

UNCLASSIFIED

AD **427701**

DEFENSE DOCUMENTATION CENTER

FOR

SCIENTIFIC AND TECHNICAL INFORMATION

CAMPBELL STATION, ALEXANDRIA, VIRGINIA



UNCLASSIFIED



NOTICE: When government or other drawings, specifications or other data are used for any purpose other than in connection with a definitely related government procurement operation, the U. S. Government thereby incurs no responsibility, nor any obligation whatsoever; and the fact that the Government may have formulated, furnished, or in any way supplied the said drawings, specifications, or other data is not to be regarded by implication or otherwise as in any manner licensing the holder or any other person or corporation, or conveying any rights or permission to manufacture, use or sell any patented invention that may in any way be related thereto.



AD No. 427701

DDC FILE COPY

427701



# TRANSACTIONS

OF THE EIGHTH  
SYMPOSIUM ON  
BALLISTIC MISSILE  
AND SPACE  
TECHNOLOGY

## VOLUME II

HELD AT THE U.S. NAVAL TRAINING CENTER, SAN DIEGO, CALIFORNIA, 16-18 OCTOBER 1963  
SPONSORED BY SPACE SYSTEMS DIVISION AND BALLISTIC SYSTEMS DIVISION  
AIR FORCE SYSTEMS COMMAND  
CONDUCTED BY AEROSPACE CORPORATION, LOS ANGELES, CALIFORNIA



**TRANSACTIONS OF THE EIGHTH SYMPOSIUM ON  
BALLISTIC MISSILE AND SPACE TECHNOLOGY**

**Held at the United States Naval Training Center  
San Diego, California  
on  
16-18 October 1963**

**VOLUME II**

**RE-ENTRY AEROPHYSICS  
PENETRATION  
GUIDANCE AND CONTROL  
RECOVERY SYSTEMS  
SPACE ELECTROMAGNETICS**

**SPACE SYSTEMS DIVISION and BALLISTIC MISSILE DIVISION  
AIR FORCE SYSTEMS COMMAND  
and  
AEROSPACE CORPORATION**



## PREFACE

The Eighth Symposium on Ballistic Missile and Space Technology was held at the U. S. Naval Training Center, San Diego, California, on 16-18 October 1963. It was sponsored by the Space Systems Division and the Ballistic Missile Division of the Air Force Systems Command, and was conducted by the Aerospace Corporation, El Segundo, California.

The eight volumes of these Transactions contain both the unclassified and classified papers presented at the Symposium, and cover the categories as listed below:

- I. Keynote Address  
Advanced Propulsion Technology  
Vehicle Design  
Reliability and Pilot Safety  
Materials for Thermal Protection
- II. Re-entry Aerophysics  
Penetration  
Guidance and Control  
Recovery Systems  
Space Electromagnetics
- III. Re-entry Aerophysics  
Re-entry Vehicle Vulnerability and  
Hardening  
Materials for Re-entry  
Re-entry Flight Test Data
- IV. Re-entry Observables  
Radar Signature Studies  
Re-entry Systems Penetration
- V. Advanced Propulsion Technology  
High-Energy Propellants  
Launching System Concepts  
Reliability and Pilot Safety
- VI. Vehicle Design  
Guidance and Control  
Space Electromagnetics
- VII. Satellite Systems  
Space Systems Survivability  
Recovery Systems



**VIII. Nuclear Explosion Environment and  
Effectiveness of Nuclear Warheads**

Volumes I and II are unclassified; Volumes III through VII are classified Secret; Volume VIII is classified Secret-Restricted Data.

Requests for any one or all of the volumes, by agencies of the Department of Defense, their contractors, and other government agencies, should be directed to the:

**Defense Documentation Center  
Cameron Station  
Alexandria, Virginia**

Department of Defense contractors must be established for DDC services, or have their need-to-know and clearance status certified by the contracting military agency or the military agency monitoring the project.

**Charles T. Morrow  
Symposium Chairman**

**Lawrence D. Ely  
Associate Symposium Chairman**



## VOLUME II

## CONTENTS

### Re-entry Aerophysics

- Finite Rate Plasma Generation in the Laminar Air Boundary  
Layer of Slender Reentry Bodies  
F. G. Blottner and M. Lenard, General Electric Company,  
Missile and Space Division, Philadelphia, Pennsylvania 3
- Effects of Nonequilibrium on the Hypersonic Laminar Boundary  
Layer  
P. DeRienzo and A. D. Wood, Avco Research and Advanced  
Development Division, Wilmington, Massachusetts, and  
F. Berner and J. D. Teare, Avco-Everett Research  
Laboratory, Everett, Massachusetts 35
- Chebyshev Method for the Calculation of Radar Cross Section  
of Plasma Wakes  
K. Fong, Lockheed Missiles and Space Company,  
Electromagnetics Research, Sunnyvale, California 65
- Analysis of Electromagnetic Wave Propagation Through Re-entry  
Induced Plasma Sheaths  
R. R. Gold, Aerospace Corporation, Laboratories Division,  
El Segundo, California 83
- Interaction of High Power Microwaves with a Reentry Vehicle  
Plasma Sheath  
M. Epstein, Aerospace Corporation, Laboratories Division,  
El Segundo, California 97

### Penetration

- A Simulation of Multiple Re-entry Vehicle Delivery  
H. C. Sebring and S. Matlin, General Electric Company,  
Missile and Space Division, Philadelphia, Pennsylvania 123

### Guidance and Control

- The Present and Future Roles of Strapped-Down Inertial  
Systems  
J. C. Powell, Minneapolis-Honeywell Regulator Company,  
Aeronautical Division, Minneapolis, Minnesota 161



Attitude Control of Satellites and Determination of Orbital  
Parameters by Use of Accelerometers  
H. Winter, Textron's Bell Aerosystems Company,  
Avionics Division, Buffalo, New York 179

Orbit Determination Error Analysis  
D. R. Speece, Aerospace Corporation, Engineering Division,  
El Segundo, California 197

### Recovery Systems

Evolution of the Hyperflo Parachute  
L. W. Sims, Cook Electric Company, Tech-Center  
Division, Morton Grove, Illinois 231

A Recovery System for a Controlled Descent Through the  
Martian Atmosphere  
R. D. Turner, Cook Electric Company, Tech-Center  
Division, Morton Grove, Illinois 263

Paraglider Booster Recovery Systems  
J. E. Crawford and J. D. McNerney, Space-General  
Corporation, El Monte, California 293

### Space Electromagnetics

Resonant-Scatter Detection of Midcourse Vehicles: Minimum  
Detectable Numbers of Resonant-Scattering Particles  
L. Glatt, Space Technology Laboratories, Inc., Physical  
Research Division, Redondo Beach, California 309

A 2.5 Watt X-Band Traveling-Wave Tube Amplifier for Satellite  
Applications  
R. E. Pospisil, Watkins-Johnson Company, Systems  
Division, Palo Alto, California 335

Manned Anti-Satellite System  
E. E. Honeywell, General Dynamics Corporation, Pomona  
Division, Pomona, California 369

Electromagnetic Radiation Hazards to Electroexplosive Devices  
Lt. Col. Reuben B. Moody, Deputy The Inspector General,  
USAF, Directorate of Aerospace Safety, Norton Air Force  
Base, California 411



FINITE RATE PLASMA GENERATION IN THE LAMINAR AIR  
BOUNDARY LAYER OF SLENDER REENTRY BODIES

F. G. Blottner  
M. Lenard

Space Sciences Laboratory  
Missile and Space Division  
General Electric Company  
Box 8555, Philadelphia 1, Pennsylvania

ABSTRACT

Numerical calculations of the chemically reacting laminar air boundary layer equations are presented at several points along cone-shaped reentry bodies at several flight conditions and different wall temperatures. These results use a seven component, ten reaction model of air ( $N$ ,  $O$ ,  $N_2$ ,  $O_2$ ,  $NO$ ,  $NO^+$ ,  $e^-$ ). Thermodynamic and transport properties are completely general and use the latest available information. Corresponding solutions of the locally similar and non-similar boundary layer equations are compared. The resulting electron densities are noted.

The work described in this paper was performed under Air Force Contract No. AF 04(694)-222.



## FINITE RATE PLASMA GENERATION IN THE LAMINAR AIR BOUNDARY LAYER OF SLENDER REENTRY BODIES

F. G. Blottner and M. Lenard

Space Sciences Laboratory  
Missile and Space Division  
General Electric Company  
Box 8555, Philadelphia 1, Pennsylvania

### INTRODUCTION

Accurate determination of electron densities in the plasma sheath surrounding reentry bodies is important for several reasons. The presence of electrons can interfere with the transmission of signals to and from the vehicle; furthermore, electrons furnish one of the observables present in the wake of reentry bodies. At high altitudes, the effect of finite reaction rates on the amount of ionization can not be neglected.

Calculations of electron densities in the plasma sheath surrounding a reentry vehicle are usually based on an accurate description of the inviscid shock layer surrounding the vehicle. Viscous effects are neglected because they are limited to a thin boundary layer near the surface of the vehicle, which, due to its small size relative to the shock layer thickness, can be neglected as a significant source of electrons. Most of the energy is imparted to the air by means of the shock and pressure forces rather than surface friction or shear forces; this corresponds to a large pressure drag and a comparatively small friction drag for the vehicle, the usual case for blunt reentry bodies. For small tipped slender shapes, the situation is different; much of the energy is imparted to the air by means of surface friction, consequently, the boundary layer will be a very significant (if not the only) source of high temperature air. Therefore, for slender reentry shapes, it is necessary to calculate air boundary layer properties accurately, based on a realistic model of high temperature air which accounts for the principal ionized species. For the flight conditions corresponding to ballistic reentry, it was found that a model including  $\text{NO}^+$  as the only ionized species is adequate. In order to account for the possibility of the absence of chemical equilibrium, chemical changes must be accounted for by incorpora-



ting the chemical kinetics into the boundary layer equations. The seven component-ten reaction model described by Bortner and Golden (1) is the simplest realistic model that can account for the production of  $\text{NO}^+$  ions; it forms the basis of this study.

### THE BOUNDARY LAYER EQUATIONS

The boundary layer equations for steady axially-symmetric flow of a multi-component reacting mixture have been stated in the literature several times (2), (3); they are repeated below for reference.

Continuity:

$$\frac{\partial \rho u r}{\partial x} + \frac{\partial \rho v r}{\partial y} = 0 \quad (1)$$

Momentum:

$$\rho u \frac{\partial u}{\partial x} + \rho v \frac{\partial u}{\partial y} + \frac{\partial p}{\partial x} = \frac{\partial}{\partial y} \mu \frac{\partial u}{\partial y} \quad (2)$$

Energy:

$$\left[ \rho u \frac{\partial T}{\partial x} + \rho v \frac{\partial T}{\partial y} \right] \sum_{i=1}^n c_i \frac{dh_i}{dT} - u \frac{dp}{dx} = \frac{\partial}{\partial y} k \frac{\partial T}{\partial y} + \mu \left( \frac{\partial u}{\partial y} \right)^2 - \rho \frac{\partial T}{\partial y} \sum_{i=1}^n q_i c_i \frac{dh_i}{dT} - \sum_{i=1}^n w_i h_i \quad (3)$$

Species Conservation:

$$\rho u \frac{\partial c_i}{\partial x} + \rho v \frac{\partial c_i}{\partial y} + \frac{\partial}{\partial y} (\rho c_i q_i) = w_i \quad (4)$$

These are the principal differential equations. Additional differential equations are needed to relate the diffusional flux velocities of the species across the boundary layer,  $q_i$ , to the concentration gradients. Two alternate formulations are given by Hirschfelder, Curtiss and Bird (4) as follows:

$$\sum_{\substack{j=1 \\ j \neq i}}^n \frac{M^2}{m_j} \frac{c_i c_j}{D_{ij}} (q_j - q_i) = \frac{\partial}{\partial y} M c_i \quad (5)$$



or, alternately;

$$c_i q_i = \sum_{j=1}^n \frac{m_i}{M^2} D_{ij} \frac{\partial}{\partial y} M c_j \quad (6)$$

where the binary diffusion coefficients  $\phi_{ij}$  in Eq. (5) are functions of temperature only, but the mixture diffusion coefficients  $D_{ij}$  in Eq. (6) depend both on temperature and local concentrations and are actually calculated by solving the system of  $n-1$  independent Eqs. (5) for the  $q_i$  - s. The formulation of the flux velocities of ionized species in a neutral mixture is somewhat different from the above and will be subsequently discussed.

In addition to the above system of differential equations, which can be thought of as representing equations for the principal variables  $v$ ,  $u$ ,  $T$  and the  $n-1$  independent  $c_i$  - s, additional equations are available that relate the thermodynamic properties, transport properties, and composition of the mixture of each other; e. g. :

Equation of State:

$$\frac{p}{R} = \frac{\rho T}{M} = \text{constant} \quad (7)$$

Mixture Molecular Weight:

$$\frac{1}{M} = \sum_{i=1}^n \frac{c_i}{m_i} \quad (8)$$

Mass Concentrations:

$$\sum_{i=1}^n c_i = 1 \quad (9)$$

Species Enthalpies:

$$h_i = h_i(T) \quad (10)$$

The dependence of species enthalpies on temperature is based on Langelo's (5) work.



## Chemical Mass Generation Rates:

$$w_i = w_i(\rho, T, c_j) \quad (11)$$

are based on an updated version of those given in (1). The chemical system described in this reference is based on seven species (N, N<sub>2</sub>, O, O<sub>2</sub>, NO, NO<sup>+</sup>, e<sup>-</sup>) and ten reactions.

Transport properties of the mixture are calculated by means of Wilke's semi-empirical formula [e.g. (6)]. The temperature dependence of the species viscosities and binary diffusion coefficients is based on unpublished work by Baulknight (7) and on results published by Yun, Weissman, and Mason (8), (9). For the details of the kinetic system, thermodynamic and transport properties, the reader is referred to (10).

The diffusion coefficients for electrons need not be calculated separately, because under all conditions of practical interest the Debye shielding length in the ionized air will be so small that the gas will be electrically neutral at every point, implying simultaneous diffusion of ions and electrons. This simultaneous diffusion of the combined ion-electron species can be calculated by a method suggested by K. T. Yen and confirmed by C. Curtiss, as follows. Let there be a separation between the ions and electrons on a microscopic scale, so that a local electric field is created in the flowing ionized gas. For the ions and electrons, Eq. (5) is then modified to include the effect of an electrostatic body force caused by this local microscopic electric field:

$$\sum_{\substack{j=1 \\ j \neq \text{NO}^+}}^n \frac{M^2}{m_j m_{\text{NO}^+}} \frac{c_{\text{NO}^+} c_j}{\delta_{\text{NO}^+ j}} (q_j - q_{\text{NO}^+}) = \frac{\partial}{\partial y} M \frac{c_{\text{NO}^+}}{m_{\text{NO}^+}} - \mathcal{E} \frac{c_{\text{NO}^+}}{m_{\text{NO}^+}} \quad (12)$$

$$\sum_{\substack{j=1 \\ j \neq e^-}}^n \frac{M^2}{m_j m_{e^-}} \frac{c_{e^-} c_j}{\delta_{e^- j}} (q_j - q_{e^-}) = \frac{\partial}{\partial y} M \frac{c_{e^-}}{m_{e^-}} + \mathcal{E} \frac{c_{e^-}}{m_{e^-}}$$

where the body force  $\mathcal{E}$  has the same magnitude but the opposite sign for the ions and electrons.



Since in a neutral plasma

$$q_{e^-} = q_{NO^+}$$

$$\frac{c_{e^-}}{m_{e^-}} = \frac{c_{NO^+}}{m_{NO^+}} \quad (13)$$

Eqs. (12) can be added to eliminate the body force term;

$$\sum_{\substack{j=1 \\ j \neq NO^+}}^n \frac{M^2}{m_j} c_{NO^+} + c_j (q_j - q_{NO^+}) \left[ \frac{1}{D_{NO^+ j}} + \frac{1}{D_{e^- j}} \right] = 2 \frac{\partial}{\partial y} M c_{NO^+} \quad (14)$$

where this equation describes the diffusion of the combined  $NO^+ - e^-$  ion-electron species in the mixture. The additional assertion can now be made that the mobility of the electrons is much larger than that of the ions or neutrals, so that

$$D_{e^- j} \gg D_{ij} \quad (15)$$

for all  $i$  and  $j$ . Terms of the order  $D_{ij}/D_{e^- j}$  can then be neglected in the equations so that the final expressions for the interdiffusion of the various neutral species and the combined ion-electron species become;

$$\sum_{\substack{j=1 \\ j \neq i, e^-}}^n \frac{M^2}{m_j} \frac{c_i c_j}{D_{ij}} (q_j - q_i) = \frac{\partial}{\partial y} M c_i \text{ for } i \neq NO^+ \quad (16)$$

$$\sum_{\substack{j=1 \\ j \neq NO^+, e^-}}^n \frac{M^2}{m_j} \frac{c_{NO^+} c_j}{D_{NO^+ j}} (q_j - q_{NO^+}) = 2 \frac{\partial}{\partial y} M c_{NO^+}$$

which is a generalization of the ambipolar diffusion in a neutral-ion-electron mixture. Eqs. (16) replace (5); correspondingly, Eq. (6) is modified by solving for the  $n - 2$  independent  $q_i$  - s from Eq. (16).



## BOUNDARY CONDITIONS

Eqs. (1) through (4), (7) through (11), and (16) represent the system of equations that have to be solved for the seven component model of air under consideration. Boundary conditions for the equations are furnished by specifying conditions at the wall and in the external (inviscid) flow.

At the wall ( $y = 0$ );

$$\begin{aligned} u(x, 0) &= v(x, 0) = 0 \\ T(x, 0) &= T_w(x) \end{aligned} \tag{17}$$

In addition to Eq. (17), boundary conditions on concentrations  $c_i$  must also be stated at the wall. At a wall where there is no mass injection two types of boundary conditions are usually considered. On a wall that is not catalytic, there are no surface reactions, therefore there can be no flux of species to and from the wall. Thus,

$$q_i(x, 0) = 0 \tag{18}$$

for all  $i$ , which implies that

$$\frac{\partial c_i}{\partial y} \bigg|_{y=0} = 0 \tag{19}$$

at  $y = 0$ . A catalytic wall can cause sudden changes in composition due to surface reactions; usually the assumption is made that the mixture is at chemical equilibrium at the local (wall) temperature. This can be denoted by:

$$c_i(x, 0) = c_{i \text{ eq}}(T_w, p, c^j) \tag{20}$$

where the above expression indicates that in order to determine the chemical equilibrium concentrations of the various species, it is necessary to know in addition to temperature and pressure the mass fractions of the chemical elements (denoted by superscript  $j$ ) that comprise the reacting mixture. Due to the interdiffusion of the various species, the mass fraction of the various elements in the boundary layers cannot be known a priori, not even if instantaneous local chemical equilibrium can be assumed everywhere. In order to show this, one may relate the mass fraction of the  $j$ -th element in the mixture to the mass fractions of the  $n$  species by



$$c^j = \sum_{i=1}^n \frac{m_i^j}{m_i} \alpha_i^j c_i \quad (21)$$

where  $\alpha_i^j$  is the number of atoms of element  $j$  in the  $i$ -th species, and the  $m_i$  are the respective molecular (or atomic) weights. Since elements are conserved in a chemical reaction, i. e. :

$$\sum_{i=1}^n \frac{m_i^j}{m_i} \alpha_i^j w_i = 0 \quad (22)$$

an equation for the conservation of elements can be written by utilizing Eqs. (20), (21), in conjunction with Eq. (4);

$$\rho u \frac{\partial c^j}{\partial x} + \rho v \frac{\partial c^j}{\partial y} + \frac{\partial}{\partial y} \left( \rho \sum_{i=1}^n \frac{m_i^j}{m_i} \alpha_i^j c_i q_i \right) = 0 \quad (23)$$

Eq. (23) above indicates that in general, the mass fraction of the elements in the boundary layer will change irrespective of what the reaction rates are. In particular then, the mass fraction of the elements will not be known at the wall, which implies that additional information is necessary to define the boundary conditions for species concentrations at a catalytic wall. If the  $n$  species are made up of  $m$  elements, then there will be only  $n - m$  independent boundary conditions of the type shown in Eq. (20) (one less if  $e^-$  is one of the species and a neutral plasma is specified). To obtain the  $m - 1$  additional boundary conditions necessary at the wall, the conservation of elements in the surface reactions that are implied by the catalytic wall must be stated;

$$\sum_{i=1}^n \frac{m_i^j}{m_i} \alpha_i^j q_i(x, 0) c_i(x, 0) = 0 \quad (24)$$

where there are  $m - 1$  independent boundary conditions of the type shown in Eq. (24), corresponding to the  $m - 1$  independent elemental concentrations, for the present seven component mixture under consideration, over-all mass conservation (Eq. 9) and charge conservation leave essentially five independent species conservation Eq. (4) to be considered. The mixture contains two elements, O and N, the concentration of one of which is independent. Thus, there will be four boundary conditions of the type shown in Eq. (20) available; the four species must include at least, but not more than, one charged species and at least one species which is comprised of pure N and pure O each. In addition, one boundary condition of the type



shown in Eq. (24) is available to relate the slopes of the concentration profiles at the wall.

Far from the wall the boundary layer solution must merge into the external inviscid flow, which is specified. This implies that as

$$\begin{aligned} y &\rightarrow \infty \\ u &\rightarrow u_e \\ T &\rightarrow T_e \\ c_i &\rightarrow c_{ie} \end{aligned} \tag{25}$$

Corresponding to the seven boundary conditions shown in (25) there will be seven unknown boundary values of the appropriate variables at the wall, which can be determined only by solving the boundary layer equations. In a numerical computation scheme, an iteration on these seven unknowns has to be performed in order to integrate the equations and obtain the proper solutions that satisfy boundary conditions (25). Two of the seven unknown boundary values are;

$$\begin{aligned} \left. \frac{\partial u}{\partial y} \right|_{y=0} \\ \left. \frac{\partial T}{\partial y} \right|_{y=0} \end{aligned} \tag{26}$$

For a wall that is not catalytic, the additional unknown boundary values are;

$$c_i(x, 0) \tag{27}$$

which corresponds to Eq. (18) and (19). For a catalytic wall, the unknown quantities are;

$$\begin{aligned} c^N_i(x, 0) \text{ or } c^O_i(x, 0) \\ q_i(x, 0) \end{aligned} \tag{28}$$

where the four species  $i$  in Eq. (28) correspond to the four species for which boundary conditions are specified by Eq. (20).



## TRANSFORMATION OF THE EQUATIONS

Solution of the foregoing system of partial differential equations can be greatly simplified if the independent variables are transformed in accordance with the combined Mangler and Howarth-Dorodnitsin transformations (cf. (2), (3), (11));

$$\xi = \int_0^x \rho_w \mu_w u_e r^2 dx \quad (29)$$

$$\eta = \frac{u_e r}{\sqrt{2\xi}} \int_0^y \rho dy$$

If, in addition, the velocity is expressed as

$$u = u_e \frac{\partial f}{\partial \eta} \quad (30)$$

the continuity Eq. (1) can be used to express  $v$  in terms of  $f$ , and the remaining differential equations can be written in terms of the new variables  $\eta$  and  $\xi$ . The present development is essentially the same as that of (2), except for the more exact formulation of the species flux velocities [Eqs. (16), (5) and (6)]. The final form of the transformed boundary layer equations becomes:

Momentum:

$$\frac{\partial}{\partial \eta} \left( \ell \frac{\partial^2 f}{\partial \eta^2} \right) + f \frac{\partial^2 f}{\partial \eta^2} + \beta \left[ \frac{\rho_e}{\rho} - \left( \frac{\partial f}{\partial \eta} \right)^2 \right] = 2\xi \left[ \frac{\partial f}{\partial \eta} \frac{\partial^2 f}{\partial \eta \partial \xi} - \frac{\partial f}{\partial \xi} \frac{\partial^2 f}{\partial \eta^2} \right] \quad (31)$$

Energy:

$$\begin{aligned} & \frac{\partial}{\partial \eta} \left[ \frac{\ell}{Pr} \sum_{i=1}^7 c_i \frac{dh_i}{dT} \left( \frac{T_e}{h_e} \right) \frac{\partial}{\partial \eta} \left( \frac{T}{T_e} \right) \right] + f \sum_{i=1}^7 c_i \frac{\partial}{\partial \eta} \left( \frac{h_i}{h_e} \right) - \\ & - \sum_{i=1}^7 \frac{\beta w_i}{\rho \frac{du_e}{dx}} \frac{h_i}{h_e} + \frac{u_e^2}{h_e} \left\{ \ell \left( \frac{\partial^2 f}{\partial \eta^2} \right)^2 + \right. \end{aligned}$$



$$+ \beta \frac{\partial f}{\partial \eta} \left[ \frac{T}{T_e} \left( \frac{\sum_{i=1}^7 c_i \frac{dh_i}{dT}}{\sum_{i=1}^7 c_{ie} \frac{dh_{ie}}{dT}} + \frac{2h_e}{\beta u_e^2} \sum_{i=1}^7 \frac{\partial c_{ie}}{\partial \ln \xi} \frac{h_{ie}}{h_e} \right) - \frac{\rho_e}{\rho} \right] \left. \vphantom{\frac{\partial f}{\partial \eta}} \right\} - \quad (32)$$

$$- \frac{\rho^2}{h_e \rho_w \mu_w} \frac{\partial T}{\partial \eta} \sum_{i=1}^7 \frac{q_i}{\eta_y} c_i \frac{dh_i}{dT} = 2\xi \sum_{i=1}^7 c_i \left\{ \frac{\partial f}{\partial \eta} \frac{\partial}{\partial \xi} \left( \frac{h_i}{h_e} \right) - \frac{\partial f}{\partial \xi} \frac{\partial}{\partial \eta} \left( \frac{h_i}{h_e} \right) \right\}$$

where

$$Pr \equiv \frac{\mu}{k} \sum_{i=1}^7 c_i \frac{dh_i}{dT} \quad (33)$$

$$t \equiv \frac{\rho \mu}{\rho_w \mu_w}$$

and where the flux velocities are determined from a transformation of Eqs. (16);

$$\sum_{\substack{i=1 \\ j \neq i, e^-}}^n \frac{M^2}{m_j} \frac{c_i c_j}{\phi_{ij}} \frac{q_i - q_j}{\eta_y} = \frac{\partial}{\partial \eta} M c_i \text{ for } i \neq NO^+ \quad (34)$$

$$\sum_{\substack{j=1 \\ j \neq NO^+, e^-}}^n \frac{M^2}{m_j} \frac{c_{NO^+} c_j}{\phi_{NO^+ j}} \frac{q_j - q_{NO^+}}{\eta_y} = 2 \frac{\partial}{\partial \eta} M c_{NO^+}$$

Noting first that in accordance with transformations (29);

$$\frac{1}{\eta_y} \frac{\partial}{\partial \eta} \eta_y f(\eta) = \frac{1}{\rho} \frac{\partial}{\partial \eta} \rho f(\eta)$$

for any function  $f(\eta)$  of  $\eta$ , the species conservation equations can finally be written;



$$\begin{aligned}
& f \frac{\partial c_i}{\partial \eta} - \frac{1}{\rho_w \mu_w} \frac{\partial}{\partial \eta} \left( \rho^2 c_i \frac{q_i}{\eta_y} \right) + \frac{\beta}{\frac{du_e}{dx}} \left[ \frac{w_i}{\rho} - f \eta \frac{c_i}{c_{ie}} \left( \frac{w_i}{\rho} \right)_e \right] \\
& = 2\xi \left[ \frac{\partial f}{\partial \eta} \frac{\partial c_i}{\partial \xi} - \frac{\partial f}{\partial \xi} \frac{\partial c_i}{\partial \eta} - \frac{\partial f}{\partial \eta} \frac{c_i}{c_{ie}} \frac{\partial c_{ie}}{\partial \xi} \right]
\end{aligned} \tag{35}$$

The pressure gradient parameter,  $\beta$ , that appears in the above equation is defined by:

$$\beta = \frac{2\xi}{u_e} \frac{du_e}{d\xi} = \frac{2\xi}{\rho_w \mu_w u_e} \frac{du_e}{dx} \tag{36}$$

Auxiliary Eqs. (7) through (11) are not affected by the transformations; the boundary conditions are likewise unaffected, except for the velocities at the wall, instead of Eq. (17) the boundary conditions are:

$$f(\xi, 0) = \left. \frac{\partial f}{\partial \eta} \right|_{\eta=0} = 0 \tag{37}$$

$$T(\xi, 0) = T_w(\xi)$$

The boundary conditions at the wall for the concentrations are unchanged from those specified by either Eq. (19) (non-catalytic surface) or Eqs. (20) and (24) (catalytic surface). Far from the wall, boundary conditions shown in Eq. (25) are equivalent to

$$\begin{aligned}
\eta & \rightarrow \infty \\
\frac{\partial f}{\partial \eta} & \rightarrow 1 \\
T(\xi, \eta) & \rightarrow T_e(\xi) \\
c_i(\xi, \eta) & \rightarrow c_{ie}(\xi)
\end{aligned} \tag{38}$$

The terms that appear on the right hand sides of the foregoing system of seven simultaneous differential equations are the so called "non-similar" terms. At the stagnation point these non-similar terms vanish and the partial differential equations simplify to ordinary ones. Fay and Ridell (2) have pointed out that these terms can sometimes be neglected as an approximation based on physical considerations other than the rigorously justifiable



stagnation point case. This approximation results in the so called "locally similar" solutions, which can always be justified a posteriori, provided the profile shapes change slowly. The role that local similarity and non-similarity play in numerical solutions of the foregoing problem will be discussed in subsequent sections.

## NUMERICAL RESULTS

Numerical calculations to solve the foregoing system of boundary layer equations have been performed by two entirely distinct methods. One method adapts the complete system of partial differential equations to an implicit finite difference calculation scheme. An initial boundary layer profile is specified and the successive development of the boundary layer flow is determined by proceeding in finite steps along the wall, calculating consecutive profiles at each point. This procedure is similar to the one described in Blottner's earlier work (12) for a binary mixture. The other method makes the assumption of local similarity and computes the results at a certain specified point along the body. To solve the resulting system of seven ordinary differential equations, seven unknown boundary conditions at the wall are assumed and a numerical integration performed to the edge of the boundary layer. There the results are compared with the seven required boundary conditions, and then an iteration procedure performed on the seven assumed wall boundary conditions, repeating the integration a sufficient number of times to reach agreement with the edge boundary conditions to the required accuracy. (This type of procedure is described in detail in Appendix B of (13).)

The results of these calculations, which are all based on a fully catalytic wall assumption, are shown in Figs. 1 through 13 and Table 1. The principal example that was considered was that of a  $10^\circ$  half angle pointed cone at 22,000 fps speed and 150,000 ft. altitude. Ramifications of possible boundary layer-inviscid flow interactions were not considered; the inviscid flow was assumed to be at chemical equilibrium. (Due to the low temperatures the thermo-chemical model assumed for the inviscid flow is immaterial.) The surface speed, pressure and temperature are 21,590 fps, .02756 atm., and  $1061^\circ\text{K}$  respectively. The wall temperature was assumed to be  $1000^\circ\text{K}$ .

The variation of temperature in the boundary layer is shown in Fig. 1. These profiles are substantially the same from the tip to 10 ft. downstream from the tip for both the locally similar and non-similar solutions. This is in contrast with the profile based on chemical equilibrium where the peak temperatures have been greatly reduced. Fig. 2 which shows the variation of maximum temperature along the body indicates that for the conditions that were considered it would take a distance much longer than 10 ft. to approach chemical equilibrium in the boundary layer. The approximation of



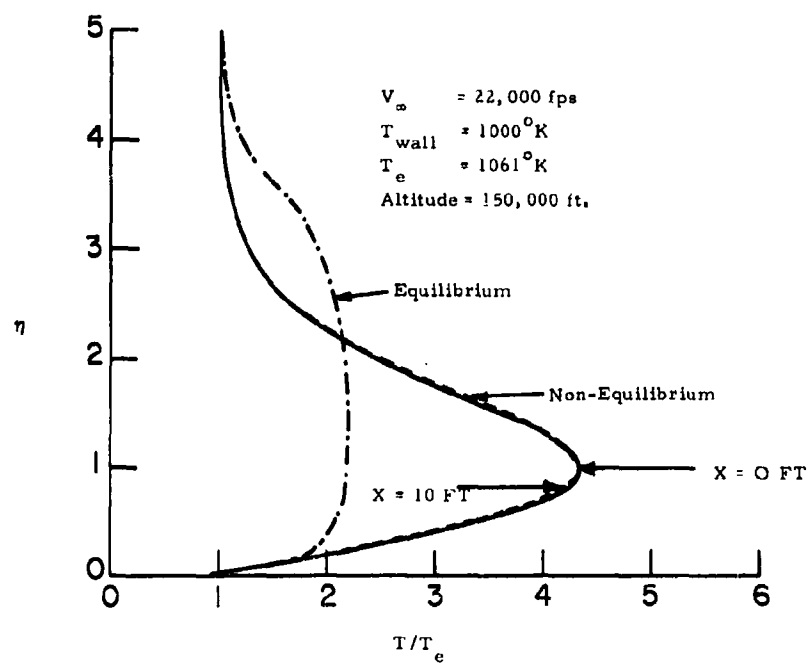


Fig. 1. Temperature Profiles for the Non-Equilibrium Boundary Layer Flow for a  $10^{\circ}$  Cone



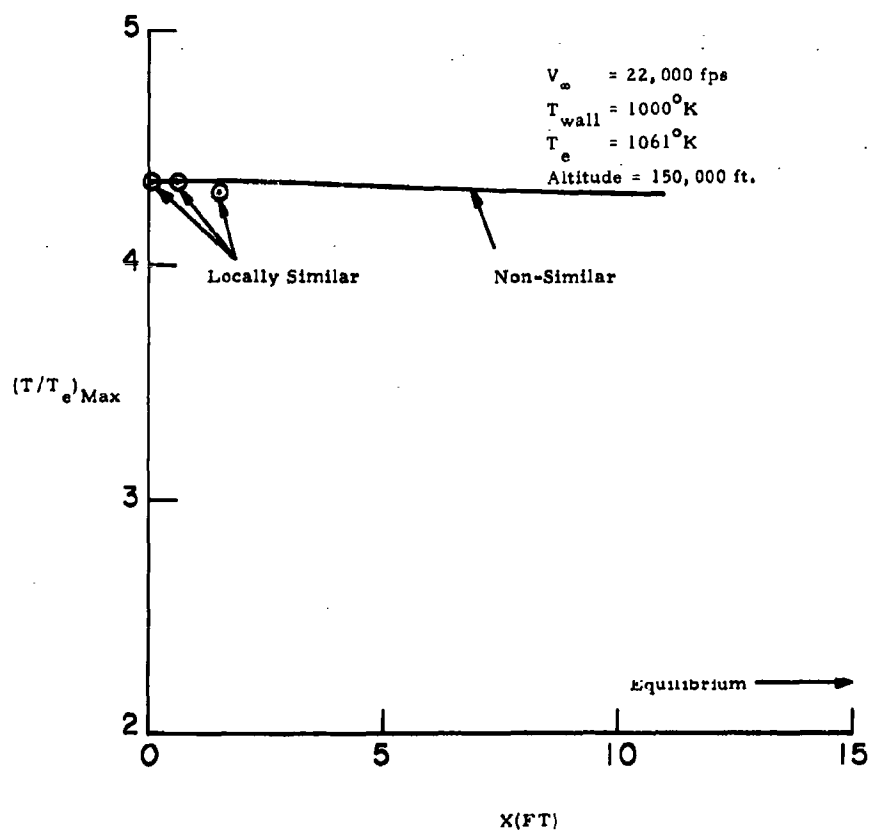


Fig. 2. Maximum Temperature in the Non-Equilibrium Boundary Layer on a  $10^{\circ}$  Cone



local similarity appears to result in an increased rate of adjustment towards equilibrium along the body. These conclusions are even more apparent from the composition profiles for the species O, N, NO and the electron densities, (Fig. 3 - 6) and the corresponding variation of the respective maxima along the body (Fig. 7 - 10). Atomic oxygen is the principal new species in the boundary layer due to the relative ease of oxygen dissociation. Atomic nitrogen is a comparatively minor species but it is important because of its role in the generation of nitric oxide ions and electrons. Both the profiles (Fig. 4) and the variation of maximum along the body (Fig. 8) clearly indicate that there is an "overshoot" in the concentration of this important species as compared to the equilibrium value. The reason for this is the higher temperature in the non-equilibrium boundary layer as compared to the equilibrium case, and the comparative ease with which the so called "shuffle" reactions are able to produce nitrogen atoms, provided sufficient amounts of atomic oxygen and nitric oxide are present. Such "overshoot" phenomena have been observed in the relaxation processes behind hypersonic shocks in inviscid flow; they arise from the non-linearities of coupled fluid mechanic and complicated chemical kinetic systems. No such "overshoot" phenomena are exhibited by the nitric oxide concentrations (Fig. 5 and 9) and the electron densities (Fig. 6 and 10) in the boundary layer. However, the possibility of an electron density "overshoot" occurring for longer bodies or at different flight conditions cannot be ruled out, particularly because such excess electron densities have been predicted behind shocks in inviscid flow (14). This is significant because it indicates that under some circumstances the electron densities in the non-equilibrium boundary layer can exceed the corresponding equilibrium values.

Fig. 6 also shows an electron density profile calculated by an approximation which appears reasonable; the two-body nitric oxide ionizing reaction was assumed to be at instantaneous equilibrium in conjunction with the locally similar chemical non-equilibrium solution. The resulting prediction was three orders of magnitude too large, indicating that care must be exercised when attempting to simplify complicated chemistry in this problem. (This is in contrast with heat transfer rate calculations where the simplifications of separate decoupled oxygen and nitrogen dissociation reactions, or even the binary atom-molecule fluid assumption have resulted in adequate predictions).

Further insight into the complexities of the reacting air boundary layer can be gained from Figs. 11 through 13. Due to the complex transport properties which govern the interdiffusion of the various reacting species, there will be a variation in the total oxygen content of the boundary layer, as shown in Fig. 11. Fig. 12 shows that the production of electrons occurs mainly in the narrow high temperature region near the wall from where diffusion towards the wall and free stream take place. The sensitivity of the resulting electron densities to the ionizing rate constants and the ambipolar



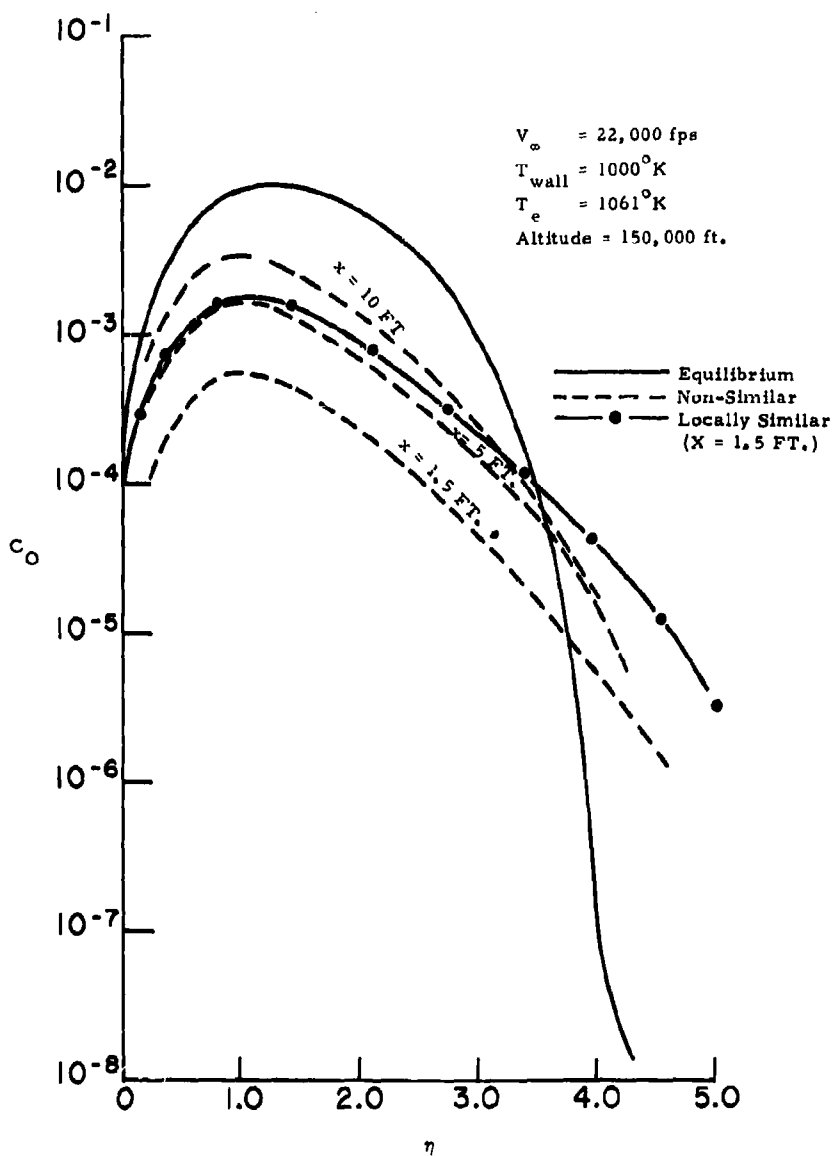


Fig. 3. Mass Fraction of Atomic Oxygen Across the Boundary Layer on a  $10^{\circ}$  Cone



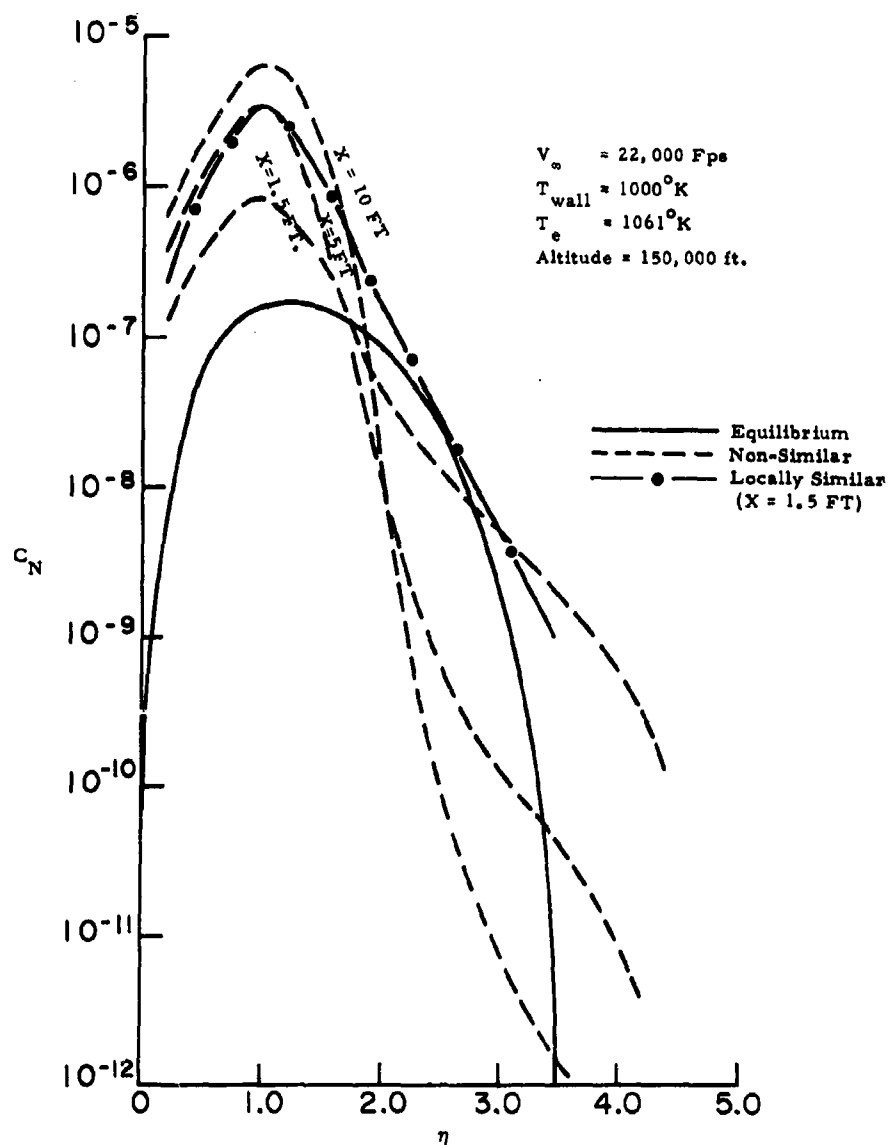


Fig. 4. Mass Fraction of Atomic Nitrogen Across the Boundary Layer on a  $10^{\circ}$  Cone



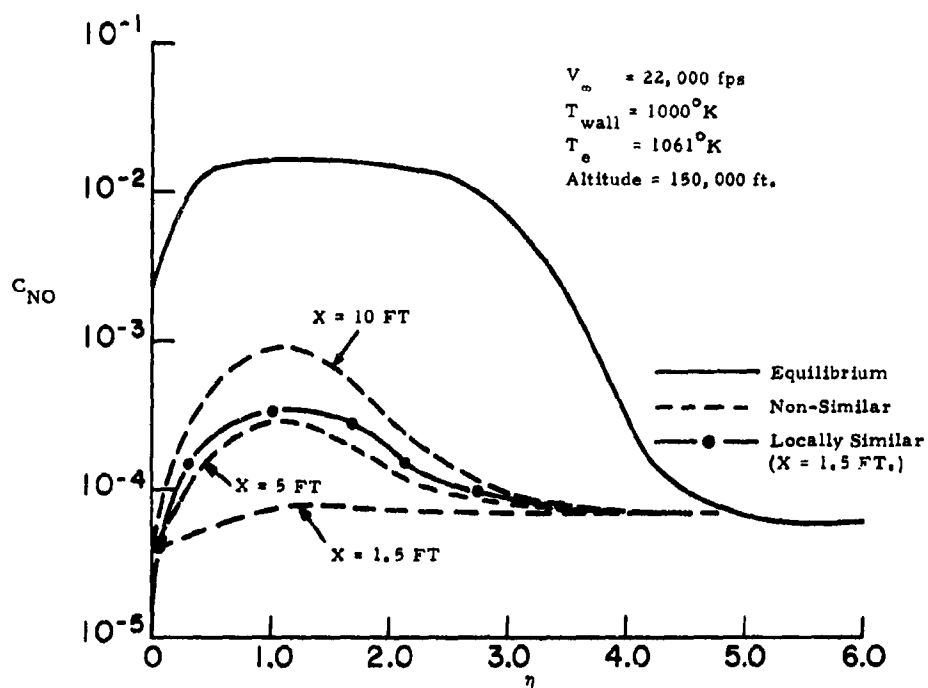


Fig. 5. Mass Fraction of Nitric Oxide Across the Boundary Layer on a  $10^{\circ}$  Cone



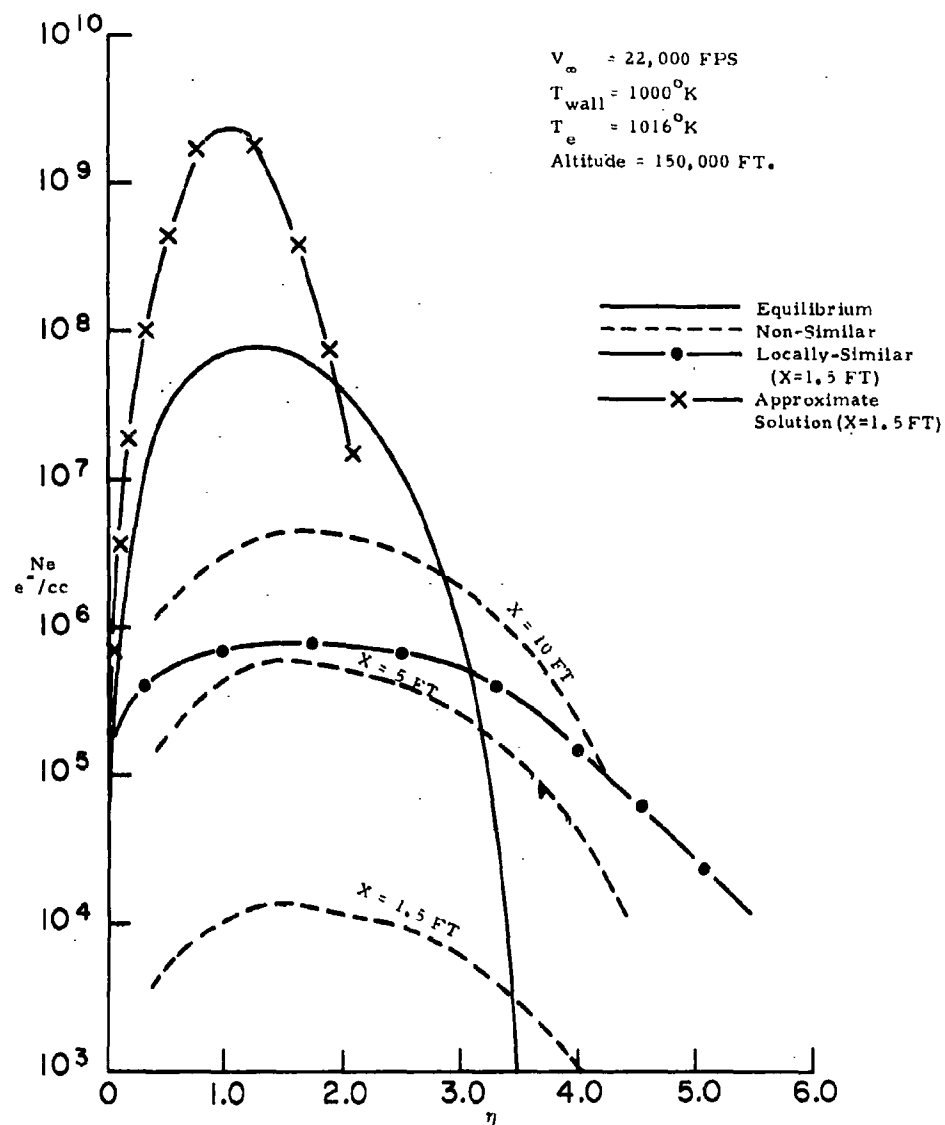


Fig. 6. Electron Density in the Boundary Layer on a  $10^{\circ}$  Cone



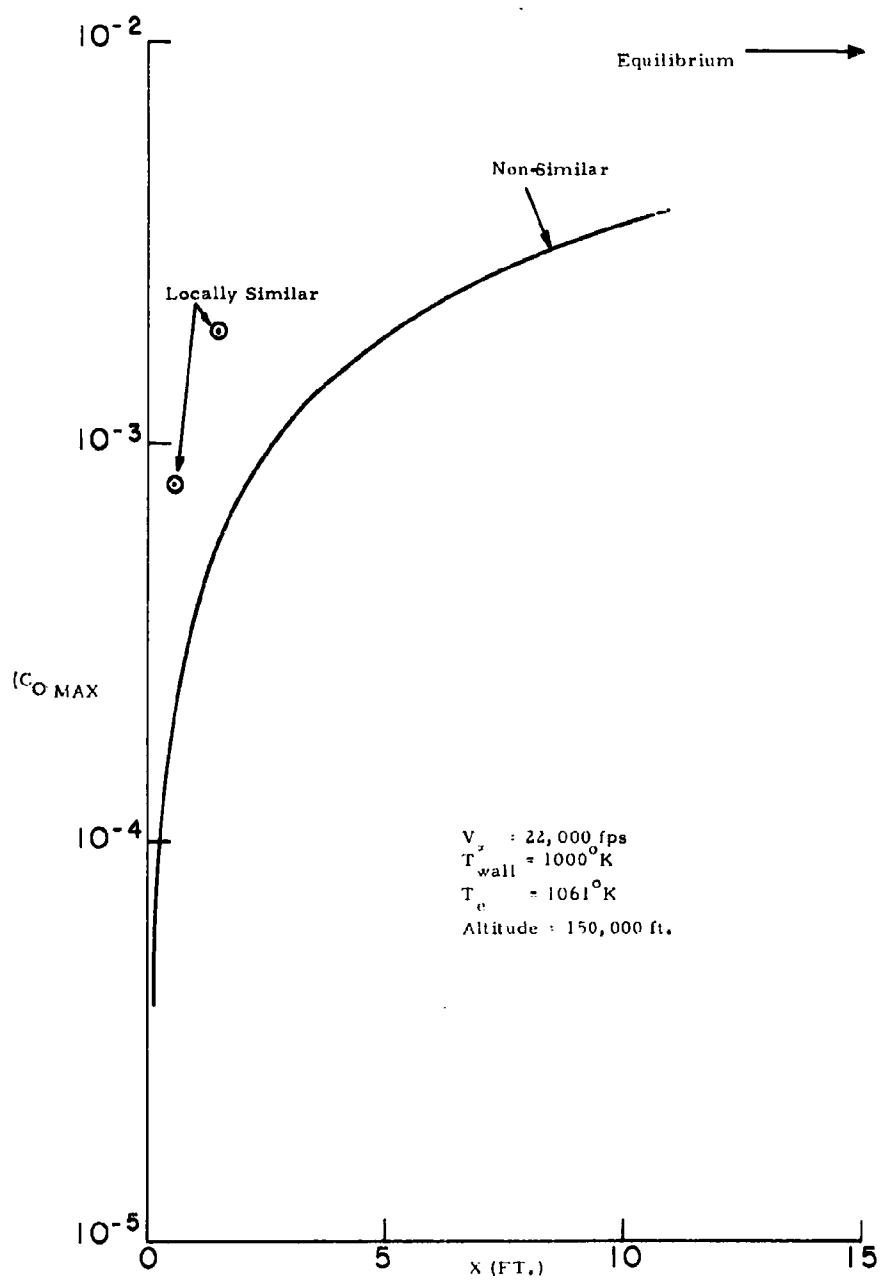


Fig. 7. Maximum Mass Fraction of Atomic Oxygen in the Boundary Layer on a  $10^\circ$  Cone



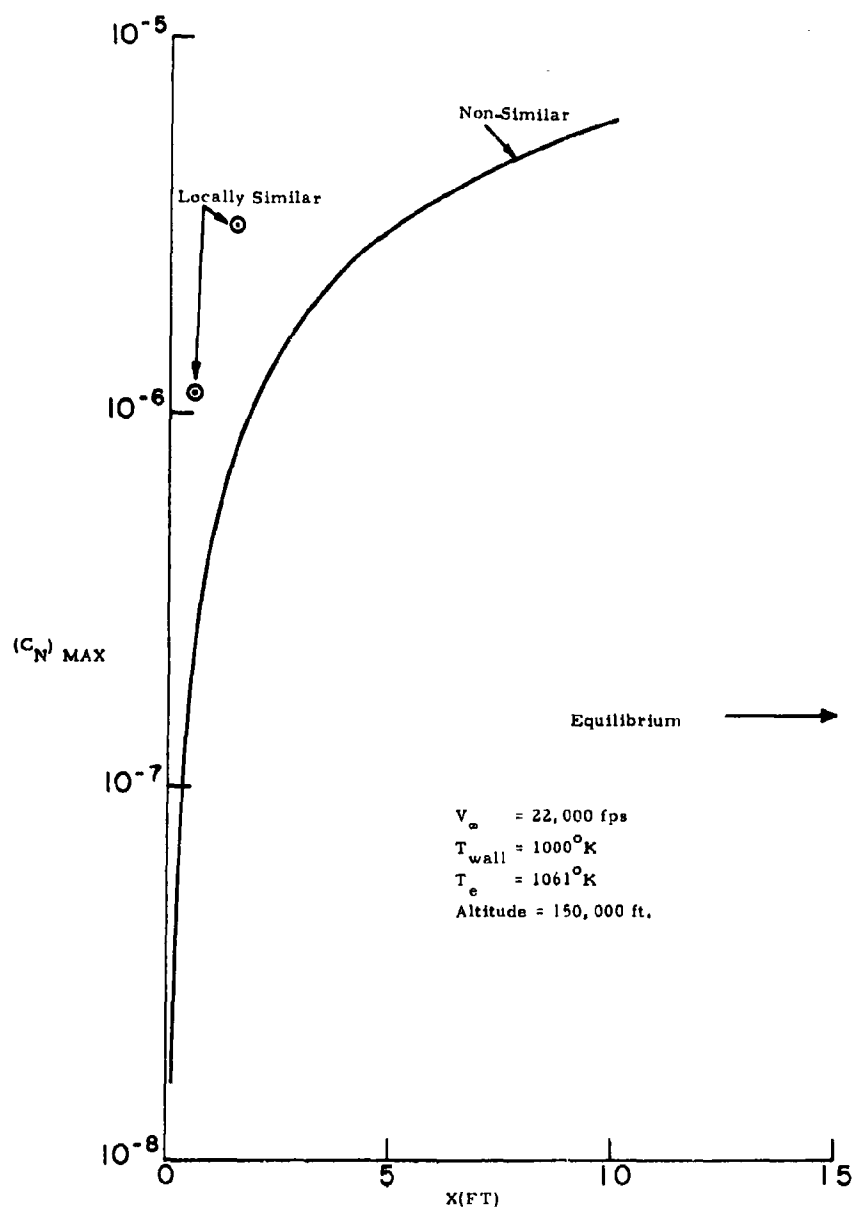


Fig. 8. Maximum Mass Fraction of Atomic Nitrogen in the Boundary Layer on a  $10^\circ$  Cone



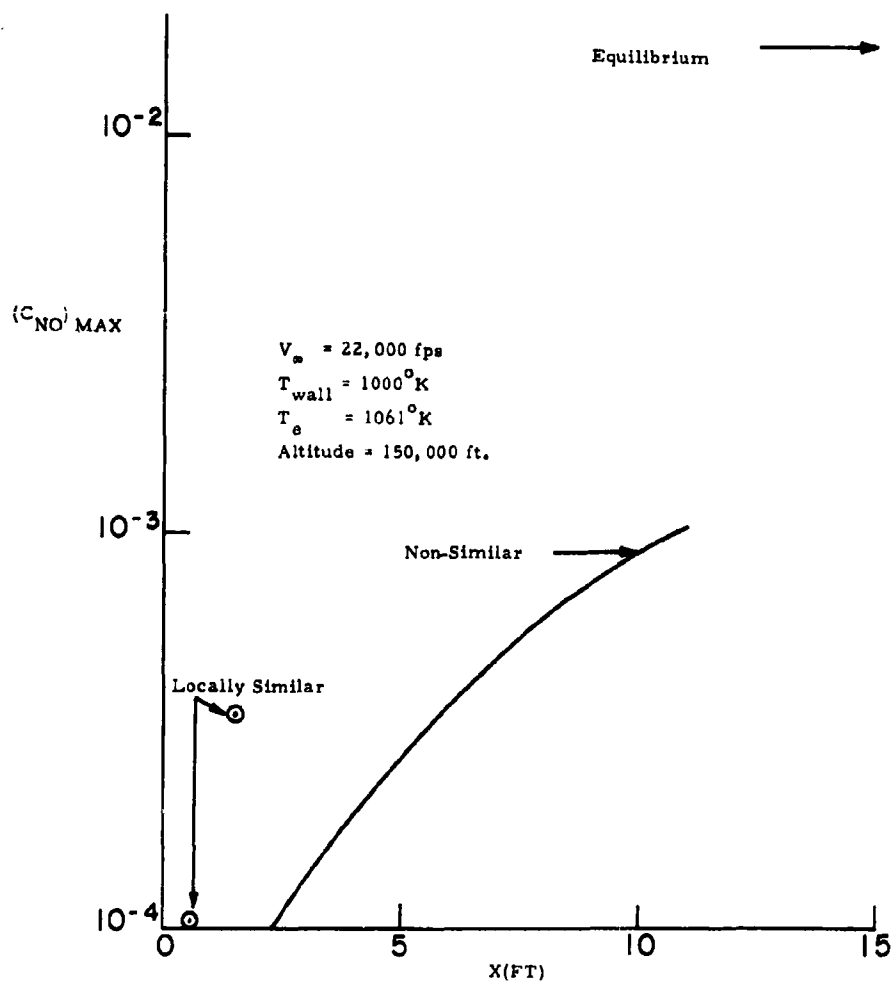


Fig. 9. Maximum Mass Fraction of NO in the Boundary Layer on a  $10^{\circ}$  Cone



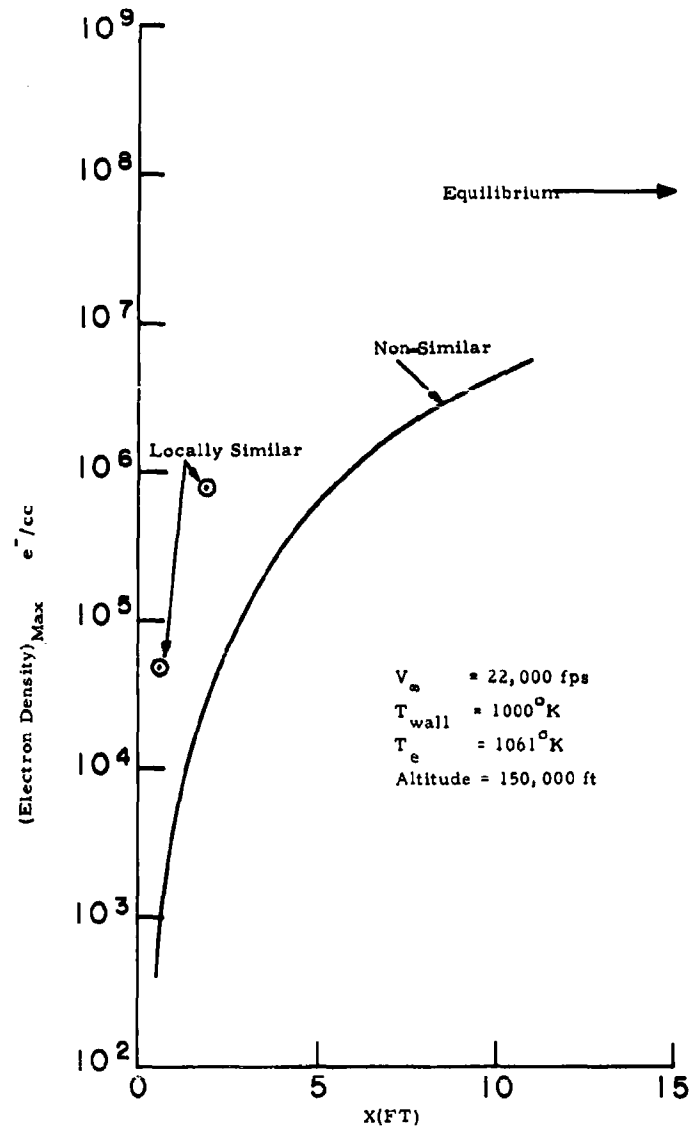


Fig. 10. Maximum Electron Density in the Boundary Layer on a  $10^\circ$  Cone



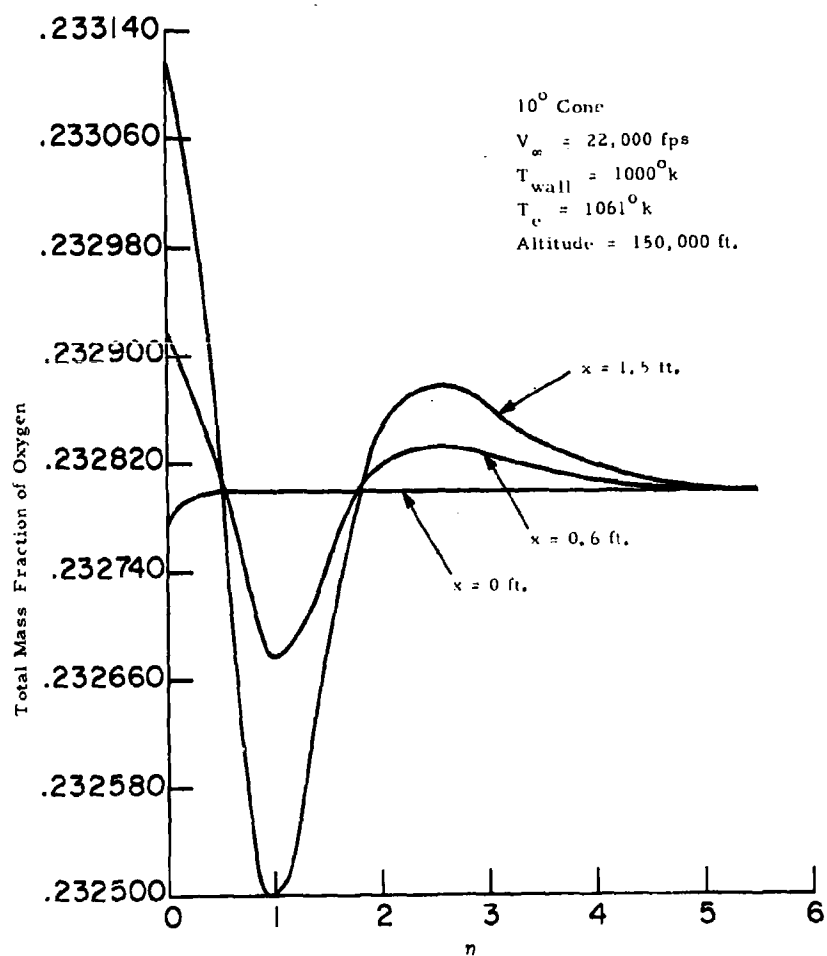


Fig. 11. Total Oxygen Content in Boundary Layer



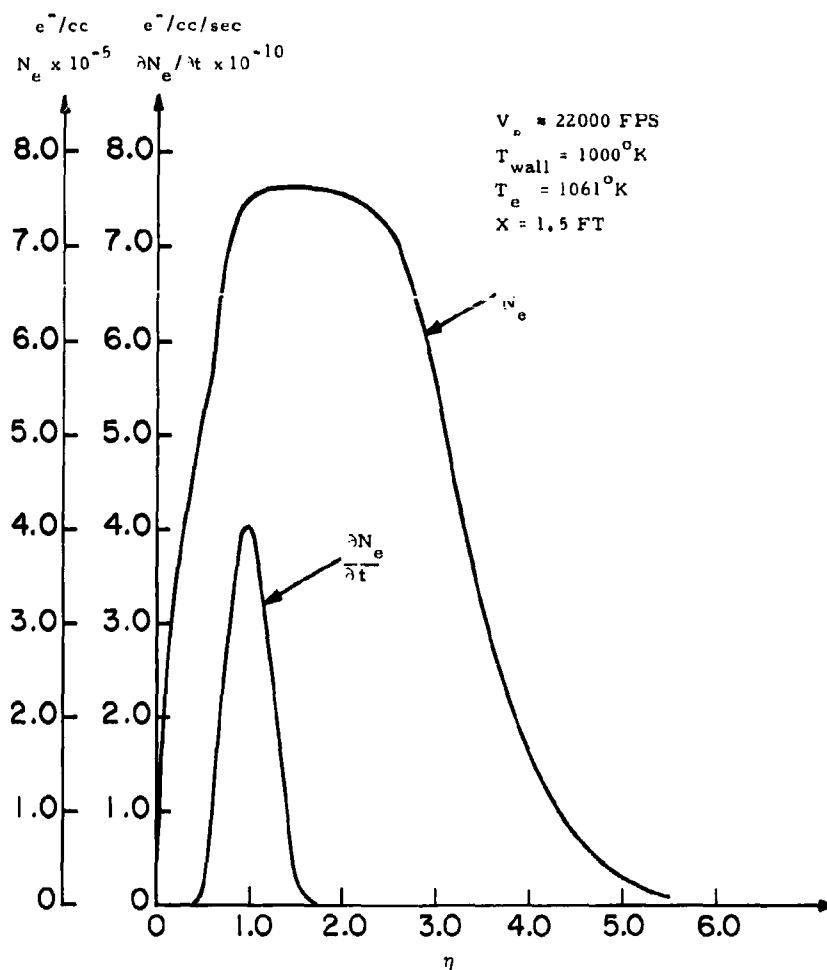


Fig. 12. Electron Densities and Generation Rates in the Locally Similar Boundary Layer on a  $10^\circ$  Cone



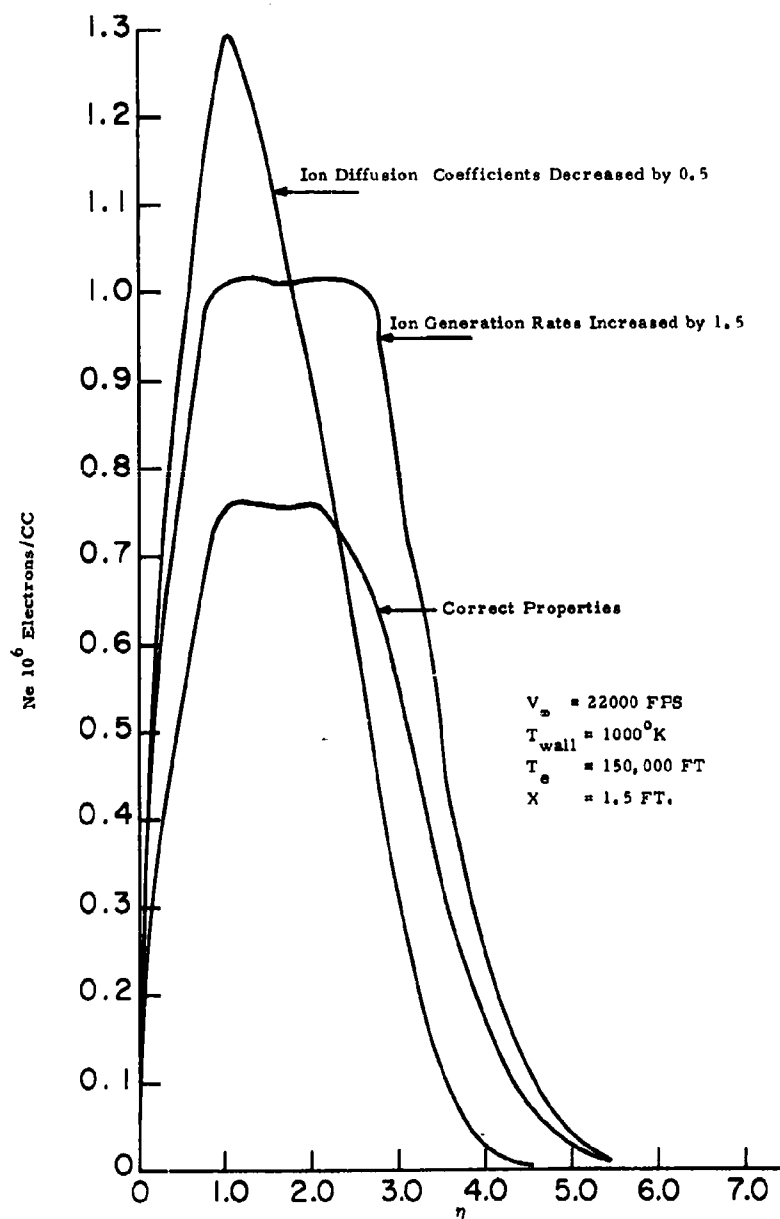


Fig. 13. Effect of Ion Generation Rates and Ion Diffusivities on Electron Densities in Locally Similar Boundary Layer on a  $10^\circ$  Cone



diffusivities is shown in Fig. 13 where the effect of a 1.5-fold increase in ionizing rates and a halving of the ambipolar diffusivities is demonstrated.

Table 1 shows the effects of changing wall temperature and altitude for this problem as it effects the principal properties of the resulting non-equilibrium air boundary layer. As expected, a rise in wall temperature increases the chemical activity in the boundary layer whereas an increased altitude diminishes it greatly.

Table 1. Locally Similar Boundary Layer Properties on  $10^\circ$  Cone at 22,000 fps 1.5 ft. Downstream from Tip

<u>Altitude, ft.</u>	<u>150,000</u>	<u>150,000</u>	<u>200,000</u>
$P_e$ , atmospheres	0.02756	0.02756	0.0046706
$U_e$ , fps	21,590	21,590	21,590
$T_e$ , $^\circ K$	1061	1061	1041.5
$T_w$ , $^\circ K$	1000	1050	1000
$T_{max}$ , $^\circ K$	4580	4604	4570
$C_{O_{max}}$	$1.88 \times 10^{-3}$	$2.00 \times 10^{-3}$	$0.328 \times 10^{-3}$
$C_{N_{max}}$	$3.18 \times 10^{-6}$	$3.52 \times 10^{-6}$	$0.378 \times 10^{-6}$
$C_{NO_{max}}$	$2.52 \times 10^{-4}$	$4.02 \times 10^{-4}$	$0.549 \times 10^{-4}$
$N_{e_{max}}$ , $e^- / cc$	$7.74 \times 10^5$	$9.30 \times 10^5$	$0.510 \times 10^3$

#### ACKNOWLEDGMENTS

The numerical results presented here are partly due to the efforts of Dr. James Jewell who designed one of the computer programs, and particularly to the efforts of Mr. Edward Meyer of CEIR Inc. who did the programming and performed the actual computations, thereby furnishing the key ingredient to obtain these numerically difficult results.



## NOMENCLATURE

$c_i$	Mass fraction of i-th species
$c^i$	Mass fraction of i-th element
$D_{ij}$	Mixture diffusion coefficient
$D_{ij}$	Binary diffusion coefficient
$\mathcal{E}$	Body force due to microscopic electric field
$f$	Non-dimensional stream function (Equation 30)
$h$	Mixture enthalpy
$h_i$	Species enthalpy
$k$	Mixture (frozen) heat conductivity
$\ell$	Density-viscosity product (Equation 33)
$m_i$	Molecular weight of i-th species
$M$	Molecular weight mixture
$n$	Numer of species in mixture
$p$	Pressure
$Pr$	(Frozen) Prandtl number (Equation 33)
$q_i$	Diffusional flux velocity of i-th species
$r$	Radial coordinate of axi-symmetric surface
$R$	Universal gas constant
$T$	Absolute temperature
$u, v$	Parallel and normal velocities in boundary layer



$w_i$	Chemical mass generate rate of i-th species
$x, y$	Parallel and normal coordinates in boundary layer
$\alpha_i^j$	Number of atoms of element j in species i
$\beta$	Pressure gradient parameter (Equation 36)
$\xi, \eta$	Transformed parallel and normal coordinates in boundary layer (Equation 29)
$\mu$	Viscosity
$\rho$	Density

## SUBSCRIPTS

e	At the outer edge of the boundary layer
eq	In chemical equilibrium
i, j, O	Refers to species (i-th, j-th, O, etc.)
W	Wall

## SUPERScript

i, j, O	Refers to element (i-th, j-th, O, etc.)
---------	---

## REFERENCES

1. Bortner, M.H., and Golden, J., "A Critique On Reaction Rate Constants Involved in the Chemical System of High Temperature Air", G.E. - MSD TIS R61SD023, February 1961.
2. Fay, J. A., and Riddell, F. R., "Theory of Stagnation Point Heat Transfer In Dissociated Air", Journal of the Aero/Space Sciences, vol. 25, February 1958.
3. Scala, S. M., and Baulknight, C. W., "Transport and Thermodynamic Properties In a Hypersonic Laminar Boundary Layer, Part 2 Applications", ARS Journal, vol. 30, no. 4, 1960, 329.
4. Hirschfelder, J. O., Curtiss, C. F., and Bird, R. B., Molecular Theory of Gases and Liquids, John Wiley and Sons, 1954.



5. Langelo, V. A., "Reacting Gas Flow Field", G.E. MSD Space Sciences Laboratory TIS Report (to be published).
6. Bird, R. B., Stewart, W. E., Lightfoot, E. N., Transport Phenomena, John Wiley & Sons, 1960.
7. Baulknight, C. W., "Binary Diffusion Coefficients for  $\text{NO}^+$ ", G.E. MSD internal communication, unpublished.
8. Yun, K. S., and Mason, E. A., "Collision Integrals for the Transport Properties of Dissociating Air at High Temperatures", Physics of Fluids, vol. 5, no. 4, 1962, p. 380.
9. Yun, K. S. Weissman, S., and Mason, E. A., "High Temperature Transport Properties of Dissociating Nitrogen and Dissociating Oxygen", Physics of Fluids vol. 5, no. 6, 1962, p. 672.
10. Lenard, M., "Chemically Reacting Boundary Layers", G.E. MSD Space Sciences Laboratory TIS Report (to be published).
11. Lees, Lester, "Laminar Heat Transfer Over Blunt-Nosed Bodies at Hypersonic Flight Speeds", Jet Propulsion, vol. 26, 1956.
12. Blottner, F. G., "Chemical Non-Equilibrium Boundary Layer", AIAA Paper #63-443, August 1963; also "Non-Equilibrium Laminar Boundary Layer Flow of a Binary Gas", G.E. TIS Report R63SD17, June 1963.
13. Reshotko, E., and Beckwith, I. E., "Compressible Laminar Boundary Layer Over a Yawed Infinite Cylinder with Heat Transfer and Arbitrary Prandtl Number", NACA Rept. 1379, 1958.
14. Langelo, V. A., "Chemical Non-Equilibrium Gas Shock Flow", G.E. TIS R63SD66, 1963.



## EFFECTS OF NONEQUILIBRIUM ON THE HYPERSONIC LAMINAR BOUNDARY LAYER

P. DeRienzo\*  
F. Berner\*\*  
A. D. Wood\*  
J. D. Teare\*\*

\*Avco Research and Advanced Development Division  
Wilmington, Massachusetts

\*\*Avco-Everett Research Laboratory  
Everett, Massachusetts

### ABSTRACT

An approximate method is formulated for the determination of the non-equilibrium compressible laminar boundary layer, both with and without the restriction of vibrational equilibrium. The method involves solution of the rate equations for species production and vibrational relaxation along "effective" particle paths determined from mass continuity considerations. The velocity and enthalpy time histories along these paths are then specified from the appropriate locally similar equilibrium or frozen boundary layer analyses.

Application of the method is illustrated for the hypersonic laminar boundary layer along a sharp cone. Results are compared with more exact numerical solutions of the nonequilibrium boundary layer equations, and the limitations of the approximate method are indicated.

Finally, the technique is used to determine the effects of altitude and cone angle on the nonequilibrium boundary layer, together with the influence of variations in the chemical rate constants and vibrational relaxation models. The application of binary scaling is discussed.

The work described in this paper was performed under Air Force Contracts No. AF 64(694)-239 and AF 64(694)-33.



## EFFECTS OF NONEQUILIBRIUM ON THE HYPERSONIC LAMINAR BOUNDARY LAYER

P. DeRienzo\*, F. Berner\*\*, A. D. Wood\* and J. D. Teare\*\*

\*Avco Research and Advanced Development Division  
Wilmington, Massachusetts

\*\*Avco-Everett Research Laboratory  
Everett, Massachusetts

### INTRODUCTION

Most of the gross characteristics of the flow field surrounding an object entering a planetary atmosphere at hypersonic speed can be calculated with sufficient precision to determine heat transfer rates and aerodynamic performance. However, for many applications it is necessary to make detailed estimates of the electrical and radiative properties of the gas in the flow field, and in such cases it is frequently inadequate to assume thermodynamic equilibrium. Considerable success has been obtained with the well-known stream-tube method (1), (2) for inclusion of finite rate air chemistry into the aerothermodynamics of the inviscid flow field surrounding blunt bodies. The results obtained by this method have compared satisfactorily with more accurate calculations of the subsonic nose region (3) and of the expanding flow region downstream of the sonic line (4).

Because of the presence of the strong normal shock associated with a blunted nose, most of the electrons and radiating species are produced in the hot gas of the inviscid region, so that the effect of chemical reactions proceeding in the cooler boundary layer can frequently be neglected. For a slender re-entry vehicle, however, precisely the opposite conditions apply. The gas in the inviscid flow field is relatively cool, whereas the static enthalpy in the boundary layer can increase to a significant fraction of the stagnation enthalpy, leading to temperatures high enough to permit dissociation and ionization processes to occur.

The calculation of a hypersonic laminar boundary layer on a slender body is a straightforward procedure when either equilibrium or frozen flow is assumed (5), (6). Inclusion of finite reaction rates and relaxation times, however, greatly complicates the calculation by introducing a time dependence into the equation of state of the gas. While methods for the numerical solution of the exact nonequilibrium boundary layer equations have recently been published for both binary mixtures (7) and multi-component air (8), they are generally quite complex.

The present paper discusses a simplified procedure which was originally developed before these more exact techniques were available. It represents



an adaptation of the streamtube method mentioned above, and is based on two fundamental assumptions:

1. The enthalpy and velocity profiles calculated for a locally similar boundary layer under frozen or equilibrium conditions are assumed to provide an adequate description of the profiles in a chemically reacting boundary layer.
2. The effect of diffusion on the species concentrations is assumed to be negligible compared with the chemical rates of production.

On the basis of these assumptions it is possible by simple geometrical means to locate the position of an "effective" path for a fluid element as it travels through the inviscid region and becomes immersed in the boundary layer. For such a path,  $\eta$  may then be determined as a function of  $\xi$ , where  $\eta$  and  $\xi$  are the boundary layer similarity variables (see Fig. 1). Knowing velocity and enthalpy as functions of  $\eta$  from the self-similar boundary layer calculation, it is thus possible to specify their time histories along the particle path. These histories can then be used as input for the streamtube calculation procedure with finite rate chemistry. For inviscid applications (1), such streamtube calculations are usually made for a prescribed pressure variation, with constraints provided by a momentum equation and the conservation of energy. In the present viscous case the pressure variation is determined from the calculation of the inviscid flow field but the momentum equation is discarded with the static enthalpy history providing the only other constraint necessary. The velocity serves to provide correlation between time and distance along the particle path.

Using the streamtube program of Ref. 1, the above approach was adopted independently at AERL and RAD. The respective authors were able to compare results with each other, but until recently there was no other standard of comparison which would serve to test the validity of the assumptions made. The considerable risk in ignoring diffusion processes was recognized, but it was hoped that the method would provide some upper limit estimate on the nitric oxide and electron concentrations which could be produced by the chemical reactions.

The present paper provides comparisons between the streamtube method and the multiple-strip integral method of Ref. 8. These comparisons show the limitations of the streamtube method, and stress the importance of inclusion of diffusion processes in any quantitative studies. The paper also points out the areas in which the streamtube method could be useful, and stresses the uncertainties inherent in any slender body boundary layer calculation due to the uncertainties in the appropriate chemical model and in the rate constants which should be used in this temperature regime.

#### DESCRIPTION OF METHOD

The basic assumptions stated in the previous section permit the decoupling of the chemistry from the boundary layer calculation. The validity of the assumption that the effect of diffusion is negligible can only be assessed by comparison with results obtained from more accurate procedures.



$$\text{MASS FLOW} = \int_0^y 2\pi r \rho u dy = 2\pi \sqrt{2\xi} \int_0^\eta (u/u_e) d\eta$$

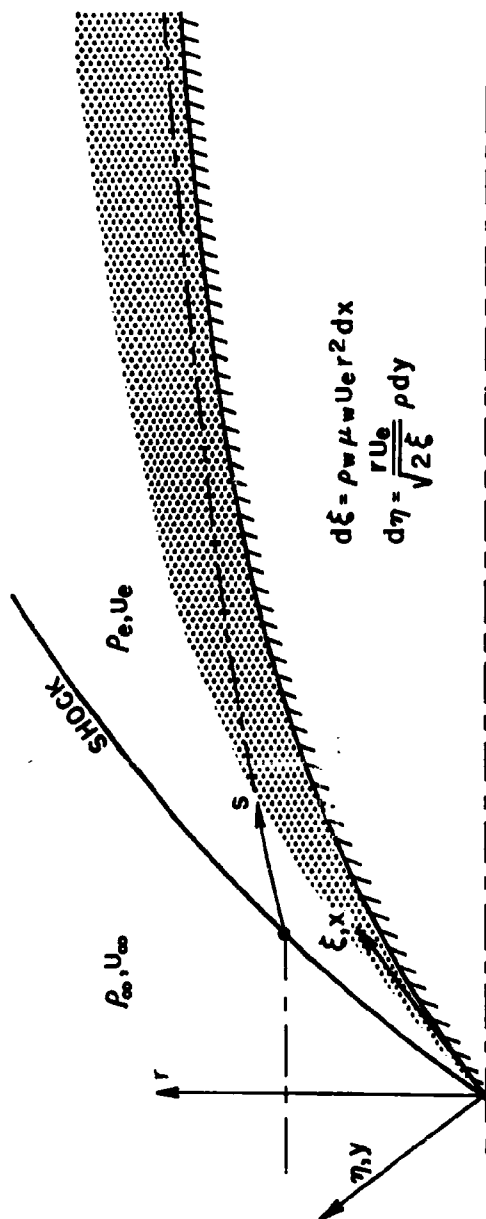


Fig. 1. Schematic of slender body flow field, showing an "effective" particle path entering the boundary layer. The coordinate systems and boundary layer transformations are also shown. The suffix  $e$  denotes conditions in the inviscid flow external to the boundary layer, and the suffix  $w$  denotes conditions at the wall.



However, it is certainly reasonable to assume that the velocity and enthalpy distributions (in terms of the usual boundary layer variable  $\eta$ ) are relatively insensitive to the chemical state of the gas in the boundary layer. This is borne out by reference to Fig. 2, which shows velocity and enthalpy profiles for an  $8^\circ$  semi-vertex angle cone under the two extremes of equilibrium and frozen air. Also shown are the corresponding profiles for a thermally perfect (frozen chemistry) calorically imperfect gas, with vibrational degrees of freedom in equilibrium with the translational temperature. The frozen ( $\gamma = 1.4$ ) profiles are certainly appropriate for the boundary layer very close to the apex of the cone, while the equilibrium profiles would obtain under conditions where the flow times were large compared with the characteristic chemical relaxation times. For intermediate nonequilibrium situations the appropriate profiles should lie between these extremes.

In practice, then, the velocity and enthalpy distributions may be calculated for any of the situations shown in Fig. 2, the choice depending on which is expected to be closest to the true state of the gas. Some of the results presented below made use of the intermediate profile (frozen chemistry, vibrational equilibrium), while calculations which included relaxation of the vibrational degrees of freedom in the gas made use of the frozen ( $\gamma = 1.4$ ) profiles.

The boundary layer calculation from which these profiles are determined is based on the corresponding external pressure, and makes use of the usual assumption of local similarity (5). This is followed by a determination of the enthalpy and velocity time histories along an "effective" particle path satisfying mass continuity, with diffusion neglected. These flow variables, together with the known starting temperature and pressure for each path, are then used as input to the streamtube calculation applied along the path. Integrating over this path with a Runge-Kutta technique, the species concentrations and electron density, together with the vibrational energies and the temperature of the mixture, are calculated. The remaining properties are found by application of the appropriate equations of state. The nonequilibrium density so determined is used to transform the boundary layer variable  $\eta$  back to the physical normal coordinate.

The chemical and ionization reactions used are those thought to be most significant in air, as summarized in Ref. 1, and included here in Table 1. The actual calculations have been carried out using both the rate constants of Ref. 1 and the more recent results of Ref. 9.

The vibrational relaxation of both the oxygen and nitrogen molecules is also considered. It is coupled to the dissociation process by a CVD representation, as described in Ref. 10 (i. e., the effect of vibrational relaxation on the dissociation rates has been considered, but the simultaneous influence of the dissociation rate on the vibrational relaxation has been excluded, since it is negligible over most of the temperature range encountered in the present paper).

The fundamentals of both the chemical and vibrational relaxation models are discussed more fully in Refs. 11 and 12.



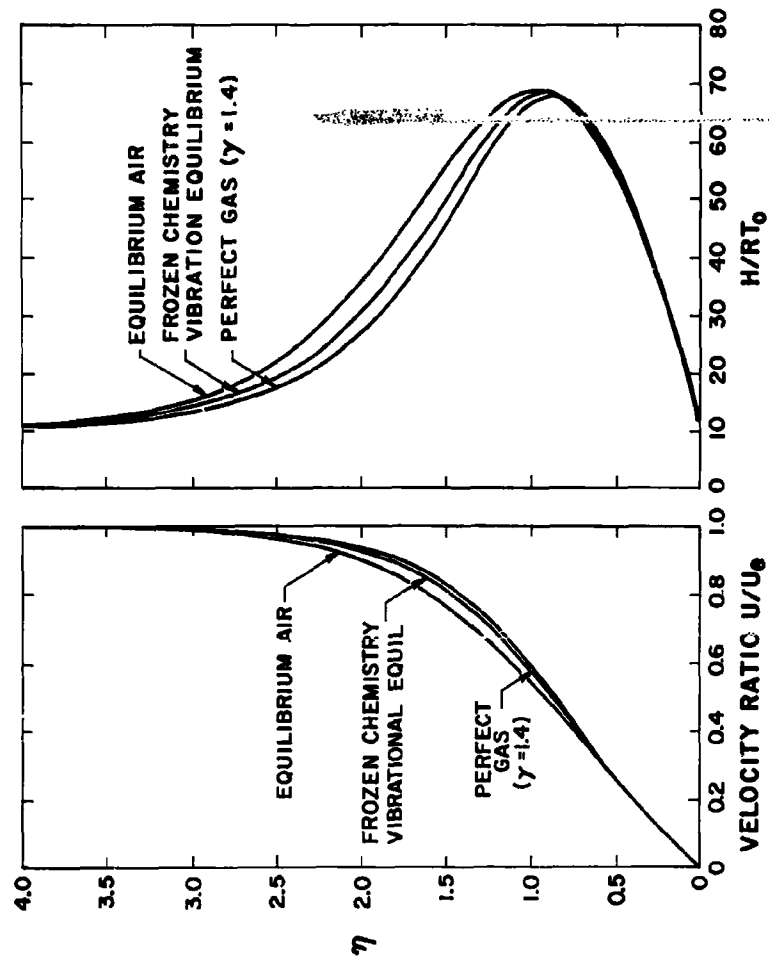


Fig. 2. Velocity and enthalpy profiles for locally similar lamina flow over a compressible boundary layer for  $8^\circ$  semi-vertex angle cone,  $u_\infty = 22,000$  fps, altitude = 150,000 ft.



Table 1. Rate Constants for Chemical Processes

(T in °K, concentrations in particles/cm<sup>3</sup>, time in seconds)

Reaction	Reference 1 - AMP 77		Reference 9 - RR 115	
	Catalyst M	Rate Constant	Catalyst M	Rate Constant
$\text{O}_2 + \text{M} + 5.1 \text{ ev } \frac{k_D}{k_R} \text{ O} + \text{M}$  E = 59373 °K	$\text{O}_2$	$k_D = \frac{0.2}{T^2} \exp(-E/T)$	$\text{O}_2$	$k_R = 2.2 \times 10^{-28} T^{-3/2}$
	O	$k_D = \frac{0.53}{T^2} \exp(-E/T)$	O	$k_R = 6.2 \times 10^{-28} T^{-3/2}$
	N, N <sub>2</sub> , NC	$k_D = \frac{6.0 \times 10^{-6}}{T} \exp(-E/T)$	N <sub>2</sub>	$k_R = 1.7 \times 10^{-32} T^{-1/2}$
			N, NO	$k_R = 8.3 \times 10^{-33} T^{-1/2}$
$\text{N}_2 + \text{M} + 9.8 \text{ ev } \frac{k_D}{k_R} \text{ N} + \text{M}$	N	$k_R = 4.1 \times 10^{-27} T^{-3/2}$	N	$k_R = 6.5 \times 10^{-27} T^{-3/2}$
	N <sub>2</sub>	$k_R = 4.2 \times 10^{-28} T^{-3/2}$	N <sub>2</sub>	$k_R = 7.6 \times 10^{-32} T^{-1/2}$
	O <sub>2</sub> , O, NO	$k_R = 1.4 \times 10^{-28} T^{-3/2}$	O <sub>2</sub> , O, NO	$k_R = 3.0 \times 10^{-32} T^{-1/2}$
$\text{NO} + \text{M} + 6.5 \text{ ev } \frac{k_D}{k_R} \text{ N} + \text{O} + \text{M}$	C, O <sub>2</sub> , N N <sub>2</sub> , NO	$k_R = 2.4 \times 10^{-27} T^{-3/2}$	NO	$k_R = 5.5 \times 10^{-27} T^{-3/2}$
			O <sub>2</sub> , O, N <sub>2</sub> , N	$k_R = 2.8 \times 10^{-28} T^{-3/2}$
$\text{NO} + \text{O} + 1.4 \text{ ev } \frac{k_1}{k_2} \text{ N} + \text{O}_2$	$k_2 = 1.7 \times 10^{-12} T^{1/2} \exp(-3120/T)$		$k_2 = 2.2 \times 10^{-11} T \exp(-3560/T)$	
$\text{N}_2 + \text{O} + 3.3 \text{ ev } \frac{k_1}{k_2} \text{ N} + \text{NO}$	$k_2 = 2.2 \times 10^{-11}$		$k_2 = 2.7 \times 10^{-11}$	
$\text{N}_2 + \text{O}_2 + 1.9 \text{ ev } \frac{k_1}{k_2} \text{ NO} + \text{NO}$	$k_2 = 0.4 T^{-5/2} \exp(-43,000/T)$		$k_2 = 0.4 T^{-5/2} \exp(-43,000/T)$	
$\text{N} + \text{O} + 2.8 \text{ ev } \frac{k_1}{k_2} \text{ NO}^+ + \text{e}^-$	$k_2 = 3 \times 10^{-3} T^{-3/2}$		$k_2 = 3 \times 10^{-3} T^{-3/2}$	



The rate equations for species production have the form

$$\frac{DX_i}{Dt} = \Gamma_i (\rho, T, X_1, \dots, X_n, e_{v_1}, \dots, e_{v_m}) \quad i = 1, 2, \dots, n \quad (1)$$

where  $X_i$  denotes the concentration of species  $i$  (in moles per mole of undissociated mixture) for each of the  $n$  species of the mixture, while  $e_{v_j}$  ( $j = 1, \dots, m$ ) is the vibrational energy (per unit mass) for each of the  $m$  vibrationally relaxing species. Density and translational temperature are indicated by the symbols  $\rho$  and  $T$ , respectively. For these calculations  $n = 7$  ( $O_2, N_2, O, N, NO, NO^+$  and electrons) and  $m = 2$  ( $O_2$  and  $N_2$ ). The notation  $D/Dt$  represents the Stokes (substantial) derivative. The quantities  $\Gamma_i$  are known functions of the variables indicated in Eq. (1), and are based on the known species partition functions and experimentally determined reaction rate expressions and relaxation times. The presence of the vibrational energy terms in Eq. (1) represents the coupling of the vibrational relaxation with the dissociation.

The corresponding rate equations for vibrational relaxation are

$$\frac{De_{v_j}}{Dt} = \frac{e_{v_j}(T) - e_{v_j}}{\tau_j} \quad j = 1, 2, \dots, m \quad (2)$$

with  $e_{v_j}(T)$  being the vibrational energy which would exist if the vibrational degrees of freedom were in equilibrium with the translational temperature. The quantity  $\tau_j$  is the experimentally determined vibrational relaxation time and is, in general, a function of pressure and translational temperature. The  $e_{v_j}$  are defined in terms of the corresponding vibrational temperatures  $T_{v_j}$  from the usual simple harmonic oscillator model

$$e_{v_j} = \frac{R_j \theta_j}{\theta_j / T_{v_j} - 1} \quad (3)$$

where  $R_j$  is the universal gas constant divided by the molecular weight of species  $j$ , and  $\theta_j$  is the characteristic temperature of molecular vibration of species  $j$ .

In this formulation, where the integration of the rate equations take place along predetermined paths and makes use of predetermined pressure, velocity and enthalpy distributions, the equation for conservation of mass is replaced by

$$dt = ds/u \quad (4)$$

where  $s$  is the streamline coordinate and  $u$  is the total velocity. The momentum conservation equation in the streamwise direction is replaced by the specified velocity  $u_{BL}$  obtained from the appropriate locally similar boundary layer calculation

$$u(\xi, \eta) = u_{BL}(\xi, \eta) \quad (5)$$



Conservation of momentum normal to the streamline is expressed in the usual boundary layer form

$$\frac{\partial p}{\partial y} = 0 \quad (6)$$

where  $p$  denotes pressure, as determined from the appropriate inviscid flow field calculation. Finally, the equation of energy conservation is replaced with the specified enthalpy per unit mass  $h_{BL}$ , also obtained from the locally similar boundary layer calculation,

$$h(\xi, \eta) = h_{BL}(\xi, \eta). \quad (7)$$

The system of equations is completed by introduction of the thermal and caloric equations of state. The thermal equation of state is given as

$$p = \rho Z R T \quad (8)$$

where

$$Z = \sum_{i=1}^n X_i \quad (9)$$

and  $R$  is the universal gas constant divided by the molecular weight of the undissociated mixture.

The caloric equation of state is written as

$$h = Z R T + e(T, X_1, \dots, X_n, e_{v_1}, \dots, e_{v_m}) \quad (10)$$

where  $e$  is the internal energy of the mixture (per unit mass) and is a known function of the indicated variables.

The system of Eqs. (1-10), together with the specified pressure external to the boundary layer, forms a complete system sufficient to determine the state of the gas as a function of position in the flow field. (S)

## RESULTS

### a. Comparison with Multiple-Strip Integral Method

In order to assess the validity of the streamtube approximation, results are compared with those of the more exact multiple-strip integral technique of Ref. 8. In this technique, the basic nonequilibrium boundary layer equations are reduced to a set of first order ordinary differential equations, using Dorodnitsyn's "method of integral relations." The original application of this technique to the solution of boundary layer equations is presented in Ref. 13.



The reduction to a system of ordinary differential equations is accomplished by dividing the boundary layer into a number of separate strips. The basic equations are then integrated with respect to the local body normal from the body surface to the edge of each strip by introducing polynomial expressions for velocity, stagnation enthalpy, and species concentrations in the integrals. The coefficients of these polynomials are chosen to satisfy conditions at the strip boundaries. Five strips have been used in the calculations presented here.

With the exception of electron diffusion, which is assumed to be described by a binary diffusion coefficient for electron-ion pairs through air molecules, a complete multi-component formalism is assumed for the mixture transport properties, each species having its own diffusion coefficients. As a consequence, the Prandtl number, species Lewis numbers, etc., are nowhere explicitly introduced, but adjust to their proper local values. A summary of the appropriate species transport properties used in the analysis is included in Ref. 14.

The thermodynamic properties of the species and the mixture are calculated by the usual procedures of statistical mechanics, assuming the internal degrees of freedom of the molecules are in equilibrium with the translational mode. The reactions considered are the same as those of Table 1 with the rate constants being those of Ref. 9. The equilibrium constants, in tabular form as functions of temperature, closely follow the simplified expressions of Ref. 11.

The comparison of the two methods is given in Figs. 3-5, where profiles of temperature and species concentrations 15 ft back on an  $8^\circ$  half-angle cone are presented. In order to facilitate the comparison, the species concentrations are given as mass fractions (the variable which is used in the strip technique formulation). For the strip technique, the boundary layer is considered chemically and vibrationally frozen for the first six inches, the initial profile for the nonequilibrium calculation being taken from the appropriate locally similar laminar boundary layer solution. A fully catalytic wall, with a wall temperature of 1000°K, is assumed.

Results of the streamtube analysis, also assuming vibrational equilibrium, are presented for two sets of rate constants, namely those of Refs. 1 and 9. It is seen that, while the effect of the different rates on the temperature and the nitric oxide and atomic oxygen concentrations is negligible, the atomic nitrogen concentrations do exhibit significant differences, with a consequent even greater difference in the electron concentration.

In addition to the general strip method calculation, where diffusion effects are included and the velocity and enthalpy profiles are calculated locally as a coupled part of the nonequilibrium analysis (designated "free"  $h$ ,  $u$ ), two models of a more restricted nature are included. In one the velocity and enthalpy profiles are constrained to be identical to the locally similar profiles used in the streamtube analysis (designated "fixed"  $h$ ,  $u$ ). In the other, the strip method has been further restricted to eliminate the effects of diffusion. The restrictions and the results of this case are the closest to those of the streamtube analysis. Complete agreement with the streamtube results is



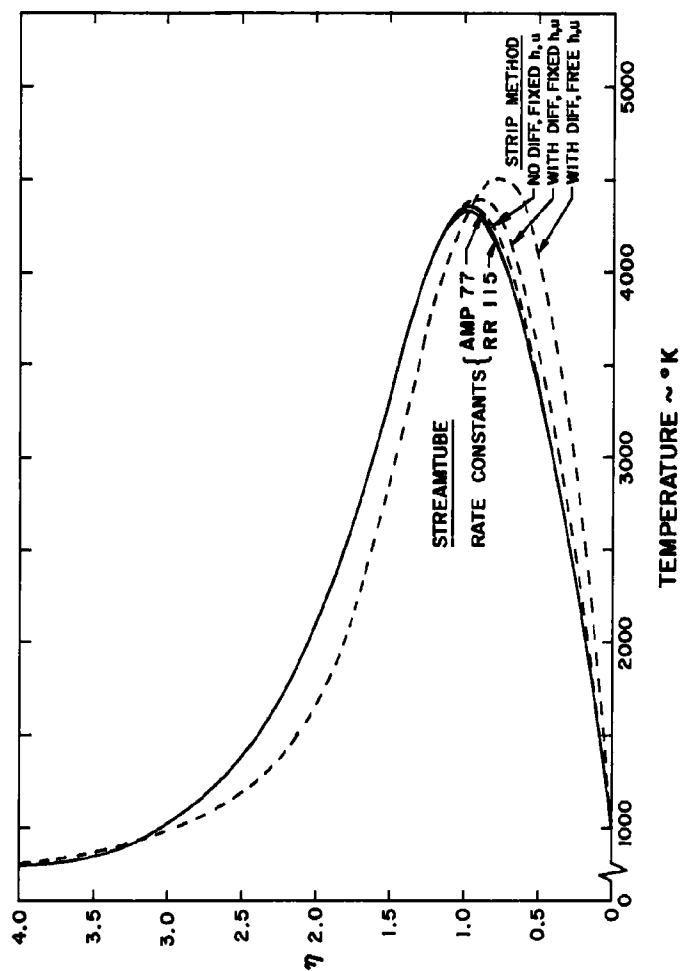


Fig. 3. Nonequilibrium temperature profiles at station  $x = 15$  ft for  $8^\circ$  semi-vertex angle cone,  $u_\infty = 22,000$  fps, altitude = 150,000 ft. The profiles are obtained by the streamtube and the multiple-strip integral methods. Rate constants are obtained from Ref. 9 (designated RR 115, used by both methods) and from Ref. 1 (designated AMP 77, used by streamtube method only).



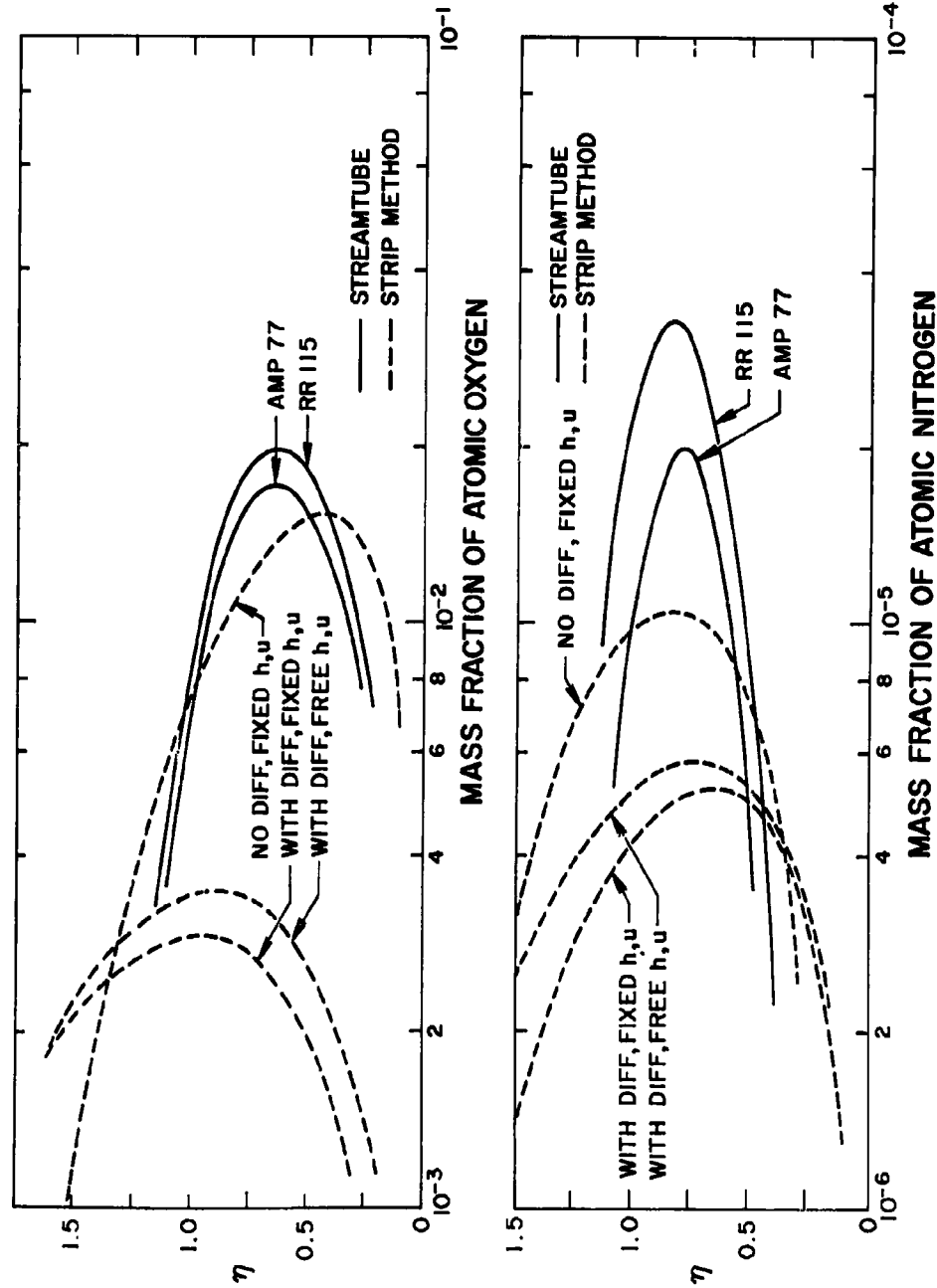


Fig. 4. Nonequilibrium concentration of atomic oxygen and nitrogen at station  $x = 15$  ft for  $8^\circ$  semi-vertex angle cone,  $u_\infty = 22,000$  fps, altitude = 150,000 ft. Methods and rates used same as for Fig. 3.



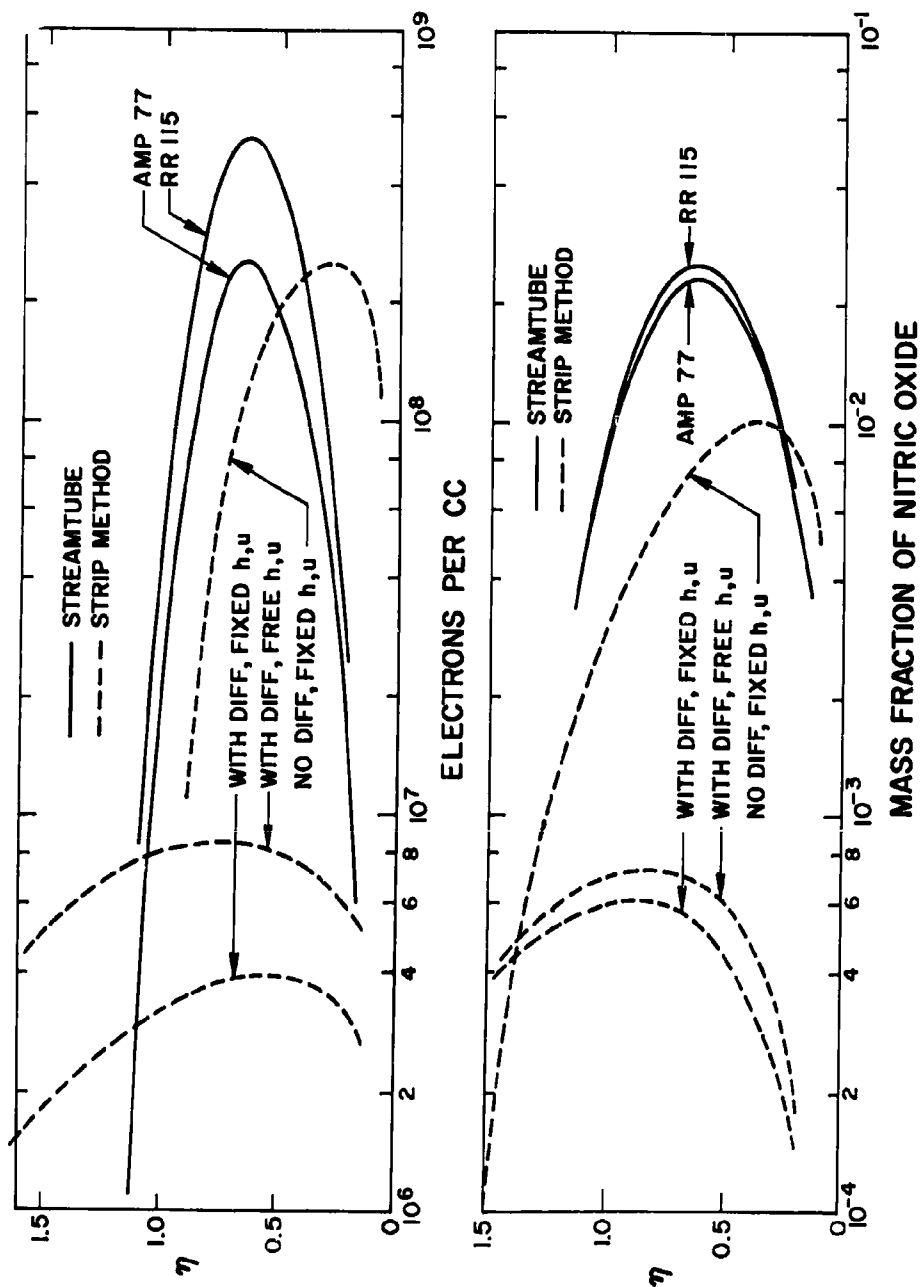


Fig. 5. Nonequilibrium concentration profiles of electrons and nitric oxide at station  $x = 15$  ft for  $8^\circ$  semi-vertex angle cone,  $u_\infty = 22,000$  fps, altitude = 150,000 ft. Methods and rates used same as for Fig. 3.



still not achieved, however, due to differences in the thermodynamic and transport properties used in the two methods, as well as a greater degree of coupling between the thermodynamics and the chemistry for even this simplified strip analysis. (In the strip method the species concentrations are based on the properties across the entire boundary layer, while in the streamtube technique these concentrations depend only on the properties along the "effective" pathline under consideration.)

Aside from these property and coupling differences, the remaining discrepancy between the streamtube and most general strip method (with diffusion, and "free" velocity and enthalpy profiles) is then seen to be due to the approximations of neglecting diffusion and requiring the velocity and enthalpy to be specified by the fixed locally similar profiles. The strip method results indicate that, while the temperature again is not greatly affected by the various approximations, the species concentrations are. The neglect of diffusion generally has the greater effect on the profiles and, in fact, apparently accounts for the major portion of the difference between the streamtube and general strip method techniques.

Although the precise details of the boundary layer profiles are of importance for many applications, there are also cases where the total quantities of atoms, radiating species and electrons produced within the boundary layer are more significant. Certain telemetry considerations and some aspects of far wake behavior fall into this category. The overall rate of deposition of any species produced within the boundary layer is obtained by integration of the particle flux across the boundary layer. The result is given by

$$D_i = 2\pi r \int_0^{y_e} n_i u dy \text{ particles/sec,} \quad (11)$$

where  $y_e$  is the value of  $y$  at the edge of the boundary layer, and  $n_i$  is the number density of the relevant species.

When such integrals are evaluated for the profiles shown in Figs. 4 and 5, it is found that the discrepancies between the streamtube and multiple-strip integral methods are somewhat reduced. The reason is that, although the peak concentrations given by the strip method are always smaller for the species considered here, larger quantities are produced at large values of  $\eta$ , thus contributing more heavily to the integral of Eq. (11). For example, when the integrations are carried out for the atomic oxygen profiles of Fig. 4, the streamtube profile yields a total deposition rate which is 1.5 times the corresponding rate for the strip method profile with diffusion. This represents a considerably closer agreement than is obtained from a comparison of peak values, where the streamtube result is approximately 6 times greater than that of the strip method. Similarly, for the electron profiles of Fig. 5, the streamtube method yields a deposition rate 11 times that for the strip method, while the peak value for the streamtube method is 35 times that of the strip method.



### b. Sensitivity to the Chemical Model and Rate Constants

The sensitivity to the choice of rate constants illustrated in Figs. 3, 4, and 5 is shown from a different point of view in Figs. 6 and 7 for the same geometry and flight conditions. Here the temperature and concentrations are plotted as functions of distance along a particular path within the boundary layer. The path is chosen to pass through the peak of the enthalpy profile at a distance of about 5 ft from the cone apex. The temperature is seen to peak at approximately the same location. In addition to the effect of rate constants, the figures also illustrate the influence of the chemical model. Of the six cases shown in Figs. 6 and 7, the two labelled "vibrational equilibrium" correspond to the streamtube calculations of Figs. 3, 4 and 5. For the other four cases, the vibrational degrees of freedom are assumed unexcited when the particle path enters the shock layer, with subsequent relaxation at finite rates. Vibrational excitation accounts for almost negligible energy ( $\sim 20^\circ\text{K}$ ) in the inviscid region, but the conditions are such that the nitrogen does not achieve vibrational equilibrium until some 10 ft from the apex. Near the 5-ft station, therefore, the peak translational temperature is increased by some  $400^\circ\text{K}$  if the vibrational degrees of freedom are not assumed fully excited. This increased temperature affects the nitric oxide production and, to a greater degree, the atomic nitrogen concentration and associated electron production.

Two of the vibrational nonequilibrium curves use the CVD model, with the rate constants of Refs. 1 and 9. The remaining two cases (also with the rate constants of Refs. 1 and 9) use a non-CVD model, in which dissociation is allowed to proceed at a rate determined by the translational temperature, even when the vibrational degrees of freedom are not fully excited. This permits slightly greater atom production and yields the greatest electron production for a given choice of rate constants.

The results of these calculations show that the nitric oxide and electron concentrations can be extremely sensitive to slight variations in the chemical model and rate constants used. Until there is more adequate experimental data to clarify these details, any boundary layer calculations in this temperature regime (with or without diffusion) will be subject to the same uncertainties.

### c. Variations with Cone Angle

The effects of variation of cone angle on the profiles obtained by the streamtube method are shown in Figs. 8, 9 and 10 for the 15-ft station. For the family of curves drawn with solid lines the rate constants used are those of Ref. 1, and the chemical model includes vibrational nonequilibrium with CVD with the integrations starting from conditions immediately behind the shock wave (calculated for  $\gamma = 1.4$ ). The enthalpy and velocity profiles used are for the locally similar frozen boundary layer.

In the case of the more slender cones the region in which the temperature exceeds  $3000^\circ\text{K}$  forms a relatively narrow band inside the boundary layer. For cones with larger semi-vertex angles this region becomes wider and for the  $25^\circ$  cone it actually extends beyond the boundary layer out to the shock. Moreover, for the frozen boundary layer ( $\gamma = 1.4$ ) in which the temperature



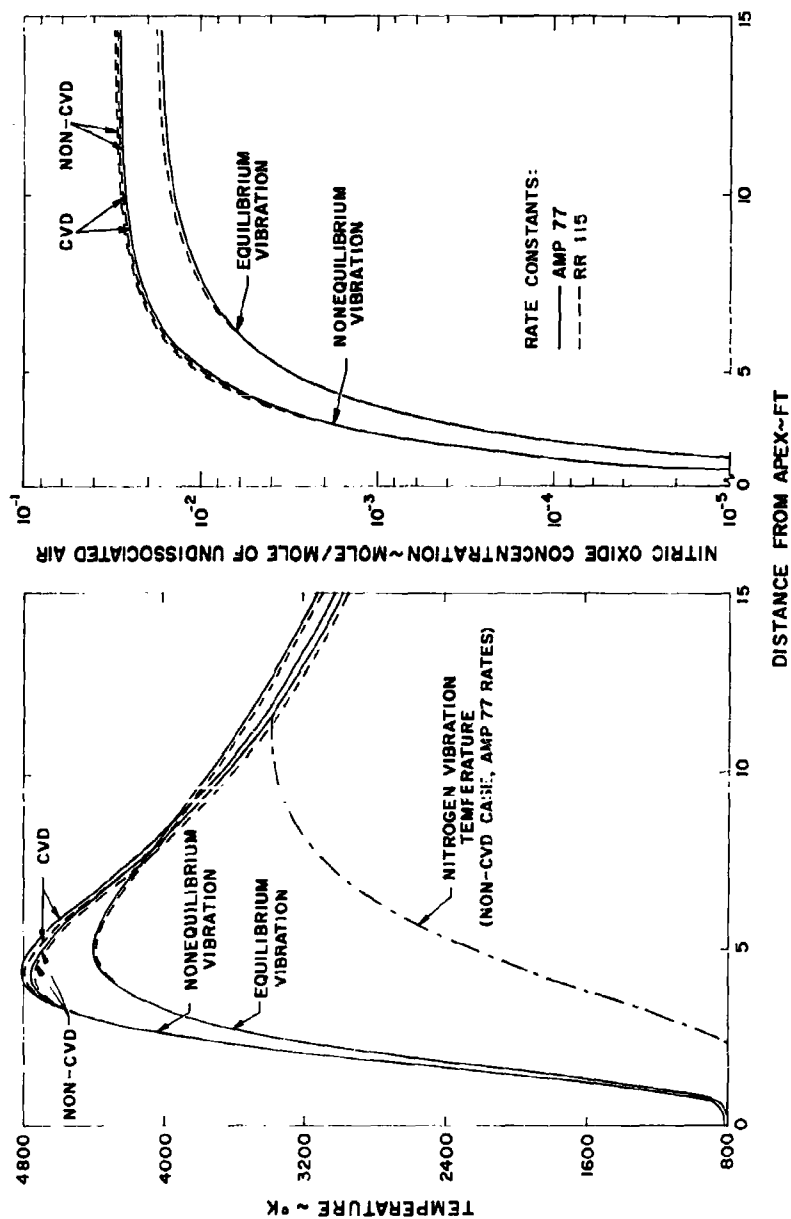


Fig. 6. Temperature and nitric oxide concentration histories along an effective particle path in the boundary layer for 80 semi-vertex angle cone,  $u_\infty = 22,000$  fps, altitude = 150,000 ft. The calculations are for both vibrational equilibrium and nonequilibrium, and show the effect of slight changes in the chemical model and rate constants used.



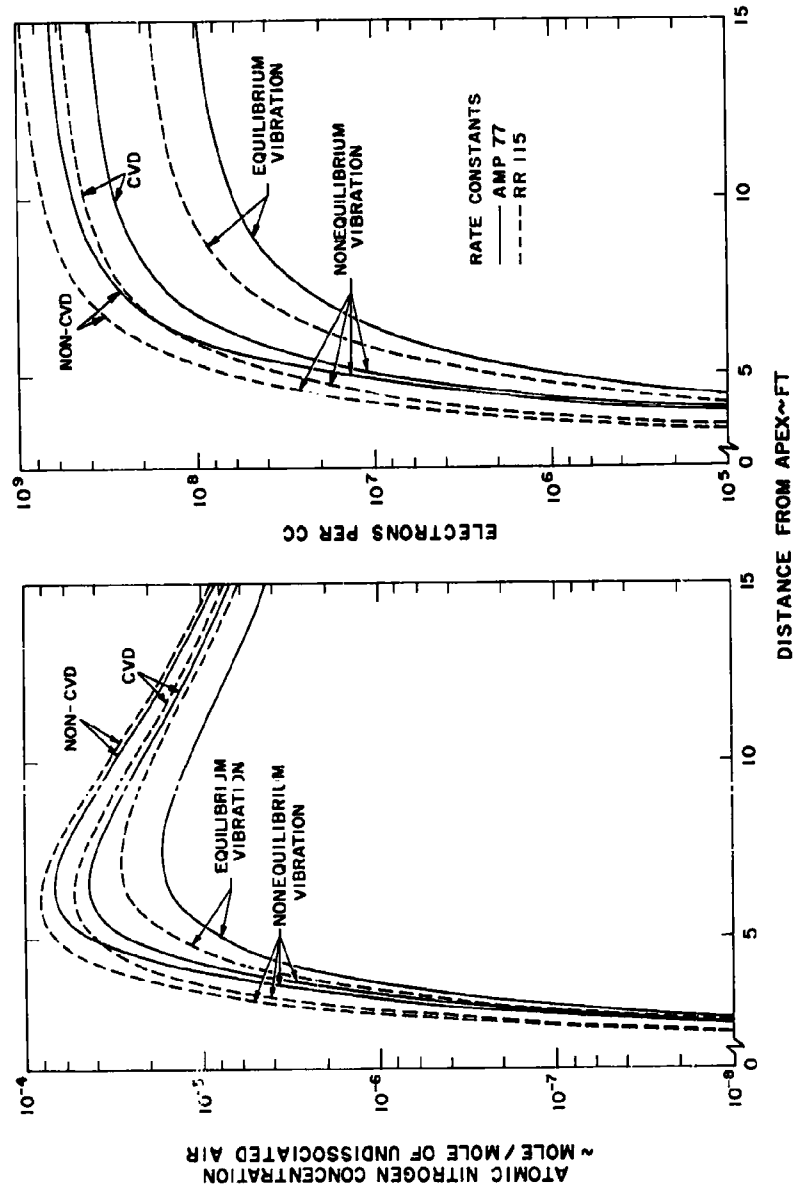


Fig. 7. Atomic nitrogen concentration and electron density histories along an effective particle path in the boundary layer for 8° semi-vertex angle cone,  $u_\infty = 22,000$  fps, altitude = 150,000 ft. The calculations are for both vibrational equilibrium and nonequilibrium, and show the effect of slight changes in the chemical model and rate constants used.



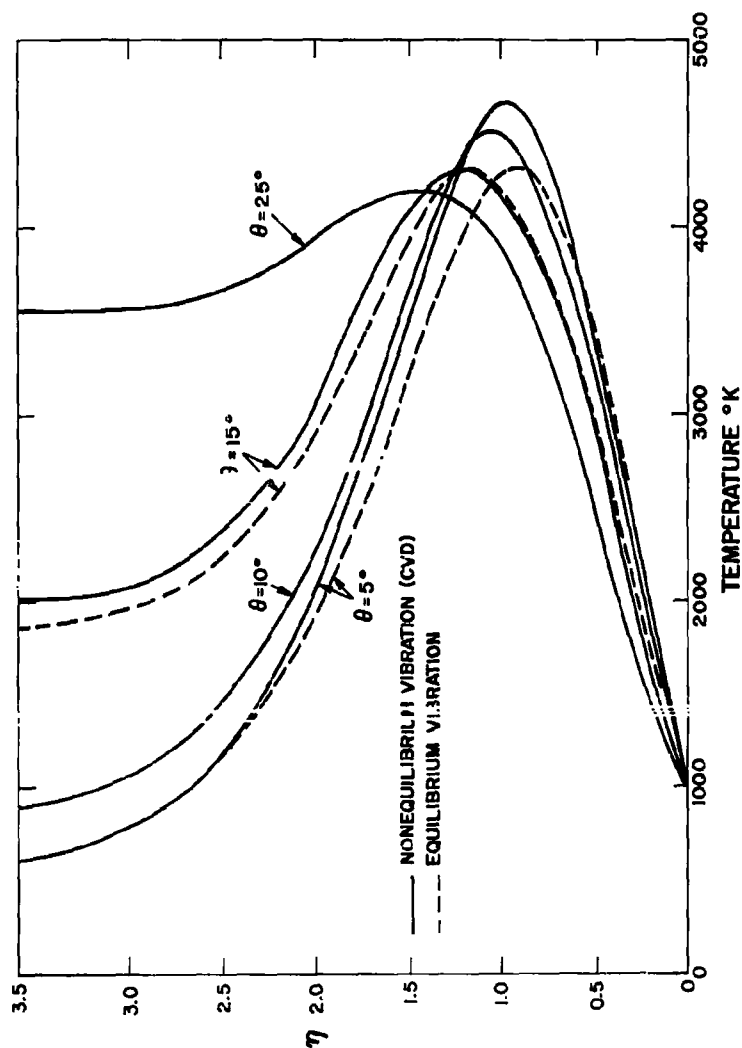


Fig. 8. Nonequilibrium temperature profiles in the boundary layer at  $x = 15$  ft for various cone angles,  $u_\infty = 22,000$  fps, altitude = 150,000 ft. The calculations include finite-rate vibrational relaxation with CVD for semi-vertex angles  $\theta = 5, 10, 15$  and  $25^\circ$ . Profiles with vibrational equilibrium are shown for  $\theta = 5^\circ$  and  $15^\circ$ .



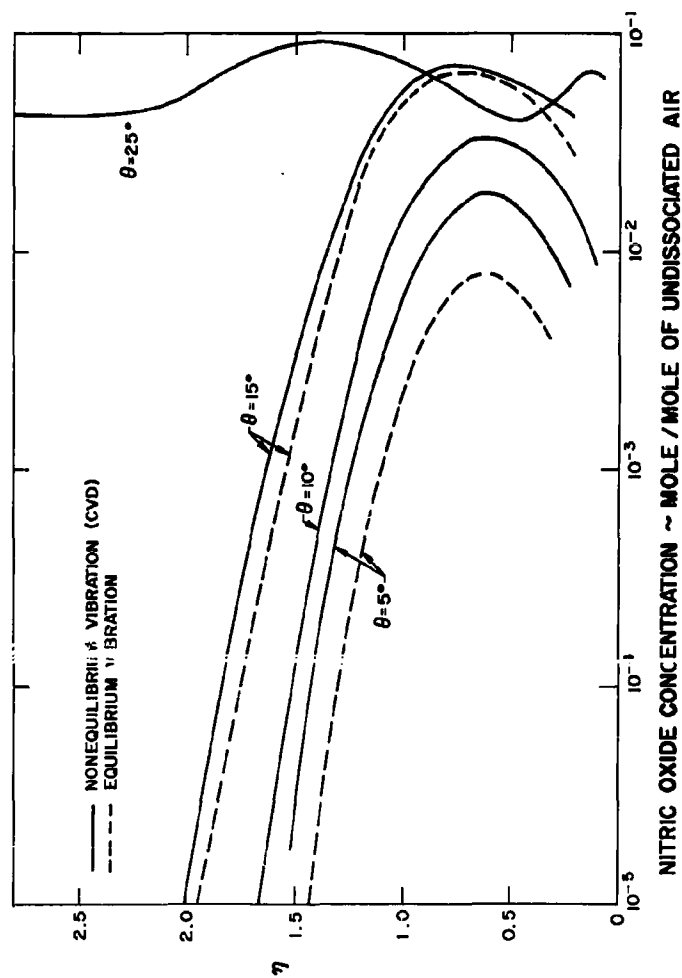


Fig. 9. Nonequilibrium nitric oxide concentration profiles in the boundary layer at  $x = 15$  ft for various semi-vertex angles  $\theta$ ,  $u_\infty = 22,000$  fps, altitude = 150,000 ft. The calculations include both finite-rate vibrational relaxation with CVD and vibrational equilibrium, as in Fig. 8.



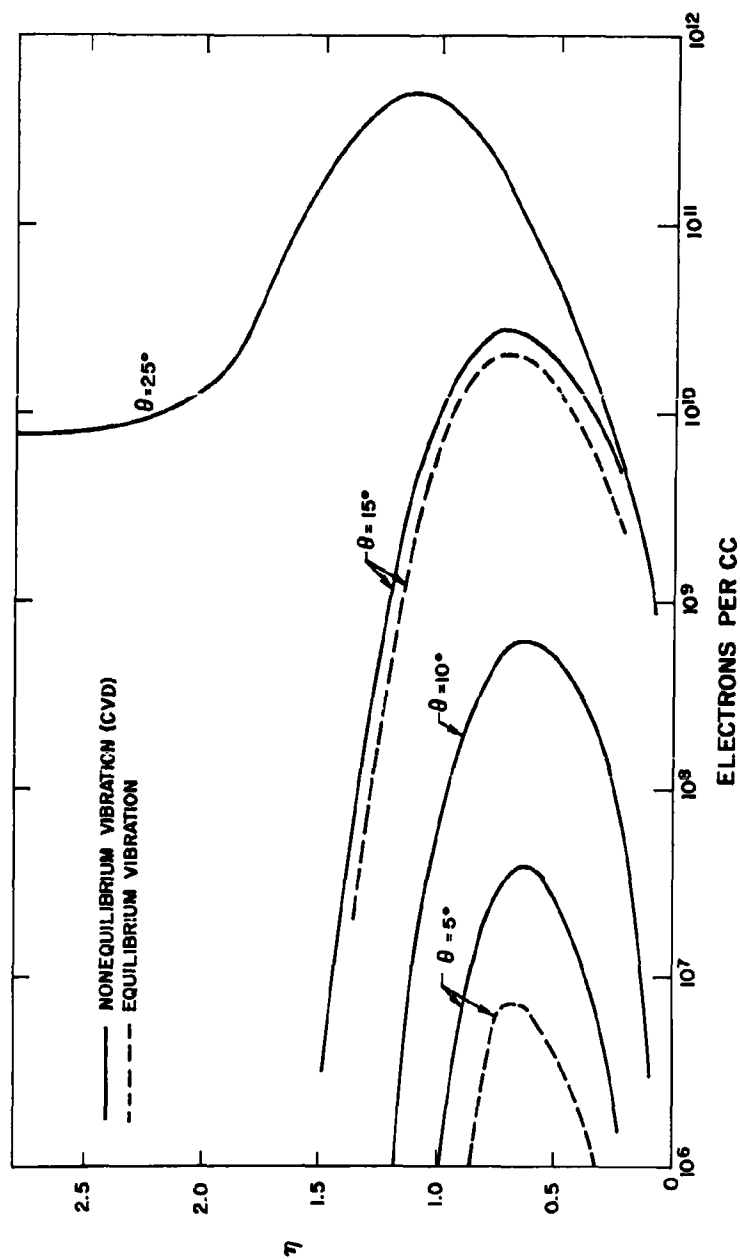


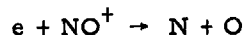
Fig. 10. Nonequilibrium electron density profiles in the boundary layer at  $x = 15$  ft for various semi-vertex angles  $\theta$ ,  $u_\infty = 22,000$  fps, altitude  $= 150,000$  ft. The calculations include both finite-rate vibrational relaxation with CVD and vibrational equilibrium, as in Fig. 8.



is proportional to the enthalpy, both the peak temperature and peak static enthalpy increase with increasing cone angle. For the flight conditions considered here (altitude = 150,000 ft, flight speed = 22,000 ft/sec) the peak temperature increases from 5250°K to 6650°K if the semi-vertex angle is increased from 5° to 25°.

Even though the peak static enthalpy in the boundary layer increases with cone angle, Fig. 8 shows that the nonequilibrium peak temperature decreases with increasing cone angle. This trend can be explained by considering differences in the enthalpy-time histories with cone angle for particles arriving in the region of peak temperatures at a fixed distance from the apex. In contrast to the flow times from the shock to this region, which are about the same for all cone angles considered, the residence times of particles in the high enthalpy region increase with cone angle. Furthermore, the pressure rise across the shock also increases with cone angle, resulting in higher density levels throughout the inviscid flow region and boundary layer. These factors all lead to a higher chemical activity which in turn is responsible for the lower peak temperatures for larger cone angles.

Of course, the higher chemical activity also leads to a larger production of NO and electrons, both with respect to the peak concentrations achieved, and to the extent of the chemically-active region in a direction normal to the cone surface. A particularly large NO production occurs in the high temperature region in the case of the cone with 25° semi-vertex angle. The rather anomalous shape of the NO concentration profile near the wall at the 15-ft station can be explained in the light of the above discussion. Fluid elements entering the boundary layer close to the apex of the cone undergo violent chemical reactions, resulting in NO and electron concentrations close to local equilibrium. As the fluid element approaches the lower temperature region near the wall, the concentrations of these species become in excess of the local equilibrium requirements. The reactions reverse direction and work toward the removal of the excess, as for example, on particle paths which arrive at the 15-ft station with  $\eta \approx 0.5$ . However, for particle paths at smaller values of  $\eta$  the fluid elements reach the low temperature region so rapidly that the reaction rates become too slow for effective removal of the NO within a 15-ft length. This accounts for the high levels of nitric oxide for the 25° cone at small values of  $\eta$ . On the other hand, the binary recombination process



can be effective in reducing the electron concentration by one or two orders of magnitude within the same axial flow distance. Of course the fine details of the profiles obtained from the streamtube method are not significant because of the neglect of diffusion, but the information obtainable on the chemical behavior is of value.

Another aspect of the 25° cone result is seen in Fig. 10, which shows considerable production of electrons in the outer edges of the boundary layer at the 15-ft station. Most of this production occurs in the inviscid flow field, since the static enthalpy is too high to permit the gas to remain frozen.



The results obtained under the assumption of vibrational equilibrium are shown by the dashed curves of Figs. 8, 9 and 10 for cone angles of  $5^\circ$  and  $15^\circ$ . Again the rate constants are those of Ref. 1, but the enthalpy and velocity profiles used are for the locally similar boundary layer for a thermally perfect, calorically imperfect gas. The sensitivity of the profiles to the extent of vibrational excitation for small cone angles has already been mentioned in Section b. As the cone angle is increased the vibrational relaxation distance in the inviscid flow field for 150,000 ft altitude becomes small compared with the flow length of 15 ft. Consequently, the differences between vibrational equilibrium and nonequilibrium are fairly small for a  $15^\circ$  cone, and practically negligible for a  $25^\circ$  cone. For this reason the vibrational equilibrium profiles have been omitted for the latter case.

#### d. Binary Scaling, and Variation with Station and Altitude

All of the results presented above have applied to an altitude of 150,000 ft. For the more slender cones, the chemical and excitation processes occurring in the heated gas are dominated by binary reactions, even at the 15-ft station. For the larger cone angles, of course, the shorter chemical relaxation times permit over-dissociation to occur, and lead to situations where three-body recombination processes are important within the boundary layer. However, as long as binary processes dominate, the well-known concept of binary scaling can be invoked. As far as the chemical and excitation processes are concerned, this permits a calculation obtained for a body of characteristic dimension  $x$  at an ambient density  $\rho_\infty$  to be applied to a geometrically similar body of different size (at the same flight velocity), as long as the ambient density is chosen to maintain  $\rho_\infty x$  invariant. For a constant wall temperature, and neglecting viscosity changes due to variations in atmospheric temperature with altitude this scaling criterion also implies that the Reynolds number is left practically unchanged. Thus it is clear that the boundary layer is also virtually unaffected by the scale change. Thus the entire chemical and thermodynamic behavior for a given body at one altitude can be applied to the appropriate geometrically similar body at a different altitude. In any application of this principle, of course, it is necessary to express species concentrations non-dimensionally, (in moles per mole of undissociated air, for example). Concentrations expressed in particles per unit volume would then scale linearly with the ambient density.

The binary scaling principle is equally applicable to more accurate nonequilibrium boundary layer calculations which include the effects of diffusion, since the diffusion is also a binary process. The only problem which arises in the application of such scaling is in the determination of its limits of validity. As soon as atoms are produced, three-body recombination processes begin, though they are entirely negligible over most of the range of the slender cone calculations presented here. However, when the results presented are applied to smaller and smaller bodies at higher and higher densities, the three-body processes gain in importance and ultimately vitiate the binary scaling concept.

The onset of such a breakdown may be readily determined by means of the streamtube method. In the present case some calculations were made to assess the validity of binary scaling for the profiles shown for the  $10^\circ$  cone



of Figs. 8, 9 and 10. The profiles plotted are for the 15-ft station with  $\rho_{\infty}/\rho_0 = 1.5 \times 10^{-3}$  (150,000-ft altitude), and they are indistinguishable from the corresponding profiles for the 0.0225-ft station on a conical pellet at  $\rho_{\infty}/\rho_0 = 1$  (sea level). While the reactions occurring on particle paths near the wall at the high density are not entirely binary, the three-body reactions do not predominate until the temperature is too low for significant chemical changes to be effected. This situation is similar to that discussed in connection with the 25° cone in Section c.

The effects of variation of station location are graphically illustrated in Fig. 11, where nonequilibrium temperature profiles at three different axial stations for the 10° cone of Fig. 8 are shown. The nonequilibrium calculations are carried out under the same restrictions as those used for Fig. 8, and vibrational nonequilibrium with CVD is assumed. The initial frozen ( $\gamma = 1.4$ ) profile is observed to relax through a series of values which tend to approach equilibrium conditions downstream. It should be noted that, whereas the peak temperatures vary over a wide range, the peak value of static enthalpy can change by only a few percent, as pointed out in the discussion of Fig. 2.

The effects of variation of both altitude and station location for a given body size are shown in Figs. 12, 13 and 14. Here the calculations are carried out by the streamtube technique for an 8° semi-vertex angle cone, under conditions of vibrational equilibrium, and with the rate constants of Ref. 1. In these figures the profiles are given in terms of actual distance normal to the body surface, rather than as functions of  $\eta$ , to provide more graphic illustration of the effects of altitude and station location. Altitudes of 115,000 ft, and 200,000 ft are considered, as well as stations 5, 10 and 15 ft from the apex of the cone.

The profiles of temperature, nitric oxide concentration and electron density show variations with altitude and station which reflect the increase in boundary layer thickness both with altitude and with distance downstream. While the peak temperature does not exhibit any great variation over the range of conditions considered, the peak values of nitric oxide concentration and electron density do, a fact which is of some importance in any precise flow field determination.

For purposes of comparison the electron density profiles for equilibrium air at the 15-ft station are included in Fig. 14. A large difference between equilibrium and nonequilibrium results is exhibited at higher altitudes. The difference is seen to decrease with altitude, indicating a general approach to equilibrium conditions at the lower altitudes, as far as the 15-ft station is concerned. For a shorter cone length, of course, the approach to equilibrium would occur at still lower altitude, in accordance with the binary scaling principle discussed above.

## CONCLUSIONS

An approximate technique has been developed for the determination of nonequilibrium effects within a laminar boundary layer, based on the assumptions that the effect of diffusion on the species concentrations may be neglected, and that the velocity and enthalpy distributions are given with sufficient



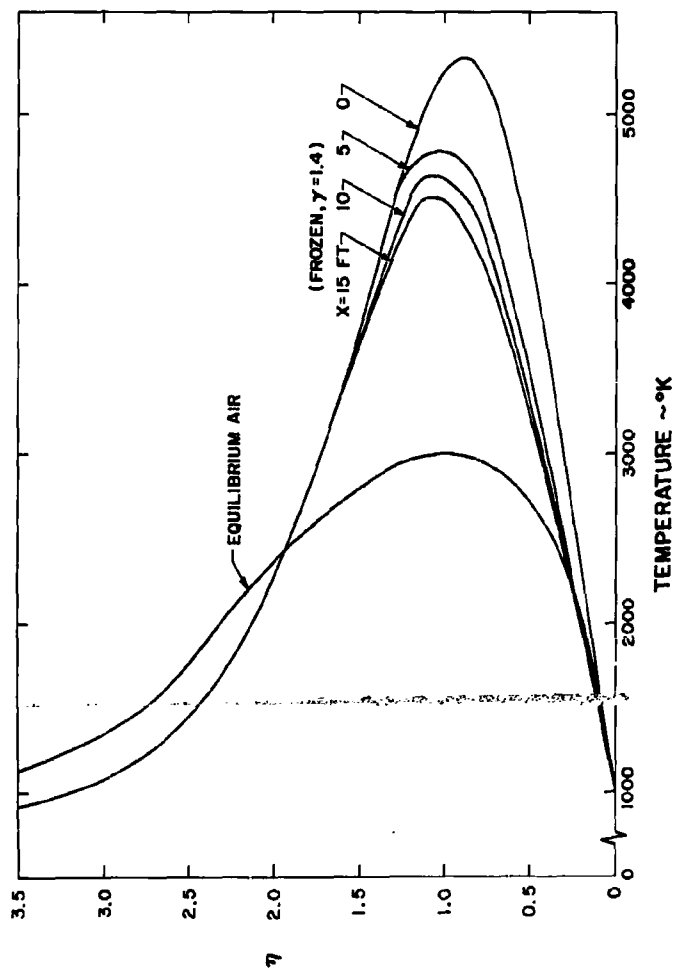


Fig. 11. Temperature profiles in the boundary layer for  $10^\circ$  semi-vertex angle cone  $u_\infty = 22,000$  fps, altitude = 150,000 ft. The profile labeled  $x = 0$  ft is for a perfect gas with frozen chemistry and represents the initial profile. The profiles at distances 5, 10 and 15 ft from the apex are obtained by the streamtube technique using finite-rate vibrational relaxation with CVD. Also shown is a corresponding profile for equilibrium air.



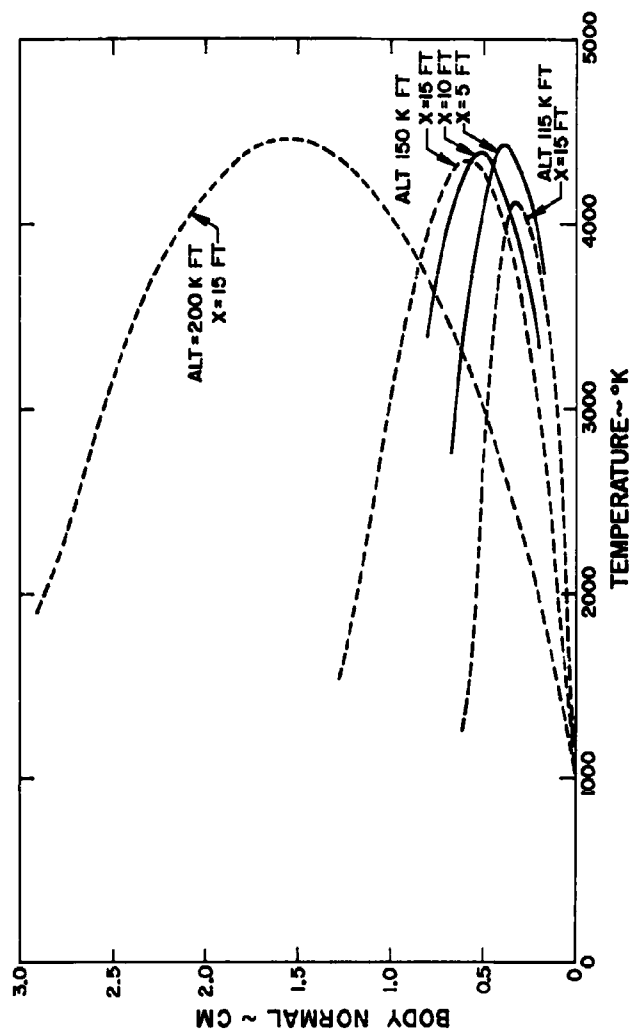


Fig. 12. Variation of nonequilibrium temperature profiles with altitude and station for 8° semi-vertex angle cone,  $u_{\infty} = 22,000$  fps. Vibrational equilibrium is assumed.



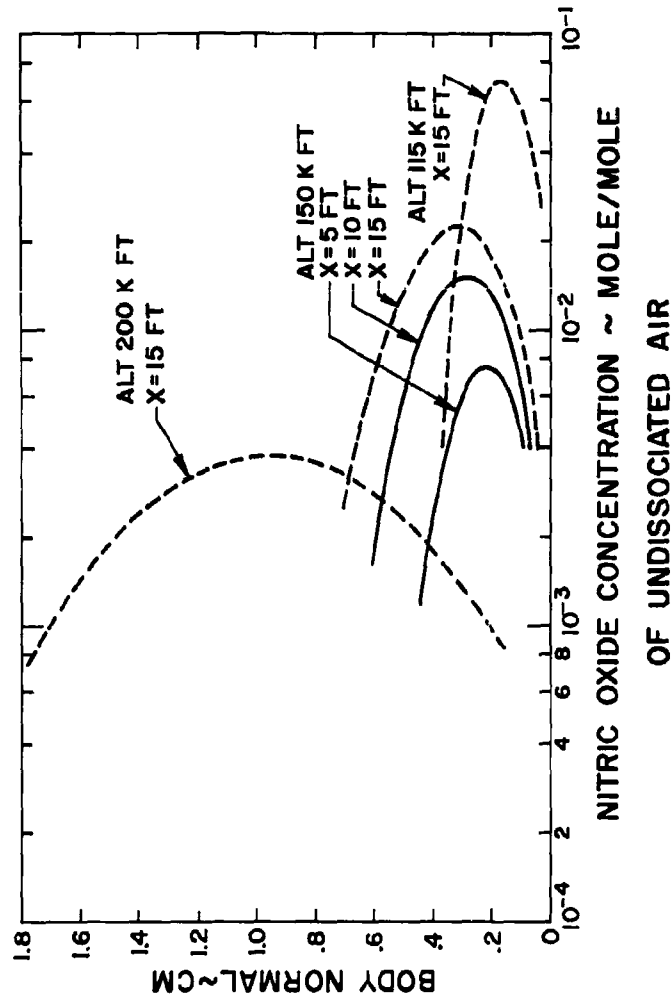


Fig. 13. Variation of nitric oxide concentration profiles with altitude and station for 80 semi-vertex angle cone,  $u_{\infty} = 22,000$  fps. Vibrational equilibrium is assumed.



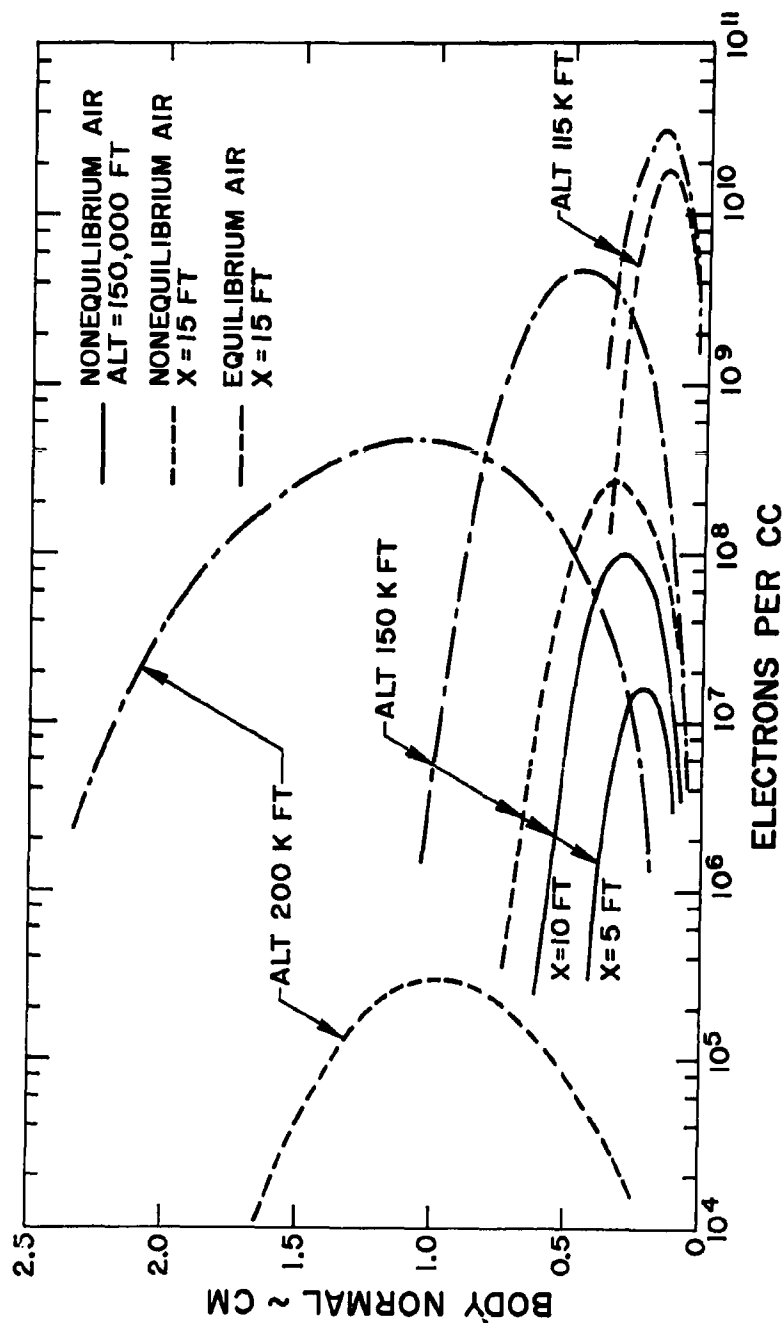


Fig. 14. Variation of nonequilibrium electron density with altitude and station for  $8^\circ$  semi-vertex angle cone,  $u_\infty = 22,000$  fps. Equilibrium profiles for the  $x = 15$ -ft station are also shown. Vibrational equilibrium is assumed.



accuracy by a locally similar analysis which neglects nonequilibrium effects. A comparison with results from a more accurate multiple-strip integral technique indicates that the approximate technique tends to over-predict peak values of some of the species concentrations, particularly nitric oxide and electrons. The primary cause of the discrepancy is shown to be the neglect of diffusion, with the enthalpy and velocity approximations being of secondary importance.

While the neglect of diffusion in the streamtube method is seen to over-predict peak atom, nitric oxide and electron concentrations, integration across the boundary layer to determine the overall deposition of these species results in a much closer agreement between the two methods.

In spite of the discrepancy brought about by the neglect of diffusion, the streamtube method does have certain applications, particularly for those cases where general nonequilibrium trends, rather than detailed flow field computations, are desired. In these circumstances an adequate description of the profiles at a given station can be obtained by calculations made for a limited number of suitably chosen effective particle paths, resulting in a considerable reduction of machine time as compared with a more exact method. Certain nonequilibrium trends have been considered here for the boundary layers on pointed cones. They include the uncertainty due to the rate constants and the vibration-dissociation coupling, both of which have been shown to be appreciable. In fact, it is seen that the combined effects of these uncertainties, together with other differences in the thermodynamics and transport properties, may well approach the order of the difference between the streamtube and multiple-strip integral methods in some cases.

Parametric effects, such as the variations due to altitude and body geometry, also have been considered, together with the application of the binary scaling concept. The difference between the equilibrium and nonequilibrium results at higher altitudes is appreciable, with equilibrium being approached as the altitude is decreased.

In summary, it is clear that diffusion effects cannot be neglected in comparison with chemical production processes, as in the streamtube method. Any quantitative estimates of species production in cone boundary layers must be supported by calculations which include the effect of diffusion. However, as long as such supporting calculations are made, it is possible that the streamtube method has some usefulness for estimation of trends with cone angle or altitude, or for evaluation of the effect of changes in the chemical model or in the rate constants. Such changes in the chemical model could include, for example, seeding or reactions with ablation products.

#### ACKNOWLEDGMENTS

The authors are pleased to acknowledge the advice and cooperation of Adrian Pallone, Peter Rose and Nelson Kemp, and are grateful for the assistance of Anthony Pappas (RAD), Allan Amoling, Robert Yanover, Harvy Cohen, Gerard Dreiss and other members of the AERL Computer Group during the course of this investigation.



## REFERENCES

1. Lin, S. C., and J. D. Teare, "A Streamtube Approximation for Calculation of Reaction Rates in the Inviscid Flow Field of Hypersonic Objects," Avco-Everett Research Laboratory AMP 77, August 1961. Proceedings of the Sixth Symposium on Ballistic Missile and Aerospace Technology, vol. 4, New York Academic Press, 1961.
2. Bloom, M. H., and M. Steiger, "Inviscid Flow with Nonequilibrium Molecular Dissociation for Pressure Distributions Encountered in Hypersonic Flight," J. Aerospace Sci., vol. 27, November 1960, p. 821.
3. Hall, J. G., A. Q. Eschenroeder, and P. V. Marrone, "Blunt-Nose Inviscid Airflows with Coupled Nonequilibrium Processes," J. Aerospace Sci., vol. 29, September 1962, p. 1038.
4. Wood, A. D., J. F. Springfield, and A. J. Pallone, "Determination of the Effects of Chemical and Vibrational Relaxation on an Inviscid Hypersonic Flow Field," AIAA Preprint No. 63-441, August 1963.
5. Van Tassell, W., and A. J. Pallone, "Similar Solutions of the Compressible Laminar Boundary Layer Equations for Air in Equilibrium Dissociation and Ionization with and without Air Injection in the Stagnation Region," Avco Corporation, Research and Advanced Development Division, TM 61-22, June 1961.
6. Fay, J. A., and N. H. Kemp, "Theory of Stagnation-Point Heat Transfer in a Partially Ionized Diatomic Gas," Avco-Everett Research Laboratory Research Report 144, November 1962.
7. Blotther, F. G., "Chemical Nonequilibrium Boundary Layers," AIAA Pre-print No. 63-443, August 1963.
8. Pallone, A. J., J. Moore, and J. Erdos, "Nonequilibrium, Non-Similar Solutions of the Laminar Boundary Layer Equations," Avco/RAD TM 63-58, Research and Advanced Development Division, Avco Corp., Wilmington, Mass., August 1963.
9. Lin, S. C., and J. D. Teare, "Rate of Ionization Behind Shock Waves in Air, Part II: Theoretical Interpretation," Avco-Everett Research Laboratory Research Report 115, September 1962. Phys. of Fluids, vol. 6, March 1963, p. 355.



10. Hammerling, P., J. D. Teare and B. Kivel, , Theory of Radiation from Luminous Shock Wave in Nitrogen, " Avco-Everett Research Laboratory Research Report 49, June 1959. Phys. of Fluids, vol. 2, July-August 1959, p. 422.
11. Wray, K. L. , "Chemical Kinetics of High Temperature Air, " Avco-Everett Research Laboratory Research Report 104, June 1961. Hypersonic Flow Research (Proceedings of American Rocket Society International Hypersonics Conference, Cambridge, Mass. August 1961, New York Academic Press, 1962.
12. Wray, K. L. , and J. D. Teare, "A Shock Tube Study of the Kinetics of Nitric Oxide at High Temperatures, " Avco-Everett Research Laboratory Research Report 95, June 1961. J. Chem. Phys., vol. 36, May 1962, p. 2582.
13. Pallone, A. J. , "Non-Similar Solutions of the Compressible-Laminar Boundary Layer Equations with Applications to the Upstream-Transpiration Cooling Problem, " J. Aerospace Sci., vol. 28, June 1961, p. 449.
14. Pallone, A. J. , and J. A. Moore, "Similar Solutions to the Laminar Boundary Layer Equations for Nonequilibrium Air, " Avco/RAD TR-62-59, July 1962.



CHEBYSHEV METHOD FOR THE CALCULATION  
OF  
RADAR CROSS SECTION OF PLASMA WAKES

K. Fong

Electromagnetics Research  
Lockheed Missiles and Space Company  
Sunnyvale, California

ABSTRACT

To calculate the radar cross-section of a plasma wake, it is necessary to solve the electromagnetic field within the cylindrical plasma. This is a formidable problem and, to date, only limited progress has been made.

This paper presents the Chebyshev method by which the field equation of a radially varying plasma wake is numerically solved. Using the computed values, along with values for the Bessel and Hankel functions, the radar cross section of the cylindrical wake can be computed. The advantage of this method, against the use of power series, is that strong convergence is assured due to the use of Chebyshev series in the present method.

The method described in this paper was performed under Navy Contract N0w 63-0050-c (U).



# CHEBYSHEV METHOD FOR THE CALCULATION OF RADAR CROSS SECTION OF PLASMA WAKES

K. Fong  
Electromagnetics Research  
Lockheed Missiles and Space Company  
Sunnyvale, California

## INTRODUCTION

The plasma wake of a body re-entering the atmosphere can modify its radar return. This depends on the electron density, the manner in which the electrons are distributed, and the electron-atom collision frequency. Because the flow is both laminar and turbulent, the assumption of uniform electron distribution in the wake is unrealistic. Also, the assumption that the electron density, therefore the plasma frequency, in the wake region is a function of the radial distance only may not be correct, but is often used as a mathematical model for theoretical calculation of backscattering cross-section. To simplify things further, the collision frequency is often assumed constant at each altitude. Even with these assumptions, the field equation, which must be solved, is complicated enough to require the service of electronic computers.

With the permittivity of the wake expressed in a finite polynomial of the radial variable, (which may be obtained from experimental data by curve-fitting techniques), numerically solving the field equation by assuming an infinite Taylor or power series results in slow convergence. This difficulty cannot be easily overcome even with the use of high speed computers.

The numerical method proposed in this paper alleviates the slow convergence problem.

The Chebyshev polynomials have been known to the network theorist for its "equal ripple" approximation in filter synthesis, and the Chebyshev series possesses the property of approximating a function with fewer terms than any other series in its class. Because of this bounded magnitude of the Chebyshev polynomial and the strong convergence that the Chebyshev series possesses, Clenshaw (1) has used the Chebyshev expansion method for approximating solution of differential equations of real variables and real coefficients. Lanczos (2) has also used the Chebyshev series as the perturbing term (s) for solving differential equations in his  $\tau$ -method. L. Fox (3) merges Clenshaw's and Lanczos' method into a matrix equation which can be solved to obtain the coefficients of the finite Chebyshev series approximating the solution of a differential equation.

This matrix form of L. Fox is used here for solving the field equation of the plasma wake so that radar cross-section can subsequently be computed. The matrices suggested by Fox consist of real elements, whereas the matrix equation resulting in solving the field equation inside the plasma wake is



complex since its permittivity is complex. Also, in this paper, Fox's matrix form has been re-arranged so that computation of numerical values by programming the computer can be conveniently performed by employing Crout's method for solving sets of simultaneous equations (4).

#### SOLVING THE HELMHOLTZ EQUATION

By means of curve fitting techniques,  $\epsilon(\rho)$  of a plasma cylinder may be obtained from experimental data on electron density distribution. Assume that  $\epsilon(\rho)$  is expressible by a finite polynomial of the form

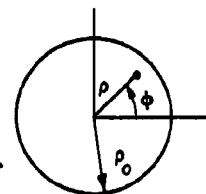
$$\epsilon(\rho) = \epsilon_1 + \epsilon_2 \rho^2 + \epsilon_3 \rho^4 + \epsilon_4 \rho^6 + \epsilon_5 \rho^8 + \dots \quad (1)$$

The  $\epsilon$ 's are complex. For parallel polarization and normal incidence, the field equation is given by

$$\frac{\partial^2 u_z}{\partial \rho^2} + \frac{1}{\rho} \frac{\partial u_z}{\partial \rho} + \frac{1}{\rho^2} \frac{\partial^2 u_z}{\partial \phi^2} + \omega^2 \mu_0 \epsilon_0 \epsilon(\rho) u_z = 0 \quad (2)$$

By the method of separation of variables one obtains

$$u_z = E_m(\rho) e^{jm\phi} \quad \text{direction of propagation} \rightarrow \quad (3)$$



Combining eqs. (3) and (2) gives

$$\frac{d^2 E_m(\rho)}{d\rho^2} + \frac{1}{\rho} \frac{dE_m(\rho)}{d\rho} + \left( k^2 \epsilon(\rho) - \frac{m^2}{\rho^2} \right) E_m(\rho) = 0 \quad (4)$$

Using the first four terms of the series for  $\epsilon(\rho)$  from (1),

$$\begin{aligned} \frac{d^2 E_m(k\rho)}{d(k\rho)^2} + \frac{1}{k\rho} \frac{dE_m(k\rho)}{d(k\rho)} + \left[ \epsilon_1' + \epsilon_2'(k\rho)^2 + \epsilon_3'(k\rho)^4 + \epsilon_4'(k\rho)^6 \right. \\ \left. - \frac{m^2}{(k\rho)^2} \right] E_m(k\rho) = 0 \end{aligned} \quad (5)$$

Since the range of  $x$  in the Chebyshev polynomial,  $T_n(x)$ , is  $-1 \leq x \leq 1$ ,  $k\rho$  in eq. (5) is changed to

$$k\rho = \beta x \quad (6)$$

where  $\beta$  is chosen so that  $0 < x \leq 1$ .

Now eq. (5) becomes



$$\frac{d^2 E_m(x)}{dx^2 \beta^2} + \frac{1}{x\beta} \frac{dE_m(x)}{dx\beta} + \left[ (\epsilon'_1 + \epsilon'_2 \beta^2 x^2 + \epsilon'_3 x^4 \beta^4 + \epsilon'_4 \beta^6 x^6) - \frac{m^2}{(\beta x)^2} \right] E_m(x) = 0 \quad (7)$$

With the transformation

$$E_m(x) = x^m R_m(x) \quad (8)$$

eq. (7) gives

$$x^2 \frac{d^2 R_m(x)}{dx^2} + (2m+1) x \frac{dR_m(x)}{dx} + \left[ \beta^2 x^2 (\epsilon'_1 + \epsilon'_2 \beta^2 x^2 + \epsilon'_3 x^4 \beta^4 + \epsilon'_4 \beta^6 x^6) \right] R_m(x) = 0 \quad (9)$$

The even power of  $x$ 's in the expression for the permittivity suggests the use of the even order of Chebyshev polynomial in the approximating Chebyshev series

$$R_m(x) = \sum_{n=0}^N A_{2n} T_{2n}(x) \quad (10)$$

where the prime indicates that the first term in series (10) is

$$\frac{1}{2} A_0 T_0$$

The  $A$ 's are the coefficients of the Chebyshev series.

It can be easily shown (see Appendix A) that

$$x^2 \frac{d^2 T_{2n}(x)}{dx^2} = 2n(2n-1) T_{2n} + 2n \sum_{k=1}^{n-1} (8kn - (2k)^2 - 2) T_2(n-k) + 2n(2n^2 - 1) T_0(x) \quad (11)$$

$$x \frac{dT_{2n}(x)}{dx} = 2n(T_{2n} + 2T_2(n-1) + 2T_{2n-4} + \dots + T_0) \quad (12)$$

$$x^2 T_{2n}(x) = \frac{T_{2n} + 2 + 2T_{2n} + T_{2n-2}}{4} \quad (13)$$

$$x^4 T_{2n}(x) = \frac{T_{2n+4} + 4T_{2n+2} + 6T_{2n} + 4T_{2n-2} + T_{2n-4}}{16} \quad (14)$$

$$x^6 T_{2n}(x) = \frac{T_{2n+6} + 6T_{2n+4} + 15T_{2n+2} + 20T_{2n} + 15T_{2n-2} + 6T_{2n-4} + T_{2n-6}}{64} \quad (15)$$



and

$$x^8 T_{2n}(x) = \frac{T_{2n+8} + 8T_{2n+6} + 28T_{2n+4} + 56T_{2n+2} + 70T_{2n}}{256} \\ + \frac{56T_{2n-2} + 28T_{2n-4} + 8T_{2n-6} + T_{2n-8}}{256} \quad (16)$$

Using eqs. (10) through (16) and after adding the perturbing Chebyshev polynomial ( $\tau$ -method)(2) eq. (9) is approximated by

$$\sum_{n=0}^N A_{2n} \left\{ 2n(2n-1)T_{2n} + 2n \sum_{k=1}^{n-1} [8kn - (2k)^2 - 2] T_{2(n-k)} + 2n(2n^2-1)T_0(x) \right. \\ + 2n(2n+1)(T_{2n} + 2T_{2n-2} + 2T_{2n-4} + \dots + T_0) + \beta^2 \epsilon_1' \left[ \frac{T_{2n+2} + 2T_{2n} + T_{2n-2}}{4} \right] \\ + \beta^4 \epsilon_2' \left[ \frac{T_{2n+4} + 4T_{2n+2} + 6T_{2n} + 4T_{2n-2} + T_{2n-4}}{16} \right] + \beta^6 \epsilon_3' \left[ \frac{T_{2n+6} + 6T_{2n+4} + 15T_{2n+2}}{64} \right. \\ \left. + \frac{20T_{2n} + 15T_{2n-2} + 6T_{2n-4} + T_{2n-6}}{64} \right] + \beta^8 \epsilon_4' \left[ \frac{T_{2n+8} + 8T_{2n+6} + 28T_{2n+4} + 56T_{2n+2}}{256} \right. \\ \left. + \frac{70T_{2n} + 56T_{2n-2} + 28T_{2n-4} + 8T_{2n-6} + T_{2n-8}}{256} \right] \left. \right\} = \tau_1 T_{2N}(x) + \tau_2 T_{2N+2}(x) \\ + \tau_3 T_{2N+4}(x) + \tau_4 T_{2N+6}(x) + \tau_5 T_{2N+8}(x) \quad (17)$$



[illegible]

$$\begin{aligned} b_{11} &= T_0(0) = 1 \\ b_{12} &= T_2(0) = -1 \\ b_{13} &= T_4(0) = 1 \\ b_{14} &= T_6(0) = -1 \end{aligned}$$

and so on.  $R_m(0) = 1$  is assumed in eq. (19).



For  $N=10$ , eq. (17) becomes

$$\begin{bmatrix}
 b_{11} & b_{12} & b_{13} & b_{14} & b_{15} & b_{16} & b_{17} & b_{18} & b_{19} & b_{1,10} & b_{1,11} \\
 b_{21} & b_{22} & b_{23} & b_{24} & b_{25} & b_{26} & b_{27} & b_{28} & b_{29} & b_{2,10} & b_{2,11} \\
 b_{31} & b_{32} & b_{33} & b_{34} & b_{35} & b_{36} & b_{37} & b_{38} & b_{39} & b_{3,10} & b_{3,11} \\
 b_{41} & b_{42} & b_{43} & b_{44} & b_{45} & b_{46} & b_{47} & b_{48} & b_{49} & b_{4,10} & b_{4,11} \\
 b_{51} & b_{52} & b_{53} & b_{54} & b_{55} & b_{56} & b_{57} & b_{58} & b_{59} & b_{5,10} & b_{5,11} \\
 b_{61} & b_{62} & b_{63} & b_{64} & b_{65} & b_{66} & b_{67} & b_{68} & b_{69} & b_{6,10} & b_{6,11} \\
 0 & b_{72} & b_{73} & b_{74} & b_{75} & b_{76} & b_{77} & b_{78} & b_{79} & b_{7,10} & b_{7,11} \\
 0 & 0 & b_{83} & b_{84} & b_{85} & b_{86} & b_{87} & b_{88} & b_{89} & b_{8,10} & b_{8,11} \\
 0 & 0 & 0 & b_{94} & b_{95} & b_{96} & b_{97} & b_{98} & b_{99} & b_{9,10} & b_{9,11} \\
 0 & 0 & 0 & 0 & b_{10,5} & b_{10,6} & b_{10,7} & b_{10,8} & b_{10,9} & b_{10,10} & b_{10,11} \\
 0 & 0 & 0 & 0 & 0 & b_{11,6} & b_{11,7} & b_{11,8} & b_{11,9} & b_{11,10} & b_{11,11} \\
 0 & 0 & 0 & 0 & 0 & 0 & b_{12,7} & b_{12,8} & b_{12,9} & b_{12,10} & b_{12,11} \\
 0 & 0 & 0 & 0 & 0 & 0 & 0 & b_{13,8} & b_{13,9} & b_{13,10} & b_{13,11} \\
 0 & 0 & 0 & 0 & 0 & 0 & 0 & 0 & b_{14,9} & b_{14,10} & b_{14,11} \\
 0 & 0 & 0 & 0 & 0 & 0 & 0 & 0 & 0 & b_{15,10} & b_{15,11} \\
 0 & 0 & 0 & 0 & 0 & 0 & 0 & 0 & 0 & 0 & b_{16,11}
 \end{bmatrix}
 \begin{bmatrix}
 A_0 \\
 A_2 \\
 A_4 \\
 A_6 \\
 A_8 \\
 A_{10} \\
 A_{12} \\
 A_{14} \\
 A_{16} \\
 A_{18} \\
 A_{20}
 \end{bmatrix}
 =
 \begin{bmatrix}
 1 \\
 0 \\
 0 \\
 0 \\
 0 \\
 0 \\
 0 \\
 0 \\
 0 \\
 0 \\
 0 \\
 \tau_1 \\
 \tau_2 \\
 \tau_3 \\
 \tau_4 \\
 \tau_5
 \end{bmatrix}$$

The expressions for the  $b$ 's are given in Appendix B.

(19)

The latter matrix equation is not directly suitable for computer calculation because computer subroutines for solving simultaneous equations are usually written for matrix equation of the form

$$VX = C$$

where the elements of  $V$  and  $C$  are known and the elements of the column matrix  $X$  are to be computed. With a little algebraic manipulation, the following form is obtained for eq. (19)



$$\begin{array}{c} \text{original} \\ \text{b-matrix} \end{array} \begin{bmatrix} 0 & 0 & 0 & 0 & 0 \\ 0 & 0 & 0 & 0 & 0 \\ 0 & 0 & 0 & 0 & 0 \\ 0 & 0 & 0 & 0 & 0 \\ 0 & 0 & 0 & 0 & 0 \\ 0 & 0 & 0 & 0 & 0 \\ 0 & 0 & 0 & 0 & 0 \\ 0 & 0 & 0 & 0 & 0 \\ 0 & 0 & 0 & 0 & 0 \\ -1 & 0 & 0 & 0 & 0 \\ 0 & -1 & 0 & 0 & 0 \\ 0 & 0 & -1 & 0 & 0 \\ 0 & 0 & 0 & -1 & 0 \\ 0 & 0 & 0 & 0 & -1 \end{bmatrix} \begin{bmatrix} A_0 \\ A_2 \\ A_4 \\ A_6 \\ A_8 \\ A_{10} \\ A_{12} \\ A_{14} \\ A_{16} \\ A_{18} \\ A_{20} \\ \tau_1 \\ \tau_2 \\ \tau_3 \\ \tau_4 \\ \tau_5 \end{bmatrix} = \begin{bmatrix} 1 \\ 0 \\ 0 \\ 0 \\ 0 \\ 0 \\ 0 \\ 0 \\ 0 \\ 0 \\ 0 \\ 0 \\ 0 \\ 0 \\ 0 \\ 0 \end{bmatrix} \quad (20)$$

The original b-matrix has been augmented and is now a square matrix. All unknowns are in the right places for computation. For a given set of  $\epsilon$ 's, values of  $E_m(\rho)$  are shown in Table 1, and the terms of  $R_1(x)$  are in Table 2.

Having solved the field inside the plasma cylinder, the next step is to formulate the expression for the backscattering radar cross section of the cylinder.



Table 1. Values of  $E_m(\bar{\rho}_0)$  and  $E'_m(\bar{\rho}_0)$ 

$$\epsilon = -40 + j12 + (60.4 + j13.6) x^2 - (18 + j12) x^4 + 3.5 + j5.3) x^6; \frac{\nu_0}{\lambda_0} = 0.05$$

M	$E_m(\bar{\rho}_0)$	$E'_m(\bar{\rho}_0)$
0	$1.025 - j 7.47 \times 10^{-3}$	$.29 + j .103$
1	$.1008 - j 1.67 \times 10^{-4}$	$.115 + j 1.22 \times 10^{-3}$
2	$.01 - j 1 \times 10^{-5}$	$3 \times 10^{-3} + j 1.96 \times 10^{-5}$
3	$1 \times 10^{-3} - j 7.55 \times 10^{-7}$	$1.1 \times 10^{-4} - j 1.29 \times 10^{-6}$
4	$1 \times 10^{-4} - j 6 \times 10^{-8}$	$7 \times 10^{-6} - j 2.5 \times 10^{-7}$
5	$1 \times 10^{-5} - j 5.06 \times 10^{-9}$	$5.6 \times 10^{-7} - j 2.94 \times 10^{-8}$
6	$1 \times 10^{-6} - j 4.4 \times 10^{-10}$	$4.8 \times 10^{-8} - j 3.1 \times 10^{-9}$
7	$1 \times 10^{-7} - j 3.8 \times 10^{-11}$	$4.3 \times 10^{-9} - j 3.05 \times 10^{-10}$
8	$1 \times 10^{-8} - j 3.42 \times 10^{-12}$	$3.88 \times 10^{-10} - j 2.97 \times 10^{-11}$
9	$1 \times 10^{-9} - j 3.09 \times 10^{-13}$	$3.52 \times 10^{-11} - j 2.87 \times 10^{-12}$
10	$1 \times 10^{-10} - j 2.818 \times 10^{-14}$	$3.22 \times 10^{-12} - j 2.75 \times 10^{-13}$
11	$1 \times 10^{-11} - j 2.59 \times 10^{-15}$	$2.97 \times 10^{-13} - j 2.63 \times 10^{-14}$
12	$1 \times 10^{-12} - j 2.4 \times 10^{-16}$	$2.76 \times 10^{-14} - j 2.5 \times 10^{-15}$
13	$1 \times 10^{-13} - j 2.23 \times 10^{-17}$	$2.57 \times 10^{-15} - j 2.4 \times 10^{-16}$
14	$1 \times 10^{-14} - j 2.09 \times 10^{-18}$	$2.41 \times 10^{-16} - j 2.3 \times 10^{-17}$
15	$1 \times 10^{-15} - j 1.96 \times 10^{-19}$	$2.27 \times 10^{-17} - j 2.2 \times 10^{-18}$
16	$1 \times 10^{-16} - j 1.85 \times 10^{-20}$	$2.14 \times 10^{-18} - j 2.11 \times 10^{-19}$
17	$1 \times 10^{-17} - j 1.74 \times 10^{-21}$	$2.025 \times 10^{-19} - j 2.03 \times 10^{-20}$
18	$1 \times 10^{-18} - j 1.66 \times 10^{-22}$	$1.92 \times 10^{-20} - j 1.95 \times 10^{-21}$
19	$1 \times 10^{-19} - j 1.58 \times 10^{-23}$	$1.83 \times 10^{-21} - j 1.88 \times 10^{-22}$
20	$1 \times 10^{-20} - j 1.5 \times 10^{-24}$	$1.75 \times 10^{-22} - j 1.81 \times 10^{-23}$

$$\bar{\rho}_0 = \frac{\rho_0}{\lambda_0}$$



Table 2. Values of Coefficients  $A_{2n}$ 

$n$	$A_{2n}$
0	$1.44 - j .1719$
1	$.452 - j .204$
2	$9.23 \times 10^{-3} - j 3.3 \times 10^{-2}$
3	$-1.987 \times 10^{-3} - j 1.08 \times 10^{-3}$
4	$-8.29 \times 10^{-5} + j 7.24 \times 10^{-5}$
5	$2.75 \times 10^{-6} + j 3.5 \times 10^{-6}$
6	$1.29 \times 10^{-7} - j 9.9 \times 10^{-8}$
7	$-1.64 \times 10^{-9} + j 6.19 \times 10^{-9}$
8	$-1.46 \times 10^{-9} - j 8.72 \times 10^{-9}$
9	$1.03 \times 10^{-9} + j 6.68 \times 10^{-9}$
10	$-7.38 \times 10^{-10} - j 4.8 \times 10^{-9}$
11	$4.88 \times 10^{-10} + j 3.17 \times 10^{-9}$
12	$-2.393 \times 10^{-10} - j 1.55 \times 10^{-9}$
13	$6.05 \times 10^{-11} + j 3.91 \times 10^{-10}$



# FORMULATING RADAR CROSS SECTION EXPRESSION

(6) The incident electric field polarized in the z-direction is given by

$$u_z^i = u_0 e^{-j k \rho \cos \phi} \quad (20)$$

Using wave transformation technique (6), eq. (20) becomes

$$u_z^i = u_0 \sum_{m=-\infty}^{\infty} j^{-m} J_m(k\rho) e^{j m \phi} \quad (21)$$

The scattered field takes the form

$$u_z^s = u_0 \sum_{m=-\infty}^{\infty} j^{-m} A_m^{(2)}(k\rho) e^{j m \phi} \quad (22)$$

Similarly, the field inside the cylinder is given by

$$u_z = u_0 \sum_{m=-\infty}^{\infty} j^{-m} B_m E_m(k\rho) e^{j m \phi} \quad (23)$$

Where  $A_m$  and  $B_m$  are constants which are determined later by applying the boundary condition on the "surface" of the cylinder.  $E_m(\rho)$  is given in eq. (8) and its numerical value for each value of  $m$  is computed with the aid of the matrix eq. (19). Knowing the electric fields the corresponding magnetic field can be easily derived by using the Maxwell equation

$$\nabla \times \mathbf{E} = -\mu \frac{\partial \mathbf{H}}{\partial t}$$

They are

$$H_\phi^i = \frac{u_0}{\eta_0} \sum_{m=-\infty}^{\infty} j^{-(m+1)} \frac{\partial J_m(k\rho)}{\partial(k\rho)} e^{j m \phi} \quad (24)$$

$$H_\phi^s = \frac{u_0}{\eta_0} \sum_{m=-\infty}^{\infty} j^{-(m+1)} A_m \frac{\partial H_m^{(2)}(k\rho)}{\partial(k\rho)} e^{j m \phi} \quad (25)$$

and

$$H_\phi = \frac{u_0}{\eta_0 k} \sum_{m=-\infty}^{\infty} j^{-(m+1)} B_m \frac{\partial E_m(\rho)}{\partial \rho} e^{j m \phi} \quad (26)$$

where

$$\eta_0 = \sqrt{\frac{\mu_0}{\epsilon_0}}$$



At the "surface" of the cylinder, where  $\rho = \rho_0$ , the following boundary condition applies:

$$H_\phi = H_\phi^i + H_\phi^s \quad (27)$$

and

$$u_z = u_z^i + u_z^s \quad (28)$$

Substituting the field expressions from eqs. (21) to (26) into eqs. (27) and (28) and solving for  $A_m$  gives

$$A_m = - \frac{E_m(\rho_0) \frac{\partial J_m(k\rho)}{\partial(k\rho)} \Big|_{\rho=\rho_0} - J_m(k\rho_0) \frac{E(\rho)}{(k\rho)} \Big|_{\rho=\rho_0}}{\frac{\partial H_m^{(2)}(k\rho)}{\partial(k\rho)} \Big|_{\rho=\rho_0} E_m(\rho_0) - H_m^{(2)}(k\rho_0) \frac{\partial E(\rho)}{\partial(k\rho)} \Big|_{\rho=\rho_0}} \quad (29)$$

The backscattering radar cross section is defined by

$$\sigma = 2k L^2 \left| \frac{u_z^s}{u_z^i} \right|^2 \quad (30)$$

where  $k = \frac{2\pi}{\lambda_0}$ ,  $L$  is the length of the cylinder and  $u_z^s$  is evaluated at the point where the radar is located, and  $u_z^i$  is evaluated usually at  $\rho = 0$ .

So using the asymptotic expression for  $H_m^{(2)}(k\rho)$ , substituting eqs. (22) and (21) into eq. (30), and setting  $\phi = \pi$  (because of backscattering), the following expression is obtained

$$\sigma = \frac{4L^2}{\pi} \left| \sum_{m=0}^{\infty} \epsilon_m (-1)^m A_m \right|^2 \quad (31)$$

where  $\epsilon_m$  is the Neumann number.

Expression (31) is not easy to compute numerically.  $A_m$  given by eq. (29) involves besides  $E_m(\rho)$  and its derivative, Bessel functions of the first and second kind and their derivatives. In those cases where the numerical values of  $E_m(\rho)$  are obtained by summing a large number of terms, high order Bessel function and derivatives are required in computing  $\sigma$ . But the magnitude of high order Bessel functions of first kind becomes very small



whereas that of the second kind increases to a rather high value making the summation very difficult. The method used in obtaining  $E_m(\rho)$  in this paper enables the summation in (31) to be terminated at a small value of  $m$  before the Bessel function behaves radically different from each other. For example, using values of

$$E_m(\bar{\rho}_0) \text{ and } \left. \frac{\partial E_m}{\partial \bar{\rho}} \right|_{\bar{\rho} = \bar{\rho}_0}$$

from Table 1, 18 terms of eq. (31), gives  $\sigma \approx 1.69 \times 10^2 \text{ ft}^2$  for  $L = 100 \text{ ft}$ .

#### DISCUSSION

Numerical results presented here are for illustrative purposes. In cases where the ratio of radius to propagation frequency is large, either an iteration process or an increase in the number of terms of the Chebyshev series in approximating the field equation is necessary.

Although error analysis (2, 3) is difficult in applying the Chebyshev method to the field equation, yet if the values of  $r$ 's are much smaller than those of the first few coefficients of the finite Chebyshev series, a good approximate solution is obtained.

#### ACKNOWLEDGEMENT

The author is grateful to Mr. N. A. Logan for his numerous suggestions on the use of the Chebyshev method and to Dr. T. H. Lee for his encouragement and valuable suggestions in the preparation of this paper.



### Appendix A

Derivation of  $x T_n'(x)$  And  $x^2 T_n''(x)$  In Terms of  $T_n(x)$ 's.

The  $T_n(x)$ 's are the Chebyshev polynomials of the first kind (5). In order to find  $xT_n'(x)$  in terms of the  $T_n(x)$ 's, start with the following:

$$\begin{aligned} T_3(x) &= 4x^3 - 3x \\ T_3'(x) &= 12x^2 - 3 \\ &= 6(T_2(x) + T_0(x)) \\ T_4(x) &= 8x^4 - 8x^2 + 1 \\ T_4'(x) &= 32x^3 - 16x \\ &= 8(4x^3 - 3x) + 8x \\ &= 8(T_3(x) + T_1(x)) \end{aligned}$$

and

$$\begin{aligned} T_5(x) &= 16x^5 - 20x^3 + 5x \\ T_5'(x) &= 80x^4 - 60x^2 + 5 \\ &= 10(8x^4 - 8x^2 + 1) + 10(2x^2 - 1) + 5 \\ &= 10(T_4(x) + T_2(x) + T_0(x)) \end{aligned}$$

From the above one has in general

$$T_n'(x) = 2n (T_{n-1}(x) + T_{n-3}(x) + \dots + \begin{matrix} T_1 \\ T_0 \end{matrix}) \quad \begin{matrix} \text{for } n \text{ even} \\ \text{for } n \text{ odd} \end{matrix} \quad (\text{A})$$

so

$$xT_n'(x) = 2n \left[ xT_{n-1} + xT_{n-3} + \dots + \begin{matrix} xT_1 \\ x \cdot T_0 \end{matrix} \right] \quad (\text{B})$$

By the use of the recurrence relation

$$xT_n(x) = \frac{T_{n+1}(x) + T_{|n-1|}(x)}{2} \quad (\text{C})$$

(B) can be written

$$xT_n'(x) = n \left[ T_n(x) + 2T_{|n-2|} + 2T_{|n-4|} + \dots + \begin{matrix} 2T_1(x) \\ T_0(x) \end{matrix} \right] \quad \begin{matrix} n \text{ odd} \\ n \text{ even} \end{matrix} \quad (\text{D})$$

Replacing  $n$  by  $2n$  one has

$$xT_{2n}'(x) = 2n \left[ T_{2n}(x) + 2T_{2|n-1|} + 2T_{2|n-2|} + \dots + T_0(x) \right] \quad (\text{E})$$



From (A), the second derivative is

$$T_n''(x) = 2n[T_{n-1}'(x) + T_{n-3}'(x) + \dots] \quad (F)$$

again using (A), (F) becomes

$$\begin{aligned} T_n''(x) = 2n[ & 2(n-1)(T_{n-2}(x) + T_{n-4}(x) + T_{n-6}(x) + \dots) \\ & + 2(n-3)(T_{n-4}(x) + T_{n-6}(x) + \dots) + 2(n-5)(T_{n-6}(x) \\ & + T_{n-8}(x) + \dots) + \dots] \end{aligned}$$

or

$$T_n''(x) = 4n \left\{ (n-1) T_{n-2}(x) + [(n-1) + (n-3)] T_{n-4}(x) \right. \\ \left. + [(n-1) + (n-3) + (n-5)] T_{n-6}(x) + \dots \right\}$$

Multiplying the last expression by  $x$  and using (C) gives

$$\begin{aligned} xT_n''(x) = 2n \left\{ (n-1) T_{n-1}(x) + [2(n-1) + (n-3)] T_{n-3}(x) \right. \\ \left. + [2(n-1) + 2(n-3) + (n-5)] T_{n-5}(x) + \dots \right. \\ \left. + [2(n-1) + 2(n-3) + 2(n-5) + 2(n-7) + \dots] \right. \\ \left. \begin{matrix} T_1 \\ T_0 \end{matrix} \right\} \quad \begin{matrix} n \text{ even} \\ n \text{ odd} \end{matrix} \quad (G) \end{aligned}$$

Multiplying by  $x$  again and using (C)

$$\begin{aligned} x^2 T_n''(x) = n \left\{ (n-1) T_n(x) + \left\{ 3(n-1) + (n-3) \right\} T_{n-2}(x) \right. \\ \left. + \left\{ 4(n-1) + 3(n-3) + (n-5) \right\} T_{n-4}(x) \right. \\ \left. + \left\{ 4(n-1) + 4(n-3) + 3(n-5) + (n-7) \right\} T_{n-6}(x) \right. \\ \left. + \left\{ 4(n-1) + 4(n-3) + 4(n-5) + \dots \right\} \right. \\ \left. \begin{matrix} T_1(x) \\ T_0(x) \end{matrix} \right\} \quad \begin{matrix} n \text{ odd} \\ n \text{ even} \end{matrix} \quad (H) \end{aligned}$$

After replacing  $n$  by  $2n$ , expression (H) can be written

$$\begin{aligned} x^2 T_{2n}''(x) = 2n(2n-1) T_{2n}(x) + 2n \sum_{k=1}^{n-1} (8kn - (2k)^2 - 2) T_{2(n-k)}(x) \\ + 2n(2n^2-1) T_0(x) \quad (I) \end{aligned}$$



Appendix B

Elements of the b-matrix:

For  $n=0$ , from (17)

$$b_{21} = \frac{2}{4} a_0 + \frac{6}{16} a_1 + \frac{20}{64} a_2 + \frac{70}{256} a_3$$

$$b_{31} = \frac{2}{4} a_0 + \frac{8}{16} a_1 + \frac{30}{64} a_2 + \frac{112}{256} a_3$$

$$b_{41} = \frac{2}{16} a_1 + \frac{12}{64} a_2 + \frac{56}{256} a_3$$

$$b_{51} = \frac{2}{64} a_2 + \frac{16}{256} a_3$$

$$b_{61} = \frac{2}{256} a_3$$

$$\text{and } b_{71} = b_{81} = \dots = 0$$

$$a_0 = \left( \frac{2\pi}{\lambda_0} \beta \right)^2 \epsilon_1, \quad a_1 = (2\pi)^2 \epsilon_2 \left( \frac{\beta}{\lambda_0} \right)^4, \quad a_2 = (2\pi)^2 \epsilon_3 \left( \frac{\beta}{\lambda_0} \right)^6$$

$$\text{and } a_3 = (2\pi)^2 \epsilon_4 \left( \frac{\beta}{\lambda_0} \right)^8$$

Similarly, for  $n=1$ 

$$b_{22} = 4(2m+1) + \frac{1}{4} a_0 + \frac{4}{16} a_1 + \frac{15}{64} a_2 + \frac{56}{256} a_3$$

$$b_{42} = \frac{1}{4} a_0 + \frac{4}{16} a_1 + \frac{16}{64} a_2 + \frac{64}{256} a_3$$

$$b_{52} = \frac{1}{16} a_1 + \frac{6}{64} a_2 + \frac{29}{256} a_3$$

$$b_{62} = \frac{1}{64} a_2 + \frac{8}{256} a_3$$

$$b_{72} = \frac{1}{256} a_3$$

$$\text{and } b_{82} = b_{92} = \dots = 0$$

Elements of column 3 are

$$b_{23} = 28 + 4(2m+1) + \frac{1}{16} a_1 + \frac{6}{64} a_2 + \frac{28}{256} a_3$$

$$b_{33} = 40 + 8(2m+1) + \frac{1}{4} a_0 + \frac{4}{16} a_1 + \frac{16}{64} a_2 + \frac{64}{256} a_3$$

$$b_{43} = 12 + 4(2m+1) + \frac{2}{4} a_0 + \frac{6}{16} a_1 + \frac{20}{64} a_2 + \frac{71}{256} a_3$$

$$b_{53} = \frac{1}{4} a_0 + \frac{4}{16} a_1 + \frac{15}{64} a_2 + \frac{56}{256} a_3$$

$$b_{63} = \frac{1}{16} a_1 + \frac{6}{64} a_2 + \frac{28}{256} a_3$$

$$b_{73} = \frac{1}{64} a_2 + \frac{8}{256} a_3$$

$$b_{83} = \frac{1}{256} a_3$$

$$\text{and } b_{93} = b_{10,3} = \dots = 0$$



Elements of column 4 are

$$b_{24} = 102 + 6(2m+1) + \frac{1}{64}a_2 + \frac{8}{256}a_3$$

$$b_{34} = 180 + 12(2m+1) + \frac{1}{16}a_1 + \frac{6}{64}a_2 + \frac{29}{256}a_3$$

$$b_{44} = 108 + 12(2m+1) + \frac{1}{4}a_0 + \frac{4}{16}a_1 + \frac{15}{64}a_2 + \frac{56}{256}a_3$$

$$b_{54} = 30 + 6(2m+1) + \frac{2}{4}a_0 + \frac{6}{16}a_1 + \frac{20}{64}a_2 + \frac{70}{256}a_3$$

$$b_{64} = \frac{1}{4}a_0 + \frac{4}{16}a_1 + \frac{15}{64}a_2 + \frac{56}{256}a_3$$

$$b_{74} = \frac{1}{16}a_1 + \frac{6}{64}a_2 + \frac{25}{256}a_3$$

$$b_{84} = \frac{1}{64}a_2 + \frac{8}{256}a_3$$

$$b_{94} = \frac{1}{256}a_3$$

$$\text{and } b_{10,4} = b_{11,4} = \dots = 0$$

Elements of column 5 are

$$b_{25} = 248 + 8(2m+1) + \frac{1}{256}a_3$$

$$b_{35} = 464 + 16(2m+1) + \frac{1}{64}a_2 + \frac{8}{256}a_3$$

$$b_{45} = 368 + 16(2m+1) + \frac{1}{16}a_1 + \frac{6}{64}a_2 + \frac{28}{256}a_3$$

$$b_{55} = 56 + 8(2m+1) + \frac{2}{4}a_0 + \frac{6}{16}a_1 + \frac{20}{64}a_2 + \frac{70}{256}a_3$$

$$b_{65} = \frac{1}{4}a_0 + \frac{4}{64}a_1 + \frac{15}{64}a_2 + \frac{56}{256}a_3$$

$$b_{75} = \frac{1}{16}a_1 + \frac{6}{64}a_2 + \frac{28}{256}a_3$$

$$b_{85} = \frac{1}{64}a_2 + \frac{8}{256}a_3$$

$$b_{95} = \frac{1}{256}a_3$$

$$\text{and } b_{10,5} = b_{11,5} = \dots = 0$$

Elements of column 6 are

$$b_{26} = 490 + 10(2m+1)$$

$$b_{36} = 940 + 20(2m+1) + \frac{1}{256}a_3$$

$$b_{46} = 820 + 20(2m+1) + \frac{1}{64}a_2 + \frac{8}{256}a_3$$

$$b_{56} = 620 + 20(2m+1) + \frac{1}{16}a_1 + \frac{6}{64}a_2 + \frac{28}{256}a_3$$

$$b_{66} = 340 + 20(2m+1) + \frac{1}{4}a_0 + \frac{4}{16}a_1 + \frac{15}{64}a_2 + \frac{56}{256}a_3$$

$$b_{76} = 90 + 10(2m+1) + \frac{2}{4}a_0 + \frac{6}{16}a_1 + \frac{20}{64}a_2 + \frac{70}{256}a_3$$



$$b_{86} = \frac{1}{4} a_0 + \frac{4}{16} a_1 + \frac{15}{64} a_2 + \frac{56}{256} a_3$$

$$b_{96} = \frac{1}{16} a_1 + \frac{6}{64} a_2 + \frac{28}{256} a_3$$

$$b_{10,6} = \frac{1}{64} a_2 + \frac{8}{256} a_3$$

$$b_{11,6} = \frac{1}{256} a_3$$

$$\text{and } b_{12,6} = b_{13,6} = \dots = 0$$

Elements of column 7 are

$$b_{27} = 852 + 12 (2m+1)$$

$$b_{37} = 1656 + 24 (2m+1)$$

$$b_{47} = 1512 + 24 (2m+1) + \frac{1}{256} a_3$$

$$b_{57} = 1272 + 24 (2m+1) + \frac{1}{64} a_2 + \frac{8}{256} a_3$$

$$b_{67} = 936 + 24 (2m+1) + \frac{1}{16} a_1 + \frac{6}{64} a_2 + \frac{28}{256} a_3$$

$$b_{77} = 504 + 24 (2m+1) + \frac{1}{4} a_0 + \frac{4}{16} a_1 + \frac{15}{64} a_2 + \frac{56}{256} a_3$$

$$b_{87} = 132 + 12 (2m+1) + \frac{6}{16} a_1 + \frac{20}{64} a_2 + \frac{70}{256} a_3$$

$$b_{97} = \frac{1}{4} a_0 + \frac{4}{16} a_1 + \frac{15}{64} a_2 + \frac{56}{256} a_3$$

$$b_{10,7} = \frac{1}{16} a_1 + \frac{6}{64} a_2 + \frac{28}{256} a_3$$

$$b_{11,7} = \frac{1}{64} a_2 + \frac{8}{256} a_3$$

$$b_{12,7} = \frac{1}{256} a_3$$

$$\text{and } b_{13,7} = b_{14,7} = \dots = 0$$

Up to this point, the pattern of the b's for each column has been established and the b's of columns 8, 9, and so on, can be written down easily.

#### BIBLIOGRAPHY

- 1) C. W. Clenshaw, "The Numerical Solution of Linear Differential Equations in Chebyshev Series", Proc. Camb. Phil. Soc., 53, 1957, pp 134-119
- 2) C. Lanczos, Applied Analysis, Prentice Hall, Inc., 1961
- 3) L. Fox, "Chebyshev Methods for Ordinary Differential Equations", pp 318-331, The Computer Journal, 1962
- 4) F. B. Hildebrand, Methods of Applied Mathematics, 8th Printing, December 1961, Prentice Hall
- 5) Tables of Chebyshev Polynomials, National Bureau of Standards Applied Mathematics Series No. 9, 1952
- 6) R. F. Harrington, Time Harmonic Electromagnetic Fields, McGraw Hill, 1961, page 232



ANALYSIS OF ELECTROMAGNETIC WAVE PROPAGATION  
THROUGH RE-ENTRY INDUCED PLASMA SHEATHS

Richard R. Gold

Aerospace Corporation  
Laboratories Division  
El Segundo, California

ABSTRACT

An exact solution is obtained to the general problem of propagation of plane harmonic electromagnetic waves across a stratified plasma layer. The variation of the plasma properties in the direction normal to the layer is arbitrary, and oblique incidence is considered with no applied magnetic field. A constant magnetic field applied normal to the layer is included for the case of normal incidence. The solution is based on an integral equation formulation of the problem and is expressed as an infinite series. It is particularly useful when the ratio of slab thickness to free space wavelength ( $L/\lambda_0$ ) is small. The resultant, relatively simple algebraic expressions for the reflection and transmission coefficients give an excellent approximation in many applications of current interest.

The work described in this paper was performed under the sponsorship of the Air Force Space Systems Command, Contract No. AF 04(695)-169.



## ANALYSIS OF ELECTROMAGNETIC WAVE PROPAGATION THROUGH RE-ENTRY INDUCED PLASMA SHEATHS

Richard R. Gold

Aerospace Corporation  
Laboratories Division  
El Segundo, California

### INTRODUCTION

Virtually all of our space programs require, for one purpose or another, some consideration of electromagnetic wave propagation through the re-entry induced plasma sheath or wake. Although a number of formal solutions to the general problem of one-dimensional propagation through stratified media have been obtained (1,2,3), relatively few boundary value problems have been treated in detail (4,5). The utility of such solutions for design calculations is limited by the difficulty in abstracting numerical results since the arguments and/or orders of the special functions involved are complex numbers. High speed computers can be employed to evaluate these functions or solve the boundary value problem directly, however, it is difficult, in general, to generate meaningful computations readily. (The reader is referred to Ref. 5 for the exact analysis involving Fig. 1. Detailed calculations were made for  $L/\lambda_0 = 0.5$  and 1 covering a wide range of conditions. In addition, the asymptotic expansion of the exact solution for the Kinked-Trapezoid profile for larger values of  $L/\lambda_0$  is relatively easy to evaluate numerically.)

As a consequence of the study of this problem (5), a simplified analysis was obtained which is particularly appropriate to many applications of current interest. Thus, accurate slide rule calculations of transmission and reflection can be made for thin plasma sheaths including arbitrary distributions of electron density and collision frequency normal to the layer and oblique incidence. An applied magnetic field normal to the layer is included (for the case of normal incidence) because of the interest shown in its use to alleviate the communication "blackout" problem. The analytical solutions are of considerable value also in the study of related phenomena as is demonstrated in a companion paper by Dr. M. Epstein.

### ANALYSIS

A right-handed Cartesian coordinate system with the positive  $z$ -axis vertical is chosen, and the planes  $z = 0$  and  $z = L$  constitute abrupt boundaries between free space in the regions  $z < 0$  and  $z > L$ , and the plasma region  $0 < z < L$ . The plasma is assumed to be stratified so that its properties are functions only of  $z$ . We consider a plane wave to be obliquely



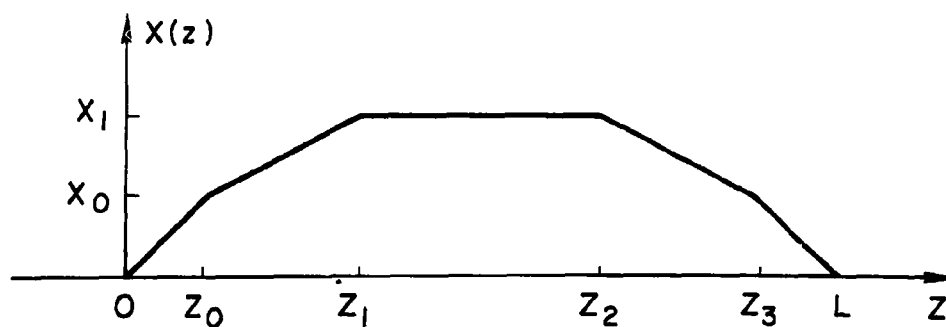


Fig. 1a. Kinked-Trapezoid Distribution of  $X(z)$

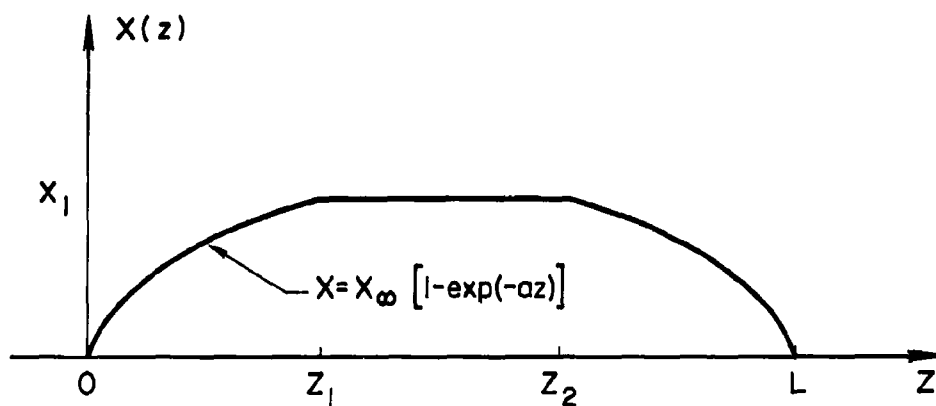


Fig. 1b. Exponential-Homogeneous-Exponential Distribution of  $X(z)$

Fig. 1. Specified Electron Density Profiles (Ref. 5)



incident at the abrupt free space-plasma boundary,  $z = 0$ , with its wave-normal in the  $x$ - $z$  plane at an angle  $\theta_I$  to the positive  $z$ -axis. Further, a steady biasing magnetic field of constant induction  $B_0$  may be applied in the positive  $z$ -direction for the case  $\theta_I = 0$ . The governing differential equation for the  $z$ -dependent electric field is of the general form (2):

$$w''(\zeta) + (n_0 L)^2 (C^2 - mX) w(\zeta) = 0 \quad (1)$$

where  $\zeta = z/L$ ,  $n_0 = 2\pi/\lambda_0$  is the free space wave propagation constant,  $\lambda_0$  is the free space wavelength, and  $C = \cos \theta_I$ . If no magnetic field is applied, Eq. (1) determines the horizontally polarized field  $w = E_y$ . In the presence of a magnetic field the governing equations for the propagation of both the right- and left-handed circularly polarized waves are of the form (1), provided that  $\theta_I = 0$ , where  $w = F_{x,l}$ ;  $F_x = E_x + iE_y$ ,  $F_l = E_x - iE_y$ . The quantities  $m$  and  $X$  which may be functions of  $\zeta$  are defined as follows:

$$X = \left(\frac{\omega_p}{\omega}\right)^2 = \frac{Ne^2}{\epsilon_0 \bar{m} \omega^2}, \quad m_r = (1 - Y - iZ)^{-1}, \quad m_l = (1 + Y - iZ)^{-1}$$

$$Y = \frac{\omega_B}{\omega} = \frac{|e| B_0}{\bar{m} \omega}, \quad Z = \frac{\omega_c}{\omega} \quad (2)$$

where  $\omega$  is the angular signal frequency,  $\omega_p$  the plasma frequency,  $\omega_c$  the collision frequency,  $\omega_B$  the electron gyrofrequency,  $N$  is the number density of electrons,  $e$  the charge,  $\bar{m}$  the mass, and  $\epsilon_0$  is the free space dielectric constant. The customary boundary conditions require that  $w$  and  $w'$  be continuous at the interfaces  $\zeta = 0$  and  $\zeta = 1$ .

The solutions in the free space regions where  $X = 0$  are,

$$w = \exp(-in_0 L C \zeta) + R \exp(in_0 L C \zeta), \quad \zeta \leq 0, \quad (3)$$

$$w = T \exp(-in_0 L C \zeta), \quad \zeta \geq 1, \quad (4)$$

where  $R$  is the reflection coefficient,  $T$  is the transmission coefficient, and the incident wave of unit amplitude is assumed to be linearly polarized, say along the  $x$ -axis,  $w = E_y = \exp(-in_0 L C \zeta)$ . Applying the boundary conditions specified above we obtain the following relations in which  $w$  refers to the solution in the plasma ( $0 \leq \zeta \leq 1$ ), the subscript "0" denoting the value of  $w$  or  $w'$  at  $\zeta = 0$  and "1" the value at  $\zeta = 1$ :

$$w'_0 = in_0 L C (w_0 - 2), \quad R = w_0 - 1, \quad (5a, b)$$

$$w'_1 = -in_0 L C w_1, \quad T = \exp(in_0 L C) w_1 \quad (6a, b)$$



Integrating (1) twice with respect to  $\zeta$  from 0 to  $\zeta$  and using (5a), one obtains the inhomogeneous Volterra integral equation of the second kind\*

$$w(\zeta) = \phi(\zeta) + (n_0 L)^2 \int_{\xi=0}^{\zeta} K(\zeta, \xi) w(\xi) d\xi, \quad 0 \leq \zeta \leq 1 \quad (7)$$

where:

$$\phi = w_0 + in_0 LC \zeta (w_0 - 2), \quad K = (\xi - \zeta) [C^2 - m(\xi) X(\xi)] \quad (8)$$

The infinite series

$$w(\zeta) = \phi(\zeta) + \sum_{r=1}^{\infty} (n_0 L)^{2r} I_{\zeta}^r \phi(\zeta) \quad (9)$$

converges to the unique continuous solution of the Volterra equation (7) for all values of  $n_0 L$ , in any interval in which the Kernel  $K(\zeta, \xi)$  is continuous; the integral operator  $I_{\zeta}$  is defined by the relation

$$I_{\zeta} \phi(\zeta) \equiv \int_{\xi=0}^{\zeta} K(\zeta, \xi) \phi(\xi) d\xi \quad (10)$$

Applying the boundary condition (6a) we obtain the following relation for the unknown  $w_0$ :

$$\begin{aligned} w_0 \left[ iC(2 + in_0 LC) - n_0 L \left[ A_1 + (n_0 L)^2 A_2 + (n_0 L)^4 A_3 + \dots \right] \right] \\ = 2iC \left[ 1 + in_0 LC - (n_0 L)^2 \bar{A}_1 - (n_0 L)^4 \bar{A}_2 - (n_0 L)^6 \bar{A}_3 - \dots \right] \quad (11) \end{aligned}$$

$$A_1 = \int_{\xi=0}^1 q^2 h g d\xi, \quad A_2 = \int_{\xi=0}^1 q^2 g d\xi \int_{\xi_1=0}^{\xi} (\xi_1 - \xi) q^2 h d\xi_1,$$

$$A_3 = \int_{\xi=0}^1 q^2 g d\xi \int_{\xi_1=0}^{\xi} (\xi_1 - \xi) q^2 d\xi_1 \int_{\xi_2=0}^{\xi_1} (\xi_2 - \xi_1) q^2 h d\xi_2$$

\*The integral equation formulation and resultant formal solution were developed jointly by Dr. M. Epstein and the Author.



where  $q^2 = C^2 - mX$ ,  $g(\xi) = 1 + in_0LC - in_0LC\xi$ ,  $h(\eta) = 1 + in_0LC\eta$ , and  $\bar{A}_1, \bar{A}_2, \bar{A}_3$  are obtained by substituting  $\bar{h}(\eta) = \eta$  in place of  $h$ . The number of terms which must be retained will depend on the magnitude of  $n_0L$  and the integral expressions. Solving the resultant linear algebraic equation for  $w_0$  we obtain the reflection coefficient from (5b), determine  $w_1$  from (7) in a consistent manner, and hence the transmission coefficient from Eq. (6b).

The solution outlined above involves three independent parameters, namely,  $n_0L$ ,  $|mX|_{\max}$ , and the functional form of  $mX$  which affects the integral expressions. Let us introduce the following notation:

$$\delta = |m(\xi)X(\xi)|_{\max} = \{X(\xi)[(1 - Y)^2 + Z^2(\xi)]^{-1/2}\}_{\max},$$

$$\mu_0 = \delta \int_{\xi=0}^1 f d\xi = \delta \mu'_0, \quad \mu_1 = \delta \int_{\xi=0}^1 \xi f d\xi = \delta \mu'_1, \quad (12)$$

$$\nu = \delta^2 \int_{\xi=0}^1 \int_{\xi_1=0}^{\xi} (\xi_1 - \xi) f(\xi_1) f(\xi) d\xi_1 d\xi = \delta^2 \nu',$$

where  $X^{1/2}$ ,  $Z$ , and  $Y$  are the ratios of plasma frequency, collision frequency, and cyclotron frequency to the signal frequency, respectively, and  $f(\xi) = m(\xi)X(\xi)/\delta$ , hence,  $|f| \leq 1$ . Note that when  $\delta$  is very large it is essentially a measure of the maximum magnitude of the index of refraction  $n^*(n^{*2} = 1 - mX)$ , that is,

$$\delta \approx |n^{*2}|_{\max} \text{ for } \delta \gg 1$$

It should be noted also that the maximum magnitudes of the integrals, corresponding to  $|f| = 1$ , are of the order:  $|\mu'_0| \sim 1$ ,  $|\mu'_1| \sim 1/2$ ,  $|\nu'| \sim 1/6$ . The actual magnitude of these quantities may be substantially smaller in view of the variation of  $mX$ . To illustrate, let  $Z = \omega_c/\omega$  be constant so that the functional dependence is real, say of the quadratic form:  $f(\xi) = mX(\xi)/|m|X_1 = 4m(\xi - \xi^2)/|m|$ , where  $m$  is now constant and  $X_1$  is the maximum value of  $X$  in the plasma. The corresponding magnitude of  $\mu'_0$ ,  $\mu'_1$ , and  $\nu'$  is  $2/3$ ,  $1/3$ , and  $1/45$ , respectively; the latter is almost an order of magnitude less than the maximum value noted above.

Further examination of Eq. (11) shows that in order to obtain reasonably simple expressions for calculation purposes the quantity  $n_0L$  should be at most of order 1. Assuming that  $n_0L (= \epsilon, \text{ say}) \ll 1$  and  $|\mu'_0|$ ,  $|\mu'_1|$ , and  $C$  are of order 1, expressions for the reflection and transmission coefficients are obtained by systematically ordering  $\delta$  and  $|\nu'|$  with respect to  $\epsilon$ . The following principal results are obtained subject



to the formal requirement:

$$|(n_0 L)^3 \nu|_{\max} = \left| \frac{(n_0 L)^3 X^2(\zeta)}{(1 - Y)^2 + Z^2(\zeta)} \int_{\xi=0}^1 \int_{\xi_1=0}^{\xi} (\xi_1 - \xi) f(\xi_1) f(\xi) d\xi_1 d\xi \right|_{\max} \leq 0(1) \quad (13)$$

(A number of re-entry communication applications can be shown to satisfy this condition as will be noted in the next section.) For  $\delta = 0(1/\epsilon^2)$  [that is, the maximum magnitude of the index of refraction is of order  $(n_0 L)^{-1}$ ]:

$$R = \frac{-n_0 L \mu_0 + (n_0 L)^2 (2iC \mu_1 - iC \mu_0 + n_0 L \nu)}{n_0 L \mu_0 + [2iC + (n_0 L)^2 (iC \mu_0 - n_0 L \nu)]} + 0(\epsilon^2) \quad (14)$$

$$T = \frac{2iC}{n_0 L \mu_0 + [2iC + (n_0 L)^2 (iC \mu_0 - n_0 L \nu)]} + 0(\epsilon^2) \quad (15)$$

In this case,  $|R| = 0(1)$ ,  $|T| = 0(\epsilon)$ . If  $\delta \leq 0(1/\epsilon)$  Eqs. (14) and (15) can be further simplified; in particular, when  $|(n_0 L)^3 \nu| = 0(\epsilon^2)$ , the zeroth order solution for the transmission coefficient becomes:

$$T = \frac{2iC}{2iC + n_0 L \mu_0} + 0(\epsilon^2) \quad (16)$$

Equation (16) is valid formally, therefore, if  $\delta = 0(1/\epsilon)$  [that is,  $|n^*|_{\max}$  of order  $(n_0 L)^{-1/2}$ ] and  $|\nu| = 0(\epsilon)$ . It is also valid, to the given order, if  $\delta = 0(1)$ , regardless of the value of  $|\nu|$  in which case  $|R| = 0(\epsilon)$  and  $|T| = 0(1)$ , as expected. The same limiting result was obtained in the appendix of Ref. 1 using a delta function representation for  $mX$  in Eq. (1).

## DISCUSSION

By means of the preceding formal consideration, relatively simple expressions have been derived for  $R$  and  $T$  involving integrals of the form shown in Eq. (12). The solutions are valid for small values of  $n_0 L$ , provided that  $|(n_0 L)^3 \nu|$  is at most of order 1 [Eq. (13)]. If  $\delta \leq 0(1/\epsilon)$ , accurate results may be obtained from the simple zeroth order solution (16). When  $\delta = 0(1/\epsilon^2) \approx |n^*|_{\max}^2$ , Eq. (15) should be used in which case  $|T| \ll 1$ . In the remainder of this section we will analyze these results quantitatively using available exact solutions. An illustrative application will be cited also to demonstrate the appropriateness and utility of the present solutions. It is of particular interest, however, to emphasize the following observation. The solutions (14), (15), and (16), perhaps fortuitously, give the correct limiting values,  $|R| = 1$  and  $|T| = 0$  as  $\delta \rightarrow \infty$  for fixed  $n_0 L$ . In addition, since (14) and (15) apply when  $|R|$  is close to one



and  $T$  is small, useful results may be obtained even outside the formal interval (13) (in the analysis of propagation through re-entry plasma sheaths, for example, accurate estimates are frequently not necessary in such cases). This point will be examined also in the following discussion.

Exact solutions to the present boundary value problem using the differential Eq. (1) were derived in Ref. 5 assuming constant collision frequency and the two classes of electron density distributions shown in Fig. 1. In this case,

$$\mu_0 = mX_1 c_0, \quad \nu = (mX_1)^2 c_2, \quad \delta = X_1 [(1 - Y)^2 + Z^2]^{-1/2}$$

where,

$$c_0 = \int_{\xi=0}^1 \chi d\xi, \quad c_2 = \int_{\xi=0}^1 \int_{\xi_1=0}^{\xi} (\xi_1 - \xi) \chi(\xi_1) \chi(\xi) d\xi_1 d\xi,$$

$\chi(\xi) = X(\xi)/X_1$ ,  $X_1$  is the maximum value of  $X(\xi)$  in the interval and  $m$  is constant [Eq. (2)]. For the exponential profile  $c_0 = 0.62$  and  $c_2 = -0.0382$ , when  $z_1/L = 0.5$ ,  $aL = 3$ . Similarly, for the triangular distribution ( $X_0/X_1 = z_0/z_1$ ,  $z_1/L = 0.5$ )  $c_0 = 0.5$  and  $c_2 = -0.0292$ . The exact values obtained for the exponential profile (normal incidence) are compared with the present approximate results in Figs. 2 through 5. The parameters  $\delta$  and  $|(n_0 L)^3 \nu|$  are annotated on the graphs.

Since  $\delta$  is at most of order  $1/n_0 L$  in Fig. 2 ( $n_0 L = 0.00628$ ) and  $|(n_0 L)^3 \nu| \ll 1$ , the zeroth order results obtained from Eq. (16) cannot be distinguished from the exact values. A similar situation exists in Fig. 3 ( $n_0 L = 0.0628$  for  $Z = 10$  and  $100$ ). For  $Z = 1$  the formal limit (13) is satisfied. Agreement is good at  $X_1 = 1,000$  using (16) even though  $\delta = 0 [1/(n_0 L)^2]$  and is excellent when the appropriate Eq. (15) is used. Note the small level of transmission involved, namely  $\text{db}_T = -24.60$ . In Fig. 4 ( $n_0 L = 0.628$ ),  $(n_0 L)^2 \delta = 4.07$  and  $|(n_0 L)^3 \nu| = 1.0$  at  $X_1 = 14.6$ . The agreement indicated for larger values of  $X_1$  is due in part to the fortunate form of the solutions discussed above. Thus, depending on the accuracy required, (16) or (15) may be used to estimate transmission for values of  $X_1$  as large as  $100 [|(n_0 L)^3 \nu| = 47.2]$  where the level of transmission is extremely small. The present results are considerably less accurate in Fig. 4 than in the preceding two figures (for the same value of the parameter) due to the increase in  $n_0 L$ . It follows that for smaller values of  $n_0 L$  substantially better agreement is obtained than shown in Fig. 4 for the corresponding value of  $|(n_0 L)^3 \nu| \gg 1$ . A non-zero value of  $Y$  for a given set of conditions would decrease  $\delta$  and hence improve the correlation, as shown in Fig. 5. The parameter  $|(n_0 L)^3 \nu|$  is reduced by an order of magnitude for  $Y = 5$  so that it is equal to  $1.38$  at  $X_1 = 50$ . The level of accuracy at this point and for larger values of  $X_1$  is comparable to that shown in Fig. 4, however, by contrast, larger losses are now predicted by the approximate expressions.



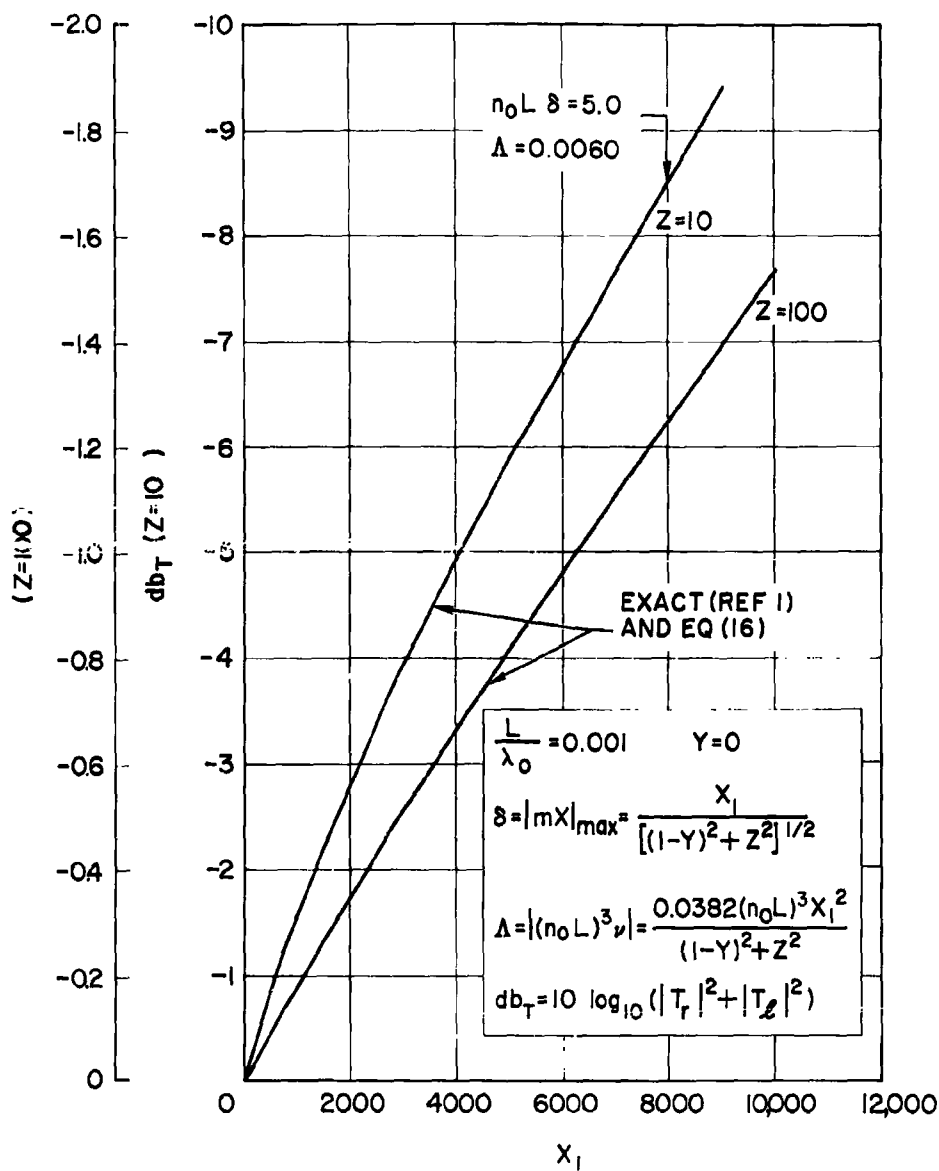


Fig. 2. Degradation in Transmitted Energy,  $db_T$ , versus  $X_1$   
 $(L/\lambda_0 = 0.001, Y = 0)$



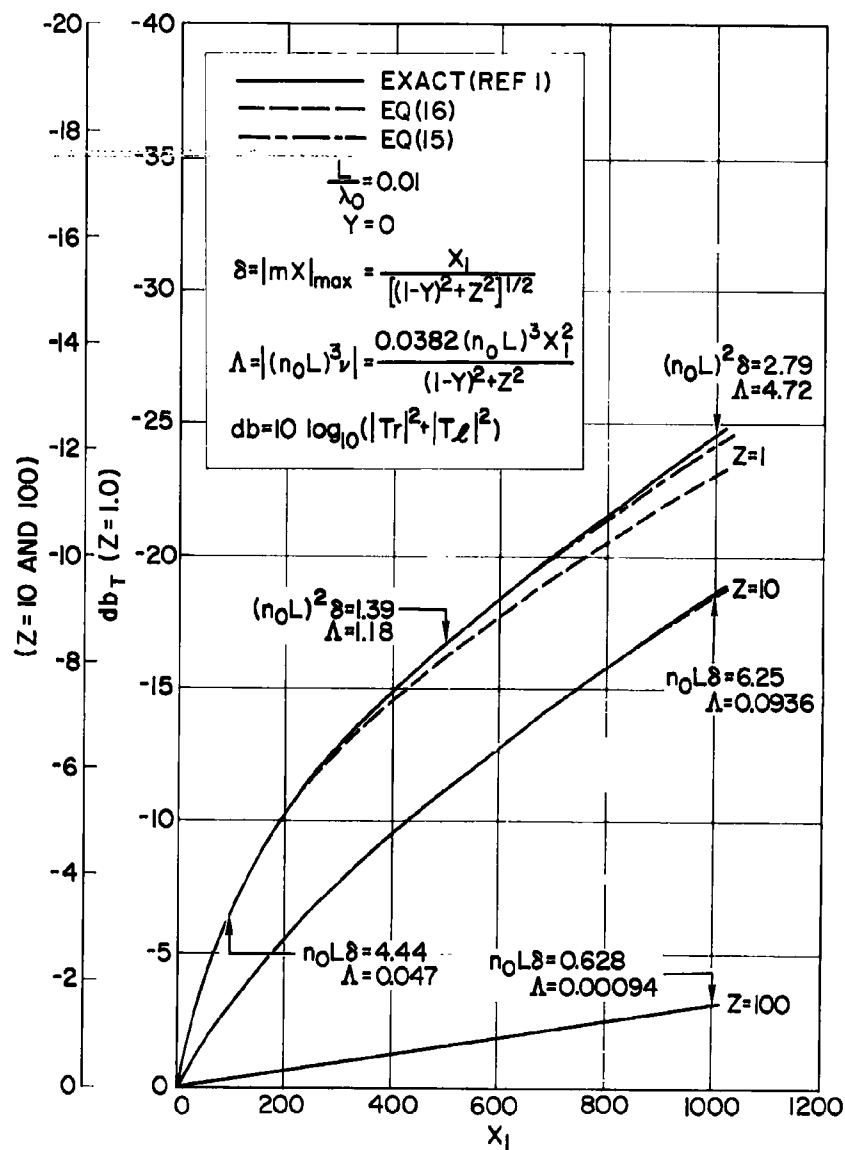


Fig. 3. Degradation in Transmitted Energy,  $dbT$ , versus  $X_1$   
 $(L/\lambda_0 = 0.01, Y = 0)$



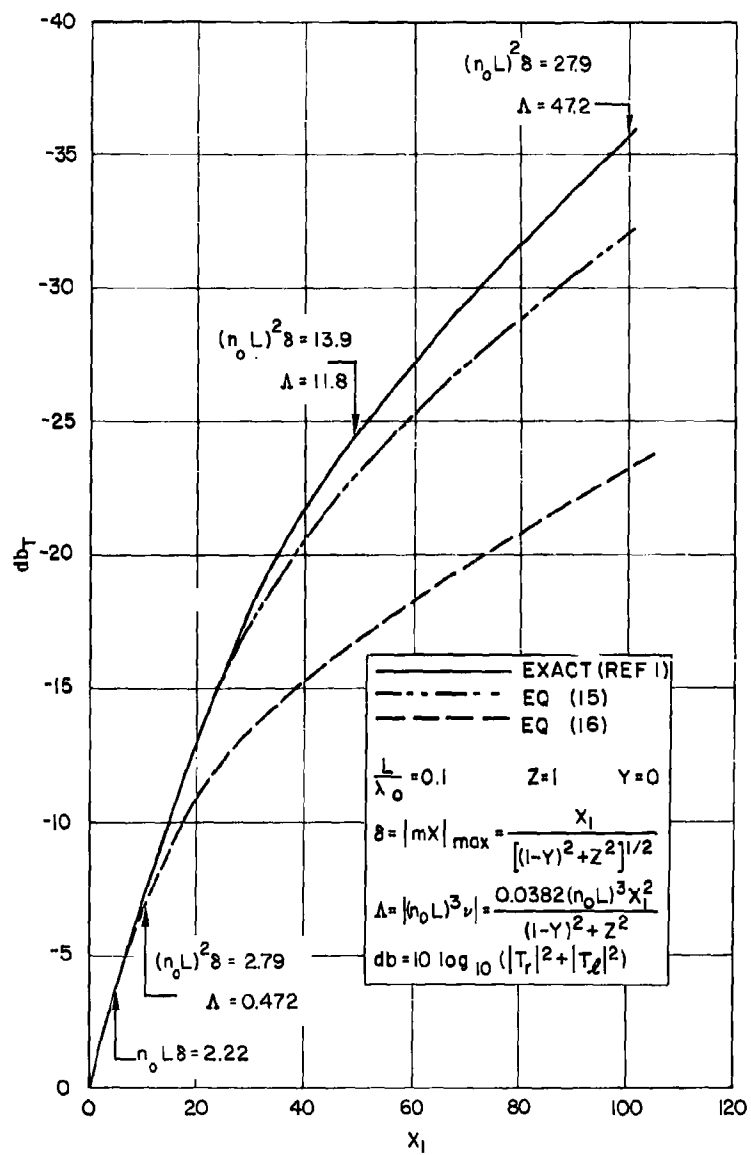


Fig. 4. Degradation in Transmitted Energy,  $db_T$ , versus  $X_1$   
 $(L/\lambda_0 = 0.1, Y = 0)$



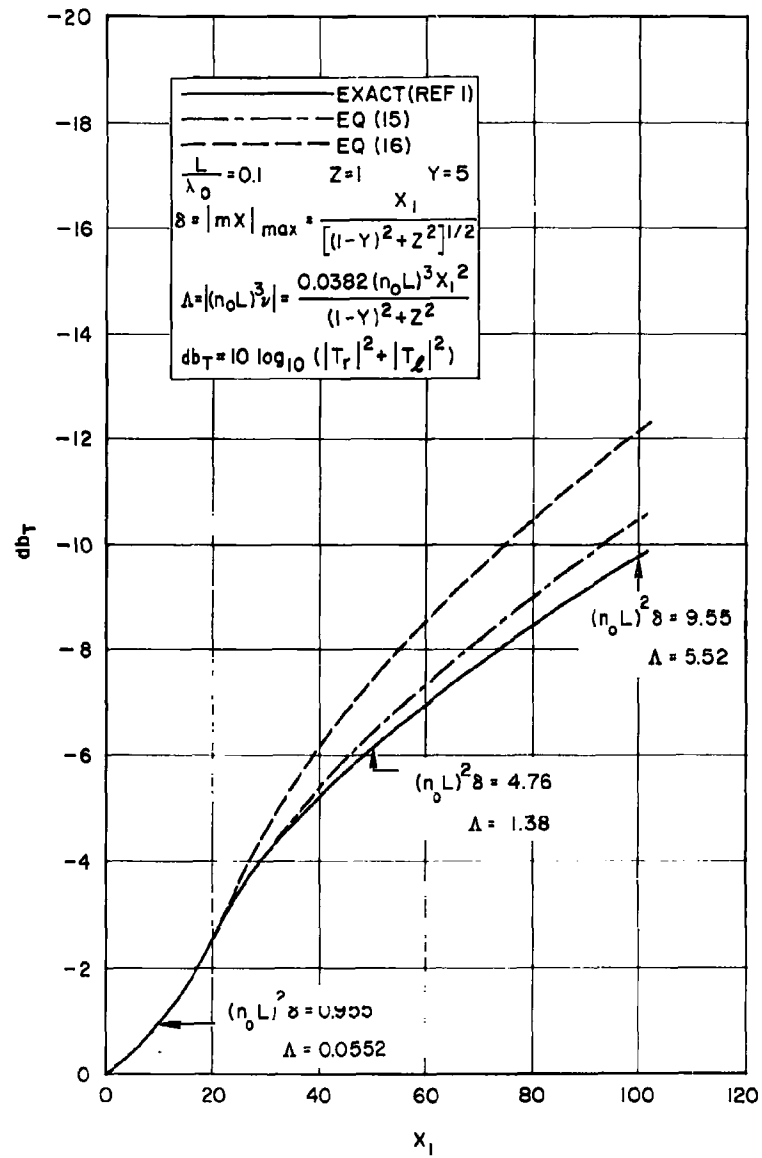


Fig. 5. Degradation in Transmitted Energy,  $db_T$ , versus  $X_1$   
 $(L/\lambda_0 = 0.1, Y = 5)$



To demonstrate the applicability of the present analysis, a 10-degree half-angle cone was considered at zero angle of attack. Equilibrium boundary layer calculations were made for a range of flight conditions (22,000 to 26,000 ft per sec re-entry velocity at altitudes from 50,000 to 150,000 ft) to determine the maximum enthalpy and temperature, from which the maximum plasma properties were obtained. The boundary layer or slab thickness was computed for a wall temperature of 1500°K and axial length of 11 ft. Several detailed computations resulted in the following interesting conclusion with respect to the actual variation of collision frequency  $\omega_c$ . The maximum value occurs at the outer edge of the boundary layer. As much as an order of magnitude decrease may be experienced from this value to the minimum value in the boundary layer. A hot wall condition would result in a subsequent increase as the wall is approached. One can show readily, however, that in thin re-entry induced plasma sheaths of this type the strong variation in  $\omega_c$  occurs in those regions in which the plasma frequency is small. The use of  $\omega_c = \text{constant}$ , evaluated at the point where  $X = X_1$ , is a good approximation, therefore, since the integrated value of the product  $m(z)X(z)$  is only slightly altered.

Frequencies of 240 Mc and 3 kMc were assumed. A quadratic distribution of  $X$  was considered based on the maximum values and the corresponding constant value of  $Z$  was computed. In every case it was found that  $|(n_0 L)^3 \nu| < 1$ . It was found further that the conditions calculated were all within the parametric range included in Figs. 2 through 4. Extremely accurate transmission calculations would be obtained from (16) for the majority of the cases considered since  $n_0 L \ll 1$ . Sufficient accuracy would be obtained also using (16) in the several cases where  $n_0 L = 0.7$  since the maximum value of  $X$  involved was less than 10. More specific examples of interest may be derived using the results given in Ref. 6.

### CONCLUSION

A formal series solution has been obtained which is found to be particularly useful in the analysis of plane electromagnetic wave propagation through re-entry induced plasma sheaths or wakes. Arbitrary variations of the plasma properties in the direction normal to the layer and oblique incidence are considered. A constant magnetic field applied normal to the layer is included for the case of normal incidence. Simple expressions are obtained for the reflection and transmission coefficients when  $L/\lambda_0$  is small. In particular, if  $n_0 L = 2\pi L/\lambda_0 = \epsilon \ll 1$  and if  $\delta = 0(1/\epsilon^2)$  [that is, the maximum magnitude of the index of refraction is of order  $1/\epsilon$ ],  $R$  and  $T$  are given by Eqs. (14) and (15), respectively. The limiting solution (16), for  $\delta \leq 0(1/\epsilon)$ , which was obtained in Ref. 1 by a different method, is extremely convenient for calculation purposes due to the simplicity of the complex algebra involved and the absence of complicated integral expressions ( $\mu_0$  can be evaluated readily, say graphically). Although  $|(n_0 L)^3 \nu| \leq 1$  is required [Eq. (13)], the form of the approximate solutions is such that useful results may still be obtained outside this range.



The accuracy of these expressions was established using the exact solutions obtained in Ref. 5 for the case of normal incidence, constant collision frequency, and the electron density distributions shown in Fig. 1. Excellent agreement was found using the zeroth order solution (16) when  $|(n_0 L)^3 \nu| \ll 1$ , that is,

$$|(n_0 L)^3 c_2 X_1^2 [(1 - Y)^2 + Z^2]^{-1}| \ll 1$$

as shown in Figs. 2 through 5, where  $X_1$  is the maximum value of  $X$  and  $C_2 = -0.0382$  for the exponential profile assumed. Although (16) ceases to be valid formally as this parameter approaches one and (15) should be used, accurate results are nevertheless still obtained from the former. By the same token, Eq. (15), and to some extent (16), continue to be useful even for large values of the parameter, particularly when  $n_0 L \ll 1$ .

Results of calculation for a 10-degree half-angle cone at zero angle of attack was considered to demonstrate the applicability of the present analysis. A large number of conditions of interest were examined. In every case it was found that  $|(n_0 L)^3 \nu| < 1$ . The conditions computed were all within the parametric range included in Figs. 2 through 4, and it was established that (16) could be used to provide accurate transmission calculations.

#### REFERENCES

1. Ginzburg, V. L., Propagation of Electromagnetic Waves in Plasma, New York, Gordon and Breach Science Publishers, Inc., 1961.
2. Budden, K. G., Radio Waves in the Ionosphere, New York, Cambridge University Press, 1961.
3. Mason, R. and Gold, R. R., "Electromagnetic Wave Propagation Through Magnetoactive Plasmas," Aerospace Corporation Report No. TDR-69(2119)TR-3, 1 February 1962.
4. Albini, F. A. and Jahn, R. G., "Reflection and Transmission of Electromagnetic Waves at Electron Gradients," J. Applied Physics, Vol. 32, No. 1, 1961, p. 75.
5. Gold, R. R., "Reflection and Transmission of Electromagnetic Waves from Inhomogeneous Magnetoactive Plasma Slabs," Aerospace Corporation Report No. TDR-169(3230-11)TN-12, 29 March 1963.
6. Vicente, F. A., "Approximate Calculation of RF Attenuation for a Lifting Re-Entry Vehicle," Aerospace Corporation Report No. TDR-169(3116-40)TN-2, 11 June 1963.



INTERACTION OF HIGH POWER MICROWAVES WITH A REENTRY  
VEHICLE PLASMA SHEATH

Melvin Epstein  
Aerospace Corporation  
Laboratories Division  
El Segundo, California

ABSTRACT

An exact solution has been derived for the propagation of electromagnetic waves through an inhomogeneous plasma slab. Although the solution is expressed in terms of an infinite series, an accurate approximation is obtained using just the first two terms provided that the slab is sufficiently thin. This result is used in developing an approximate analysis of the interaction between a strong electromagnetic wave and a thin plasma sheath. The results of the analysis indicates that even at power levels below breakdown, the absorption of electromagnetic energy by the plasma may significantly alter the propagation characteristics of the plasma. Further, the presence of plasma in the irradiated region is found to markedly affect the character of the breakdown process. Small amounts of plasma are found to eliminate breakdown in the usual sense. Instead, the electron density increases rapidly, but continuously, as the incident power is increased.

The work described in this paper was performed under the sponsorship of the Air Force Space Systems Command, Contract No. AF 04(695)-169.



## INTERACTION OF HIGH POWER MICROWAVES WITH A REENTRY VEHICLE PLASMA SHEATH

Melvin Epstein  
Aerospace Corporation  
Laboratories Division  
El Segundo, California

### INTRODUCTION

Considerable effort has been spent in recent years studying the interaction between electromagnetic waves and plasmas. Much of this research has been motivated by the problem of propagation of electromagnetic signals through the plasma sheath surrounding re-entry vehicles for the purpose of communication. It is now well known that the ionized gas layer which surrounds a vehicle re-entering the earth's atmosphere impedes the transmission of electromagnetic waves from the vehicle. Both analytical and experimental investigations have shown that only a certain fraction of the energy of the electromagnetic wave emanating from the antenna leaves the environment of the vehicle. The rest of the energy is partially absorbed by the plasma and partially reflected at the plasma vehicle surface. The fraction of the energy that is transmitted depends principally on the electron density, collision frequency, signal frequency, and thickness of the plasma sheath. The way in which the fraction of transmitted energy depends on these parameters is fairly complicated; but generally speaking, the larger the ratio of plasma frequency to signal frequency, and/or the ratio of sheath thickness to wave length, the smaller will be the transmitted energy.

Several methods have been proposed for increasing the amount of energy transmitted from the vehicle. Perhaps the most effective method is to reduce the angle of the nose cone to a small value. In that way the inviscid flow becomes relatively cool and the sheath is confined almost entirely to the viscous boundary layer.

Another possible scheme for the improvement of transmission is to apply a dc magnetic field along the direction of propagation. A sufficiently strong magnetic field has been found to increase the net energy transmitted. Such a device appears as an attractive solution for those vehicles with sufficient spare weight and room to accommodate the necessary equipment.

Although transmission may be considerably increased by these techniques, the effects of attenuation and reflection may still degrade the transmitted signal to an unacceptable level. In that case one must use a more powerful transmitter to obtain a satisfactory level of transmitted energy. However, if the energy density of the electromagnetic field becomes very large, then that part of the energy absorbed by the plasma may significantly alter the propagation characteristics of the plasma. In particular, one would expect that the increased energy level of the plasma would result



in an increase in electron density. If this occurs, it is conceivable that the resulting increase in attenuation and reflection may actually reduce the net transmitted power. In fact, if the electric field becomes sufficiently intense, then electrical breakdown of the plasma will occur and the incident signal will be almost totally reflected.

It is the purpose of this paper to present an approximate analysis which will allow the prediction of the breakdown power level and the strong interaction at power levels below breakdown. The analysis proceeds in the following manner. First, the plasma sheath in the vicinity of the antenna is approximated by a constant thickness plasma slab whose properties vary only in the direction of propagation (see Fig. 1). An exact formal solution of Maxwell's equations is then developed for such a plasma slab. It is then shown that if the ratio of the thickness of the slab to the free space wave length is sufficiently small, the exact solution can be approximated by a simple expression which involves only the average values of the plasma properties. From this development, it is possible to write a simple expression for the energy absorbed by the plasma from the electromagnetic field in terms of the average values of the plasma properties. Since the interaction changes the electron density and collision frequency, the new plasma properties are not known. Therefore, the next step is to write an energy balance equation which relates the change in the plasma properties to the amount of energy added. By solving this equation simultaneously with Maxwell's equations, it is possible to determine the new state of the plasma and the amount of energy transmitted.

#### SOLUTION OF MAXWELL'S EQUATIONS\*

Attention will be restricted to advanced type reentry vehicles (i. e., vehicles with small cone angles). In that case the plasma sheath is confined entirely to within the boundary layer. Since the boundary layer grows rather slowly, it will be assumed that the boundary layer thickness is constant in the region of the antenna. All boundary layer properties will be assumed to be functions only of  $z$ , the distance along the normal to the vehicle surface. In addition, it will be assumed that the antenna emits plane waves. These last two approximations may be very poor in some cases but they are generally accepted as necessary because of the present state-of-the-art in this field. For simplicity, the present analysis will be restricted to normal incidence at the plasma-surface interface. However non-normal incidence does not introduce any essential difficulty.

---

\*The formal development of the exact solution to Maxwell's equations displayed in this section was accomplished jointly by Dr. R. R. Gold and the author. Subsequent developments of this approach followed by Dr. Gold and the author follow somewhat different lines because of the different applications being considered.



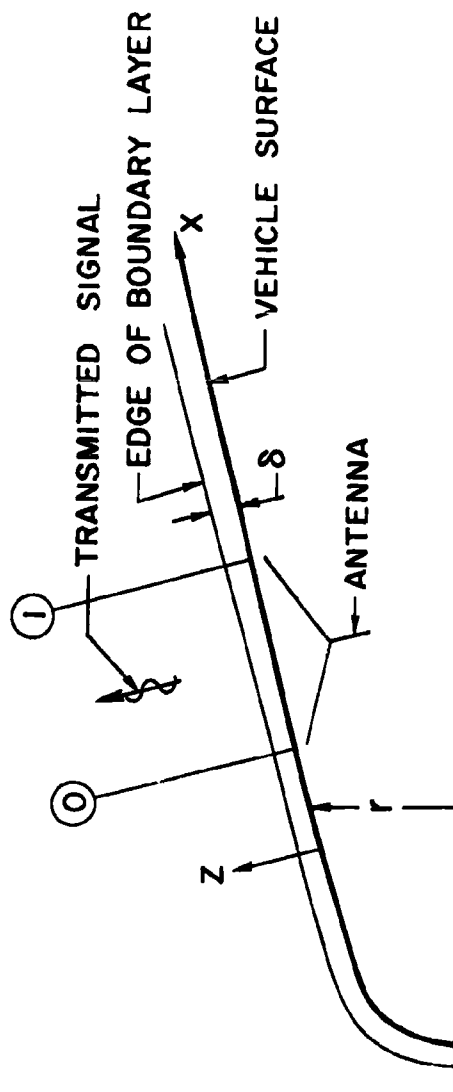


Fig. 1. Geometry of the Model



Under these conditions, Maxwell's equations may be reduced to the following form:

$$\frac{\partial^2 E}{\partial z^2} = \mu \frac{\partial j}{\partial t} + \epsilon \mu \frac{\partial^2 E}{\partial t^2} \quad (1)$$

where  $E$  is the electric field strength,  $\epsilon$  is the dielectric constant,  $\mu$  is the permeability, and  $j$  is the current density. The current density may be related to the electric field strength by means of the electrical conductivity,  $\sigma$ .\*

$$j = \sigma E = \frac{ne^2}{m(\nu + i\omega)} E \quad (2)$$

where  $n$  is the electron density,  $e$  is the electron charge,  $m$  is the electron mass,  $\nu$  is the collision frequency, and  $\omega$  is the signal frequency. In this problem  $n$  and  $\nu$  are assumed to be arbitrary functions of  $z$ . If Eq. (2) is substituted into Eq. (1) and the following nondimensional notation is introduced [assuming  $E = E_0 \exp(i\omega t)$ ]

$$\mathcal{E} = \frac{E_0}{E_{0i}}, \quad y = \frac{z}{\delta}, \quad \beta = 2\pi \frac{\delta}{\lambda} \quad (3)$$

$$a = \frac{iX}{Z+1}, \quad X = \frac{\omega^2}{\omega^2 - \nu^2} = \frac{ne^2}{\epsilon m \omega^2}, \quad Z = \frac{\nu}{\omega}$$

where  $E_{0i}$  is the amplitude of the incident wave,  $\delta$  is the slab thickness, and  $\lambda$  is the free-space wave length, then Eq. (1) reduces to

$$\frac{d^2 \mathcal{E}}{dy^2} + \beta^2 (1 - a) \mathcal{E} = 0 \quad (4)$$

where  $a$  is a function of  $y$ .

Equation (4) is the classical Helmholtz equation which arises in the study of propagation of waves through plane, stratified media. Exact analytical solutions to Eq. (4) have been obtained only for certain special forms of  $a(y)$ . (See (1) for a review of the exact solutions.) It will now be demonstrated how a formally exact solution of this equation can be obtained for arbitrary  $a(y)$ .

\*At very high field strengths the conductivity depends on the field strength. However, for air, the appropriate form for this nonlinear effect is not yet known. Hence, in this paper, the classical form displayed in Eq. (2) will be used.



If Eq. (4) is integrated twice with respect to  $y$ , then, with the help of an integration by parts, it takes the form

$$\mathcal{E}(y) = F(y) + \beta^2 \int_0^y K(y, \eta) \mathcal{E}(\eta) d\eta \quad (5)$$

where

$$F(y) = \mathcal{E}(0) + \left( \frac{d\mathcal{E}}{dy} \right)_{y=0} y \equiv \mathcal{E}_0 + \mathcal{E}'_0 y \quad (6)$$

and

$$K(y, \eta) = (\eta - y)[1 - a(\eta)] \quad (7)$$

Equation (5) is a Volterra integral equation of the second kind. Its exact solution is given by (2)

$$\mathcal{E}(y) = F(y) + \sum_{i=1}^{\infty} \beta^{2i} K^i F(y) \quad (8)$$

where  $K$  is an integral operator defined by

$$Kf(x) = \int_0^x K(x, \xi) f(\xi) d\xi \quad (9)$$

The constants  $\mathcal{E}_0$  and  $\mathcal{E}'_0$  are determined by requiring that the electric and magnetic fields be continuous at  $z = 0$  and  $\delta$ . The details of this part of the calculation will be indicated shortly. The theory of integral equations guarantees that in the limit as  $i \rightarrow \infty$ , Eq. (8) converges to the solution of Eq. (4) regardless of the value of  $\beta$ , provided only that  $a$  be continuous. In practice, the evaluation of more than just the first few terms in Eq. (8) may become tedious. However, examination of the structure of Eq. (8) indicates that convergence should be rapid if  $\beta$  is small and  $a$  does not become too large.

For the physical conditions of the present problem,  $\beta$  is generally a very small number. For example, for a frequency of  $10^9$  cps at a point one ft back on a six deg cone moving at Mach 18 at 50,000 ft altitude,  $\beta \approx 1/3000$ . It will now be shown that if the average value of the magnitude of  $a$  is at most of order of magnitude,  $1/\beta$ , then the first two terms in Eq. (8) provide a simple and accurate solution to Maxwell's equations.

It can be shown (see (2)) that if only the first two terms in Eq. (8) are retained, then the error incurred is of the order of

$$\beta^2 K^2 \mathcal{E}^{(0)}(y) \quad (10)$$



where  $\mathcal{E}^{(0)}(y)$  is the zeroth approximation to  $\mathcal{E}$ . Since  $\mathcal{E} = 0(1)$  and the operator  $K = 0(a) = 0(1/\beta)$ , the error is seen to be  $0(\beta)$ . The first two terms of Eq. (8) are

$$\mathcal{E}(y) = \mathcal{E}_0 + \mathcal{E}'_0 y + \beta^2 \int_0^y (\eta - y)(\mathcal{E}_0 + \mathcal{E}'_0 \eta)[1 - a(\eta)] d\eta \quad (11)$$

The constants  $\mathcal{E}_0$  and  $\mathcal{E}'_0$  may be eliminated by requiring that the electric and magnetic fields in the plasma be continuous with the corresponding fields in the free space regions  $z < 0$  and  $z > \delta$ . For this problem, it can be shown that continuity of the magnetic field is equivalent to continuity of  $dE/dz$ . Differentiating Eq. (11), one obtains

$$\frac{d\mathcal{E}}{dy} = \mathcal{E}' = \mathcal{E}'_0 - \beta^2 \left( \mathcal{E}_0 y + \frac{1}{2} \mathcal{E}'_0 y^2 \right) + \beta^2 \int_0^y (\mathcal{E}_0 + \mathcal{E}'_0 \eta) a d\eta \quad (12)$$

For the free space region,  $z < 0$ ,  $a = 0$  and the solution is

$$\mathcal{E}(y) = \exp(-i\beta y) + R \exp(i\beta y) \quad (13)$$

where the first term represents the incident wave, the second term represents the reflected wave, and  $R$  is the reflection coefficient. For the free space region,  $z > \delta$ ,  $a$  is also zero and hence

$$E(y) = T \exp(i\beta y) \exp(-i\beta y) \quad (14)$$

where  $T$  is the transmission coefficient.

Equating Eqs. (11) and (13) and their respective derivatives at  $y = 0$  yields

$$1 + R = \mathcal{E}_0 \quad (15)$$

$$i\beta(R - 1) = \mathcal{E}'_0 \quad (16)$$

Equating Eqs. (11) and (14) and their respective derivatives at  $y = 1$  yields

$$\mathcal{E}_0 + \mathcal{E}'_0 - \beta^2 \left( \frac{1}{2} \mathcal{E}_0 + \frac{1}{6} \mathcal{E}'_0 \right) + \beta^2 \int_0^1 \left[ \mathcal{E}_0 - (\mathcal{E}_0 - \mathcal{E}'_0)\eta - \mathcal{E}'_0 \eta^2 \right] a(\eta) d\eta = T \quad (17)$$

$$\mathcal{E}'_0 - \beta^2 \left( \mathcal{E}_0 + \frac{1}{2} \mathcal{E}'_0 \right) + \beta^2 \int_0^1 (\mathcal{E}_0 + \mathcal{E}'_0 \eta) a(\eta) d\eta = -i\delta T \quad (18)$$



If  $a$  were known, Eqs. (15), (16), (17), and (18) could be solved simultaneously for  $T$ ,  $R$ ,  $\mathcal{E}'_0$  and  $\mathcal{E}_0$ . Since the integrands involving  $a$  appear in the form  $\eta^n a$ , it is convenient to define the moments of  $a$ ,

$$\mu_n = \frac{\int_0^1 \eta^n a(\eta) d\eta}{\int_0^1 \eta^n d\eta} = (n+1) \int_0^1 \eta^n a(\eta) d\eta \quad (19)$$

Then, Eqs. (17) and (18) become

$$\mathcal{E}_0 + \mathcal{E}'_0 - \beta^2 \left( \frac{1}{2} \mathcal{E}_0 + \frac{1}{6} \mathcal{E}'_0 \right) + \beta^2 \left[ \mathcal{E}_0 \mu_0 - (\mathcal{E}_0 - \mathcal{E}'_0) \frac{\mu_1}{2} - \mathcal{E}'_0 \frac{\mu_2}{3} \right] = T \quad (20)$$

$$\mathcal{E}'_0 - \beta^2 \left( \mathcal{E}_0 + \frac{1}{2} \mathcal{E}'_0 \right) + \beta^2 \left( \mathcal{E}_0 \mu_0 + \mathcal{E}'_0 \frac{\mu_1}{2} \right) = i\delta T \quad (21)$$

Solving Eqs. (15), (16), (20) and (21) simultaneously and dropping terms which are  $O(\beta)$ , one obtains

$$\mathcal{E}_0 = \frac{2i}{2i + \beta\mu_0} \quad (22)$$

$$\mathcal{E}'_0 = O(\beta) \quad (23)$$

$$R = -\frac{\beta\mu_0}{2i + \beta\mu_0} \quad (24)$$

$$T = \frac{2i}{2i + \beta\mu_0} \quad (25)$$

It is seen that, neglecting terms of  $O(\beta)$  (which, as previously pointed out, is extremely small in the problem considered here), these constants of integration depend only on the average value of  $a$  in the boundary layer.

The quantity of principal interest here is the rate at which energy is deposited into the plasma from the electromagnetic field. This can be determined by calculating the difference between the energy entering the plasma at  $z = 0$  and the energy leaving the plasma at  $z = \delta$ . The flux of electromagnetic energy across a surface is given by the Poynting vector  $\vec{P}$ ,

$$\vec{P} = \vec{E} \times \vec{H} \quad (26)$$



Integrating over a cycle of the electromagnetic field, the time averaged flux can be shown to be

$$\bar{P} = \frac{E_{0i}^2}{2\omega\mu\lambda} \mathcal{L}m \left( e^{\frac{d\tilde{E}}{d\eta}} \right) \quad (27)$$

where the tilde denotes a complex conjugate value. Applying this to Eqs. (11), (22), (23), (24) and (25), one finds that the ratio of the rate at which energy is absorbed by the plasma to the rate at which energy is incident on the plasma is

$$\frac{W_{ab}}{W_i} = 1 - R\tilde{R} - T\tilde{T} \quad (28)$$

where  $R$  and  $T$  are given by Eqs. (24) and (25). It is noted that the rate at which energy is absorbed by the plasma depends only on the average value of  $a$ , if terms of  $O(\beta)$  are neglected. Hence, if a reasonable approximation is available for the distribution of the electron density and the collision frequency, and the rate at which energy is being emitted by the antenna is known, then the rate at which energy is being absorbed by the plasma can be determined. Since the plasma properties in the presence of an intense microwave field are not known, Eq. (28) must be solved simultaneously with the equations describing the response of the plasma to an energy source. An approximate model for this part of the problem will be developed in the next section.

#### THE ENERGY EQUATION FOR THE ELECTRONS\*

In order to evaluate Eq. (28), one must be able to determine the electron density and the collision frequency. The latter in turn depends on the electron temperature, since for a slightly ionized gas

$$\nu = \frac{4\rho Q}{3m_n} \sqrt{\frac{8kT_e}{\pi m}} \quad (29)$$

where  $\rho$  is the gas density,  $Q$  is the electron-neutral collision cross section,  $m_n$  is the neutral particle mass, and  $T_e$  is the electron temperature. The electron temperature is necessarily different from the neutral gas temperature since the electromagnetic field acts directly only on the electrons (the ions are too massive to be significantly affected at microwave frequencies). The electron temperature can be determined by striking a balance between the energy gained by the electrons from the microwave field and the energy lost by the electrons to the neutrals by elastic and inelastic collisions. In

---

\*The author wishes to thank Dr. T. A. Jacobs for his discussions regarding the development of the energy equation.



general, it is rather difficult to write an accurate version of such an energy balance because the various processes are quite complicated and the rates at which they proceed are not well known, especially in the presence of an applied electromagnetic field. Attention will therefore be restricted here to a particular limiting case. This is consistent with one of the objectives of this paper, that is, to show the existence of a problem area (that is, increased attenuation at pre-breakdown power levels) which has apparently not received sufficient consideration.

It will henceforth be assumed that all reactions induced by the applied electromagnetic field have characteristic times much smaller than the time it takes for a particle to flow through the irradiated region. That is, it will be assumed that the plasma is in a quasi-equilibrium state defined in the following way. The electrons, having absorbed energy from the electromagnetic field, will undergo both elastic and inelastic collisions with the neutrals. The inelastic collisions will take the form of excitation of the electronic degrees of freedom of the neutral particles, and ionization. For the species present in air, the principal energy absorbing type of collision is the excitation process. Even though the excitation energy is somewhat less than the ionization energy, its cross section is very much greater. On the other hand, unless the electron temperature becomes extremely large compared to the gas temperature, the rate of energy transfer through excitation greatly exceeds that due to elastic collisions. (That this is indeed the case may be assured by an *a posteriori* calculation of the final electron temperature.) In addition, if the total amount of energy added to the gas per second is much less than the flux of total enthalpy of the gas through the irradiated region, the density and temperature of the gas will not change perceptibly. Both this assumption and the assumption of very fast reaction rates will be valid if the pressure is sufficiently high since then both the collision rates and the energy density of the gas will be high. This development implies that the model just described will be most accurate at the lower altitudes. Hence, it will be assumed that all of the gas except for the free and bound electrons are at a temperature  $T$ , which is the temperature the gas would have in the absence of the applied electromagnetic field. The bound electrons and the free electrons will be assumed to be at a temperature  $T_e$ . It will be assumed that the bound electrons have the energy that they would have if they were in equilibrium with their parent atom at a temperature  $T_e$ . This is a conservative estimate since if they had less energy, the free electrons would be even more energetic and the amount of ionization caused by direct impact between an electron and a neutral particle would increase.

It will be further assumed that the ionization level instantaneously adjusts itself to the value given by an approximate form of the Saha equation, that is,

$$n = n_0 \exp[(-I/2kT)(T/T_e - 1)] \quad (30)$$

where  $n_0$  is the electron density in the absence of an applied electromagnetic field. This approximation is based on the observation that for small degrees of ionization, the Saha equation predicts that the electron density varies



essentially as  $\exp(-I/2kT)$ . That is, the electron density depends most sensitively on the ratio of the ionization energy to the thermal energy of the electrons. It seems reasonable to extrapolate Saha's equation to the present quasi-equilibrium situation by using the local electron temperature rather than the gas temperature. In that case Saha's equation becomes Eq. (30).

Using this model, it is possible to write an energy equation for the electrons in the irradiated region in the following way. The net enthalpy flux out of the irradiated region is (for the conical geometry of Fig. 1)

$$2\pi r_1 \int_0^\delta \left( \frac{5}{2} n_1 k T_e u + u \sum_i n_{i1}^+ I_i \right) dz - 2\pi r_0 \int_0^\delta \left( \frac{5}{2} n_0 k T u + u \sum_i n_{i0}^+ I_i \right) dz \equiv H_1 - H_0 \quad (31)$$

where subscripts 0 and 1 denote conditions at the upstream and downstream edges of the irradiated region, respectively,  $r$  is the local cone radius,  $n_i^+$  is the number of positive ions of the  $i$ th species, and  $I_i$  is the ionization energy per particle for the formation of an ion of the  $i$ th species.

According to the principle of conservation of energy, the above net enthalpy flux must be equal to the flux of energy into the electrons from the electromagnetic field  $W_{ab}$ , minus the flux of energy out due to inelastic collisions. According to the model that has been assumed, the last term is

$$2\pi r_1 \int_0^\delta \int_T^{T_e} \rho u \sum_i a_{i1} C_{p_{i1}}^{el} dT_e dz \equiv H_{el} \quad (32)$$

where  $a_i$  is the mass fraction of the  $i$ th species and  $C_{p_i}^{el}$  is the contribution of the electronic degrees of freedom to the specific heat of the  $i$ th species. The energy equation for the electrons then takes the following form.

$$H_1 - H_0 = W_{ab} - H_{el} \quad (33)$$

Equation (33) must be solved simultaneously with Eq. (28) to determine the final state of the gas and the propagation characteristics of the plasma. The solution of these equations for some typical re-entry conditions will be illustrated in the next section.

## DISCUSSION OF RESULTS

Before proceeding to some typical calculations, it is useful to invoke some simplifying approximations pertinent to advanced re-entry vehicles. For slender nose cones, provided that the antenna is not too close to the cone apex and that the antenna is not very long, one may take  $r_1 \approx r_0$ . Further, if the electron temperature does not become very great, most of



the additional ionization will result from one particular reaction. The following approximation will then be valid:

$$\sum_i (n_{i1}^+ I_i - n_{i0}^+ I_i) \approx (n_1 - n_0) I \quad (34)$$

where  $I$  is the ionization potential per particle of the dominant ionizing reaction. [For air in cone boundary layers on advanced reentry vehicles, the species with the lowest ionization potential that is present in reasonable quantities, is NO;  $I = 9.5$  eV (Ref. (3)). Further, the first excited state of the oxygen atom ( $\approx 1.97$  eV) is considerably lower than that of any of the other principal species. Hence unless the electron temperature becomes very high, it is reasonable to assume that

$$\sum_i a_i C_{p_i}^{el} \approx a_0 C_{p_0}^{el} \quad (35)$$

where here the subscript 0 stands for oxygen atoms.

Using these approximations and the following non-dimensional notation

$$y = \frac{z}{\delta}, \quad V = \frac{u}{u_e}, \quad \tau = \frac{T}{T_e} \quad (36)$$

where  $u_e$  is the inviscid flow velocity outside the boundary layer ( $u_e = \text{constant}$  for a cone), Eq. (33) may be written as

$$\begin{aligned} W_{ab} = & 5\pi r k u_e \delta \int_0^1 \tau \{ \exp[(I/2kT)(\tau - 1)/\tau] - 1 \} n_0 T V dy \\ & + 2\pi r u_e I_2 \delta \int_0^1 \{ \exp[(I/2kT)(\tau - 1)/\tau] - 1 \} n_0 V dy \\ & + \pi r u_e \delta \int_0^1 \rho V T a_0 \left[ \int_1^\tau C_{p_0}^{el}(Tw) dw \right] dy \end{aligned} \quad (37)$$

whereas  $\mu_0$ , which enters into Eq. (28) becomes

$$\mu_0 = \frac{ie^2}{\epsilon m \omega^2} \int_0^1 \frac{n_0 \{ \exp[(I/2kT)(\tau - 1)/\tau] \}}{i + \frac{4\rho Q}{3\omega m_n} \sqrt{\frac{8kT}{\pi m}} \sqrt{\tau}} dy \quad (38)$$



Equation (37) must be solved together with Eq. (28) which also contains integrals of functions of  $\tau$ . Since an integral formulation of the problem has been given, one cannot hope to determine a unique variation of  $\tau$  with  $y$ . However, if a reasonable form for the dependence of  $\tau$  on  $y$  is assumed containing one arbitrary constant, then the simultaneous solution of Eqs. (28) and (37) will give the value of that constant.\* As a first approximation, it will be assumed here that the electron temperature profile has the same shape as the neutral gas temperature profile. In that case  $\tau$  is independent of  $y$ . Although this is certainly not accurate, the fact is that the integrands contain either the electron density or atom concentration as factors. Since both of these are rather sharply peaked near the center of the boundary layer, the detailed shape of the functions which multiply them do not affect the values of the integrals very much.

Since Eqs. (28) and (37) are nonlinear in  $\tau$ , the simplest way of carrying out the calculation is to assume several values of  $\tau$  and evaluate  $W_{ab}$  from Eq. (37) (assuming that the unperturbed boundary layer profiles are known). To each value of  $\tau$  there corresponds a particular value of  $W_{ab}$ , the total energy absorbed by the plasma in the irradiated region. Since the properties of the plasma vary between the upstream and downstream ends of the irradiated region, it is proper to evaluate Eq. (28) using some mean properties in the irradiated region. The procedure used is perhaps best described with the use of Fig. 2 which shows the total energy absorbed as a function of  $\tau$  at the downstream end of the irradiated region. For the case where  $\tau = \tau_1$  at the downstream end of the irradiated region, the energy absorbed is  $W_{ab}(\tau_1)$ . It seems proper to evaluate Eq. (28) at a point in the irradiated region where half of this amount of energy is absorbed. This defines a value of  $\tau_2$  (which is a function of  $\tau_1$ ) as shown in Fig. 2. Using this in Eq. (28) and  $W_{ab}$  from Eq. (37), the value of  $W_i$  which is necessary to give  $\tau = \tau_1$  at the downstream end of the irradiated region can be found.

This procedure has been used to calculate the interaction between a strong microwave signal (frequency =  $10^9$  cps) and the plasma generated by viscous dissipation in the boundary layer of a 6 deg semi-apex angle cone. The boundary layer properties are taken from the equilibrium flow field calculations of Ref. (4). The irradiated region is taken to be approximately one ft downstream of the apex of the cone. The results presented in Figs. 3-6 are for a vehicle altitude and Mach number of 50,000 ft and 18.4, respectively. Results are shown for four different wall temperatures ( $1500^\circ$ ,  $2500^\circ$ ,  $3500^\circ$ , and  $4500^\circ$  K). Figure 3 shows the variation of absorbed power,  $W_{ab}$ , as a function of  $\tau$  as calculated from Eq. (37). These curves are seen to be rapidly varying functions of  $\tau$ . This may be explained by noting that the dominant term in Eq. (37) is the one corresponding to electronic excitation. Since the contributions of the electronic degrees of freedom vary essentially exponentially with electron temperature, the power absorbed curves vary in a similar way.

---

\* This is somewhat analogous to the integral method in boundary layer theory.



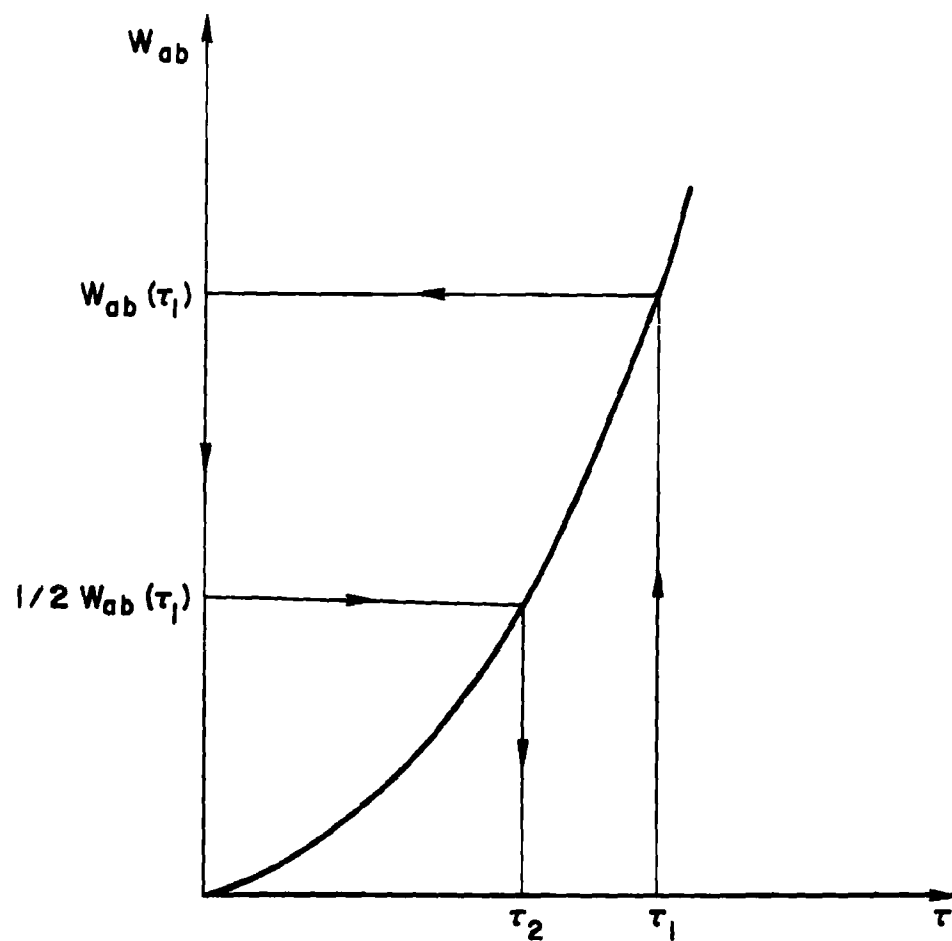


Fig. 2. Scheme for Determining Appropriate Average Electron Temperature Used in Eq. (28)



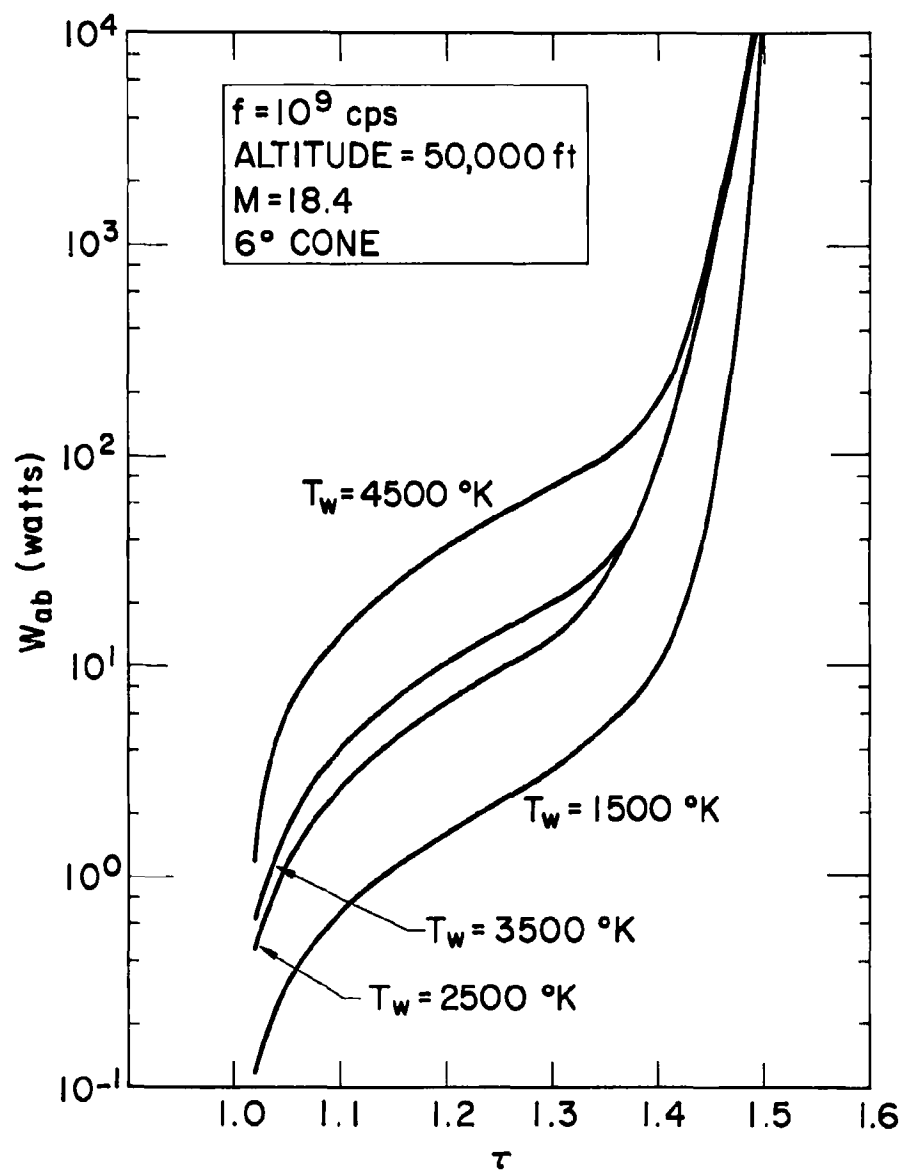


Fig. 3. Variation of Energy Absorbed as a Function of  $\tau$



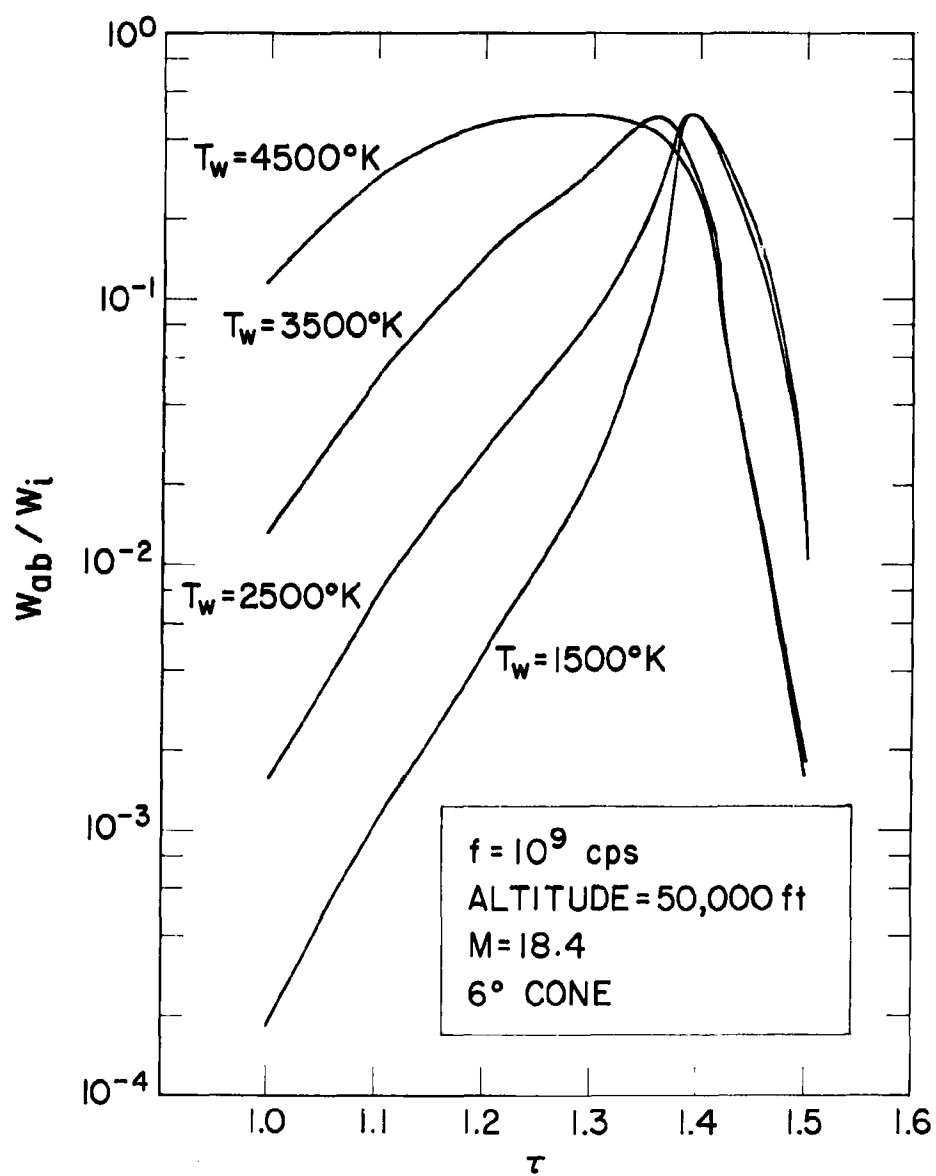
The curves of  $W_{ab}/W_i$ , as determined from Eq. (28), are shown in Fig. 4 as a function of  $\tau$ . These curves are characteristically peaked at some moderate value of  $\tau$ . For the particular physical conditions considered here, the unperturbed plasma is under-dense and the absorption is small. As the electron temperature is increased, the modified Saha equation requires that the electron density also increases and the relative absorption increases. When the plasma becomes over-dense, the absorption decreases again, going to zero as the electron density becomes very large.

These curves may be combined in the manner described above to show the variation of  $\tau$  with  $W_i$ , the incident power level (Fig. 5). These curves are characteristically S-shaped. At small incident power levels the small fraction of absorbed power increases the electron density and temperature slightly. This increase makes the plasma slightly more absorptive. When the power level is increased, a greater fraction of the incident power is absorbed. This situation further increases the absorptive properties of the plasma, leading to a faster and faster increase in electron temperature and density as the power is increased. This condition eventually leads to a catastrophic situation where the tangent to the curve becomes vertical. For slightly higher electron temperatures, a stable situation does not exist. A further increase in power results in a vertical jump to the upper branch of the S-curve. The incident power corresponding to this situation is therefore the breakdown power. Note that after breakdown has occurred a reduction in power is possible along the upper branch of the S-curve. When the upper vertical tangent is reached, a discontinuous change in plasma properties again occurs as the incident power is lowered and the solution jumps again to the lower branch. Thus, the familiar hysteresis associated with electrical breakdown of gases is both predicted and explained by this calculation.

An important result to note here is that at the higher wall temperature (which produces a higher unperturbed electron density level) breakdown does not occur in the usual way. The reason for this can be explained by referring to Fig. 4. It is seen that for a wall temperature of  $4500^\circ\text{K}$ , the relative absorption for the unperturbed plasma is already close to its maximum. Although a slight increase in power makes it slightly more absorptive, further increases in power decrease the absorptivity and the catastrophic situation described above never develops. This is not meant to imply that large changes in electron density do not occur, but rather that the change in electron density varies continuously with change in incident power. Thus, the presence of plasma may significantly affect the character of electrical breakdown.

From the shapes of the curves in Figs. 3-5 one may conclude that if the absorptivity (that is,  $W_{ab}/W_i$ ) of the unperturbed plasma is at a point to the right of the maximum [that is, if  $d(W_{ab}/W_i)/d\tau < 0$ ], then a classical or "jump" type of electrical breakdown cannot occur. Only if the unperturbed state is sufficiently low on the left hand side of the absorptivity curve may the classical catastrophic breakdown occur. This phenomenon, of course, is exactly what happens in the classical, initially plasma-free, breakdown. In that case the electric field in the irradiated region is equal to the incident field since there is no plasma (except for the few ambient free electrons) to modify the field. This situation persists until the few free electrons present



Fig. 4. Relative Absorption as a Function of  $\tau$



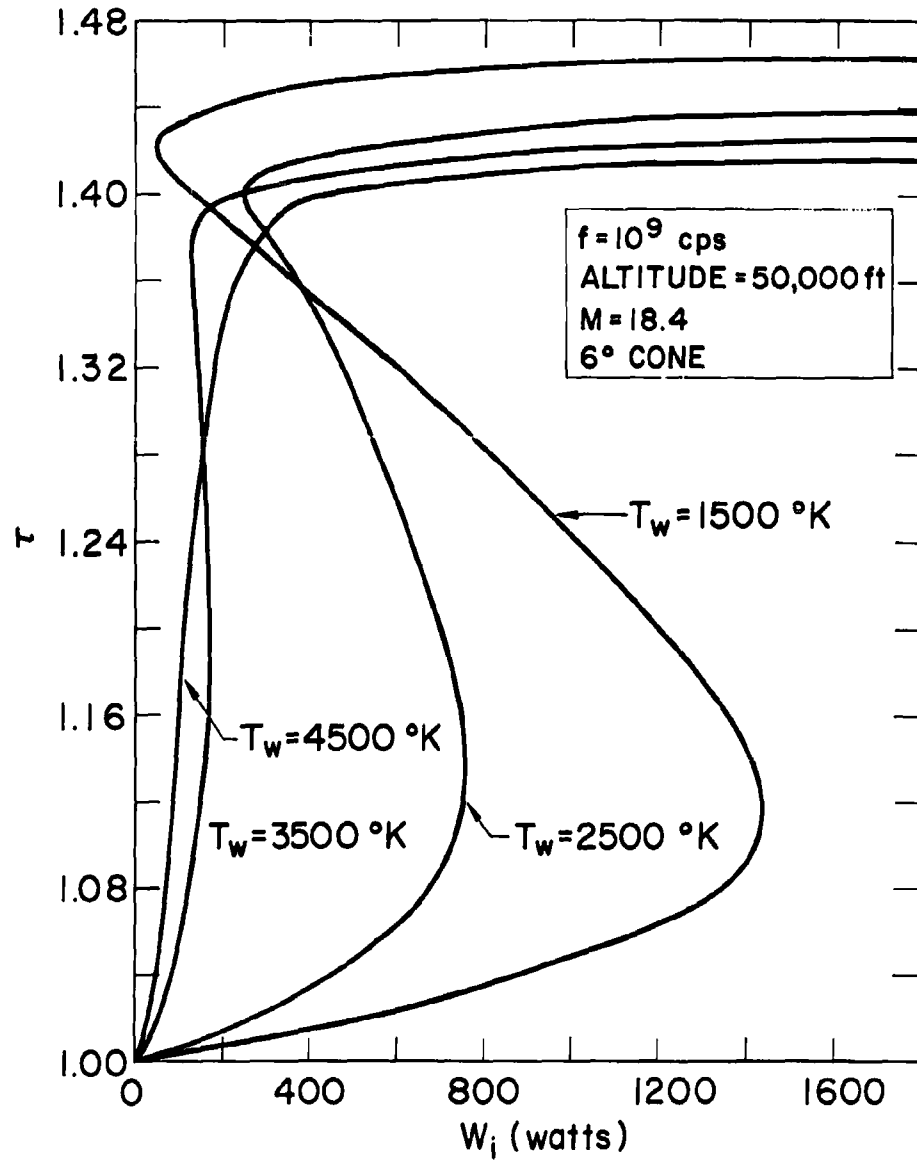


Fig. 5. Ratio of Electron to Gas Temperature as a Function of Incident Power



gain enough energy to increase their ionization rate above the recombination rate (at least for high pressure breakdown). When this occurs, the gas undergoes a tremendous increase in absorptivity leading to a catastrophic breakdown. On the other hand, if the unperturbed gas is already ionized, then the electric field strength within the plasma may be quite different from the incident field strength. The absorptivity may be rather high to start with so that a considerable fraction of the incident energy may be readily absorbed. Thus, rather large changes in plasma properties may occur at field strengths well below those predicted neglecting the presence of the plasma.

To illustrate this, the variation of the loss in transmitted power as a function of incident power level is shown in Fig. 6. In the particular example shown, the boundary layer is so thin that nearly perfect transmission is obtained at all power levels below breakdown. However, the significant effect of power level on the relative power loss is apparent. For other conditions where the transmitted power level may be calculated to be marginal at low field strengths, increasing the incident power level may actually lower the transmitted power level. This is especially the case for an overdense but thin plasma sheath, such as, for example, the 4500°K wall temperature case in Fig. 6.

These new effects are even more pronounced at higher altitudes where the Mach number and hence the unperturbed electron density are higher. Typical results are shown in Figs. 7 and 8 for the same configuration at an altitude of 75,000 ft and a Mach number of 21.6. At small power levels the degradation of the signal is still acceptable although somewhat greater because of the increased electron density and boundary layer thickness. However, it is seen that at the higher wall temperatures the transmitted signal may be degraded to an unacceptable level without obtaining breakdown in the usual sense, if the power delivered to the antenna is too large.

In all cases, it is noted that once breakdown occurs, increasing the incident power results in a slight further reduction in transmission coefficient.

## CONCLUSIONS

An exact solution has been derived for the propagation of plane, transverse, electromagnetic waves through an inhomogeneous plasma slab for the case wherein the inhomogeneity is in the direction of propagation. The solution takes the form of an infinite series. If the slab thickness is small compared to the free space wave length of the signal, the first two terms of the series provide an accurate solution even for highly over-dense plasmas.

Using this solution, an approximate analysis of the interaction between a strong microwave signal and a thin plasma sheath was developed. Illustrative calculations were presented for the case of a microwave signal propagating through the plasma sheath formed in the boundary layer of a reentry vehicle nose cone. The following conclusions are drawn from these results:



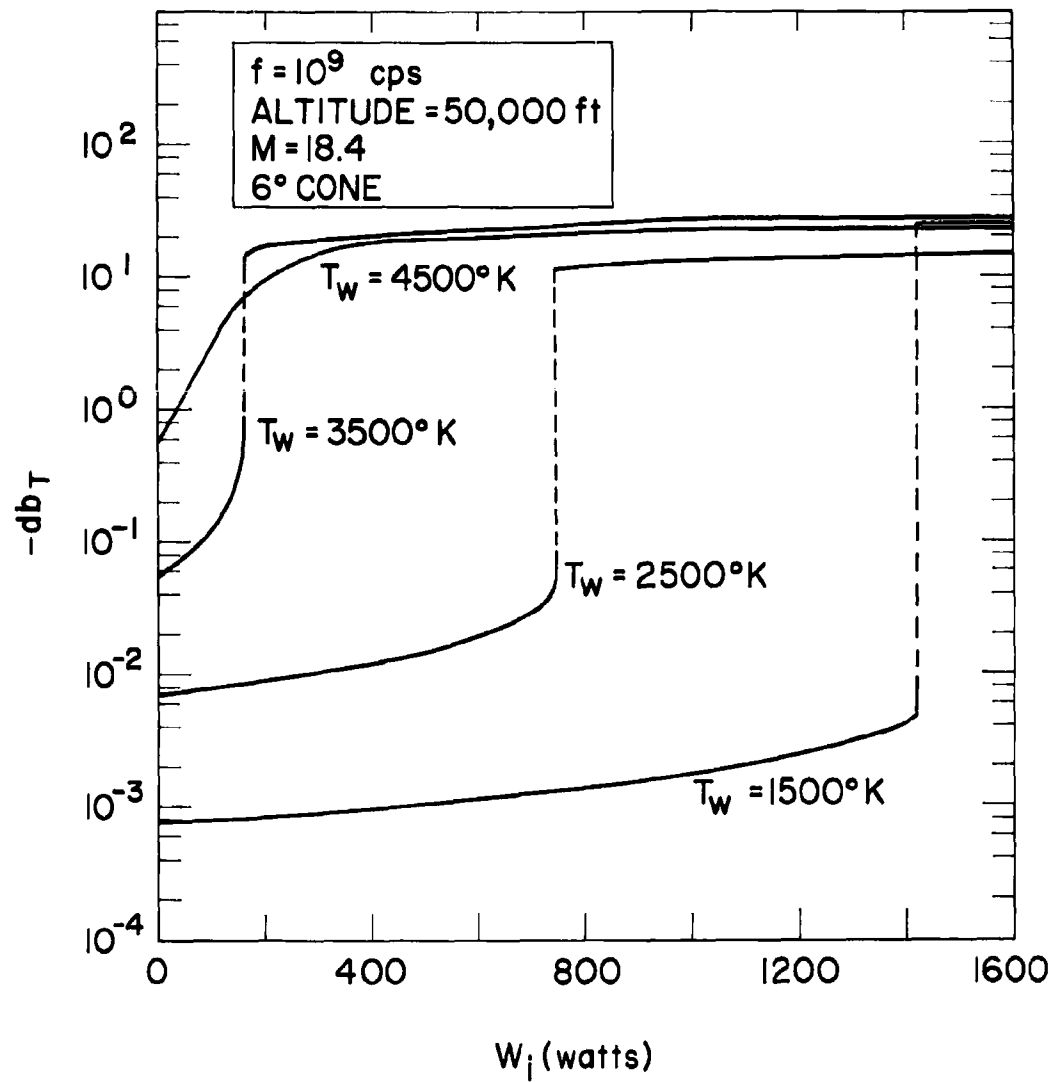


Fig. 6. Transmitted Energy as Function of Incident Power



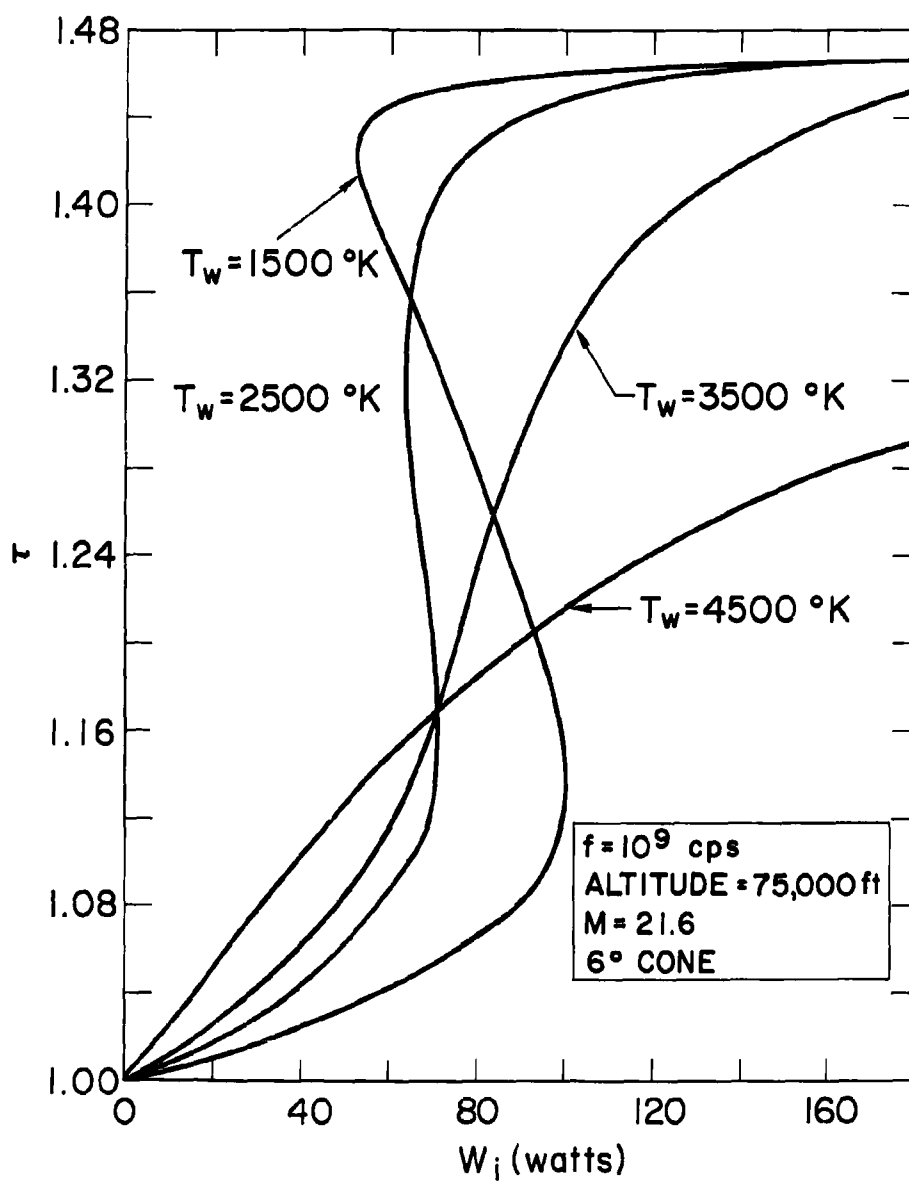


Fig. 7. Ratio of Electron to Gas Temperature as a Function of Incident Power



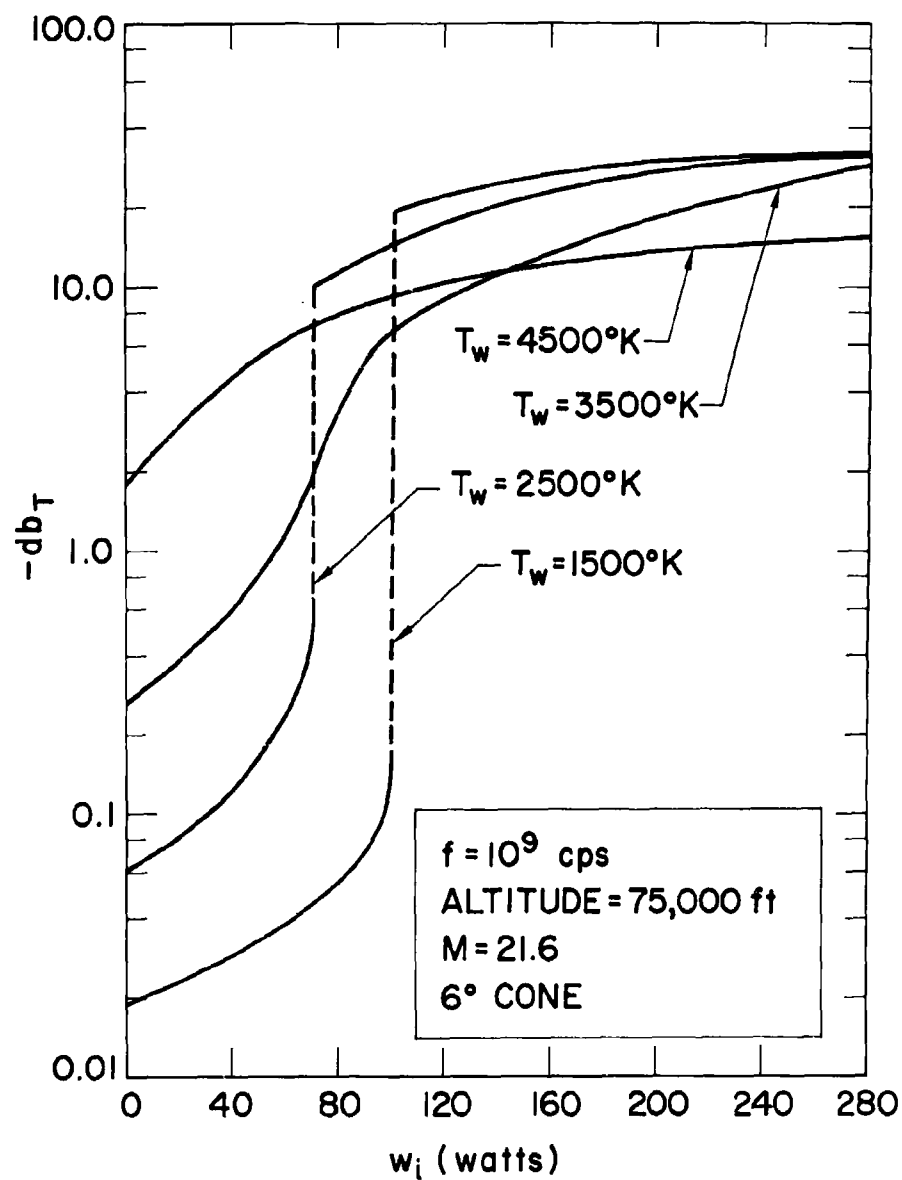


Fig. 8. Transmitted Energy (db down) as a Function of Incident Power



1. The energy absorbed by the plasma from the electromagnetic field at power levels below breakdown may significantly alter the propagation characteristics of the plasma. It seems reasonable to expect that under certain conditions, increasing the power emitted by the antenna may reduce the power transmitted through the plasma sheath.
2. The presence of plasma may significantly alter the breakdown characteristics of the gas. The calculations indicate that increasing amounts of ambient plasma lead to a lowering of the power level required for breakdown. In fact, if the ambient electron density is sufficiently high, the classical type of electrical breakdown does not occur. Instead, the plasma properties change continuously as the incident power level is increased.
3. Once breakdown has occurred, increasing the incident power level still further results in a slight further decrease in transmission coefficient.

It is concluded that interactions of the sort just described should receive consideration whenever high power microwave or telemetry equipment are used on re-entry vehicles.

#### REFERENCES

1. Mason, R. and Gold, R. R., "Electromagnetic Wave Propagation Through Magnetoactive Plasmas," Aerospace Corporation Report No. TDR-69(2119)TR-3, 1 Feb. 1962.
2. Hildebrand, F. B., Methods of Applied Mathematics, Prentice-Hall, Inc., N. Y., 1952.
3. Massey, H. S., W. and Burhop, E. H. S., "Electronic and Ionic Impact Phenomena," Clarendon Press, Oxford, 1952.
4. Coleman, E. R., "Preliminary Analysis of a Hypersonic, Slender, Pointed Cone Frontal Flow Field," Bendix Corp. Report FS-62TN-1020, Jan. 1962.



## PENETRATION



A SIMULATION OF MULTIPLE  
RE-ENTRY VEHICLE DELIVERY

H. C. Sebring\*  
Dr. S. Matlin\*\*

General Electric Company  
Missile and Space Division  
P. O. Box 8555  
Philadelphia 1, Pennsylvania

\*Systems Engineer, Advanced Requirements Operation  
Re-entry Systems Department

\*\*Mathematician, Engineering Technologies Operation  
Advanced Space Projects Department

ABSTRACT

A Monte Carlo simulation of multiple re-entry vehicle delivery is presented, followed by applications and results. The model is unique in that it has six options which permit a variety of inquiries with economy in cost and time. Applications reveal advantages in using multiple re-entry vehicles (R/V's) in comparison with a larger single R/V, to attack point and area targets and spaced multiple targets. Optimum aimpoint patterning relative to R/V survival probability is discussed. Mission effectiveness and systems error analyses are made and the translations to R/V design criteria are indicated. The investigations may help to develop a future course for military technology in re-entry systems.

The work described in this paper was Company sponsored.



# A SIMULATION OF MULTIPLE RE-ENTRY VEHICLE DELIVERY

H. C. Sebring\* and Dr. S. Matlin\*\*

General Electric Company  
Missile and Space Division  
P. O. Box 8555  
Philadelphia 1, Pennsylvania

\*Systems Engineer, Advanced Requirements Operation  
Re-entry Systems Department

\*\*Mathematician, Engineering Technologies Operation  
Advanced Space Projects Department

## INTRODUCTION

If two or more re-entry vehicles are given trajectories with a single missile booster, their denotation is "multiple re-entry vehicles." The purpose of this paper is threefold: (1) to present a method for simulating the use of multiple re-entry vehicles, (2) to review some principal applications, and (3) to discuss a few results of the investigations.

Re-entry vehicle delivery analysis must consider statistically distributed parameters. For example, there are the bias errors of missile guidance and attitude, and random quantities such as ejection velocity and defense penetration. Analyzing the ejection, re-entry, and subsequent target attack requires a Monte Carlo computer simulation model.

The simulation is also applicable to objects such as decoys, precursor warheads, BDA data link transceivers, ECM devices, etc.

The discussion is presented in the following sequence: (1) logic of the model, (2) composition of the model, (3) some applications and results, and (4) conclusions.

## LOGIC OF THE MODEL

The simulation uses Keplerian trajectory equations and assumes a spherical non-rotating earth. Figure 1 shows the trajectory geometry and vector orientation, the regions of interest being insertion, re-entry, and ground.



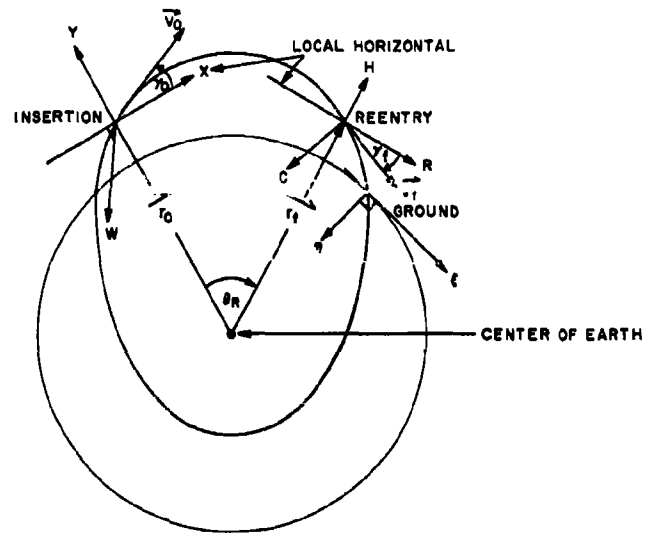


Figure 1. Trajectory Vector Geometry

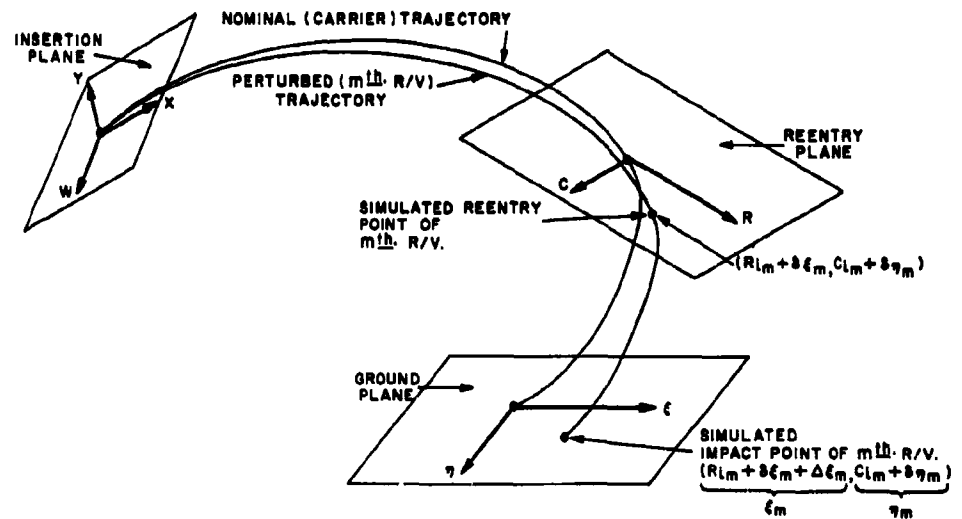


Figure 2. Trajectory Geometry for the Insertion, Re-Entry and Ground Planes



Figure 2 indicates the propagation of a vector perturbation on the insertion plane to the re-entry and ground planes. The simulated ground impact point represents a sampled deviation from the aimpoint.

In the simulation, aimpoints are transferred to re-entry plane coordinates, and then to ejection requirements on the insertion plane. A Monte Carlo process then selects values from the bias and random ejection error distributions, and a resultant perturbation vector is determined. The errors are random selections from Gaussian distributions having zero means and known  $\sigma$ 's. Bias errors, such as guidance, or pitch, yaw, and roll rates, are related to the R/V carrier and affect each R/V. Superimposed on bias errors are the individual R/V random errors such as ejection angle and velocity. Using the projection on the orbit plane of the ejection perturbation vector  $\Delta V_m$  (magnitude  $\Delta V_{mxy}$ ), insertion angle ( $\beta_m$ ), and orbit plane angle ( $\alpha_m$ ), errors are propagated to the re-entry plane. Next, the R/V re-entry velocity and angle, the re-entry altitude assumed (400,000 ft), and the R/V  $W/C_{DA}$  are used to convert the errors to the ground plane. With a given survival probability, a Monte Carlo process is again applied to eliminate non-surviving R/V's. Finally, the impact points of the surviving R/V's are used, with lethal radii, to compute a kill frequency distribution. The target analysis will be discussed in more detail in the sequel.

The number of computer simulations, to obtain convergence stability of the Bernoullian kill probability, is calculated according to the desired combination of confidence and accuracy. Figure 3 shows examples of kill probability stabilization

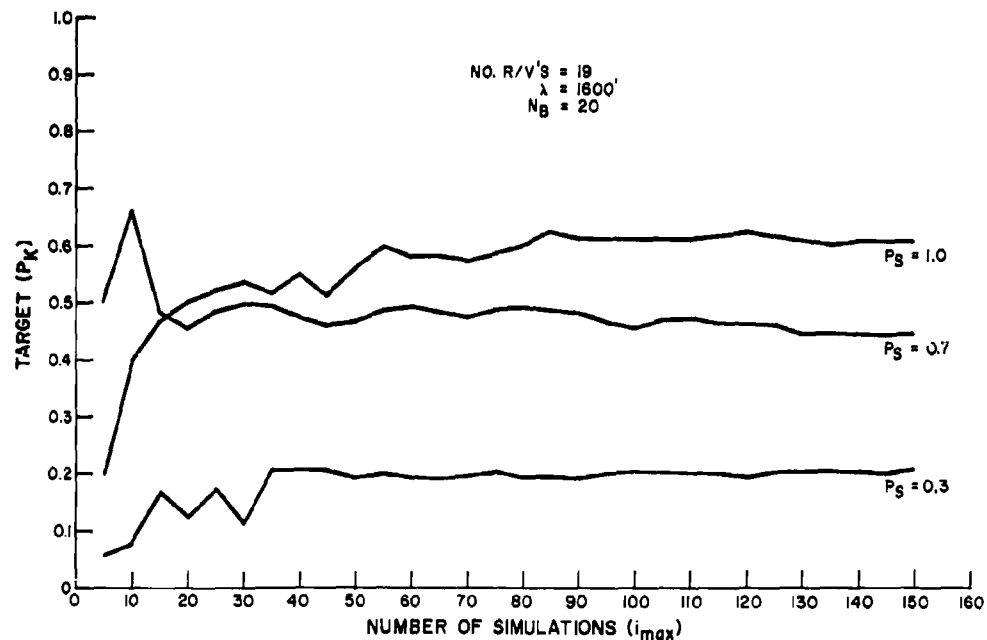


Figure 3. Convergence of Simulated Bernoullian Target Kill Probabilities



with an increasing number of simulations. Nineteen patterned R/V's were used against a point target. A lethal radius of 1600 feet was selected for each R/V. Survival probabilities of 0.3, 0.7, and 1.0 were used. The number of random draws per simulation,  $N_B$ , to determine survival was 20. Multiple Monte Carlo survival determinations are used for a faster kill probability stabilization for the lower survival probability values,  $P_S$ . This technique permits reduction in the number,  $i \max$ , of simulations.

### COMPOSITION OF THE MODEL

In the previous discussion, et seq., reference is made to the bias and random ejection errors. These are shown in Table 1 in terms of standard deviations of

Table 1. Ejection Errors and Linearly Multiplying Error Sensitivity Coefficients

	Type (Error Due to:)	$\sigma$	Range	Crossrange
			Sensitivity Coefficient	Sensitivity Coefficient
<b>BIAS ERRORS</b> Affects carrier vehicle and so all R/V's similarly	Guidance: Range Impact	$a_1$ ft	$D_{1m} = 1$	$F_{1m} = 0$
	Crossrange Impact	$a_2$ ft	$D_{2m} = 0$	$F_{2m} = 1$
	Missile Attitude: Pitch	$a_3$ radians	$D_{3m}$	$F_{3m} = 0$
	Yaw	$a_4$ radians	$D_{4m}$	$F_{4m}$
	Roll	$a_5$ radians	$D_{5m}$	$F_{5m}$
	Target Uncertainty: Range	$a_6$ ft.	$D_{6m} = 1$	$F_{6m} = 0$
	Crossrange	$a_7$ ft.	$D_{7m} = 0$	$F_{7m} = 1$
	Atmospheric (Density & Wind)	set $A_8 = 1$	$D_{8m}$ ( $D_{8m} = N(0, \sigma_{matm})$ )	$F_{8m} = N(0, .98 \sigma_{matm})$
	W/C <sub>D</sub> Bias	$a_9$ (fraction)	$D_{9m}$ ( $D_{9m} = \frac{D_{8m}}{2R/\phi (W/C_D A)} \cdot (W/C_D A)_{m}$ )	$F_{9m} = 0$
	Spares	$\begin{cases} a_{10} = 0 \\ a_{11} = 0 \\ a_{12} = 0 \end{cases}$	$\begin{cases} D_{10m} = 0 \\ D_{11m} = 0 \\ D_{12m} = 0 \end{cases}$	$\begin{cases} F_{10m} = 0 \\ F_{11m} = 0 \\ F_{12m} = 0 \end{cases}$
	Missile Attitude Rate: Pitch	$a_{13}$ rad/sec	$D_{13m}$	$F_{13m} = 0$
	Yaw	$a_{14}$ rad/sec	$D_{14m}$	$F_{14m}$
	Roll	$a_{15}$ rad/sec	$D_{15m}$	$F_{15m}$
<b>RANDOM ERRORS</b> Affects each R/V individually	Fractional Error in $\Delta V_m$	$c_1$ (fraction)	$E_{1m}$	$G_{1m}$
	Angular Error @ Missile: Pitch	$c_2$ radians	$E_{2m}$	$G_{2m} = 0$
	Yaw	$c_3$ radians	$E_{3m}$	$G_{3m}$
	Roll	$c_4$ radians	$E_{4m}$	$G_{4m} = 0$
	W/C <sub>D</sub> Random	$c_5 = a_9$ (fraction)	$E_{5m} = D_{9m}$	$G_{5m} = 0$
	Spares	$\begin{cases} c_6 = 0 \\ c_7 = 0 \end{cases}$	$\begin{cases} E_{6m} = 0 \\ E_{7m} = 0 \end{cases}$	$\begin{cases} G_{6m} = 0 \\ G_{7m} = 0 \end{cases}$
	Angular Error in Velocity Range	set $C_8 = 1$	$F_{8m}$	$G_{8m} = 0$
	due to Thrust Misalignment: Crossrange	set $C_9 = 1$	$E_{9m} = 0$	$G_{9m}$

Note:

$$A_8 D_{8m} = N(0, \sigma_{matm})$$



Gaussian distributions with zero means. Also given are the symbols for the sensitivity coefficients, which may be considered as amplification factors. An input error standard deviation can be multiplied by the related sensitivity coefficient to give an impact (landing point) standard deviation.

Figure 4 is a schematic indicating the sources of bias errors in the R/V carrier at ejection time.

Figure 5 illustrates the sources of random errors for each R/V.

The symbols that follow are defined in the Appendix. The program consists of four routines. In Routine 1, re-entry parameters ( $V_f$ ,  $\gamma_f$ ,  $\theta_R$ ) are computed using the carrier vehicle parameters at insertion ( $r_0$ ,  $\bar{V}_0$ ,  $\gamma_0$ ) and the re-entry height ( $r_f$ ), (see Figure 6). Also calculated are the "sensitivity coefficients"  $K_{RX}$ ,  $K_{RY}$ ,  $K_{HX}$ ,  $K_{HY}$ , which indicate the values for range and height displacements at re-entry for unit changes in  $\bar{V}_0$  in the local horizontal and vertical directions. Thus, the propagation of a deviation from  $\bar{V}_0$  to re-entry may be found. Routine 1 may be used alone or with the other routines. If it is used alone, there is an option of calculating  $\frac{\partial \text{Range}}{\partial (W/C_{DA})_m} (\Delta \bar{g}_m)$ , if  $W/C_{DA}$  varies among R/V's. Figure 7 gives a simplified logic flow for Routine 1.

The R/V's must be ejected to impact in the desired burst pattern. In Routine 2 are computed the velocity impetus needed ( $\Delta \bar{V}_{mxy}$ ) in the trajectory plane, the ejection angle with the local horizontal ( $\beta_m$ ), and the angle with the trajectory plane ( $\alpha_m$ ) required for the  $m^{\text{th}}$  R/V to impact the re-entry plane at a certain point ( $R_{im}$ ,  $C_{im}$ ) and at a certain trajectory spacing ( $\phi_m$ ) from nominal (see Figure 8). Spacing along a trajectory plane separates the re-entry times, thus making it difficult for the defense to attack more than one R/V with one AMM. Also computed in this routine are additional "sensitivity coefficients," which indicate how unit deviations in insertion velocity propagate to re-entry. Routines 1 and 2 may be used alone, if optioned. Figure 9 gives the program instructions for Routine 2.

Routine 3 generates R/V impact points. Assuming the errors are normally distributed, a Monte Carlo technique is used to select errors randomly. Since stochastic variables are involved, multiple selections ( $i_{\text{max}}$ ) are required before the landing point of an R/V can be identified (via its range and cross range standard deviations). For each simulated landing, a set of bias errors ( $A_{ip}$ ) is chosen; then random errors ( $C_{jip}$ ) are chosen for each R/V separately ( $p = 1, 2, \dots, i_{\text{max}}$ ). The errors are multiplied by the appropriate sensitivity coefficients ( $D_{im}$ ,  $F_{im}$ ,  $E_{jm}$ ,  $G_{jm}$ ) and a linear combination is taken, which converts the aimpoint to a simulated landing point (Subroutine Part 3X). The deviations of simulated from intended landing points are stored by bias, random, range and cross range categories. These data are then processed to yield appropriate statistical means and standard deviations. Figure 10 shows the logic of Routine 3.



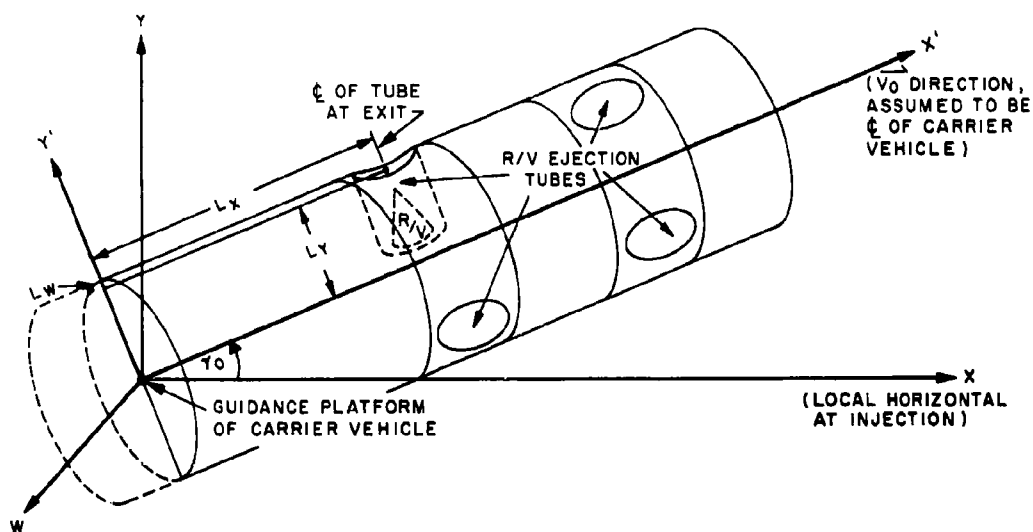


Figure 4. Schematic of a Multiple R/V Carrier

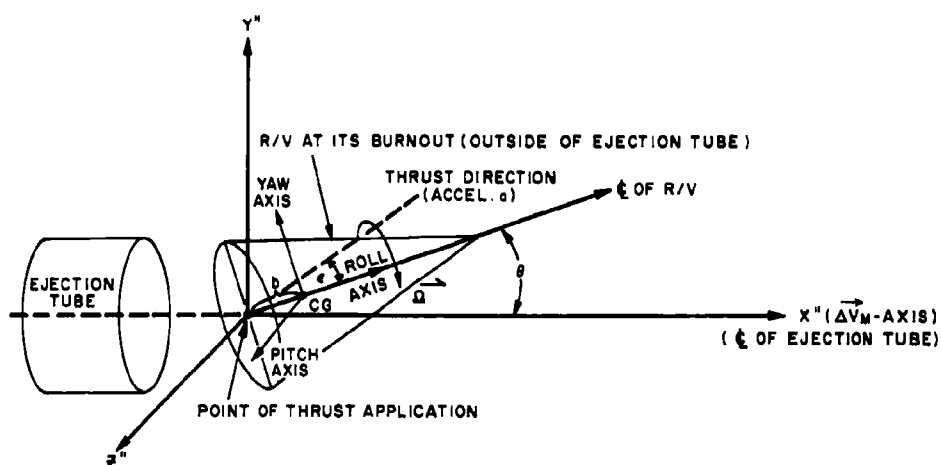


Figure 5. Sources of R/V Random Ejection Errors



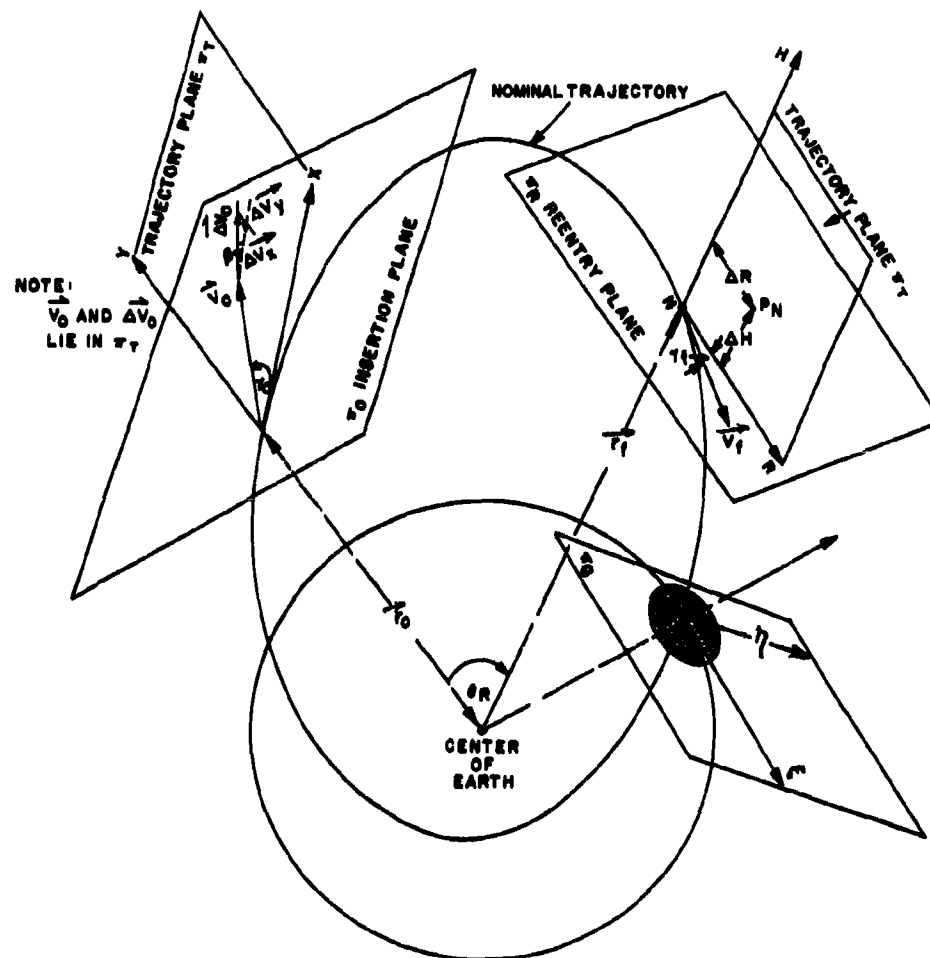


Figure 6. Schematic of Coordinate Systems Used in the Simulation



## MAIN FLOW

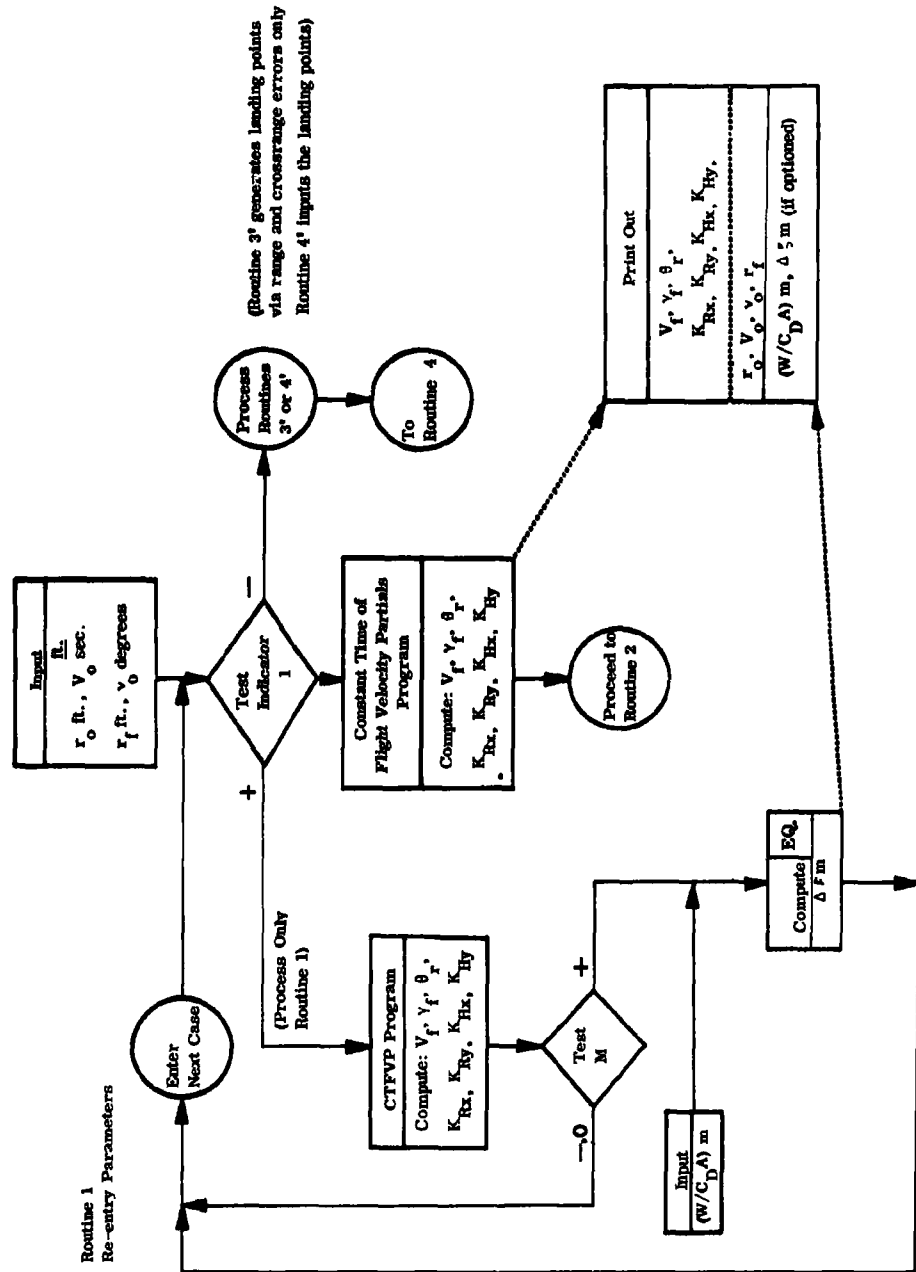


Figure 7. Routine 1 (Re-entry Parameters)







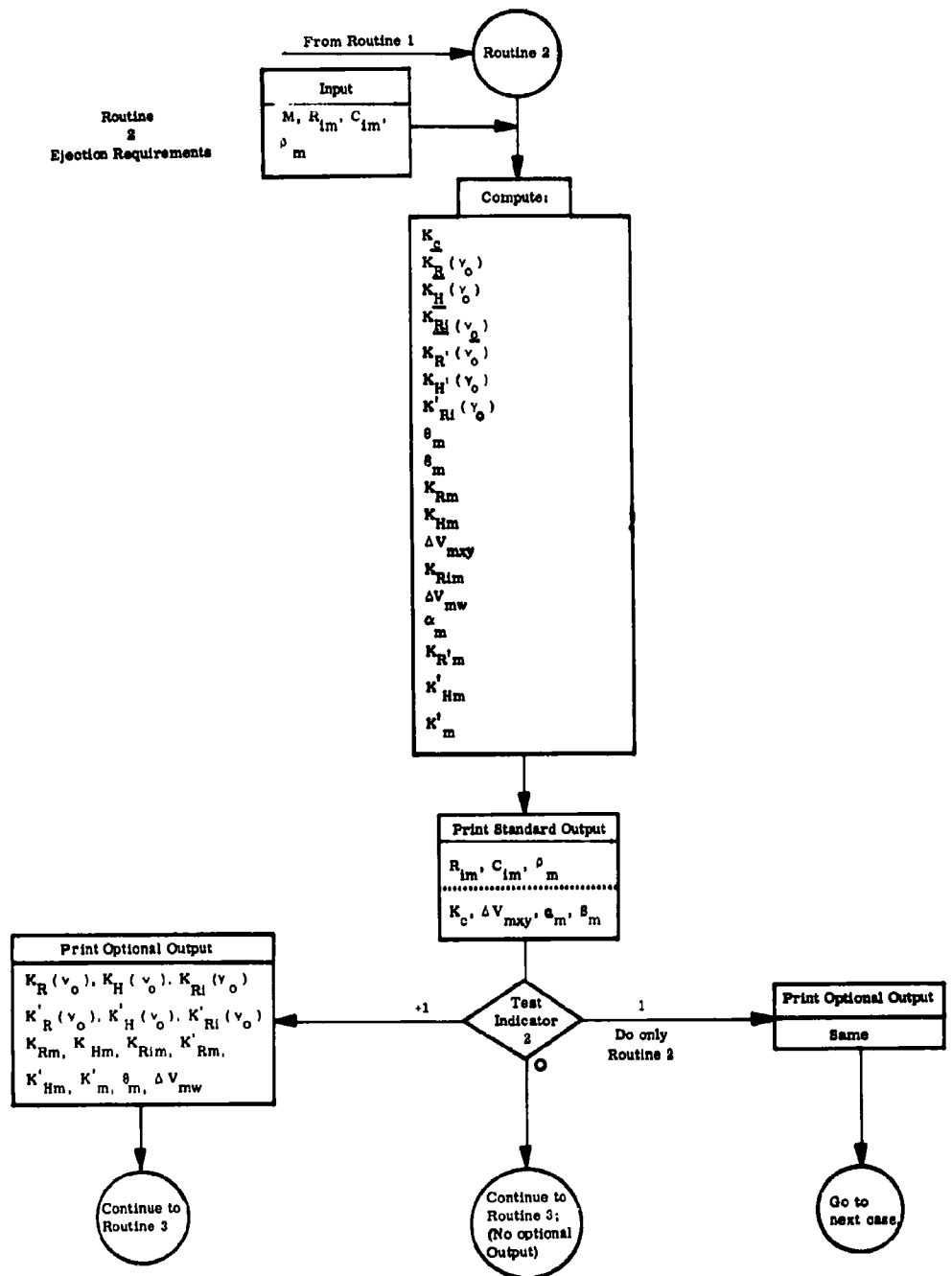


Figure 9. Routine 2 (Ejection Requirements)



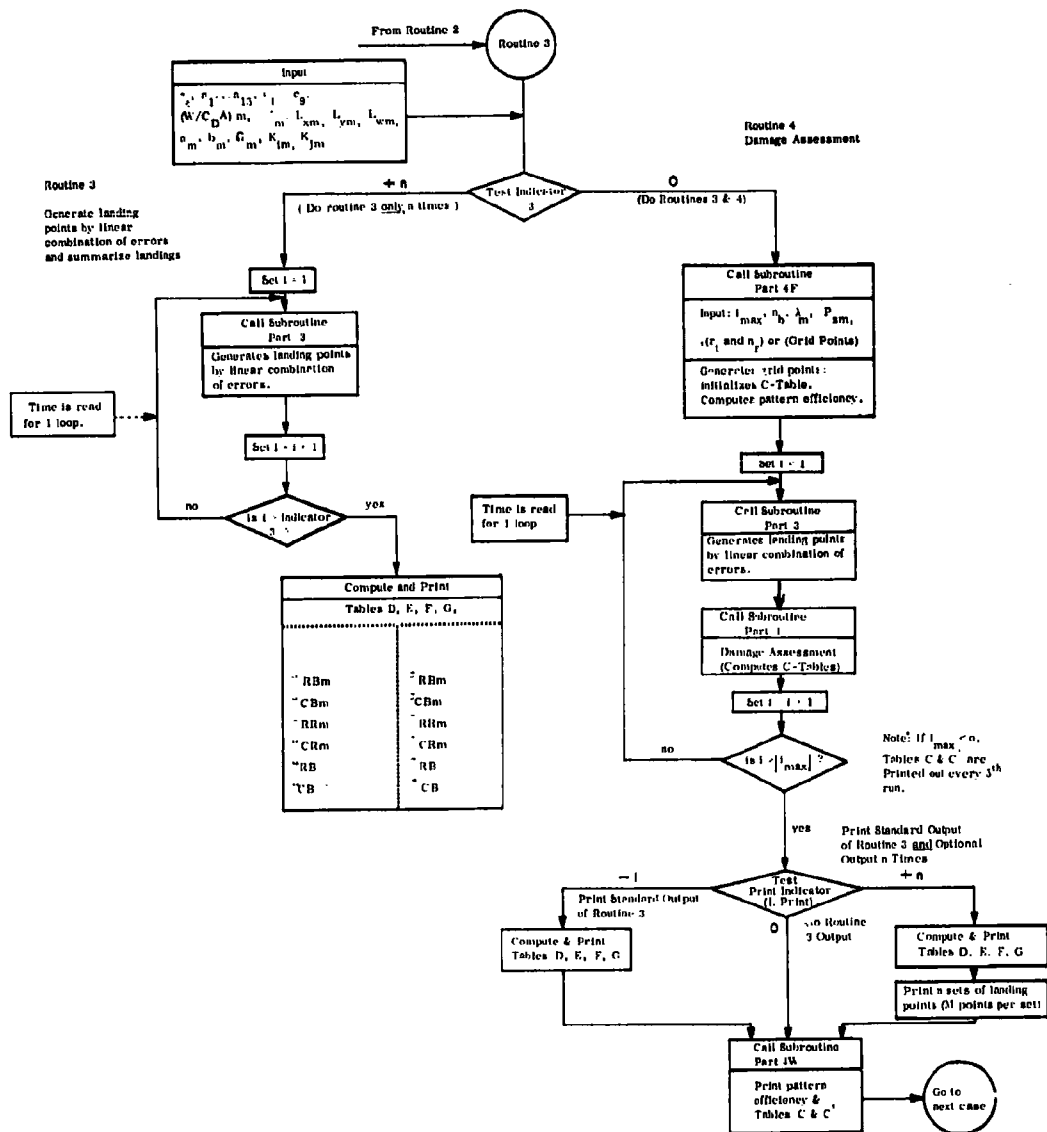


Figure 10. The Logic of Routines 3 and 4



If statistical tests show that the landing point deviations are normally distributed in range and cross range, both for bias and random components, then further landing points may be generated by Routine 3' instead of by Routines 1, 2 and 3 (the three routines may be used alone if so optioned). In Routine 3', landing points are generated by adding to the nominal point the propagated errors obtained with the simulation.

The Monte Carlo approach used in Routines 3 and 3' may be bypassed, and Routine 4' used as a preliminary to Routine 4. In Routine 4', landing points are entered as inputs.

In Routine 4, target damage is assessed. First, the "pattern efficiency" is computed. That is, if all warheads burst at their intended aimpoints, the percentage of target area that would be destroyed is computed. The area target is given as a set of grid points. If a circular target is considered, the program generates the grid points from the target radius ( $r_T$ ), and the number of grid lines ( $n_T$ ) per target radius (which establishes the grid point density). If the target perimeter is irregular, a descriptive set of grid points is generated by giving the ordinate of the first grid line, a spacing ( $\epsilon$ ), and the abscissa of the first grid point on each subsequent grid line, together with the number of grid points on each of these lines. A point target may be defined as circular with  $r_T = 0$ . Figure 10 gives the logic of Routine 4. The "pattern efficiency" and generation of target grid points are executed in Subroutine Part 4F of Routine 4. Part 4F is shown in Figure 11. Routine 4 also uses outputs from Subroutine Part 3 (Figure 12), and Subroutine Part 4 (Figure 13).

In Part 4 of Routine 4, the percentage of area killed is computed for each  $i_{\max}$  run, using (by another Monte Carlo process) the probability,  $P_S$ , of the  $m^{\text{th}}$  R/V penetrating the target's defenses and also the simulated landing point of the  $m^{\text{th}}$  R/V. Routine 4 yields a table (C') in which an entry in the  $i^{\text{th}}$  cell is the probability that  $\leq i$  percent of the target is killed. For a point target, the cell values are equal and represent target survival probability.

#### Options

In summary, the program includes the following options:

1. Routine 1 may be used alone, as a separate program.
2. Routines 1 and 2 only may be used.
3. The target in Routine 4 may be: (a) a circular area target; (b) a point target; or (c) any irregular area, the target being generated by giving the highest horizontal grid line, the spacing between grid lines and grid points ( $\epsilon$ ), the number of horizontal lines, the first point on each line and the number of points on each line.
4. The actual landing points ( $\xi_m, \eta_m$ ) required by Routine 4 may be obtained in three ways: (a) via Routines 1, 2 and 3, in which linear combinations of randomly



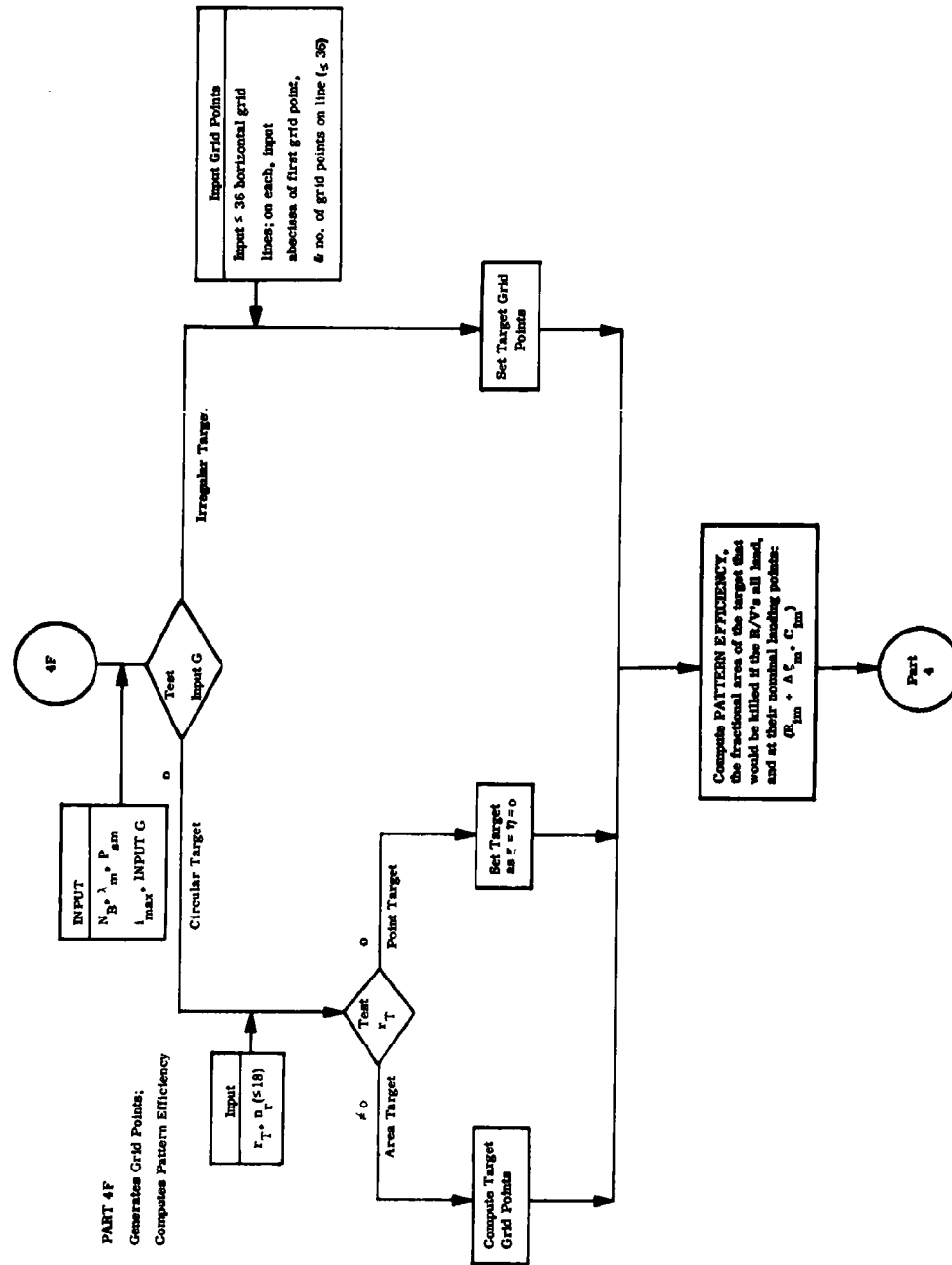


Figure 11. Subroutine Part 4F



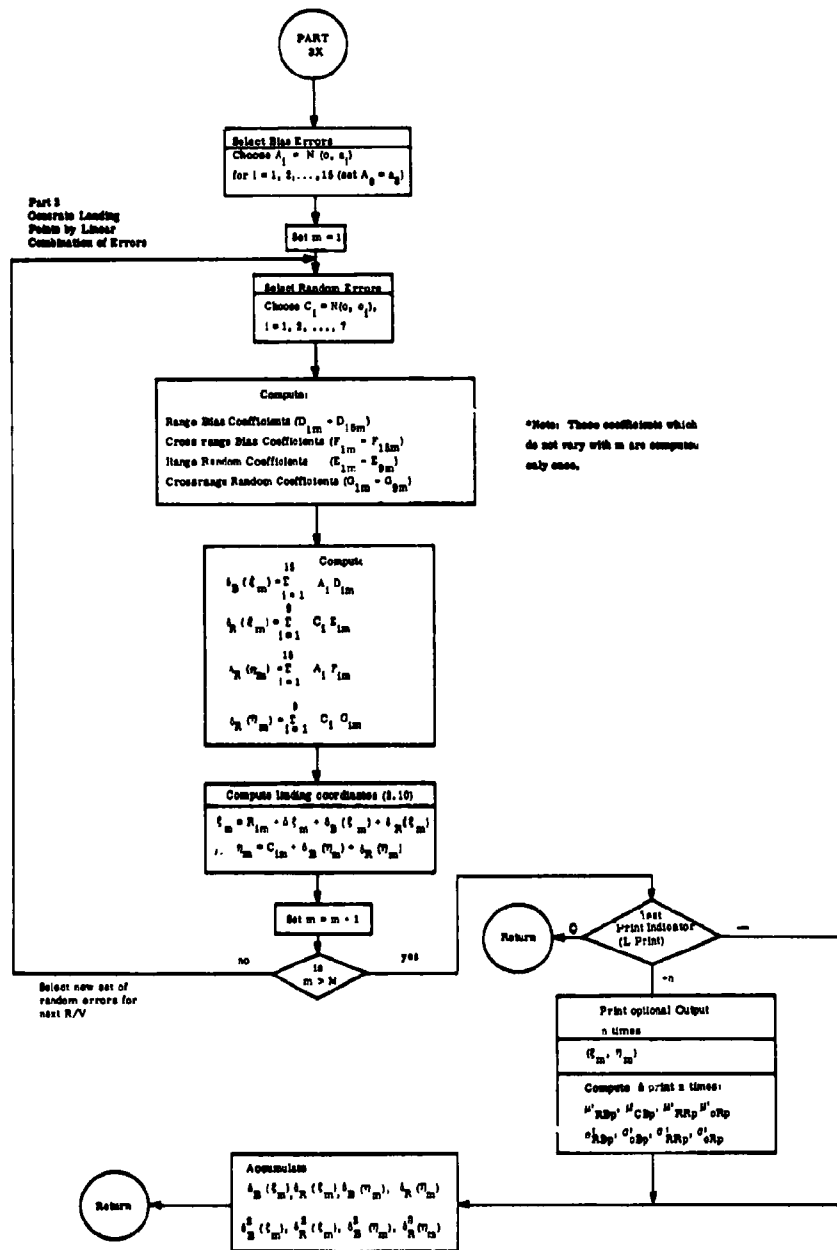


Figure 12. Subroutine Part 3



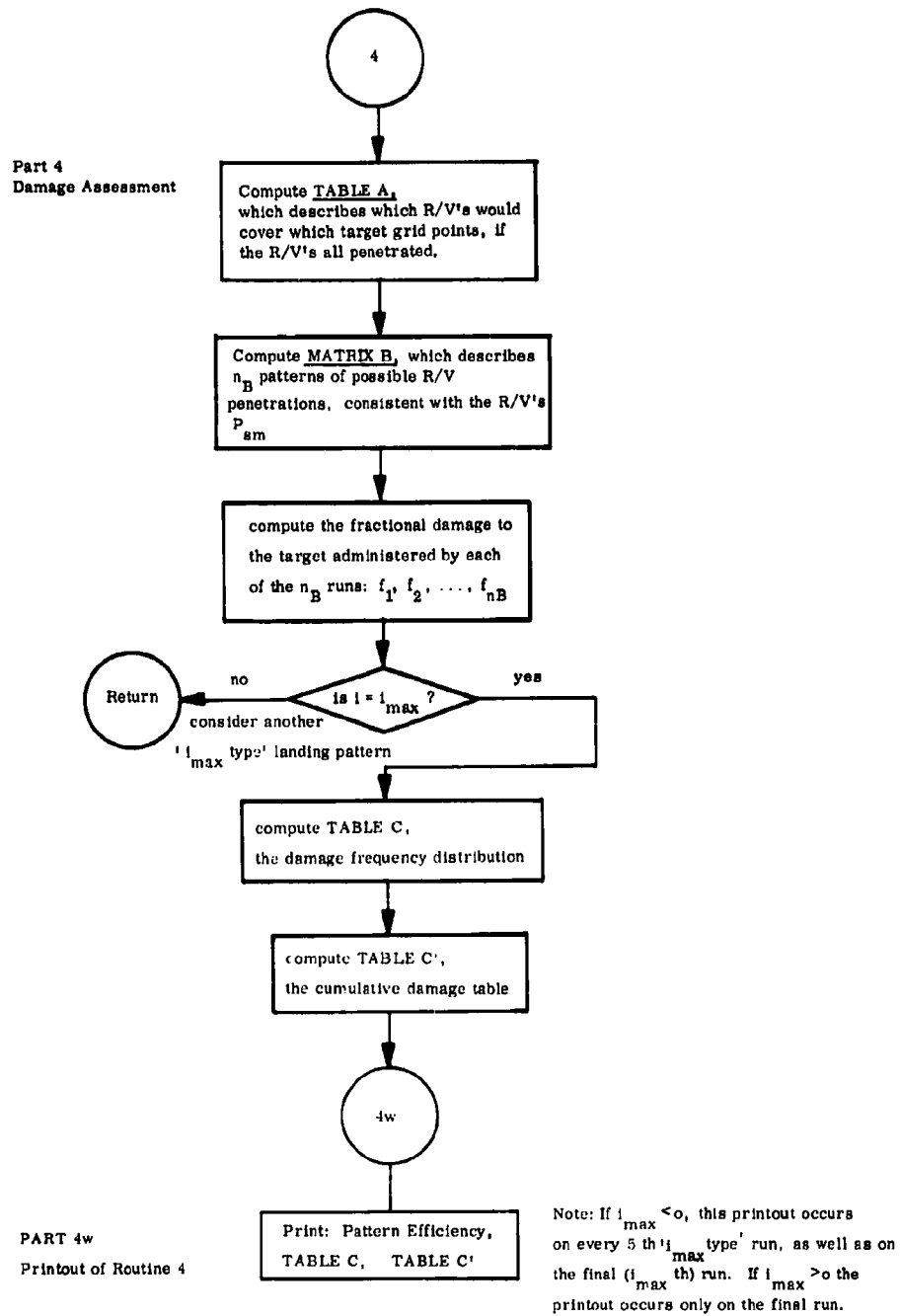


Figure 13. Subroutine Part 4 (w)



selected normal errors are added to the nominal range and cross range; (b) if the actual landing points are normally distributed on the range ( $\sigma_R$ ) and cross range ( $\sigma_C$ ) directions, errors randomly selected from these distributions are added to the aim-point coordinates; or (c) sets of ( $\xi_m$ ,  $\eta_m$ ) may be given as inputs, bypassing all the random features associated with the landing points (except for  $P_{S_m}$ ).

5. In all cases, the "pattern efficiency" is computed. It is the fractional area damage attained by a pattern of R/V's, all of which land at their intended landing points. For a point target, it is unity.

6. Routines 1, 2 and 3 may be run, as a separate program, to provide information on R/V input error sensitivities.

Using only Routines 1, 2, and 3,

$\left. \begin{matrix} \delta \xi_m \\ \delta \eta_m \end{matrix} \right\}$ , the deviation in  $\left. \begin{matrix} \text{range} \\ \text{crossrange} \end{matrix} \right\}$  of the  $m^{\text{th}}$  R/V due to delivery errors on the  $i_{\text{max}}^{\text{th}}$  run, is separated into the bias and random error contributions

$$\left. \begin{matrix} \delta B_p \xi_m \\ \delta B_p \eta_m \end{matrix} \right\} \quad \text{and} \quad \left. \begin{matrix} \delta R_p \xi_m \\ \delta R_p \eta_m \end{matrix} \right\}.$$

These contributions are processed to yield the standard output of Routine 3, which consists of the mean and standard deviation of each of the four error contributions across  $i_{\text{max}}$  runs (for each R/V) and the over-all mean and standard deviation of the bias errors across  $m$  R/V's and  $i_{\text{max}}$  runs. The optional output of Routine 3 may be printed, up to  $n$  times, presenting the actual landing points of the R/V's on each of the  $n$  simulations, together with the mean and standard deviation of each of the four error contributions across  $m$  R/V's for each of the  $n$  simulations.

### SOME APPLICATIONS AND RESULTS

The final objective in the use of the simulation is to balance effective mission performance with the best engineering design characteristics.

A considerable number of investigations have been made with the model. Within the constraints of space, proprietary information, and a decision to keep the paper unclassified, the following three will be discussed: (1) aimpoint patterning, (2) R/V ejection error sensitivity analysis, and finally, (3) an examination of R/V ejection and selected re-entry parameters (design criteria).

#### Aimpoint Patterning

Patterning studies were made by orienting lethal circles over point and area



targets. For the former, the pattern geometry was fitted to the ellipse of the delivery error distribution. Figure 14 shows the results of aiming an elliptical pattern of 17 R/V's at a 500 psi target. The three curves are for R/V survival probabilities of 1.0, 0.7, and 0.3. Target kill probability is related to the ratio of aimpoint spacing distance to lethal radius. The dashed line indicates how the optimum  $r/\lambda$  decreases with reduced survival probability. For small survival probabilities, say  $\leq 0.3$ , direct target aiming for each R/V is best.

Figure 15 presents target kill probability variations with numbers of R/V's for point target hardness values of 50 psi, 30 psi, 1,000 psi, and 4,000 psi. The payload weight is fixed, and the warhead yield decreases with increasing numbers of R/V's. Six to 12 R/V's are preferred for any combinations of  $P_g$  and psi, the exception being the softest (50 psi) undefended target. Excess R/V's can be used against multiple spaced targets or for patterned attacks against area targets. Or, decoys, precursor warheads, BDA data link transceivers, or ECM devices may be substituted.

Compared with a single R/V, multiple R/V's provide a higher chance of at least one penetration of the defenses. Military history shows that the stray bomb, or even a bullet, has played a significant part in the victory. Figure 16 shows that a single R/V survival probability of 0.3 is raised, with 10 R/V's, to 0.98, redefined as the chance that at least one survives. The  $P_g$  variation with R/V numbers and defense KP is also given in Figure 16.

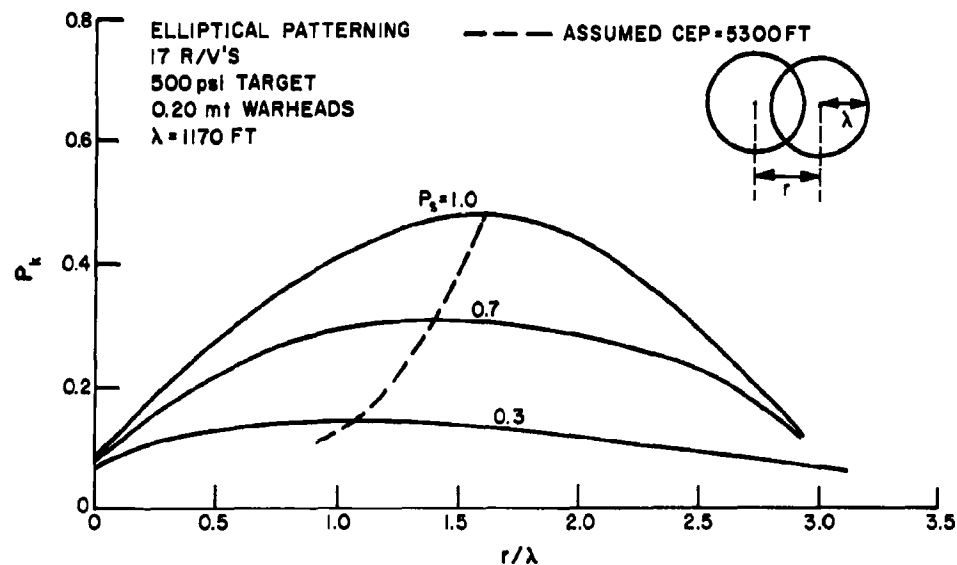


Figure 14. Patterning Compactness Optimization



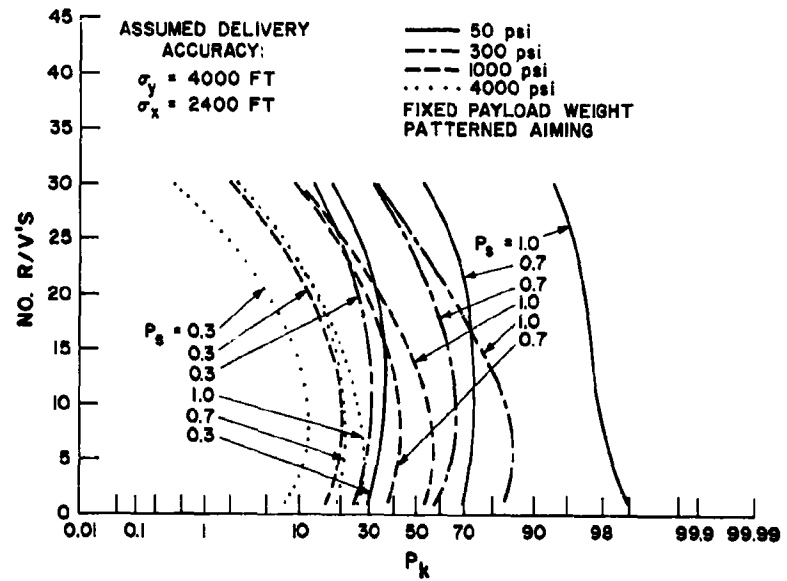


Figure 15. Optimization of No. R/V's for  $P_K$ ,  $P_S$  and Target Vulnerability (psi)

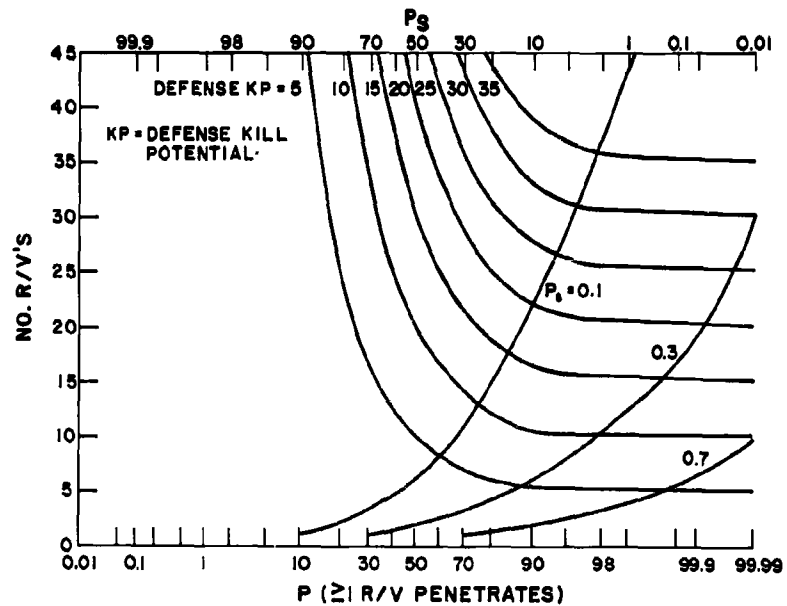


Figure 16. The Relationship of Multiple R/V's to Survival Probability and the Chance of at Least One Defense Penetration



For area targets of low psi values, the accumulative lethal area is normally large relative to target area, even for low R/V survival probabilities. Patterning was therefore designed to fit the target shape, there being little gain expected in fitting the pattern to the elliptical error distribution. If accuracy is poor, the area pattern is tightened; center aiming is most effective for the case of large delivery CEP's.

Figure 17 shows the results of a simulated attack on a circular area of 5.0 nm radius;  $P_g = 0.3$ , and vulnerability is 3.0 psi. Nineteen "beehive" patterned R/V's were used in three separate attacks, with assumed warhead yields of 100 Kt, 50 Kt, and 25 Kt.

For the 100 kt case (curve 1), there is a 90 percent chance of subjecting at least 50 percent of the area to 3.0 psi, a 75 percent chance of attaining 3.0 psi over at least 60 percent, etc. Obviously, the chance of destroying any of the area cannot exceed 30 percent for the case of a single R/V, regardless of warhead yield.

#### Re-entry Vehicle Ejection Error Sensitivities

Particular error sensitivity coefficients were derived such that a linear combination of the product of any ejection error standard deviation and the appropriate coefficient, yields a landing point standard deviation. Figure 18 shows the linear divergence of these coefficient values with range offset aiming from the nominal point. The most sensitive errors are seen to be the bias missile attitude pitch,

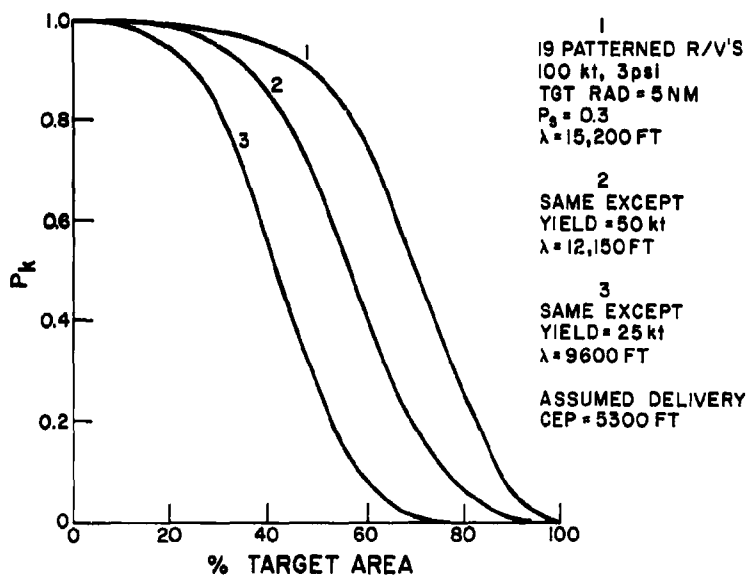
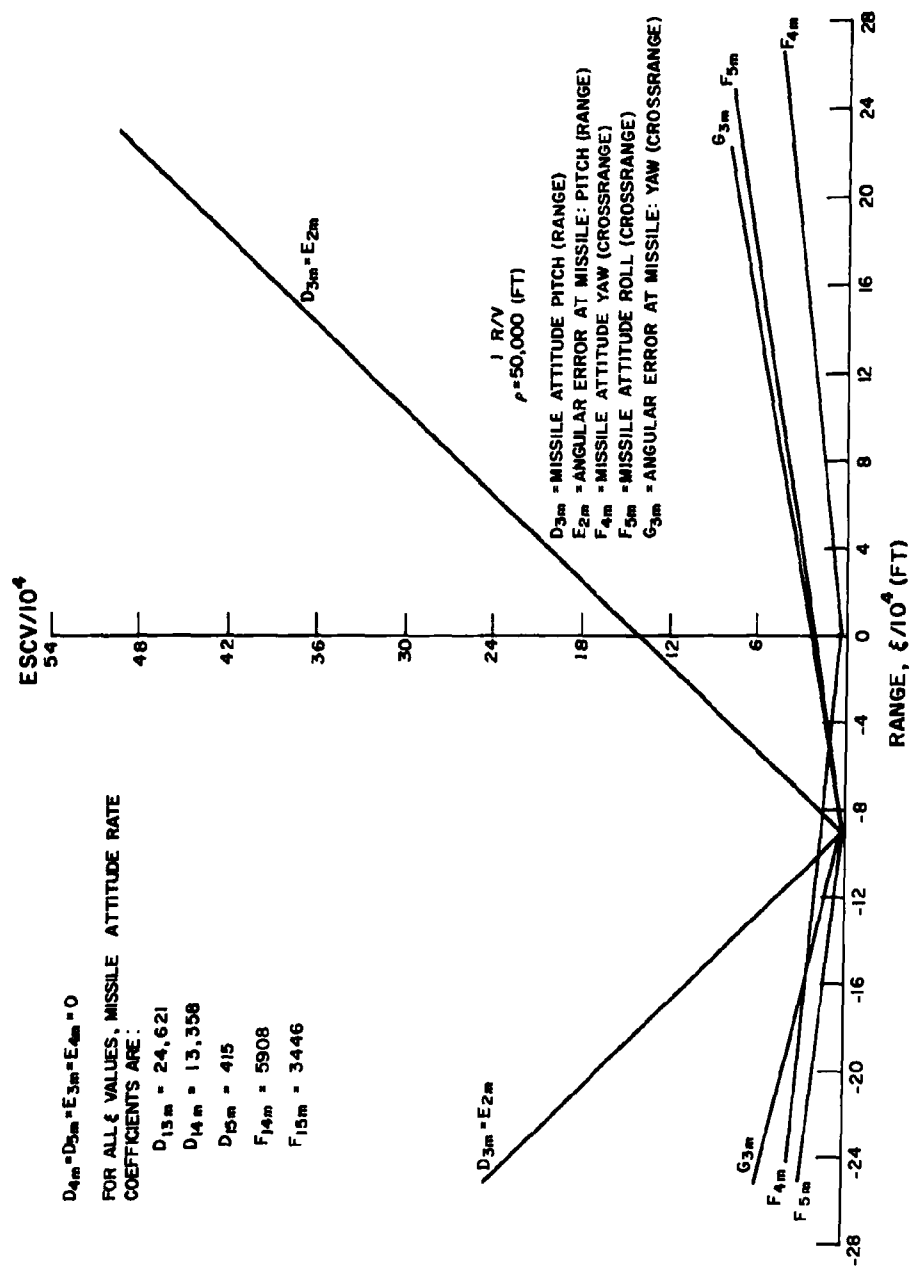


Figure 17. Area Target Attack





**Figure 18. Divergence of the Amplification Factors (Error Sensitivity Coefficients) With Respect to Offset Aimpoint Range Distance**



affecting the range impact error; and the random pitch angular error of the R/V at the missile, affecting the range error. A trajectory spacing from the nominal,  $\rho$ , of 50,000 feet is assumed. The small values in the negative range direction are peculiar only to the particular input error values.

Figure 19 relates the error sensitivity coefficients to cross range offset distance. The largest values are found for E4m, the range error sensitivity coefficient for angular random roll error at the missile; and for D4m, the range sensitivity coefficient for the bias missile attitude yaw error. It is apparent that offset aiming in crossrange can give large range errors if payload stabilization and design tolerances are not carefully considered.

Figure 20 gives the variations, with offset aiming distance, of the error sensitivity coefficients which are inputs to the computation of the D, E, F, and G amplification factors previously discussed. These coefficients serve to propagate ejection errors to the re-entry plane. Three of the coefficients are unaffected by offset distances (note the vertical curves).  $K_{Rim}$  and  $K'_{Rim}$  are range deviations at the re-entry plane due to unit changes in the insertion velocity vector  $\vec{V}_0$  ( $\Delta V_{xy} = 1$ ) in the  $\beta$  direction and  $\beta + \pi/2$  direction, respectively.

#### Some Ejection and Re-entry Parameters - Design Criteria

Simulations have provided data to relate payload and R/V design parameters to the desired mission performance. Some of these data are presented.

Figure 21 parametrically interrelates crossrange aimpoint offset distance ( $\eta$ ) crossrange ejection angle ( $\alpha_m$ ), spacing on the trajectory plane ( $\rho$ ), and R/V velocity requirement ( $\Delta V_{mw}$ ) in the w-direction.

Figure 22 illustrates the requirements for R/V velocity adjustment in the trajectory plane and the ejection elevation angle, for offset aiming in a positive or negative range direction.

Figure 23 relates the burnout angle and burnout velocity with R/V re-entry angle of attack and delivery range, assuming in-line deployment and R/V alignment with the ejection vector.

Space has permitted discussion of some of the model applications and results. Further investigations have been made as follows:

1. Aimpoint patterning (additional studies)
2. R/V survival analyses
  - a. Weight tradeoffs using decoys, chaff, ECM devices
  - b. Defense capabilities



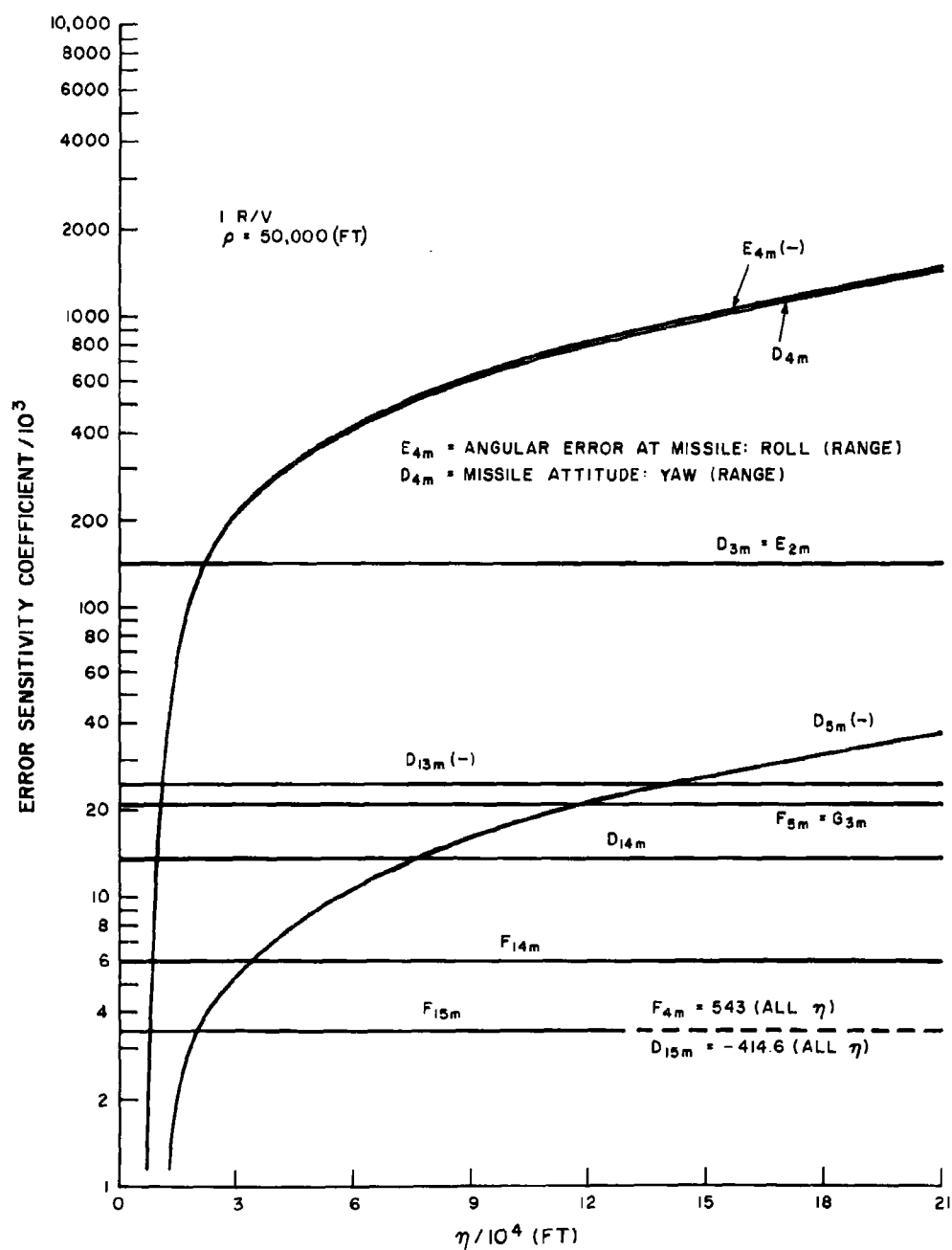


Figure 19. Error Sensitivity Coefficient Value vs. Crossrange Aimpoint from Nominal



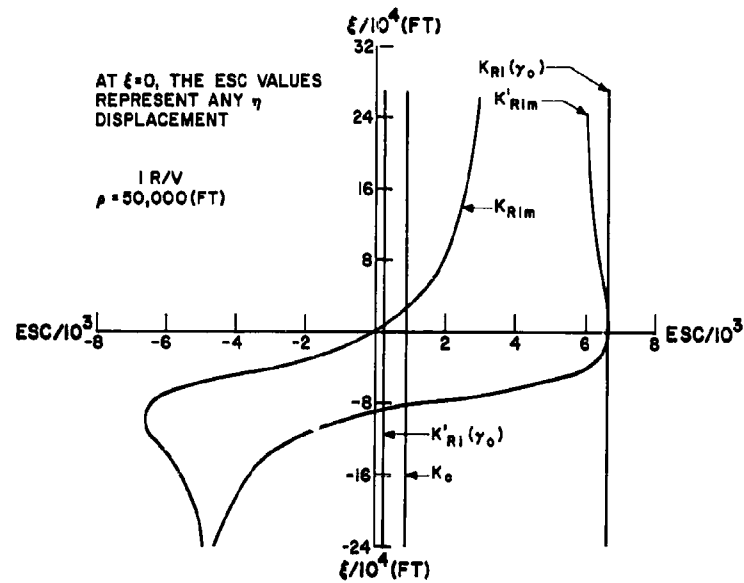


Figure 20. The Behavior of Re-entry Error Sensitivity Coefficients (ESC) With Offset Aimpoint Distance

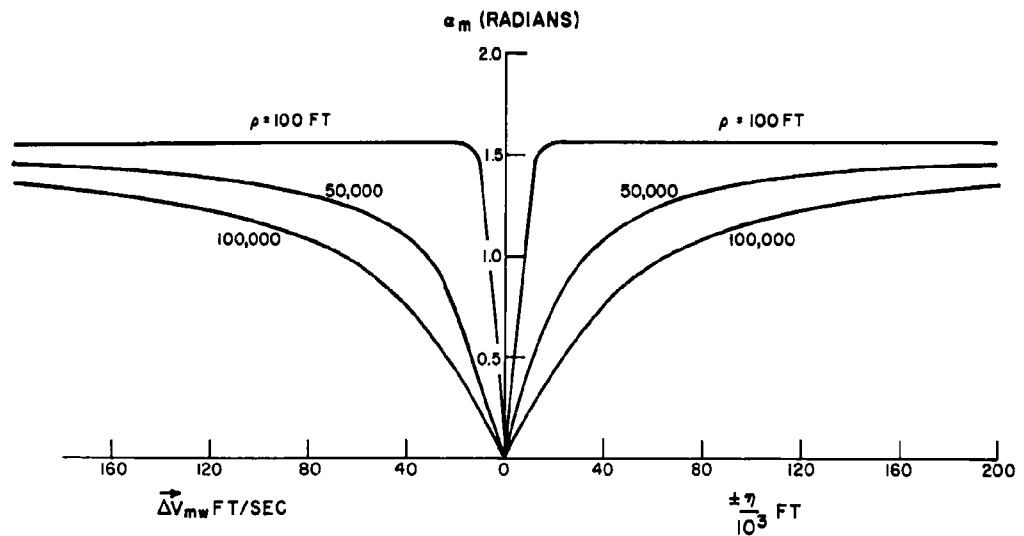


Figure 21. Ejection Parameters for Cross Range Aiming With Trajectory Spacing



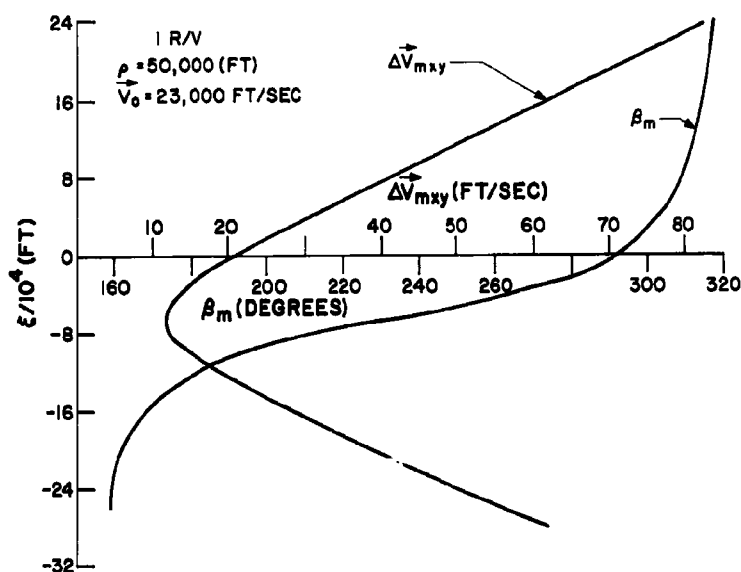


Figure 22. Changes in the Trajectory Plane Elevation Angle and Velocity Components With Respect to Offset Range Distance

3. R/V trajectory spacing with respect to W/C<sub>D</sub>A and AMM lethal envelopes
4. Practicability of attacking multiple targets with multiple R/V's
5. Missile guidance accuracy effects on the use of multiple R/V's
6. Lethal envelope attacks, e. g. for runway cratering
7. Superhard target attacks, e. g. for  $\psi = 6,000$
8. Mixed warhead sizes and W/C<sub>D</sub>A's
9. Cost exchange ratio comparisons
10. Cost effectiveness comparisons
11. Design optimization studies



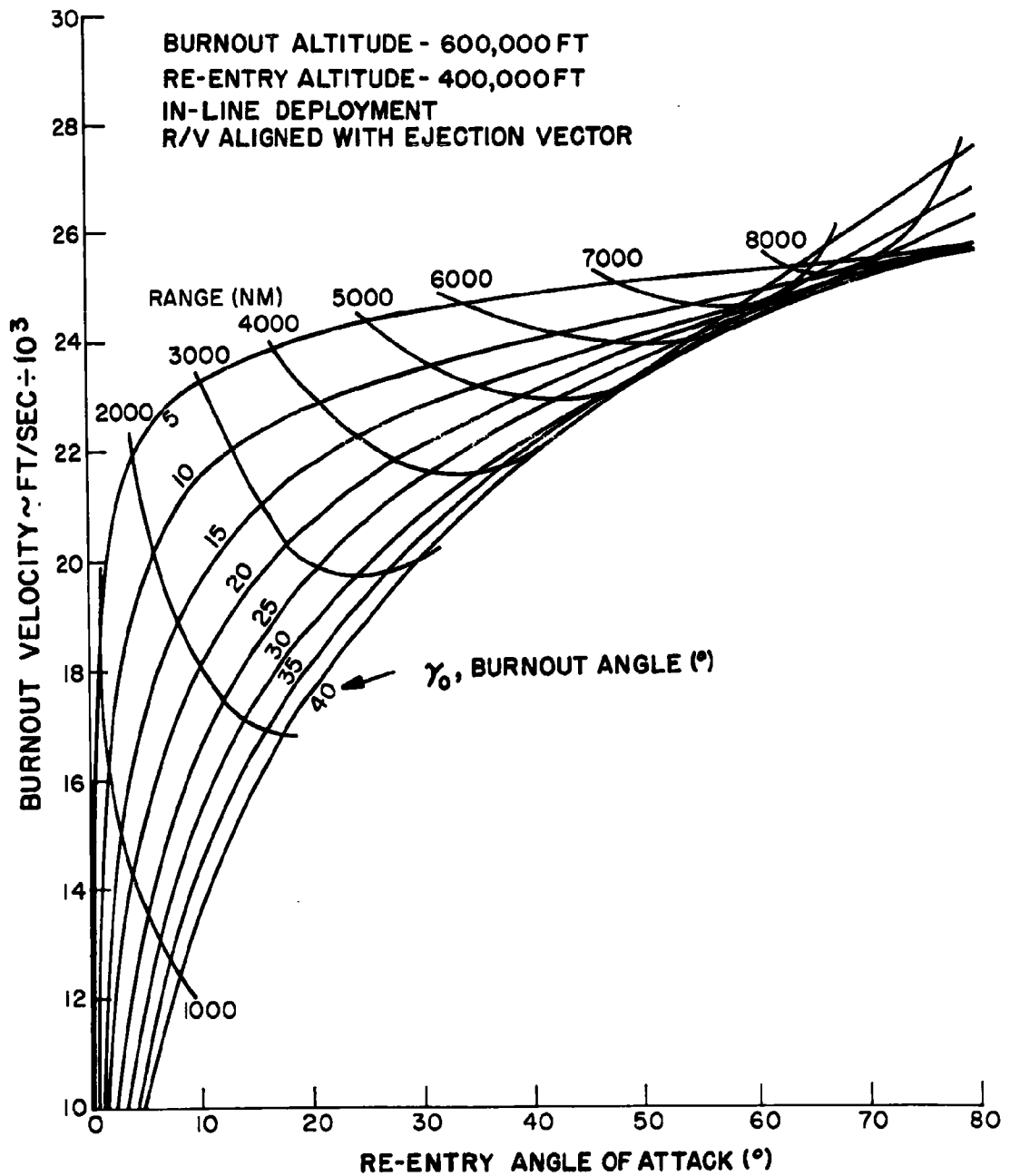


Figure 23. Nomogram Relating Burnout Velocity, Range, Burnout Angle, and Re-entry Angle of Attack



12. R/V ejection parameters handbook preparation. Parametric interrelation of  $V_o, \gamma_o, V_f, \gamma_f, \rho$ , offset  $\xi$  and  $\eta, \beta_m, \Delta V_{mxy}, \Delta V_{mw}, \alpha_m, \theta_R, r_o, r_f$ , etc.
13. Attack economy determination by testing overkill
14. Statistical analyses to test the distributions of separate and combined output errors.

### CONCLUSIONS

A Monte Carlo computer model has been developed for the simulation of multiple re-entry vehicle ejection and target attack. It enables translation of the selected mission strategy to the proper missile payload and to the optimum ejection and design requirements for R/V's, decoys, and other devices. As a corollary, the best attainable design parameters can be converted to the optimum mission performance. A number of options enable a variety of investigations with minimum time and computer costs.

Applications of the model reveal appreciable advantages in using multiple R/V's. The probability of any damage for a single R/V is limited by its survival probability, regardless of warhead yield. Multiple R/V's, however, can achieve high probabilities of large area kill, even with small survival probabilities, with a bonus of a much higher chance of at least one warhead penetrating to the target.

Multiple R/V's with patterned aimpoints can give a point target kill probability exceeding that for a single weapon of maximum payload weight. Six to 12 R/V's are preferred for any R/V survival and target hardness combinations. The exception is found for relatively soft ( $\leq 50$  psi), undefended point targets, for which case one R/V (maximum weight) has a slight advantage, at least for good delivery accuracies.

There is an excellent potential for the use of multiple R/V's to attack multiple, spaced targets. For the offense, booster, launching, and logistics costs are higher for single R/V delivery per target. And defense costs must rise significantly to ensure reasonable multiple target protection against multiple R/V's per booster.

The ambiguities in defining future enemy defense systems makes it difficult to recommend decoy weights. This uncertainty, along with the tendency of increasing payload weights, strengthens the potential of, and the utility of developing, a multiple R/V system.

### ACKNOWLEDGMENTS

Dr. J. D. M. Cameron, Manager, Systems Synthesis, Re-entry Systems Department, effected the trajectory analyses necessary for the Monte Carlo simulation.



This included formulation of the error sensitivity coefficients and the mathematical relation of re-entry vehicle ejection requirements to re-entry kinematics and offset aiming strategies.

Miss Lora Marlette, Advanced Space Projects Department, programmed the model.

#### REFERENCES

1. Cameron, Dr. J. D., "Monte Carlo Program for Computing Kill Probability With Multiple Re-entry Vehicles," unpublished manuscript, Re-entry Systems Department, General Electric Company, Philadelphia, Pennsylvania, June, 1962. (U)
2. Cameron, Dr. J. D., AWSE Memo No. 71, "Approximate Calculation of Normal Velocity Perturbation Due to Thrust Misalignment in a Spinning Vehicle," Re-entry Systems Department, General Electric Company, Philadelphia, Pennsylvania, 23 July 1962. (U)
3. Marlette, L., "Multiple R/V Effectiveness Program," unpublished manuscript, General Electric Company, Valley Forge Space Technology Center, General Electric Company, 1962.
4. Matlin, Dr. S., and Dr. J. Cameron, TIS No. 62SD208, "Multiple Re-entry Vehicle Effectiveness - A Monte Carlo Program," Missile and Space Division, General Electric Company, P. O. Box 8555, Philadelphia 1, Pennsylvania, 19 October 1962. (U)
5. Sebring, H. C., "The Validity of Simulated Target Attacks," a paper presented at the 22nd National Meeting of the Operations Research Society of America, November 1962. (U)
6. Sebring, H. C., ARO Memo No. 8, "Operations Analysis With The Multiple Re-entry Vehicle Simulation Model," Re-entry Systems Department, General Electric Company, Philadelphia, Pennsylvania, 1 February 1962. (C) Unclassified parts used.
7. Sebring, H. C., ARO Memo No. 29, "The Practicability of Attacking Multiple Targets With Multiple Re-entry Vehicles," Re-entry Systems Department, General Electric Company, Philadelphia, Pennsylvania, 8 April 1963. (S) Unclassified portions used.
8. Van Dusen, H., "Re-entry Functions for the Monte Carlo Analysis," PIR No. 8153-224, General Electric Company, Philadelphia, Pennsylvania, 23 August 1962. (U)



## APPENDIX - MULTIPLE R/V DEFINITIONS

Coordinate Systems

At insertion (xyw), re-entry (RHC), on the ground ( $\xi, \eta$ ).

At insertion, xyw is a right-handed coordinate system with the origin at the booster CG; the y-axis in the  $\vec{r}_0$  direction, and the x-axis in the local horizontal direction such that  $\vec{V}_0$  has positive component in the x-direction. The xy-plane is the trajectory plane; the xw-plane is the insertion plane (see Figure 1).

At re-entry, RHC is a right-handed coordinate system with H in the  $\vec{r}_f$  direction and R in the local horizontal direction, positive downrange (in the x-direction). The RH-plane is the trajectory plane of the booster; the RC-plane is the re-entry plane (see Figure 1).

At the ground, the origin of the coordinate system is the impact point of the booster; the  $\xi$ -axis points downrange (in the x- and R-directions), and the  $\eta$ -axis points in the w- and C-directions (see Figure 1). N.B.: to be consistent with Routine 4, the ground plane should be viewed from below the ground, to achieve the orientation:  $\eta \uparrow \xi$

Trajectory Parameters

$\left. \begin{matrix} \vec{V}_0 \\ \vec{V}_f \end{matrix} \right\}$  is the magnitude of the  $\left. \begin{matrix} \text{insertion} \\ \text{re-entry} \end{matrix} \right\}$  velocity of the booster, in ft/sec (see Figure 1).

$\left. \begin{matrix} \vec{r}_0 \\ \vec{r}_f \end{matrix} \right\}$  is the magnitude of the radius vector from the center of the earth to the booster at  $\left. \begin{matrix} \text{insertion} \\ \text{re-entry} \end{matrix} \right\}$ , in feet (see Figure 2).

$\left. \begin{matrix} \gamma_0 \\ \gamma_f \end{matrix} \right\}$  is the angle that  $\left. \begin{matrix} \vec{V}_0 \\ \vec{V}_f \end{matrix} \right\}$  makes with the local horizontal at  $\left. \begin{matrix} \text{insertion} \\ \text{re-entry} \end{matrix} \right\}$  (see Figure 1).

$\left. \begin{matrix} \gamma \\ \gamma_f \end{matrix} \right\}$  is expressed in  $\left. \begin{matrix} \text{degrees} \\ \text{radians} \end{matrix} \right\}$ .

$\theta_R$  is the angle (in radians) from  $\vec{r}_0$  measured clockwise to  $\vec{r}_f$  (see Figure 1).

Partials

$\left. \begin{matrix} K_{Ry} \\ K_{Hy} \\ K_{Riy} \end{matrix} \right\}$  is the  $\left. \begin{matrix} \Delta R \\ \Delta H \\ \Delta Ri \end{matrix} \right\}$  (in feet) at re-entry due to a unit change in  $\vec{V}_0$  in the y-direction ( $\Delta \vec{V}_{xy} = \Delta \vec{V}_y = 1$ ); i. e.,  $\beta = \frac{\pi}{2}$



$\left. \begin{matrix} K_{Rx} \\ K_{Hx} \\ K_{Rix} \end{matrix} \right\}$  is the  $\left. \begin{matrix} \Delta R \\ \Delta H \\ \Delta Ri \end{matrix} \right\}$  (in feet) at re-entry due to a unit change in  $\vec{V}_0$  in the x-direction ( $\Delta \vec{V}_{xy} = \Delta \vec{V}_x = 1$ ); i. e.,  $\beta = 0$

$\left. \begin{matrix} K_R \\ K_H \\ K_{Ri} \end{matrix} \right\}$  is the  $\left. \begin{matrix} \Delta R \\ \Delta H \\ \Delta Ri \end{matrix} \right\}$  (in feet) at re-entry due to a unit change in  $\vec{V}_0$  ( $\Delta \vec{V}_{xy} = 1$ ) in the  $\beta$  direction

$$\text{Approximately, } \begin{cases} K_R = K_{Rx} \cos \beta + K_{Ry} \sin \beta, \\ K_H = K_{Hx} \cos \beta + K_{Hy} \sin \beta, \\ K_{Ri} = K_R + K_H \cot \gamma_f. \end{cases}$$

$\left. \begin{matrix} K'_R \\ K'_H \\ K'_{Ri} \end{matrix} \right\}$  is the  $\left. \begin{matrix} \Delta R \\ \Delta H \\ \Delta Ri \end{matrix} \right\}$  (in feet) at re-entry due to a unit change in  $\vec{V}_0$  ( $\Delta \vec{V}_{xy} = 1$ ) directed normal to  $\Delta \vec{V}_{xy}$ ; i. e.,  $\beta = \beta + \frac{\pi}{2}$ .

$\left. \begin{matrix} K_R(\gamma_o) \\ K_H(\gamma_o) \\ K_{Ri}(\gamma_o) \end{matrix} \right\}$  is the  $\left. \begin{matrix} \Delta R \\ \Delta H \\ \Delta Ri \end{matrix} \right\}$  (in feet) at re-entry due to a unit change in  $\vec{V}_0$  ( $\Delta \vec{V}_{xy} = 1$ ) in the  $\vec{V}_0$  direction; i. e.,  $\beta = \gamma_o$ .

$\left. \begin{matrix} K'_R(\gamma_o) \\ K'_H(\gamma_o) \\ K'_{Ri}(\gamma_o) \end{matrix} \right\}$  is the  $\left. \begin{matrix} \Delta R \\ \Delta H \\ \Delta Ri \end{matrix} \right\}$  (in feet) at re-entry due to a unit change in  $\vec{V}_0$  ( $\Delta \vec{V}_{xy} = 1$ ), directed normal to  $\vec{V}_0$ ; i. e.,  $\beta = \gamma_o + \frac{\pi}{2}$ .

$K_C$  is the  $\Delta C_1$  (cross range displacement at impact in feet) at re-entry due to a unit change in  $\vec{V}_0$  in the w direction ( $\Delta \vec{V} = \Delta \vec{V}_w = 1$ ). (See Figure 8).

### Errors

$\delta \xi_m$  is the change in  $\left. \begin{matrix} \text{range} \\ \text{crossrange} \end{matrix} \right\}$  from nominal of the  $m^{\text{th}}$  R/V at re-entry, in feet, due to the bias and random errors. (See Figure 2, the definition of  $A_i D_{im}$  below, and Table 1).

$$\left. \begin{matrix} A_i D_{im} \\ A_i F_{im} \end{matrix} \right\} \left. \begin{matrix} D_{mj} \\ C_{mj} \end{matrix} \right\} \left. \begin{matrix} D_{jm} \\ G_{jm} \end{matrix} \right\}$$



$A_i D_{im}$  is the displacement of the  $m^{\text{th}}$  R/V from intended ground range due to the range bias error associated with  $A_i$  where  $[A_i = N(0, a_i)]$  and propagated by the "sensitivity coefficient,"  $D_{im}$ .

Similarly,  $A_i F_{im}$  is the crossrange bias error;  $C_{mj} E_{jm}$  is the range random error; and  $C_{mj} G_{jm}$  is the crossrange random error.

$$\text{Note: } \left. \begin{aligned} \delta_p \xi_m &= \sum_{i=1}^{15} A_{ip} D_{im} + \sum_{j=1}^9 C_{jmp} E_{jm} \\ \delta_p \eta_m &= \sum_{i=1}^{15} A_{ip} F_{im} + \sum_{j=1}^9 C_{jmp} G_{jm} \end{aligned} \right\} \text{ on the } p^{\text{th}} (i_{\max}) \text{ run.}$$

$$\begin{aligned} &\mu_{RBm}, \mu_{RRm}, \mu_{RB} \\ &\mu_{CBm}, \mu_{CRm}, \mu_{CB} \end{aligned}$$

$\mu_{RBm}$  is the mean range bias error of the  $m^{\text{th}}$  R/V across  $i_{\max}$  runs, equal to

$$\frac{1}{i_{\max}} \sum_{p=1}^{i_{\max}} \delta_{Bp} \xi_m, \text{ where } \delta_{Bp} \xi_m = \sum_{j=1}^{15} A_{jp} D_{jm}.$$

$\mu_{CBm}$  is the mean crossrange bias error of the  $m^{\text{th}}$  R/V across  $i_{\max}$  runs.

$\mu_{RRm}$  is the mean range random error on the  $m^{\text{th}}$  R/V across  $i_{\max}$  runs.

$\mu_{CRm}$  is the mean crossrange random error of the  $m^{\text{th}}$  R/V across  $i_{\max}$  runs.

$\mu_{RB}$  is the over-all mean range bias error across  $m$  R/V's and  $i_{\max}$  runs, equal to  $\frac{1}{m} \cdot \sum_{p=1}^m \mu_{RBp}$ .

$\mu_{CB}$  is the over-all mean crossrange bias error across  $m$  R/V's and  $i_{\max}$  runs.

$$\begin{aligned} &\sigma_{RBm}, \sigma_{RRm}, \sigma_{RB} \\ &\sigma_{CBm}, \sigma_{CRm}, \sigma_{CB} \end{aligned}$$

$\sigma_{RBm}$  is the range bias error standard deviation of the  $m^{\text{th}}$  R/V across  $i_{\max}$  runs, equal to

$$\sqrt{\frac{\sum_{p=1}^{i_{\max}} (\delta_{Bp} \xi_m)^2}{i_{\max}} - (\mu_{RBm})^2}$$



$\sigma_{CBm}$  is the crossrange bias error standard deviation of the  $m^{\text{th}}$  R/V across  $i_{\text{max}}$  runs.

$\sigma_{RRm}$  is the range random error standard deviation of the  $m^{\text{th}}$  R/V across  $i_{\text{max}}$  runs.

$\sigma_{CRm}$  is the crossrange random error standard deviation of the  $m^{\text{th}}$  R/V across  $i_{\text{max}}$  runs.

$\sigma_{RB}$  is the over-all range bias error standard deviation across  $m$  R/V's and  $i_{\text{max}}$  runs, equal to  $\sqrt{\frac{\sum_{p=1}^m \sigma_{RBp}^2}{m}}$ ; ( $\sigma_{RB}$  is merely the rms of the  $\sigma_{RBm}$ 's).

$\sigma_{CB}$  is the over-all crossrange bias error standard deviation across  $m$  R/V's and  $i_{\text{max}}$  runs, equal to  $\sqrt{\frac{1}{m} \sum_{p=1}^m \sigma_{CBp}^2}$ ; ( $\sigma_{CB}$  is merely the rms of the  $\sigma_{CBm}$ 's)

$\mu'_{RBp}$ ,  $\mu'_{RRp}$

$\mu'_{CBp}$ ,  $\mu'_{CRp}$

$\left. \begin{matrix} \mu'_{RBp} \\ \mu'_{CBp} \end{matrix} \right\}$  is the mean  $\left. \begin{matrix} \text{range} \\ \text{crossrange} \end{matrix} \right\}$  bias error on the  $p^{\text{th}}$   $i_{\text{max}}$ -type run across  $M$

$$\text{R/V's: } \mu'_{RBp} = \frac{1}{M} \sum_{m=1}^M \delta_{Bp} \xi_m$$

$$\mu'_{CBp} = \frac{1}{M} \sum_{m=1}^M \delta_{Bp} \eta_m$$

$\left. \begin{matrix} \mu'_{RRp} \\ \mu'_{CRp} \end{matrix} \right\}$  is the mean  $\left. \begin{matrix} \text{range} \\ \text{crossrange} \end{matrix} \right\}$  random error on the  $p^{\text{th}}$   $i_{\text{max}}$ -type run across  $M$

$$\text{R/V's: } \mu'_{RRp} = \frac{1}{M} \sum_{m=1}^M \delta_{Rp} \xi_m$$

$$\mu'_{CRp} = \frac{1}{M} \sum_{m=1}^M \delta_{Rp} \eta_m$$

$\sigma'_{RBp}$ ,  $\sigma'_{RRp}$

$\sigma'_{CBp}$ ,  $\sigma'_{CRp}$

$\left. \begin{matrix} \sigma'_{RBp} \\ \sigma'_{CBp} \end{matrix} \right\}$  is the  $\left. \begin{matrix} \text{range} \\ \text{crossrange} \end{matrix} \right\}$  bias error standard deviation of the  $p^{\text{th}}$   $i_{\text{max}}$ -type run

across  $M$  R/V's:



$$\sigma'_{RBp} = \left[ \frac{1}{M} \sum_{m=1}^M (\delta_{Bp} \xi_m)^2 - (\mu'_{RBp})^2 \right]^{1/2};$$

$$\sigma'_{CBp} = \left[ \frac{1}{M} \sum_{m=1}^M (\delta_{Bp} \eta_m)^2 - (\mu'_{CBp})^2 \right]^{1/2}$$

$\left. \begin{matrix} \sigma'_{RRp} \\ \sigma'_{CRp} \end{matrix} \right\}$  is the  $\left. \begin{matrix} \text{range} \\ \text{crossrange} \end{matrix} \right\}$  random error standard deviation of the  $p^{\text{th}} i_{\text{max}}$ -type run across  $m$  R/V's:

$$\sigma'_{RRp} = \left[ \frac{1}{M} \sum_{m=1}^M (\delta_{Rp} \xi_m)^2 - (\mu'_{RRp})^2 \right]^{1/2};$$

$$\sigma'_{CRp} = \left[ \frac{1}{M} \sum_{m=1}^M (\delta_{Rp} \eta_m)^2 - (\mu'_{CRp})^2 \right]^{1/2}.$$

#### R/V Parameters

$(\xi_m, \eta_m), \lambda_m, P_{Sm}$

The ground aim point  $(\xi_m, \eta_m)$  of the  $m^{\text{th}}$  R/V in feet; its lethal radius  $(\lambda_m)$  in feet; the probability that it will successfully penetrate the enemy defenses  $(P_{Sm})$ .

$\left. \begin{matrix} R_{im} \\ C_{im} \end{matrix} \right\}$  are the  $\left. \begin{matrix} \text{range} \\ \text{crossrange} \end{matrix} \right\}$  coordinates (in feet) of the intended impact point of the  $m^{\text{th}}$  R/V on the re-entry plane;  $(R_{im}, C_{im})$  is the aimpoint on the re-entry plane of the  $m^{\text{th}}$  R/V (see Figure 8).

$\Delta \xi_m$

A correction (in feet) in the range direction for the  $m^{\text{th}}$  R/V because all R/V's may not have the same  $W/C_D A$ . If the  $m^{\text{th}}$  R/V is displaced from the nominal at re-entry by  $R_{im}$  feet, it will be displaced from the nominal at the ground by  $(R_{im} + \Delta \xi_m)$  feet.

$\Delta \xi_m$  is a previously computed input (see Figure 2).

$\Delta \xi_m$  may be computed separately by using only Routine 1.



$$\frac{W}{C_D A_m}$$

The ballistic parameter of the  $m^{\text{th}}$  R/V, in  $\text{lb/ft}^2$ .

$$\rho_m$$

The spacing (in feet) of the  $m^{\text{th}}$  R/V from the R/V carrier, measured at re-entry from the plane normal to the nominal trajectory. The sign of  $\rho_m$  is positive in the +R direction.

$$\Delta \vec{V}_m, \Delta \vec{V}_{mxy}, \Delta \vec{V}_{mw}, \beta_m, \alpha_m \text{ (Ejection Requirements)}$$

$\Delta \vec{V}_m$  is the change in velocity (in ft/sec) required by the  $m^{\text{th}}$  R/V (as a perturbation on  $\vec{V}_o$ ) at ejection in order to impact the re-entry plane at the intended aimpoint ( $R_{im}, C_{im}$ ).

$\Delta \vec{V}_{mxy}$  is the component of  $\Delta \vec{V}_m$  in the xy-plane;  $\Delta \vec{V}_{mw}$  is the component of  $\Delta \vec{V}_m$  in the w-direction;  $\beta_m$  is the angle (in radians) of  $\Delta \vec{V}_{mxy}$  measured counterclockwise from the positive x-axis;  $\alpha_m$  is the angle (in radians) between  $\Delta \vec{V}_{mxy}$  and  $\Delta \vec{V}_{mw}$ , positive if  $\Delta \vec{V}_{mw}$  is positive (see Figure 8).

$$\theta_m$$

The angle of elevation (in radians) of the  $m^{\text{th}}$  R/V measured from the point where the trajectory's projection on the re-entry plane intercepts the C-axis, counterclockwise with respect to the positive R direction, at the time when the R/V carrier is at the nominal aim point on the re-entry plane (see Figure 8).

$\left. \begin{matrix} L_{xm} \\ L_{ym} \\ L_{wm} \end{matrix} \right\}$  is the distance (in feet) from the w centerline of the ejection tube at the point where the  $m^{\text{th}}$  R/V exits the tube to the  $\left. \begin{matrix} y'w \\ x'w \\ x'y' \end{matrix} \right\}$  coordinate planes depicted in Figure 4. Note that  $L_{ym} > 0$  implies  $\rho_m < 0$ ;  $L_{y'm} < 0 \Rightarrow \rho_m > 0$ .

$$\text{Thrust Misalignment Parameters } a_m, b_m, \Omega_m, K_{im}, K_{jm}, \sigma_e, V_{Tm}, V_{Cm}$$

(See Figures 4 and 5)

$a_m$ : the acceleration of the  $m^{\text{th}}$  R/V at its burnout

$b_m$ : the distance from the point of ejection thrust application to the CG of the  $m^{\text{th}}$  R/V



$\Omega_m$ : the rate at which the  $m^{\text{th}}$  R/V rolls at its burnout

$\sigma_{\epsilon'}$ : the standard deviation of  $\epsilon'$ , the angle of the thrust direction of an R/V makes with the centerline of the R/V.

$\left. \begin{matrix} K_{im} \\ K_{jm} \end{matrix} \right\}$  the radius of gyration of the  $m^{\text{th}}$  R/V about its  $\left. \begin{matrix} \text{pitch or yaw} \\ \text{roll} \end{matrix} \right\}$  axis, assuming  $I_{\text{pitch}}$  (pitch moment of inertia) =  $I_{\text{yaw}}$ .

$$K_i^2 = \frac{I_{\text{pitch}}}{m}; K_j^2 = \frac{J_{\text{roll}}}{m}$$

$\left. \begin{matrix} V_{Tm} \\ V_{Cm} \end{matrix} \right\}$  the magnitude of the velocity due to thrust misalignment  $\left. \begin{matrix} \text{in the} \\ \text{normal to the} \end{matrix} \right\}$  trajectory plane;

Target Parameters ( $r_T, \epsilon, n_r, n_G$ )

$r_T$  is the target radius in feet (when the target is circular).  $\epsilon$  is the spacing between grid points on a grid line, and between grid lines, also in feet.  $n_r$  is the number of grid lines desired per target radius ( $n_r \leq 18$ ).  $n_G$  is the total number of grid points.



## GUIDANCE AND CONTROL



THE PRESENT AND FUTURE ROLES  
OF STRAPPED-DOWN INERTIAL SYSTEMS

Jerry C. Powell

Aeronautical Division  
Minneapolis-Honeywell Regulator Company  
Minneapolis, Minnesota

ABSTRACT

The present and future roles of strapped-down inertial systems are analyzed by a differential comparison of various mechanizations based on size, weight, power, reliability, and ease of maintenance. After definition of the system mechanization problem, inertial systems are divided into those classes using rate sensing devices and those employing free gyros or other types of stable attitude reference. The computer versus gimbal trade-off is then discussed for these classes with emphasis on the strapped-down approach. Free gyro mechanizations are specialized by considering only the electrically supported gyro (ESG). The impact of the electrically supported accelerometer (ESA) and laser rate sensor on future systems is considered.

The work described in this paper was company-sponsored.



## THE PRESENT AND FUTURE ROLES OF STRAPPED-DOWN INERTIAL SYSTEMS

Jerry C. Powell  
Advanced System Specialist  
Precision Inertial Components  
Aeronautical Division  
Minneapolis-Honeywell Regulator Company  
Minneapolis, Minnesota

### INTRODUCTION

The question of whether a system should be strapped down or gimbaled, if nothing else, always seems to generate a lively discussion. System analysts generally agree that strapped-down inertial systems are less accurate than their platform counterparts, but they would probably also agree that if care in design is taken there should be very little difference in accuracy. What disagreement then would prompt a lively discussion of the topic? Proponents of strapped-down systems list these arguments in support of their case:

- Strapped-down systems are smaller, lighter weight, use less power, and are more reliable because the trade-off between replacing the isolation hardware (e. g. , gimbals, etc.) with a computer is in favor of the computer.
- Strapped-down systems have better maintainability because the sensor configuration is less complex.

This paper attempts to discuss these points in terms of present day theory and practice using available hardware, hardware available in the near future, and future system aspects.

### INERTIAL SYSTEM CONCEPTS

#### Inertial System Equation of Motion

Basic to any inertial system is the vector identity

$$\ddot{\vec{R}} = \vec{A} + \vec{G}$$

where  $\ddot{\vec{R}}$  is the second time derivative with respect to inertial space of the position vector  $\vec{R}$  of a vehicle which is to be navigated and/or guided,  $\vec{G}$  is the mass attraction acceleration experienced by the vehicle, and  $\vec{A}$  is the acceleration due to all non-mass attraction forces. The components of the vector  $\vec{A}$  are physically measurable, while the components of  $\vec{G}$  must be deduced from knowledge of the gravitational acceleration field at the position  $\vec{R}$ .



In general, the solution to the navigation problem requires that the right side of the foregoing equation be available, and therefore subsequent integration yields the position of the vehicle. "On-line" integration of  $\ddot{R}$  usually entails "closing the loop" about position by feedback of  $\dot{R}$  to calculate the mass attraction acceleration. This loop closure is sometimes referred to as the "Schuler loop."

In the case of missile guidance the feedback is sometimes "tricked" by taking advantage of prior knowledge of the approximate trajectory of the vehicle. For example, one trick which reduces computer hardware is to compute the mass attraction as a function of velocity from empirical formula if the missile flight path is well defined. By another method, "on-line" acceleration integration may be completely eliminated to reduce system complexity at the expense of accuracy. This is done by preflight computation of the equation of motion. This type of system is sometimes referred to as a flight reference system, which controls vehicle attitude and relies on a timer and predictable boost conditions to achieve its mission requirement. Various combinations of these methods are in common use. Thus, in general, to achieve system operation the acceleration vector  $\ddot{A}$  must be measured. How  $\ddot{A}$  is measured, to a large degree, determines the system configuration.

In platform mechanization the components of  $\ddot{A}$  are measured by isolating a triad of single-axis accelerometers from vehicle motion. Thus the accelerometers measure the components of acceleration while the platform is maintained in a known attitude to give "direction" to the measurement.

#### The Strapped-Down System Problem

In strapped-down system operation, the accelerometers are body-mounted to the vehicle. To give "direction" to the outputs of the accelerometers, the instantaneous attitude of the accelerometer triad must be known. In general this requires the values of the elements of a three-by-three orthogonal matrix with which transformation of the accelerometer outputs to a known frame of reference is possible. If  $T$  denotes this transformation, the vector identity mentioned above may be written as

$$\ddot{R} = T\ddot{A}' + \ddot{G}$$

where the prime on the acceleration vector  $\ddot{A}$  means that it is measured in a different coordinate frame than the rest of the elements of the equation (i. e.,  $\ddot{A} = T\ddot{A}'$ ). The fundamental problem in strapped-down inertial systems is how to deduce the transformation  $T$ .

Basically, there are two methods of obtaining the transformation:

1. On-line integration of rate information.
2. Direct observation by the use of free gyros or some other type of inertial reference.

With these basic methods, many mechanizations are possible. Some of these are now discussed.



## STRAPPED-DOWN SYSTEMS EMPLOYING RATE MEASURING DEVICES

### Differential Equations for an Orthonormal Matrix Transformation

In general, an orthonormal transformation  $T$  always exists so that the orthogonal triad defined by the sensitive axes of the accelerometers may be carried into any convenient inertial reference frame by the transformation. Application of the Coriolis law for vector derivatives to the base vectors defining the computational inertial reference axes yields a set of nine differential equations for the elements of the transformation  $T$ . In matrix notation these nine equations may be written as

$$\dot{T} = T \Omega$$

where  $\Omega$  is a skew-symmetric matrix whose three independent elements are the components of the angular rate of the accelerometer triad with respect to inertial space. These nine equations, six of which are independent, are nonlinear, and a closed form solution exists only when the angular rate is a constant. A sufficient condition for existence of a closed form solution is equivalent to the same condition that must hold for a finite rotation to be expressible as a vector. This fact gives rise to the so-called "coning problem" sometimes encountered, and extreme care must be taken in on-line computation of the transformation  $T$ . Computer requirements are discussed later.

### System Configuration

Error analysis [ see, for example, (1) ] has shown that only two of today's rate sensing devices are capable of meeting normal system requirements:

1. A hermetically sealed floated rate integrating gyro (HIG) which is digitally torqued to achieve extremely small gimbaled hangoff.
2. A HIG mounted in a single-axis platform and servoed about the gyro input axis to achieve a torque null on the gyro gimbal.

The reason why only two rate sensing devices have thus far qualified as strapped-down sensor candidates seems obvious. The rate device that is used must have a high degree of linearity all the way from the unpredictable drift rate of the gyro up to the maximum angular rate of the vehicle. This represents a dynamic range of the order of  $10^8$  to  $10^9$ .

Figures 1 and 2 illustrate the functional operation of strapped-down systems using single-axis platforms and pulse-torqued gyros, respectively. For completeness, Figure 3 illustrates the functional operation of a flight reference system. Figure 4, the functional operation of an inertial platform, is shown for comparison.



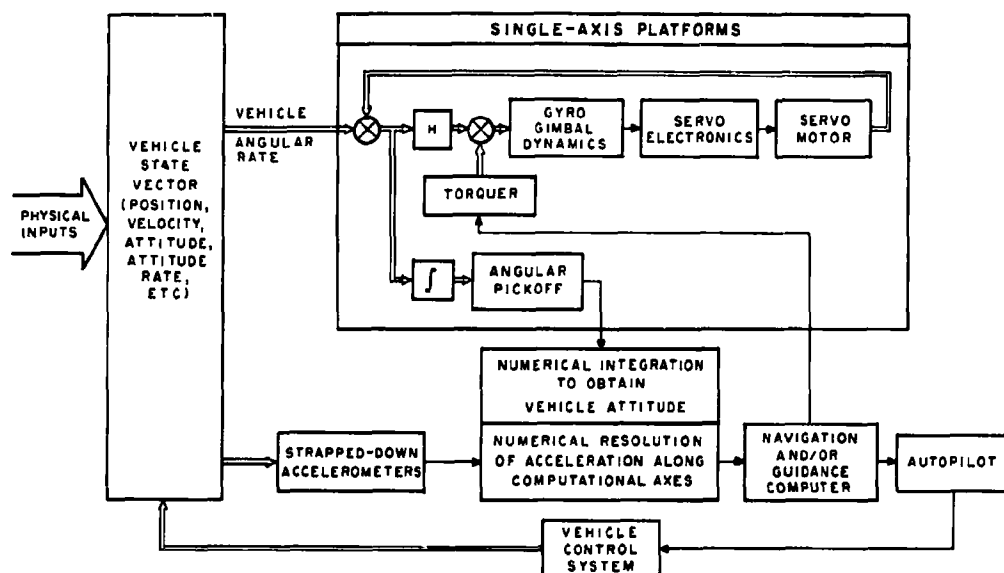


Fig. 1. Functional Operation of Strapped-Down Systems Using Single-Axis Platforms

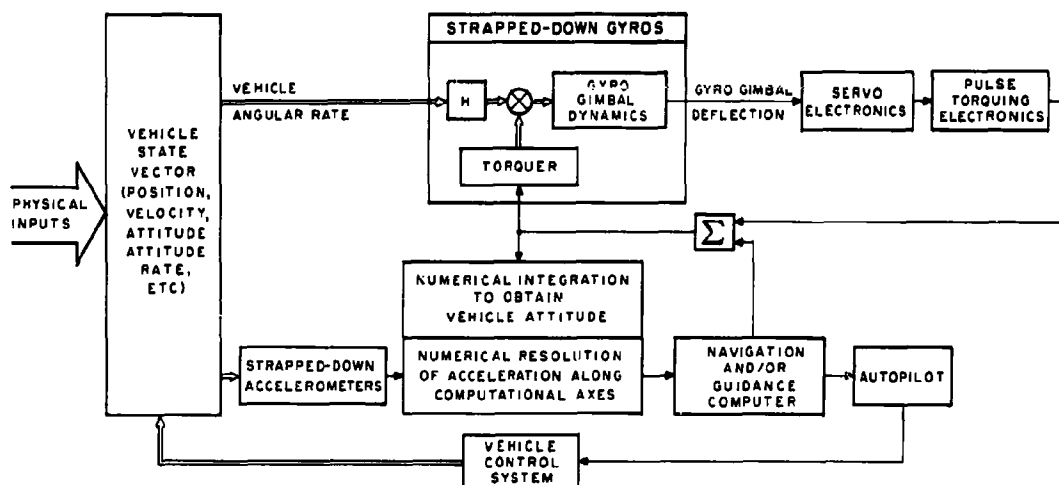


Fig. 2. Functional Operation of Strapped-Down Systems Using Pulse-Torqued Gyros



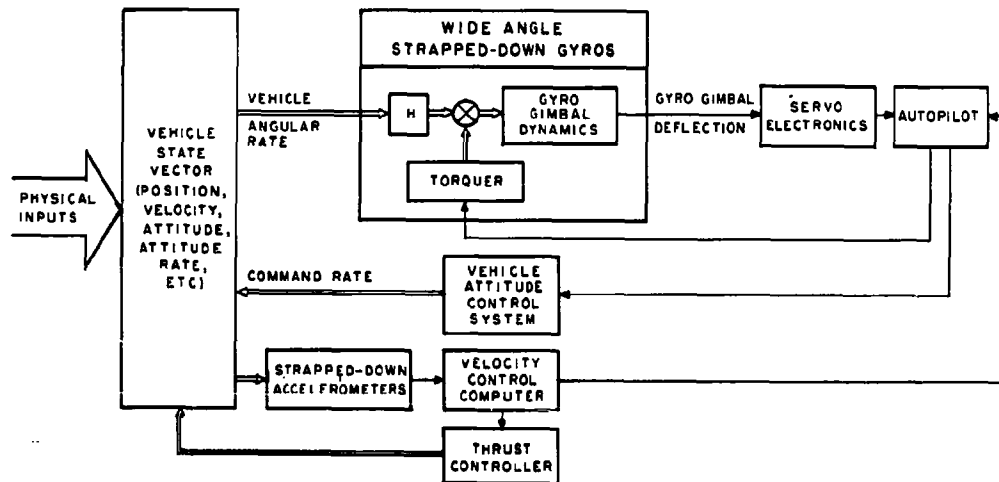


Fig. 3. Functional Operation of a Flight Reference System

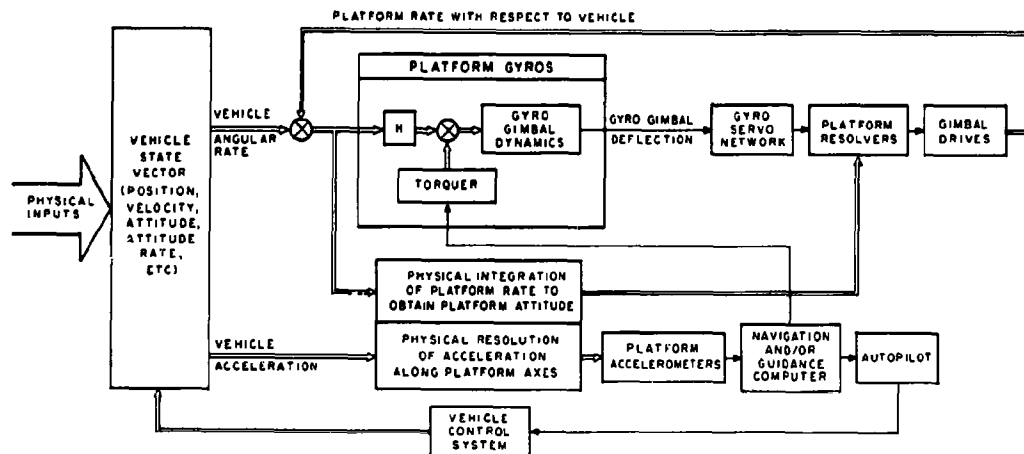


Fig. 4. Functional Operation of an Inertial Platform



In all four systems, feedback through the gyro torquer from the navigation computer is illustrated. This, of course, will vary from system to system. Some have no active feedback, while others, such as a local-vertical platform, depend heavily upon it. In addition, some systems employ accelerometer torquing. Initial alignment is accomplished in roughly the same fashion for every system by gyro torquing from accelerometer signals to obtain level alignment and by either gyro compassing or optical linkage to obtain azimuth.

Although the flight reference system is not actively included in this discussion, it deserves some comment because of its fairly wide application. The basic operation of this system depends on rate loop closure about the gyros through the vehicle attitude control system. Since the tightness of this loop is limited by the vehicle dynamics, there must be provision for fairly wide excursions of the gyro gimbals. Under these conditions, cross-coupling becomes a major factor. Insofar as missile guidance and control are concerned, the only difference in basic operation between this system and the other three is how well the cross-coupling effects can be minimized. Thus, in a sense, the strapped-down systems using pulse torquing, single-axis platforms, or the platform system itself serve only to provide a tight inner attitude control loop with more "memory" content. As shown in Figure 3, accelerometers are employed in the flight reference system. As mentioned in the introduction, however, some systems use only a timer to provide thrust cut-off. System accuracy dictates the choice of mechanization.

A modification of the system using single-axis platforms is a system using six pendulous gyro accelerometers (PGA's). For complete details see (2). These instruments differ from a single-axis platform only to the extent that they have a pendulous mass located on the gimbal. Since each of the six instruments have an output proportional to both angular rate and acceleration, sufficient information is provided for navigation and/or guidance.

The advantage of this type of system lies in continuous rotation of the sensors, which acts to attenuate some of the gyro errors. The penalty for this advantage is two-fold:

1. Extreme stability of the input axis of each unit is required to minimize acceleration effects from coupling into the rate measurement.
2. The rate information must be corrected for size or separation effect.

Size effect is due to the fact that the pendulous masses in the gyro gimbals "see" a centrifugal force proportional to the square of the angular rate environment. This effect can be designed out of the acceleration measurement but can never be designed out of the rate information channels. The effect is present in all systems, but only in the six-PGA configuration does it affect rate measurement. In platform systems the effect may be neglected.



Thus, of all rate measuring devices available today, only the pulse-torqued rate gyro, the single-axis platform, and the pendulous gyro accelerometer seem to meet the requirement of strapped-down systems if the method of integrating rate to obtain an inertial reference is to be used. These instruments may be employed in some hybrid fashion as system requirements dictate. The choice of adequate accelerometers depends on roughly the same criteria used in platform systems.

### Computer Considerations

Except for the requirement of on-line computation of the transformation matrix  $T$ , computer requirements for strapped-down or platform systems are roughly the same and shall be considered the same for discussion purposes.

The set of differential equations  $\dot{T} = T\Omega$  is only one of several possible representations of the transformation. In this representation,  $T$  is usually referred to as the direction cosine transformation. Other possible representations have been studied as being perhaps easier to mechanize in a computer:

1. Euler angle representation
2. Cayley-Klein parameter representation
3. Quaternion representation

It is the opinion of this author that the direction cosine representation is not only the most straightforward but also the easiest to mechanize.

Possible computer algorithms are now considered. If  $\Omega$  is constant, a solution of the form

$$T(t) = T(0)e^{\Omega t}$$

is obtained where  $e$  raised to the matrix  $\Omega t$  power is defined by the exponential infinite series. If  $t_{n+1} - t_n = h$  represents the time interval between successive computer cycles, the value of  $T$  at the time  $t_{n+1}$  may be written as

$$T(t_{n+1}) = T(t_n)e^{\Omega h}$$

But  $\Omega h$  for constant  $\Omega$  represents the matrix of small angles through which the vehicle rotates in the time interval  $h$ . If that matrix is represented by  $\Delta\Theta = \Omega h$ , then

$$T(t_{n+1}) = T(t_n)e^{\Delta\Theta} = T(t_n) \left[ 1 + \frac{\Delta\Theta}{1!} + \frac{(\Delta\Theta)^2}{2!} + \dots \right]$$



which defines an updating procedure. By letting the length of each computer cycle approach zero, it would be possible to obtain a solution to an arbitrary degree of accuracy. The mechanization approach which seems most straightforward then is to fix an angular resolution which is defined by the inertial sensor employed (e. g. , the angular worth of each pulse, in digital torquing, or the pickoff resolution from an angle readout on a single-axis platform) and then let the matrix  $\Delta \Theta$  represent the existence of a change in attitude of the vehicle over one computer cycle. Thus, by truncating the infinite series exhibited above, the result would be, for example,

$$T(t_{n+1}) = T(t_n) + T(t_n) \Delta \Theta$$

or

$$\Delta T(t_{n+1}) = T(t_n) \Delta \Theta(t_{n+1})$$

which now defines a gating procedure for an incremental computer mechanization. The algorithm  $\Delta T = T \Delta \Theta$  is a so-called first-order algorithm. A second-order algorithm is the updating defined by  $\Delta T = T[\Delta \Theta + (\Delta \Theta)^2/2]$ , which is the next approximation of the series. It can be shown that the first-order algorithm is the only stable algorithm that exists. The word "stability" as used here means that the error incurred by series truncation is bounded.

The problem of truncation is, of course, not the only consideration. Of major importance is the coning effect previously mentioned. Since the matrix  $\Delta \Theta$  represents a small but nevertheless finite rotation, the order in which the nine direction cosine elements of  $T$  are updated is of prime importance. This is, of course, a direct consequence of the non-commutability of finite rotations. Thus not only must adequate truncation be defined but also an order procedure for updating must be implemented.

Suppose  $p$  is the least angular change that may be sensed and issued by the sensor. (If the order of the sensor outputs is noted and implemented in the computer mechanization, coning drift may still occur due to angular motion of amplitude less than the finite pickoff resolution. This type of drift is usually much less than the unpredictable drift rate of the gyro.) If  $w$  is the angular rate along one of the coordinate axes and if the restriction is imposed that the direction cosine matrix can be updated only once per channel per computer cycle, the inequality

$$wh \leq p$$

must hold so that information from the sensors is not lost. If the pickoff resolution is, for example, 20 seconds of arc and the maximum vehicle angular rate is one rad/sec, the time interval  $h$  allowed for one computer cycle is roughly  $10^{-4}$  sec or a computer iteration frequency of about 10 kc. To put this frequency in perhaps more familiar terms, using machine language and a computer program quite close to optimum with respect to speed, this represents a computer - to - real-time ratio of roughly 6:1 or 8:1 on an IBM 7090 computer. On the basis of this example, straightforward



computer mechanization in a general-purpose airborne computer seems out of the question, and improved computer speeds in the foreseeable future will not appreciably alter this conclusion.

If the above discussion is accepted, basically two choices are available to this type of a strapped-down system:

1. Design a special-purpose high-speed "front end" that may be tied to a general-purpose computer to solve the direction cosine problem.
2. "Trick" the computer mechanization by using some not-so-straightforward method.

The first approach has many merits. Present-day computer logic has more than enough speed to solve the direction cosine problem. The difficulty seems to lie in the economics of computer development.

"Tricking" the computer mechanization may take many forms. For example, although the second-order algorithm previously discussed is unstable in the strict sense, it might be employed [as was done by at least one company; see, for example, (3)] in system applications where only short periods of operation are required and where larger angular increments can be used. In this way, the direction cosine problem could hopefully be resolved through the use of a high-speed general-purpose computer.

In summary, then, the computer problem for strapped-down inertial systems using rate information may be solved with little effort by a special-purpose computer. The decision to do so, however, must come from other considerations such as the over-all worth of the solution. In the author's opinion, it is possible to solve the computer problem adequately for ballistic missiles by employing a high-speed general-purpose computer and a "tricked" computer program.

#### Computer versus Gimbal Trade-off

The merits of a strapped-down system using the rate integrating devices previously outlined are now investigated. System analysts generally agree that, with care in design, a strapped-down system can compete with a platform in system accuracy. It is believed that present-day single-axis platform and/or pendulous gyro accelerometers can meet accuracy requirements in the body-mounted vibration environment. This may or may not require shock mounting of the sensor package. However, some gyro vibration errors must be seriously considered. For example, in many gyros the principal moments of inertia along the spin and input axes are mismatched. This may, under certain conditions, cause torque rectification. Further, the spin, output, and input axes of the gyro may not be principal axes of inertia. In steady state this causes no problem, but it is possible to get torque rectification through the off-diagonal elements of the inertia tensor of the gyro gimbal. Many of these effects become less important in platform mechanization. How important they are in strapped-down operation remains to be seen.



In a recent Honeywell study of two hypothetical systems, the smallest gimbaled system was compared with the smallest gimbaleless system. The strapped-down system employed pulse torqued gyros and pulse rebalanced pendulums for accelerometers, while the platform used the same sensors in gimbals. Numerical results are classified and therefore not included here. However, it can be reported that, although the strapped-down system had an advantage in every category except possibly accuracy, the margin in each case was within the uncertainty of the estimates. Thus, there was no overriding factor in either system. In fact, on the basis of design experience, the platform should perhaps be declared the winner. What, then, can be said for strapped-down systems using single-axis components?

The study mentioned above used the smallest inertial sensors presently available which meet the accuracy criteria defined. If larger sensors were employed, to obtain some gain in accuracy or for some other reason, the balance would probably swing toward the strapped-down system owing to the larger platform requirements. At present, however, this advantage would be slight.

Experience has shown that gimbal mechanisms are quite reliable compared to the inertial sensors they support. On the other hand, the degree of reliability of the computer that would replace the already proven gimbal structure is still questionable. In any event, it would seem that inertial sensor reliability is the dominant factor, and reliability of isolation and/or computer hardware is secondary. Thus, arguments in favor of strapped-down systems cannot at present be effectively generated from a reliability standpoint.

#### The Maintainability Argument

In maintainability, strapped-down systems can take a strong stand. Usually, if an inertial sensor in a platform fails, the entire platform must be pulled from the vehicle and proper repairs made. This is necessary because the sensors in the platform inner element are somewhat inaccessible, although some systems employ an "inside-out" gimbal arrangement. In a strapped-down sensor package, however, an individual unit (or at most, for example, a gyro-accelerometer package) may be pulled and replaced. There is, of course, the problem of physical alignment and/or calibration of the replacement item, but this may be solved by accurate machining of the mounting surfaces and possibly changing some computer alignment constants.

#### Conclusions

It must be kept in mind that the preceding discussion applies specifically to strapped-down systems employing rate measuring devices. From this discussion, the following qualified conclusions are drawn:

- With proper design care, strapped-down systems can compete with platforms in accuracy.
- For long-term navigation, a high-speed special-purpose computer is probably required to make strapped-down systems practical. For boost and/or injection or other short-term missions, a high-speed general-purpose computer is deemed adequate.



- The computer-versus-gimbal trade-off in terms of size, weight, and power may be slightly in favor of the strapped-down system, but the margin is very small.
- Over-all system reliability is still dictated by the reliability of the sensors, and the picture will probably not change in the near future.
- Ease of maintenance is generally in favor of the strapped-down system.

As the size, weight, and power requirements of computer hardware are reduced, as is being done quite rapidly, the strapped-down system concept becomes more attractive. However, even without the computer, the balance of power is not overwhelming. Considering, in addition, the over-all lead in platform production techniques, the future of strapped-down systems of the rate sensing variety is not favorable. Such systems can, nevertheless, play a valuable role, but only to complement rather than to replace platforms.

#### INERTIAL SYSTEMS EMPLOYING ELECTRICALLY SUSPENDED GYROS

The previous section of this paper was concerned with a comparison of systems using rate integrating methods. This section will deal with the second dominant system concept -- that of obtaining an inertial reference by direct observation, which includes the use of free gyros, star trackers, etc. Only the free gyro, and in particular the electrically suspended gyro (ESG), will be considered here. The choice of the ESG for making a system comparison seems logical because it is the only free gyro presently available which seems adequate for high-accuracy systems.

In the case of strapped-down versus gimballed systems using rate devices, discussion of system mechanization merits were only loosely tied to the choice of the sensor. In ESG system considerations, the gyro characteristics are more closely tied to the system analyst's approach. For this reason, a portion of this section is devoted to gyro operation.

##### Electrically Suspended Gyro Characteristics

Briefly, an ESG operates by controlling voltages applied to a set of electrodes concentric with a spherical rotor. The electric force field developed between the rotor and electrodes continuously drives the rotor toward the center of the gyro case, thus achieving support. When the rotor is spun, its angular velocity vector tends to seek a stable attitude defined by its axis of maximum inertia. This effect is accentuated by making the hollow interior of the rotor oblong. Thus the spin vector (or angular momentum vector) becomes fixed with respect to the rotor once nutation incurred during spin-up has been damped out. Gyro readout is accomplished through the aid of a pattern applied to the exterior of the rotor. By virtue of the stable spin axis, the pattern bears a fixed relationship to the spin direction.



Two fundamental readout methods have been devised, each having several possible variations. Both methods rely on an optical link between a pattern inscribed on the rotor surface and optics fixed with respect to the case. The first method employs a pattern on the rotor which is pierced by the spin axis and is such that a signal proportional to the angular distance between the spin axis and the optical line of sight is developed. This signal can then be used to close a servo loop to drive the optical line of sight and hence the gyro case so that it "follows" the spin axis. This method then may be used as the basis of a gimbaled system mechanization.

The second method of readout, a strapped-down approach, uses the timing of a series of line crossings of a pattern under a pickoff. The pattern is designed so that the frequency of crossing is a function of the angle between the spin axis and the pickoff line of sight. By using two or more pickoffs, it is then possible to deduce the "direction cosines" (i. e., the attitude) of the spin axis with respect to the gyro case.

#### System Configurations

Bearing in mind that the fundamental purpose of the ESG's is to provide "direction", two system configurations immediately present themselves:

- Use of gimbaled pickoffs of two ESG's to close a rate loop through a set of gimbal drives and thus stabilize a platform on which acceleration measurement is performed.
- Use of two strapped-down ESG's and a set of strapped-down accelerometers in conjunction with a computer. The ESG spin axis orientations can be used to mathematically construct an inertial frame of reference, and from this the transformation  $T$  relating the attitude of the accelerometer triad with respect to space is derivable. Thus the accelerometer outputs, measured in the moving frame of the vehicle, may be transformed to inertial space.

These two processes are roughly the same, and indeed would be identical if the mathematically defined reference were the same as that of the platform. Figures 5 and 6 are block diagrams of these mechanizations.

Initial system alignment for both the strapped-down and the gimbaled system may be performed in one of two ways:

1. Closed-loop torquing
2. Computer alignment



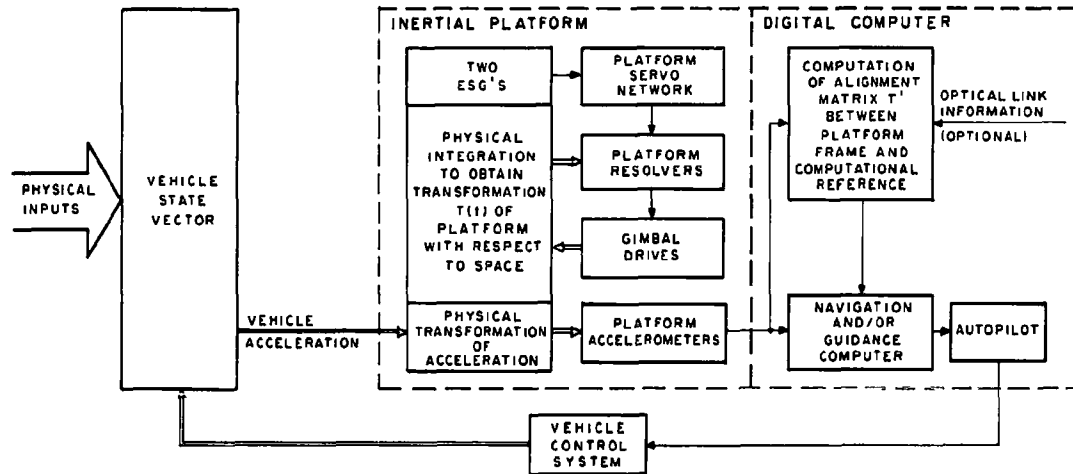


Fig. 5. Gimbaled System Configuration

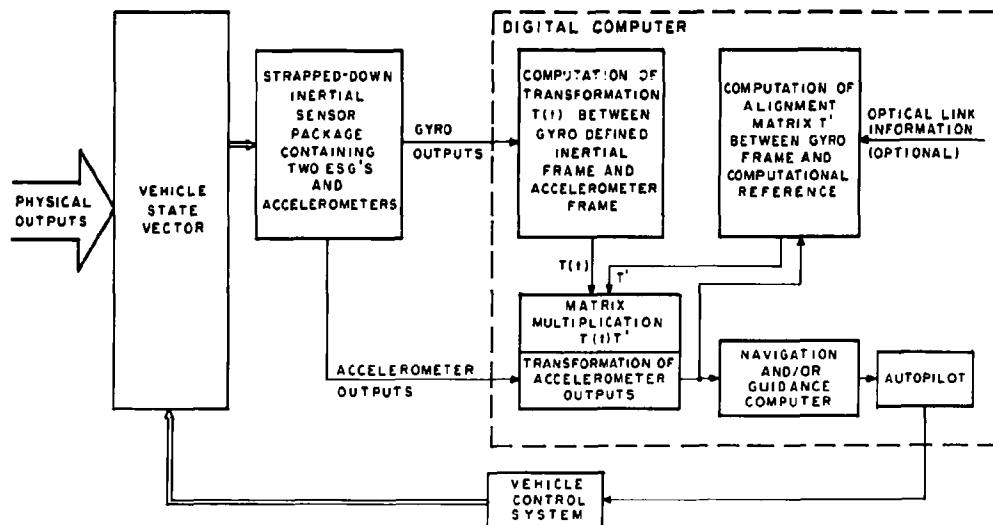


Fig. 6. Strapped-Down System Configuration



Although a "precision" torquing capability of the ESG does not exist (in the sense of precision pulse torquing of floated gyros), closed-loop torquing can still be accomplished. This is done in the same fashion as outlined in the systems configurations using rate gyros\*.

A second method -- computer alignment -- seems, in the opinion of the author, to be the most desirable however for two reasons: (1) ESG magnetic torquing produces a heating effect which, although small, may be detrimental to gyro performance and (2) the trade-off between hardware complexity is probably in favor of the computer.

Alignment by the computer method is still accomplished by using the accelerometer outputs for leveling and gyro outputs or optical link to obtain azimuth, but the information is treated differently. For example, in the case of the platform, the accelerometer outputs are with respect to an inertial reference frame defined by the initial spin-up of the gyros. If the platform is not torqued the accelerometer outputs will have to be transformed to the frame of reference convenient for computation. (It should be clear that computation could be performed in the gyro reference frame with subsequent transformation of the result, but this is usually less efficient.) The same remarks apply to the strapped-down system. Thus the transformation between the gyro defined inertial reference and the computational reference frame may still be generated from accelerometer and gyro outputs and/or optical link, but the information is used to generate a transformation matrix instead of torquing signals.

#### Reasons for Gimballing an ESG

Two solid reasons exist for using the ESG in a gimbaled mode. The first is accuracy of readout. Current pickoff technology indicates that the pickoff is roughly an order of magnitude more accurate than the strapped-down pickoff, but the gap between the two is closing quite rapidly. In either case, however, the angular readout is sufficiently accurate to match most present accelerometer accuracies.

The second reason for gimballing an ESG concerns predictable drift torque compensation. Of the sources of torques that degrade gyro performance, the two most serious but fortunately the most predictable, are mass unbalance and electric torque caused by a nonspherical rotor. In the case of gimbal mode operation, these two torques can be made to cancel each other to achieve a very low torque null uncertainty. Torque compensation in the strapped-down mode may be achieved through presently available computer compensation techniques.

Thus, on the one hand gimbaled operation achieves more accurate readout and on the other reduces computer complexity.

---

\*There is a slight difference; since ESG magnetic torquing coils are not completely orthogonal, there exists torquing signal cross-coupling. It is easily established, however, that with cross-coupling present the servo is stable and achieves a null.



### Computer Considerations

The difference in computer requirements between the strapped-down and gimbaled system configurations is that the strapped-down system must generate the time-varying transformation between the gyro-defined coordinate frame and the triad defined by the accelerometers, and must correct for effects due to mass unbalance and electric torques. The torque compensation, although somewhat complicated mathematically, is essentially a very low speed calculation since all the computer must do is keep up with the uncompensated gyro drift. This costs computer memory but very little else.

Generation of the time-varying transformation, although fast compared with torque compensation, is slow compared with direction cosine integration, for example. Computer iteration frequency is estimated at roughly 50 to 500 cps. However, as contrasted with the incremental direction cosine mechanization outlined previously, the generation of the transformation  $T$  usually requires total value multiplications which entail more computer time. To further complicate the situation, present strapped-down pickoff patterns on the rotor require square root and transcendental computations which use additional computer time. As a result, it is concluded that with the strapped-down pickoff techniques presently employed, no general-purpose computer available today is capable of solving the strapped-down problem in real time.

Fortunately, a straightforward solution exists and is being implemented. Since the most prominent factor in sapping computer time is the "gyrations" required to obtain the pickoff information in efficient form, the most obvious solution is to apply a pattern on the rotor which yields the pickoff output in efficient form. This, of course, is the pattern that gives the cosine of the angle between the pickoff and the spin axis as the time ratio of successive pattern crossings. This type of pattern is referred to as a cosine pattern.

Thus, with a cosine pattern on the rotor, the strapped-down computer problem may be solved in real time at the expense of additional memory over that required for a gimbaled system.

### Conclusions

From the discussion presented above, the following conclusions are drawn:

- ESG platform mechanizations are practical today. Strapped-down systems, while possible to implement, must await special-purpose computer development or a more efficient pickoff to make them practical.
- Platform mechanizations are more accurate than their strapped-down counterpart owing to a more accurate pickoff and greater ease in drift torque compensation. Pickoff accuracies in either case, however, are sufficient for accurate system implementation. With some effort, torque compensation in a computer can be accomplished for the strapped-down system.



It is believed that precision gyro mass unbalance correction without the aid of a computer can only be achieved in gimbaled operation in the foreseeable future\*, while accurate electric torque compensation for either system will be attained within a short time. New strapped-down pickoff designs look promising; consequently, strapped-down systems utilizing general-purpose computers should be practical very shortly. Strapped-down pickoffs may never be as accurate as those using gimbals, but in either case the rate of accuracy improvement seems to be outstripping both accelerometer accuracy improvements and system requirements.

It is as yet impossible to state with any reasonable accuracy the division of responsibility between strapped-down and gimbaled systems, but it seems safe to say that the role of strapped-down systems utilizing ESG's will be larger than that of the system using rate sensing devices.

### FUTURE INERTIAL SYSTEM ASPECTS

At least two new inertial sensor candidates are sufficiently developed to warrant a short discussion of their possible implications. These are an electrically suspended three-axis accelerometer (ESA) and the laser rate integrating sensor.

#### The Electrically Suspended Accelerometer

It has long been thought that the ESG should make a good accelerometer. Until fairly recently, however, the key to proper mechanization and the method of accurate readout were missing. It now appears that an extremely accurate accelerometer using the principle of force rebalance is achievable. The mechanization, involving a nuclear magnetic or electron resonance technique integral with the force rebalance servo loop, results in automatic digital readout with a very small fps/pulse weight.

Thus far, all of the techniques required to manufacture an accurate accelerometer coincide with the requirements of an accurate gyro. Hence, combining the gyro and accelerometer into one unit seems at present to be quite practical, and effort is proceeding along these lines. The possibility then of a system employing two instruments consisting of a combined ESG and three-axis accelerometer (ESGA) presents itself. Further, for short-term guidance missions such as ballistic missiles there is a possibility of using an ESGA as the only inertial sensor and deriving the second axis of required space reference by digital computation.

It is conjectured that if the size and number of the inertial sensors are reduced to ultimate computer size, the strapped-down approach should be in a much stronger position to usurp the present role of gimbaled systems.

---

\*Recent fine balance techniques at Honeywell may change this view. Extremely precise balance has been achieved, but the question of stability has not yet been answered.



### The Laser Rate Sensor

The laser rate sensor can be considered exactly like a conventional rate integrating floated gyro insofar as system mechanization is concerned. Hence, should it be strapped down or gimbale? It is too early to say, of course, but the following possibilities can be considered. From early estimates this sensor offers the possibility of practically zero drift. If zero gyro drift is assumed, the drift due to lags in platform servo follow-up and commutation errors in strapped-down mechanization would become the dominant error sources. The choice on an accuracy basis of a strapped-down or gimbale system then depends upon which of these errors can be most greatly minimized. As a guess this would probably be the commutation error in a strapped-down system because a platform follow-up lag can look just like a commutivity error. In a computer the size of the lag is limited by the computer speed and the gyro output angular resolution. In a platform the lag is limited by physical parameters which determine the platform "hangoff" in transient response. It would seem then that the computer would stand a better chance of minimizing this error.

A second consideration would be the stability of the optical path length. No conclusions have yet been reached on this subject.

### REFERENCES

1. MH Aero Document R-ED 6029, "The Gimballess Analytic Inertial Navigation System (U)," 1 August 1957. (Confidential)
2. MH Aero Report 2503-TR1, "Final Report - The Gimballess Analytic Inertial Navigation System (U)," 31 May 1962. (Secret)
3. Blazek, H. F., "A Strap-Down Inertial System for an IRBM (U)," Transactions of the Sixth Symposium on Ballistic Missile and Space Technology, vol. II, 28-30 August 1961. (Secret)



ATTITUDE CONTROL OF SATELLITES AND DETERMINATION  
OF ORBITAL PARAMETERS BY USE OF ACCELEROMETERS

H. Winter

Textron's Bell Aerosystems Company  
Avionics Division  
Buffalo 5, New York

ABSTRACT

Attitude control of satellites and determination of orbital parameters are common problems in present space technology. A method of inertial instrumentation to obtain attitude error signals and those orbital parameters defining size and shape of the orbit is presented. In particular, this paper proposes to provide this information by use of accurate linear accelerometers only; this is desirable due to the limited operating life of available gyros compared to the potential life of satellites. Two of many possible configurations are presented, and the accuracy associated with each method is analyzed.

The work described in this paper was company-sponsored.



## ATTITUDE CONTROL OF SATELLITES AND DETERMINATION OF ORBITAL PARAMETERS BY USE OF ACCELEROMETERS

Herbert Winter  
Textron's Bell Aerosystems Company  
Avionics Division  
Buffalo 5, New York

### INTRODUCTION

A recurrent problem in present-day space technology is attitude control and determination of orbital parameters of a satellite, especially the parameters defining size and shape of the orbit. Present plans call for the orbiting of unmanned and manned space vehicles around the moon, Venus and Mars; the farther planets will no doubt be approached in the not-too-distant future. Due to the communications problems at inter-planetary distances, a self-contained system for determining the attitude and orbit of a satellite appears to be very desirable.

The present paper establishes the feasibility of inertial instrumentation for the determination of these satellite characteristics. Other methods, using active or passive radiation instrumentation, appear possible. No attempt is made here to prove the superiority of the inertial method; a comparative study of each type of instrumentation is required to determine the best method for a particular application. It would appear, however, that the method discussed here is at least competitive with other known systems in terms of accuracy and reliability.

Previous writers have discussed the possibility of direct stabilization using the gravity gradient torque (1), (2) as well as stabilization by use of accelerometers (3). Others have described methods of obtaining orbital parameters using accurate gyros as well as accelerometers (4), (5).

Compared to the potential life of a space vehicle, the operating life of present-day gyros is limited. The present system therefore dispenses with gyros as primary instrumentation, limiting itself only to accelerometers. A low-accuracy angular reference, stellar or gyroscopic, is, however, required during the initial stages of control to avoid certain ambiguities existing in the accelerometer instrumentation.



# DERIVATION OF EXPRESSIONS FOR ACCELEROMETER OUTPUT

First, the measured acceleration at an arbitrary point within the satellite will be derived. This acceleration will appear in the form of a vector; a physical accelerometer will, of course, measure only one component of this vector acceleration.

Assuming a right-handed coordinate system, axes  $x, y, z$ , fixed to the satellite, with its center at the satellite's center of gravity, let the position vector of the accelerometer measured in this system be  $\bar{s}$  (see Fig. 1). Since the measured acceleration at the center of gravity is exactly zero for an orbiting vehicle, it is sufficient to derive the measured acceleration at point  $\bar{s}$  with respect to the center of gravity.

Since the magnitude of  $\bar{s}$  is constant, the true acceleration at this point with respect to the center of gravity is easily shown to be

$$\bar{a}_T = \dot{\bar{\omega}} \times \bar{s} + \bar{\omega} \times (\bar{\omega} \times \bar{s}), \quad (1)$$

where  $\bar{\omega}$  represents the total rotation vector of the satellite with respect to inertial space, and a dot above a quantity denotes differentiation with respect to time.

The measured gravity may be represented by

$$\bar{g} = \frac{\gamma}{r^3} \bar{r}, \quad (2)$$

where  $\bar{r}$  is the vector distance from the center of attraction, and  $\gamma$  is the product of the gravitational constant and the mass of the attracting body. Using the subscript  $o$  for quantities at the satellite's center of gravity, we may write the difference in gravity between point  $\bar{s}$  and the center of gravity as

$$\Delta \bar{g} = \bar{g} - \bar{g}_o = \frac{\gamma}{|\bar{r}_o + \bar{s}|^3} (\bar{r}_o + \bar{s}) - \frac{\gamma}{r_o^3} \bar{r}_o \approx \frac{\gamma}{r_o^3} (\bar{s} - 3 \frac{\bar{s} \cdot \bar{r}_o}{r_o^2} \bar{r}_o), \quad s \ll r_o. \quad (3)$$

It is useful at this point to define a second set of coordinate axes as follows (see Fig. 2):

- $\bar{i}$  = unit vector along horizontal component of velocity vector;
- $\bar{j}$  = unit vector parallel to orbital rotation vector;
- $\bar{k}$  = unit vector along vertical, positive up.



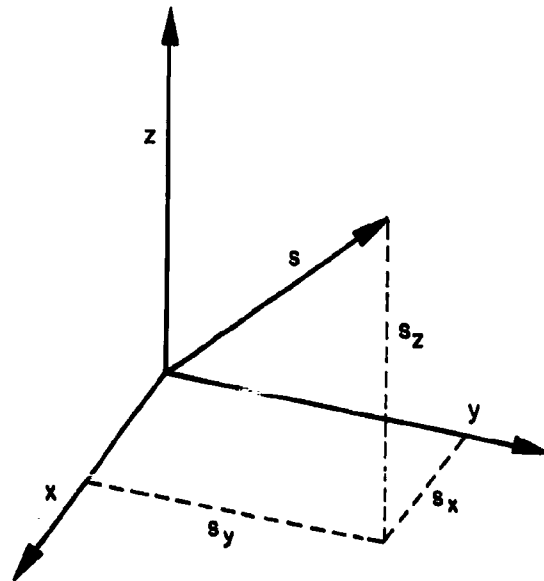


Fig. 1. Satellite Coordinate System

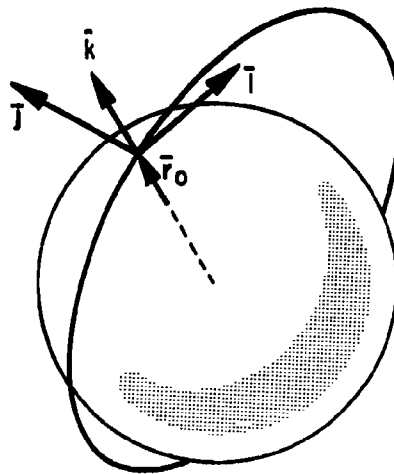


Fig. 2. Orbital Coordinate System



Noting that  $\vec{r}_0 = \vec{k} r_0$ , and expanding the triple vector product in Eq. (1), Eqs. (1) and (3) are now combined to give the total measured acceleration vector

$$\vec{a} = \vec{a}_T + \Delta \vec{g} = \dot{\vec{\omega}} \times \vec{s} + \vec{\omega} \cdot \vec{s} \vec{\omega} - \omega^2 \vec{s} + \frac{\gamma}{r_0} (\vec{s} - 3 \vec{s} \cdot \vec{k} \vec{k}). \quad (4)$$

Eq. (4) may also be expanded into a matrix equation

$$\begin{pmatrix} a_x \\ a_y \\ a_z \end{pmatrix} = \begin{pmatrix} a_{xx} & a_{xy} & a_{xz} \\ a_{yx} & a_{yy} & a_{yz} \\ a_{zx} & a_{zy} & a_{zz} \end{pmatrix} \begin{pmatrix} s_x \\ s_y \\ s_z \end{pmatrix}, \quad (5)$$

where the elements of the matrix are as follows:

$$\begin{aligned} a_{xx} &= -\omega_y^2 - \omega_z^2 + \frac{\gamma}{r_0} (1 - 3 c_{kx}^2), \\ a_{xy} &= -\dot{\omega}_z + \omega_x \omega_y - 3 \frac{\gamma}{r_0} c_{kx} c_{ky}, \\ a_{xz} &= \dot{\omega}_y + \omega_x \omega_z - 3 \frac{\gamma}{r_0} c_{kx} c_{kz}, \\ a_{yx} &= \dot{\omega}_z + \omega_y \omega_x - 3 \frac{\gamma}{r_0} c_{ky} c_{kx}, \\ a_{yy} &= -\omega_z^2 - \omega_x^2 + \frac{\gamma}{r_0} (1 - 3 c_{ky}^2), \\ a_{yz} &= -\dot{\omega}_x + \omega_y \omega_z - 3 \frac{\gamma}{r_0} c_{ky} c_{kz}, \\ a_{zx} &= -\dot{\omega}_y + \omega_z \omega_x - 3 \frac{\gamma}{r_0} c_{kz} c_{kx}, \end{aligned} \quad (6)$$



$$a_{zy} = \dot{\omega}_x + \omega_z \omega_y - 3 \frac{\gamma}{r_0} c_{kz} c_{ky},$$

$$a_{zz} = -\omega_x^2 - \omega_y^2 + \frac{\gamma}{r_0} (1 - 3 c_{kz}^2),$$

with  $c_{kx}$  denoting the cosine between the k and x axes, etc.

It should be noted that each of the elements of the matrix of Eq. (5), as expressed in Eq. (6), represents the output of an accelerometer one unit distance away from the center of gravity; for instance,  $a_{xy}$  is equal to the acceleration measured along the x axis by an instrument one unit distance along the y axis from the center of gravity (see Fig. 3). The nine terms may therefore be considered as the outputs of three triads of accelerometers, each triad mounted a unit distance along one of the axes from the center of gravity, and each consisting of three orthogonally mounted accelerometers measuring in directions parallel to these axes.

In general, the output of any accelerometer whose sensitive axis measures in the direction indicated by direction cosines  $c_x, c_y, c_z$  with the x, y, z axes is

$$a = c_x a_x + c_y a_y + c_z a_z. \quad (7)$$

Substituting Eq. (5) in Eq. (7), one obtains

$$a = \sum_i \sum_j c_i s_j a_{ij}; \quad i = x, y, z; \quad j = x, y, z. \quad (8)$$

Inspection of the terms in Eq. (6) indicates that the direction cosines between the vertical and the vehicle coordinate axes appear only as products of pairs. This makes it inherently impossible to differentiate between the upward and downward directions. Similarly, components of angular rotation appear only as products of pairs, making it impossible to determine the sense of the rotation vector. The following analysis therefore assumes initially small angular errors, on the order of less than five degrees, and angular rates small compared to the orbital rate, i.e., less than about ten degrees per hour. This permits removal of the nonlinearities in the expressions of Eq. (6).

Assume the x axis approximately aligned with the i axis, the y with the j axis, and the z with the k axis; let  $\theta_x$  be the angular error about the x axis,  $\theta_y$  about the y axis,  $\theta_z$  about the z axis. In addition, denote the orbital rate by  $\omega_s$ . Then, approximately, neglecting second-order terms,



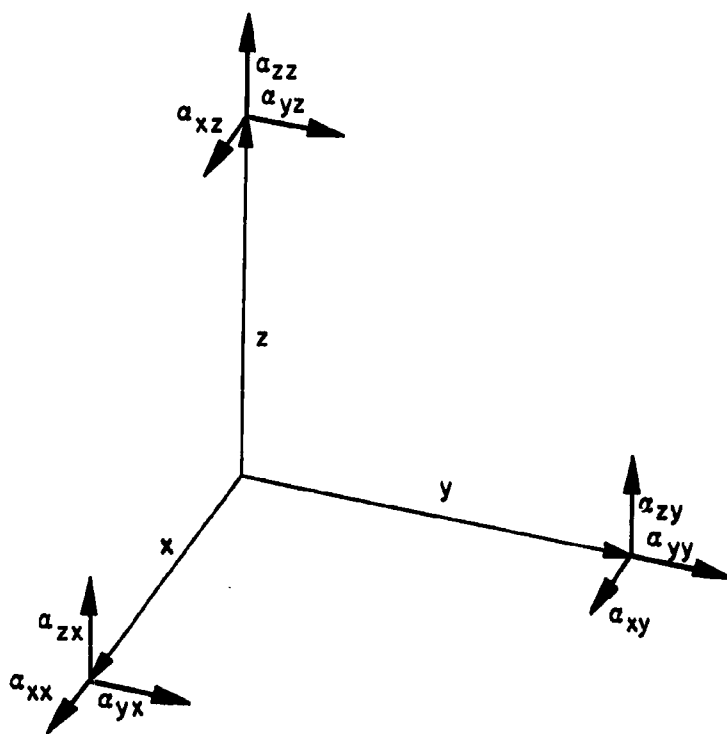


Fig. 3. Accelerometer Placement Equivalent to Matrix Elements of Eq. (5)



$$c_{kx} = -\theta_y,$$

$$c_{ky} = \theta_x,$$

$$c_{kz} = 1;$$

(9)

$$\omega_x = \omega_s \theta_z + \dot{\theta}_x,$$

$$\omega_y = \omega_s + \dot{\theta}_y,$$

$$\omega_z = -\omega_s \theta_x + \dot{\theta}_z.$$

Substituting Eqs. (9) in Eqs. (6), again neglecting second-order terms, one obtains the following:

$$a_{xx} = \frac{\gamma}{r_0^3} - \omega_s^2 - 2\omega_s \dot{\theta}_y,$$

$$a_{xy} = -\ddot{\theta}_z + 2\omega_s \dot{\theta}_x + \dot{\omega}_s \theta_x + \omega_s^2 \theta_z,$$

$$a_{xz} = \dot{\omega}_s + \ddot{\theta}_y + 3\frac{\gamma}{r_0^3} \theta_y,$$

$$a_{yx} = \ddot{\theta}_z - \dot{\omega}_s \theta_x + \omega_s^2 \theta_z,$$

$$a_{yy} = \frac{\gamma}{r_0^3},$$

(10)

$$a_{yz} = -\ddot{\theta}_x - \left(3\frac{\gamma}{r_0^3} + \omega_s^2\right) \theta_x - \dot{\omega}_s \theta_z,$$

$$a_{zx} = -\dot{\omega}_s - \ddot{\theta}_y + 3\frac{\gamma}{r_0^3} \theta_y,$$

$$a_{zy} = \ddot{\theta}_x + 2\omega_s \dot{\theta}_z - \left(3\frac{\gamma}{r_0^3} + \omega_s^2\right) \theta_x + \dot{\omega}_s \theta_z,$$

$$a_{zz} = -\left(2\frac{\gamma}{r_0^3} + \omega_s^2\right) - 2\omega_s \dot{\theta}_y.$$



## ATTITUDE CONTROL EQUATIONS

The following combinations of the terms in Eq. (10) provide useful signals for attitude control:

$$\begin{aligned}
 A_x &= \frac{1}{2} (a_{yz} + a_{zy}) = \omega_s \dot{\theta}_z - \left( 3 \frac{\gamma}{r_o} + \omega_s^2 \right) \theta_x, \\
 A_y &= \frac{1}{2} (a_{zx} + a_{xz}) = 3 \frac{\gamma}{r_o} \theta_y, \\
 A_z &= \frac{1}{2} (a_{xy} + a_{yx}) = \omega_s \dot{\theta}_x + \omega_s^2 \theta_z.
 \end{aligned} \tag{11}$$

There are several combinations of accelerometers with which the expressions of Eq. (11) can be obtained. Two of these will be described.

Method 1

Each of six accelerometers is mounted so as to provide one of the  $a$  terms in Eq. (11). The arrangement is indicated schematically in Fig. 4, and may be tabulated as shown in Table 1.

Table 1. Accelerometer Arrangement, Method 1

Instrument	$c_x$	$c_y$	$c_z$	$s_x$	$s_y$	$s_z$	Output
$a_1$	0	0	1	0	1/2	0	(1/2) $a_{zy}$
$a_2$	0	1	0	0	0	1/2	(1/2) $a_{yz}$
$a_3$	1	0	0	0	0	1/2	(1/2) $a_{xz}$
$a_4$	0	0	1	1/2	0	0	(1/2) $a_{zx}$
$a_5$	0	1	0	1/2	0	0	(1/2) $a_{yz}$
$a_6$	1	0	0	0	1/2	0	(1/2) $a_{xy}$



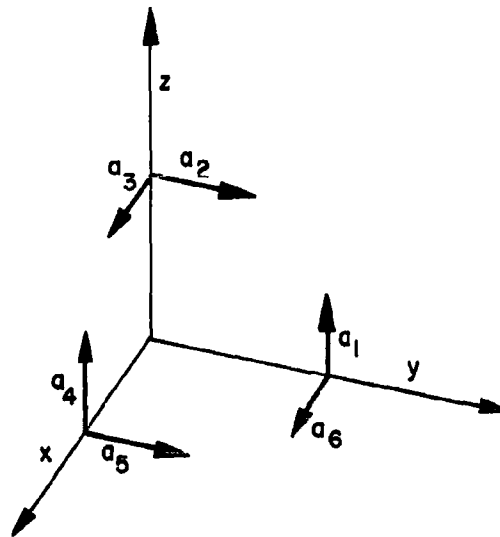


Fig. 4. Accelerometer Placement for Method 1

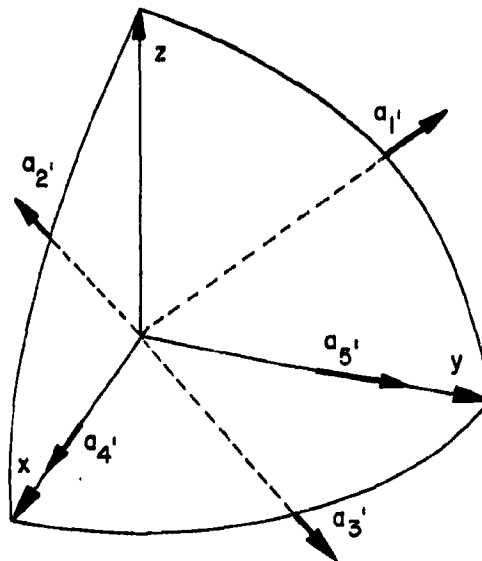


Fig. 5. Accelerometer Placement for Method 2



The expressions of Eq. (11) are obtained as follows:

$$\begin{aligned} A_x &= a_1 + a_2, \\ A_y &= a_3 + a_4, \\ A_z &= a_5 + a_6. \end{aligned} \tag{12}$$

The actual values for  $s_x, s_y, s_z$  are, of course, arbitrary; they really represent scale factors which may be adjusted by amplifier gains, potentiometers, etc. Their relative values for any one accelerometer, however, are critical.

### Method 2

Only five accelerometers are required. Two of these are located on the x and y coordinate axes, with their sensitive axes along the same coordinate axes; the other three are each located in a plane through two of the coordinate axes, and half-way between these two axes, their sensitive axes along the bisector of these two coordinate axes. This is shown in Fig. 5, and tabulated in Table 2.

Table 2. Accelerometer Arrangement, Method 2

Instrument	$c_x$	$c_y$	$c_z$	$s_x$	$s_y$	$s_z$	Output
$a_1$	0	$\sqrt{2}/2$	$\sqrt{2}/2$	0	$\sqrt{2}/2$	$\sqrt{2}/2$	$1/2 (a_{yy} + a_{yz} + a_{zy} + a_{zz})$
$a_2$	$\sqrt{2}/2$	0	$\sqrt{2}/2$	$\sqrt{2}/2$	0	$\sqrt{2}/2$	$1/2 (a_{xx} + a_{xz} + a_{zx} + a_{zz})$
$a_3$	$\sqrt{2}/2$	$\sqrt{2}/2$	0	$\sqrt{2}/2$	$\sqrt{2}/2$	0	$1/2 (a_{xx} + a_{xy} + a_{yx} + a_{yy})$
$a_4$	1	0	0	1/2	0	0	$1/2 a_{xx}$
$a_5$	0	1	0	0	1/2	0	$1/2 a_{yy}$

Noting from Eq. (10) that

$$a_{zz} = a_{xx} - 3 a_{yy}, \tag{13}$$



the expressions of Eq. (11) are as follows:

$$\begin{aligned} A_x &= a_1 - a_4 + 2a_5, \\ A_y &= a_2 - 2a_4 + 3a_5, \\ A_z &= a_3 - a_4 - a_5. \end{aligned} \quad (14)$$

Next, it will be shown how the expressions  $A_x$ ,  $A_y$ ,  $A_z$  are used to control the attitude of the vehicle.

Signal  $A_y$  may be used directly in the y-attitude channel, since it is proportional to the error about the y axis (see Eq. (11)). The gain is, of course, not constant in the general case of an elliptic orbit, but this should not be too critical. An initial estimate can be made, and, if necessary, the gain may be adjusted on the basis of the computed orbital parameters.

Eq. (11) indicates that the x and z channels are cross-coupled due to the orbital motion about the y axis. They may be separated by performing the following operations:

$$\begin{aligned} A'_x &= -A_x + \frac{1}{\omega_s} \dot{A}_z = \ddot{\theta}_x + \left( 3 \frac{\gamma}{r_o^3} + \omega_s^2 \right) \theta_x, \\ A'_z &= \left( 1 + \frac{3\gamma/r_o^3}{\omega_s^2} \right) A_z + \frac{1}{\omega_s} \dot{A}_x = \ddot{\theta}_z + \left( 3 \frac{\gamma}{r_o^3} + \omega_s^2 \right) \theta_z. \end{aligned} \quad (15)$$

Each term is now a function of the error about only one axis, and, with proper filtering, may be used for attitude control about this axis. As in the y channel, the gains may be adjusted on the basis of the orbital parameters. To the extent that the gains in instrumenting Eq. (15) are incorrect, there will be cross-coupling; in particular, the  $A'_x$  term will include a term proportional to  $\ddot{\theta}_z$ , the  $A'_z$  term one proportional to  $\ddot{\theta}_x$ . These terms will not affect the steady-state condition of the system.

#### ORBITAL PARAMETER DETERMINATION

It is recognized that, unless accurate initial conditions are available, only three of the six orbital parameters are obtainable by purely inertial means. These three parameters are the ones defining size and shape of the orbit, and the vehicle's position in the orbit (e.g.: semi-major axis, eccentricity, and true anomaly). Fortunately, it is just these parameters which are most important in accomplishing orbital missions about the bodies in our solar system.



If Method 1 is used to provide attitude stabilization, the rate of change of orbital rotation may be obtained from

$$A_0 = a_3 - a_4 = \dot{\omega}_s + \ddot{\theta}_y. \quad (16)$$

After attitude control reduces  $\ddot{\theta}_y$  to zero, only  $\dot{\omega}_s$  remains. From orbital mechanics,

$$\dot{\omega}_s = -\frac{2e\gamma}{r_m^3} \left( \frac{1 + e \cos v}{1 - e^2} \right)^3 \sin v, \quad (17)$$

where

$r_m$  = semi-major axis,

$e$  = eccentricity,

$v$  = true anomaly ( $\dot{v} = \omega_s$ ).

Standard curve-fitting methods are used to compute the orbital parameters from  $A_0$  either continuously or at known time intervals.

It is evident, however, that this method will not provide answers in the case of a circular orbit, since for this case  $A_0 = 0$  regardless of the radius of the orbit. A seventh accelerometer would have to be used to provide this information, e.g., one which is placed one unit distance along the y axis with its sensitive axis along the y axis, thus measuring  $a_{yy} = \gamma/r_0^3$  (see Eq. (10)).

If, on the other hand, Method 2 is used for stabilization, only five accelerometers are required, since  $a_{5'}$  provides the necessary instantaneous radial measurement directly, and is thus suitable for circular as well as elliptic orbits. Thus,

$$a_{5'} = \frac{1}{2} \frac{\gamma}{r_m^3} \left( \frac{1 + e \cos v}{1 - e^2} \right)^3, \quad (18)$$

from which the orbital parameters may be computed by curve fitting.

#### ACCURACY ANALYSIS

The accuracy of each accelerometer output is determined by the accelerometer accuracy itself, by the accuracy of its location, and by the accuracy of its alignment. Using Eq. (8), the output error of any given accelerometer may therefore be represented by the expression



$$\Delta a = \epsilon_a + \sum_i \sum_j (\Delta c_{ij} s_j \alpha_{ij} + c_{ij} \Delta s_j \alpha_{ij}), \quad (19)$$

where  $\epsilon_a$  denotes the error inherent in the instrument, and a  $\Delta$  before a quantity indicates an error of this quantity.

The errors in direction cosines are expressed in terms of misalignment angles of the instrument as follows:

$$\begin{aligned} \Delta c_x &= c_z \delta_y - c_y \delta_z, \\ \Delta c_y &= c_x \delta_z - c_z \delta_x, \\ \Delta c_z &= c_y \delta_x - c_x \delta_y, \end{aligned} \quad (20)$$

where  $\delta_x$  is the accelerometer misalignment angle about the x-axis, etc.

To obtain the accuracy of the system, the accelerometer output errors are determined from Eq. (19), using Eq. (20) and Table 1 or Table 2 (depending on which of the two methods is being analyzed). The errors of the attitude control signals are then obtained from the differential of Eq. (12) or Eq. (14). The attitude errors are determined from the differential of Eq. (11) for the steady state, i.e.,

$$\begin{aligned} \Delta \theta_x &= - \left( 3 \frac{\gamma}{r_o} + \omega_s^2 \right)^{-1} \Delta A_x, \\ \Delta \theta_y &= \left( 3 \frac{\gamma}{r_o} \right)^{-1} \Delta A_y, \\ \Delta \theta_z &= \omega_s^{-2} \Delta A_z. \end{aligned} \quad (21)$$

The errors of the orbital parameter indication are similarly obtained from the differential of Eq. (18):

$$\frac{\Delta a_5}{a_5} = -3 \frac{\Delta r_m}{r_m} + 3 \frac{(1 + e^2) \cos v + 2e}{(1 - e^2)(1 + e \cos v)} \Delta e - 3 \frac{e \sin v}{1 + e \cos v} \Delta v. \quad (22)$$

The following analysis is made for illustrative purposes on the basis of low-level circular earth orbits. The distance for mounting the accelerometers is taken to be one meter.



### Accelerometer Accuracy

It is assumed that the errors inherent in the various instruments are equal and independent, so that, in the error equations corresponding to Eqs. (12) and (14), addition occurs in terms of the square root of the sum of the squares, e.g., the error equation corresponding to the first equation of Eq. (12) is

$$\Delta A_x = \sqrt{\Delta a_1^2 + \Delta a_2^2} = \sqrt{2} \epsilon_a. \quad (23)$$

An accelerometer accuracy of  $10^{-9}g$  is assumed for an instrument whose total range is  $10^{-3}g$ . This implies a threshold of less than  $10^{-9}g$  and a linearity of better than  $10^{-6}$ . A range of  $10^{-3}g$  provides a large enough linear region for operation at reasonable angular velocities and accelerations. Thresholds of  $10^{-6}$  maximum range and linearities of one part in  $10^6$  appear feasible in today's advanced developments.

Using a total instrument error of  $10^{-9}g$ , the attitude errors are shown in Table 3.

Table 3. Attitude Errors Caused by Accelerometer Errors

	Method 1	Method 2
$\Delta \theta_x$	8 min	14 min
$\Delta \theta_y$	11 min	28 min
$\Delta \theta_z$	32 min	39 min

From Eq. (22), the error in indication of major axis is seen to be 28 km, the error in eccentricity about 0.004.

### Accelerometer Alignment

The effect of accelerometer misalignment is very small; if the alignment accuracy is one minute of arc about each axis, the total corresponding attitude errors are half a minute of arc about each axis for both methods of instrumentation. The effects on orbital parameter determination are negligible.

### Accelerometer Location

It will be assumed here that the position of the center of gravity is accurately known, that the accelerometers are located with respect to this position, but that this location is in error. (Errors in the location of the center of gravity are discussed in the next section.)



The standard errors in location of any accelerometer are taken to be 1 mm in each direction, and are assumed independent. The corresponding attitude errors are presented in Table 4.

Table 4. Attitude Errors Caused by Accelerometer Location Errors

	Method 1	Method 2
$\Delta \theta_x$	3 min	3 min
$\Delta \theta_y$	3 min	4 min
$\Delta \theta_z$	3 min	4 min

The major axis will be indicated to an accuracy of 4 km, the eccentricity to less than 0.001.

#### Center of Gravity Location

The location of the center of gravity will generally not be known very accurately. It will be assumed optimistically that it is known to an accuracy of 1 cm. The corresponding errors are obtained from the same equation used in the preceding section, but assuming perfect correlation between accelerometer location errors in the same direction, no correlation between errors in different directions.

The corresponding attitude errors are shown in Table 5.

Table 5. Attitude Errors Caused by CG Location Errors

	Method 1	Method 2
$\Delta \theta_x$	32 min	30 min
$\Delta \theta_y$	34 min	42 min
$\Delta \theta_z$	34 min	10 min

The errors in orbital parameters will be about 40 km for the major axis, 0.007 for eccentricity.

It is interesting to note that these errors, attitude as well as orbital parameter, are caused by center-of-gravity location errors in the y and z directions; the error along the x axis produces negligible system errors.



If necessary, the errors due to inadequate knowledge of the location of the center of gravity may be reduced considerably by using two additional accelerometers placed at what is believed to be the center of gravity, with their sensitive axes along the y and z axes. The readings of these accelerometers may then be used to correct the other instruments. Due to the insensitivity of the system to x-axis errors, as seen above, an additional accelerometer along the x axis is not required. This brings the total number of accelerometers up to seven for a complete system in which the errors in center of gravity location are compensated.

### CONCLUSION

The analysis indicates the feasibility of an accurate reliable system for attitude control and determination of three orbital parameters, using only accelerometers as sensing instruments. The biggest limitation to the system described as "Method 2", using just five accelerometers, is uncertainty of the location of the center of gravity; this error can, however, be compensated by the use of two additional accelerometers.

The figures used in the accuracy analysis are felt to be typical of instruments currently under development at Bell Aerosystems Company and, perhaps, at other companies, with spacing between instruments commensurate with proposed vehicle sizes. It therefore appears entirely feasible to provide a seven-accelerometer system with a vertical error of less than 30 minutes of arc, an azimuth error of 40 minutes, error in determination of semi-major axis within 30 kilometers, and error in determination of eccentricity within 0.004.

### REFERENCES

1. Roberson, R.E., "Gravitational Torque on a Satellite Vehicle," Journal of the Franklin Institute, vol. 265, no. 1, 1958.
2. Savet, P.H., "Attitude Control of Orbiting Satellites at High Eccentricity," ARS Journal, vol. 32, no. 10, 1962, p. 1577.
3. Taylor, H.L., "Satellite Orientation by Inertial Techniques," Journal of the Aerospace Sciences, vol. 28, no. 6, 1961, p. 493.
4. Crowley, J., Kolodkin, S.S., and Schneider, A.M., "Some Properties of the Gravitation Field and Their Possible Application to Space Navigation," Proceedings of the 5th Annual East Coast Conference on Aeronautical and Navigational Electronics, Institute of Radio Engineers, Baltimore, 1958.
5. Streicher, M., Zehr, R.M., and Arthur, R., "An Inertial Guidance Technique Usable in Free Fall," Proceedings of the 3rd National Convention on Military Electronics, Institute of Radio Engineers, Washington, 1959.



## ORBIT DETERMINATION ERROR ANALYSIS

D. R. Speece

Aerospace Corporation  
Engineering Division  
El Segundo, California

## ABSTRACT

The problem of orbit determination by radar tracking data is broken into its constituent parts, which are then subjected to detailed examination. Typical results are presented and discussed as a method of arriving at general conclusions. The behavior of orbital errors is interpreted in terms of the influence of their sources and the nature of their propagation. The emphasis of this analysis is on why orbital errors behave as they do, how well can we expect to determine orbits, and how can we do better. The conclusions are based on the results of a large number of digital simulations with the Aerospace TRACE program and the General Electric Pat-B program, plus limited experience in the reduction of "live" data from the SCF net.



## ORBIT DETERMINATION ERROR ANALYSIS

D. R. Speece

Aerospace Corporation  
Engineering Division  
El Segundo, California

## INTRODUCTION

The advent of large scale digital computer programs for the determination of the orbits of near-earth satellites has resulted in the need for criteria for the determination of the accuracy of the resultant orbits in areas remote from the tracking stations, and for techniques to improve this accuracy. This has lead, in turn, to the generation of large scale digital computer programs for the analysis of orbital errors. The results presented here were obtained by the use of such error analysis programs.

An orbital plane coordinate set is selected for the error analysis. The general characteristics and phase relationships of the position and velocity errors in this coordinate set are then presented. The dependence of the magnitudes of the orbital errors on the measurement system is presented in the form of bar charts of maximum position errors after one and two tracking passes by systems which measured various quantities to vehicles in circular orbits at altitudes of 200 nm, 2000 nm, and 100,000 nm. Because these results represent the maximum capability in orbit determination when the only sources of error are station location errors, constant measurement biases, and Gaussian noise in each measurement, they are considerably better than can actually be achieved in most cases. Because of the interdependence of orbital errors through the equations of motion, the accuracy of determination of position relative to velocity at any point in orbit is not a function of whether the determination was by range or by range rate measurements. A curve of the equivalence of range and range rate as orbit determination quantities is given. The advantages of interferometer systems in orbit determination is also discussed. In conclusion, an analysis of the factors which limit the practical accuracies of orbit determination is given.

The orbit determination simulation programs take a specified orbit, earth model, and tracking system. The ensemble average errors in the system orbital prediction are then computed by statistical combination of all the tracking data. The resultant estimates are reliable only as long as the predicted orbital errors are larger than the uncertainties due to neglected sources of error.

In the radar tracking orbit determination problem, the sources of error are:

1. Radar measurement errors



2. Coordinate reference errors
3. Earth shape and mass uncertainties
4. Atmospheric drag uncertainty
5. Uncertainties in extraterrestrial perturbations
6. Uncertainties in reference metrics such as the radius of the earth, the speed of light, and the astronomical unit
7. Computational errors.

The first two of these are dependent on the basic capability of each radar tracker and the care with which it is installed, surveyed in, and calibrated. Station timing accuracy is dependent on the accuracy of reception and use of an external reference signal such as that provided by radio station WWV. The basic measurement accuracy is limited by target characteristics and by the accuracy of atmospheric corrections. The lower limit on the coordinate reference errors is imposed by area survey accuracy which is, in turn, ultimately limited by uncertainties in the shape and mass distribution of the earth.

With respect to mass perturbations by the geopotential harmonics and by the sun and moon, these are sources of orbital error only if they are omitted from the data reduction program. If the source of perturbation is included in the program model, then only the error in its computed vector magnitude is a source of orbital error.

The accurate tracking of many satellites over long periods of time has provided data for better estimates of the data reduction program constants such as the geopotential harmonic terms, solar radiation pressure, the structure of the atmosphere, the radius of the earth, etc. For near earth orbits, the uncertainties in the speed of light and in the astronomical unit are not significant enough sources of error to allow appreciable reduction in their uncertainties by tracking data reduction. It is important to recognize that the ability to calibrate the computer program earth model and to correct measurement bias and survey errors by tracking data reduction is strongly dependent on the relative contribution of the particular error source to the resultant total error in the computed orbit. Thus, the third zonal harmonic (pear shape) was found by its cumulative long-term effect on low inclination orbits. The resultant departure of the computed orbit from the measured orbit exceeded the limits assignable to measurement bias and survey error alone.

The orbit determination programs generally compute residuals between measured quantities and computed quantities. The nonlinear orbital equations are expanded in Taylor series about a nominal solution. The resultant linear set of first difference equations is then solved by a matrix formulation to obtain agreement between the computed orbit and the measured data. The criterion for satisfactory solution is usually minimization of the weighted sums of the squares of the residuals. An alternate weighting technique is the maximum likelihood criterion which provides optimum recognition of the effects of measurement bias and survey errors.



An obvious computational error in orbit determination is computer roundoff error. The above matrices tend to be ill-conditioned. Because of this, double precision computation of the terms in the matrices is often necessary. Even then, erratic results can often be traced to computer roundoff errors.

Let us now examine some of the characteristics of orbital errors. For our purposes the most convenient coordinate set is a vehicle centered set in which position and velocity components are measured in the direction of the horizontal component of the velocity vector (in-track), normal to the orbital plane (cross-track), and along the earth-central radius vector (altitude). As will be shown, this set has close physical coupling to the conventional orbital elements.

### CUMULATIVE ERROR PROPAGATION

The orbital error analysis programs generally compute one-sigma ephemeris uncertainty matrices resulting from a tracking pass. These are analytically propagated along the orbit to the next tracking station. The new measurements result in reduced orbital errors which are then propagated to the next station. This process is continued over the period of interest for the problem at hand.

Typical behavior of the orbital errors is illustrated in figures 1a, 1b, and 1c. The general pattern of these results has been repeated in many simulations of the capabilities of a single tracking station which measures range, range rate, and/or angles once per revolution to a vehicle in a nearly circular orbit at any altitude. The curves present the components of ephemeris uncertainty at each point along the orbit as a result of errors in all preceding tracking data. The position and velocity errors are presented in pairs to emphasize the phase relationships between them. We will now investigate the reasons for this particular pattern.

Consider the behavior of the positional errors. The increase in in-track error after the first pass (figure 1a) is primarily due to period error. But it is also dependant on the uncertainty in eccentricity. Hence, it increases most rapidly on the side of the earth opposite the tracker. The composite curve has a steady rise due to period error on which is superimposed a nearly sinusoidal oscillation whose period is equal to the orbital period as a result of eccentricity error.

The cross-track error (figure 1b) depends primarily on the accuracy of determination of the orbital plane (inclination and longitude of the ascending node). Since the orbital plane intersects the center of the earth, the cross-track error drops to its minimum value at the tracker and at the point on the opposite side of the earth from the tracker. This second point is better known than the first (in real-time error propagation) because the second half of the tracking pass contributed to its determination. The variable component of cross-track error is a rectified sine-wave whose period is equal to the orbital period. The rectification is a result of the rms nature of the error computation.



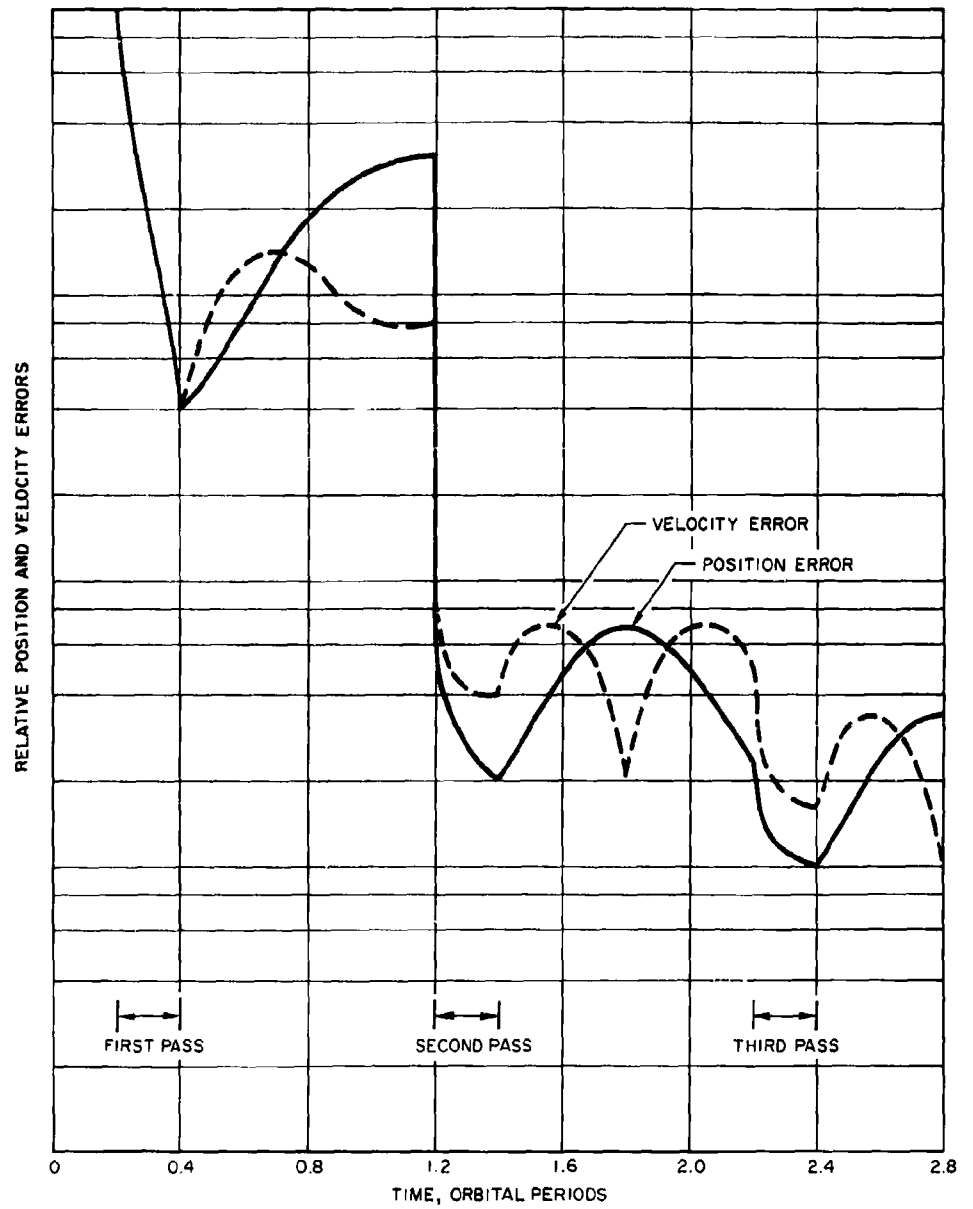


Figure 1. Typical Behavior of Orbital Errors  
1a. In-Track Error Propagation



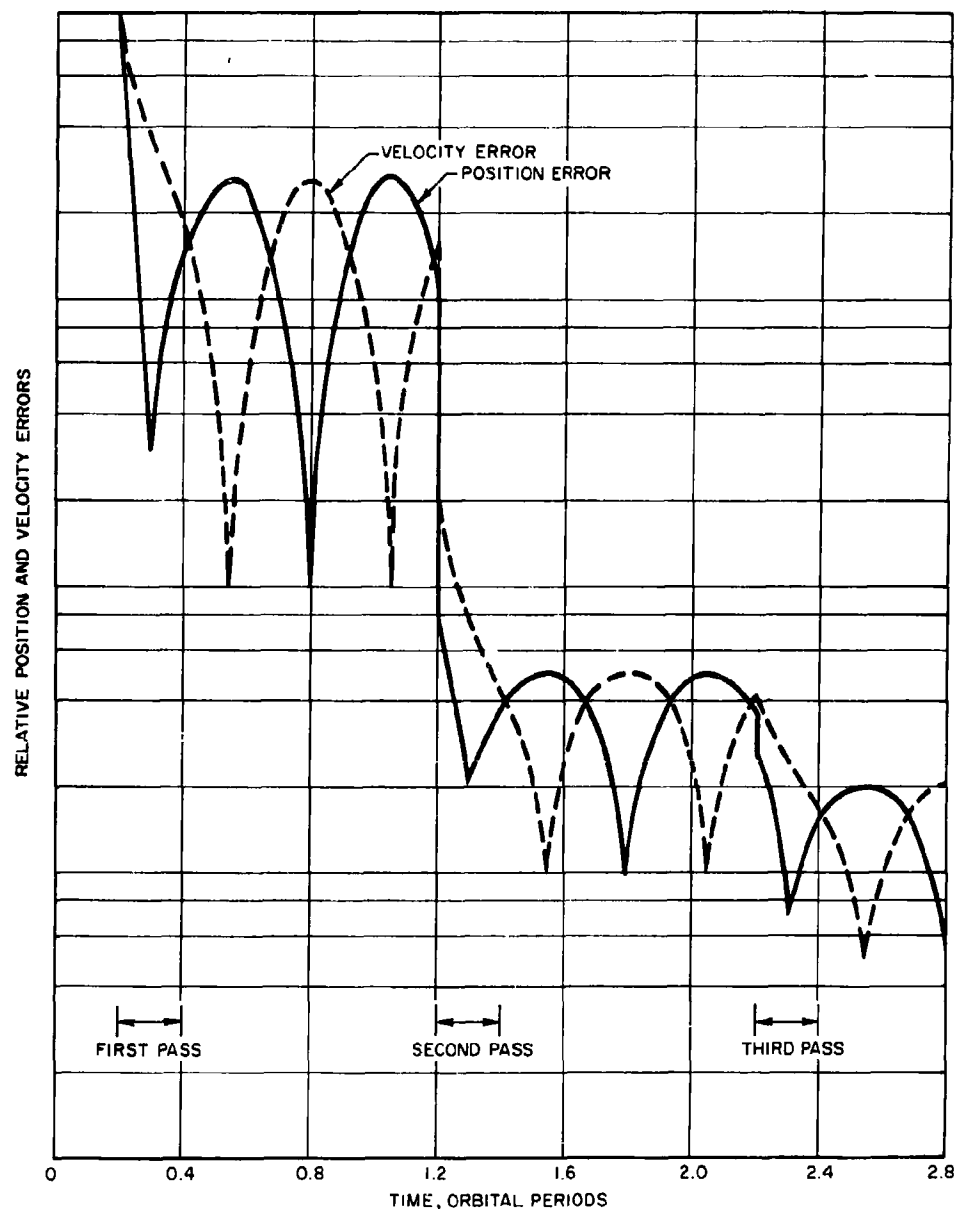


Figure 1. Typical Behavior of Orbital Errors

1b. Cross-Track Error Propagation



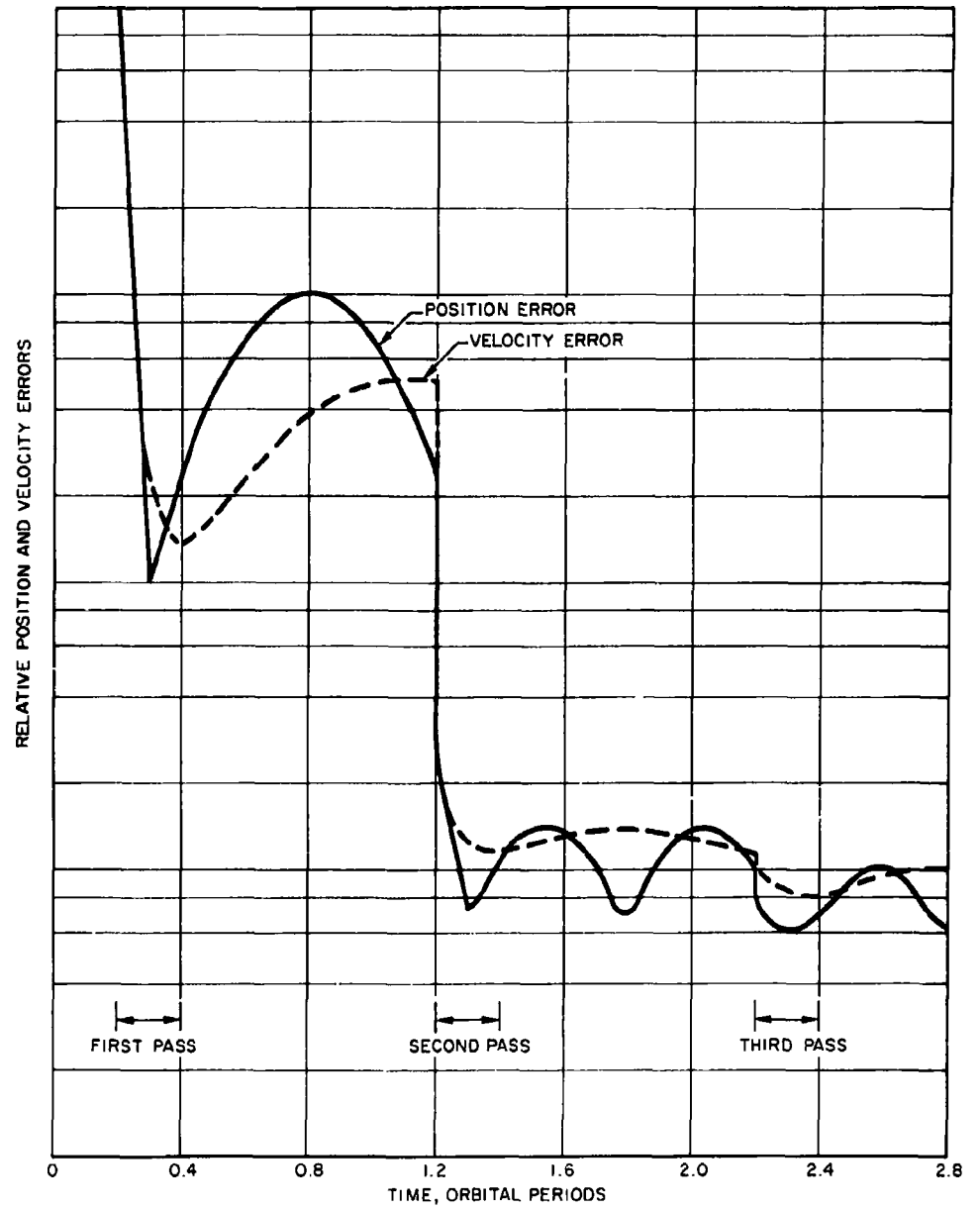


Figure 1. Typical Behavior of Orbital Errors

1c. Altitude Error Propagation



The altitude error following the first pass (figure 1c) is primarily a result of major axis uncertainty. Hence, it is roughly a half-sine wave between the first two tracking passes.

The nature of the error decrease during tracking can be explained as follows: at the minimum range from the tracker the slant range vector can be resolved into a cross-track component and an altitude component. The accuracy of the resolution is a function of the range and angle accuracy of the tracking system. The most valuable cross-track and altitude data is that obtained near the minimum range point. The best in-track data is often obtained near the radar horizon where the slant range vector is most nearly aligned with the vehicle velocity vector.

When the tracker first spots the vehicle on the second pass (roughly one revolution later) the in-track error is immediately reduced to a much lower level than before. The ballistic constraint (orbital equations of motion) allows a greatly improved estimate of orbital period. The resultant improvement in knowledge of the major axis of the orbit provides strong leverage in the computation of both altitude and in-track quantities. The eastward shift of the tracker due to earth rotation between passes provides a more accurate indication of the orientation of the orbital plane with a resultant reduction in cross-track errors.

After the second pass the in-track position error has the form of a half sine wave as would be expected if the tracker were near apogee or perigee of the orbit and the major axis were accurately known but eccentricity and the argument of perigee were still significantly in error. These same conditions explain the shape of the in-track velocity error and the altitude errors. Because of measurement errors, a tracker near perigee or apogee of an orbit invariably obtains a weaker solution for the argument of perigee (and path angle) than if the tracker were located elsewhere along the orbit. Because of the stronger solution for the path angle of the velocity vector, slightly eccentric orbits can apparently be more accurately determined than very nearly circular orbits. If the tracker is not located near apogee or perigee, then the phase of the eccentricity contribution to orbital error is shifted accordingly. It is then possible for the in-track and/or altitude position errors following the first tracking pass to continue to decrease for a short while after the end of tracking.

After two passes by the same tracking station, the orbit is often sufficiently well determined that measurement bias and station location errors result in relatively slow improvement with additional passes. However, because of some variability of physical system biases and because of the changes in the tracking geometry from pass to pass, there is some smoothing of the systematic measurement errors over succeeding passes. Also, the more accurate the measurement system, the less the relative improvement in the orbital estimate with a second pass. The effect of measurement type and accuracy is discussed later.

The velocity error curves bear a rough derivative relationship to the position error curves. This effect is most noticeable in the case of the cross-track errors. This is a result of the fact that the cross-track position



is most accurately determined at the tracker where the cross-track heading error in the velocity vector is a maximum. Because the orbital plane intersects the center of the earth, this results in errors of the following form:

$$\sigma_c \approx \sigma_{c_{\max}} \left| \sin \frac{2\pi}{P} (t - t_0) \right| ,$$

and

$$\sigma_c \approx \frac{2\pi}{P} \sigma_{c_{\max}} \left| \cos \frac{2\pi}{P} (t - t_0) \right| ,$$

where  $P$  is the orbital period and  $t_0$  is the time of the minimum slant range from the tracker. Because of the strong dependence of the first pass determination of orbital inclination on system angular (azimuth) accuracy, the maximum cross-track error after one tracking pass for low altitude orbits is

$$\sigma_{c_{\max}} \text{ (first pass)} \approx r_a^- ,$$

where  $r$  is earth central radius to the satellite and  $\bar{a}$  is the smoothed azimuth error (usually the azimuth bias). As orbital altitude increases the longer tracking arcs permit the first pass determination of the orientation of the orbital plane by the station latitude dependent effect of earth rotation on range and/or range rate measurements. This effect is inclination dependent and vanishes for equatorial orbits.

The in-track and radial velocities for an elliptical orbit are of the form

$$\dot{I} = \frac{V_0}{\sqrt{1 - \epsilon^2}} (1 + \epsilon \cos \theta) ,$$

and

$$\dot{A} = \frac{V_0}{\sqrt{1 - \epsilon^2}} \epsilon \sin \theta ,$$

where  $V_0$  is the mean orbital velocity,  $\epsilon$  is eccentricity, and  $\theta$  is angle from perigee. Assuming small eccentricity, the errors in these are of the form



$$\Delta \dot{I} \approx \Delta V_0 + V_0 (\Delta \epsilon \cos \theta - \epsilon \Delta \theta \sin \theta) ,$$

and

$$\Delta \dot{A} \approx \epsilon \Delta V_0 \sin \theta + V_0 (\Delta \epsilon \sin \theta + \epsilon \Delta \theta \cos \theta) .$$

Between tracking periods,  $\Delta V_0$ ,  $\Delta \epsilon$ , and  $\Delta \theta$  remain constant. After the orbital period has been accurately determined by a second tracking pass, the error in semi-major axis and, hence,  $V_0$  is negligible. We then have

$$\Delta \dot{I}(\theta - \frac{\pi}{2}) \approx \Delta \dot{A}(\theta) , \quad \Delta \dot{A}(\theta - \frac{\pi}{2}) \approx -\Delta \dot{I}(\theta) .$$

The statistical combination of the above components of error and their integrals produce curves of the form of figures 1a and 1c. It has been found that there is strong quarter-orbit correlation of the type suggested above. But it has been observed in the computer results that the maximum value of  $\sigma_{\dot{A}}$  is invariably larger than the maximum value of  $\sigma_{\dot{I}}$ .

After two tracking passes, the apparent form of the in-track and altitude velocity errors of figures 1a and 1c is

$$\sigma_{\dot{I}} \approx \sigma_{\dot{I}_{\max}} \left| \sin \left( \frac{2\pi(t - t_0)}{P} + \sigma_{\theta_1} \right) \right| ,$$

and

$$\sigma_{\dot{A}} \approx \sigma_{\dot{A}_{\max}} \left| \cos \left( \frac{2\pi(t - t_0)}{P} + \sigma_{\theta_2} \right) \right| ,$$

where  $P$  is again the orbital period,  $t_0$  is time of tracker passage, and the  $\sigma_{\theta_i}$  are phase errors related to the uncertainty in the location of perigee.

Because the coordinate directions in the orbital plane set rotate with orbital motion, the position errors are related to the above velocity errors as follows



$$\begin{aligned}\sigma_I &\approx \frac{1}{2} \int_0^t \sigma_{\dot{I}}(t) dt - \frac{1}{2} \int_0^t \sigma_{\dot{A}}(t - \frac{P}{4}) dt \\ &\approx \frac{P}{\pi} \left( \sigma_{\dot{I}_{\max}} + \sigma_{\dot{A}_{\max}} \right) \left[ 1 - \cos \left( \frac{2\pi(t - t_0)}{P} + \sigma_{\theta_3} \right) \right],\end{aligned}$$

and

$$\begin{aligned}\sigma_A &\approx \frac{1}{2} \int_0^t \sigma_{\dot{I}}(t - \frac{P}{4}) + \frac{1}{2} \int_0^t \sigma_{\dot{A}}(t) dt \\ &\approx \frac{P}{\pi} \left| \left( -\sigma_{\dot{I}_{\max}} + \sigma_{\dot{A}_{\max}} \right) \sin \left( \frac{2\pi(t - t_0)}{P} + \sigma_{\theta_4} \right) \right|.\end{aligned}$$

The factors  $1/2$  and the cross-coupling with a quarter-orbit phase shift are in recognition of the interchange of coordinate directions each quarter orbit as a result of coordinate rotation. The signs of the integrated terms and the algebraic rather than rms addition are a result of the statistical correlations (indicated by the computer programs) between the components of error. The resultant expressions are seen to satisfy the observed fact that the maximum altitude position error is invariably considerably smaller than the maximum in-track position error. This appears to be a necessary result of the effect of the eccentricity error.

The above formulas have been derived in an attempt to explain observed results given by the error analysis programs. Rearranging them, we find

$$\sigma_{\dot{I}_{\max}} \approx \frac{\pi}{P} \left| \sigma_{I_{\max}} - 2\sigma_{A_{\max}} \right|,$$

and

$$\sigma_{\dot{A}_{\max}} \approx \frac{\pi}{P} \left| \sigma_{I_{\max}} + 2\sigma_{A_{\max}} \right|.$$

These approximations have been found to be very nearly correct for a wide variety of orbits. Although the altitude position error is smaller than the in-track position error, the converse is true of the corresponding velocity



errors. Physically, the reason can be traced to the large effect of the uncertainty in perigee location on the altitude rate error. Because orbital altitude at the tracking station is accurately determined, this uncertainty has a much smaller effect on the altitude position error.

Because the errors of figures 1a, 1b, and 1c represent average rms values, the basic sinusoidal oscillations are rectified and the effect of phase uncertainty and constant components is to fatten the curves and fill in the low points. The indicated phase relationships and the above ratios of velocity to position error are strong functions of the orbit determination geometry and are only weakly influenced by the quantities measured for orbit determination. But, as discussed in the next section, the actual magnitudes of the orbital errors are a strong function of the measurement mix and accuracy as well as orbital altitude.

### THE CAPABILITIES OF VARIOUS MEASUREMENT SYSTEMS

Let us examine the orbital accuracy obtainable from the data of a single tracking station which measures various quantities to various accuracies. For the sake of uniformity, let the tracker be located at VAFB (34.7 deg N Latitude, 120.6 deg W Longitude), have a data rate of one set of measurements per 20 sec, a station location uncertainty of 100 ft N-S, 100 ft E-W, and 50 ft vertically, and limit the tracking to elevation angles above 10 deg. Assume the only sources of orbital error are the above survey errors plus white Gaussian noise and constant biases in each measurement. Assume data reduction is by the maximum likelihood criterion.

The results of the system comparison are given in figures 2, 3, and 4 which present the maximum one-sigma positional errors after one and two tracking passes for various measurement accuracies and orbital altitudes. The altitudes selected were 200 nm, 2000 nm, and 100,000 nm. The 200 nm orbit had an inclination of 40 deg. The satellite passed to the east of the tracker at a maximum elevation angle of 45 degrees on the first pass and to the west of the tracker at a maximum elevation angle of 45 deg on the second pass. The 2000 nm orbit was polar and also had maximum tracking elevation angles of 45 deg for the first two passes. The 100,000 nm orbit was equatorial and, hence, had a maximum tracking elevation angle of 54.1 deg.

Figure 2a compares the maximum ephemeris prediction errors of various systems after tracking a satellite for one pass in a 200 nm orbit. In each case the system which measured range rate (0.3 fps bias, 0.03 fps random) produced more accurate estimates than the system which measured range (300 ft bias, 300 ft random). As can be seen, the cross-track error increases almost linearly with angular (azimuth) bias.

Figure 2b illustrates the order of magnitude improvement in ephemeris prediction after a second tracking pass. The range rate results are now seen to be almost independent of angular accuracy. Fits to low altitude SCF net range and angular data have shown a similar lack of sensitivity of multiple pass fits to the omission or inclusion of angular measurements. But in these cases more than one station and more than two passes were used. Also, at the 200 nm altitude, the three per minute data rate of figure 2 is insufficient for good smoothing of the assumed 300 ft random range error.



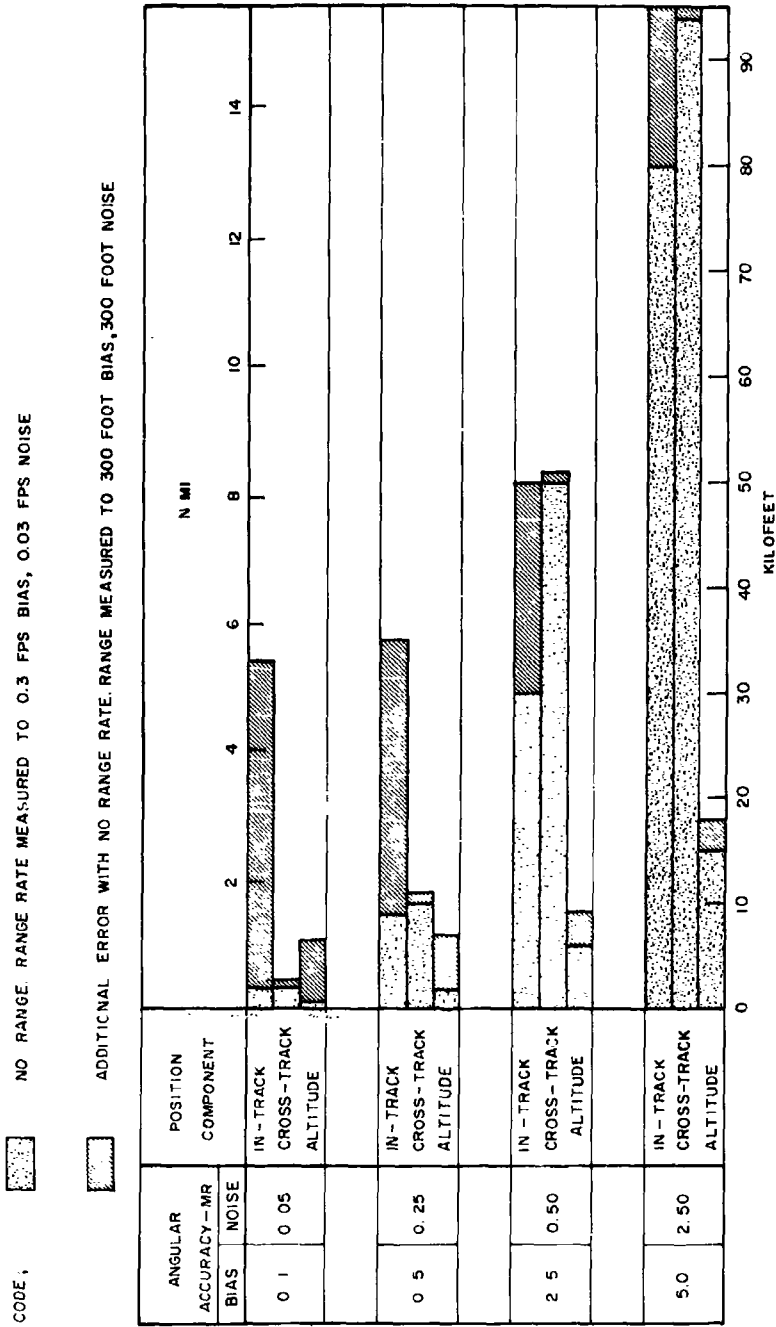


Figure 2. One-Sigma Position Errors for 200 nm Circular Orbit  
2a. Maximum Errors after First Pass



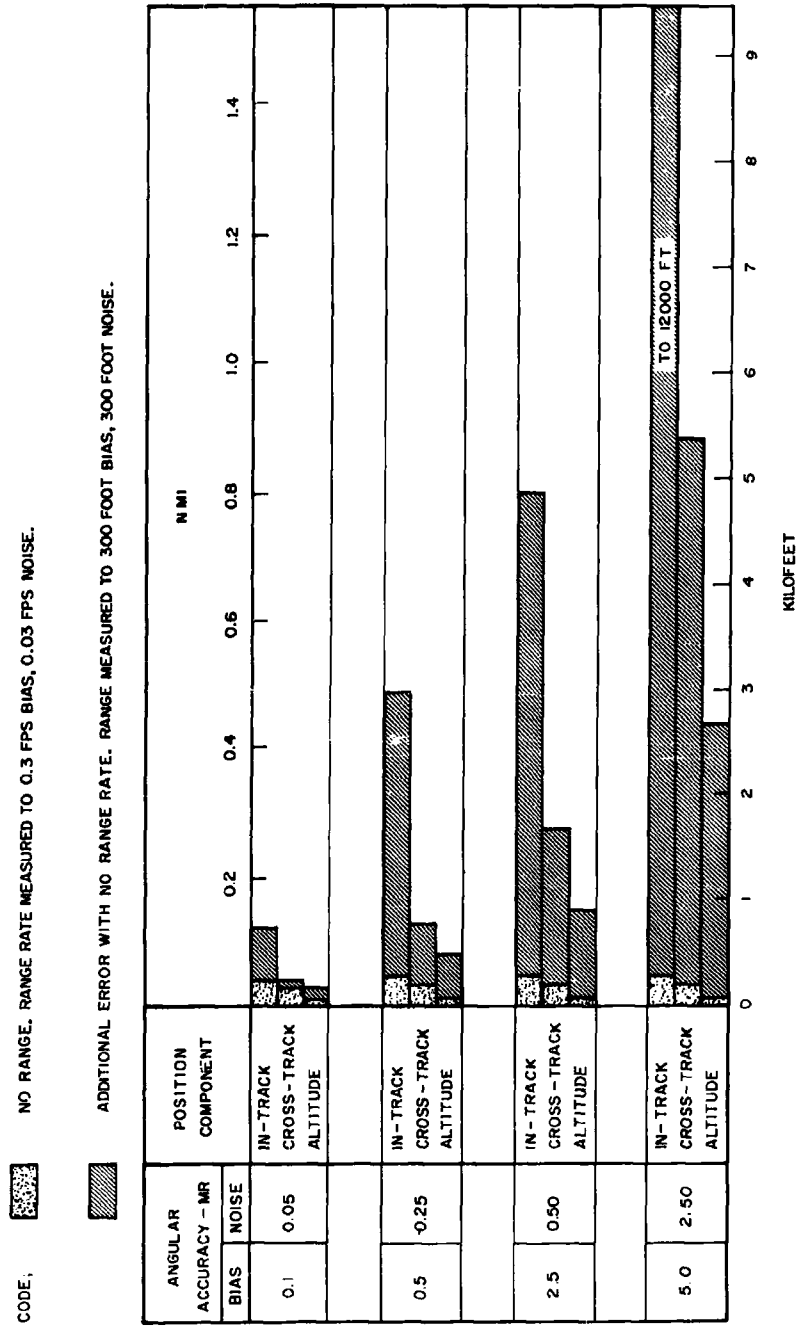


Figure 2. One-Sigma Position Errors for 200 nm Circular Orbit  
2b. Maximum Errors after Second Pass



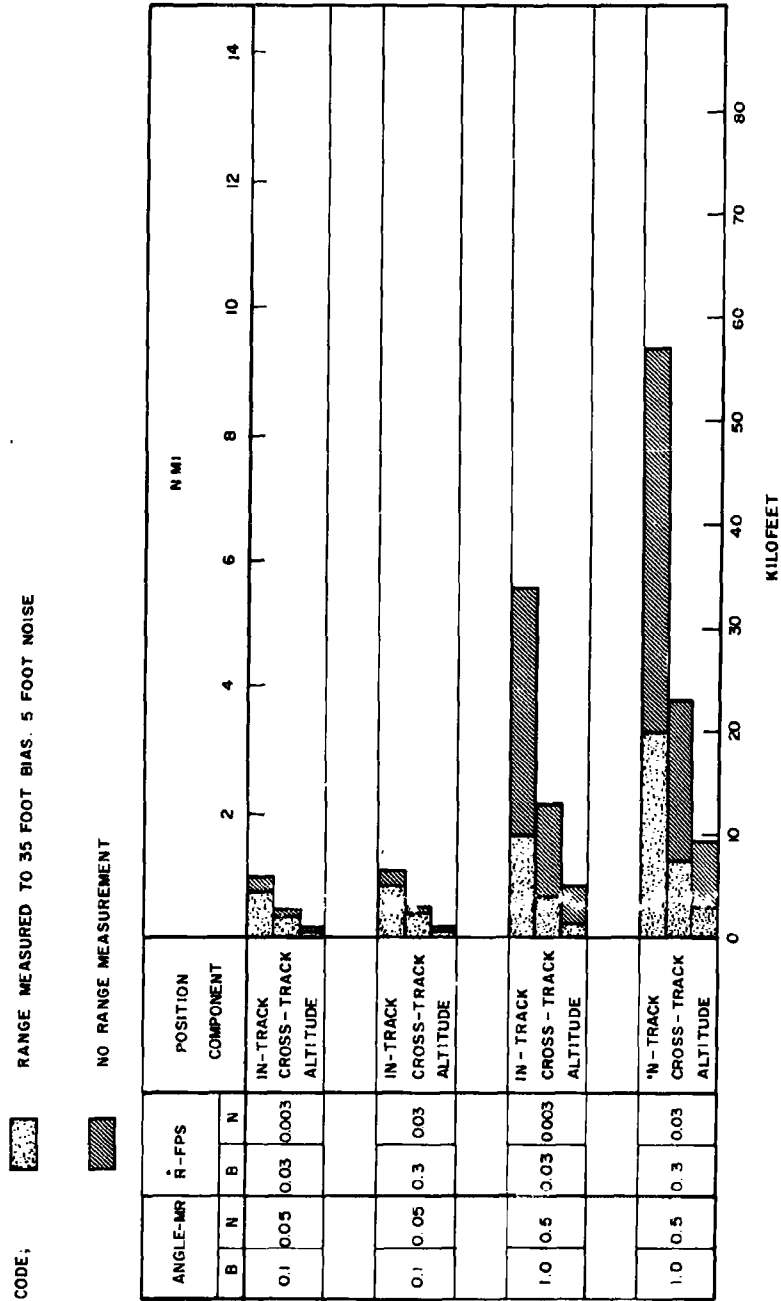


Figure 3. One-Sigma Position Errors for 2000 nm Circular Orbit  
 3a. Maximum Errors after First Pass



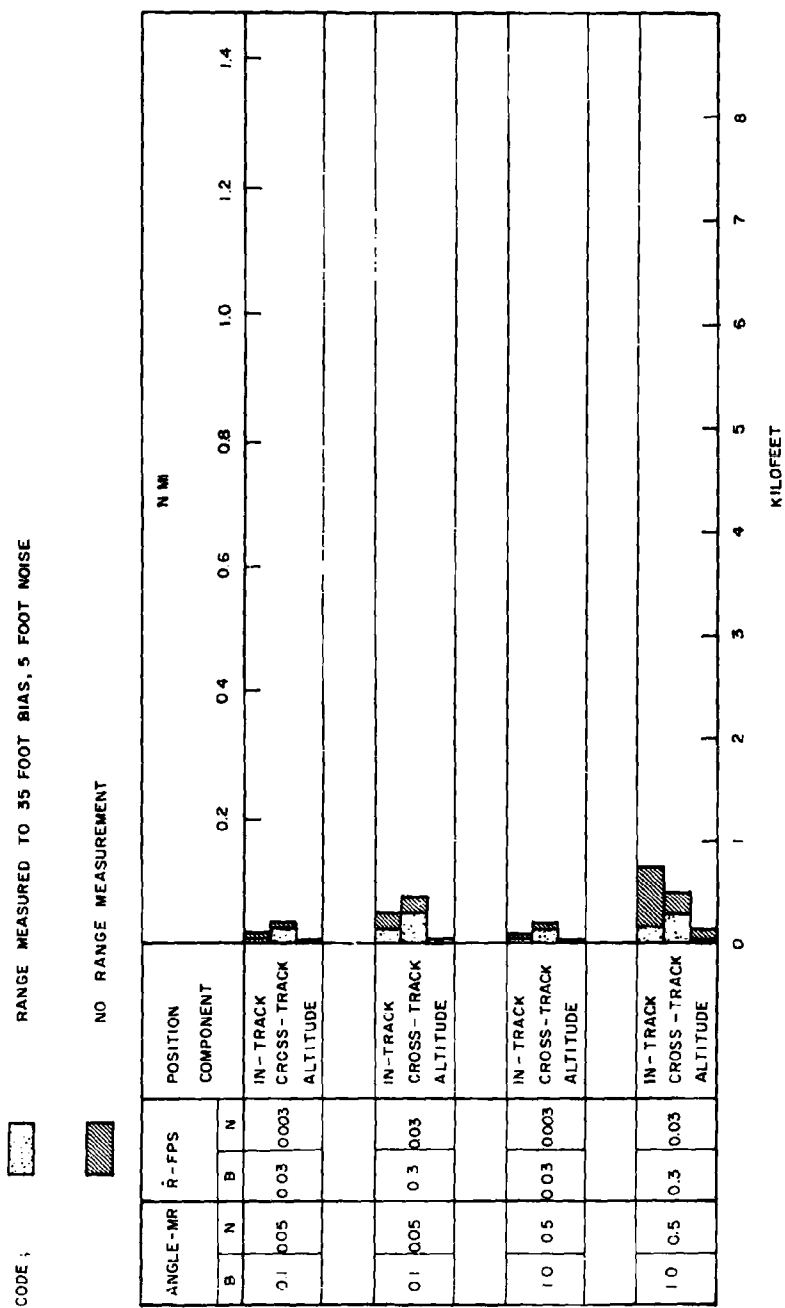


Figure 3. One-Sigma Position Errors for 2000 nm Circular Orbit  
3b. Maximum Errors after Second Pass



# ONE SIGMA MEASUREMENT ACCURACY

	ANGLES - MR	RANGE - FT	R-FPS
BIAS	1.0	35	0.30
NOISE	0.5	5	0.30

CODE; WITH RANGE  
NO RANGE MEASUREMENT

NOTE:  
THE 100,000 NMI ORBIT WAS EQUATORIAL AND WAS TRACKED A SECOND TIME  
AFTER ONLY A SMALL PART OF A REVOLUTION

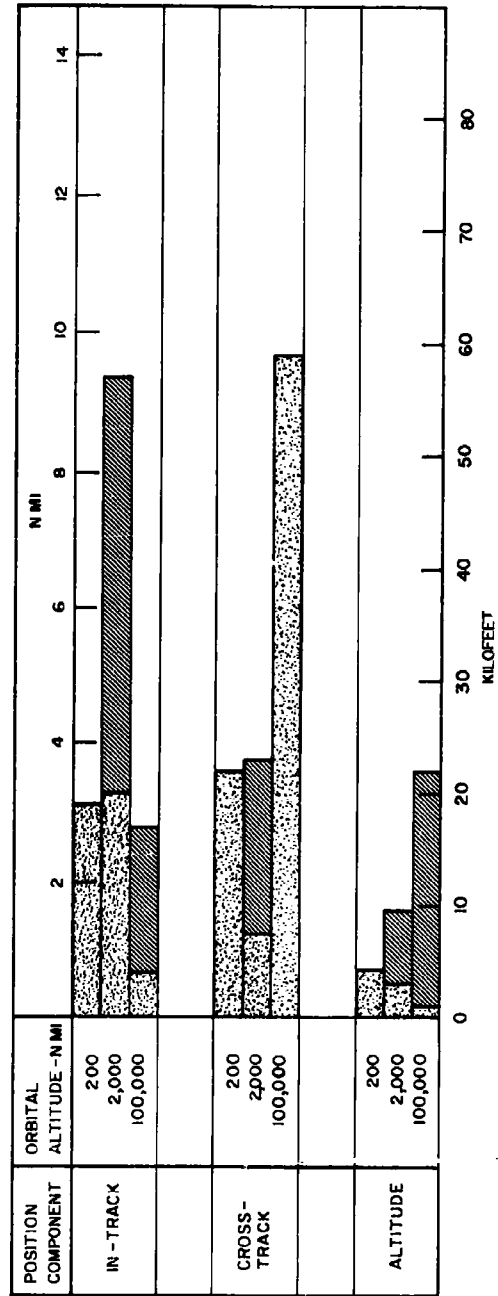


Figure 4a. Variation with Altitude of One-Sigma Position Error After First Pass



## ONE-SIGMA MEASUREMENT ACCURACY

	ANGLES-MR	RANGE - FT	$\dot{R}$ - FPS
BIAS	1.0	35	0.30
NOISE	0.5	5	0.03

CODE;  WITH RANGE NO RANGE MEASUREMENT

NOTE; THE 100,000 NM ORBIT WAS EQUATORIAL AND WAS TRACKED A SECOND TIME AFTER ONLY A SMALL PART OF A REVOLUTION

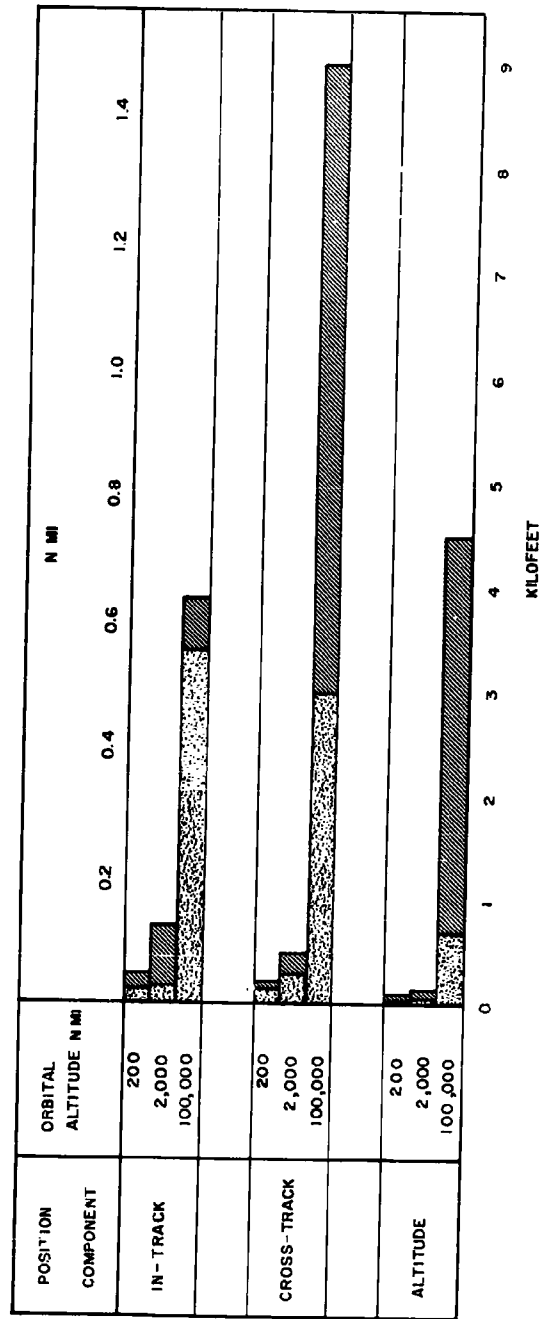


Figure 4b. Variation with Altitude of One-Sigma Position Error After Second Pass



Figure 3 shows the first and second pass ephemeris errors for a 2000 nm orbit. The relative lack of sensitivity of second pass results to angular accuracy is again evident. Also, at the higher altitude, the first pass cross-track error no longer shows a linear dependence on azimuth bias. The enhanced value of first pass range data with poorer angular data is also evident.

Figure 4 shows the value of 35 ft range measurements as a function of orbital altitude. The time between passes increased with altitude as follows:

Altitude (nautical miles)	200	2000	100,000
Time between passes (hours)	1.5	2.2	15.8
Orbital Period (hours)	1.5	3.0	232

Thus, earth rotation brought the 100,000 nm satellite back above the 10 deg tracking horizon again in one-fifteenth its orbital period. Because of this, the maximum positional errors did not correspond to the peaks of the curves of figure 1 but were considerably smaller. Keeping this in mind, the relative degradation in positional knowledge with vehicle altitude is evident in the first pass results of figure 4a and is amplified in the second pass results of figure 4b. The first pass results for the 200 nm orbit show no improvement in accuracy with the addition of range measurements, whereas there is improvement after the second pass. This is a result of the inability of the data reduction process to smooth the 100 ft station location error until after a second pass.

The 100,000 nm results are not strictly comparable to the lower altitude results. The positional errors given in figures 4a and 4b were at less than one-tenth revolution after the end of tracking rather than representing maximum values over the following revolution. Because the orbit was equatorial, the first pass cross-track error was primarily dependent on the angular tracking history. There is a generally weak dependence of first pass range and/or range rate data on inclination errors for nominally equatorial orbits (the situation is analogous to the problem of obtaining a good solution for the path angle of the velocity vector for nominally circular orbits). The second pass occurred only a small part of a revolution after the first. The small improvement in the second pass in-track position error with the measurement of slant range reflects the greater ability of the maximum likelihood data reduction technique to smooth range rate and angular biases than to smooth the combined range bias and survey error for very high altitude orbits.

In the orbit determination problem there is a rough equivalence between positional and rate measurements. Smoothed range data can be differentiated to obtain range rate. With the orbital constraints, range rate can be integrated to obtain range. The better of the two measurements in a combined system may carry practically all the weight in the orbital prediction process.

Figure 5 presents a rough curve of the above equivalence after several tracking passes. It presents the range rate accuracy required to permit the



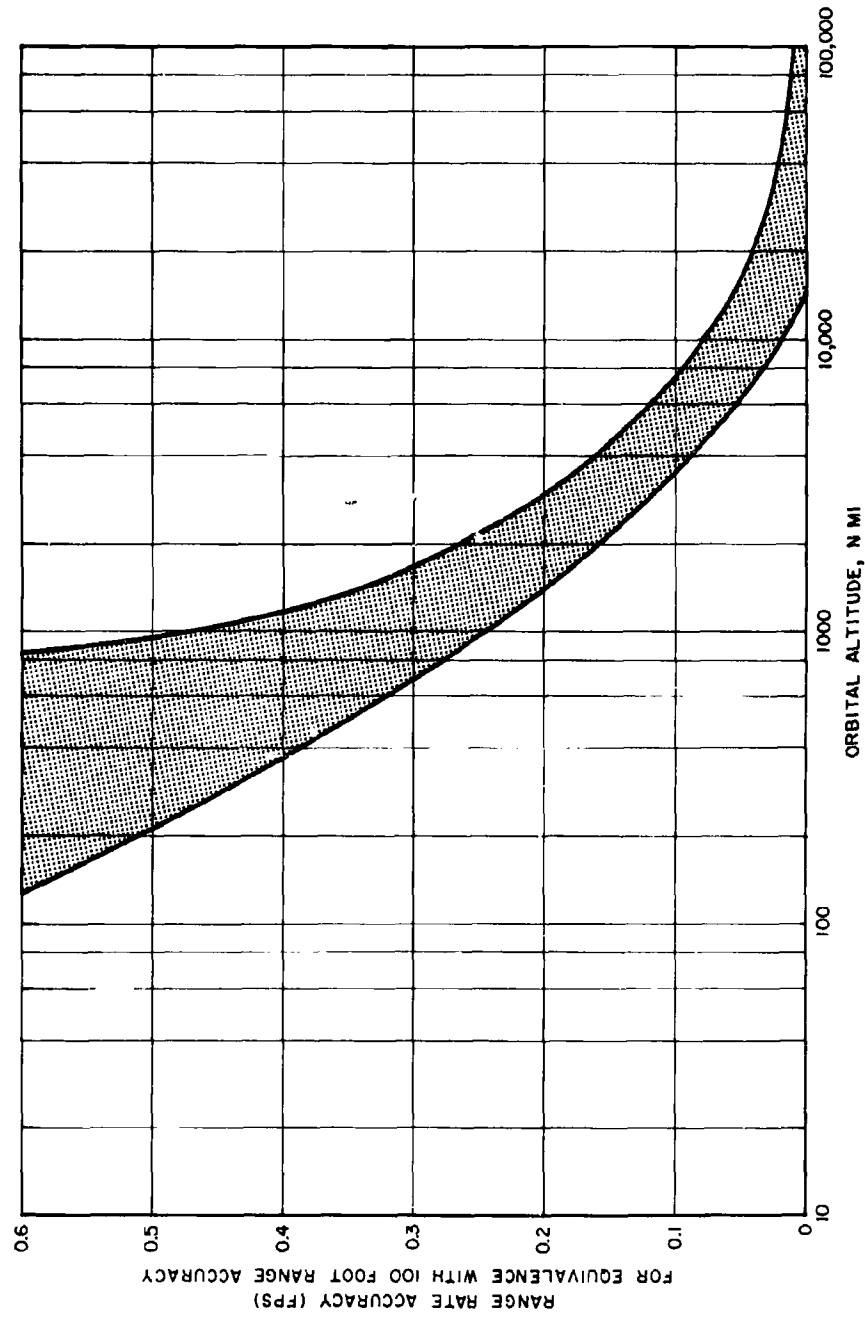


Figure 5. Relative Value of Range Rate Data



calculation of ephemerides to the accuracy to which they can be computed from 100 ft range data. The spread in the curve represents uncertainty due to the small amount of data from which it was plotted plus the following factors:

1. Since the ability to deduce range from range rate tends to be inversely proportional to range, the low altitude results are strongly dependent on the maximum tracking elevation angles of the passes.
2. At high altitudes where the largest component of range rate is earth rotation, the results are strongly dependent on orbital inclination. Range rate has no capability in the determination of the orbit of a synchronous equatorial satellite.
3. The comparison related primarily to measurement biases but the range bias is augmented by station location errors.
4. The results are somewhat sensitive to the type of data reduction used.

The comparison would favor range more strongly after only one tracking pass. The greatly improved knowledge of the velocity vector by a second pass enhances the value of range rate data. Because of the strong bias smoothing effect of the maximum likelihood criterion, the results of figures 2, 3, and 4 could not be used in the plotting of figure 5.

A recognized technique for achieving the equivalent of good angular measurements is through the use of interferometer arrangements. Base legs can be angle surveyed to the accuracy of the local geodetic reference. Because of the elimination of common errors, differential quantities can be measured to at least an order of magnitude greater accuracy than the quantities being differenced.

The reduction in orbital position errors through the use of differential range rate data is illustrated in figure 6. The basic tracker was the 0.3 fps bias, 0.03 fps noise range rate and 1 mr bias, 0.5 mr noise angular tracker of figure 4. Differential range rates (P and Q) were measured to 0.001 fps bias, 0.001 fps noise with orthogonal 10,000 ft rate legs. These are extremely good accuracies. But the same results would be obtained with longer rate legs and less accurate measurements.

The first pass cross-track error reduction of figure 6b indicates that, in conjunction with the orbital constraint, the 0.001 fps differential range rate measurements are roughly equivalent to 0.015 mr angular measurements. As shown by figures 6a and 6c the resultant precision in determination of the orientation of the orbital plane permitted an order of magnitude improvement in the determination of the in-plane orbital elements from the basic first pass range rate history. As can be seen, the differential range rate data provided little improvement in the orbital estimate after the orbital plane orientation had been determined by the second pass range rate history of the basic tracker. But orbital motion provided a base leg of one revolution (21,500 nm) for the latter determination.



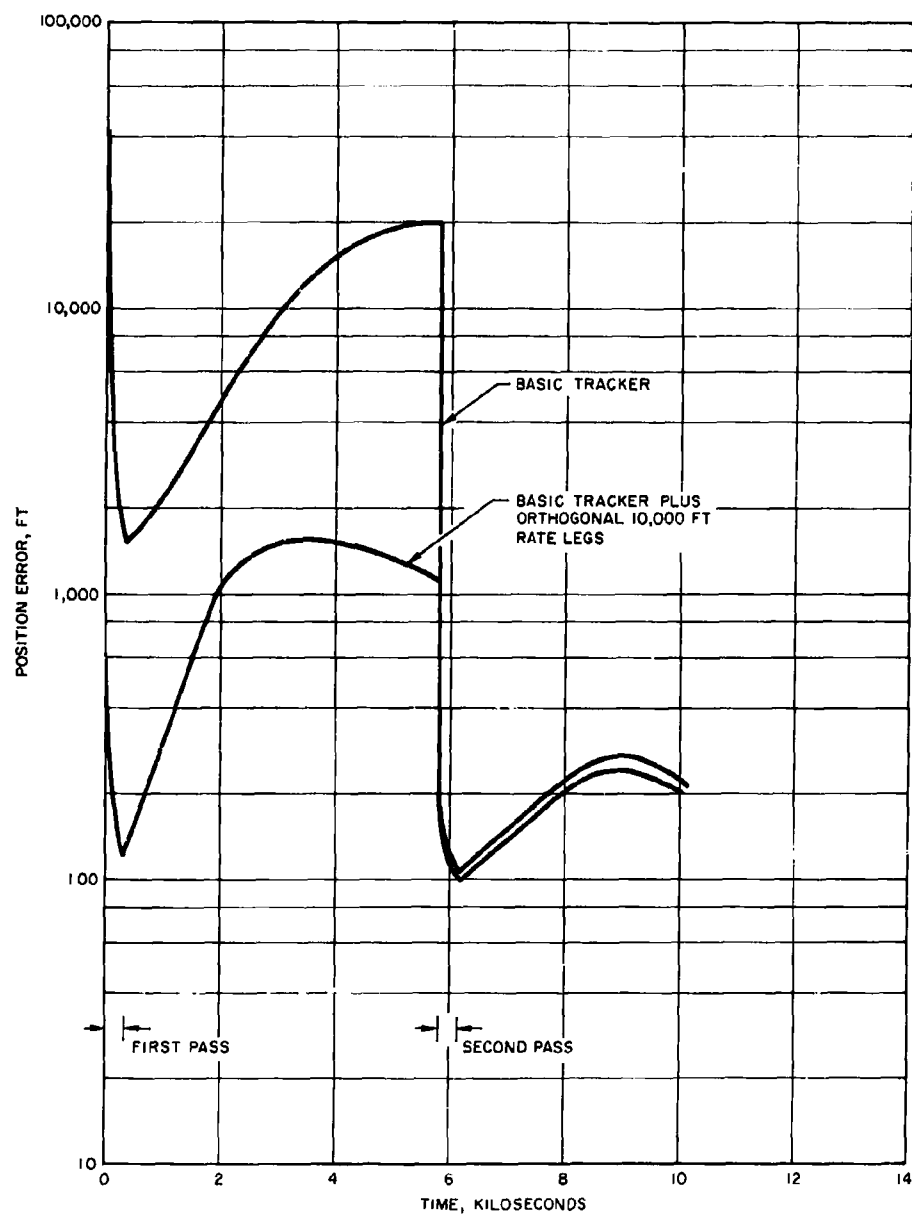


Figure 6. Ephemeris Improvements with 0.001 FPS Differential Range Rate for 200 nm Orbit

6a. One-Sigma In-Track Error



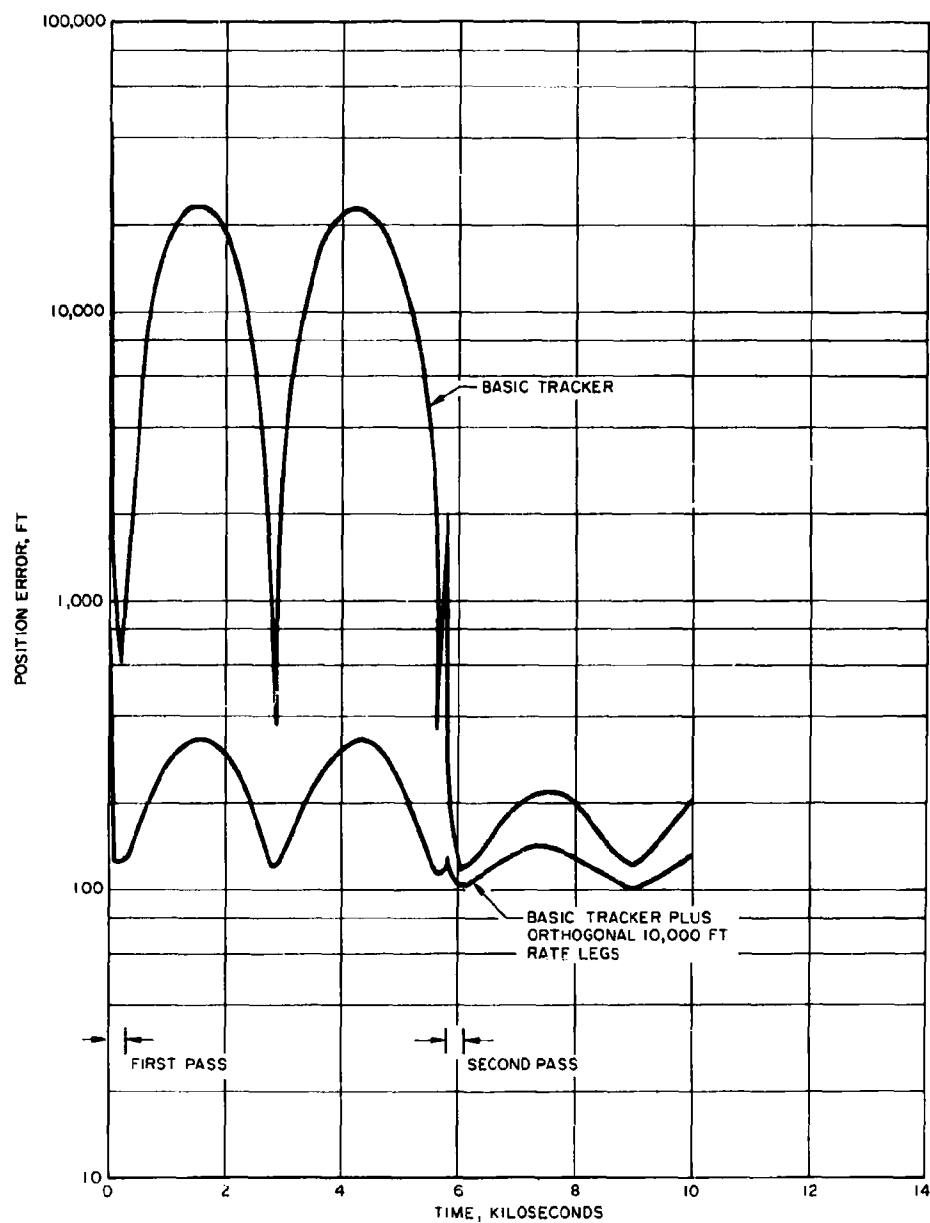


Figure 6. Ephemeris Improvement with 0.001 FPS Differential Range Rate for 200 nm Orbit

6b. One-Sigma Cross-Track Error



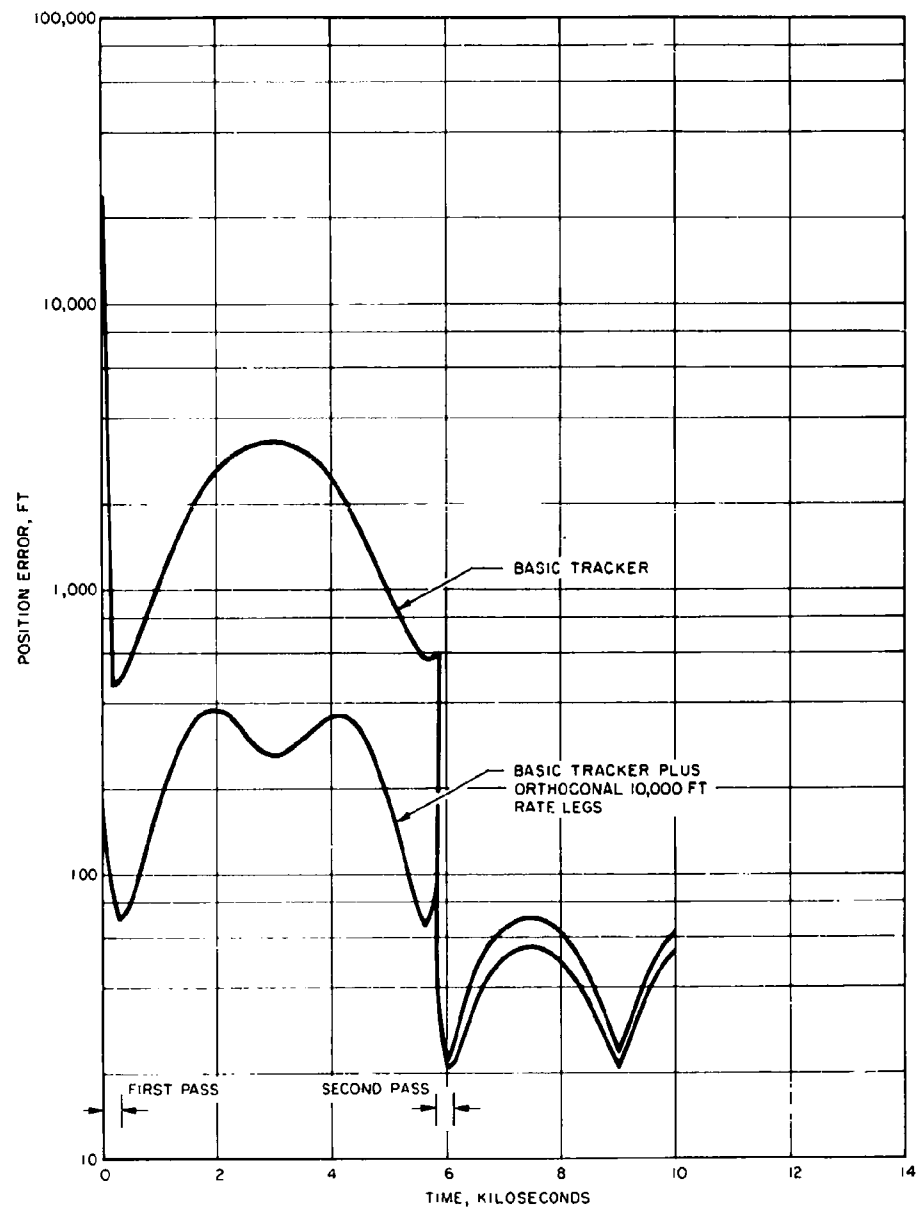


Figure 6. Ephemeris Improvement with 0.001 FPS Differential Range Rate for 200 nm Orbit

6c. One-Sigma Altitude Error



It is important to recognize that the results given in figures 2, 3, 4, and 6 represent the capabilities of maximum likelihood data reduction with no earth model errors and with truly constant measurement biases. As discussed later, the same accuracy is obtained by differential correction of the measurement biases and station location errors. But the ability to obtain the accuracies of figures 2, 3, 4, and 6, particularly the results after two passes, depends strongly upon there being no sources of orbital error other than measurement noise, constant biases, and survey errors. Thus, these results represent a true upper limit to the capabilities of the systems discussed here. With optimum bias and survey correction, this limit is set by the random measurement errors. With inverse variance weighting of only the random errors and no attempt to correct bias and survey errors, the orbital accuracy after several passes is strongly limited by the bias and survey errors and is only a weak function of the random errors. In the actual orbit determination problem, the orbital accuracy obtainable eventually approaches a limit set by geopotential and atmospheric model errors.

#### THE EFFECTS OF MEASUREMENT GEOMETRY

The relative value of differential range rate and basic angular measurements deteriorates with orbital altitude in a manner similar to that depicted in figure 5 for range rate. The value of range and differential range as orbit determination parameters is enhanced at higher altitudes. The prime value of angular and differential quantities is in the first pass determination of the orientation of the orbital plane and in aiding convergence of the data reduction program.

Any six independent measurements are sufficient to determine the vehicle position and velocity at a point (an ephemeris). If position measurements are made at a point in orbit, only three of them can be independent. Any additional position measurements at this point are redundant and can be expressed as a function of any three independent position measurements. To estimate an ephemeris by measurement at a point, three independent rate measurements are also required. But time separation will usually assure independence even in repetitions of the same measurement. Thus, if a tracker makes accurate measurements at six points in time of  $R$ ,  $A$ ,  $E$ ,  $\dot{R}$ ,  $\dot{P}$ ,  $\dot{Q}$ ,  $P$ , or  $Q$  (rate measurements are insufficient for a circular synchronous equatorial satellite and an azimuth measurement or the equivalent is required by polar and equatorial trackers) then these six measurements are sufficient to determine an ephemeris. The ephemeris is obtained as that which results in an exact fit of the equations of motion to the six independent measurements. Subsequent measurements are then redundant and allow smoothing of the measurement errors.

If the orbit is nearly circular, then it becomes difficult for one tracker to separate a slight eccentricity effect from the inclination dependent rate of ground track departure from a great circle arc because of earth rotation. If only range and/or range rate is measured and the tracking time is short, then the single pass ephemeris estimate is subject to severe loss of precision. A second tracker greatly improves the situation regardless of what quantities are measured. The accuracy of the ephemeris estimate improves as the in-track separation of the two trackers is increased. With the orbital



constraint, this separation provides an effect analogous to that of base leg length in interferometer arrangements.

Examination of the shape of the positional error curves of figure 1 indicates that for the two station case, the optimum separation for the determination of the orientation of the orbital plane (the cross-track error) is 90 earth-central degrees along the orbital plane. A separation of 180 deg is optimum for the determination of the in-plane parameters. The best period estimate is obtained by the original station tracking at some multiple of 360 deg later (the higher the multiple, the more accurate the estimate for stable orbits). The use of the original station eliminates the prime effect of station location error.

The single pass range rate results for the 200 nm circular orbit showed a 30 to 1 degradation in in-track and altitude estimates and a 5 to 1 degradation in the cross-track estimate when the maximum tracking elevation angle was reduced from 83 deg to 9 deg with a 30 percent reduction in total tracking time. There is considerably less degradation if range rather than range rate is measured or if data from more than one pass is available. The above results are based on tracking above the radar 5 deg horizon at a data rate of one set of measurements per 5 sec.

The sensitivity of the ephemeris estimate to data rate and measurement noise was investigated. The prime effect of an increased data rate is greater smoothing of the noise. After a single pass the ephemeris accuracy is a strong function of measurement noise (and data rate). After more than one pass this dependence essentially vanishes (in the practical orbit determination problem) and the accuracy is a function of measurement bias, station location error, earth model error, and other sources of systematic error in either the data or the data reduction program model. After the orientation of the orbital plane is accurately determined by a second pass, the computer programs can apparently smooth the data noise much more effectively.

Interstation timing errors are of very little importance until they result in in-track displacements comparable to the interstation survey errors. For the low altitude orbits which present the worst case, a 4 millisecond station time reference error results in only a 100 ft in-track displacement. Another timing error can arise from the assignment of range and/or range rate measurement times to the time of ground reception rather than vehicle transmission of the signal. The speed of light is only 186 mi per millisecond. The result is an average time reference shift which is not important plus a variable bias in the data which is proportional to slant range differences and can be important.

The most serious kind of measurement bias has been found to be the constant bias. Variable components of bias are smoothed by the orbital equations after more than one pass in much the same way as data noise is smoothed. If the biases fluctuate from pass to pass then their effect averages out more rapidly than if they remain constant. The truly constant biases are smoothed only by changes in tracking history from pass to pass and by interstation averaging. The same is true of survey errors.



It has been found that if there is only one tracking station then the results are relatively insensitive to station location errors. The data gives no indication of a longitudinal survey error and is only weakly affected by a moderate error in radial distance of the station from the spin axis of the earth. Survey errors have an average effect which adds to the slant range bias plus a variable effect which is relatively less important. It can be argued that if survey errors are accounted for in a data reduction program then variable range biases should be ignored because of the poor ability of the program to differentiate between the two from their effects on the measurements.

In the multiple station case it has been found that survey errors have very little effect on range rate and angular measurements. It appears that survey errors are automatically smoothed in the reduction of range rate data. But they have an almost additive effect on slant range errors. Because of this, the most serious component of survey error is usually the interstation inconsistency rather than the uncertainty in location of the center of the earth.

#### DIFFERENTIAL CORRECTION OF SYSTEMATIC ERRORS

The data reduction program must obtain an estimate of the six ephemeris components at some point in time. For low altitude orbits it has been found very beneficial to also obtain an estimate of the average atmospheric drag. Station bias and survey errors can be treated as additional parameters and also be solved for. These estimates are then incorporated into the program as it re-solves for the six ephemeris components. This process of error correction by the data reduction programs has been called differential correction.

A problem in differential correction is the resultant increase in dimensionality of the error matrices with its attendant reduction in computing speed and increase in numerical accuracy problems. Maximum likelihood data reduction accomplishes the equivalent of differential correction by allowing the estimated orbit to adjust in a simple way to the systematic errors. A danger in either approach is that the error sources will be incorrectly identified.

The bias errors are identified as the average inconsistencies between the final computed orbit and the measurement sets. The station location errors are identified by their fixed directional characteristic. The resultant error evidences itself by a change in pattern between passes which brackets the tracking station. Range rate bias is indicated by the failure of the range rate null to occur at the minimum range point.

The sophisticated tracking data reduction programs presently available use the weighted least squares criterion for ephemeris fits. Without differential correction, this can result in ephemeris estimates which deteriorate when two stations which are close together track simultaneously. If there are range biases of opposite sign, for example, the combined least squares estimate can result in a large angular error in the assigned vehicle position.



The data presented earlier assumed maximum likelihood data reduction and no earth model errors. Similar results are obtained by the weighted least squares criterion with differential correction of the systematic errors provided convergence is satisfactory. The parameters to be included in the likelihood estimator or to be differentially corrected are the important sources of ephemeris error. There is very little ability to correct minor sources of error. Even the major sources of error cannot successfully be corrected until sufficient data is available to allow a reduction in ephemeris uncertainty to a level below the upper limit of the error in the quantity to be corrected. Differential correction cannot reduce measurement biases to a level below that of the systematic effect of the smoothed random errors.

In the determination of high altitude orbits from angular tracking data the quantities to be corrected are clearly the angular measurement biases. For the low altitude orbits it is difficult to assess the relative importances of earth model errors, drag uncertainty, measurement biases, and survey errors.

#### EARTH MODEL ERRORS

The prime component of the force field of near earth satellites is the inverse radius squared gravitational attraction toward the center of the earth. This effect is represented in the program model by values of earth mass and equatorial radius. The programs solve for satellite altitude above the surface of the earth. An error in the numerical value of earth mass and/or radius results in the following period error:

$$\Delta P = \frac{P}{2} \left( - \frac{\Delta \mu}{\mu} + 3 \frac{\Delta r_e}{r_e + h} \right).$$

For a mass error of one part in  $10^5$  or a radius error of roughly 100 ft and a 2000 nm orbit, this results in a period error of 0.05 sec. Since average orbital periods have been measured by the Smithsonian system to at least an order of magnitude greater accuracy than this, we are forced to conclude that any residual errors in the present value of mass are largely balanced by compensating errors in earth radius.

In general, computer program model errors lead to orbital errors which are smaller than the positional differences which result from propagating in ephemeris with and without the source of model error. There are two reasons for this:

1. The data reflects the existence of the actual earth parameters and thus leads to a computed orbit which averages out part of the error.
2. Many of the model effects are oscillatory and a large part of the resultant error averages to zero over many sets of tracking data.



An earth mass or radius error can be compensated by assigning a corresponding altitude error to the vehicle. It has been found that in the reduction of range rate and angular data the programs readily convert earth mass and station altitude errors to vehicle altitude errors, thus maintaining the measured tracking rates and orbital periods. If the orbital estimate is based on slant range tracking histories, then this can no longer be done. Hence, slant range trackers have a greater ability to differentially correct model errors than other systems. But orbital estimates from range data without the correct computer program earth model parameters are poorer than estimates from other measurements of comparable accuracy.

The actual mass distribution of the earth can be expanded in an infinite series of spherical harmonics. If it were a rotating fluid mass of variable density, then there would be no longitudinal harmonics and the geopotential expansion would be

$$U = \frac{\mu}{r} \left[ 1 - \sum_{n=2}^{\infty} J_n \left( \frac{a}{r} \right)^n P_n(\sin \phi) \right]$$

where

$\mu$  = gravitational constant times earth's mass

$r$  = earth central radius to point

$J_n$  = mass coefficient of  $n^{\text{th}}$  harmonic

$a$  = mean equatorial radius of earth

$P_n$  =  $n^{\text{th}}$  zonal harmonic (Legendre polynomial)

$\phi$  = geocentric latitude to point .

This function is differentiated to obtain the components of gravitational force at the point of interest (the satellite location).

By far the largest harmonic is oblateness ( $J_2$ ). It has the effect of precessing the orbital plane and the major axis. By measuring the resultant long term precession rates,  $J_2$  has been determined to an accuracy which is undoubtedly much greater than the individual accuracies of the mass and radius. The negative sign in the above equation is a result of the desire to have a positive value for  $J_2$ .

Associated with  $J_2$  is the shape oblateness ( $\epsilon$ ). Its computation from  $J_2$  requires the assumption of an internal density distribution for the earth. An error in  $\epsilon$  would appear as an altitude survey error which would increase with distance of the station from the equator and would thus be primarily detrimental to slant range data from far northern (or southern) stations.



The remaining zonal harmonics are roughly three orders of magnitude smaller than  $J_2$  and their effects attenuate rapidly with orbital altitude. They have been isolated by their long term effects on low altitude, low inclination orbits.

Because of the irregular patterns of the continents and measured gravitational anomalies we would expect to also find evidence of longitudinal (tesseral) harmonics in the reduction of satellite tracking data. The geopotential expansion for these is

$$U = \frac{\mu}{r} \sum_{n=2}^{\infty} \sum_{m=1}^n J_{mn} \left(\frac{a}{r}\right)^n P_n^m(\sin \phi) \cos m(\lambda - \lambda_{mn})$$

where  $J_{mn}$  is the mass coefficient,  $P_n^m$  is the associated Legendre polynomial, and  $\lambda$  is longitude. These harmonics should have a maximum effect on low altitude polar orbits. One effect is an oscillatory orbital period. It has been found necessary to include  $J_{22}$  in the data reduction programs to obtain good fits to low altitude polar orbits. It has also been found that the best orbital prediction capability is obtained by fitting to tracking data taken over one-half day or one full day's time, thus obtaining optimum smoothing of the even tesseral harmonics. This also provides optimum smoothing of station location errors.

The orbit determination programs are forced to represent the effects of the full infinite series of geopotential harmonics by a few lower order terms. Because of the smoothing effect of the orbital constraint on local perturbations, this representation can be very good. But the results tend to be highly dependent on the inclination of the orbits used to compute the harmonics. At the present time, a set of harmonics has not been derived which will provide good fits to orbits of all inclinations. If properly interpreted, slant range data to low altitude nearly polar orbits should produce more valuable information on the longitudinal harmonics than any other data (provided drag is not a serious source of error).

The geopotential harmonic and station location errors can be handled by reducing enough different sets of data to arrive at good values for these parameters or by measuring range rate rather than slant range and thus obtaining a larger degree of smoothing of these effects. Slant range data can be converted to smoothed range rate data through the technique of one-pass fits.

In the low altitude region, drag is a major cause of ephemeris error. The atmospheric density is dependent on solar activity. Thus the 1959 ARDC standard atmosphere, which was derived from the behavior of satellites launched in 1958 (a year of high solar activity), indicated a mean density above 200 nm which is several times higher than that measured in 1962 (the year of the quiet sun). The density is higher on the daylight side of the earth.



In addition, solar radiation pressure shifts the center of the orbit away from the center of the earth toward the dark side. The radiation pressure is equal to drag at an altitude of roughly 500 nm.

The solution to the drag problem appears to be to use a sophisticated drag model with solar activity as an input and to have the data reduction program make early and repeated estimates of mean drag. Results with low altitude polar orbits suggest that the programs can estimate mean drag (the ballistic coefficient) accurately enough that, even with the ARDC 1959 atmosphere, the drag error may no longer be an important source of ephemeris error. With a more accurate set of geopotential harmonics and with good station locations this may cease to be true. At any rate, the change in drag as apogee altitude drops and as perigee shifts relative to the subsolar point should be correctly accounted for.

At lower altitudes the gravitational effects of external bodies can often be neglected. At higher altitudes drag and geopotential harmonics other than oblateness can often be neglected. Highly eccentric orbits with perigee in the drag region present an interesting case in which perturbations of perigee altitude by the sun and moon have a very great effect on orbital lifetime. For nearly circular orbits, the prime effect of the external bodies is to precess the orbital plane. If they are omitted then this precession will eventually exceed the limits of the ability of the computer program to improve its orbital estimate. As more data becomes available the ephemeris accuracy will initially improve, then level off, and eventually begin deteriorating. In the presence of any model error which has a cumulative effect, there is a maximum number of revolutions over which the computer program should obtain its fit. Beyond this point, earlier data must be dropped to maintain the accuracy of the estimate. This maximum number of revolutions is a measure of the accuracy of the computer program earth model. There is also a long time limitation due to computer numerical accuracy.

### CONCLUSIONS

It has been found that the basic changes in orbital uncertainty beyond a tracking station are a function of the equations of motion rather than measurement type or accuracy. The phase relationships and the ratio of position to velocity error in each coordinate are dictated by the geometry and by the requirement that the position errors be the integral of the velocity errors rather than by whether the tracking system measured range or range rate. Only the scale magnitudes of the orbital errors are determined by measurement type and accuracy. The ideal minimum values of these numerical orbital errors for various systems whose only sources of error were station location uncertainty plus Gaussian noise and constant biases in each measurement are presented as bar charts of maximum positional errors after one and two tracking passes.

The results of the study indicate that for low altitude orbits after only one set of tracking data, system angular accuracy is of overriding important in ephemeris prediction. After the orbital plane is accurately determined by a second tracking pass using the same or a second station, angular data loses its value and good range rate becomes the most important measurement



for ephemeris prediction. At higher altitudes where range rate changes slowly, good slant range data becomes the most valuable.

After only one pass, ephemeris accuracy is strongly dependent on data rate and measurement noise. After more than one pass this dependence essentially vanishes and accuracy is limited by measurement bias and other systematic sources of error. In the multiple pass case, angular data should be de-emphasized or it will hurt the ephemeris estimates. But it should not be discarded because it improves program convergence.

In the low altitude case, the programs should make their own drag estimates after several revolutions. These should be repeated periodically. Station locations should also be determined by tracking data reduction. After this is done, errors in the geopotential harmonics may become the greatest remaining source of multiple pass prediction error. For high inclination orbits, the longitudinal harmonics have a significant effect. This effect and that of station location errors can be minimized by performing fits to data spans which are multiples of 24 hours.

In the presence of earth model errors the ephemeris estimate may deteriorate as the data span is increased. In addition, if tracking is concentrated along a small part of the orbit, the model errors will tend to convert to an eccentricity error rather than a period error. Hence, the data from one isolated station far from the others will cause an apparent deterioration of the fit.

Because the multiple pass estimate is only weakly affected by data noise and variable biases, the data sets can be truncated symmetrically about the minimum range points to increase the speed of the programs. In a simulation of a 5000 nm orbit, tracking above the 20 deg radar horizon produced the same ephemeris accuracy in three revolutions as tracking above the 5 deg radar horizon. In addition, actual data accuracy decreases at lower elevation angles and the errors tend to be symmetrical to either side of the maximum elevation angle point.



## RECOVERY SYSTEMS



## EVOLUTION OF THE HYPERFLO PARACHUTE

L. W. Sims

Cook Electric Company  
Tech-Center Division  
Aerospace Technology Section  
Morton Grove, Illinois

### ABSTRACT

Analytical and experimental studies of the characteristics of supersonic parachutes and associated phenomena, which resulted in the development of the Hyperflo parachute, are described.

Data from wind tunnel test programs which were conducted with six and eight inch parachute models are discussed. These programs covered the Mach number range from 1.5 to 4.65 and included approximately 200 test conditions. The present paper describes the evolution of parachute canopies which performed satisfactorily through Mach 4.65 and, in a succeeding series of wind tunnel tests, through Mach 6. Results of a rocket sled test program and a free-flight program to test full-scale Hyperflo parachutes up to Mach numbers of 4.0 and altitudes of 130,000 feet are summarized.

The work described in this paper was performed under Air Force Contract No. AF 33(616)-8459 sponsored by the Retardation and Recovery Branch, Flight Accessories Laboratory, Aeronautical Systems Division, Air Force Systems Command.



## EVOLUTION OF THE HYPERFLO PARACHUTE

L. W. Sims  
Cook Electric Company  
Tech-Center Division  
Aerospace Technology Section  
Morton Grove, Illinois

### INTRODUCTION

While performing studies of the supersonic operation of parachutes and their associated flow phenomena, under contract with the Retardation and Recovery Branch, Flight Accessories Laboratory, Aeronautical Systems Division, AFSC, USAF, the Hyperflo family of high speed parachutes evolved. At the initiation of this program on June 30, 1961, satisfactory operation of conventional parachutes was limited to an upper Mach number of approximately 2. Numerous applied research programs had been conducted prior to this time aimed at evaluating conventional parachutes at transonic and supersonic speeds. These programs involved the use of high speed sleds, wind tunnels, and free-flight vehicles and resulted in the generation of much data. Typical data for such programs consisted of force measurements, high speed photographs of parachute deployments and operation, and high speed Schlieren films. As a result of the analysis of such data, the basic problems associated with the operation of conventional parachutes at supersonic speeds were indicated. Numerous conventional parachute configurations were employed in these tests, with ribbon-type constructions predominating. In the following sections of this paper, the basic problems associated with the application of conventional parachutes at supersonic speeds are discussed. Indications of design trends necessary to improve supersonic canopy performance, as deduced from previous test data of modified configurations, are discussed. In subsequent sections, the analytical procedures and test programs from which the Hyperflo canopies evolved are described.

Three wind tunnel test programs (designated Phases I, Ia, and II) representing a total of nearly 200 test conditions were completed in this study, covering a Mach number range of 1.5 to 4.65.



## BASIC PROBLEMS ASSOCIATED WITH SUPERSONIC OPERATION OF CONVENTIONAL PARACHUTE CONFIGURATIONS

In earlier test programs, conventional parachutes had been found to perform poorly at supersonic speeds, particularly above Mach 2. In the following paragraphs, the characteristics of conventional parachutes when operating in the supersonic range will be described.

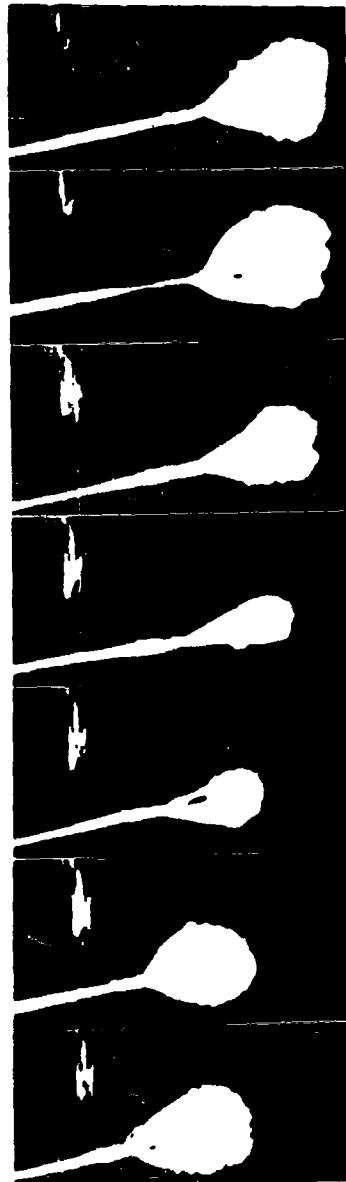
### A. Inflation Characteristics

Analysis of Schlieren movies of conventional parachute configurations has revealed a typical behavior in the supersonic range above Mach 1.8 - 2.0. This behavior is characterized by a rather violent "breathing" tendency or alternate inflation and deflation cycle, which occurs at very high frequencies (of the order of 5 to 100 cycles per second). This phenomenon is illustrated in Fig. 1 for a 4.0 foot diameter flat circular ribbon parachute with a 19 percent porosity. This film sequence (alternate frames of movies taken at 128 fps), was taken during wind tunnel tests of this configuration at a Mach number of 3.5 during the conduct of a series of tests in the NASA Lewis 10 ft by 10 ft wind tunnel by the Cook Research Laboratories. During this program, both ribbon and guide surface type parachutes were tested in the Mach number range from 2.0 to 3.5. A wide number of variations of both types of parachutes were employed. For example, the porosity of the ribbon-type parachutes was varied from 5 to 30 percent. Porosity distributions were also considered in that low skirt porosity with large vent porosity, as well as low vent porosity and high skirt porosities, were employed in the various configurations. In addition, the tests were conducted both with and without a forebody. In all instances, parachute behavior was typified by high frequency breathing.

In addition to the ribbon parachutes, various types of guide surface ribless canopies were also tested. The extremes in breathing were not as pronounced as for the ribbon canopies. However, over-inflation of the roof and indentation of the guide surfaces resulted in nearly immediate failure of the canopy at the intersection of the roof and guide surface panels. In Fig. 1, a 3.25 ft diameter guide surface ribless parachute with 20 percent slots is shown at Mach 3.5.

In order to evaluate whether these phenomena were associated with the flexible materials of which these configurations were constructed or with an unstable flow field ahead of the canopy, a further test program was conducted employing rigid canopies constructed of steel and simulating the inflated shapes of typical ribbon canopies. These tests were conducted with and without simulated lines and with various numbers and lengths of lines. Based upon the results of these tests, the existence of unsteady flow conditions and Mach number effects was confirmed. A discussion of these and





FLAT CIRCULAR RIBBON



GUIDE SURFACE RIBLESS

Fig. 1. Characteristics of Two Parachutes at  $M = 3.5$



the preceding fabric model tests, along with an analysis of the various associated flow regimes, is given in Ref. 1. As a result of this analysis, it appeared that the nature of the flow regime and shock wave structure ahead of the canopy was significantly dependent upon the forebody wake characteristics, and that parachute configurations were greatly affected by the interaction of the canopy shock wave with velocity gradients existing in the wake of the forebody. Several typical flow types which are associated with this interaction are demonstrated in Ref. 1.

In later tests, a canopy configuration which was studied in the Cook Electric Company's Tech-Center Division wind tunnel facility demonstrated that certain configurational characteristics may have a strong effect in suppressing the unfavorable interaction effects which appear to be associated with a conventional parachute configuration immersed in a nonuniform flow field provided by an upstream forebody. The canopy of this configuration consisted of a  $15^\circ$  (half angle) conical frustum fabricated of a nonporous material with a center vent which provided an exit-to-inlet area ratio of 0.29. A variation of this configuration employing a  $45^\circ$  conical frustum was also tested. Very high drag coefficients (0.46 and 0.96, respectively) based upon cloth area were realized with these models at  $M = 2$ . Extremely good inflation characteristics were also evident from Schlieren films (Fig. 2), and very little canopy breathing was evident. However, both of these canopies exhibited an instability about the point of suspension by oscillation angles up to nearly  $20^\circ$ . In spite of such high angular excursions, the canopies remained well-inflated although subjected to severe disturbances associated with these high angular displacements. The instability of these configurations was attributed to the ring-airfoil-type lift inherent in this canopy shape. A stabilizing surface extending forward of the maximum diameter had been added to the  $45^\circ$  conical canopy. However, the high inflation tendencies of this canopy resulted in material stretch of this surface to such an extent that it was ineffective in contributing stabilization. It was this basic configuration, along with the indicated necessary modifications, which served to establish some of the configurational details of the models which were selected for the first testing series of the subject program.

#### B. Stability Characteristics

Analysis of the data from early tests indicated that the stability of a parachute canopy about the point of suspension varies directly with porosity. Tests in the present program indicated this trend also. However, it is apparent that geometric details of the canopy have a significant effect also. An illustration of this, of course, is the guide surface canopy which is constructed generally of a low porosity material, yet in the subsonic and transonic ranges of Mach numbers exhibits extreme stability. The contribution of the forward guide surface is essential to the attainment of this stability. The flat roof of this configuration contributes negative lift when sufficient





Fig. 2. Characteristics of a  $15^\circ$  Conical Parachute,  $A_E/A_i = 0.29$ ,  $M = 2.0$



porosity allows flow through the canopy. The forward guide surfaces, which are inflated internally with near-stagnation pressures, serve as a stabilizing cone-frustrum and contribute the necessary compensating positive lift for stability. The basic guide surface configuration, along with modifications, served also to provide some of the canopy shapes investigated in the first testing series of this program.

### C. Shock Wave-Boundary Layer Interaction

Analysis of Schlieren photographs of conventional parachute configurations at supersonic speeds indicated significant shock wave-boundary layer interactions. It appeared from observation of parachute test data that for those configurations which exhibited low or marginal inflation characteristics, the interaction of the canopy shock wave and the suspension line boundary layer had a significant effect on the inflation stability of the canopy, and was somewhat associated with cyclic canopy collapse. In other instances (Fig. 2), it appeared that this phenomenon did not have a significant effect on the parachute performance. This latter example, of course, applied to a canopy with strong inflation properties as previously described.

This phenomenon has been most evident in those instances in which the suspension lines become normal or near normal to the canopy shock wave. This condition is readily attained in the case of a canopy which is unstable about the point of suspension, allowing excursion angles of the canopy such that the lines approach normalcy to the shock wave as illustrated in Fig. 2. This is possible since examination of Schlieren films appears to indicate that the shock wave associated with an unstable parachute translates normal to the wake axis an amount which is limited approximately to the width of the forebody wake, and very small rotation of the shock pattern about its vertex is evident. For those canopy types which sustain a strong shock, small oscillation angles are needed to attain a near normal angle between the suspension lines and the shock wave.

## HYPERFLO DEVELOPMENT

### A. Indications of Desirable Canopy Geometry Based upon Early Tests

Reference was made to a conical canopy configuration illustrated in Fig. 2 which had exhibited strong inflation tendencies as well as inflation stability at Mach 2. In the design of this canopy, three features differed extremely from conventional configurations previously applied in the supersonic speed range. These were: (1) a much lower exit-to-inlet area ratio had been used, (2) a nonporous material was used in the vicinity of the inlet or skirt region of the canopy, and (3) a much lower total porosity resulted.



The total porosity of a parachute is defined as the open area divided by the total cloth area. The open area consists of the space between ribbons, as in a ribbon canopy construction, and/or open spaces in a woven fabric which allows the passage of air. In the case of the canopy described above, which, except for the open vent, is constructed of nonporous material, the over-all porosity was considered as the area of the vent divided by the total area (which includes the vent). This definition will be at variance to some degree with porosity which is expressed as a function of permeability. The latter property of cloth is determined by measurement of the rate of flow of air under specified conditions through a fabric. Small spaces between fibers of a cloth material will define somewhat different flow conditions than flow through a large vent. However, in all calculations performed in this program to determine the open area, a strictly geometric interpretation has been made. This "open" area is used herein to determine both total porosity and "exit" area.

Accordingly, the exit-to-inlet area ratio of the conical canopy discussed above is 0.29, and the total geometric porosity is 9.5 percent. In contrast to this, a conventional ribbon parachute is constructed using a geometric porosity of 15 to 28 percent. If the canopy were constructed in a hemispherical shape, the exit-to-inlet area ratio would be 0.30 to 0.56 assuming full inflation. In ribbon configurations, the porosity at the skirt is normally greater than that near the vent. Strong inflation characteristics in the skirt or inlet regions appear to be essential to provide an outward force at least equal to the inward components of the suspension line loads.

As discussed previously, the stability of a given parachute configuration about the point of suspension appears to vary directly with porosity. In the case of the guide surface configuration, however, the total porosity is low and the stability is notably high. The stabilizing effect of the forward guide surface is apparent although the conventional angle ( $45^\circ$ ) of this surface appeared to be too great for supersonic applications.

The use of low over-all porosity, coupled with stabilizing surfaces appeared essential. Requirements to establish the effects of (1) porosity distributions in producing good inflation, (2) stabilizing surface angles and length for proper inflation and stability, and (3) the over-all geometric shape of the canopy for optimum drag-to-weight ratio appeared to prescribe the direction of effort in the Phase I parachute test program.

#### B. Effects of Forebody Wake on Supersonic Parachute Operation

The importance of the effects of the wake of a forebody on a trailing parachute configuration have been recognized. In Ref. 1, calculations were performed to determine the effects of the nonuniform flow field produced by the wake on a shock wave ahead of a blunt trailing decelerator. Significant



shock diffraction was verified by employing empirical wake theory for the determination of the wake flow ahead of the canopy and shock wave. Diffraction of the typical near-normal shock wave, which would exist under free-stream conditions ahead of a blunt body such as an inflated parachute, into a conical type shock was indicated by these calculations, and has been confirmed by numerous Schlieren photographs of parachutes operating supersonically in a forebody wake. Furthermore, the dependence upon the wake of a forebody for satisfactory parachute operation at supersonic speeds has also been indicated by past tests and applications.

A Phase Ia model configuration under test will be used as an illustration to establish the flow field ahead of a canopy and associated shock wave. To predict the flow field in the wake, an empirical wake theory was used. Drag predictions provided by this procedure on trailing decelerators have been in good agreement with test data. Total temperature is assumed constant, and static pressure is assumed equal to free-stream pressure in the wake after the wake throat.

The velocity,  $V_w$ , across the wake as given in Ref. 2 is:

$$V_w = V_\infty \left\{ 1 - \frac{V_{w1}}{V_\infty} \left[ 1 - \left( \frac{y}{b} \right)^{3/2} \right]^2 \right\}$$

where

$y$  = the distance from the wake centerline

$b$  = the wake half width

$V_\infty$  = the free-stream velocity

$\frac{V_{w1}}{V_\infty}$  = the wake centerline velocity decrement ratio  
which is determined by the expression

$$V_{w1}/V_\infty = \frac{C}{(x/d - x_t/d)^{2/3} + C}$$

where

$x$  = distance aft of forebody base

$d$  = forebody base diameter

$x_t$  = wake throat location

$C$  = constant based on test data.



Figure 3 is a trace from a Schlieren photograph of a Phase Ia configuration which was located at an  $x/d = 10$  at a test Mach number of 2.13. Various wake Mach numbers as predicted by the procedure discussed above are indicated in the wake ahead of the shock wave. Flow deviations through the shock for these Mach numbers and local shock wave angles are indicated. A wake width equal to the forebody diameter is assumed. It may be seen from Fig. 3 that a subsonic outflow resulting from the deflection through the shock has a favorable effect in maintaining the canopy fully inflated. Canopy inlet-cone half angles of nearly 25 degrees will provide a positive "angle of attack" of the canopy inlet to the local flow direction. It is apparent from Fig. 3 that the flow deviation angle based upon the free-stream Mach number is sufficient to spread the wake to near the skirt of the canopy. This is further indicated to be required since the pressure ratio across the normal portion of the shock on the centerline (for the wake centerline Mach number) is greater than the pressure ratio across the oblique shock at the free-stream Mach number. Divergence of the wake flow is further encouraged by the high (near-stagnation) pressures existing in the canopy.

### C. Experimental Program

Three wind tunnel test phases were completed in this program. The first program was conducted in the AEDC Tunnel A, VKF, Tullahoma, Tennessee, followed by an interim program in the Tech-Center Division wind tunnel, and the third phase was accomplished in the NASA Langley Research Center, LST, Langley Field, Virginia. Tests were conducted over a Mach number range of 1.5 to 4.65 in the over-all experimental test program.

#### 1. Phase I Parachute Test Program

Parachute models were deployed in the wake of a biconic forebody which was strut-mounted to the tunnel side wall. All canopies were tested with riser lengths locating the inlet of the canopy approximately 10 forebody base diameters aft of the forebody base. Drag measurements, high speed direct photography at 500 frames per second, and Schlieren movies at 1000 frames per second provided data for analysis of the test model performances.

##### a. Test Model Descriptions

In the first series of parachute tests, a study was conducted involving five modified guide surface ribless canopies, five biconic canopies, a Hemisflo canopy, and a flat circular ribbon canopy with the capability of remote variation of reefing area ratio. Variations in the basic gore designs of the guide surface types were accomplished in order to provide different inlet-to-maximum projected diameter ratios as well as inlet guide surface angles. Canopy inlet angles were selected so as to be consistent with shock wave-wake analyses. Specifications for the various configurations tested in this program are shown in Table 1.



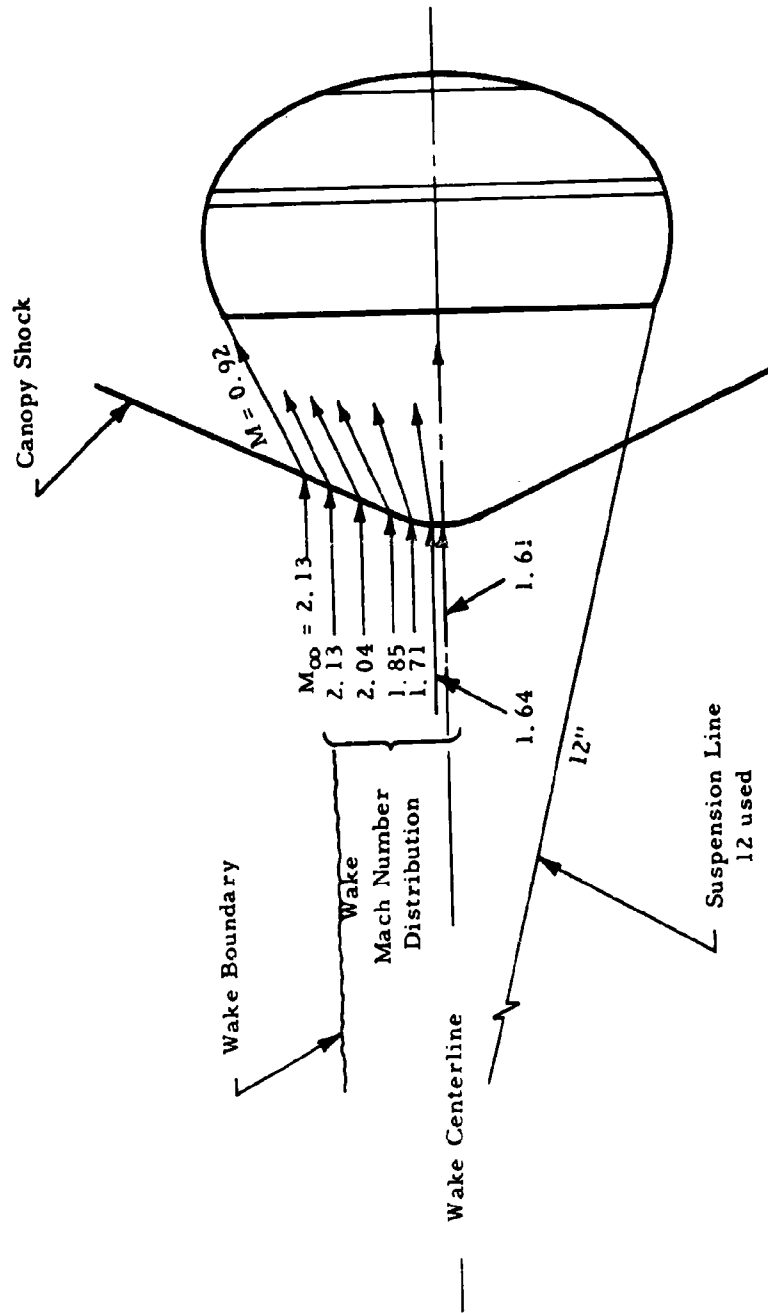


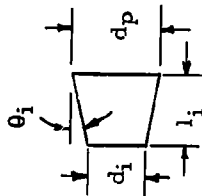
Fig. 3. Flow Field and Shock Configuration Phase Ia Test Model C-6a,  $M_{\infty} = 2.13$



Table 1. Phase I Parachute Types and Specifications

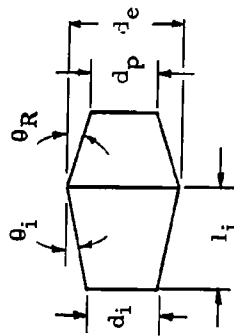
## I Modified Guide Surface Ribless Types

Parachute Model	Suspension Line Length	$\theta_i$ (deg)	$d_i/d_p$	$l_i/d_p$	Roof Type	$S_o/S_p$ (2)
A	1 $d_m$	20	0.7	0.41	(1)	2.64
C	1 $d_m$	20	0.5	0.69	(1)	5.45
D	1 $d_m$	20	0.35	0.89	(1)	4.09
E	2 $d_m$	11	0.5	1.29	(1)	5.85



## II Large Vent Bi-Conical Types

Parachute Model	Suspension Line	$\theta_i$ (deg)	$d_i/d_p$	$l_i/d_p$	$d_i/d_e$	$\theta_R$ (deg)	$S_o/S_p$
F	1 $d_m$	20	0.7	0.41	1.14	20	3.3
G	1 $d_m$	20	0.5	0.69	1.14	20	4.57
H	2 $d_m$	11	0.5	1.29	1.14	20	6.27
I	1 $d_m$	20	0.5	0.69	1.14	30	3.83
J	1 $d_m$	20	0.5	0.69	1.21	30	3.87



## III Ribbon Type

Hemisflo - 28% porosity, 10% extension -  $S_o/S_p = 2.54$  (1) Standard guide surface ribless

IV Ribbon Type (2) Ratio of total cloth area to maximum projected frontal area

Ribbon - reefed - 28% porosity, 1% vent -  $S_o/S_p = 2.25$



## b. Results of Phase I Tests

Analysis of the force data recorded on Visicorder tape, as well as motion pictures, resulted in the observation of both favorable and unfavorable performance characteristics of the tested configurations. Since the direct movies (at 500 frames per second) and the Schlieren movies (at 1000 frames per second) made possible the analysis of various phenomena at short frame-time intervals, canopy inflation, steadiness of shock wave, shock wave geometry and canopy stability characteristics were in general readily discernible. In the accomplishment of this test program, indications of favorable canopy geometry were noted. In one instance (modified guide surface type D) an over-all indication of good performance prevailed, although the drag was low compared to Types A and B.

Favorable characteristics were observed for several canopies, although in most cases other than Types A, B, and D, over-all canopy behavior was not outstanding. However, in several configurations there were indications of good inlet region inflation, roof inflation and/or stability. Outstanding among these was the Type G conical canopy. The inlet angle for this configuration was the same as the Type D guide surface model, and appeared to be very well inflated during the test when near zero angle of attack. The Type F conical appeared best of all conical types from the standpoint of stability, although the canopy was generally underinflated. The biconic parachutes (except for Type F) indicated large degrees of instability about the point of suspension. The reefed flat circular ribbon canopy exhibited very good stability and good roof inflation, particularly when reefed to 28 percent at a Mach number of 2.99.

In Table 2 are listed the essential parachute components and associated geometry which indicated good component or over-all performance in the Phase I tests. The configurations with which these components or geometric properties were associated also are tabulated.

It may be noted that the number of appearances which the various configuration types make in this tabulation directly indicate the number of favorable performance characteristics associated with a particular model configuration. Configurations A and D appear most often in the tabulation.

These results, coupled with considerations to improve drag area efficiency, were utilized in the design of configurations for the Phase Ia tests.

## 2. Phase Ia Parachute Test Program

The objective of this program was to improve the most promising Phase I configurations. Since several configurations indicated favorable



Table 2. Demonstration of Favorable Component Performance  
Phase I Test Models

Favorable Component Performance	Associated Test Model Configuration
Inlet Inflation	A, C, D, E, G
Roof Inflation	A, D, RR*
Drag	A
Stability about point of Suspension	A, C, D, E, F, RR*, Hem.**
Stability about C.G.	C, D, E, F, RR*, Hem.**

\*Reefed circular flat ribbon

\*\*Hemisflo



inlet inflation characteristics, these geometries were retained in future model designs, leaving the canopy roof study as an important investigation in this program. The nonporous biconical configurations, having indicated under-inflation characteristics particularly in the roof regions, were modified in such a way as to decrease the exit-to-inlet area ratio. Since the Type F conical canopy indicated good stability and also represented the conical type with the smallest total surface area, it was considered for further study in this interim test program.

The tests in the Phase I program involving the modified guide surface type canopies indicated excellent stability with reference to the point of suspension and except for Type A, excellent stability with reference to their center of gravity. Inflation characteristics were fair to good for some configurations (Types A, C, and D) and, as previously mentioned, were best for the Type D. In most of the tests of these configurations some oscillation of the guide surface panels was noted. The tendency to rotate, resulting in suspension line wrap-up, was also indicated in those tests in which a swivel was not used. It is apparent that malalignments of the guide surface panels due to fabrication tolerances would tend to cause rotation. Tests confirmed this, particularly when the guide surface panels were well-inflated (e.g., Type D). It was not apparent from the tests that the typical guide surface construction contributed significantly to the favorable performance of the guide surface models. Accordingly, part of the study in the interim program was aimed at evaluating the contribution of the guide surface construction. This was accomplished by designing cone frustrum models with similar over-all geometry. Simultaneously, a study of canopy roof geometry was conducted.

The instability about the center of gravity which was characteristic of Type A was attributed to excess negative lift contributed by the flat roof. This configuration indicated excellent drag, exhibited good inflation, and was constructed with the smallest cloth area of the guide surface types (all having the same frontal area). Hence, it was considered particularly worthy of further study. Modifications to improve the stability characteristics of this model were considered.

In this program, 14 model configurations were tested at approximately  $M = 2$  while deployed behind a cone cylinder forebody. Canopies were located at 10 forebody diameters aft of the forebody base, as in the Phase I program. Model diameters of 6 inches provided a ratio of parachute diameter to forebody base diameter of approximately 2.2. Schlieren photography provided the only data, since inflation and stability characteristics of the model canopies and the shock wave structure were of primary concern.

Reduction of the roof area of the Type A canopy near its periphery by means of an annular vent was considered to be the most effective and



simplest means of reducing the upsetting moment contributed by the flat roof. Accordingly, several models were so constructed and tested. Structural problems appeared in the tests of such models since the introduction of the annular vent resulted in a roof construction which had an isolated low porosity center disc. This disc was first secured by extending the suspension lines over the roof to the center of the disc. High speed photography revealed considerable relative motion between the disc and main canopy, producing asymmetries in the vent that induced canopy instability. This appeared to indicate the need for a high porosity mesh material to be used in the vent area. Numerous types of mesh were used with success. The mesh proved to be a satisfactory structural tie to provide the desired vent opening, and maintain a fixed exit geometry. Various vent sizes were used, including a model of which the entire roof was high porosity mesh. High stability, stable shock wave geometry, and strong inflation characterized models at Mach 2. The conical inlet regions of the most satisfactory configurations were constructed of a solid, low porosity nylon cloth.

Models which were constructed of nonporous materials with a center vent in general encountered structural problems, which resulted in early failure. However, those models which were so constructed (modifications of Type F) with total porosities comparable to the best porous models performed satisfactorily prior to failure.

Studies carried out in this test series to evaluate the contribution of the guide surface panel construction appeared to indicate that this particular construction does not contribute significantly to supersonic canopy performance. Since this type of construction is more complex and results in a higher ratio of total cloth area to frontal area (for a given frontal area) than that of a conical shape, attention was concentrated on the latter geometry. The inlet guide surface, however, appeared to provide the necessary stability to allow the use of very low total porosities, which contributed to the high inflation characteristics of the most satisfactory configurations. The cone-frustrum-shaped canopies which had low porosity inlet cones, low cone inlet angles and high porosity roof constructions demonstrated superior performance characteristics. The basic canopy designs which were evaluated in the final test series of the program were essentially established in the Phase Ia test series. Detail design parameters which were highly optimized in the Phase Ia program and used in the final wind tunnel test phase cannot be given because of security classification.

### 3. The Phase II Parachute Test Program

#### a. General

To further evaluate the effects of the forebody wake on parachute performance, parachute inflated diameters of both 6 and 8 inches were tested



for some configurations. These two model sizes provided ratios of parachute diameter to forebody diameter of 2.5 and 3.33, respectively. Figure 4 is a photograph of some of the Phase II test models.

Models were deployed in the wake of a cone-cylinder forebody mounted to the NASA Langley Research Center Large Supersonic Tunnel side walls.

In addition to the study of the effect of the ratio of parachute diameter to forebody diameter, the effects of canopy location aft of the forebody base were examined. This was accomplished during tunnel operation by the use of an externally controlled motor driven winch located in the forebody. This mechanism, as well as the forebody and mount, was part of the NASA tunnel facility equipment and contributed greatly to the large amount of data gathered in this final test phase.

#### b. The Test Program

In all, ten parachute configurations were studied in this program and approximately 140 test conditions (configuration, Mach number, dynamic pressure and canopy position aft of the forebody) were attained. Both force measurements and Schlieren photography (1000 frames per second) provided data at each condition.

In addition to the configurations which were developed through Phase I and Ia test programs, a conventional Hemisflo canopy was tested. This was the same model used in the Phase I test program, and was re-run in part to confirm the data derived for this model in the Phase I tests and to extend the data for this configuration for comparative purposes.

In general, models were deployed at that Mach number which corresponded to the upper Mach number limit of a given wind tunnel mode, with Mach number successively reduced with the model deployed. Models were deployed at Mach numbers as high as 4.0. In all but two instances, tunnel mode changes (accompanied by the tunnel shock excursion through the test section) were carried out with the test model deployed. The survival of test models through the tunnel mode changes as well as through long periods of sustained exposure to tunnel conditions during data acquisition contributed significantly to the amount of data obtained in this test program. Several test models survived, without damage, several hours of tunnel testing. In particular, one test model survived four hours of continuous exposure to Mach numbers above  $M = 2.3$ . This in itself attests to the excellent behavior of the canopies, since most conventional parachutes in this range of Mach numbers would do well to survive several minutes of operation without extensive damage resulting from the dynamic loadings associated with the typical





Fig. 4. Typical Phase II Test Models Including Several Hyperflo Configurations



inflation instabilities characteristic of such canopies at Mach numbers in excess of 2.

The completed program on the Phase II tests is shown in Table 3. It may be noted from this table that three configurations were subjected to tests over the Mach number range from 2.3 through 4.0 and two of these three were tested to the upper tunnel Mach number limit of 4.65. Most other models were tested over the range of  $M = 2.3$  to  $M = 3.75$ , since available tunnel time did not permit the accomplishment of the highest Mach number conditions for all models.

### c. Test Results

#### (1) Parachute Drag

Drag coefficients for several configurations and canopy positions are shown in Fig. 5. These are based on the model design frontal area, which in general was greater than the constructed frontal area. It may be noted that the drag for most configurations reaches a peak at  $M = 3.75$ , drops rapidly after this Mach number and levels off above  $M = 4.0$ . A similarity to these data may be noted in Fig. 6 for the case of a solid cone with a  $45^\circ$  half angle tested in the wake of a forebody. Figure 6 is based on data from Refs. 3 and 4.

Either a Reynolds number effect or a dynamic pressure effect may be suspected in the parachute case. The latter is evidenced by Fig. 7 in which the drag coefficients of two Phase II configurations are plotted vs. Mach number, and on which is superimposed the tunnel test dynamic pressure vs. Mach number. It may be noted that the maximum drag coefficients correspond to the minimum dynamic pressure condition at  $M = 3.75$ . The inflated diameters of these models, however, as measured from Schlieren photographs, do not appear to vary significantly at  $M = 3.75$  from those measured at other Mach numbers. For example, the average inflated-to-constructed diameter ratio for configuration VI at  $M = 3.75$  is 0.89 and the value of this ratio at  $M = 4.0$  is 0.90. A significant reduction in drag coefficient would normally be expected to be associated with a reduction in inflated area. The effect of Reynolds number on supersonic parachute performance has not generally been found to be significant in previous parachute test programs. Further, the tests involving the solid cone referred to above were all conducted with Reynolds numbers per foot in excess of  $2 \times 10^6$ .

In considering the drag effectiveness of the tested model canopies, reference may be made to Fig. 3. Flow deviation through the canopy shock was shown to result in the spreading of the wake after the shock into a conical region which extends to near the canopy inlet. It is expected



Table 3. Phase II Test Schedule Summary

Configuration	Max. Dia. (in. )	Mach No.	x/d
C-6a (I)	8	2.3 - 4.0	8 - 10
C-6b (II)	8	2.75 - 3.75	8 - 10
C-9 (III)	8	3.0 - 3.75	4 - 10
C-3b(IV)	8	3.0 - 3.75	6 - 10
C-6b (V)	6	2.5 - 4.65	7 - 13
C-7a(VI)	6	2.3 - 4.65	7 - 13
CR-2a (VII)	6	2.3 - 3.75	7 - 13
C-6a (VIII)	8	2.5 - 3.75	6 - 9
CR-2b (IX)	8	3.75	8 - 12
Hemisflo (X)	8	2.3 - 3.5	8 - 13



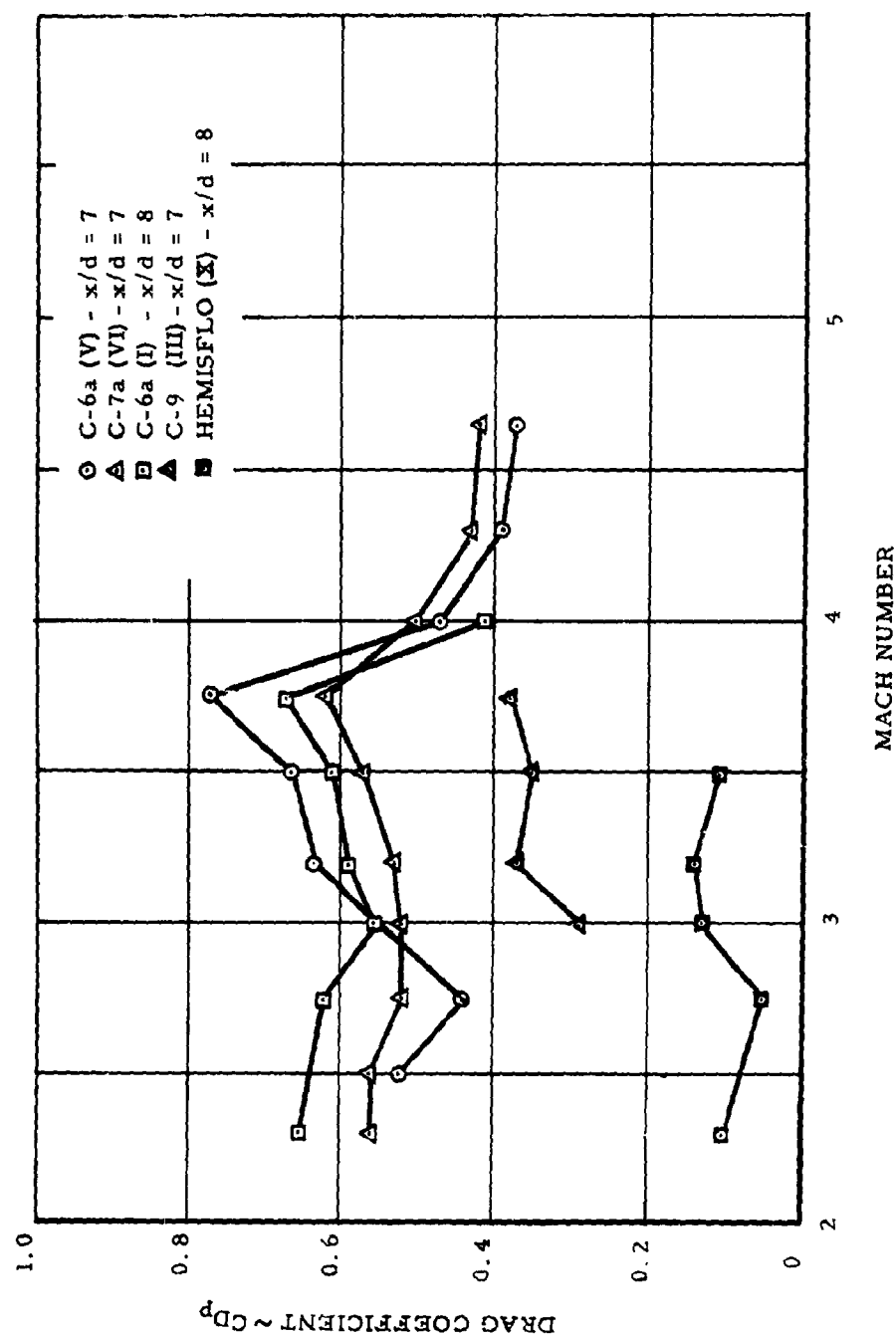


Fig. 5. Drag Coefficient vs. Mach Number, Several Phase II Models



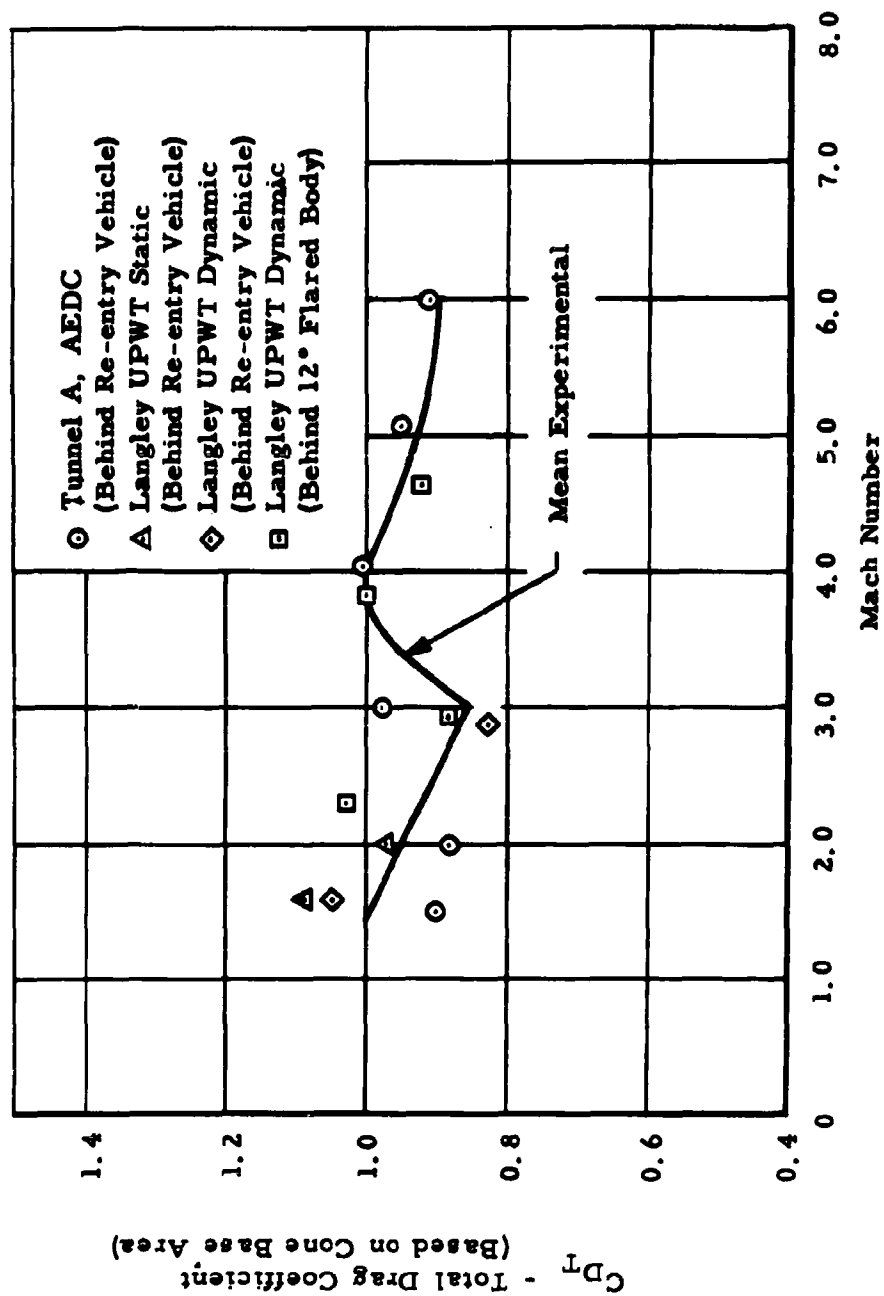


Fig. 6. Drag Coefficient vs. Mach Number of Solid 45° Half Angle Cone in Wake of Forebody



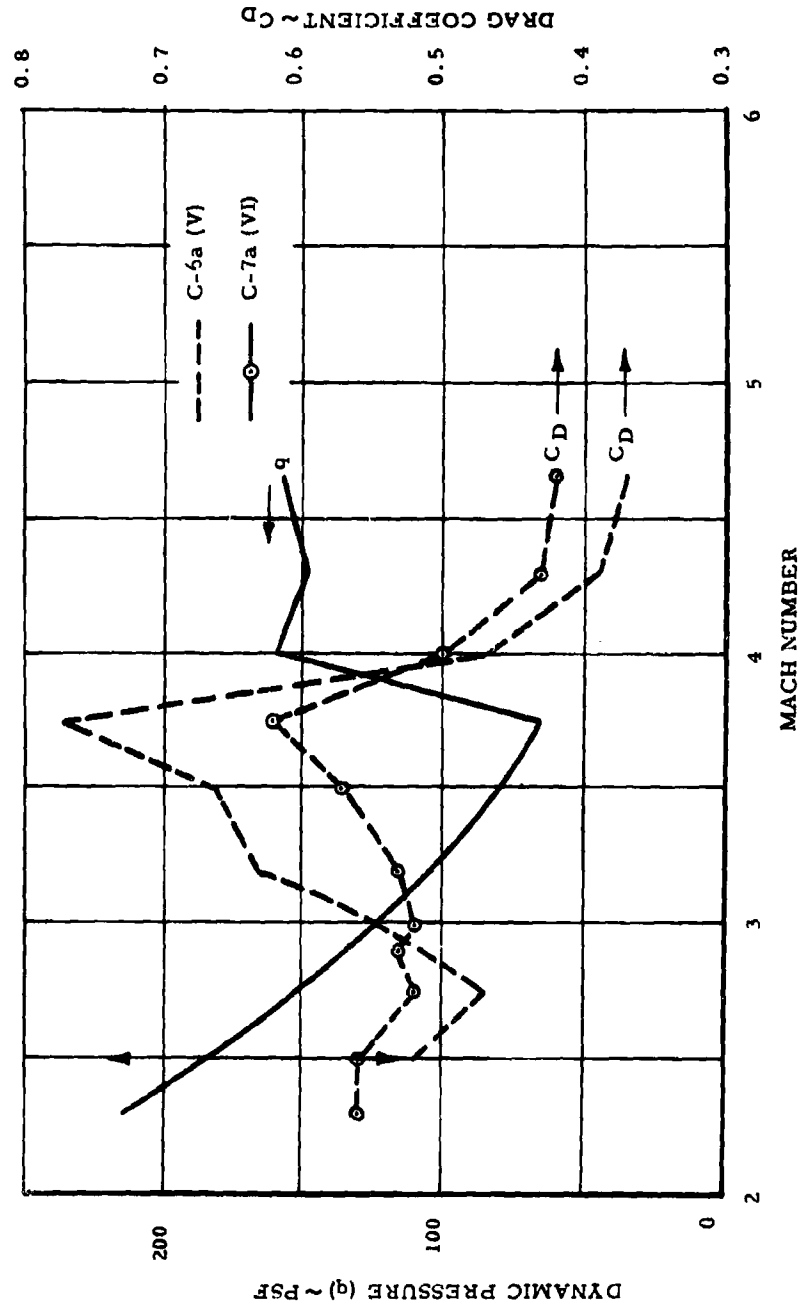


Fig. 7. Tunnel Dynamic Pressure and Drag Coefficient vs. Mach Number for Two Phase II Test Models at  $x/d = 7$



that within this region an essentially constant pressure exists which satisfies pressure boundary requirements across the normal portion of the shock on the wake centerline, and on the diverging flow boundary.

It may be considered that the drag of the canopy under these conditions is equivalent to the drag on a cone having the same half angle as that represented by conical diverged flow region. In Fig. 8 is shown the average conical shock wave angle as measured from Schlieren photographs of Model VI tests. Also shown is the half-angle cone which would produce the drag equivalent to that measured in the tests, and the corresponding conical shock wave angles. Figure 8 represents a canopy location of 7 forebody diameters, and Fig. 9 represents similar characteristics at 9.5 forebody diameters aft of the forebody base.

That a stable flow condition may be maintained which satisfies pressure boundary requirements will now be discussed. By the employment of the methods to determine wake flow characteristics described earlier, pressure ratios across the normal portion of the canopy shock wave on the wake centerline are determined for various  $x/d$  locations aft of the forebody. Examples of these calculations are shown in Figs. 10 and 11. Conical surface pressure coefficients for various cone half-angles at the corresponding free stream Mach numbers are also shown.

The agreement of the above calculated data with the performance of configuration VI is shown in Table 4 and illustrated in Figs. 10 and 11. Close agreement of the measured and calculated data is apparent.

During the conduct of the Phase II tests it was found that the canopy location had a very marked effect on the performance of all configurations tested, and optimum canopy locations appeared generally to be 6 to 8 calibers aft of the forebody. All canopy models exhibited markedly increased stability, inflation, and drag characteristics at the close-in locations as compared to downstream positions, although no serious reduction in performance occurred in the tested  $x/d$  range.

Upon examination of Figs. 10 and 11, it may be noted that as  $x/d$  is increased, the cone angle for equilibrium conditions also increases. Although the apparent deflection angles realized in the examined cases are greater than those through an oblique shock, the high pressure (near stagnation) existing within the canopy should cause the flow to deviate further. It may be anticipated that there will be a limiting downstream canopy location for which stable flow conditions will prevail. This is based on the assumption that the flow conditions described earlier are responsible for the excellent canopy performance realized, particularly at low  $x/d$  canopy positions.



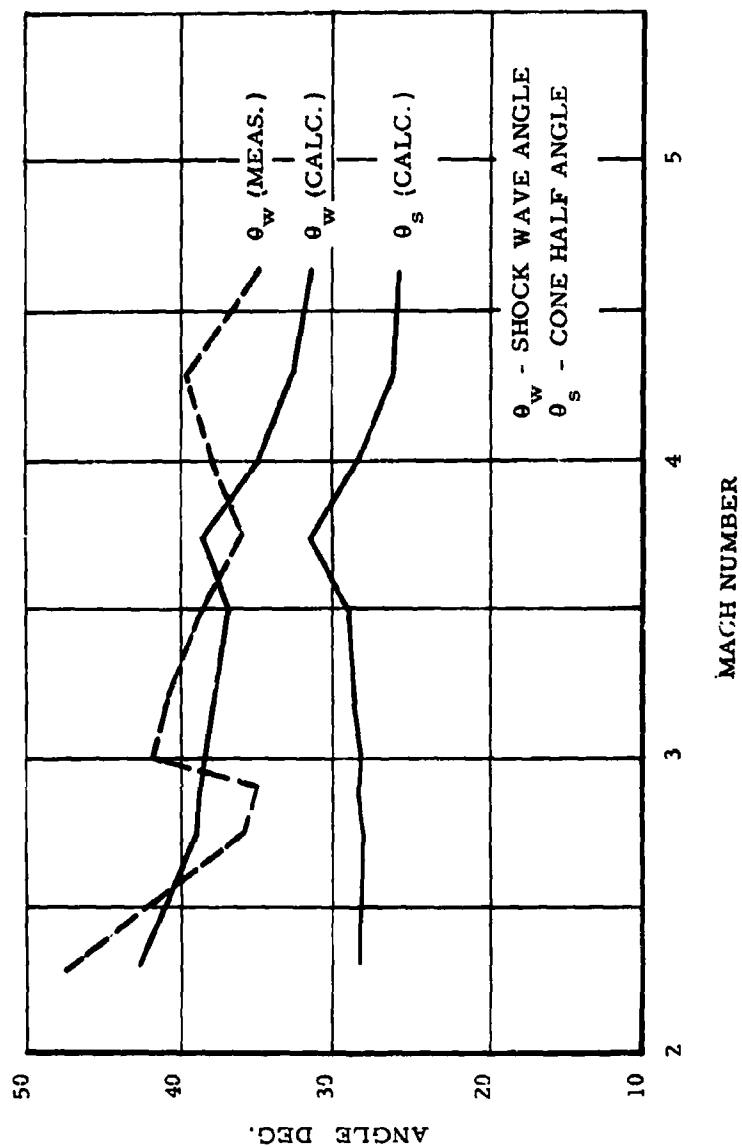


Fig. 8. Comparison of Measured and Calculated Shock Wave Angles  
 Based upon Drag Measurements; Phase II Tests, Model c-7a(VI),  
 $x/d = 7$



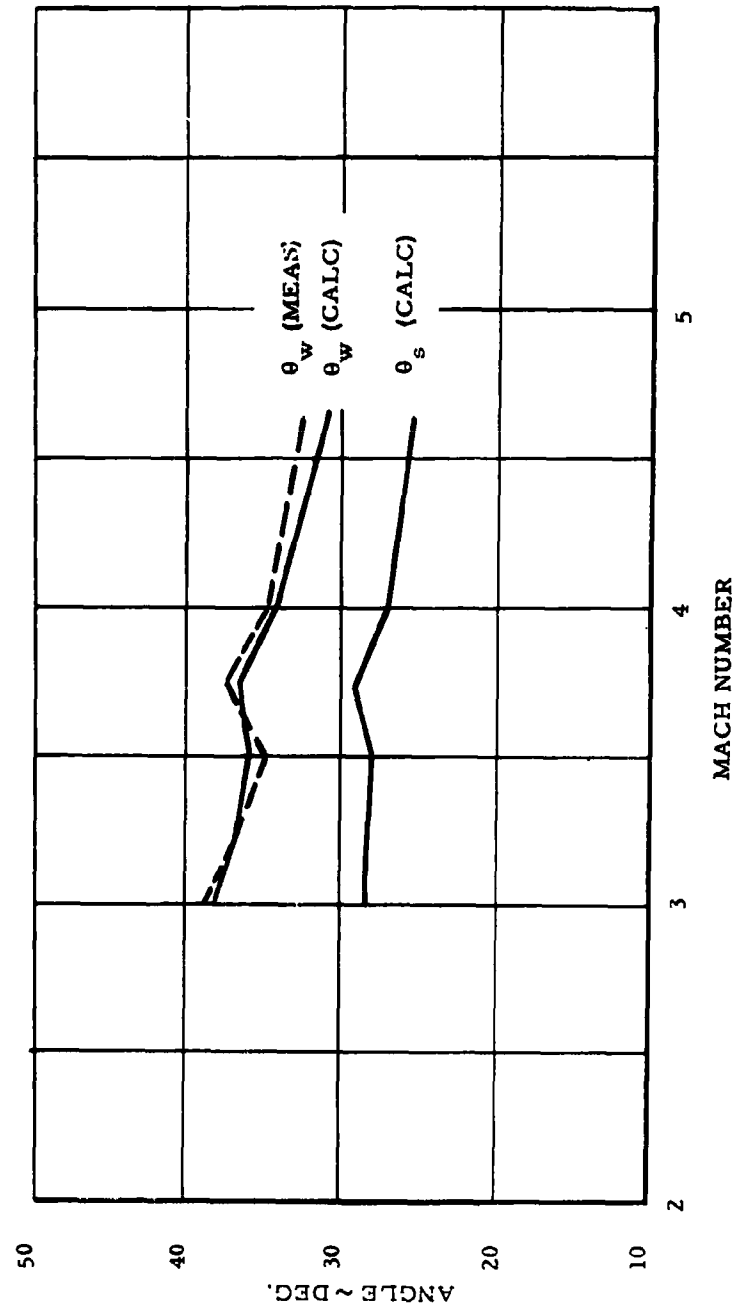


Fig. 9. Comparison of Measured and Calculated Shock Wave Angles  
Based upon Drag Measurements; Phase II Tests, Model C-7a(VI)  
 $x/d = 9.5$



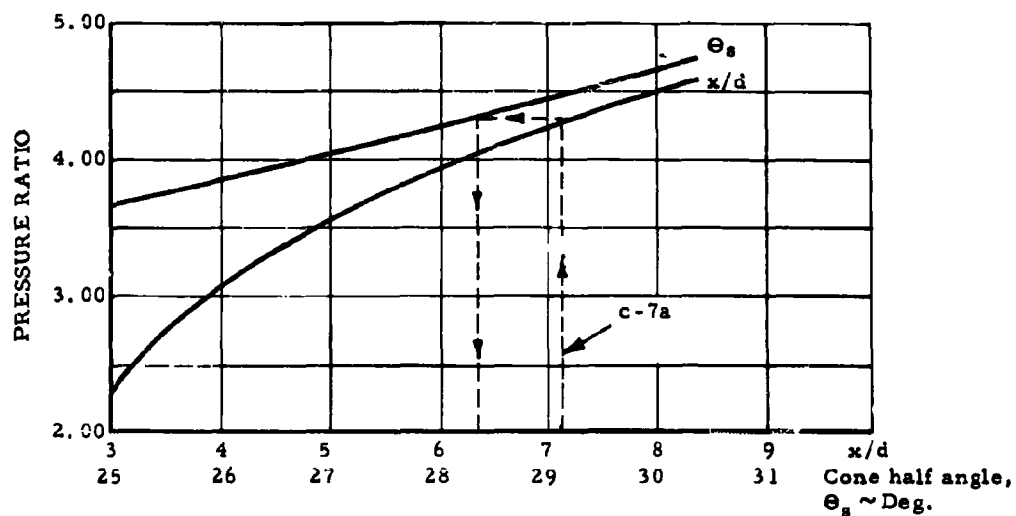


Fig. 10. Wake Centerline Normal Shock (Vertex)  
Pressure Ratio vs.  $x/d$ , and Cone Surface  
Pressure Ratio vs. Cone Half Angle at  $M_\infty = 3.00$

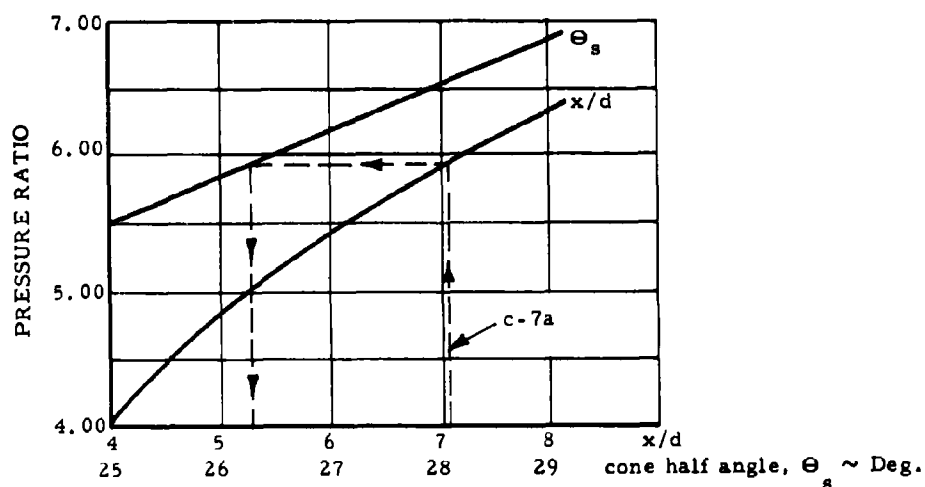


Fig. 11. Wake Centerline Normal Shock (Vertex)  
Pressure Ratio vs.  $x/d$ , and Cone Surface  
Pressure Ratio vs. Cone Half Angle at  $M_\infty = 4.00$



Table 4. Correlation of Calculated Shock Vertex Position and Equilibrium Diverged Conical Region with Parachute Drag Measurements for Model C-7a(VI)

Mach No.	Shock Vertex (x/d)	Equilibrium Half Cone Angle (deg)	Equivalent Drag Half Cone Angle (deg)
2.75	7.0	28	-
3.0	7.2	28.4	28.2
3.2	7.0	28.0	28.2
3.5	7.3	27.7	28.0
3.75	7.3	27.2	29.3
4.00	7.1	26.5	27.4
4.30	7.0	25.6	-
4.65	6.4	24.5	25.2



## (2) Parachute Stability

In general, the models tested in this program were highly stable with respect to the point of suspension. A definite trend, however, was noted in the stability of the canopy as a function of canopy location aft of the forebody. The close-in, low  $x/d$  positions resulted in marked increases in stability about the point of suspension, as compared to downstream locations. Oscillations about the point of suspension were of the order of 5 degrees or less at the low  $x/d$  positions.

## (3) Parachute Inflation

Inflation characteristics were, in general, good. In particular, the 6 inch maximum diameter models were outstanding. In Fig. 12 are shown typical Schlieren photographs of Test Model VI at various Mach numbers. Average inflated diameter to constructed diameter ratios for Phase II configurations generally ranged from 0.8 to 1.05. Average inflated to constructed diameter ratios of the 6 inch diameter models in most cases were greater than those for the 8 inch models. One model (VII) maintained inflated to constructed diameter ratios of 0.93 to 1.05 over the Mach number range from 2.3 to 3.75.

## 4. Program Conclusions

The following specific conclusions were drawn during the conduct of this program:

- (1) The use of proper canopy design geometry, coupled with appropriate total porosity and porosity distribution, provides a parachute configuration which operates satisfactorily in the high supersonic speed ranges. Such canopies were found to suppress the unfavorable characteristics associated with the operation of conventional parachutes in the high Mach number environments.
- (2) The use of a relatively low total canopy porosity distributed so as to provide a low inlet region porosity leads to both high stability and high inflation characteristics in the Hyperflo configurations.
- (3) Observation of these canopies under subsonic conditions during wind tunnel shutdown has indicated excellent inflation and stability characteristics. It is therefore felt that successful operation of the high speed canopies will be assured with perhaps minor variation of the design parameters for subsonic speed applications.
- (4) Although relatively low total porosities were used in the design of the test models as compared to previously applied (conventional)





$M = 2.3, x/d = 7$



$M = 2.98, x/d = 10$



$M = 3.75, x/d = 7$



$M = 4.65, x/d = 7$

Fig. 12. Schlieren Photographs of Phase II Model C-7a(VI)  
at Several Mach Numbers. Film Speed: 1000 fps



parachute designs, wide ranges of porosity were used with successful results.

- (5) The canopy location aft of the forebody appeared to affect significantly the performance of all configurations in the high speed ranges. The most favorable location appeared to be in the close-in or low  $x/d$  positions. This should result in a significant reduction in the over-all parachute system weight, since the riser length will be minimized. The weight of a parachute riser frequently represents a large percentage of the total parachute system weight.
- (6) The effect of diameter ratio of the canopy to that of the forebody was not clearly established, although there were indications of a slight reduction in canopy performance at a ratio of 3.33 as compared to a ratio of 2.5.
- (7) The effects of dynamic pressure on canopy performance are not definitely established, although some data gathered in this program appear to indicate high drag coefficients with low dynamic pressure. The effects of dynamic pressure or of Reynolds number were not investigated sufficiently in this program to establish a definite correlation with canopy performance.
- (8) Several roof designs were employed in the models tested in this program. No significant effect on canopy performance could be attributed to the roof design variation. All canopies which were constructed using the basic Hyperflo design geometry performed in a comparable manner when designed with equivalent total porosities. This provides a wide latitude of techniques to be used in the fabrication of full scale canopies.
- (9) In the determination of satisfactory parachute canopy designs for high supersonic speed applications, the drag efficiency (ratio of gross surface area to projected frontal area) did not deteriorate. In fact, the efficiency of the Hyperflo configuration is significantly higher than those for previously employed designs.
- (10) The over-all test series conducted in this program indicated no appreciable Mach number sensitivity of the Hyperflo canopies to a Mach number of 4.65. Subsequent tests with models fabricated according to specifications determined in this program extended the range to a Mach number of 6 with similar satisfactory results.



### 5. Current Status of the Hyperflo Parachute

Subsequent to the analytical and experimental development program described above, several additional test programs have been implemented to explore and extend the potentialities of the Hyperflo parachute. The first of these was an in-house wind tunnel program conducted by the Retardation and Recovery Branch, Flight Accessories Laboratory, Aeronautical Systems Division, AFSC, USAF. In this program wind tunnel testing was extended to Mach number 6.0, the maximum limit of the particular tunnel used. Results were similar to those previously described; excellent inflation and stability characteristics were obtained.

Under contract to the above Agency, the Tech-Center Division of Cook Electric Company has carried out full-scale testing of Hyperflo parachutes in two separate programs. In the first of these the Tomahawk rocket sled has been used to test the Hyperflo under subsonic and transonic conditions at near sea level conditions so that high dynamic pressures and loads were developed. Tests were conducted up to Mach number 1.5 and a dynamic pressure of about 2900 psf. Very satisfactory parachute performance was demonstrated.

Currently nearing completion is the second program which uses the CREE missile system for free-flight testing of the Hyperflo. Test conditions include Mach numbers up to 4.0 and altitudes to 130,000 ft. Again the agreement between free-flight tests and wind tunnel tests is remarkably good.

The first project involving actual operational use of the Hyperflo parachute recently has been initiated. Continued use of the Hyperflo for deceleration and stabilization in the supersonic and hypersonic regimes may be expected due to a parachute's inherent advantages of self-inflation and minimum weight and volume for a given drag area.

### REFERENCES

1. Fredette, R. O., Parachute Research Above Critical Aerodynamic Velocities, Cook Electric Company, 1961.
2. Schlichting, H., Boundary Layer Theory, McGraw-Hill Book Co., Inc. 1955.
3. Charezenko, N., and McShera, J. T., "Aerodynamic Characteristics of Towed Cones Used as Decelerators at Mach Numbers from 1.57 to 4.65," NASA TN D-994, December 1961.
4. Coats, J. D., "Static and Dynamic Testing of Conical Trailing Decelerators for the Pershing Re-Entry Vehicle," AEDC TN-60-188, October 1960.



A RECOVERY SYSTEM FOR A CONTROLLED DESCENT  
THROUGH THE MARTIAN ATMOSPHERE\*

R. D. Turner

Cook Electric Company  
Tech-Center Division  
Aerospace Technology Section  
Morton Grove, Illinois

ABSTRACT

This paper presents a summary of a parametric investigation of a parachute recovery system for a Mars entry vehicle. The parameters which were investigated were entry vehicle velocity, entry angle, estimated atmospheric variations as of mid 1962 and parachute system weight. The primary objectives of this study were to determine if a parachute decelerator system could provide a minimum of four minutes time of descent under the most severe entry conditions and to determine the minimum altitude at which deployment would take place if the first objective, i.e., four minute time of descent, was achieved.

The analysis performed in connection with this study has shown that under the most severe expected entry conditions a four minute time of descent cannot be achieved utilizing conventional state-of-the-art parachute designs. To achieve this desired descent time with a reasonable parachute system weight requires that the first stage parachute be deployed at a Mach number of approximately 3. Based on the advent of the Hyperflo parachute which is presently being developed by Cook Electric Company, under the auspices of the Flight Accessories Laboratory, Aeronautical Systems Division, USAF, this first stage deployment Mach number is considered practical for recovery applications in late 1963 and 1964.

It has been concluded that a three stage parachute system with the first stage deployed at a maximum dynamic pressure of 500 psf and weighing approximately 17 pounds would provide a minimum weight decelerator system. The weight of the entire recovery system which includes the 17 pounds for parachutes and associated equipment is estimated to be 28.2 pounds for a 200 pound entry vehicle.

---

\*This work was performed for the Jet Propulsion Laboratory, California Institute of Technology, sponsored by the National Aeronautics and Space Administration, under Contract NAS 7-100.



## A RECOVERY SYSTEM FOR A CONTROLLED DESCENT THROUGH THE MARTIAN ATMOSPHERE

R. D. Turner  
Cook Electric Company  
Tech-Center Division  
Aerospace Technology Section  
Morton Grove, Illinois

### INTRODUCTION

The advent of propulsion systems capable of propelling a payload to a distant planet has spurred industry to investigate the problems associated with landing a payload under controlled conditions. Many problems associated with this type of mission arise as a result of the unknowns associated with the constituents of the atmosphere, the long space flight at near vacuum conditions and the variable entry conditions which will be due to the long space flight.

This study has been performed to determine the effects of these variables as they affect a recovery system operation. Included in this study are design constraints for which an optimized recovery system was defined.

### PROGRAM OBJECTIVES AND DESIGN CONSTRAINTS

The objectives which have guided the study are as follows:

- (1) Maximum parachute descent time
- (2) Maximum deployment altitude consistent with descent time
- (3) Minimum parachute oscillation
- (4) Minimum weight
- (5) Minimum impact velocity.

To start the analysis, it was necessary to specify an atmospheric density profile and entry angle. The choices made for these two parameters were atmosphere B (Figs. 1 and 2) and 90 degrees, respectively. These parameters were chosen since atmosphere B represents a mean density and temperature variation and a 90 degree entry imposes the most severe requirement in terms of obtaining the highest decelerator deployment altitude and maximum time of descent. For this study, the entry vehicle weight used was 200 lb and the recoverable capsule weight was 120 lb.



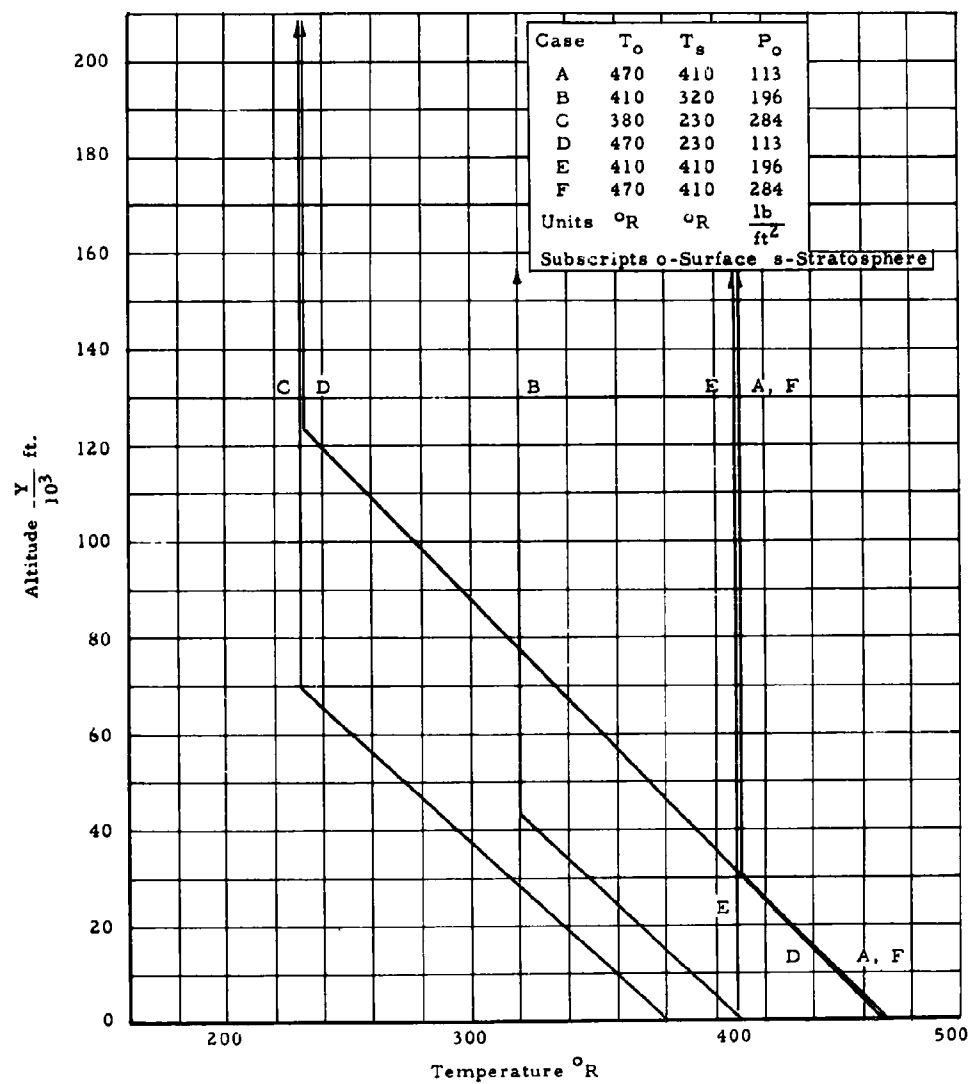


Fig. 1. Temperature of Mars Atmosphere



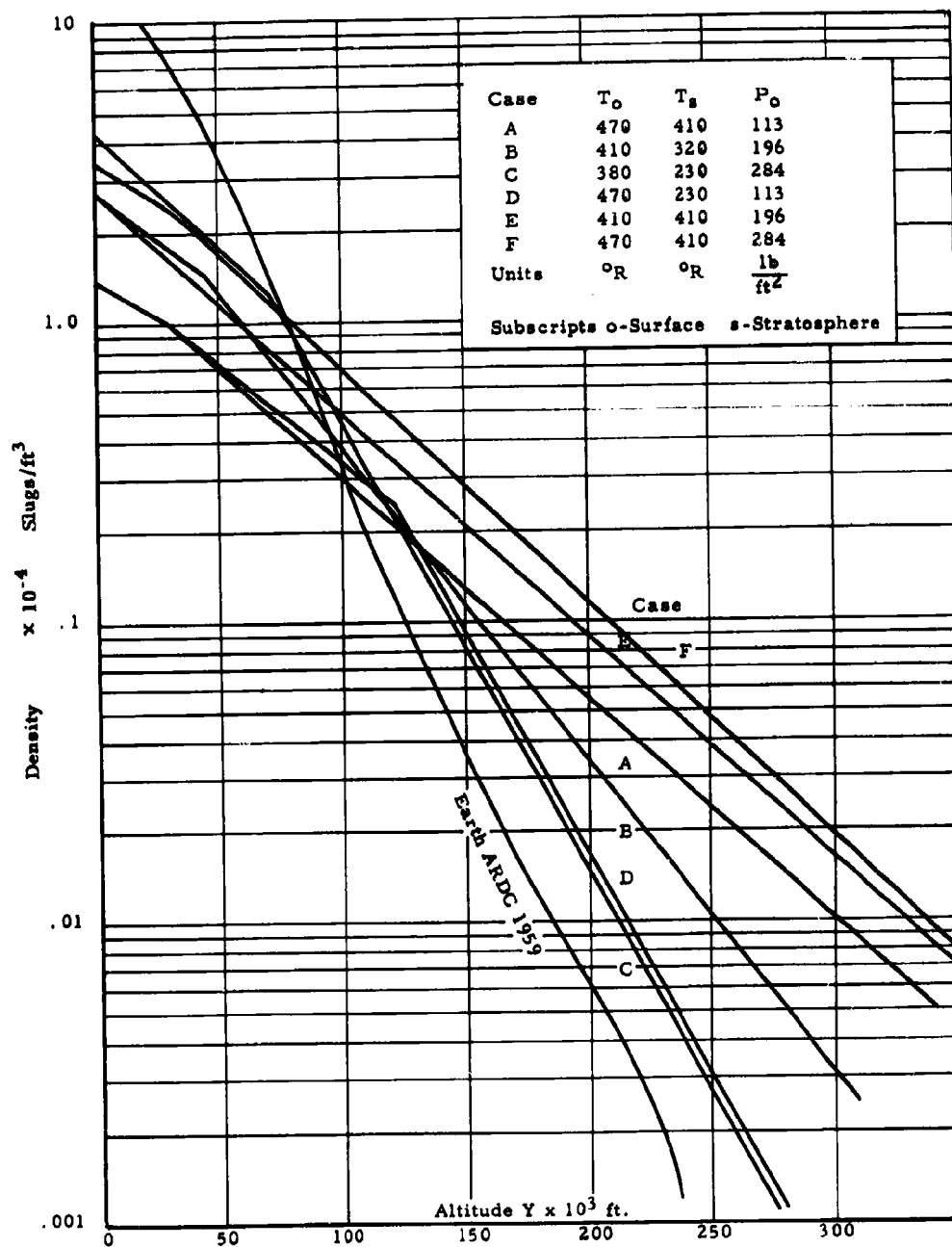


Fig. 2. Density of Mars Atmosphere



Throughout this paper, the weights quoted for the entry vehicle and parachute systems are in Earth pounds. This procedure was utilized to avoid confusion since for the different Mars atmospheres different accelerations of gravity were considered, hence, different effective weights were used in computer calculations. The magnitude of this variation for the different atmospheres (A through F, Figs. 1 and 2) is 11.8 to 12.8 ft/sec<sup>2</sup>.

To determine the maximum parachute deployment altitude, deployment Mach numbers were chosen as 2, 3, and 4. The choice of these Mach numbers is predicated on the present state of the art and recent studies coupled with wind tunnel tests which suggest an extension of the state of the art in the near future.

The Mach number of 2 is accepted throughout the industry (1) as an approximate limit to present supersonic application for what is commonly referred to as conventional parachutes, i.e., conicals, Equiflo, and Hemisflo, the latter two being Cook Research Laboratory designs. These designs were tested by Cook Research Laboratories and were found to be effective in the low supersonic speed range, but exhibited erratic tendencies at high supersonic Mach numbers. The Hyperflo (Fig. 3) which has recently evolved from a study program performed by these Laboratories, suggests that reliable parachute operation above a Mach number of 2 is feasible. Wind tunnel tests conducted by Cook over a Mach number range of 1.5 to 4.65 show satisfactory operation of the Hyperflo throughout this Mach number range. A program conducted by an Air Force agency from Mach 4 to 6 shows the same results. Based on these results and a free-flight test program which is currently in progress to validate wind tunnel tests of the Hyperflo configuration up to Mach numbers of 4 and altitudes up to 200,000 ft, the deployment conditions of Mach 2, 3 and 4 are considered within the range of practical limits for obtaining maximum descent time.

Operation of the terminal descent parachute has been restricted somewhat arbitrarily to a maximum Mach number of 0.9. This restriction is based on obtaining maximum reliability and maintaining a minimum weight system since deployment of a large terminal descent parachute is not advisable above a Mach number of 1.0.

#### SELECTION OF POTENTIAL PARACHUTES

It was the object of this study to select a parachute system such that the maximum drag area (consistent with prescribed g limitations) was deployed at any given time, hence producing the greatest descent time for the recoverable package. To optimize such a system, i.e., provide minimum weight, consideration had to be given to the types of parachutes to be used.



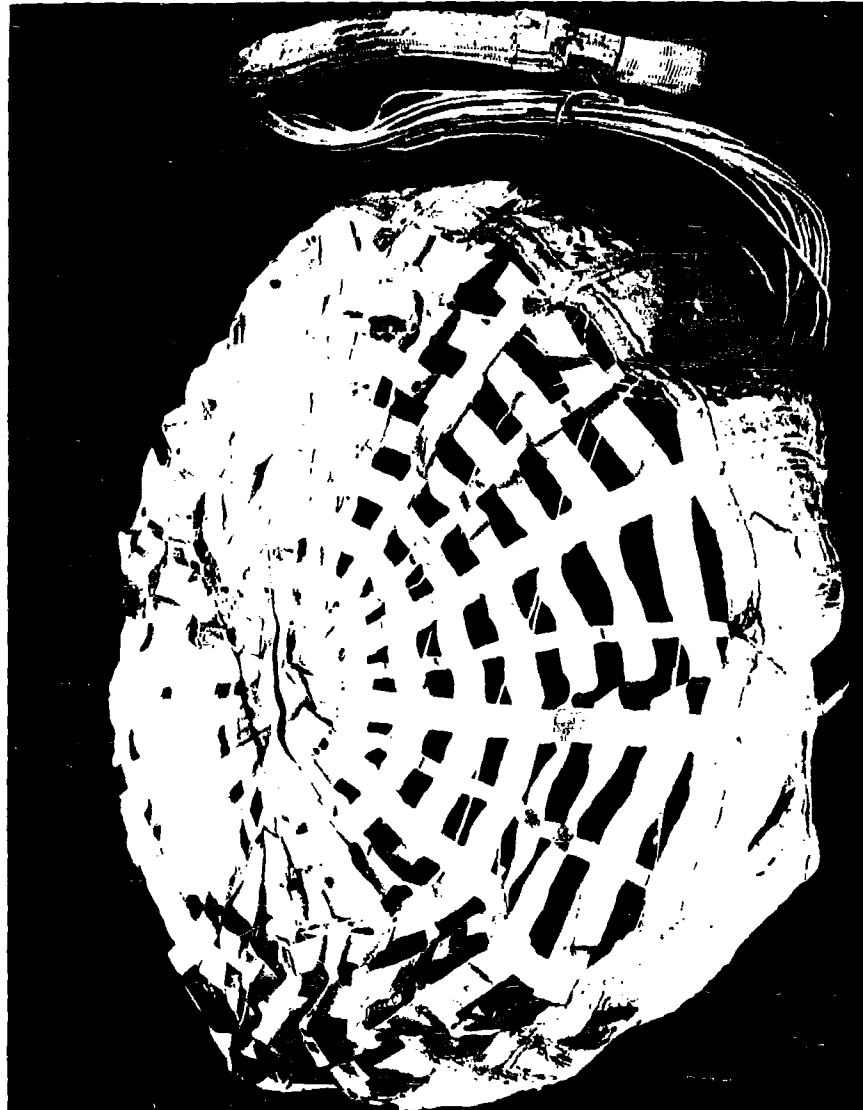


Fig. 3. Hyperflo Parachute Tested in the CREE Program at a Mach Number of 2.8 at 103,000 ft



Based on evaluation of empirical data and past experience, the solid flat, extended skirt, and the slotted type parachutes are suitable for the subsonic stages.

Although the solid flat configuration yields the most drag per pound of parachute, oscillations of greater than  $\pm 20$  deg can be expected. The slotted type canopies have stability of  $\pm 7$  deg which is well within the required limits of  $\pm 10$  deg. However, these canopies are not best suited for a high drag and low system weight since effective drag coefficients are low (0.55 to 0.75).

Extended skirt canopies have been designed to exhibit oscillation limits of  $\pm 5$  deg and to have the quality of quick damping of any wind-shear-induced oscillations. Under the light canopy loadings considered in this program, the extended skirt canopy exhibits a drag coefficient of 0.9 based on total geometric area.

Based upon the above analysis, the terminal descent parachute which affords the best stability and maximum drag-to-weight ratio within the prescribed stability limits is the extended skirt canopy. Therefore, for all trajectory calculations, the extended skirt canopy has been utilized as the final stage parachute.

For first stage supersonic application over the Mach numbers of interest, the Hyperflo configuration is the only canopy shape which has shown satisfactory test data performance. As discussed earlier, this configuration is presently undergoing free-flight test validation up to a Mach number of 4, and based on wind tunnel results, shows very good stability characteristics.

In addition to the free-flight tests, high speed sled tests are being conducted with the Tomahawk sled. To date, five free-flight tests have been performed over a Mach number range of 2.1 to 4 and altitudes varying from 85,000 to 130,000 ft. Augmenting these tests are six sled tests at dynamic pressures of 2170 - 2890 psf (Mach 1.3 and 1.5, respectively). Results of these tests confirm the optimism which was instilled as a result of the wind tunnel program.

Preliminary data indicate drag coefficients of the order of 0.9 at subsonic and transonic speeds. This value is reduced to approximately 0.6 at Mach 2, at which point it is approximately constant to Mach 3. From 3 to 4 the value reduces to approximately 0.45. From Mach 4 to 6 the drag coefficient appears to remain approximately constant. All the above coefficients are based on the projected frontal area.

Due to the performance requirements of the proposed recovery system, the Hyperflo and extended skirt parachute canopies have been selected,



respectively, as initial and final stage decelerators, using the reefed extended skirt canopy for any intermediate stage. The Hyperflo canopy is intended for parachute deployment at supersonic velocities, whereas reefed and fully inflated stages of the extended skirt canopy are intended for all subsonic applications.

#### PARACHUTE SYSTEM SELECTION

Based on a review of parachute weight as a function of terminal velocity and the use of the lightest Mil Spec cloth (1.1 oz/yd) for the terminal parachute, a range of practical last stage  $C_{DA}$ 's was obtained. Considering this range in final descent parachute weight with a first stage parachute which would produce the maximum allowable opening shock (130 earth g's) resulted in a nominal parachute system weight of 26 lb. The three deployment dynamic pressures resulting from a trajectory computation for a 90 deg entry angle, 21,730 fps entry velocity, 200 lb entry vehicle weight and Mach numbers of 2, 3, and 4 are  $q = 277$ ,  $q = 510$  and  $q = 805$  psf respectively. In order to show effects of recovery system weight change upon descent time, systems weighing approximately 17 lb and 11 lb were also selected for analysis under the same deployment conditions. Table 1 gives the physical characteristics of these systems.

Cursory consideration was also given to two single parachute systems to be deployed at subsonic velocities and weighing 17 and 26 lb.

#### TRAJECTORY COMPUTATIONS

The results of computations showing the descent time vs parachute weight for the initial conditions given below are given in Fig. 4.

$V_E$  = entry velocity at 800,000 ft = 21,730 fps

$\gamma_0$  = initial flight path angle = 90 deg

$W_1$  = initial entry weight = 200 lb (earth)

$W_2$  = final weight = 120 lb (earth)

B Atmosphere

Mach 2 deployment  $q = 277$  psf

Mach 3 deployment  $q = 510$  psf

Mach 4 deployment  $q = 805$  psf



Table 1. Description of Parachute Systems Studied

Nominal System Weight	1st Stage Deploy. Mach. No.	1st Stage Size $D_p$ (ft)	Design Opening Load g's	Wt. of Chute and Access.'s (lbs)	Main Canopy Reefed $C_{DA}$ (ft <sup>2</sup> )	Main Canopy Reefed Dia. Ratio (Percent)	Main Canopy Area $S_0$ (ft <sup>2</sup> )	Main Canopy Terminal Velocity (ft/sec)	Main Canopy & Access.'s Total Wt. (lbs)	Total Parachute Weight (lbs)
<b>Two Chute System</b>										
26 lbs	4	6.5	130	10.3	30.93	6.2	1120	18.3	15.3	25.6
	3	7.07	130	8.8	30.93	6.2	1120	18.3	15.3	24.1
	2	9.60	130	11.4	100.8	12.7	1120	18.3	15.3	26.7
17 lbs	4	5.62	97.5	5.9	27.38	8.0	700	23.1	9.6	15.5
	3	6.14	97.5	8.0	27.38	8.0	700	23.1	9.6	17.6
	2	7.98	97.5	9.0	63.0	12.7	700	23.1	9.6	18.6
11 lbs	4	4.60	65.0	4.2	22.30	8.7	466	28.3	6.6	10.8
	3	5.00	65.0	4.4	22.30	8.7	466	28.3	6.6	11.0
	2	6.76	65.0	4.9	42.00	12.7	466	28.3	6.6	11.5
<b>Single Chute System</b>										
17 lbs					25.78	6.3	934	20.0	18.1	18.1
26 lbs					58.25	8.0	1479	16.0	27.8	27.8



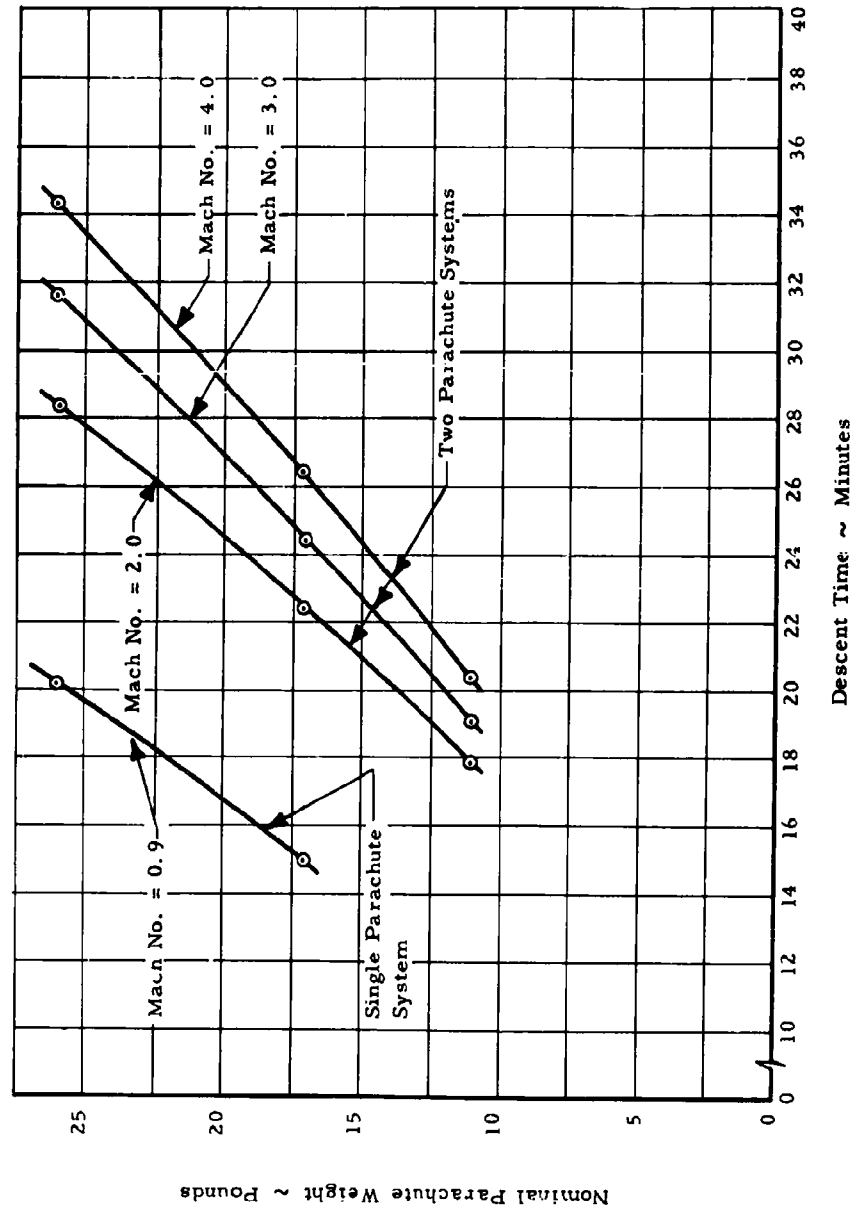


Fig. 4. Descent Time vs Nominal Parachute Weight for Various Deployment Mach Numbers and "B" Atmosphere



For these calculations, the reefed second stage was deployed at Mach 0.9 and a dynamic pressure of 50 psf. This dynamic pressure limit is due to parachute design restraints and closely corresponds to 0.9 Mach number for the altitudes associated with a 90 deg entry angle. For the single parachute systems, the dynamic pressure at deployment was 76.5 psf. All terminal descent parachutes were disreefed at a dynamic pressure of 5 psf.

From these analyses it is obvious that all of the systems analyzed easily exceeded the four minute minimum time limitation as imposed by the contract. It is also noteworthy that for a fixed deployment Mach number, the variation in descent time with parachute weight is almost linear. However, the slope (minutes per pound) increases with deployment Mach number for the range considered. As would be expected, the single parachute system provides significantly less descent time than do the two parachute systems for a fixed nominal parachute total weight.

Figure 5 shows the effect of parachute weight and the first stage deployment dynamic pressure on the altitude where deployment of first stage, deployment of second stage reefed, and second stage disreefed occur for the atmosphere B calculations. These results indicate that the range of deployment altitudes for the two parachute system varies from 37,000 to 49,000 ft, the highest being the Mach 4 deployment and the lowest being the Mach 2 condition.

The loss in altitude from deployment of the first stage to disreefing of the second parachute over the range of parachute weights considered for the Mach 2 case is approximately 2,500 ft. For the Mach 3 case, the range is larger and varies from 4,000 ft for the 26 lb system to 7,000 ft for the 11 lb system. For the Mach 4 system, the heavyweight system requires a minimum altitude loss of 6,000 ft whereas the lightweight system required 10,000 ft of altitude. In all nominal parachute weight cases, the higher the deployment Mach number the higher the altitude is at time of disreef for a fixed weight parachute system.

The terminal, i.e., impact velocities, were 18.3, 23.1 and 28.3 for the 26, 17, and 11 lb parachute systems, respectively. It is therefore obvious that the increase in descent time for a fixed Mach number of deployment and varying parachute weight system is a function of both the altitude loss in deploying the final descent parachute and the terminal velocity of the parachute. For the systems considered, increasing parachute weight has a favorable effect for both conditions.

Since these calculations show that all systems are feasible for this atmosphere's density variation, the most severe atmospheric environment was then considered. It was found that the characteristics of atmosphere D and a 90 deg entry impose the most severe requirements in terms of



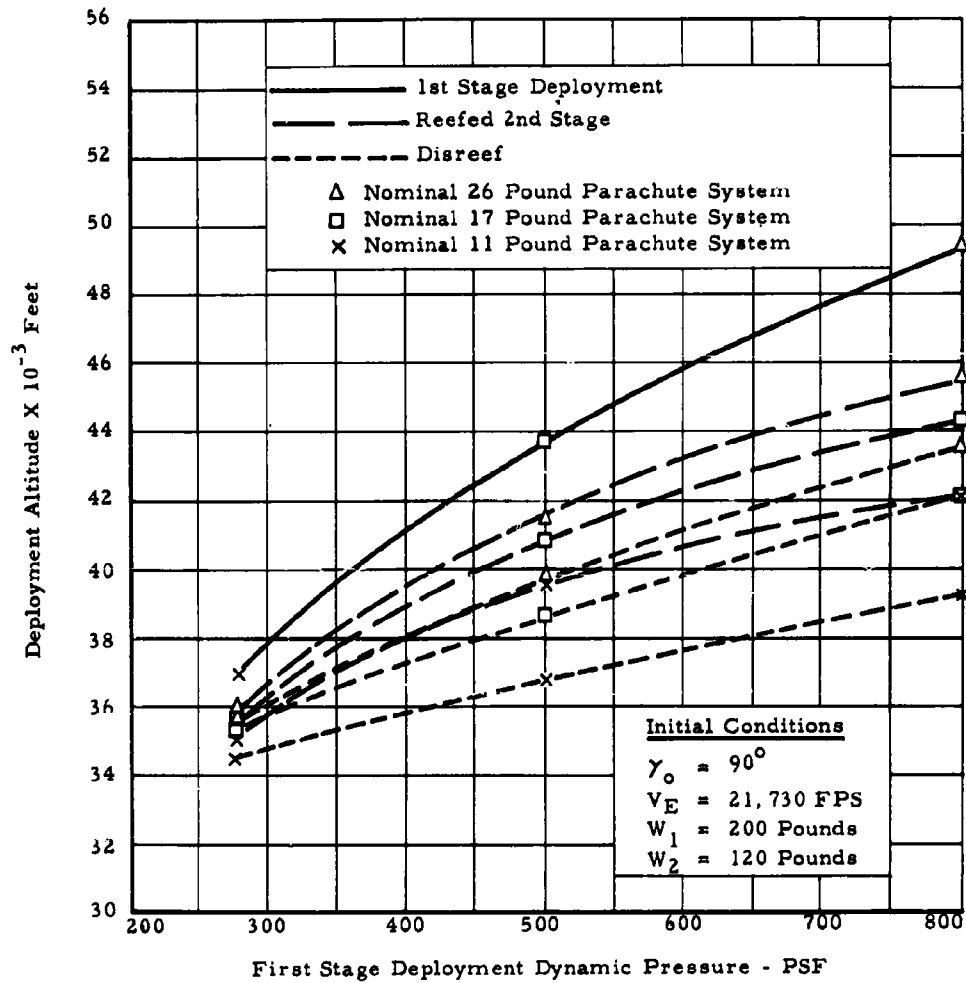


Fig. 5. Effect of Nominal Parachute Weight and First Stage Deployment Dynamic Pressure on Deployment Altitude for Atmosphere "B"



deploying a decelerator at the maximum altitude since for a given deployment dynamic pressure this atmospheric variation produces the lowest altitude.

Using this atmospheric profile, it becomes obvious that a single parachute system is not satisfactory since impact occurs at a Mach number slightly in excess of 0.90. This condition violates the restraint that a single parachute not be deployed above a Mach number of 0.9. As a result of this violation of restraint, further analysis using a single parachute for the recovery system was terminated.

Figure 6 shows the descent time for various deployment dynamic pressures for atmosphere D. It should be noted that the deployment Mach number of 2 was maintained for this series of runs since conventional parachutes are Mach number sensitive. The dynamic pressure (235 psf) for Mach number 2 in atmosphere D is less than that in B and hence does not impose a structural problem. For the other cases, deployment dynamic pressure was approximately retained, i.e., 500 and 800 psf, since Hyperflo test data to date does not indicate a Mach number sensitivity. To achieve maximum efficiency, this parachute should be deployed at design dynamic pressure.

Results of these computations indicate that the 17 lb system is still above the four minute limit in descent time although considerably reduced from that obtained for the B atmosphere. For this series of runs, the Mach 2, 500 psf and 800 psf dynamic pressure cases were run for the 17 lb parachute system and 11 and 26 lb systems were calculated for the 500 psf dynamic pressure. From these calculations and the almost linear relationship again exhibited in the 500 psf deployment condition, estimated variations are shown in Fig. 6 for the Mach 2 and 800 psf dynamic pressure deployment conditions. These variations were obtained by assuming that the relationship among the approximate slopes of the Mach 2, 500 psf and 800 psf curves for atmosphere D would be the same as that shown in Fig. 4 for atmosphere B. Based upon these estimates, deployment at a Mach number of 2 with the 11 lb system closely approaches the 4 minute limit.

Figure 7 shows the effect of dynamic pressure on deployment altitude for atmosphere B and D with a 17 lb nominal parachute system. From this figure, it is seen that the deployment altitude variation for the two atmospheres is most adversely affected at the lowest dynamic pressure. It is also seen that the first stage deployment altitude for atmosphere D varies from 18,000 ft to 39,000 ft for the low and high dynamic pressure deployment conditions, respectively. This variation is for all nominal parachute weight systems and is not applicable solely to the 17 lb system.

The results of this series of computations again show that all the systems considered fulfill the minimum time requirement; however, the Mach 2 or state-of-the-art case is closely approaching this limit for the low



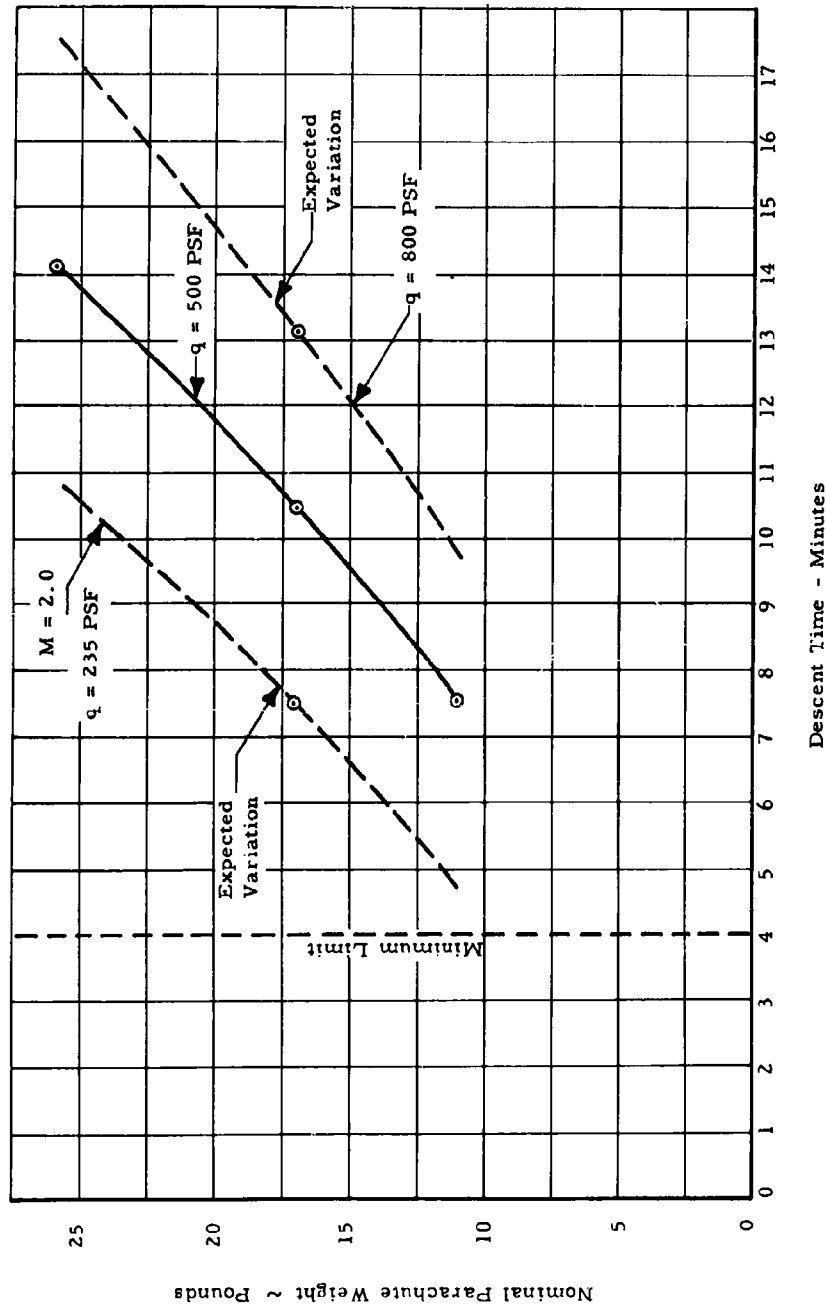


Fig. 6. Descent Time vs Nominal Parachute Weight for Various Deployment Dynamic Pressures and Atmosphere "D"



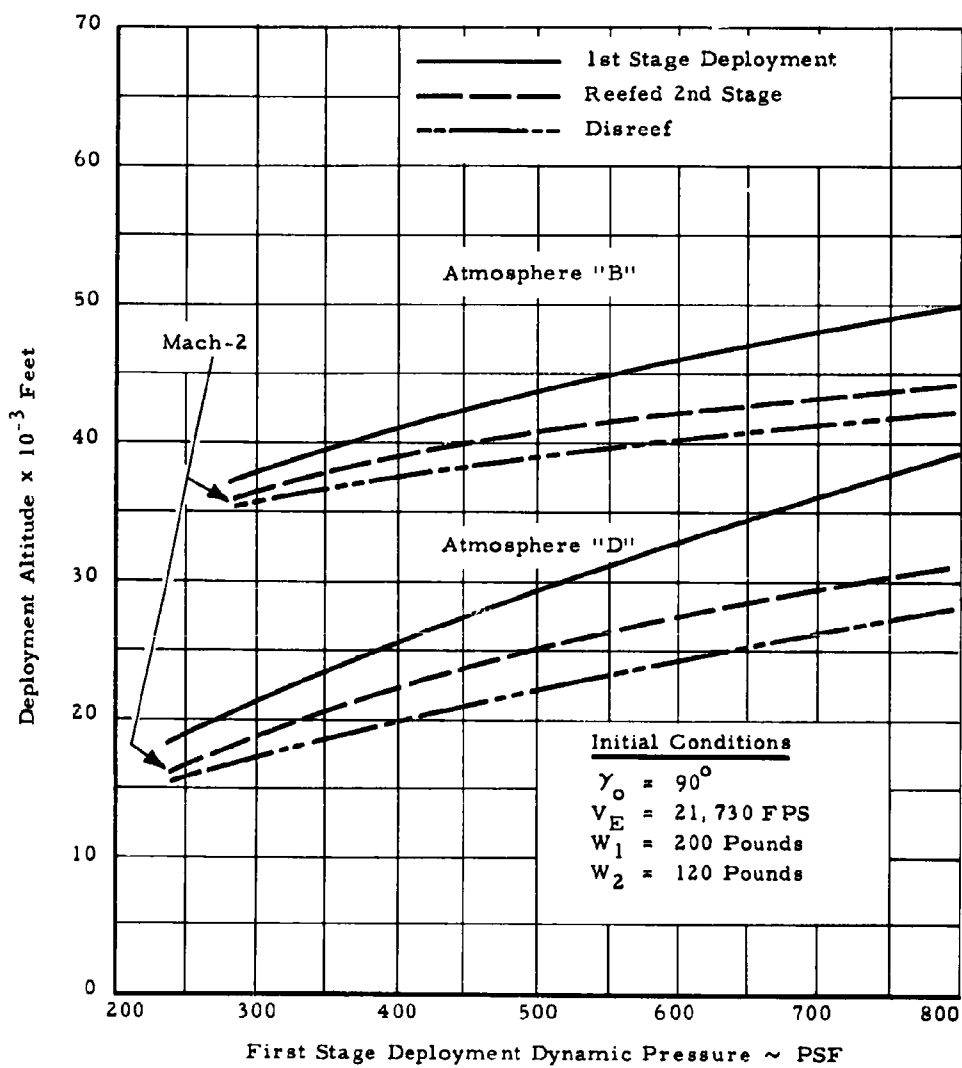


Fig. 7. Effect of First Stage Deployment Dynamic Pressure on Deployment Altitude for Atmosphere "B" and "D" with a Nominal 17 lb Parachute System



nominal parachute weight system.

To determine the minimum system capability, the most severe entry condition was imposed. This condition, which is at variance with the initial conditions as set forth previously, consists of an entry velocity of 37,000 fps at an altitude of 800,000 ft. Figure 8 shows the results of calculations using this entry velocity with a 90 deg entry angle.

For this series of runs, calculations were performed for all three nominal parachute weights at deployment conditions of 500 and 800 psf dynamic pressure. Only the 17 lb parachute system was investigated for the Mach 2 condition. The expected variation shown for the Mach 2 condition was obtained in the same manner as discussed previously for the D atmosphere case and nominal entry velocity.

The results of these calculations clearly show that a Mach 2 deployment is unsatisfactory in obtaining the desired four minute terminal descent time.

It is also evident that an 11 lb system does not fulfill the time requirement for all deployment dynamic pressure less than or equal to 800 psf. For the nominal 17 lb system and a deployment dynamic pressure of 500 psf, a descent time of approximately 3.7 minutes is achieved, and as a result, is considered worthy of additional investigation since it represents a near borderline condition for the worst possible initial entry conditions and requires the minimum extension to the present state of the art.

For the trajectory calculations performed, estimates have been made of the magnitude of the aerodynamic heating which the parachutes will encounter. For these calculations the reference temperature used for the parachute was 160°F. This temperature was chosen since it represents the extreme limit which will be encountered in space flight. Figure 9 shows the time the recovery temperature, assumed to be  $T_{\infty} [1 + (\gamma - 1)/2 (0.9) M^2]$ , is above 160°F vs the recovery temperature at time of deployment for the nominal lightweight entry vehicle. Both of the cases shown are for an entry velocity of 21,730 fps since it was found that the higher entry velocities in D atmosphere produced lower maximum deployment recovery temperatures. This condition prevailed since for a fixed deployment dynamic pressure, the Mach number at deployment for the higher entry velocities was lower because the deployment altitude was lower.

From these calculations, it has been determined that the maximum recovery temperature is approximately 1300°F for the 800 psf deployment condition. Using a cold wall method for computing the stagnation heat input results in a maximum integrated heat input of 2.56 BTU per square foot. Assuming a representative nylon tape which has adequate strength for the roof of the canopy, 3/4 in. MIL-T-5038 results in a temperature rise of



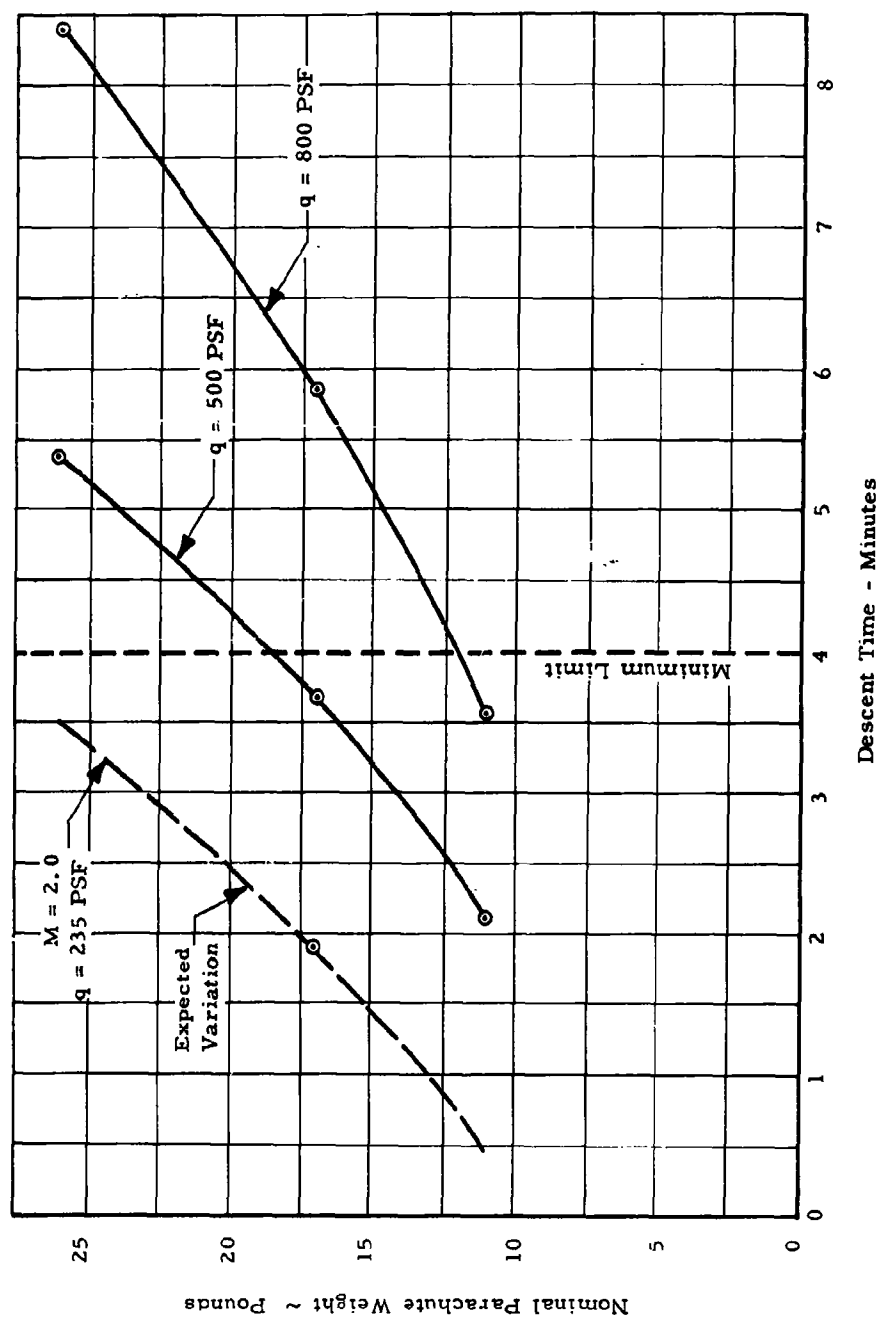


Fig. 8. Descent Time vs Nominal Parachute Weight for a 90 Deg Entry Angle, "D" Atmosphere, and an Entry Velocity of 37,000 fps



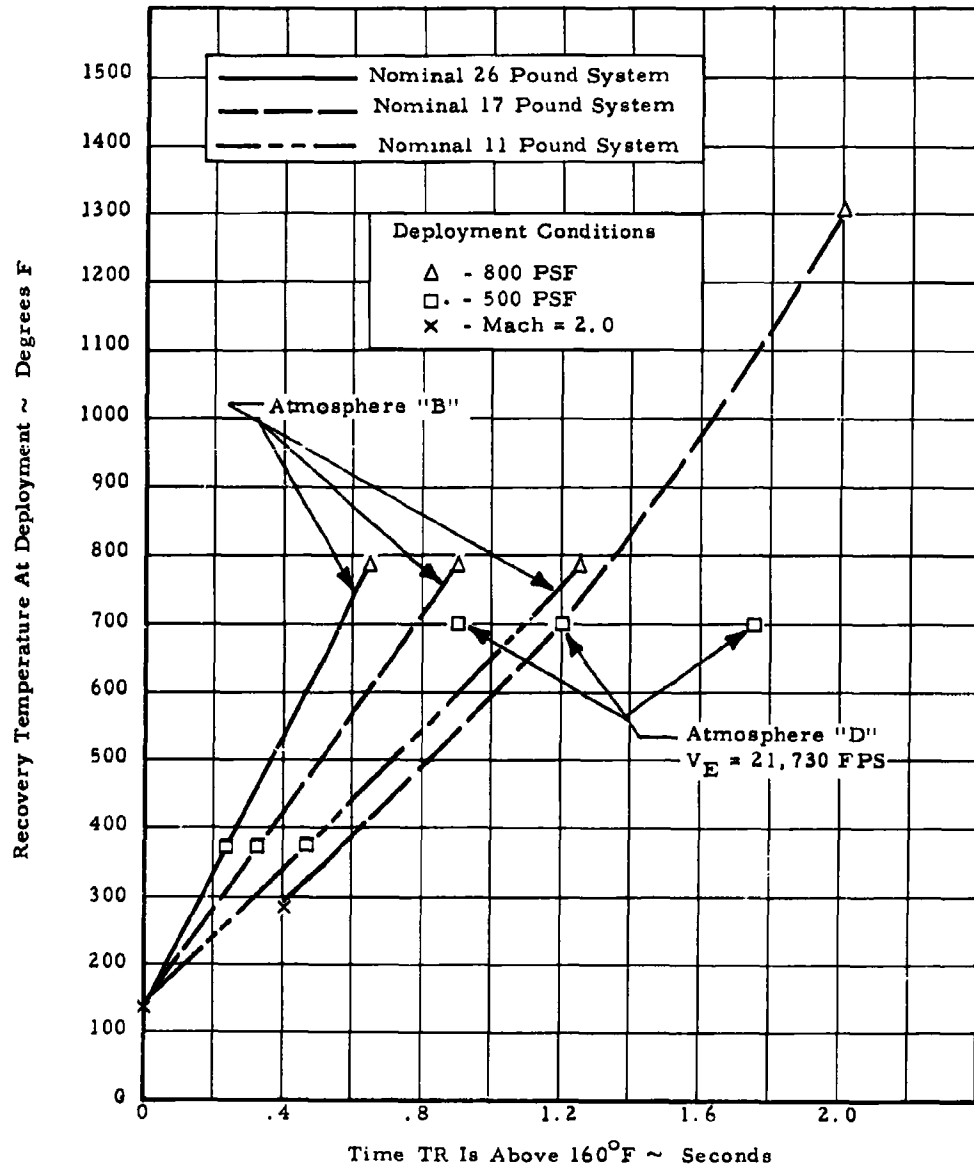


Fig. 9. Recovery Temperature at Time of First Stage Deployment vs Time TR Is Above 160°F for Atmospheres "B" and "D"



96°F or a final maximum temperature of 256°F. It should be emphasized that theoretical procedures available to calculate the aerodynamic heating encountered by a parachute have not been verified by test data; hence, the results of the above calculations at best can be considered as estimates. Tests have been performed at elevated Mach numbers with conventional parachutes. The effect of aerodynamic heating for these tests is not readily distinguishable since these parachutes exhibited violent oscillations and abrasion of the material precluded accurate analysis of the results. A test has been performed for a Mach number of 2.45 at an altitude of 60,000 ft where no visible damage occurred.

To finalize the descent time history information, computations were made for the 200 lb entry vehicle, nominal entry velocity, B atmosphere, 17 lb parachute system, and entry angles of 20, 45 and 70 deg. To perform these computations, constraints were imposed on the deployment timing based on the results obtained from the 90 deg entry computations and a knowledge of the potential problem areas associated with shallow entry angles.

The constraints chosen for this series of computations were as follows:

- (1) The recovery temperature at deployment must not exceed 700°F.
- (2) The deployment of first stage must be at a dynamic pressure not exceeding 500 psf.
- (3) The first stage is released at a dynamic pressure of 50 psf providing the Mach number is less than or equal to 0.9.
- (4) The second stage is disreefed 7 seconds after its deployment.

The first constraint is consistent with the maximum first stage deployment recovery temperature encountered for a 500 psf deployment on a 90 deg entry in D atmosphere. The second constraint is inherent in the first stage parachute structural design. The third constraint allows for the deviation in entry angle and atmosphere properties, that is, rate of change in density with time of flight and variation in the local speed of sound and atmospheric pressure. This constraint insures that two requirements will be satisfied. The first is that the parachute must be deployed at subsonic speeds and the second is that the opening loads must be within design tolerance. For the nominal 17 lb system deployed at a dynamic pressure of 500 psf, the time between first stage deployment and release of the second stage varies from 2.02 to 2.65 seconds for all 90 deg computations previously performed. The fourth constraint was based on 90 deg entry angle computations where it was found that the time to decelerate from a Mach number of 0.9 to  $q = 5$  psf varied from 6 to 7 seconds.



Figure 10 shows the results of the entry angle computations for descent time using the above constraints for deployment conditions. As would be expected, decreasing the entry angle significantly increases the descent time. For the 20 deg entry angle, the descent time is more than double that obtained for a 90 deg entry. Figure 11 shows the effect of deployment altitudes as a function of entry angle. It is seen from this figure that for the 20 deg entry angle, deployment of the final stage is above 100,000 ft.

The effect of constraint number 3 was quite pronounced in these calculations. The delay time in releasing the first stage varied from 2.02 seconds for the 90 deg case to 10.6 seconds for the 20 deg entry angle. The major factors contributing to this change in release time were the high deployment Mach number, the low dynamic pressure associated with a recovery temperature of 700°F, and the low dynamic pressure associated with a Mach number of 0.9.

#### SELECTION OF DEPLOYMENT CONDITION AND NOMINAL PARACHUTE SYSTEM WEIGHT

Based upon the trajectory analysis performed, the following considerations have led to the selection of a parachute system. The factors which have influenced the system choice are maximum reliability, maximum time of descent, and minimum weight.

From the analysis performed, it is estimated that the 800 psf dynamic pressure deployment condition closely borders the limit of acceptable tolerances for nylon due to aerodynamic heating. This condition also extends the state of the art in parachute operation to its highest value, and due to sensing tolerances, may result in deployment Mach numbers which will not be validated by free-flight tests until approximately early 1964. An additional problem associated with this deployment condition is the rise in drag coefficient as obtained from wind tunnel tests in the range of Mach 4 to 3. The rise in drag becomes significant if deployment takes place at a lower Mach number than the nominal 4 at the design dynamic pressure, since parachute load limits would be exceeded. As a result of these problems, it is not desirable to deploy at this condition unless descent time requirements specifically dictate its use without regard to the possible reduction in reliability.

The 500 psf deployment condition appears to be the most promising. Parachute performance at the Mach numbers expected to be encountered will be flight validated by mid 1963 on the CREE parachute test vehicle. The computed heat inputs resulting from the 90 deg entry angle trajectory analysis indicate the maximum fabric temperature to be below 180°F and on the 20 deg entry case to be below 210°F. All of these characteristics coupled with the almost constant drag coefficient for Mach numbers between 3 and 2



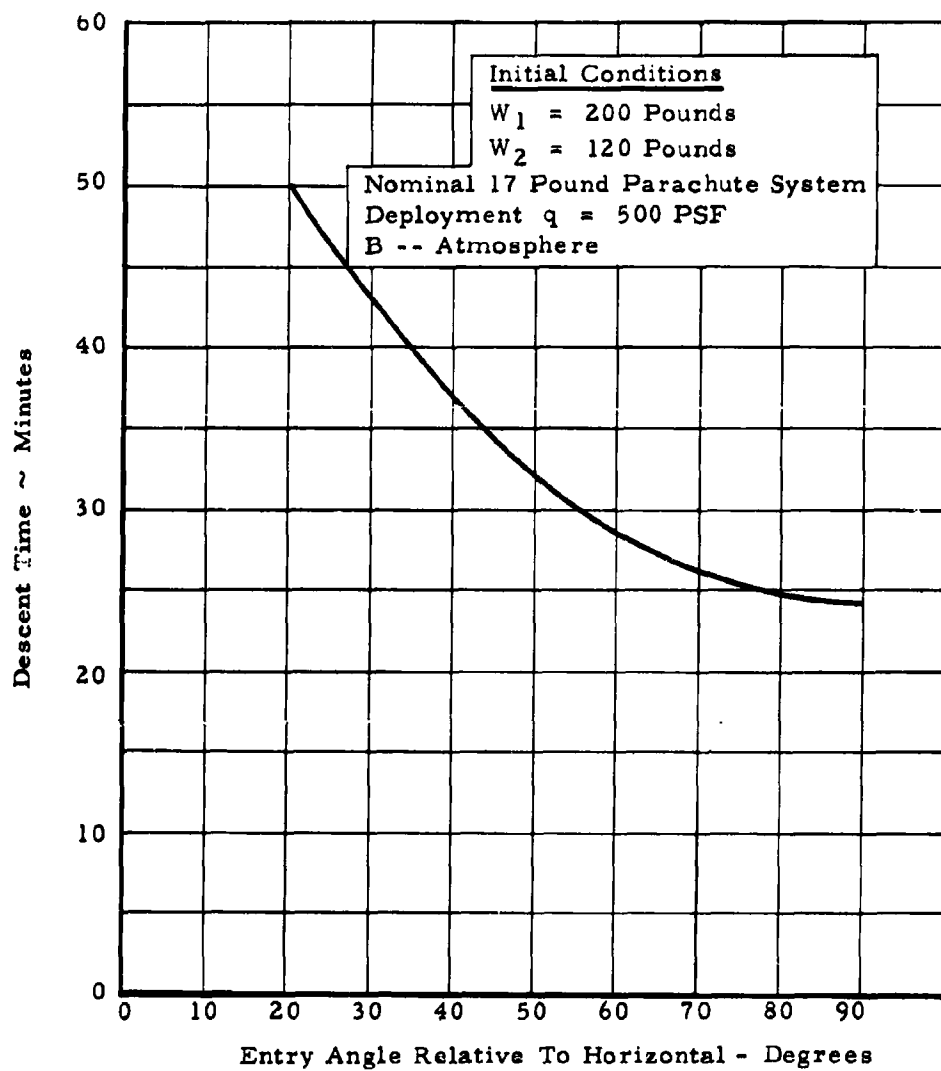


Fig. 10. Effect of Entry Angle on Descent Time



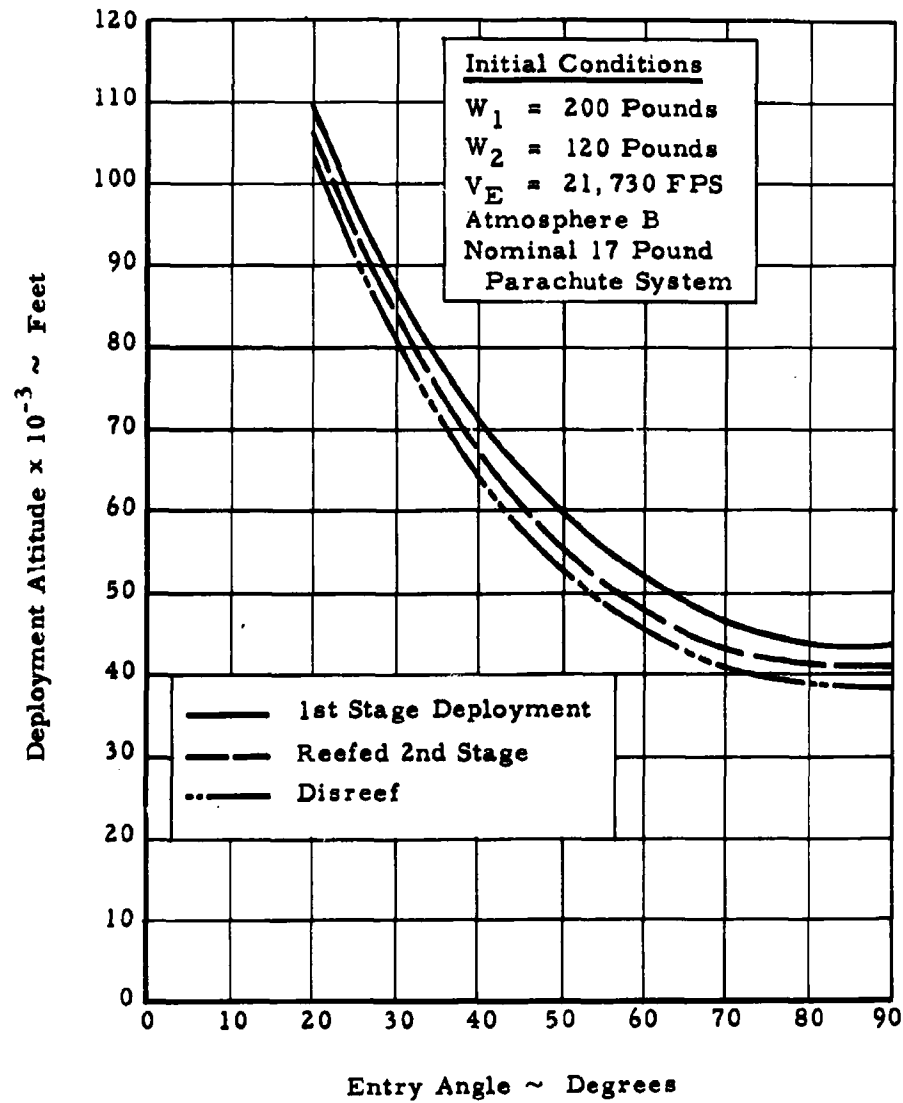


Fig. 11. Effect of Entry Angle on Deployment Altitude



indicate favorable characteristics with respect to loading conditions and number of tests required to prove flight reliability.

The Mach 2 deployment condition is obviously not satisfactory since under the most favorable loading condition (130 g's) for obtaining maximum time of descent it does not fulfill the minimum time requirement.

From the above discussion it is concluded that the 500 psf deployment environment requires the least extension to the state of the art and hence suggests the highest reliability with a minimum amount of proof testing. Based upon obtaining a system with the maximum reliability for the early flights, where only estimates can be made of the environmental parameters, it is suggested that the first stage be deployed at a dynamic pressure of 500 psf. The parachute system weight becomes the remaining significant parameter to be selected. The nominal 26 lb system introduces two problems. The most severe problem is that this system subjects the vehicle to the maximum loading condition. Hence, the sensing system requirements must be extremely stringent and possess tolerances in a direction which will only reduce the design load. The second problem, which is not as crucial but still significant, is the sizeable weight increase over the nominal 17 lb system.

Due to the weight savings and increased over-all flexibility of the nominal 17 lb system over the nominal 26 lb system, the 17 lb system is recommended. This system fulfills the four minute descent time requirement for all entry velocities less than 36,000 fps for all entry angles. At 37,000 fps entry velocity and 90 deg entry angle, it fulfills the four minute descent time for all entry vehicle weights less than 197 lb. The small region where the 17 lb system does not fulfill the desired descent time on the most severe entry condition is not considered significant enough to exclude its selection.

#### SENSING REQUIREMENTS FOR THE NOMINAL 17 LB PARACHUTE SYSTEM

To determine the requirements for the sensing system, it was first necessary to define an optimum sensing system. The parameters which are known to influence the deployment conditions are:

- (1) Allowable deceleration
- (2) Aerodynamic and structural limit of parachutes
- (3) Temperature capability of parachutes.



Based on fulfilling the above criteria, an optimum sensing system was defined as a system which would provide the maximum descent time independent of the entry parameters which might be encountered on a flight to Mars. To obtain a description of a system that would provide a maximum time of descent, the following constraints have been imposed on the deployment environment. The constraints are considered to be sequenced as in a series circuit, i.e., the first constraint must be met prior to the second being allowed to function.

#### First Stage

- (1)  $\frac{\partial g}{\partial t} > 0$
- (2) Dynamic pressure  $q \leq 500$  psf
- (3) Recovery temperature  $T_R \leq 700^\circ\text{F}$

#### Second Stage - Reefed

Mach number must be less than 0.9 and the dynamic pressure be equal to or below 50 psf.

#### Third Stage

Deployed 7 seconds after second stage is deployed.

These constraints are based on limiting the parachute loads and aerodynamic heating to safe limits for nylon materials.

Considering first the constraints which affect the first stage deployment, it follows that the first constraint assures that deployment of the system occurs after peak deceleration has been encountered and hence assures that peak heating has passed. The second constraint limits the opening shock load to the design values for the onboard instrumentation and recovery system. The third constraint (and the one hardest to fulfill) assures that the Mach number at deployment is within bounds and that the aerodynamic heating will not produce material temperatures which will result in failures under the initial loading condition.

To measure the three limiting constraints mentioned previously requires instrumentation components which are not standard purchase items. The first constraint requires, for example, an electrical device which will sense that maximum deceleration has occurred independent of the absolute magnitude of the peak deceleration. This device must have a sufficiently low response rate that it will not be triggered by variations in angle of



attack while the vehicle deceleration is increasing. A cursory examination of these requirements indicates that two methods may be used to perform this function. The first method is to measure the vehicle deceleration and sense when it passes through a specified g level when g's are increasing, and when it passes through the same g level when g's are decreasing. This method has been utilized by this company for nose cone recovery and is considered reliable when the g level at which deployment is to be initiated is well below the value measured by the triggering device. From the trajectories analyzed, it appears that for 20 deg entry angles in atmosphere, A, B, and F the peak dynamic pressure encountered is quite close to 500 psf. Should minimum expected entry angles be less than 20 deg, maximum time of descent would not be obtained using this system if a 90 deg entry angle actually was experienced. If it were certain that a shallow entry angle would be encountered, it would be possible to set the g value for less than the 500 psf condition since under these conditions the calculations performed indicate that the recovery temperature limits the deployment rather than the dynamic pressure.

A second approach to this problem is the development of a meter which will measure the rate of change of acceleration with time. This device would eliminate the problem discussed above, i. e., sensing an absolute value; however, a cursory examination of present standard equipment indicates that no device will cover the extreme ranges in deceleration which will result from the large variations in possible entry angles, entry velocities, and atmospheric variations. Hence, if the first approach is not acceptable due to possible deviations in entry angle, a "jerk meter" would have to be developed.

The second constraint is easily satisfied by use of an accelerometer. Examination of the drag area variation for the 200 lb entry vehicle shows a maximum spread of less than 7 percent for a Mach number range of 2.8 to 4.8. Based upon this small variation in drag area and the relationship between drag area, dynamic pressure, and deceleration the deployment dynamic pressure can be held within  $\pm 3.5$  percent, or approximately 20 psf. This is well within required limits. The required accelerometers (to the best of our knowledge) have not been investigated under hard vacuum and sterilization requirements, however.

Fulfillment of the third constraint is the most difficult. This constraint, however, is of prime importance since without it being fulfilled, deployment could occur at a Mach number in excess of 11 for a 20 deg entry angle. This Mach number is after peak deceleration and at a dynamic pressure of 500 psf; however, the recovery temperatures and ensuing total heat inputs would be considerably in excess of those allowable for nylon parachutes.



It should be emphasized that in optimizing time of descent it is not possible to fix the Mach number at deployment since different atmospheres and entry angles provide different maximum Mach numbers for which acceptable environmental conditions prevail. If the Mach number for deployment is fixed it can be shown that a loss in descent time would result for some entry conditions. As a result, the parameter which most closely predicts the extremes in acceptable environmental conditions is the total heat input. This parameter has been found to be controlled reasonably well by restricting the first stage deployment to a fixed recovery temperature as discussed earlier. Unfortunately, recovery temperatures encountered during a hypersonic entry are well above those that existing temperature measuring devices can sustain. The amount of ablation of the heat shield itself is not a direct measure since varying entry angles and atmospheric variations will produce varying degrees of ablation.

A second approach to this problem is to deploy at a specific Mach number. As stated previously, this does not provide an optimum system, but neither does it require the development of an exotic temperature measuring device. The Mach number at deployment would be limited to approximately 3.0, since for different atmospheric and resulting static temperature variations this Mach number would limit the recovery temperature to a value less than 700°F. A means by which Mach number could be sensed is by measuring base pressure ( $P_B$ ) and free stream static pressure. The static pressure port could be located on the side of the entry body, for example, and a correlation of surface pressure with static pressure would then be required as a function of Mach number. Once these values are known, the value of the ratio could be used to give the free stream Mach number.

Problem areas associated with this type of system are the sensing accuracies of absolute pressure transducers and the measuring of free stream pressure at the high Mach numbers. The sensing errors would limit the deployment altitude to pressure levels where accurate pressure ratios, hence Mach number determination, could be made.

The second stage deployment in the reefed condition requires a Mach number sensing device if wide ranges in entry angle are to be anticipated. Based upon the trajectory analysis, it is expected that if the entry angle could be held to a value greater than approximately 50 deg, a fixed time delay could be used without sacrificing a large percentage of the terminal descent time. If these conditions cannot be met, a pressure sensing device must be installed to limit the deployment Mach number to a value less than or equal to 0.9. Should the temperature sensing device be used for the first stage sensor, deployment of the second stage would probably rely on sensing Mach number by the ratio of static to total pressure. This method does not present any significant problem areas since the total pressure probe would be protected by the heat shield during the entry into the Mars atmosphere.



and would be exposed when the heat shield is removed at the time of first stage deployment. The use of these pressures provides the advantage that higher absolute values would be obtained resulting in increasing the altitude where accurate measurements could be easily made. If the pressure sensing device for first stage is chosen, the same system would be used in a two-fold purpose to trigger both first and second stages.

Third stage deployment or disreefing can be accomplished by a fixed time delay reefing cutter since the deployment requirement is dependent only on limiting the deployment to a maximum dynamic pressure.

The results of this investigation of the sensing requirements show that several methods can possibly be used to perform the desired function. The type of system required is largely a function of the possible error in entry angle predictions and the tolerable sacrifice in the potential deployment altitude. These factors, coupled with the environmental conditions associated with the sterilization process which the equipment must survive, eliminates any accurate determination of specific measuring devices. To perform this selection boundary conditions on both entry angle and maximum and minimum entry velocities must be finalized. With this information, an exhaustive error analysis coupled with further research on the problem must be performed to enable the prediction of design criteria for the sensing system.

#### SYSTEM SEQUENCING AND WEIGHT BREAKDOWN

The system deployment operation considered for this application is shown in Fig. 12. The decelerator system deployment sequence is initiated by mortaring off the rear cover. This cover then extracts the first stage parachute. It is anticipated that at the time the first stage is deployed the heat shield would be free and hence separated from the recoverable vehicle once sizeable drag loads are encountered.

Release of the first stage would be accomplished by a pyrotechnic release which would allow the first stage to extract the main stage. The main stage would incorporate standard time delay reefing cutters which would be actuated by lanyards at time of deployment. Based on preliminary estimates of the system components, it is expected the total recovery system weight would be approximately 28 lb for the nominal 17 lb parachute system.

#### SUMMARY

A parametric investigation with 3 nominal parachute system weights has been performed. The parameters which received the most attention were atmospheric density profile, entry angle, and entry velocity. It is concluded that to fulfill a four minute time of descent requirement for the expected



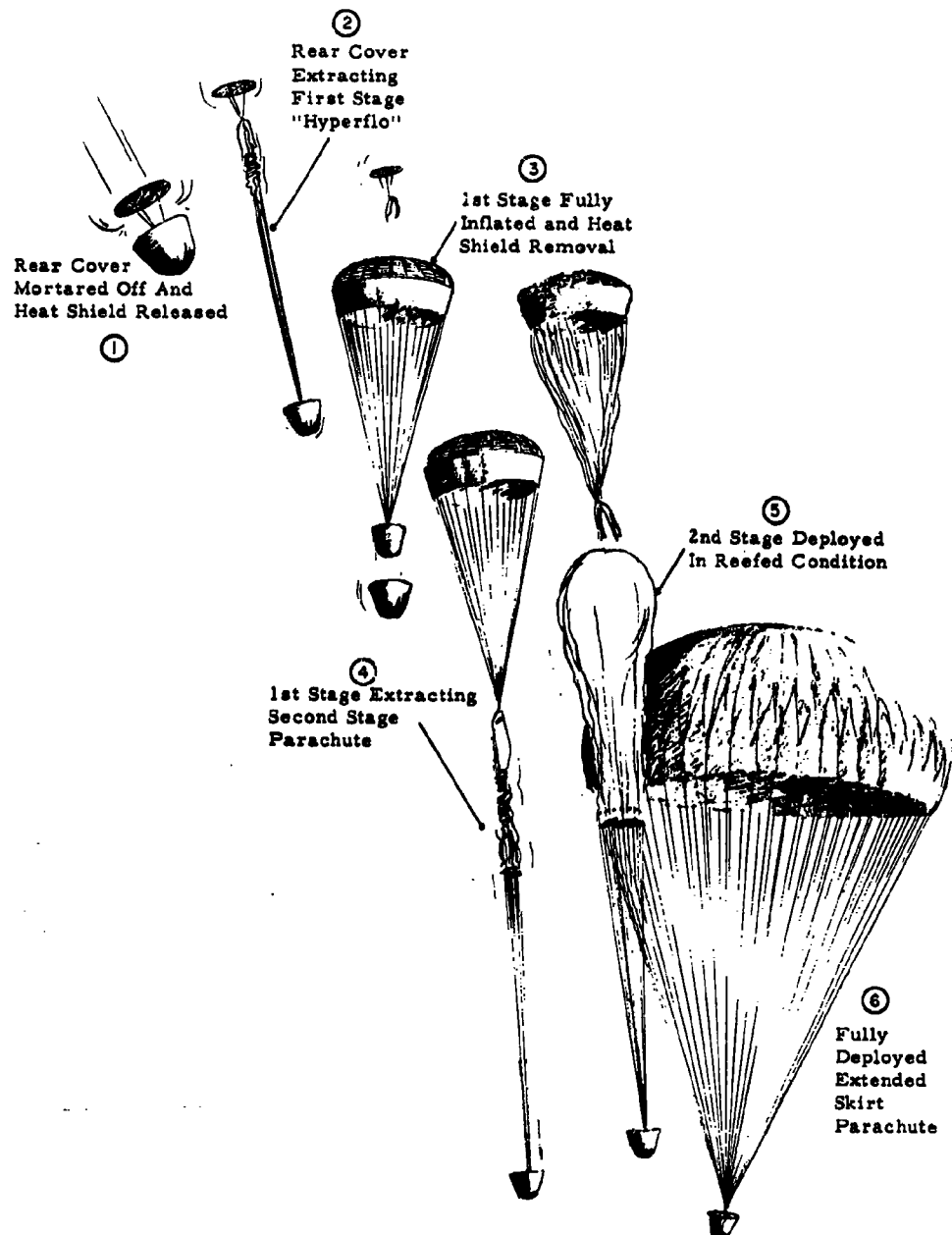


Fig. 12. Recovery System Deployment Sequence



entry velocities, and a 90 deg entry angle, present state-of-the-art parachutes are impractical due to a weight consideration. Due to the favorable test results obtained with the Hyperflo parachute configuration to date, this conclusion does not appear to produce a serious problem. It is anticipated however, that the major problem associated with such a mission is the sterilization and hard vacuum environment sensing devices and parachute fabrics must survive. This problem area requires further investigation prior to obtaining a final system design.

#### REFERENCES

1. Engstrom, B. A., "Performance of Trailing Aerodynamic Decelerators at High Dynamic Pressures, Phases 5 and 6," WADC TR 58-284, February 1962.



## PARAGLIDER BOOSTER RECOVERY SYSTEMS

J. E. Crawford  
J. D. McNerney

Space-General Corporation  
El Monte, California

## ABSTRACT

The study of techniques for the recovery of boosters is rapidly gaining increased attention as the pace of space exploration gains momentum. The operational requirements for recovery systems are discussed and the aerothermodynamic and structural characteristics for a family of paraglider recovery systems are presented. Re-entry equilibrium stagnation temperatures are typically below 500°F, permitting the use of low-cost, low-temperature materials of construction. Inflatable and erectable configurations, as well as various control schemes, are also discussed. Weight estimates for the complete recovery systems range from 5% to 12% of the payload weight, as a function of burnout velocity and re-entry heating and pull-out accelerations.

The work described in this paper was company-sponsored.



## PARAGLIDER BOOSTER RECOVERY SYSTEM

J. E. Crawford  
J. D. McNerney

Space-General Corporation  
El Monte, California

INTRODUCTION

The development of an efficient and successful recovery system for aeroballistic devices and orbital spacecraft demands the serious attention of the aerospace industry. The reliable recovery of man from space missions is a universally accepted requirement, while unmanned systems are considered as experiments and expendable. While this logic has probably been valid for most of the relatively rudimentary experiments conducted so far, the imminent transition to the operational phase of the exploration of space, with the launching of an ever increasing number and complexity of systems, demands that recovery of these systems be given serious consideration for the following reasons.

The economics of the expendability of space systems has been analyzed and presented in many publications. Unfortunately, however, the majority of these arguments have too often been refuted by customer cost analysis based on only the quantities of each system as are now funded; i.e., there are some valid arguments that the cost to develop a recovery system for fifteen Titan III or twenty Saturns may not show a cost reduction in the total program. However, if the ultimate quantities that will be produced of such systems is reasonable estimated from past experience, an efficient recovery system will show large program cost reductions.

Perhaps of greater importance are several less tangible considerations. Vast sums of money are being expended on environmental test facilities to simulate space environment effects, especially for long periods of exposure. The validity of the results of this testing is often questionable, while the recovery of actual vehicles from space could provide factual data on the effects of the mission environment, or the true cause of system failures or malfunctions.

At the September 1963 Symposium on "Space Rendezvous, Rescue and Recovery" at Edwards Airforce Base it was repeatedly stated by Government and industry authorities that the recovery of large boosters is essential to the success of our future space program. A NASA analysis of reliability predictions estimated that space mission reliability would be increased from 0.75 to greater than 0.92 by 1970 principally by failure analysis of recovered boosters.

Finally, and perhaps of most immediate importance is the necessity to recover intelligence data and secret vehicles from space before our opponents succeed in intercepting and eventually retrieving them from space for their own counter-intelligence purposes.



High density payloads can be reentered from orbit on a ballistic trajectory, and retrieved successfully, if we continue to accept the high cost of maintaining vast air and marine recovery fleets. Low density systems do not lend themselves to efficient ballistic reentry systems, but are generally adaptable to recovery if reentered through the atmosphere in the relatively gentle environment that a lifting, controlled glide vehicle is capable of producing.

#### PERFORMANCE CRITERIA

The Space-General Corporation has conducted numerous studies, employing the paraglider concept, for the recovery of manned and unmanned space systems and boosters. The system design criteria assumed that the reentry system must be simple, produce a minimum of performance penalty to the basic vehicle system, provide long maneuverable glide range capability, and be low in cost.

Historically, parachutes have served as the terminal deceleration system after the initial velocity has decayed to subsonic speeds. The complete reentry system is therefore the heat shield, the guidance and control system, etc., as well as the parachute; therefore, the total reentry is relatively heavy and complex. The parachute system, as with any other drag system, permits very limited or no maneuverability and control.

Rigid lifting surfaces, typically characterized by moderate wing loadings, produce tolerable reentry aerodynamic and heating loads but usually impose considerable penalties on the launch vehicle system. The Rogallo wing paraglider suggests the advantages of both systems with minimum constraints on the parent vehicle and very moderate reentry heating conditions. The pressure stabilized inflatable structure can be stowed in a high density configuration similar to the parachute, but when deployed, will provide the high L/D and maneuverability desired for shallow reentry and controlled low speed landing.

Studies of various wing and payload arrangements indicate that the under-slung or suspended payload (as typical of the system under development for the Gemini paraglider recovery system) provides relatively simple aerodynamic control by shifting the payload position relative to the wing, and also distributes the deadweight more uniformly over the wing booms. However, the lift to drag ratio for the suspended payload is typically 30% to 50% lower than for a clean configuration which incorporates the payload in the keel. The suspended payload cables or supporting truss weight, and heat protection system required to protect the small diameter cables from the high stagnation temperatures generated, imposes weight penalties considerably in excess of that for the integral payload arrangement (ref. 1). The suspended payload also imposes problems of deployment and the hazard of collision of the payload with the wing during deployment, gusts, or inadvertent maneuvers.

Optimum shaping of the wing camber and wing tip shape of an integral paraglider-payload configuration can increase the lift to drag ratio to 15 or as high as 17 as demonstrated by wind tunnel tests (ref. 2, 3, 4). It was concluded from these studies that the integral payload system provided the most simple, light weight system with minimum aerothermodynamic problems and greatly extended range and maneuverability characteristics.



### SATURN SI-C RECOVERY SYSTEM

Three booster recovery studies are described including a review of the earlier studies of the Saturn SI-C booster configuration as shown in Figure 1.

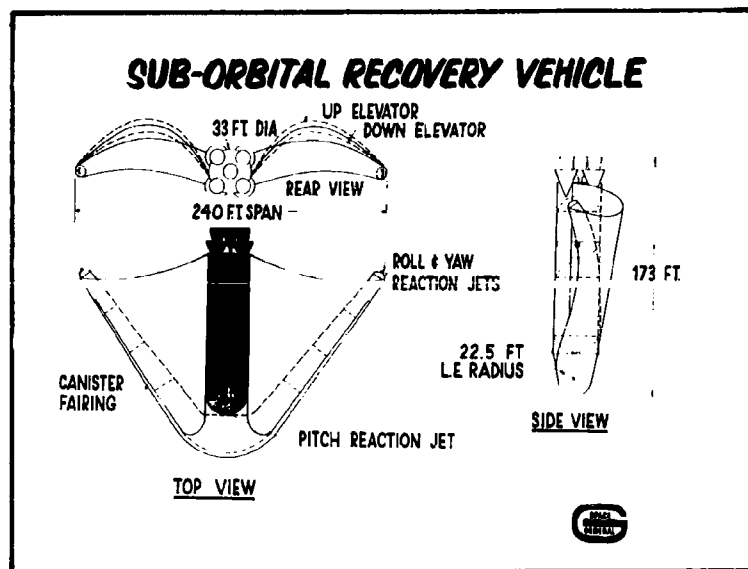


FIGURE 1

This study assumed a booster burn-out weight of 384,000 lbs and a burn-out velocity of 6890 fps at a 196,800 ft. altitude with a flight path angle of  $60^\circ$  from the vertical. The influence of wing loading on trajectory characteristics is shown in Figure 2.

A hypersonic  $L/D_{\max} = 1.1$ ,  $C_{L\max} = 0.8$  and subsonic  $L/D_{\max} = 8.0$ , and  $C_{L\max} = 1.1$  was assumed. From this parametric analysis a wing loading of 20 was selected which produced a wing area of approximately 20,500 sf. The wing membranes and inflatable structures utilize a fiberglass cloth or metallic filament fabric reinforcing material impregnated with silicone matrix material. As the stagnation temperatures were under  $800^\circ\text{F}$ , exotic metals are not required for this application and fiberglass fabric may provide a low cost reinforcing material for the structure. The structure was analyzed for a maximum load factor of 6.4g at pull-out and 2g for subsonic gust loading. The residual propellant system pressurization gas at 30 psi was assumed to be available for pressurization of the paraglider. A weight breakdown of recovery system is shown in Figure 3.



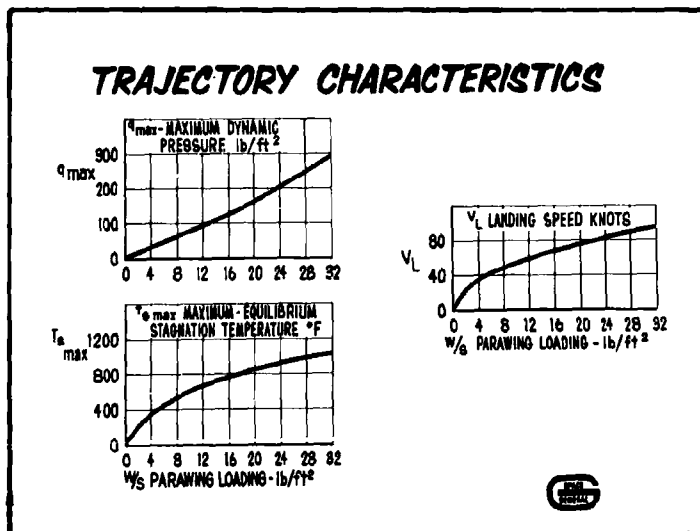


FIGURE 2

WEIGHT BREAKDOWN  
SATURN SI-C RECOVERY SYSTEM

Paraglider Structure	38,120 lb
Pressurization System Plumbing	67
Reaction Control System	35
Guidance and Command System	240
Aerodynamic Control System	330
Canister	<u>750</u>
Total System Weight	39,492 lb

FIGURE 3



An analysis of a suspended payload arrangement and the integral payload configuration indicated that the suspended system produced a weight approximately twice that of the integral system. The principal weight differences resulted from the weight of the suspension system and the center keel (or boom) required in the suspended payload arrangement. The lower L/D also greatly penalized the range and maneuverability characteristics. Reentry heating of the small diameter shroud lines may be a critical problem but this penalty was not included in the weight estimate.

Pull-out load factors were calculated for trajectory profiles considered to be typical of various boosters is shown in Figure 4a.

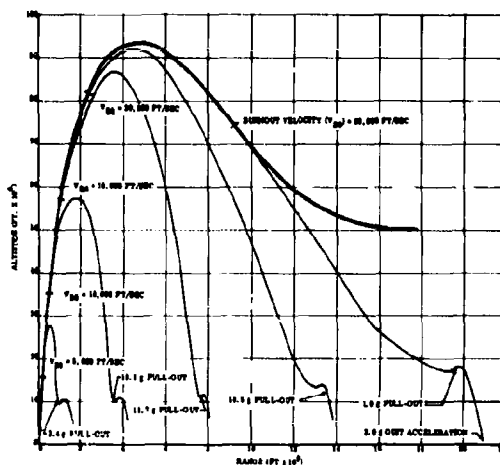


FIGURE 4a

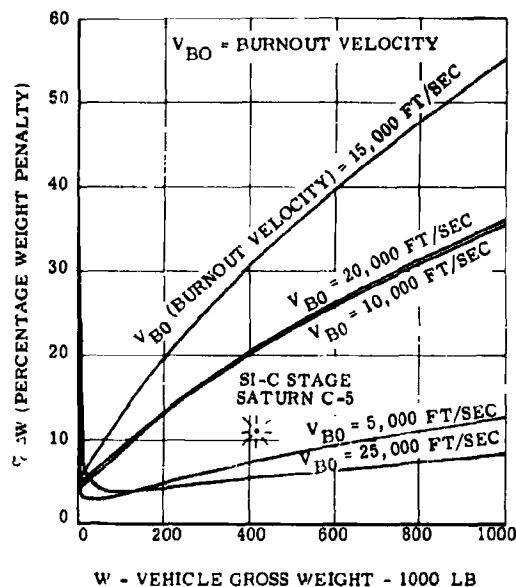


FIGURE 4b

These analyses indicate that high "g" pull-outs result from burn-out velocities between 14,000 and 18,000 fps, however vehicle staging is usually scheduled outside of the critical range. Flight path angle at time of burn-out is, of course, also a critical factor. The Saturn SI-C trajectory is not shown in this figure but would be between the two lower trajectory curves. A parametric analysis (ref. 7) of the paraglider recovery system weight, as a percentage of booster burn-out weight is shown in Figure 4b for burn-out velocities from 5,000 to 25,000 fps.



### TITAN III RECOVERY SYSTEMS

A study of the recovery of preliminary configurations of Titan III solid boosters generated the general arrangement for a pressure stabilized inflatable structure shown in Figure 5.

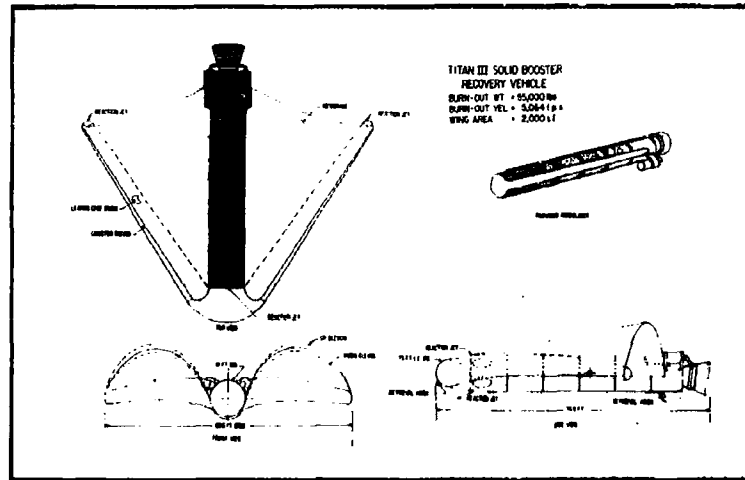


FIGURE 5

The pressure stabilize structural concept is shown here although analysis of the booster trajectory in Figures 7, 8, and 9 show that the aero-heating is relatively insignificant and extendable rigid leading edge booms should produce a lighter weight structure and more optimum aerodynamic characteristics. The weight estimate for a 3000 sf wing area inflatable structure configuration is shown in Figure 6. The 10 psi inflation pressure required to stabilize the structure with a 50% allowance for pressure schedule with altitude required a 557 lb. helium tank. However, this was a conservative analysis which assumed the tank soaked to a temperature in equilibrium with the maximum skin temperatures.

#### WEIGHT BREAKDOWN TITAN III SOLID BOOSTER INFLATABLE STRUCTURE

Paraglider Structure	4125 lb
Helium Tank	557 lb
Pressurization Gas (H <sub>2</sub> )	38 lb
Pressurization System Plumbing	55 lb
Reaction Control System	46 lb
Aerodynamic Control System	275 lb
Sub Total	5,096 lb
Titan Booster	49,914 lb
Total Recovery Wt. =	55,010 lb

FIGURE 6



Figure 7a and 7b data were computed for a trajectory with a burn-out velocity of 5,064 fps at an altitude of 182,600 ft and flight path angle of  $34.7^\circ$  above the local horizontal. As the payload coasted to the apogee of 256,500 ft. the dynamic pressures approached zero for approximately two minutes, during which time the paraglider would be deployed. By allowing the vehicle to coast to the fringe of the atmosphere the deployment sequence is accomplished in essentially a zero  $q$  and acceleration environment, thereby minimizing deployment loads. During the subsequent pull-out at the 100,000 ft. altitude level the dynamic pressure peaks out at 148 psf.

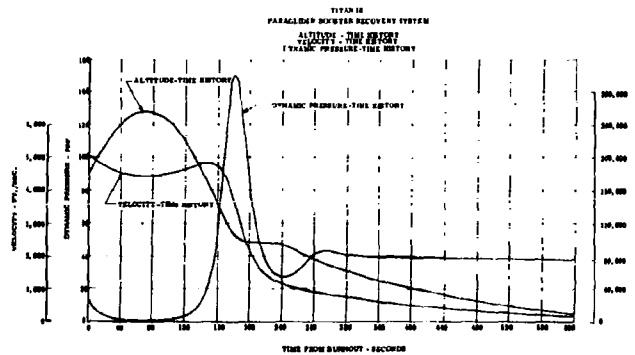


FIGURE 7a

TITAN III  
PARAGLIDER RECOVERY SYSTEM  
TIME HISTORY  
OF  
NORMAL & LONGITUDINAL ACCELERATION

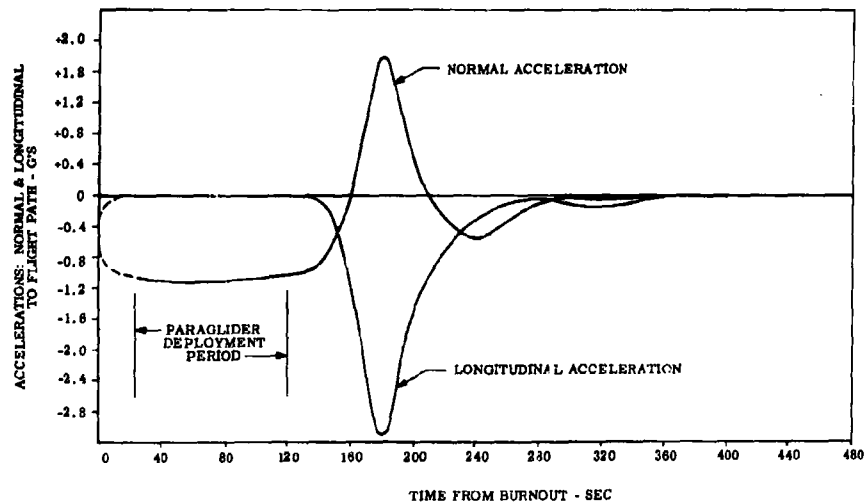


FIGURE 7b



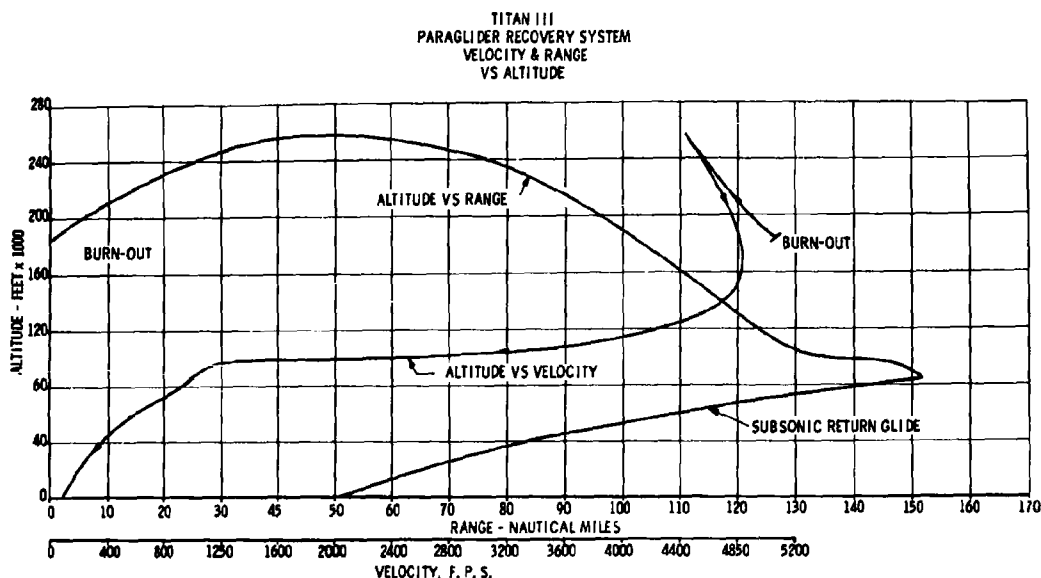


FIGURE 8

Figure 8 shows the Altitude vs Velocity and Altitude vs Range curves assuming a subsonic turn after the vehicle velocity has decelerated through the transonic range, 152 nm down range. Flying at a maximum  $L/D = 8.0$  the system is able to glide 100 nm to within 52 nm of the launch site. An increase of subsonic maximum lift to drag ratio from 8 to 12, by the use of a more optimum canopy shape, would permit a subsonic glide range sufficient to return the booster to the launch site. A supersonic turn would, of course, greatly increase this return glide range.

Figure 9 shows the aerodynamic heating characteristics for this trajectory. The very low heat flux rate and stagnation temperatures indicate that a more optimum trajectory might use a modulated lift reentry to reduce the  $6g$  acceleration for a trade-off with increased skin temperatures. However, the low temperatures produced by this configuration would allow the use of low temperature materials of construction and minimize the temperature exposure of the payload.

Figures 10 and 11 illustrate a recent study of a paraglider using rigid leading booms which retract flush with the sides of the booster in the stowed configuration. The phantom view shown in Figure 11 illustrates the erection mechanism and an alternate leading edge configuration.



TITAN III  
PARAGLIDER RECOVERY SYSTEM  
AERODYNAMIC HEATING PARAMETERS  
L. E. BOOM

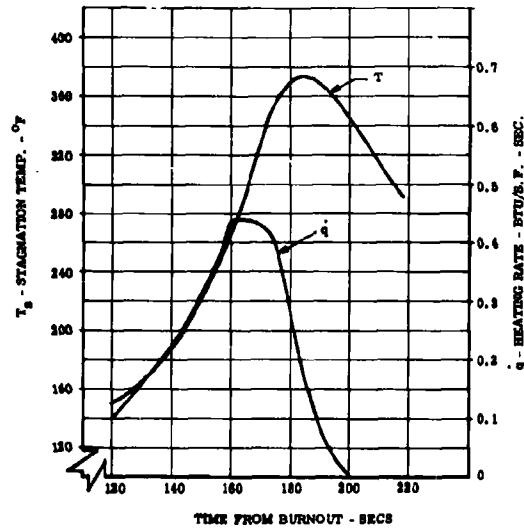


FIGURE 9

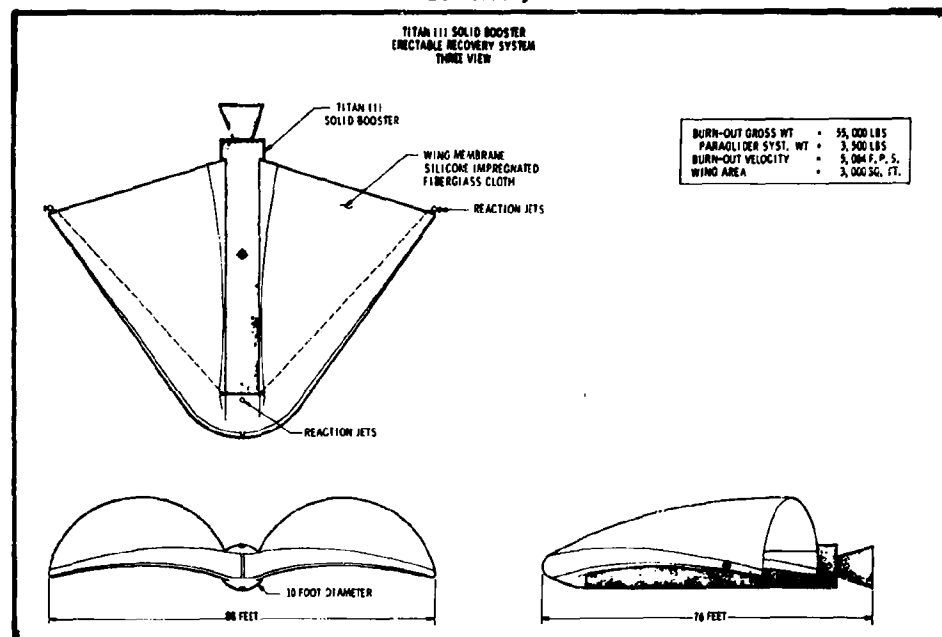


FIGURE 10



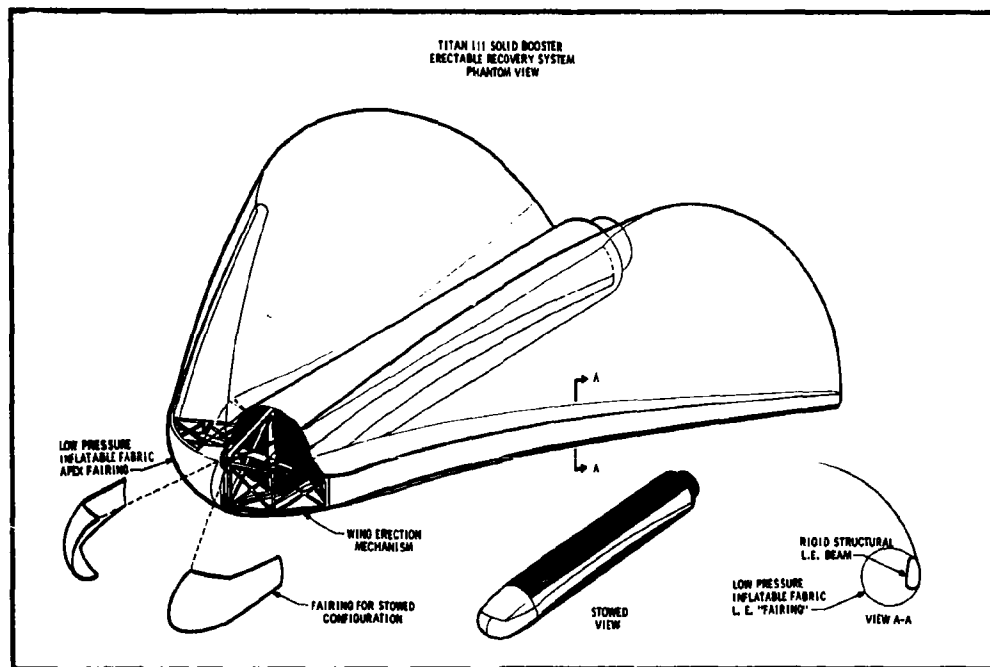


FIGURE 11

A 1.0 psi inflatable leading edge fairing is incorporated to reduce stagnation temperatures for higher velocity burn-out trajectory studies. As leading edge stagnation temperatures are inversely proportional to the  $1/8$  power of the L.E. radius, the reduction in the L.E. radius from 3.7 ft to 0.5 ft, by elimination of the inflated low pressure "thermal fairing", increases the maximum equilibrium stagnation temperatures from 3700°F to only 4750°F with a corresponding maximum heat flux increase by a factor of 2.7. For high reentry velocities the low pressure inflatable leading edge fairings may be sized to provide a system concept for trade-off of stagnation temperature and structural material temperatures, weight strength ratio at elevated temperature, material costs, and total system weight.

The erectable, rigid leading edge configuration minimizes the sharp-edge creasing of the flexible fabric in the stowed position and also permits more rapid deployment of the wing. The beam may also serve as the stowage fairing thereby reducing the total system weight. The disadvantages of this arrangement include geometric restraints on the hinge and stowage configuration and reduced chordwise bending stiffness and torsional stiffness. A weight estimate for a rigid beam structure without the low pressure inflatable boom fairing is shown in Figure 12. A silicone coated aluminum alloy honeycomb structure was utilized with a fiberglass wing membrane fabric impregnated with silicone matrix material.



WEIGHT BREAKDOWN  
TITAN III SOLID BOOSTER ERECTABLE STRUCTURE

L. E. Boom Structure	2,510 lb
Erection Truss Structure	175 lb
Wing Membrane	1,015 lb
Erection Mechanism	45 lb
Nose Fairing	95 lb
Reaction Control System (N <sub>2</sub> )	46 lb
Aerodynamic System	<u>275 lb</u>
Sub-Total	3,161 lb
Titan Solid Booster	<u>49,914 lb</u>
Total Recovered Weight	54,075 lb

FIGURE 12

UPPER STAGE OR SATELLITE RECOVERY SYSTEMS

Figure 13 shows a phantom view of a recovery system design study for the recovery from orbit or sub-orbital velocities of a 2000 lb. class upper stage or satellite payload. The wing loading of 9.5 psf would permit a landing speed of 50 knots and with a landing flare maneuver the sink rates can be reduced to less than 5 fps. This structural arrangement is similar to the system discussed in the previous paragraph. However, the higher reentry heating temperatures experienced by the orbital velocity vehicle (ref. 5) requires the use of stainless steel or super-alloy materials of construction and phenolic or silicone ablative coatings on the leading edge surfaces. The X994 fiberglass wing membrane fabric has excellent high temperature properties but is susceptible to damage from sharp edge creasing. An efficient, but more costly, alternate wing membrane material is the ultra-fine filament super alloy fabrics under development for similar high temperature applications. Fabrication processes for the development of full scale paragliders utilizing these high temperature fabrics is currently under contract at Space-General (ref. 6)

RETRIEVAL AND LANDING

The development of high lift to drag ratio paraglider wings will permit extended subsonic glide ranges of several hundred miles to the original launch sites or alternate retrieval areas. A study (ref. 1) of the Saturn booster



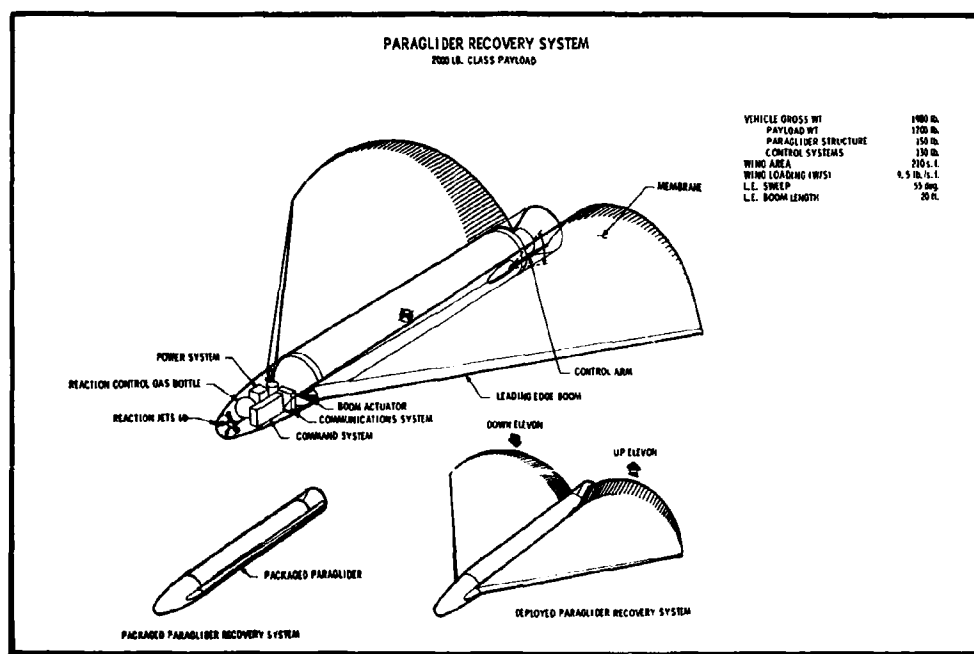


FIGURE 13

paraglider system carrying three 20,000 lb. thrust fan jet engine with an installed weight of 8300 lbs. would provide an additional range increment of 102 nm using only the 30,000 lbs. of on-board Saturn reserve fuel. An additional thirty thousand pounds of fuel would increase the incremental range by 200 nm.

Another study, by All American Engineering Co., showed that a C-130 B cargo airplane could air-snatch a 50,000 lb. Titan III solid booster paraglider reentry system and air tow it 200 nm at 140 mph to a landing site with a fuel reserve of 6400 lbs. of fuel.

Landing techniques for unmanned vehicles has been thoroughly demonstrated by the SM-62 and Regulus missiles. Numerous remote controlled landings were made successfully with the 30,000 lb. SM-62 with approach speeds above 250 knots. The extremely low landing speeds of a typical paraglider system would greatly simplify the automatic or command control landings of similar payloads.

Landings over rough terrain or high seas could be accomplished by guiding the recovery vehicle into a balloon supported arresting cable network. The balloons would be moored to sea anchors with nylon cables to absorb the engagement energy. After engagement the payload could be lowered to the surface, or deck of the ship, or towed back to a prepared site while supported by the balloons.



### SUMMARY

These booster recovery system analyses and other Space-General orbital velocity recovery system studies indicate the paraglider reentry system provides a simple, low weight, low volume concept for the control and recovery of missile payloads. The flexibility of these configurations imposes minimum restraints and penalties on the launch system and payload. Existing wind tunnel, low speed flight test, and materials test data is available to permit the initiation of a full scale development program at the present time.

The economic, security, and reliability considerations of the space program requires that we initiate this development program at the earliest possible date. A recent two-year government funded study has shown that a manned rigid winged recovery system for large boosters can be developed with a payload penalty of 20%. The development cost was estimated to be less than the savings of 30% in operating costs. The studies summarized in the paper presented today indicate that an unmanned paraglider recovery system could be developed for 5% to 10% of the payload weight with only minor modification of current vehicles and correspondingly larger program savings.

### REFERENCES

1. Brodsky, R.F., and J.D. McNerney, "Booster Recovery by Paraglider Methods", Interplanetary Missions Conference, American Astronautical Society, Los Angeles, Calif. 1963.
2. Rogallo, F.M., "Flexible Wing Research and Development", NASA Langley Research Center, presented at Symposium on Retardation and Recovery at WADC, Nov. 1962.
3. Penland, J.A., "A Study of the Aerodynamic Characteristics of a Fixed Geometry Paraglider Configuration and Three Canopies with Simulated Variable Canopy Inflation at Mach Number of 6.6.," NASA TN D-1022 dated March 1962.
4. Johnson, J.L., "Low Speed Wind Tunnel Investigation to Determine Flight Characteristics of a Model Parawing Utility Vehicle", NASA TN D-1255 dated August 1962.
5. Crawford, J.E., "Single and Multicrew Inflatable Reentry Vehicles", Advances in the Astronautical Sciences Vol. 16 Part One, Western Periodics Co., Sept. 1962.
6. Warren, F., and Keville, J.F., "The Design and Environmented Standard Testing of a Reentry Paraglider", Advances in the Astronautical Sciences Vol. 16 Part One, Sept. 1962; Western Periodics Co.
7. Brodsky, R.F. and J.D. McNerney, "Parametric Study of Space Recovery Vehicles", AIAA No. 63-275 dated June 1963.



## SPACE ELECTROMAGNETICS



RESONANT-SCATTER DETECTION OF MIDCOURSE VEHICLES:  
MINIMUM DETECTABLE NUMBERS OF RESONANT-SCATTERING PARTICLES

Leonard Glatt

Space Technology Laboratories, Inc.  
Physical Research Division  
Redondo Beach, California

ABSTRACT

Consideration is given to the possibility of resonant-scatter detection of the rarefied clouds surrounding midcourse vehicles. Minimum detectable numbers of resonant species particles are determined for two detection configurations: 1) A satellite-based downward-looking detection system operating in the 3000 to 2000 Å spectral domain; 2) An upward-looking detection system flown at altitudes of 25 or 30 kilometers. It appears likely that the rarefied fuel residual accompanying a midcourse vehicle will contain detectable amounts of some gaseous species. It will require further study to determine whether or not detectable numbers of atoms or molecules can result from outgassing or from sputtering processes.

The work described in this paper was performed under Air Force Contract No. AF04(694)-1 for the Ballistic Systems Division, AFSC.



RESONANT-SCATTER DETECTION OF MIDCOURSE VEHICLES:  
MINIMUM DETECTABLE NUMBERS OF RESONANT-SCATTERING PARTICLES

Leonard Glatt  
Space Technology Laboratories, Inc.  
Physical Research Division  
Redondo Beach, California

1. INTRODUCTION

The purpose of this report is to delineate parameters pertinent to the problem of passive detection and tracking of a rocket during its midcourse phase by observation of solar photons scattered from an associated gaseous cloud. It has been established that most space vehicles carry along their orbit a highly rarefied collection of gaseous constituents resulting either from fuel tank residual or from the outgassing of the vehicle. This tenuous gaseous cloud will scatter a fraction of the solar radiation impinging upon it. It is reasonable that efficient resonance scattering should occur at spectral frequencies characteristic of strong quantum transitions of the various species of molecules, atoms or ions. Owing to the rarefied condition of the gaseous matter, the spectrally degrading effect of nonradiative collision processes, which is dominant at higher pressures, will be reduced to insignificance. The possibility then exists that the solar radiation scattered by a strong resonance line may prove to be sufficient for passive detection and tracking.

Two types of detection-tracking configurations will be considered. In the first, a satellite-based optical system will scan in its lower hemisphere. The middle, or perhaps the extreme, ultraviolet will give the optimum ratio of signal to background noise for this type of configuration. In the second type of configuration, an optical system utilizing visible or near ultraviolet radiation will scan in its upper hemisphere. This latter type of system should be flown at 25 or 30 kilometers or higher to minimize background noise.

An appropriate signal-to-noise relation is developed in Section 2, and then reduced to equations suitable for background and for system noise limited conditions. These two conditions apply respectively to the first and second of the detection configurations specified in the preceding paragraph. The signal is assumed to arise from primary resonant scattering of solar beam photons of wavelength  $\lambda_1$  by some  $i$ th species of atom, molecule or ion in the rarefied gaseous cloud surrounding the "target"



vehicle. The diffuse background radiation field is assumed to arise from a "residual" of nonresonant primary scattering of  $\lambda_1$ -photons by upper atmosphere molecules within the field of view  $\Omega$  of the detection system. The background radiation field then is characterized by a spectrally dependent atmospheric coefficient of diffuse reflection,  $r_\lambda$ . Similarly, the "background noise" is characterized by a parameter  $\delta r_\lambda$ , which represents the spatial-temporal fluctuations of  $r_\lambda$  as averaged over an elementary (least resolvable) field of view,  $\Omega_e$ , of the detecting optical system. Background noise is to be minimized by proper choice of operating spectral region and, for the upward-looking configuration, by a sufficiently high altitude of operation.

In accordance with the assumptions of the preceding paragraph, the output voltages generated by both the resonant scattered photon signal and by the nonresonant scattered background field are similarly dependent upon certain optical system parameters, and upon the spectral intensity  $H_\lambda$  of the solar beam and the angle  $\Psi$  through which it is scattered into the optical system. The system noise voltage, on the other hand, is usually independent of radiation field and optical parameters.

The resonant scattered photons of wavelength  $\lambda_1$  generate a signal voltage  $V_s$  at each "least resolvable" retina element upon which they are focussed. Assume that  $m_i$  resonant species particles are subtended by the elementary field of view  $\Omega_e$  corresponding to a given retina element. These  $i^{\text{th}}$  species of particles will exhibit an effective resonant scatter cross section  $\sigma_\lambda^i$ . An integrated line strength parameter  $\Sigma_i$  is defined by the relation,

$$\Sigma_i = \int_{\lambda_1 - \delta_1 \lambda}^{\lambda_1 + \delta_1 \lambda} \sigma_\lambda^i d\lambda \quad (1)$$

where  $\delta_1 \lambda$  represents a few "line widths". It is clear that, to at least a first approximation, signal voltage  $V_s$  should be directly proportional to the  $m_i \Sigma_i$  product.

The  $m_i$  parameter is dependent upon  $\Omega_e$  and the "target range"  $R$ , as well as upon the number and spatial distribution of  $i^{\text{th}}$  species particles in the tenuous cloud. Let  $n_i$  represent the number of  $i^{\text{th}}$  species cloud particles projected on a unit area normal to the direction of view. Then  $m_i$  is equal to  $n_i R^2 \Omega_e$ . For a realistic selection of  $R$  equal to  $10^3$  kilometers and  $\Omega_e$  equal to  $10^{-6}$  steradians,  $m_i$  is numerically equal to  $n_i$  when the latter is expressed in units of particles per square kilometer. The value  $n_i$  should be defined to represent a suitable mean value of the projected area density of  $i^{\text{th}}$  species



particles evaluated over the corresponding  $\Omega_p$  field of view. If this is done, the minimum detectable value of  $n_i$  should be relatively insensitive to changes in range R.

The signal-to-noise relations presented in Section 2 follow directly from an elaboration of the considerations discussed in the preceding paragraphs. Section 3 evaluates  $\Sigma_i$  and a radiative transfer parameter  $\gamma$  which appears as an "occlusion" factor in the signal-to-noise relations. The integrated line strength  $\Sigma_i$  is directly proportional to  $\lambda_i^2 f_i$ , where  $f_i$  is a dimensionless quantity defined as the effective oscillator strength for resonant scattering transitions. The parameter  $f_i$  is of the order unity for strong atomic resonance lines in a highly rarefied low temperature gas. Resonant scatter oscillator strengths for molecular bands are one to three orders of magnitude weaker than for atomic lines.

Sections 4 and 5 present sample computations of minimum detectable values,  $n_d$ , of the  $n_i$  parameter. (The  $i$  subscripts and superscripts used to denote a particular species of atom, ion or molecule often will be omitted hereafter.) Reasonable assumptions are made concerning the various system parameters. The computed  $n_d$  values of resonant species particles per square kilometer of projected area of the gaseous cloud are:  
 1)  $5 \cdot 10^{21} f^{-1}$  for the (background noise limited) downward-looking configuration; 2)  $10^{20} f^{-1}$  for the (system noise limited) upward-looking configuration. For comparison there are  $6 \cdot 10^{23}$  molecules in a gram molecular weight, and  $2.5 \cdot 10^{19}$  per  $\text{cm}^3$  of gas at STP. These are the most significant results presented by this paper. It appears likely that the rarefied fuel residual accompanying a vehicle during its midcourse phase will contain detectable amounts of one or more gaseous species. Further study will be required to determine whether detectable number of atoms or molecules can result from outgassing or sputtering processes.

Appendix A presents a discussion of the relation between the "resonant scatter oscillator strengths" utilized in this paper and the more commonly encountered absorption (or emission) oscillator strengths for spectral transitions. A discussion of possible resonant scattering constituents in the rarefied clouds accompanying midcourse vehicles is presented in Appendix B. Appendix C presents tables of absorption oscillator strengths for suitable transitions of selected atoms and molecules.

## 2. SIGNAL-TO-NOISE RELATIONS

It has become customary to specify sensitivity of detecting optical systems in terms of "Noise Equivalent Power" or NEP. For an image tube NEP is defined as the intensity of the radiant input signal, in watts per least resolvable retina element,



required to produce an output signal voltage  $V_s$  just equal to the internally generated rms noise voltage of the system. The smaller the NEP, the more sensitive is the system response. Most optical radiation sensors are linear in the sense that under operation conditions their signal voltage output is directly proportional to the signal input of radiant power. The output ratio of signal-to-system-noise is then equal to the ratio of an effective radiant power input signal to the system NEP.

The background noise power input to a least resolvable detector retina element will be designated by the symbols BNP. Since the background and system noises may be assumed to possess zero cross correlation, the total effective noise input may be represented by an rms combination of NEP and BNP terms. Let  $P_s$  represent an effective radiant power input signal.  $P_s$  will be defined as equal to the increment of total radiant power input to a least resolvable retina element upon which the resonant scattered radiation is focussed, as compared to the background radiation inputs to adjacent retina elements of equal extent. The desired ratio of signal and noise output voltages,  $V_s$  and  $V_n$ , is then given by the expression,

$$V_s V_n^{-1} = P_s \left[ (\text{NEP})^2 + (\text{BNP})^2 \right]^{-1/2} \quad (2)$$

The discussion presented in the Introduction leads directly to a specification of the  $P_s$  and BNP terms appearing in Eq. (2). Consider first the BNP term. The background radiation field has been assumed to arise from a residual of primary Rayleigh scattering in the upper atmosphere. Assume that the background radiation directed into the optical system was scattered through an angle  $\Psi$  by a hypothetical "background surface" of mean diffuse spectral reflectance  $r_\lambda$ . Let  $R_b$  represent the optical range to this "surface". Each unoccluded retina element will view a projected area  $R_b^2 \Omega_e$  of this "surface". The hypothetical background range  $R_b$  cancels out, since the objective of the optical system will subtend an incremental solid angle  $A_o R_b^{-2}$  at each point of this projected area. The mean power input of  $d\lambda$ -background radiation to retina elements which do not "see" intervening resonant scattering particles thus is equal to

$$(3/16\pi)(1 + \cos^2\Psi) A_o \Omega_e H_\lambda r_\lambda \alpha_\lambda d\lambda \quad *$$

The desired BNP term then is obtained by substituting  $\delta r_\lambda$  for  $r_\lambda$ , and integrating over a  $2 \delta_2 \lambda$  interval determined by the spectral decay of the system filter function  $\alpha_\lambda$ . That is,

\*The presence of an appreciable optical density of aerosol particles in the upper atmosphere would require modification of the  $(3/16\pi)(1 + \cos^2\Psi)$  term.



$$\text{BNP} = (3/16\pi)(1 + \cos^2\psi)A_0\Omega_e \int_{\lambda_1-\delta_2\lambda}^{\lambda_1+\delta_2\lambda} H_\lambda \delta r_\lambda \alpha_\lambda d\lambda \quad (3)$$

The  $P_s$  term can be derived in a similar fashion. A retina element viewing the gaseous cloud surrounding the midcourse vehicle will "see"  $R\Omega_e n \gamma_\lambda$  resonant scattering particles, each of which will scatter into the objective lens an amount of  $d\lambda$ -increment radiant power equal to  $(3/16\pi)(1+\cos^2\psi)A_0 R^{-2} H_\lambda \sigma_\lambda d\lambda$ . The  $\gamma_\lambda$  occlusion factor is discussed in Section 3. In addition to spectral filtering losses, however, this input "target power" will suffer an "image degradation" spreading into contiguous retina elements. This signal degradation, which is contributed to by both optical and electronic read-out components of the detection system, will be symbolized by a reduction factor  $\Delta$ . A typical value of  $\Delta$  for a total of  $m_1$  isolated resonant scattering centers all distributed within a solid angle less than  $\Omega_e$  might be of the order of 0.6. However, if the  $m_1$  particles were a fraction of an appreciably larger number which were fairly uniformly imaged upon a retina area subtending several least resolvable elements, then the  $\Delta$  value near the image center would be essentially unity. No degradation factors  $\Delta$  are required to describe the response to the fairly uniform background radiation field.

The effective  $d\lambda$ -increment radiant power input to a specified retina element from the resonant scatter centers that it "sees" is equal, thus, to  $(3/16\pi)(1+\cos^2\psi)A_0\Omega_e n \Delta H_\lambda \gamma_\lambda \sigma_\lambda d\lambda$ . But this same retina element receives, in addition, a background radiation input from an incremental solid angle equal to  $\Omega_e(1-n\sigma_\lambda\gamma_\lambda)$ . By definition,  $P_s$  is equal to a  $\lambda$ -integral over the amount by which the sum of these target and partial background contributions exceeds the full background input to neighboring retina elements. That is,

$$P_s = (3/16\pi)(1 + \cos^2\psi)A_0\Omega_e n \int_{\lambda_1-\delta_1\lambda}^{\lambda_1+\delta_1\lambda} H_\lambda \alpha_\lambda \gamma_\lambda \sigma_\lambda (\Delta - r_\lambda) d\lambda \quad (4)$$

It will be noticed that the target range  $R$  does not appear explicitly in Eq. (4). Target range dependence appears implicitly, however, in the number density parameter  $n$ , which has been defined as the mean value, evaluated over an  $\Omega_e$ , of the number of resonant species particles projected on to a unit area. It is clear that  $n$  eventually will begin to decrease as  $R^{-2}$ . Also,  $\Delta$  is unity for sufficiently small  $R$ , but begins to decrease somewhat when the solid angle subtended by the resonant



scattering cloud shrinks to less than a few  $\Omega_0$ .

The integral in Eq. (4) extends over a spectral domain of width  $\delta_1\lambda$  on either side of  $\lambda_1$ , the center of the resonance line of interest;  $\delta_1\lambda$ , which will be of the order of  $5 \cdot 10^{-3} \text{ \AA}$ , represents a small multiple of the half-width of the Doppler broadened profile of the absorption cross section  $\sigma_\lambda$ . The  $\delta_2\lambda$  increment which sets the limits of the integral in Eq. (3) is determined by the optical system filter function  $\alpha_\lambda$ . System design considerations demand that  $\delta_2\lambda$  be appreciably larger than  $\delta_1\lambda$ . The Doppler profile of  $\sigma_\lambda$  is determined by the dispersion in the velocities of the individual resonant-scattering particles in the gas cloud surrounding the midcourse vehicle. The observed wavelength  $\lambda_1$  of the resonance line center is, however, dependent upon the mean velocity of the gas cloud (approximately the velocity of the midcourse vehicle) relative to the observing optical system. Ideally,  $\alpha_\lambda$  should be unity within and zero outside of a selected  $2 \delta_2\lambda$  interval just broad enough to include the ensemble of probable Doppler shifted  $\lambda_1$  lines (approximately  $0.2 \text{ \AA}$ ). The transmissions of actual filters, however, exhibit spectral decay characteristics considerably less steep than that of the ideal step-function. Achievable  $\delta_2\lambda$  values also probably will be very much wider than those for optimum width. Moreover, the transmission for spectrally narrow filters is usually appreciably less than unity, with the maximum transmission decreasing inversely with the width of the optical pass band  $2 \delta_2\lambda$ . It appears that there would have to be a system design trade-off between the decreased transmission of the radiant power "target signal" input owing to the lowered  $\alpha_{\lambda_1}$  (perhaps lower than 0.1 or even 0.01) of a very narrow filter, and the increased input of background noise arising from the use of a broader filter  $\alpha_{\lambda_1}$  closer to unity. Practical limitations on realizable optical filters may demand that  $2 \delta\lambda$  be at least  $25 \text{ \AA}$  in width, and perhaps considerably wider.

The  $r_\lambda$  and  $\delta(r_\lambda)$  symbols appearing in Eqs. (3) and (4) have been defined as representing, respectively, a mean value and a spatial-temporal fluctuation of the diffuse upward reflection by the atmosphere of impinging solar radiation. Both of these quantities are to be evaluated for the specific field of view scanned by the search-track system. These quantities will vary temporally and as a function of the geographical location of the background air mass and underlying terrain. They are also dependent upon the cosines of the respective zenith angles of the impinging solar beam and of the viewed scattered radiation. The effective contamination of the output signal arising from background noise is dependent also upon characteristics of the optical system and the space scanning process. It is often possible to utilize fairly effective techniques to help discriminate "target signals" from background noise.



It appears, however, that any possibility of implementing midcourse detection by observation of resonance scattering against a background of atmospheric radiance would depend upon finding a strong resonance line in a favorable spectral region where  $r_\lambda$  and particularly  $\delta(r_\lambda)$  are orders of magnitude less than unity. This restriction eliminates the visible spectral region from consideration except for detection configurations in which the optical system is at a lower altitude than the target of interest. When the sun is near the horizon and the air is clear, and when diffuse reflection occurs from freshly fallen snow or from the top of thick stratus clouds, then  $r_\lambda$  can be as high as 0.9 for visible radiation. The corresponding spatial fluctuations of diffuse reflectivity in the visible region may then produce  $\delta(r_\lambda)$  values of order of magnitude 0.1 or greater. In contrast,  $r_\lambda$  is the order of  $10^{-2}$  or less for wavelengths shorter than approximately 2900 Å, and is of the order of  $10^{-3}$  between 2700 and 2300 Å. The  $\delta(r_\lambda)$  values for this spectral domain should be at least one order of magnitude (and probably two orders of magnitude) lower than the corresponding  $r_\lambda$  values. The atmospheric reflection properties for the middle and extreme ultraviolet spectral regions therefore are the most favorable for use in satellite-based optical systems.

The greatly reduced  $r_\lambda$  and  $\delta(r_\lambda)$  values for wavelengths shorter than 3000 Å arise from intense absorption by atmospheric ozone molecules and by  $O_2$  molecules above the ozone layer. Owing to dissociation and predissociation processes, and to nonradiative transitions caused by molecular collisions, at most a very small fraction of the absorbed solar beam photons are re-emitted as resonance-fluorescence radiation. The very weak background radiation field arises almost entirely from a small residual of nonresonant scattering by upper atmosphere molecules (and perhaps by upper atmosphere aerosols). The  $r_\lambda$  values then represent the minute fraction of solar photons which escape absorption both in their downward path before being scattered upward and in their consequent upward path back out of the atmosphere. Since attenuation owing to absorption is so predominant, multiple scattering processes can be neglected, and Rayleigh type angular dependence previously assumed should be valid unless the aerosol concentration is quite appreciable.

## 2.1 System and Background Noise Limited Conditions

While for some choices of system parameters the background and system noise terms may turn out to be of the same order of magnitude, it is more common for one of these terms to predominate sufficiently so that the other noise term may be neglected. The respective detection (or tracking) configurations are said to be "system noise limited", or "background noise limited".

It is seen from Eqs. (4) and (3) that both the target



signal and the BNP are directly proportional to  $A_0$  and to  $\alpha_\lambda$ . The NEP term, however, is not dependent upon these optical system parameters. The  $V_s/V_n$  ratio for a "system noise limited" configuration can be improved, thus, by increasing the objective lens area  $A_0$  or by obtaining a filter with as near unity as possible transmission at  $\lambda_1$ . In theory, a sufficient increase in the  $A_0\alpha_\lambda$  product at  $\lambda = \lambda_1$  eventually would increase the BNP (and the target signal) to the point where it would equal the NEP. A further increase of this product, if realizable, then would shift the configuration from a "system noise limited" to the optimum "background noise limited" condition. No appreciable improvement in signal-to-noise ratio would result from a still further increase, even if such an increase were realizable. System constraints and physical limitations sometimes prevent the realization of an optimum "background noise limited" condition. For the "system noise limited" condition, Eq. (2) reduces to the form:

$$V_s/V_n \approx \frac{\left\{ (3/16\pi)(1 + \cos^2\psi) A_0 \bar{\alpha}_\lambda n \langle H\alpha \rangle_1 \Delta / \Sigma_1 \right\}}{\text{NEP}}, \quad (5)$$

System Noise Limited

where  $\Sigma_1$  was defined by Eq. (1). It has been assumed that  $\lambda_1$  falls in a suitable spectral region so that  $1 > \Delta > r_\lambda$ . The term  $\langle H\alpha \rangle_1$  represents a suitable mean value of the relatively slowly varying  $H_\lambda \alpha_\lambda \gamma_\lambda$  product for the  $2 \delta_1 \lambda$  interval about  $\lambda_1$ .

For the "background noise limited" condition,

$$V_s/V_n \approx \frac{n \langle \gamma \rangle_1 \Delta \Sigma_1}{\langle \delta r \rangle_2 (2\delta_2 \lambda)}. \quad (6)$$

The effective occlusion factor  $\langle \gamma \rangle_1$  represents an average of  $\gamma_\lambda$  evaluated over a relatively narrow  $2 \delta_1 \lambda$  spectral interval centered on  $\lambda_1$ , while the effective atmospheric reflection factor  $\langle \delta r \rangle_2$  is a mean value of  $\delta r_\lambda$  evaluated over an appreciably larger  $2 \delta_2 \lambda$  interval.

A currently realizable NEP value for a system designed merely to track a target previously "acquired" by some auxiliary mechanism would be of the order of  $10^{-17}$  watts. A system designed to perform search and acquisition as well as tracking functions might be limited by the current state of the art to an NEP of the order of  $10^{-14}$  to  $10^{-13}$  watts or greater. It is reasonable to expect, however, that within a few years predictable improvements in the state of the art may reduce this latter figure to  $10^{-16}$  or even to  $10^{-17}$  watts (1).

The radiant power input of background noise arising from



spatial-temporal gradients of diffuse upward atmospheric reflectance is delineated in Eq. (3). It is evident that the magnitude of the RNP term is dependent upon the wavelength  $\lambda_1$  of the resonance line to be detected. If the position of  $\lambda_1$  and the (constrained) choice of system parameters determine a BNP greater than  $10^{-13}$  or perhaps  $10^{-14}$  watts, then an optimum "background noise limited" detection configuration could be achieved by the use of the best current state-of-the-art imaging tubes (1). A detection configuration whose system parameters determine a BNP of the order of  $10^{-16}$  to  $10^{-14}$  watts quite possibly may be reduced to the "background noise limited" condition by the near future development of improved imaging tubes.

Neglecting the relatively slowly varying angular dependence, Eq. (3) may be expressed as,

$$\text{BNP} \propto A_0^2 \langle H_{\lambda} \delta r_{\lambda} \rangle_2^2 \delta_2 \lambda \quad (3a)$$

The  $H_{\lambda}$  and  $\delta r_{\lambda}$  terms can be expected to exhibit relatively slow variation over the  $2 \delta_2 \lambda$  filter function transmission band.

Both  $H_{\lambda}$  and  $\delta r_{\lambda}$  are relatively quite large in the visible and near ultraviolet, and drop off rapidly with extension to shorter wavelengths. Detection of upward hemisphere directed reradiation from a visible or near ultraviolet resonance line undoubtedly would be "background noise limited" even with relatively small diameter optics. It would appear from Eq. (6), however, that an implausibly large  $n \Sigma_1$  product would be required to produce a detectable signal when  $\delta r_{\lambda}$  is of the order of 0.1. Below 2000 Å,  $H_{\lambda}$  falls off so rapidly that an excessively large optical aperture  $A_0$  might be required to produce an optimum "background noise limited" condition. It appears, however, that such an optimum condition could be realized with reasonable system parameters if the resonance line to be detected falls within approximately the 2200 to 2900 Å spectral region. A predictable improvement over the system NEP's of the best current imaging tubes may be required to achieve this goal.

Numerical computations based upon the "background noise limited" expression are given in Section 4. These computations apply primarily to the favorable middle ultraviolet spectral region. It is assumed that the detection system is in orbit at a higher altitude than that of the midcourse rocket to be detected, and that the upward direction diffuse background radiation field arises from a residual of nonresonant scattering by the atmosphere.

A lower altitude detection system below the rocket but above most of the atmosphere would minimize the background



radiation input arising from atmospheric scattering. This would permit the utilization of resonance lines in the visible or near ultraviolet spectral regions where the solar intensity  $H_\lambda$  is near maximum. It is probable that satellite orbits of sufficiently low altitudes to utilize upper hemisphere scanning detection systems would be ruled out by systems constraints. However, it is possible that this type of scanning configuration might be implemented by the use of high flying balloons or of U-2 aircraft. It appears probable that an optical detection system operating in the visible or near ultraviolet, and scanning in the upward hemisphere, would be "system noise limited" rather than "background noise limited" if it were flown at altitudes above 25 or 30 kilometers. This statement is based upon current understanding of the (scattering) "optical density" of the upper atmosphere, and of the expected spatial-temporal fluctuations of this parameter for the visible spectral region. A numerical computation embodying a "system noise limited" condition is given in Section 5.

### 3. EVALUATION OF THE $\gamma$ AND $\Sigma$ PARAMETERS

#### 3.1 The Occlusion Factors $\gamma_\lambda$ and $\langle \gamma \rangle_1$

The occlusion factor  $\gamma_\lambda$  represents the ratio to  $n\sigma_\lambda$  of the true spectral absorption factor for the gaseous cloud. Likewise, the mean value term  $\langle \gamma \rangle_1$  represents the ratio to  $n\Sigma_1$  of the integrated absorption factor for the resonance line at  $\lambda_1$ . Consider first a narrow column aligned parallel to the direction of the solar beam. Let the length of this column be represented by  $x$ , and the spatially variable number density of the resonant species of particles be represented by  $N$ . The absorption optical density  $\tau_\lambda$  of the column is defined by

$$\tau_\lambda = \sigma_\lambda \int_0^x N_\xi d\xi \quad (7)$$

Or, taking a mean value over an elementary field of view  $\Omega_e$ ,

$$\langle \tau_\lambda \rangle_{\Omega_e} = n\sigma_\lambda \quad (7a)$$

The  $d\lambda$ -increment of solar radiation absorbed by a unit cross section of the gaseous column is  $H_\lambda d\lambda(1 - e^{-\tau_\lambda})$ . Thus, by definition of  $\gamma_\lambda$  it follows that,



$$\gamma_\lambda \approx \frac{H_\lambda d\lambda \langle 1 - e^{-\tau_\lambda} \rangle_{\Omega_e}}{H_\lambda d\lambda n \sigma_\lambda} \approx \left\langle \frac{1 - e^{-\tau_\lambda}}{\tau_\lambda} \right\rangle_{\Omega_e} \quad (8)$$

Similarly, for the integrated absorption by the complete resonance line,

$$\langle \gamma \rangle_1 \approx (n \Sigma_1)^{-1} \left\langle \int (1 - e^{-\tau_\lambda}) d\lambda \right\rangle_{\Omega_e} \quad (9)$$

where the integration is over a  $2 \delta_1 \lambda$  interval about  $\lambda_1$ .

It is seen that both  $\gamma_\lambda$  and  $\langle \gamma \rangle_1$  approach unity for sufficiently small values of resonance optical thickness  $\tau_\lambda$ . For very large values of  $\tau_\lambda$  these  $\gamma$ -parameters approach  $\langle \tau_\lambda \rangle^{-1}$ , where the average is evaluated over an  $\Omega_e$ . The value of  $\langle \gamma \rangle_1$  for intermediate values of  $\tau_\lambda$  depends upon the shape of the resonance line as well as upon its spectrally integrated intensity  $\Sigma_1$ . Doppler line profiles are pertinent to the problem of current interest. Numerical values of a quantity equivalent to  $\langle \gamma \rangle_1$  for lines with Doppler contour have been calculated by Ladenburg (2), and are plotted by Penner in his recent book (3). The ordinate  $\bar{e}$  in Penner's Fig. 4-1 is equivalent to  $\langle \gamma \rangle_1$ , while his abscissa symbolized as P'X is proportional to the denominator of Eq. (9). Values of

$$\Sigma_1 \int_0^x N_t d\xi$$

characteristic of reasonable gaseous cloud models containing a sufficient number of resonant particles for detection purposes lead to equivalent P'X values of the order of 0.5, and then to corresponding  $\langle \gamma \rangle_1$  values between 0.95 and 0.8. However, there will be some spectral degradation of the absorbed solar photons resulting from nonresonant de-excitation processes. Conservative  $\langle \gamma \rangle_1$  values of 0.7 and 0.9 therefore will be used in the computations given in Sections 4 and 5.

### 3.2 The Integrated Line Strength $\Sigma_1$

Chapter 2 of Penner's book (3) defines several quantities proportional to the parameter here designated as  $\Sigma_1$ . His  $S_{lu}$  parameter, for example, can be specified by the relation,



$$S'_{lu} = c\lambda_i^{-2} N\Sigma_i \quad (10)$$

Here  $c$  has its usual meaning of the speed of light, while the other symbols have been defined previously (the  $lu$  subscript is equivalent to the  $i$  subscript or superscript). Then, from Penner's Eq. (2-20),

$$\Sigma_i = (\pi e^2/mc^2) \lambda_i^2 (N_l/N) (1 - \exp \frac{-hc}{kT\lambda_i}) f_i \quad (11)$$

Here  $e$  and  $m$  denote, respectively, the electronic charge (in esu) and mass (in gm/electron), while  $h$ ,  $k$  and  $T$  have their usual meanings.  $N_l$  and  $N$  denote respectively, the population density of the lower quantum state and the total number density of the resonating species. The dimensionless parameter  $f_i$  represents the "oscillator strength" of the transition. The sum of the oscillator strengths for all possible transitions and states of an atom equals the total number of electrons in the atom. For tightly bound nonparticipating, inner electron shells the sum of the oscillator strengths equals the number of valence electrons. The  $f$ -values for the strongest atomic lines (or sum of the  $f$ -values for a multiplet) is approximately 1 for atoms or ions with a single valence electron, and approaches 2 for atoms with a pair of valence electrons in an  $ns$  subshell (delineated by  $ns^2$ ).

For conditions of current interest,  $(N_l/N)$  is essentially unity, while  $hc\lambda_i^{-1} \gg kT$ . This reduces Eq. (11) to the form,

$$\Sigma_i \approx (\pi e^2/mc^2) \lambda_i^2 f_i \quad (11a)$$

For  $\lambda_i$  in the vicinity of  $2500 \text{ \AA}$  (or  $2.5 \cdot 10^{-5} \text{ cm}$ ), this gives a  $\Sigma_i$  value of approximately  $6 \cdot 10^{-14} (\text{cm}^2 \text{ \AA}) f_i$ . In the visible spectral region  $\Sigma_i$  would be approximately  $2 \cdot 10^{-13} (\text{cm}^2 \text{ \AA}) f_i$ .

#### 4. AREA DENSITY OF RESONANT PARTICLES REQUIRED FOR "BACKGROUND NOISE LIMITED" DETECTION FROM A SATELLITE

The following computation is based upon the "background noise limited" expression given in Eq. (6). It will be assumed that the detecting optical system is responsive to a selected narrow  $2 \delta_2 \lambda$  increment of the middle ultraviolet spectral region, is mounted on a satellite, and scans a selected portion of its lower hemisphere. A  $V_s/V_n$  ratio of the ten to one will be assumed, since this should suffice for detection (a weaker target



signal could be tracked after acquisition and lock-on). The assumed values for least resolvable field of view  $\Omega_e$  and optical system degradation factor  $\Delta$  will be  $10^{-6}$  sterad and 0.6, respectively. Unless some clever technique for utilizing a monochromator in an imaging system could be developed, it appears that the optical filter pass band would have to be of the order of 25 Å. This 25 Å value, therefore, will be used for the  $2 \delta_2 \lambda$  term, even though an appreciably smaller value would be highly desirable. A 25 Å filter pass band would have the advantage of allowing close multiplet lines to be utilized. A value of  $5 \cdot 10^{-3}$  will be used for  $\langle \delta r \rangle_2$ . This small value for the fluctuations of diffuse reflectance should be of approximately the right order of magnitude for the middle ultraviolet domain, and might be reduced even further by the application of sophisticated background cancellation techniques. In accordance with the results of the preceding section, respective values of 0.7 and  $6 \cdot 10^{-14} \text{ (cm}^2 \text{ Å)} f_1$  will be assumed for  $\langle \gamma \lambda \rangle$  and for  $\Sigma_1$ .

The "background noise limited" expression of Eq. (6) is reproduced below, solved for the mean area density,  $n$ , of resonant particles subtended by an elementary field of view  $\Omega_e$ .

$$n \approx \frac{(V_s/V_n) \langle \delta r \rangle_2 (2 \delta_2 \lambda)}{\langle \gamma \lambda \rangle \Delta \Sigma_1} \quad (6a)$$

Upon substitution of the preceding numerical values, the minimum detectable number  $n_d$  of resonant species particles is,

$$n_d \approx 5 \cdot 10^{11} f_1^{-1} \text{ cm}^{-2} \quad \text{or} \quad 5 \cdot 10^{21} f_1^{-1} \text{ km}^{-2} \quad (12)$$

Mid U.V.: Background  
Noise Limited

Thus, approximately  $5 \cdot 10^{21}$  resonant species particles per square kilometer would suffice for the detection of an intense resonance line of oscillator strength  $f_1$  near unity and with a resonance wavelength  $\lambda_1$  in the middle ultraviolet. This corresponds approximately to  $10^{-2}$  gram-molecules of the resonant species, or to  $2 \cdot 10^2 \text{ cm}^3$  of the pure gas at STP. As indicated in Eq. (12), the minimum detectable number of resonant species particles is inversely proportional to the oscillator strength of the resonance line.

##### 5. AREA DENSITY OF RESONANT PARTICLES REQUIRED FOR SYSTEM NOISE LIMITED DETECTION

The following computation is based on the assumption of an upward-hemisphere-looking detection system flying at an altitude above 25 or 30 kilometers and utilizing the reradiation of solar



photons absorbed by a visible or near ultraviolet resonance line. Equation (5) is used, but in a form solved for  $n$ , and with the angular dependence term  $(3/16\pi)(1 + \cos^2\psi)$  replaced by its spatial mean value of  $1/4\pi$ . That is

$$n \approx \frac{(V_s/V_n)(NEP)(4\pi)}{A_o \gamma_e \langle H \gamma \rangle_1 (\Delta) \Sigma_1} \quad (5a)$$

The values assumed for these parameters are:

- 1)  $V_s/V_n = 10$ ;
- 2)  $\gamma_e = 10^{-6}$  sterad;
- 3)  $\Delta = 0.6$ ;
- 4)  $\langle \gamma \rangle_1 = 0.9$ ;
- 5)  $\langle \alpha \rangle_1 = 0.5$ ;
- 6)  $A_o = 10^2 \text{ cm}^2$ ;
- 7)  $\langle H \rangle_1 = 2 \cdot 10^{-5} \text{ watts cm}^{-2} \text{ \AA}^{-1}$ ;
- 8)  $NEP = 10^{-14} \text{ watts per resolvable element}$ ;
- 9)  $\Sigma_1 = 2 \cdot 10^{-13} \text{ f}_1 \text{ cm}^2 \text{ \AA}$ .

The first three values are the same as those assumed in the computation given in the preceding section. The larger  $\langle \gamma \rangle_1$  value used here results from the reduced density of resonant particles required for detection. The value of 0.5 for  $\langle \alpha \rangle_1$  should be reasonable since better filters are available for visible radiation and since the spectral filter used for background rejection need not be excessively narrow. An objective lens of  $10^2 \text{ cm}^2$  area may be prohibited by the constraints of some systems, but in general should not be excessive. The  $\langle H \rangle_1$  value specified is met or exceeded by the solar beam over a broad visible spectral region. The NEP value of  $10^{-14}$  watts per resolvable element is merely a projection into the near future of currently available image tubes utilizing circuitry, electrical bandwidths, and scanning frame rates similar to those of commercial television. In the near ultraviolet  $\langle H \rangle_1$  drops below  $2 \cdot 10^{-5} \text{ watts cm}^{-2} \text{ \AA}^{-1}$ , but there exists a potential for improvement of the NEP of image tubes responding to this shorter wavelength spectral region to  $10^{-15}$  watts, or perhaps even better. The increase in  $\Sigma_1$  from the value used in the preceding section arises from the  $\lambda_1^2$  term in Eq. (11a).

Upon substitution of the preceding parameter values into Eq. (3a), the minimum detectable area density  $n_d$  of resonant species particles is



$$n_d \approx 1 \cdot 10^{10} f_1^{-1} \text{ cm}^{-2} \quad \text{or} \quad 1 \cdot 10^{20} f_1^{-1} \text{ km}^{-2} \quad (13)$$

Visible and Near  
UV; System Noise  
Limited

Thus, for a sufficiently high altitude upward-viewing optical system approximately  $10^{20}$  resonant species particles per square kilometer would suffice for the detection of an intense resonance line of oscillator strength near unity and with  $\lambda_i$  in the visible or near ultraviolet. This corresponds approximately to  $4 \text{ cm}^3$  of the pure gas at STP, or to  $2 \cdot 10^{-4}$  gram-molecules.

It should be stated here that an upward-looking optical system flown above 25 or 30 kilometers also should be able to detect solar visible radiation diffusely reflected by a mid-course phase nose-cone, or by aluminum oxide particles arising from a solid propellant residual. It is quite possible that the spectral filter pass band could be opened up to a few hundred Å or perhaps even wider before the detection system became background noise limited. However, the detection of certain resonance lines possibly could provide an additional means of discriminating the nose-cone from the fuel tank or from accompanying decoys.

#### APPENDIX A

##### EFFECTIVE OSCILLATOR STRENGTHS FOR THE RESONANT-SCATTER PROCESS

The atomic oscillator strengths presented in the literature are generally those for absorption-induced transitions from a lower state  $m$  to an upper state  $n$ . In the resonant scatter process the lower state  $m$  is usually, but not always, the ground electronic state. The "effective oscillator strength" for the resonant scatter process,  $f_{m \leftrightarrow n}$ , is the product of the absorption  $f$ -value  $f_{m \rightarrow n}$ , by the probability of a spontaneous radiative transition from the excited  $n$  state back to the initial  $m$  state. If the gas is sufficiently rarefied so that non-radiative transition processes are unimportant, then,

$$f_{m \leftrightarrow n} \approx \frac{f_{m \rightarrow n} f_{m \leftarrow n}}{\sum_{\mu < n} f_{\mu \leftarrow n}}, \quad (A-1)$$

where the summation extends over all of the quantum states  $\mu$  that lie below the excited state  $n$ . The symbols  $f_{m \leftarrow n}$  and  $f_{\mu \leftarrow n}$  denote emission oscillator strengths, which are equal to the product of the corresponding absorption  $f$ -value multiplied by the ratio of the degeneracy factors  $g$  of the lower and upper state. That is, for example,



$$f_{m \leftarrow n} = \frac{g_m}{g_n} f_{m \rightarrow n} \quad (A-2)$$

For true "resonance lines" resulting from transitions between the ground and lowest excited states, the dummy symbol  $\mu$  in Eq. (A-1) can refer only to the ground state  $m$ . It is evident from Eq. (A-1) that the effective resonant scatter parameter  $f_{m \leftrightarrow n}$  then is essentially equal to the absorption parameter  $f_{m \rightarrow n}$ . The same holds true when radiative transitions to all excited states lying between the upper state  $n$  and the ground state are forbidden by the selection rules and thus have either zero or relatively very low  $f_{m \leftarrow n}$  values. In other transitions to states  $n$  above the first excited state, however,  $f_{m \leftrightarrow n}$  can be appreciably smaller than the absorption oscillator strength  $f_{m \rightarrow n}$ .

#### A.1 Oscillator Strengths for Molecular Transitions

The preceding discussion and Eqs. (A-1) and (A-2) are valid for electronic transitions in molecules as well as in atoms. However, some qualifications are required. A line or multiplet of an atomic spectrum corresponds to the totality of the vibration-rotation structure of a molecular band system. The total intensities of some types of electronic transitions of molecules are of the same order as for similar electronic transitions in an atom, but are distributed over a large number of lines and possibly a continuous spectrum (4a).

Let, as for atoms,  $m$  and  $n$  represent the electronic excitation of the lower and upper states. The symbols  $v''$  and  $J''$  will represent the respective vibrational and rotational excitations of the lower state  $m$ , while  $v'$  and  $J'$  will represent these quantities for the upper state. The absorption oscillator strength for a single line of a band system will be represented by the symbol  $f_{mv''J'' \rightarrow nv'J'}$ . The oscillator strength of the band system is the sum of these single line  $f$ -values over all the permitted transitions from a typical ( $v''$ ,  $J''$ )-level of the lower  $m$  state. That is,

$$f_{m \rightarrow n} \approx \sum_{v'} \sum_{J'} f_{mv''J'' \rightarrow nv'J'} \quad (A-3)$$

Band System

It is this summed band system parameter which corresponds to the oscillator strength of an atomic line. The oscillator strength  $f_{mv'' \rightarrow nv'}$  for a specified vibrational band of the system is given by the approximate expression

$$f_{mv'' \rightarrow nv'} \approx \sum_{J'} f_{mv''J'' \rightarrow nv'J'} \quad (A-4)$$

Vibrational Band



Here  $J''$  is some representative rotational level of the lower state.

Oscillator strengths for certain band systems of some molecules, and sometimes for individual vibrational bands of these systems, are available in the literature. The  $f$ -values for individual lines of a band system are seldom computed or measured.

The oscillator strengths for the various vibrational bands of a given band system are proportional to their respective Franck-Condon factors  $q(v'', v')$ . If these Franck-Condon factors (4) have been computed, and if the band system oscillator strength is known, then the  $f$ -values for a specified vibrational band is given by the expression,

$$f_{mv'' \rightarrow nv'} \approx \frac{f_{m \rightarrow n} q(v'', v')}{\sum_{v'} q(v'', v')} = f_{m \rightarrow n} q(v'', v') \quad (\text{A-5})$$

The second (reduced) form of Eq. (A-5) follows from a vibrational sum rule (4b), derived from the elementary properties of systems of orthogonal functions. This sum rule states that for proper normalization,

$$\sum_{v'} q(v'', v') = \sum_{v'} q(v'', v') = 1 \quad (\text{A-6})$$

#### A.1.1 Resonant-Scatter by Molecular Bands

It is quite possible that the rotational substructure of a single vibrational band could be utilized for the resonant scatter detection problem of current interest. Indeed, physical restrictions on spectral filters may well demand a  $2\delta_{2\lambda}$  transmission region wide enough to encompass more than an entire vibrational band. If all of the stronger bands in an electronic band system are passed, however, the resultant background noise might be prohibitive. Attention will be concentrated, therefore, upon resonant scattering by molecular  $(v'' \leftrightarrow v')$ -bands rather than by complete band systems, or by individual lines.

Again, as for atoms, it will be assumed that the initial state  $m$  represents either the ground electronic state or a very close multiplet component whose excitation energy is small compared to  $kT$ . It also will be assumed that the vibrational excitation of the lower state is zero ( $v'' = 0$ ). The vibrational excitation energy is generally large compared to  $kT$ , even for  $v'' = 1$ , except for elevated temperatures. Rotational energies are sufficiently small, however, so that several of the first few  $J''$  values may contribute. There are no restrictions on  $v'$  and  $J'$  other than those imposed by the selection rules



( $\Delta J=0, \pm 1$ , etc.)

Molecular electronic bands differ from atomic lines in that there are always excited energy levels between the upper level ( $n, v'$ ) and the ground state. These intervening excited levels consist of all the vibrationally (and rotationally) excited levels for which  $v''$  is not equal to zero, plus those vibrational levels of the  $n$ -state lying below the  $v'$ -level of interest. Thus, even if the upper state  $n$  is the first electronically excited state above the ground state (i.e., a "resonance band system"), consideration must be given to re-emitting radiative transitions of the types  $nv' \rightarrow nv'_i (v'_i < v')$  and  $nv' \rightarrow mv'_i (v'_i > 0)$ . The first type of purely vibrational-rotational transitions can be neglected in comparison to the second since the lifetimes for electronic excitation usually are several orders of magnitude shorter than the lifetimes for vibrational excitation.

A suitable expression for the effective resonant scatter oscillator strength of a vibrational band is then,

$$f_{mv'' \leftrightarrow nv'} \approx \left[ \frac{g_m g_n^{-1} f_{m \rightarrow n}}{\sum_{\mu < n} g_\mu g_n^{-1} f_{\mu \rightarrow n}} \right] \frac{f_{mv'' \rightarrow nv', q(v', v'')}}{\sum_{v''} q(v', v'')} \\ \approx \frac{g_m f_{m \rightarrow n} f_{mv'' \rightarrow nv', q(v'', v')}}{\sum_{\mu < n} g_\mu f_{\mu \rightarrow n}} \quad (A-7)$$

The bracketed term, which arises from Eqs. (A-1) and (A-2), reduces to unity when the  $n$  state is the first excited electronic state above the ground state; i.e., for resonance band systems. The second (reduced) form of the equation follows from Eq. (A-6) and from the fact that the Franck-Condon factors are the same for emission as for absorption. It is seen from Eq. (A-5) that Eq. (A-7) also can be expressed in the form,

$$f_{mv'' \leftrightarrow nv'} \approx \frac{g_m (f_{m \rightarrow n})^2 q^2(v'', v')}{\sum_{\mu < n} g_\mu f_{\mu \rightarrow n}} \quad (A-7a)$$

Resonant-Scatter  
by Molecular Band

For a resonance band system, this reduces to

$$f_{mv'' \leftrightarrow nv'} \approx (f_{m \rightarrow n})^2 q^2(v'', v') \quad (A-7b)$$

Resonant-Scatter by  
Molecular Band of a  
Resonance Band System



Taking the preceding reduction factors into consideration, a typical value for the effective resonant scatter  $f$ -value of a moderately intense molecular band would be of the order of  $10^{-3}$ . Thus, approximately one thousand times as many molecules as atoms would be required to furnish a detectable source of resonant scatter radiation. A substitution of  $f \approx 10^{-3}$  into Eq. (12) and into Eq. (13) gives minimum detectable numbers  $n_d$  of  $5 \cdot 10^{24}$  and of  $10^{23}$  molecules per square kilometer of gaseous cloud cross section for the respective detection configurations of Sections 4 and 5. Larger  $f$ -values, and hence smaller  $n_d$ 's, could result for bands of very intense systems ( $f_{m \rightarrow n} \sim 0.1$  to  $0.4$ ), particularly if the  $q(O, v')$  Franck-Condon factors were strongly peaked in one particular ( $v'' = 0 \rightarrow v'$ ) band.

## APPENDIX B

### POSSIBLE RESONANT SPECIES

It was mentioned in the Introduction that the constituents of the rarefied cloud accompanying a midcourse vehicle may arise from fuel tank residual, or from outgassing by the vehicle. For solid propellant rockets, the dominant contribution to the gaseous cloud probably would result from gases expelled from the reverse thrust ports during the detachment of the re-entry body. For liquid propellant rockets, the dominant contributions probably would result from leakage and evaporation of residual fuel from the closely following last-stage fuel tank. A third source of gaseous constituents arises from sputtering off of atoms from the skin of the vehicle by collisions with the ambient air molecules. While this sputtering loss is insignificant compared to the ablation loss at re-entry, it is possible that it would produce detectable numbers of atoms of some resonant species.

The principle products of rocket fuel combustion are  $CO$ ,  $CO_2$ ,  $H_2O$ ,  $N_2$ ,  $NO$  and  $NO_2$ . In addition, liquid propellant rockets give rise to appreciable quantities of high molecular weight organic compounds, originating primarily in the turbines, while  $HCl$ ,  $AlO$ , and liquid and solid  $Al_2O_3$  are abundant in the exhausts of solid fuel rockets. None of these substances are optimum targets for resonant scatter detection, but some of them should be present in sufficient quantity to make their detection feasible.

A vertical atmospheric column of one square kilometer cross section extending upward from an altitude of 50 km should contain approximately  $10^{26}$  molecules of  $NO$ . The column would contain a smaller number of  $NO_2$  molecules, but increasing orders of magnitude larger numbers of  $CO$ ,  $H_2O$ ,  $CO_2$  and  $N_2$ . The resonance lines of this set of molecules thus should be relatively prominent features of the background noise spectrum. The minimum detectable number of resonant molecules of one of these



species then would have to be at least several orders of magnitude greater than the  $n_d$  values given in Eqs. (12) and (13). In the derivation of these equations, there was an implicit assumption that the background radiance field for the spectral region of the selected  $\lambda_1$  resonance lines was not dominated by resonance scattering by atmospheric molecules of the same species serving as the target for detection.

Background contributions from resonant scattering by atmospheric molecules should not be a problem for HCl, the high molecular weight organic compounds, and the aluminum oxides. It was pointed out in Section A.1.1, however, that moderately strong effective resonant scatter oscillator strengths for molecular bands are of the order of  $10^{-3}$ , and that consequently approximately one thousand times as many molecules as atoms are required for detection. In general, the effective resonant scatter  $f$ -values will be appreciably less for polyatomic than for diatomic molecules. The strongest vibrational band of the  $X^1\Sigma^+ \rightarrow B^1\Pi$  band system of HCl is of the Rydberg type and possibly may have an oscillator strength of the order of  $10^{-2}$  or even greater. This band system, however, falls in the neighborhood of  $1330 \text{ \AA}$  in the far ultraviolet where the solar intensity is relatively very low. Also, the HCl molecule is readily dissociated by the lower energy  $X^1\Sigma^+ \rightarrow A^1\Pi$  transition. It exhibits continuous absorption for wavelengths shorter than  $2290 \text{ \AA}$ .

The predicted minimum detectable numbers of molecules, while relatively large compared to the  $n_d$  values for strong atomic lines, is not prohibitive for HCl (if its rate of dissociation does not turn out to be too rapid). The detection of resonant scatter by AlO bands also remains a possibility. The possibility also exists that leakage from certain types of rockets may provide sufficient quantities of CO and NO molecules for detection against the background noise originating from the resonant scattering by these species in the ambient atmosphere. This possibility deserves some further study.

More promising, however, is the possibility of detecting the strong resonance lines of certain trace elements present as fuel impurities. There exists also a somewhat smaller probability of detecting resonance scattering from atoms sputtered off the skin of the vehicle during the upper portion of the launch phase. Among possible trace impurities or combustion products in various types of rocket fuels are Na, K, Li, Rb, Ca, Sr, Mg, C, and  $C_2$ . The elements Na, Ca, K, Li, Rb, Sr, Mg, Pb, Ti, Si, Al, Cr, Cu, Fe, Ba, and their oxides may be present as re-entry ablation products, and presumably also would occur to some extent as a result of the sputtering process. Such first positive ions as RbII, SrII, BaII and CaII also require consideration, since the solar radiation field would tend to ionize the corresponding atoms within an order of ten minutes or less.



Minute quantities of the preceding species of atoms in addition to  $N_2$  and  $O_2$ , also probably would be outgassed from the vehicle during the midcourse and upper launch phases. The numbers of these various substances which could be expected to be present in the tenuous clouds surrounding various types of midcourse vehicles remains a topic for further study. It is intended to pursue this investigation at a later date if sufficient interest is aroused by this report.

## APPENDIX C

### TABLES OF ABSORPTION OSCILLATOR STRENGTHS FOR SELECTED ATOMS AND MOLECULES

Table 1 lists wavelengths, types of electronic transitions (mostly from the ground state), and when available the absorption  $f$ -values for some of the strongest lines of selected atoms. Table 2 gives similar information for selected molecular band systems, and when available, for individual ( $0 \rightarrow v'$ )-bands. Strong resonance lines of some substances such as Be, Cd, Zn, B and Si that were not mentioned in Appendix B are also included in Table 1. Some of these atoms may be of future interest for resonant scatter detection. The same is true for some of the substances such as CH, OH, CN and NH listed in Table 2. Some far ultraviolet lines and bands are included in the tables. These possibly could be detected by a satellite-based system if a sufficiently large objective mirror could be utilized (since good imaging is not an important requirement, rather poor quality optics might suffice).

It should be noted that the oscillator strengths listed are those for absorption rather than effective  $f$ -values for the complete resonant scatter process. As was explained in Appendix A, these two types of parameters are the same only for true resonance lines of atoms (or when downward transitions to intervening excited states are of relatively small probability). Effective resonant scatter  $f$ -values will be computed for selected nonresonance lines of atoms or for selected molecular bands if sufficient interest is aroused to justify the labor.

Most of the listed absorption  $f$ -values for atomic lines were taken from tables presented by Landolt-Börnstein (5). Later and more complete information on oscillator strengths has been tabulated, but the requested reports have not yet arrived. The information on  $f$ -values of molecular bands and band systems was taken mostly from Herzberg (4), Penner (3), or from references given by these authors.

Some of the  $f$ -values given in the literature are a result of empirical measurement, while others are based primarily upon theoretical considerations. The measured  $f$ -values given in the



Table 1. Selected Atomic Lines

Atom	Transition	Wavelength (in Å)	Absorption f-values	Atom	Transition	Wavelength (in Å)	Absorption f-values
Li	$2^2S_{1/2} \rightarrow 2^2P$	6707.85 R	0.71	Be	$2^1S_0 \rightarrow 2^1P$	2349 S	1.82
	$2^2S_{1/2} \rightarrow 4^2P$	2741.93	$M 1 \cdot 10^{-2}$		$3^1S_0 \rightarrow 3^1P$	2852 S	1.745
Na	$3^2S_{1/2} \rightarrow 3^2P_{3/2}$	5889.95 R	M 0.67	Zn	$4^1S_0 \rightarrow 4^1P_1$	2139 S	?(G1.5)
	$\rightarrow 3^2P_{1/2}$	5895.92 R	M 0.33		$5^1S_0 \rightarrow 5^3P_1$	73261 R	$M 1.9 \cdot 10^{-3}$
	$3^2S_{1/2} \rightarrow 4^2P$	7102	$M 1.4 \cdot 10^{-2}$		$5^1S_0 \rightarrow 5^1P_1$	2288 S	M 1.19
	$3^2S_{1/2} \rightarrow 5^2P$	2853	$2.2 \cdot 10^{-3}$	Hg	$6^1S_0 \rightarrow 6^3P_1$	2536.52 R	$M 2.6 \cdot 10^{-2}$
K	$4^2S_{1/2} \rightarrow 4^2P_{3/2}$	7664.94 R	0.70		$6^1S_0 \rightarrow 6^1P_1$	1849.57 S	M 1.184
	$\rightarrow 4^2P_{1/2}$	7699.01 R	0.35	Ca	$4^1S_0 \rightarrow 4^1P_1$	4226.73 S	2.27
Cu	$4^2S_{1/2} \rightarrow 4^2P_{1/2}$	73247.55 R	M 0.62		$4^1S_0 \rightarrow 5^1P_1$	2721.65	?(G0.1)
	$\rightarrow 4^2P_{3/2}$	73273.97 R	M 0.32	CaII	$4^2S_{1/2} \rightarrow 4^2P_{3/2}$	3933.66	1.19
	$4^2S_{1/2} \rightarrow 5^2P_{1/2}$	2024.33	?(G0.05)		$\rightarrow 4^2P_{1/2}$	3968.47	
Rh	$5^2S_{1/2} \rightarrow 5^2P_{3/2}$	7800.20	?(G ~ 1)	Al	$3^2P_{1/2} \rightarrow 4^2S_{1/2}$	3944.03	0.13 f
	$\rightarrow 5^2P_{1/2}$	7947.64			$3^2P_{3/2} \rightarrow 4^2S_{1/2}$	3961.54	
Sr	$5^1S_0 \rightarrow 5^1P_1^0$	4607.34 S	?(G2)		$3^2P \rightarrow 5^2S$	2660; 2652	?(G10 <sup>-2</sup> )
	$5^1S_0 \rightarrow 6^1P_1^0$	2931.88	?(G0.1)		$3^2P \rightarrow 4^2D$	2575; 2568	?(G10 <sup>-2</sup> )
	$5^1S_0 \rightarrow 7^1P_1^0$	2569.50	?(G0.1)	C	$2p^3P \rightarrow 3s^3P$	~1657	?
SrII	$5^2S_{1/2} \rightarrow 5^2P_{3/2}$	4077.71	~1	Si	$3p^3P_0 \rightarrow 4s^3P_1$	2514.32	?
	$\rightarrow 5^2P_{1/2}$	4215.52			$3p^3P_1 \rightarrow 4s^3P_{0,1,2}$	2524.2519; 2507	?
Ba	$6^1S_0 \rightarrow 6^1P_1^0$	5535.53 S	$2.10 \pm 0.25$		$3p^3P_2 \rightarrow 4s^3P_{1,2}$	2528.5; 2516.1	?
	$6^1S_0 \rightarrow 8^1P_1^0$	2702.65	?(G0.05)				
BaII	$6^1S_{1/2} \rightarrow 6^2P_{3/2}$	4554.04	~1				
	$\rightarrow 6^2P_{1/2}$	4934.10					
B	$2^2P_{1/2}^0 \rightarrow 3^2S_{1/2}$	2496.78	?(G0.5)				
	$2^2P_{3/2}^0 \rightarrow 3^2S_{1/2}$	2497.73					
	$2^2P \rightarrow 3^2D$	~1826	?(G0.5)				
	$2^2P \rightarrow 4^2S_{1/2}$	~1818	?(G0.01)				



Table 2. Selected Molecular Bands

Molecule	Electronic Band System	Band $v' \rightarrow v''$	Wavelength (in Å)	Absorption Oscillator Strength
$C_2^{12}$	$X^3\Pi_u \rightarrow A^3\Pi_g$	$0 \rightarrow 0$	$\uparrow 5160$	? (G0.01)
		$0 \rightarrow 1$	$\uparrow 4840$	? (G0.005)
		$\sum_i (0 \rightarrow v_i')$		$\sim 0.048$
	$X^3\Pi \rightarrow B^3\Pi_g$	$0 \rightarrow 0$	$\uparrow 2514$	?
	$a^1\Sigma_g^+ \rightarrow b^1\Pi_u$	$0 \rightarrow 0$	$\uparrow 12,095$	$M 2 \cdot 10^{-2}$
$C^{12} N^{14}$	$X^2\Sigma^+ \rightarrow A^2\Pi_i$	$0 \rightarrow 0$	$\uparrow 10,970$	$\sim 0.02$
		$\sum_i (0 \rightarrow v_i')$		$\sim 0.1$
	$X^2\Sigma^+ \rightarrow B^2\Sigma^+$	$0 \rightarrow 0$	$\uparrow 3876$	$M 0.026$
		$\sum_i (0 \rightarrow v_i')$		$\sim 0.1$
$C^{12} O^{16}$	$X^1\Sigma^+ \rightarrow A^1\Pi$	$0 \rightarrow 0$	$\uparrow 1543$	?
		$0 \rightarrow 1$	$\uparrow 1509$	?
		$\sum_i (0 \rightarrow v_i')$		? (G0.01)
$Al^{27} O^{16}$	$X^2\Sigma^+ \rightarrow A^2\Sigma^+$	$0 \rightarrow 0$	$\uparrow 4845$	?
		$0 \rightarrow 1$	$\uparrow 4650$	?
		$0 \rightarrow 2$	$\uparrow 2880$	?
	$X^2\Sigma^+ \rightarrow B^2\Sigma^+$	$0 \rightarrow 0$	$\uparrow 2333$	?
$B^{11} O^{16}$	$X^2\Sigma^+ \rightarrow A^2\Pi_i$	$0 \rightarrow 1$	$\uparrow \begin{matrix} 3662 \\ 3685 \end{matrix}$	?
		$0 \rightarrow 2$	$\uparrow \begin{matrix} 3830 \\ 3855 \end{matrix}$	?
		$0 \rightarrow 4$	$\uparrow \begin{matrix} 3510 \\ 3530 \end{matrix}$	?
	$X^2\Sigma^+ \rightarrow B^2\Sigma^+$	$0 \rightarrow 0$	$\uparrow 2333$	?
$N^{14} O^{16}$	$X^2\Pi \rightarrow A^2\Sigma^+$	$\sum_i (0 \rightarrow v_i')$	$\uparrow (\sim 2200 \text{ to } 1880)$	$M 2.5 \cdot 10^{-3}$
		$0 \rightarrow 0$	$\uparrow \begin{matrix} 2272 \\ 2260 \end{matrix}$	$M 4.1 \cdot 10^{-4}$
		$0 \rightarrow 1$	$\uparrow \begin{matrix} 2155 \\ 2148 \end{matrix}$	$M 8.8 \cdot 10^{-4}$
		$0 \rightarrow 2$	$\uparrow \begin{matrix} 2053 \\ 2045 \end{matrix}$	$M 6 \cdot 10^{-4}$
$O^{16} H^1$	$X^2\Pi_i \rightarrow A^2\Sigma^+$	$0 \rightarrow 1$	$\uparrow 2827$	? (G1.5 $\cdot 10^{-4}$ )
$C^{12} H^1$	$X^2\Pi \rightarrow A^2\Delta$	$0 \rightarrow 0$	$\uparrow 4300$	$1.9 \cdot 10^{-3}$
$N^{14} H^1$	$X^1\Sigma^+ \rightarrow A^1\Pi_i$	$0 \rightarrow 0$	$\uparrow 3360$	$1 \cdot 10^{-3}$
$H^1 Cl^{35}$	$X^1\Sigma \rightarrow B^1\Pi$	$0 \rightarrow 0$	$\uparrow 1330$	? (G0.1)
	$X^1\Sigma \rightarrow C^1\Pi$	$0 \rightarrow 0$	$\uparrow 1290$	? (G0.1)



tables are preceded by an M. In some cases, no  $f$ -values were readily available, but sufficient data was available in the literature for more or less reliable estimates to be made. The  $f$ -values estimated by the present author on the basis of relative intensity data, similarities of electronic states to those of other molecules or atoms, Franck-Condon factors, etc., are listed as ?(G -).

Resonant scatter lines or bands of wavelength shorter than 3000 Å would be detectable only by a downward-looking satellite system. This is indicated in the tables by the symbol ↓. Lines and bands in the visible and near ultraviolet would be suitable for a detection system flown above 25 or 30 kilometers and scanning within its upper hemisphere. This is indicated by the symbol ↑. No lines or bands belonging to the 2950 to 3250 Å region are included in the tables. The 2950 to 3100 Å region is not useful for either type of detection configuration. The 3100 to 3250 Å region is of doubtful value. These spectral intervals lie on the shoulder of the intense absorption by the Hartley bands of the atmospheric ozone layer. The background noise for the downward-looking configuration is therefore appreciably greater than for radiation of wavelength shorter than 2900 Å. The absorption in the shoulder of the ozone band is sufficient to cause appreciable attenuation of the resonant scattered radiation input to an upward-looking detection system unless the latter is located at an altitude above the ozone layer (say at an altitude above 60 kilometers). Also, the spatial-temporal fluctuations in this attenuation would act as background noise.

The wavelengths listed in Table 2 are approximate values for the band origin; i.e., for the (often forbidden)  $J'' = 0$  to  $J' = 0$  rotationless transition. The separation of the rotational lines of a ( $v'' \rightarrow v'$ )-band of a diatomic molecule is inversely proportional to the moment of inertia of the molecule. The rotational structure extends to both sides of the band origin. Quite often the center of intensity of this structure is displaced appreciably from the band origin.

#### REFERENCES

1. Private Communication, received from R. Schneeberger, Westinghouse Research Labs., Pittsburgh, Penna.
2. Ladenburg, R., *Z. Physik*, vol. 65, 1930.
3. Penner, S., Quantitative Molecular Spectroscopy and Gas Emissivities, Reading, Mass., Addison-Wesley Publishing Co., Inc., 1959.
4. Herzberg, G., Molecular Spectra and Molecular Structure, Princeton, N. J., D. Van Nostrand Company, Inc., 2nd ed., 1950; a) Chapter VI, Section 5; b) Chapter IV, Section 4.



## REFERENCES (Continued)

5. Landolt-Börnstein, Tabellen, Berlin, Germany, Springer-Verlag, 6th ed., vol. I, Part I, 1950.
6. Clementi, E., J. Chem. Phys., vol. 32, 1960, p. 656.



A 2.5 WATT X-BAND TRAVELING-WAVE TUBE AMPLIFIER  
FOR SATELLITE APPLICATIONS

R. E. Pospisil

Watkins-Johnson Company  
Systems Division  
Palo Alto, California

ABSTRACT

This paper describes a high efficiency, high reliability, 2.5 watt, X-band amplifier which is designed specifically for long life satellite environments. The amplifier is an integration of the latest "state-of-the-art" advances in both microwave and solid state circuitry.

The total program encompasses a thorough analytical study, design, development, production and subsequent life testing of sixty-three amplifiers.

The work described in this paper is being accomplished under Air Force Contract No. DA 36-039-AMC-00093(E).



## A 2.5 WATT X-BAND TRAVELING-WAVE TUBE AMPLIFIER FOR SATELLITE APPLICATIONS

R. E. Pospisil  
Watkins-Johnson Company  
Systems Division  
Palo Alto, California

### INTRODUCTION

In the past few years the number of desired telemetry channels and the bandwidth desired per channel has increased tremendously, so that more and more emphasis is being placed on the utilization of wide band devices. When this requirement must be fulfilled in addition to high efficiency, high gain, high reliability, light weight and small volume the traveling-wave tube is the only answer. Other devices such as amplitrons, triodes and klystrons while possessing several of these desirable characteristics, do not encompass all of them.

The wide bandwidth characteristics of the traveling-wave tube are also being utilized for the transmission of several carriers through the same amplifier. Of prime importance also is the fact that for deep space probes the optimum frequency range, relative to the ambient galactic noise level is between 4-9 Gc.

This paper will describe a 2.5 watt, 7-8.5 Gc amplifier which is being designed for Military Communication Satellite Applications. The amplifier will be characterized by:

#### 1. High Reliability Goals

Tube MTTF	50,000 hours
Power Supply and Telemetry Conditioning Package MTTF	200,000 hours

- |                    |                     |
|--------------------|---------------------|
| 2. Weight          | 5 pounds            |
| 3. Volume          | 65 in. <sup>3</sup> |
| 4. Power Output    | 2.5 w min.          |
| 5. Frequency range | 7.0-8.5 Gc          |



In an attempt to obtain the optimum package from both performance and size weight considerations two design approaches were investigated: periodic permanent magnet and single reversal focusing.

The following sections will describe in detail the tube design, power supply-telemetry conditioning package design and over-all amplifier configuration, including RFI considerations.

The important electrical and environmental specifications which are being designed into this amplifier are outlined in Table 1. Throughout the design and development phases of this program the key considerations relative to performance have been reliability, long life, efficiency, light weight and small size.

#### TUBE DESIGN PHILOSOPHY

The design of satellite communication tubes presents special problems to the tube designer. He must in no way permit mediocrity in accomplishing the program specification. Because of its application, the tube must have the following characteristics: high efficiency, long life, extreme reliability, and light weight. Efficiency is important because the input power which must be supplied to the tube costs several pounds per watts. Long life, extreme reliability, and light weight are evident for satellite applications.

In an effort to obtain the most practical solution to the amplifier requirement two different tube focusing designs, single reversal and periodic permanent magnet were investigated. While it is obvious that the PPM approach would ultimately provide many desirable features such as small size and light weight, it was necessary since time was of the essence to finally pursue the single reversal approach. During the investigative portion of the contract several PPM tubes were built and tested, but it became evident that the solution to some of the mechanical problems could jeopardize the contract delivery dates. In addition the single reversal approach had adequately demonstrated certain design requirements such as efficiency, power output and gain. For these reasons Watkins-Johnson is presently developing the 2.5 watt amplifier, using a single-reversal tube.

#### EFFICIENCY

##### High Beam Efficiency is of Crucial Importance

There are two important aspects to high over-all efficiency. The first consists of extracting the maximum amount of rf energy from the beam energy available in the interaction region. The second is in reducing the amount of excess beam energy which is lost in heating the collector or other tube electrodes. The maximum rf energy extraction is optimized by the proper design of the circuit and beam parameters in the tube. The excess beam energy can be reduced by the use of a depressed



Table 1. Tentative Specification, WJ-130 Satellite Microwave Amplifier

PERFORMANCE CHARACTERISTICS

Frequency range	7.0 - 8.5 Gc
Power output (saturation)	2.5 watts min. CW
Spurious, coherent output (7.2 - 7.7 Gc)	>70 db below carrier
Saturation gain	36 db min.
Power output variation	
Over frequency range	3 db max.
Over any 10 Mc within frequency range	0.3 db max.
VSWR (operating, tube only)	
Input	1.4:1
Output	1.4:1
Load VSWR for $P_{out}$ 2.5 watts	1.5:1
Noise figure	33 db max.
Maximum load VSWR for stable operation	$\infty$ , any phase
Phase linearity (over any 10 Mc within frequency range)	2.5°/10 Mc max.
AM-PM conversion (over any 10 Mc within frequency range)	50/3 db max.
Duty cycle (CW)	100 percent

ELECTRICAL REQUIREMENTS

Voltage input	24 to 30 v dc
Total DC power input for 2.5 watts min. rf saturated output (includes heater and time delay)	13.5 watts max.
Tube focusing	single reversal PM
Tube voltages (provided by power supply)	
Anode voltage	1750 v
Anode current	Less than 50 $\mu$ a
Helix voltage	1700 v
Helix current	Less than 300 $\mu$ a
Collector voltage No. 1	700 v
Collector current No. 1	5.5 ma
Cathode current	13 ma
Heater voltage	3 v
Heater current	.34 a
Collector voltage No. 2	450 v
Collector current No. 2	7.5 ma

MECHANICAL

Weight: Power Supply



Table 1. Continued

Regulator	.38 lb
Low voltage converter	.24 lb
High voltage converter	.83 lb
RFI module	.38 lb
Output low pass filter, misc. hardware	.25 lb
Tube	
Single reversal	2.92 lb
Total amplifier (excluding RFI shield)	5 lb
Volume: Power Supply	
Regulator	4.5 in <sup>3</sup>
Low voltage converter	4.00 in <sup>3</sup>
High voltage converter	14 in <sup>3</sup>
RFI module	7.0 in <sup>3</sup>
Output low pass filter	4.0 in <sup>2</sup>
Tube	
Single reversal	18 in <sup>3</sup>
Total amplifier including RFI packaging	65 in <sup>3</sup>
DC connections	Bendix Pygmy
RF input	BRM
RF output	UG - 51/U
Operating position	Any

ENVIRONMENTAL

Cooling	Conduction to baseplate
Baseplate temperature	
Operating	-10°C to +65°C
Storage	-54°C for 24 hrs and +71°C for 24 hrs
Pressure	10 <sup>-10</sup> mm/Hg
Vibration	
Sinusoidal, period of 45 minutes	5 to 2000 cps @ 5g rms (any axis, amplitude limited to 0.5 inch peak- to-peak)
Random, period of 5 minutes	20 to 300 cps @ 0.04g <sup>2</sup> /cps and 300 to 2000 cps @ 0.16g <sup>2</sup> / cps (any axis)
Acceleration	12 g for 10 min. (any axis)
Shock (all six directions)	100 g, 6 msec
Radiation	as encountered in the Van Allen Belt
Humidity	100 percent
Explosive atmosphere	No ignition of such atmosphere



Table 1. Concluded

RELIABILITY AND LIFE CHARACTERISTICS

Tube	
Beam transmission	98 percent min.
Cathode	Sprayed oxide
Cathode current density	150 ma/cm <sup>2</sup>
Cathode temperature	720°C
Life time	50,000 hrs min.
Power supply	
Failure rate (based on high rel. parts)	0.5 percent/1000 hrs
MTTFF	200,000 hrs



collector which is insulated and operated at a lower voltage than that of the circuit. With no rf modulation on the beam a large percentage of the electrons can be collected at a very low voltage so that a large amount of power can be recovered. However, as the beam is more heavily modulated, the velocity spread in the beam causes excessive returned electrons at very low collector voltages. The maximum over-all efficiency then occurs at a collector voltage higher than the optimum value in a weekly modulated beam. The important fact in the design of high over-all efficient tubes is that the basic beam efficiency has to be very high because there is a limit to the amount of improvement which can be obtained with a depressed collector. This ultimate theoretical limit is not reached in every tube.

#### High-Perveance High-Impedance Design Essential

The design considerations necessary for good beam efficiency are understood fairly well. It has been shown by several authors<sup>1,2,3,4</sup> that the efficiency of a traveling-wave tube is proportional to the gain parameter,  $C$ .

This parameter,  $C$ , is given by

$$C = \frac{I_0}{4V_0} K^{1/3} \quad (1)$$

where

$I_0$  = Beam current

$V_0$  = Beam voltage

$K$  = Interaction impedance

The two obvious ways of increasing  $C$  are then to increase the beam perveance and to increase the interaction impedance. As the beam perveance is increased, the current density in the beam increases rapidly which in turn increases the required focusing field and area convergence of the electron gun.

These conditions unfortunately are not in accord with some of the other design criteria relative to weight and size. Therefore a compromise must be made as to the magnitude of the perveance chosen so as to optimize the efficiency/gain parameter ( $N/C$ ).

Any tube which is being designed for long life requires low cathode loading (i. e., current density - milliamps per (centimeter)<sup>2</sup>) which leads to higher convergent guns and hence demands a stronger magnetic field.

Ideally a PPM design is the choice in that it will result in minimum weight and size. However, at higher frequencies the PPM approach becomes harder to focus



in that the scalloping wave length should be kept longer than the period of the magnet and as such the mechanics of producing the tube components is more difficult. In addition as the frequency increases the beam diameter is reduced and the current density increases, thereby increasing the space charge and compounding the focusing problems. Due to the numerous magnetic field reversals and as such the large number of pole pieces, the magnetic field has many small perturbations, which result in lower over-all efficiency.

A comparison between the primary design trade-offs which must be considered between a PPM and single reversal focusing approach are listed in Table 2. Representative data taken on a single reversal focused WJ-251 is shown in Figure 1.

Another important area in the design of the tube is the realization of a good depressed collector. Considerable work has been done on depressed collectors. Sterzer<sup>5</sup> has measured 57 percent efficiency using a two stage collector which represented an improvement ratio of 2.33 and a ratio of 1.88 with a single stage collector.

## LIFE

### Causes of Failure

The primary cause of failure in a well designed highly reliable tube is in loss of emission from the cathode. This can be the result of depletion of the emitting material, a change in the amount of reducing agents in the cathode or the presence of some type of contaminating material (such as O<sub>2</sub>, CO<sub>2</sub>, CO etc.). The first two of these should be the primary causes of failure for well-processed and aged tubes in a final production design.

Depletion of the emitting material (BaO, SiO, and CaO) and changes in the amounts and types of reducing agents are a result of chemical reactions occurring in the oxide layer during operation. The rate at which these reactions occur depends critically upon the temperature of the cathode. At typical operating temperatures these rates double, with a temperature increase of 20 to 30°C. The necessary operating temperature of the cathode in turn, depends upon the current density that is required. Therefore, in order to achieve a long life design, it is necessary to reduce the required emission density at the cathode surface to a limit known to be consistent with life in excess of that required.

### Life Data

There is only a small amount of life data on traveling-wave tubes, with the major portion of this at Bell Telephone Laboratories.<sup>6</sup> Recent communication with J. P. Laico of BTL indicates that the 12 tube sample is still in progress with all tubes still operating. The minimum life at present is 31,000 hrs., the maximum is 37,000 hrs., and the average is 35,000 hrs. The emission density of 200 ma/cm<sup>2</sup>



TABLE 2. - Design Trade Offs Between Single Reversal and Periodic Permanent Magnet Focused 2.5 Watt, 7 - 8.5 Gc Tube.

	Single Reversal	PPM
Weight	2.6 lb	0.75 lb
Volume	18 in. <sup>3</sup>	5.5 in. <sup>3</sup>
Efficiency	31%	27%
Mechanical Reproducibility	Single reversal construction due primarily to fewer alignment problems relative to the pole pieces is easier to build. Thereby resulting in a higher degree of confidence relative to reliability.	



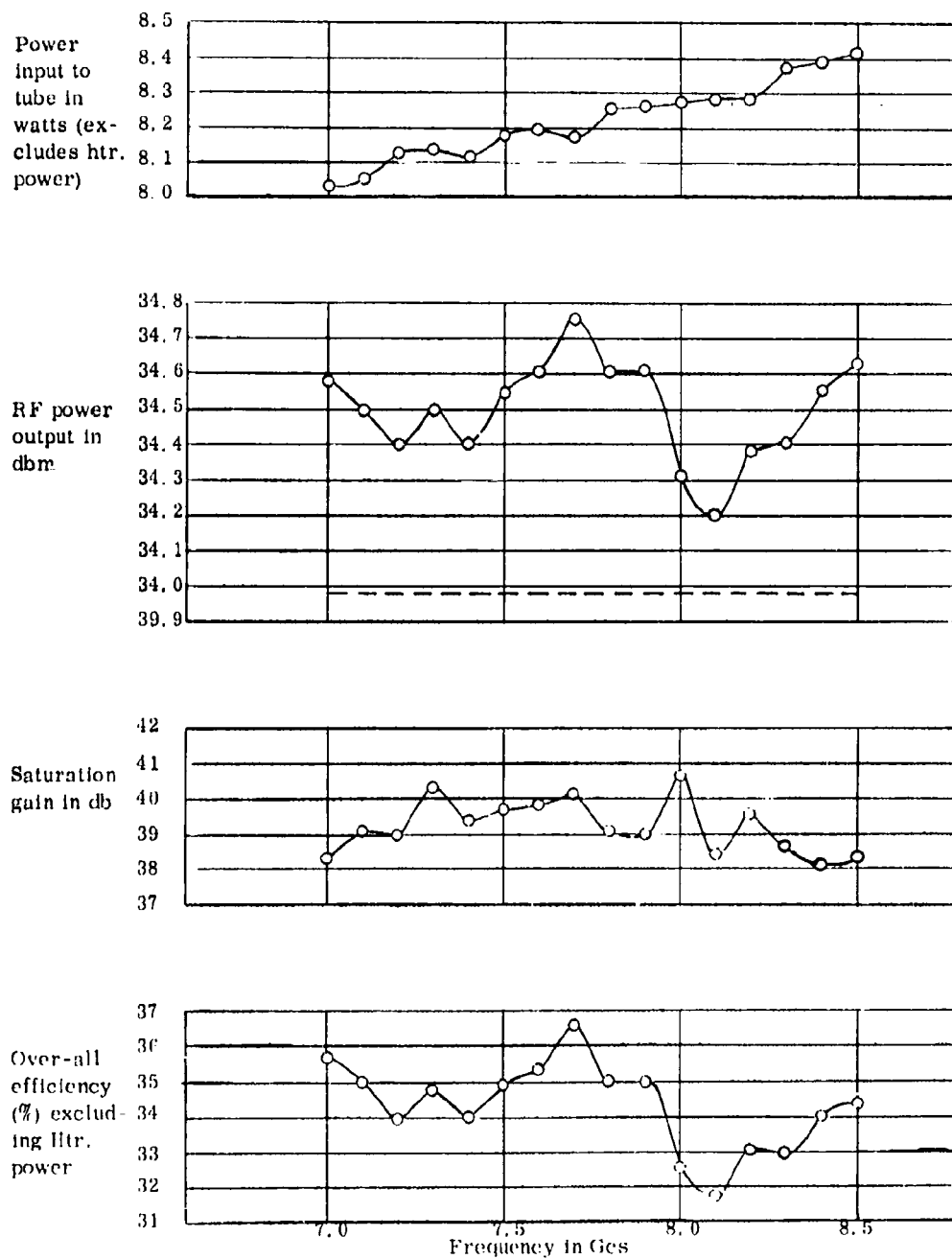


Figure 1. Data Taken on WJ-251B Tube



was achieved with cathode temperature between 720° and 760°C.

Another source of life data can be obtained from the RCA transmitter at Rockey Point, Long Island. Transmitting tubes with oxide cathodes have been operating under CW conditions for over 100,000 hrs.<sup>7</sup>

In addition Watkins-Johnson has placed ten S-band, WJ-227, 10 watt tubes on life test and these units have accrued an average of 32,583 hours (using acceleration factors). Also five complete amplifier packages (tube, power supply and telemetry) units designed and developed by Watkins-Johnson under contract with the Philco Corporation, Palo Alto, California are presently under life test at Philco with an average actual test time per amplifier of 3032 hours. The test conditions are as follows; 100% duty cycle, 3-4 days at -35°C, 3-4 days at room ambient temperature, 3-4 days at +75°C, and then repeat.

The basic design of the 2.5 watt tube closely matches the conditions which have been proven to give long life. The cathode is designed to operate at 150 ma/cm<sup>2</sup> and cathodes of similar design in the 10 watt S-band tube have been operated successfully in the range from 700° to 750°C. At these low temperatures the reaction rates are low enough to ensure an adequate supply of free barium for a period of greater than 50,000 hours.

#### Very Low Tube Pressure Essential

In addition to emission density, other requirements for low cathode temperature operation include very low tube pressure, lack of contaminating materials, and prevention of ion bombardment on the cathode.

A low tube pressure ( $10^{-9}$  mmHg) may be assumed by the use of only certain types of materials which have proven to be suitable for vacuum tube use. Careful quality control must be maintained with only certified materials permitted for tube parts. The assembly work is done in an enclosed area supplied with filtered air and pressurized to maintain 3" of static pressure. The enclosed assembly area physically separates the operator and tube components to ensure cleanliness. The filter system has prefilters and "Aerosolve" absolute filters based on NBS 100 HP specifications. It is capable of removing smoke, pollen, dust, and fumes. A photograph of the clean assembly facility is shown in Fig. 2.

The assembly technicians are experienced and well trained as to the importance of cleanliness. All parts from the machine shop are stored in an area outside this clean facility and after these have been degreased and processed they are stored in the clean area. Hooded and pressurized benches are available for final assembly work. Increased attention is being given to this important aspect of tube processing, particularly as research and development tubes are now moving into production. Modern cleaning and plating facilities are available with ultrasonic cleaning being a





Fig. 2. Photograph of the super-clean assembly facility at Watkins-Johnson. This unit provides filtered air and the operator and tube components are physically separated to ensure cleanliness.



standard procedure. Water break and atomizer tests found at BTL to be of value in detecting organic contaminants are being evaluated at Watkins-Johnson Company.

Table 3 lists the performance specifications of the 2.5 w, X-band tube.

The problems associated with a design of this type are to a large degree mechanical in nature. An example of this is the construction details associated with the helix assembly. Figure 3 is a cross-sectional drawing of the helix showing the support structure. Beryllia wedges are glazed to the helix and a copper cylinder is broached to be 1 mil less than the diameter of the helix and wedge assembly. This technique has been perfected on the 35 watt X-band tube developed under Army Signal Corps contract no. DA 36-039 SC-87480.

The ID of the helix is 50 mils and the helix is made of 5 by 9 mil tape. The beryllia wedges are made from 60 mil rods ground so that the smaller and larger surfaces are 10 and 40 mils respectively.

Heat flow measurements were made on a helix similar in construction to that described above. The helix and beryllia assembly were pressure fitted in a copper body and 60 cycle power was applied between the two ends of the helix. The test was conducted in a vacuum with 70 watts per inch dissipated before failure occurred.

The ultimate test of any structure is when it is placed in a tube. A helix assembly, as described, was placed in a 2.5 w tube assembly and a full 3 watts of CW power in X-band was obtained with practically no fading. The tube was run continuously for 8 hours with no degradation in performance.

The 2.5 w tube uses a helix assembly which is scaled by 0.6 of the 35 watt X-band tube. As far as heat conduction is concerned, assume that for the 35 watt tube a safe upper limit for heat flow is 35 watts per inch. Then, the safe upper limit of heat flow for the proposed tube is 12.5 watts per inch. Note that the proposed beam power is 12 watts with a helix length of 1.5 inches, hence the design is conservative.

#### DESCRIPTION OF AMPLIFIER EQUIPMENT

This section outlines a high reliability, high efficiency, lightweight amplifier equipment described in Table 1, which includes the 3.0 watt traveling-wave tube discussed previously and the necessary power supplies and telemetry equipment to make up an integrated power amplifier package.

The power supply unit consists of a line voltage regulator followed by independent dc converter units for the filament and beam voltages, and a time delay network to permit cathode preheating before application of high voltage to the tube. Packaging of these units, in general, will employ three dimensional modules. The entire amplifier package including traveling-wave tube will have an over-all efficiency of at least 20



TABLE 3. - Specification - WJ-251, 7.6 Gc Traveling-Wave Tube for Satellite Communication.

PERFORMANCE CHARACTERISTICS

Frequency	7.00-8.5 Gc
Power output at saturation	3.0 w (min) CW
Spurious coherent output	>70 db below carrier
Gain saturated	36 db min.
Gain variation over frequency range	3 db max.
Gain variation over any 10 Mc within frequency range	0.3 db max.
Noise figure	33 db max.
VSWR, input and output (tube operating)	1.4:1
Phase linearity over any 10 Mc within frequency range	2.5 degrees/10 Mc max.
AM-PM conversion over any 10 Mc within frequency range (linear)	5 degrees/3 db max.
(saturated)	3 degrees/db
Efficiency at saturation power output (without heater)	40 percent min
(with heater)	31 percent min
Focusing	Single reversal PM

LIFE AND RELIABILITY-RELATED CHARACTERISTICS

Beam transmission	98 percent min.
Cathode	Sprayed oxide
Cathode current density	150 ma/cm <sup>2</sup>
Life time	50,000 hours

ELECTRICAL CHARACTERISTICS

Anode voltage	1750 v
Anode current	Less than 50 $\mu$ a
Helix voltage	1700 v
Helix current	Less than 140 $\mu$ a
Collector voltage No. 1	700 v
Collector current No. 1	5.5 ma
Cathode current	13 ma
Heater voltage	3 v
Heater current	.34 a
Collector voltage No. 2	450 v
Collector current No. 2	7.5 ma



MECHANICAL CHARACTERISTICS (continued)

Length	7.1 inches
Cross section	3.0 inch dia. (single rev.)
Weight	2.7 lb (single rev.)
Cooling	Conduction only
RF connections	BRM
Operating position	Any

ENVIRONMENTAL REQUIREMENTS

Operating temperature	-10 to +65°C
Humidity	To 95 percent
Salt atmosphere	As encountered in coastal regions for checkout
Radiation	As encountered in Van Allen Belt
Operation pressure range	Tube will operate in vacuum

ENVIRONMENTAL CHARACTERISTICS

Shock, two shocks in each six directions	100 g 6 ms triangular
Acceleration, six directions, three minutes per direction	11 g
Sinusoidal vibration three planes	5-100 cps 2.5 g
17 minutes per plane	100-300 cps 10 g
Gaussian random vibration	300-2000 cps 15 g
three planes, 17 minutes per plane	20-300 cps .03 g <sup>2</sup> /cps
	300-2000 cps. 2g <sup>2</sup> /cps



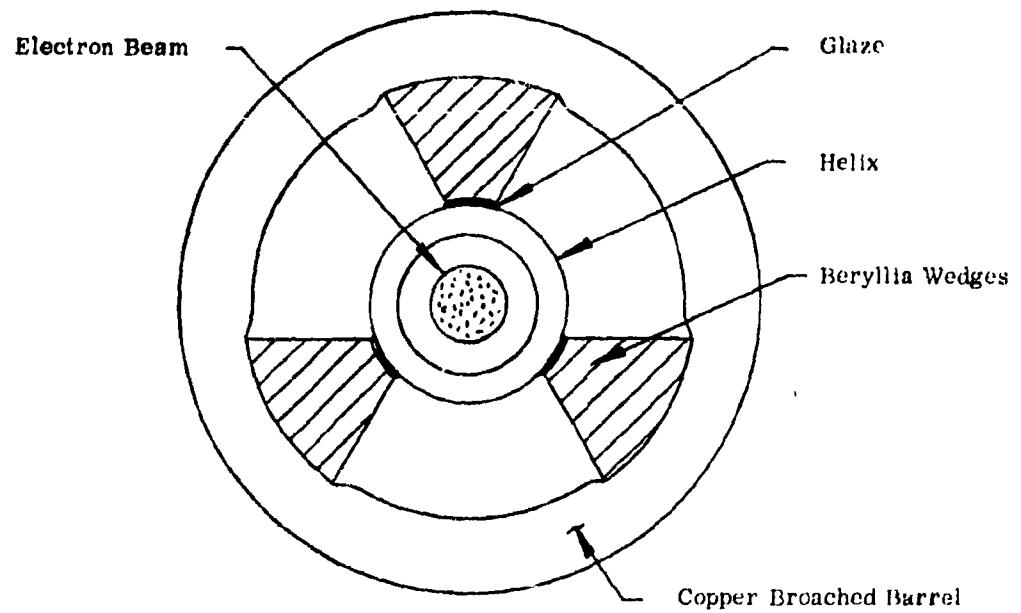


Fig. 3. Cross-sectional sketch of circuit and support structure. Beryllia wedges are glazed to the helix and this assembly is inserted into a broached copper tubing while at elevated temperature in an oven. The outer tubing shrinks tightly over the helix and support structure proving a very rigid structure with good thermal conduction.



percent (at maximum dc input voltage and maximum base plate temperature) and a total weight of 5.0 pounds.

#### Design Approach for Power Supply-Telemetry Package

Since the amplifier package is intended for use in a space environment for long periods of time, the uppermost consideration in the design of the power supply-telemetry package has been reliability and efficiency.

In an effort to increase the over-all reliability, a careful analysis as to total number of components vs redundancy, the best components presently available which have proven reliability figures and a careful incoming inspection of all components has been made and is being continued under our present programs.

The requirements for a successful traveling-wave tube amplifier power supply are:

1. High reliability
2. High efficiency
3. Small size and light weight
4. Low standby power
5. Insensitivity to input transients
6. Low feedback ripple to the satellite supply

The solution to the above requirements of necessity has been a compromise between the best operating features of transistor circuitry and magnetic circuitry. The system described in the following text satisfies all the requirements previously set forth.

The block diagram, Fig. 4, breaks down the supply into its main components.

The use of high temperature transistors throughout the entire power supply allows for extended thermal operation. Increasing the line regulator frequency to approximately 20 kc and the converter frequency to 10 kc has resulted in a reduction in filter size, (both physical and electrical) thus allowing high reliability capacitors to be utilized.

Representative data taken on a potted (filled epoxy) power supply is given in Table 4.

#### Switching Regulator

The relatively simple circuit shown in Fig. 5 is capable of .05 percent regulation for a 60 percent line change with better than 94 percent efficiency at an output power of up to 80 watts. The high efficiency is attained by switching the power to



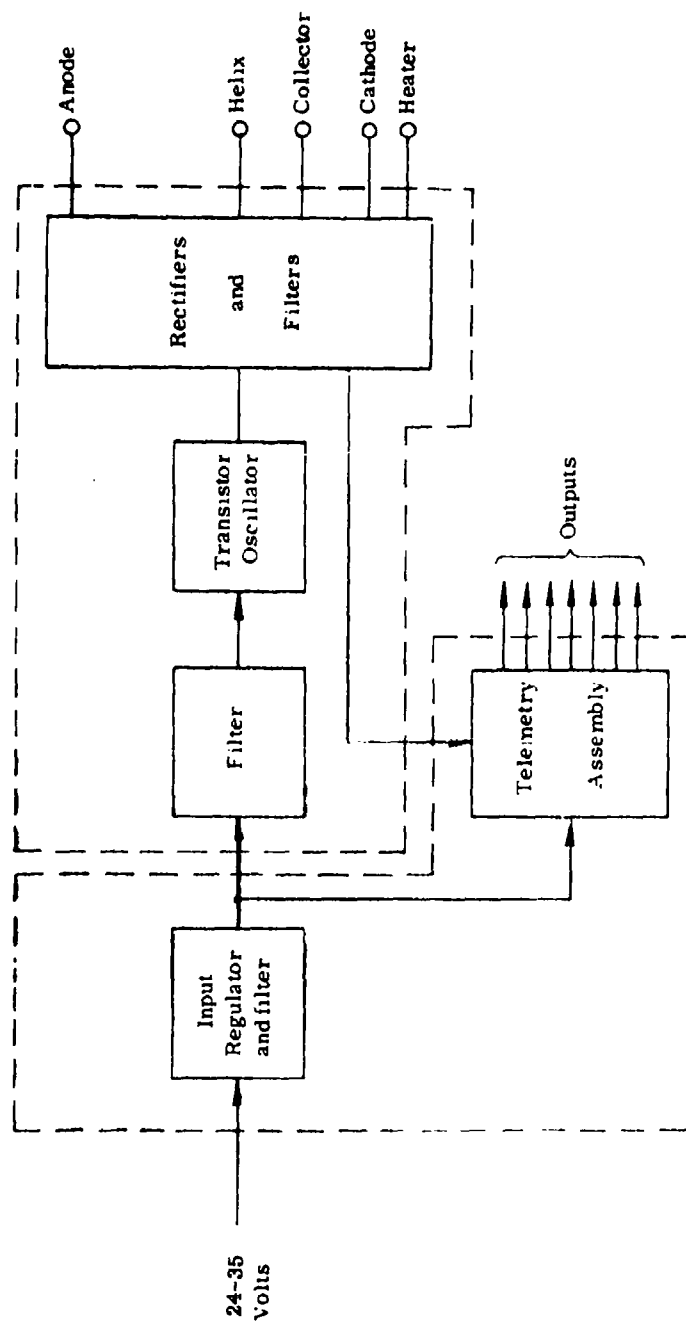


Fig. 4. Block diagram breaking down the power supply into its major components. This design results in highest efficiency. The telemetry assembly is for diagnostic and monitoring purposes.



TABLE 4. Power Supply Performance Data

Temp.	V <sub>in</sub>	Reg.	Drift (Relative to 25°C)	Efficiency	Time Delay
-40°C	24	0.06%	0.55%	85.0	71 sec
	35			81.3	
+25°C	24	0.002	---	85.4	80 sec
	35			82.4	
+80°C	24	0.14%	0.05%	82.0	68 sec
	35			80.1	



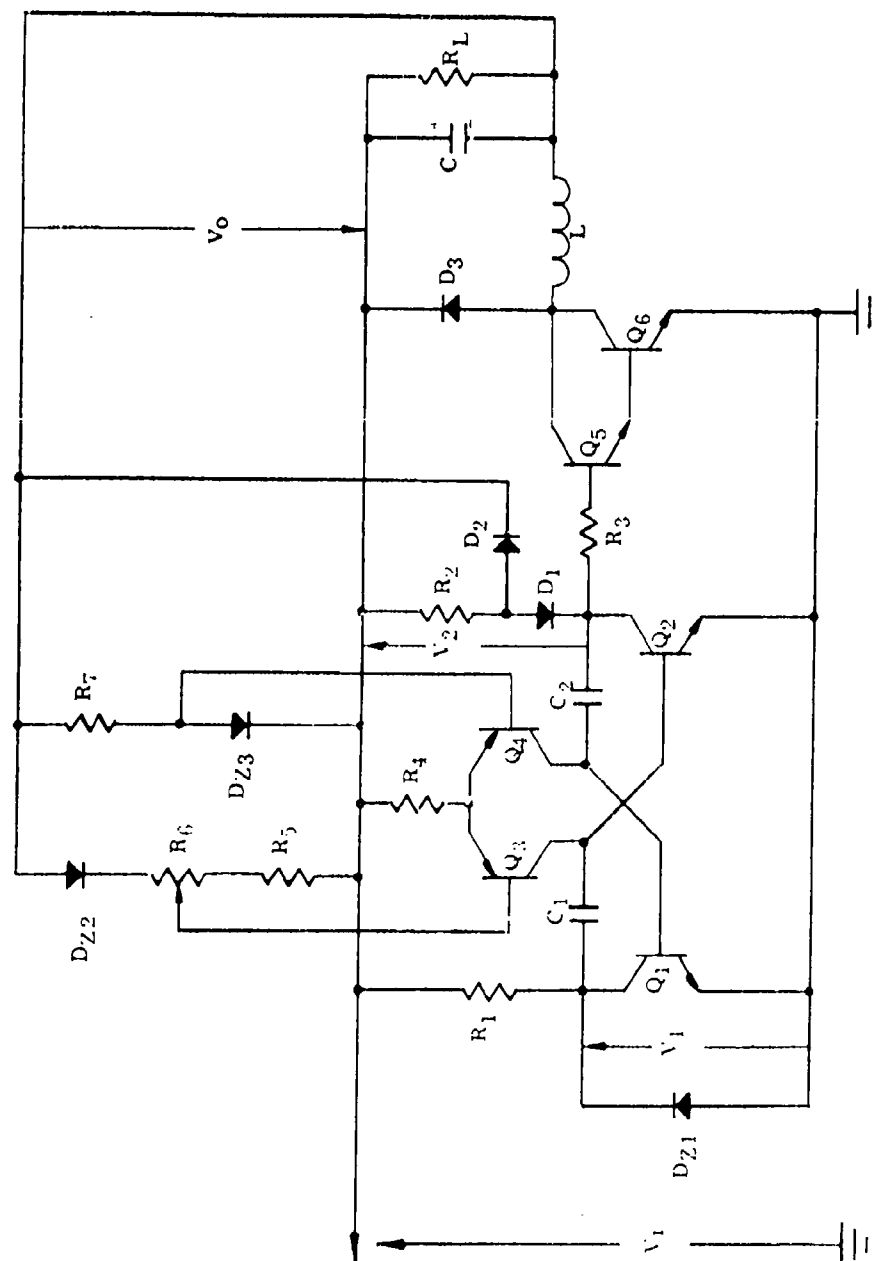


Fig. 5. Self-compensating switching regulator.



the load and the regulation is accomplished by varying the duty cycle of the switch ( $Q_6$ ).

High efficiencies are typical of this type of regulator; the extremely close regulation with a reduced number of components, however, is obtained by a more efficient use of the free running multivibrator ( $Q_1 Q_2$ ). By a proper choice of variables the M-V can be made to "pre-regulate" with no information fed-back from the load.

In order to illustrate this "pre-regulation" effect we shall disconnect the main feedback loop from the load ( $R_L$ ) and terminate it with a battery of value  $V_0$ , thus preserving equilibrium conditions in the multivibrator.

The voltage waveshape at the collector of  $Q_3$  under these conditions is shown in Fig. 6.

Since there is no external feedback, constant currents  $I_3$  and  $I_4$  flow in the collectors  $Q_3$  and  $Q_4$  respectively. This being the case it can be easily shown that

$$T_1 = \frac{V_1 C_1}{I_3} = \text{Constant (since } I_3 \text{ is constant)} \quad (2)$$

and

$$T_2 = \frac{(V_1 - V_2) C_2}{I_4} \quad (3)$$

Combining the above quantities into the expression for the output voltage ( $V_0$ ) we have:

$$V_0 = \frac{T_1 V_1}{T_1 + T_2} = \frac{T_1 V_1}{T_1 + \frac{V_1 C_2}{I_4} - \frac{V_2 C_2}{I_4}} \quad (4)$$

If we make

$$T_1 = \frac{V_2 C_2}{I_4} \quad \text{then} \quad (5)$$

$$V_0 = T_1 \frac{I_4}{C_2} \quad (6)$$

which is a constant, independent of  $V_1$ . We can thus obtain perfect line "pre-regulation".



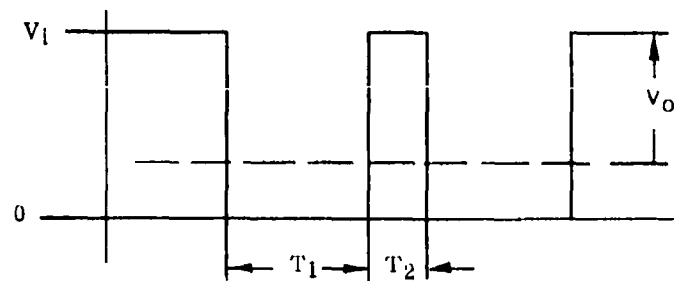


Fig. 6. Voltage waveshape at collector of series switching transistor (Q<sub>6</sub>).



Since this ideal situation is difficult to obtain in practice, the external feedback is needed to correct for the discrepancies and load variations. This is accomplished by varying  $I_3$  and  $I_4$ .

The upper limit of the line voltage change is dictated solely by the breakdown voltages of the transistors and the decrease in efficiency. The lower limit is obviously  $V_0$ . A 100 percent line change was demonstrated with a drop in regulation to 0.07 percent at 25°C.

Since the "pre-regulation" circuit reacts very rapidly this regulator does not have to rely on the slow response of an inductor-capacitor feedback network to correct for fast transients in the input line voltage.

#### High Voltage Converter

In order to obtain the maximum efficiency out of a free-running converter, the circuit configuration shown in Fig. 7 has been designed.

The Darlington connection increases the effective  $\beta$  and thereby reduces the power supplied to the bases of  $Q_1$  and  $Q_2$ . For the same reason the value of the starting resistor,  $R_S$ , may be made large and once again save power. Taps are provided to reduce the saturation drop across  $Q_3$  and  $Q_4$ . The circuit has been designed and tested for operation down to -40°C, and operates satisfactorily even under the conditions where the power supply voltage is brought up very gradually.

The converter is shut-off by grounding point  $x$  through a resistor in the timer. This action reverse biases the b-e junctions of the H.V.C. transistors and prevents regeneration.

#### Output Rectifier and Filters

The output transformer has several output windings which are rectified, filtered and then added to obtain the necessary high voltages. This method of developing high voltage outputs places much less stringent PIV ratings on the rectifiers and thus provides a higher degree of reliability.

Additional protection against high voltage surges damaging the rectifiers when the supply is turned off can be realized by the addition of a small input capacitor. Since the voltage transient is of only a very short duration, the capacitor size must, of course, be a compromise between high turn on current transients and high turn off current transients.

#### Timer

The timer circuit shown in Fig. 8 serves a dual purpose. It delays the application of the high-voltage until a proper warmup of the heater is accomplished and it



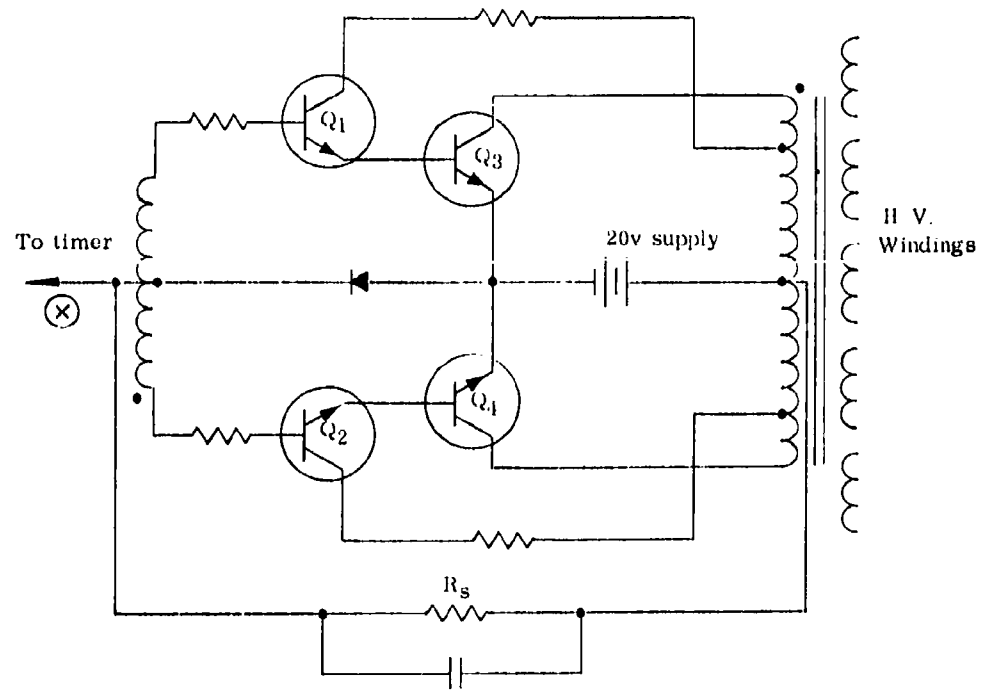


Fig. 7. Free running converter.



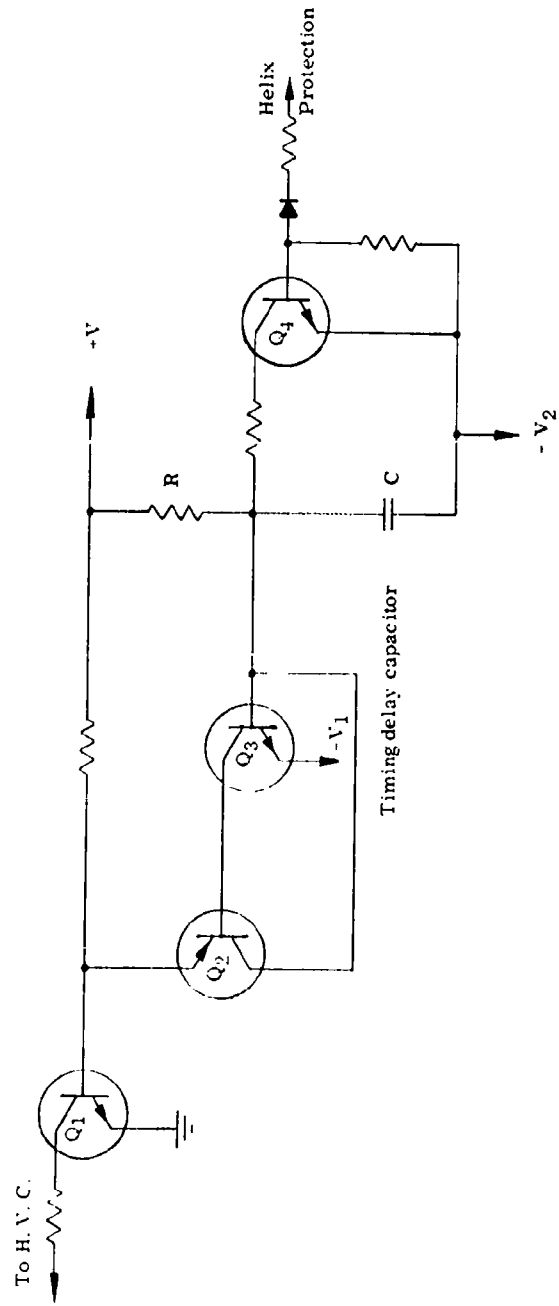


Fig. 2. Timer for high voltage converter



disconnects the high voltage if excessive helix current is developed.

The circuit consists of an R-C network with the provision (Q<sub>4</sub>) to discharge the capacitor when the helix current becomes excessive. Transistors Q<sub>2</sub> - Q<sub>3</sub> make up a Schmidt-trigger type circuit operating around - V<sub>1</sub>. This combination is required to ensure proper switching action. Q<sub>1</sub> is needed to isolate the timer from the H. V. C. and provide proper phasing of the bias control to the bases of the HV transistors.

### Telemetry

In an attempt to adequately be capable of diagnosing any problems within the amplifier five points are signal conditioned for telemetry purposes; (regulator voltage, low and high voltage converter outputs, helix current and cathode current).

Since the helix is physically tied to ground, an indication of its current may be obtained by measuring the voltage drop across a series resistor as shown in Fig. 9. Since the cathode is 1750 v below ground, its current will be monitored by means of an isolation transformer (Fig. 10) and will be accomplished relative to the ac equivalent of the cathode current. This method of ac sampling and subsequent rectification provides linearity and accuracy of better than 1 percent.

Monitoring of the voltage regulator will be accomplished with the aid of the circuit in Fig. 11. Since the 20 v dc supply is referenced to the positive side of the input voltage instead of ground the above circuit will yield a scaled down indication of the regulator output. This is accomplished by making the gain from point 1 to the output equal and opposite to that from point 2. If the voltage regulator telemetry output is to stay constant when the 20 v supply is constant we must have the equality that:

$$R_2 R_3 = R_4 (R_1 + R_2) \quad (7)$$

The voltage outputs of both the low and high voltage converters are conditioned by circuits such as that shown in Fig. 12. The H. V. C. output measures the anode to helix potential which is 100 volts and is referenced to ground.

All of the above telemetry outputs are non-inverting, have an output impedance of less than 2.5 k, have +6 volt positive limiting and are "short-circuit proof".

### Output Harmonic Filters

The output of the TWT is fed into a harmonic filter in order to reduce the second harmonic level to the specified level.

Assuming that the 2nd harmonic power is 18 db below the carrier, then an additional 52 db is required to meet the specification of 70 db below the carrier. This will require a low pass filter in series with the tube output. Using a noise figure of



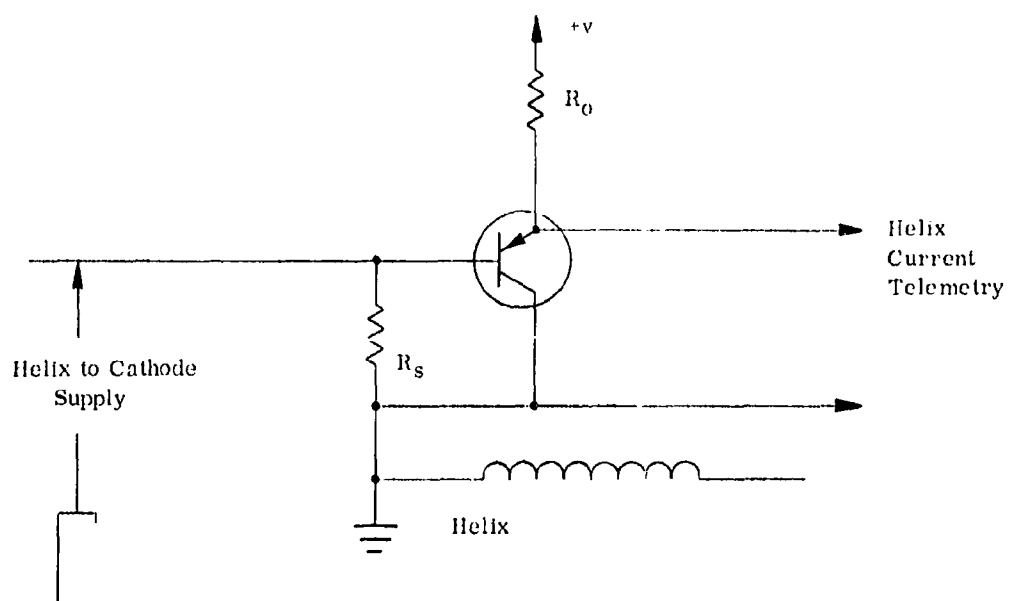


Fig. 9. Helix current telemetry conditioning circuitry.



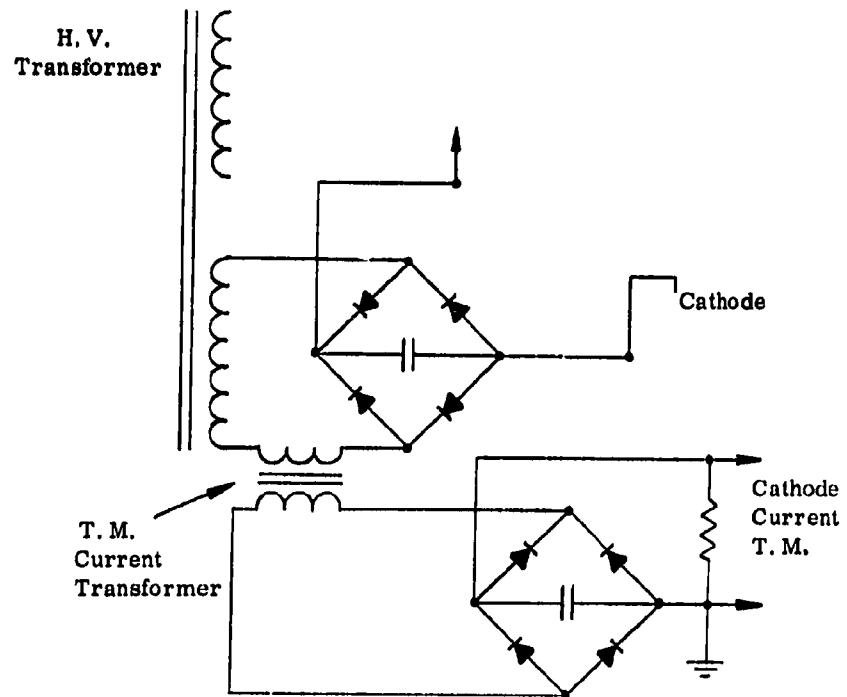


Fig. 10. Cathode current telemetry conditioning circuitry.



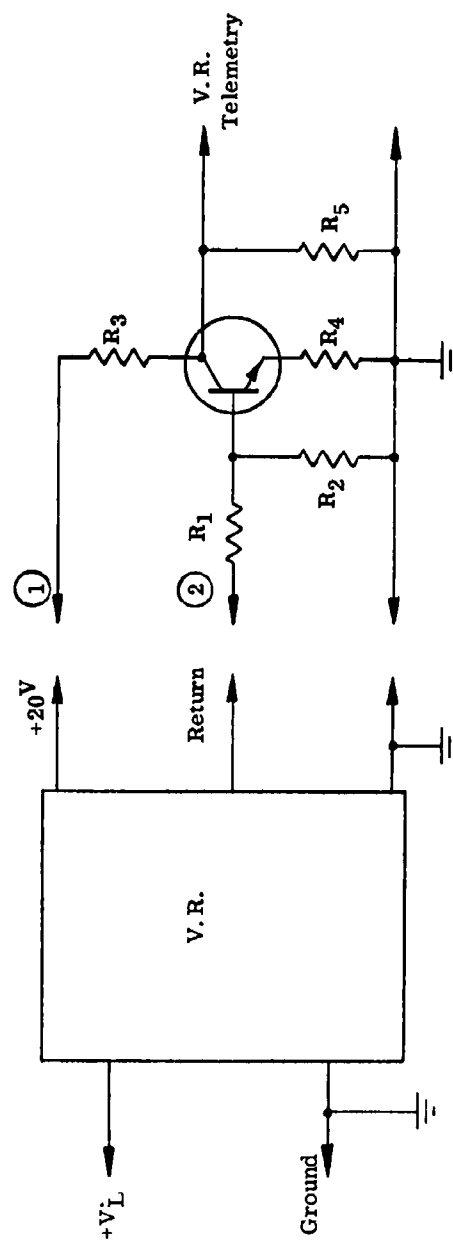


Fig. 11. Regulator voltage output telemetry conditioning circuitry.



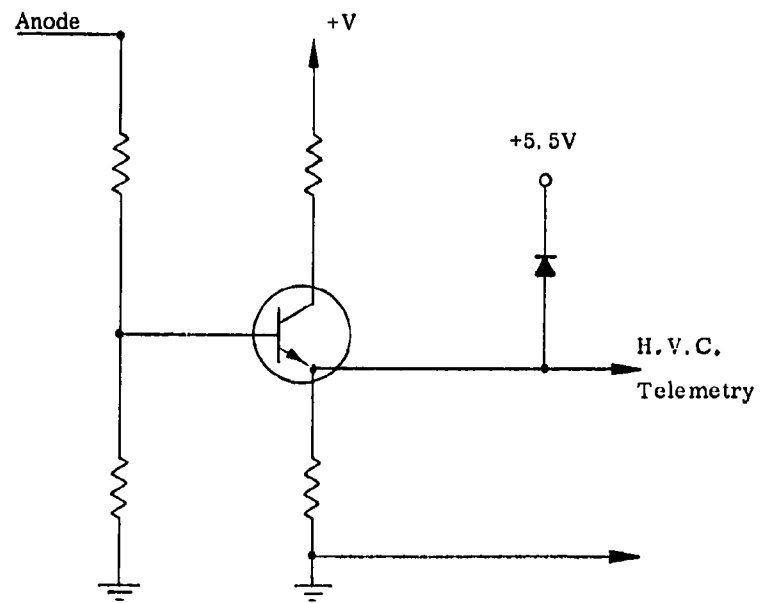


Fig. 12. High voltage converter telemetry conditioning circuitry.



30 db and a gain of 35 db, the noise power within the band is calculated to be -49 dbm/Mc which is well below the carrier level of 34 dbm. Assuming a bandwidth of 1 Mc, the noise power will then be 83 db below the carrier.

#### Mechanical Considerations (Amplifier)

The demands placed on the system for minimum volume and weight, in combination with the ability to operate in a vacuum environment place very stringent requirements on the packaging and excapsulation portion of the over-all design.

The entire power supply is contained in a single package since not only does this approach reduce the weight and volume, but enhances the solution to the RFI problems (Fig. 13).

The supply is completely encapsulated with the outer can providing only RFI shielding. The major sub-assemblies inside the can are the regulator, low voltage converter, high voltage converter and RFI modules.

The power transistors are mounted directly to the bottom of the can so as to keep the thermal resistance between the vehicle frame and the transistor case a minimum. The RFI filter will be installed into the assembly first and as such will form an integral portion of the power supply can.

The high voltage transformer is mounted close to the output headers, which in turn are located next to the tube pin connections. The anode and helix taps are brought out to a header so that the operation of each tube can be optimized. In this manner, all that is required to change either the anode or helix voltage is the jumpering of these output taps.

The basic package configuration has been dictated by RFI considerations so as to minimize the level of interference propagated or conducted from the various sub-assemblies.

The input power connector, which also contains the telemetry outputs, feeds into a RFI filter can, in which each output and input lead is decoupled and contains feed thru capacitive terminals. The entire assembly is solder sealed to prevent any rf energy escaping around possible mechanical discontinuities. It is presently contemplated, even though further testing is required, to provide tiny air holes which, while not passing the undesired radio frequencies, will allow air to flow around the potting compound. This is deemed necessary due to the stringent environmental conditions ( $10^{-9}$  mm/Hg) and the fact that out-gassing will be taking place within the encapsulant. If some type of venting is not allowed and volume is to be kept to a minimum, it is strongly felt that a rupture might take place.



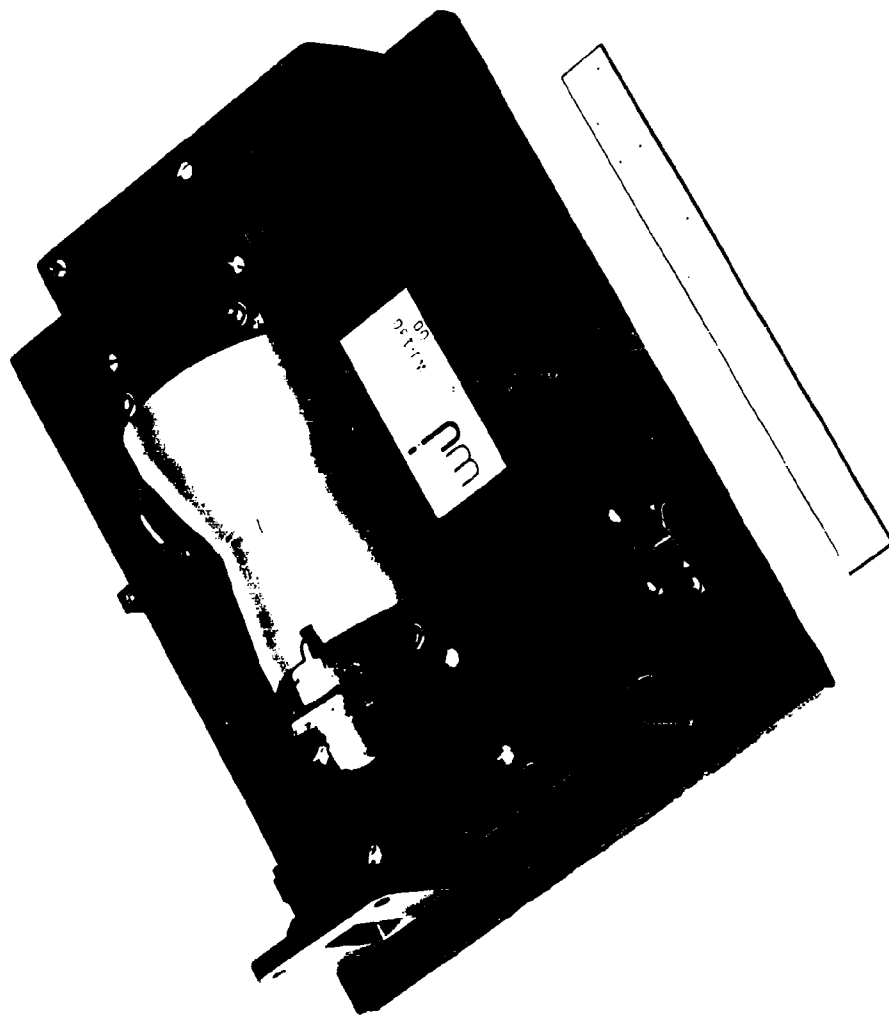


Fig. 13. WJ-130 high efficiency, high reliability traveling-wave tube amplifier (power 2.5 watts, frequency 7.0 - 8.5 Gc).



## RELIABILITY

Reliability to be an actuality, rather than just a word, must be initially designed into the equipment along with other basic performance parameters. This marriage can best be accomplished by considering the reliability program to be an integral part of the total effort. This is effectively done in that level of the company having over-all project responsibility.

No single factor in the design of a reliable equipment is more important than selection of parts and materials of adequate quality and their application in the design at levels within their capabilities.

Economic considerations also demand that parts costs and materials be kept to a minimum while still meeting requirements for performance (including reliability). It thus becomes essential to know with a considerable degree of certainty the demands of and operating conditions in the circuit application (determined by the designer) and to match these needs with capabilities having adequate factors of safety commensurate with cost, size, weight, performance, etc. It should be noted quite emphatically, however, that at no time in this program did other factors take precedence over reliability and performance.

All aspects of the present program are aligned towards one goal -- reliability. All of the 63 amplifiers which are being produced are destined for various life and evaluation tests so as to increase the confidence level associated with this piece of equipment.

As a measure of the completeness of the over-all testing program the acceptance level tests, which are to be performed on all amplifiers, are outlined below.

1. 200 hours stabilization
2. Functional check
3. Physical check
4. Complete vibration test (each of three coordinate directions)
5. Functional and physical check
6. Continuous 1000 hour life test (ambient conditions)
7. Functional and physical check
8. 1000 cycle life test (ambient conditions, 15 min. on and 15 min. off)
9. Functional and physical check
10. Thermal vacuum test for six days ( $10^{-5}$  mm/Hg)
11. Functional and physical check



Following the satisfactory completion of the tests listed above the units will be placed on test under the following conditions.

1. Five amplifiers -- ambient temperature, pressure  $10^{-5}$  mm/Hg for 30 days at full power.
2. Thirty-five amplifiers -- ambient temperature, pressure  $10^{-5}$  mm/Hg for one (1) year at full power.
3. Five amplifiers -- ambient temperature and pressure for one (1) year at full power.
4. Five amplifiers -- ambient temperature and pressure, cycled 15 minutes on, 15 minutes off for one (1) year.
5. Eight amplifiers -- certification tests.
6. Five amplifiers -- flight proof tests which include vibration, temp-altitude, acceleration, humidity, thermal vacuum, acoustic field, shock and RFI.
7. The 35 amplifiers of Item 2 will continue tests into the second year or until such time as the units have failed.

#### CONCLUSION

The integration and implementation of the total amplifier in a single facility has led to the close coordination and solution of the interface problems between the traveling-wave tube and power supply. In particular problems associated with mating the tube and power supply and eliminating RFI have been more easily solved. The end result of this close integration has been a state-of-the-art amplifier which possesses the qualities so desirable for satellite application -- efficiency, reliability, small weight and volume, and optimum performance.

#### REFERENCES

1. J. R. Pierce, Traveling-Wave Tubes, p. 160, D. Van Nostrand, 1950.
2. A. Nordsieck, "Theory of the Large Signal Behavior of the Traveling-Wave Amplifier", Proceedings of the IRE, 41, pp. 630-647, May 1953.
3. J. C. Slater, Microwave Electronics, D. Van Nostrand, 1950, pp. 298-299.
4. P. K. Tien, L. R. Walker, V. M. Wolontis, "A Large Signal Theory of Traveling-Wave Tube Amplifiers", Proc. of IRE, 43, pp. 260-277, March 1955.
5. F. Sterzer, "Improvement of Traveling-Wave Tube Efficiency Through Collector Potential Depression", IRE Trans., ED-5, Vol. 4, pp. 300-306, October 1958.
6. J. P. Lalco, H. L. McDowell and C. R. Moster, "Traveling-Wave Tube for 6,000 Mc Radio Relay", BSTJ Vol. 35, pp. 1285-1346, November 1956.
7. Private Communication from R. W. Peter, formerly of RCA Laboratories.



## MANNED ANTI-SATELLITE SYSTEM

E. E. Honeywell  
General Dynamics Corporation  
Pomona Division  
Pomona, California

## ABSTRACT

The major problem of satellite defense within the framework of the present political environment is the determination of the military value of a particular orbiting vehicle. Inspection of satellites by ground-based equipment is inadequate and inspection by unmanned satellites has many shortcomings. In this paper, a conceptual design of a manned orbital inspection system is presented. The concept provides for close inspection of the target satellite while still allowing the crew to remain a relatively safe distance from the potentially hostile satellite. In addition, the concept includes a means of destroying the target satellite if it is determined to be hostile. The command module of the system is a re-entry body which is capable of returning the crew to a selected landing site and landing in the manner of a high performance airplane. The Titan III booster is considered as the launch vehicle in the concept.

The work described in this paper is the result of General Dynamics/Pomona-funded research and in no way can be construed as having the endorsement of the Department of Defense or the U.S. Air Force.



## MANNED ANTI-SATELLITE SYSTEM

E. E. Honeywell  
General Dynamics Corporation  
Pomona Division  
Pomona, California

## INTRODUCTION

This paper presents a conceptual design of a system which provides for close inspection of earth satellites by man and, in addition, a satellite negation capability which can be employed in the event the target satellite is determined to be hostile. It is not proposed that the system (or any of the major sub-systems) is the optimum solution to the problem of satellite defense; it is merely one of several plausible approaches.

## SYSTEM CONCEPT

General Description

The system to be presented is tailored to the following specific concept. Upon designation of a target satellite a manned vehicle ascends from a ground launch site (or from a parking orbit) on a trajectory whose apogee is at a point of tangency between the paths of the two vehicles. Initiation of the ascent is timed so that the manned vehicle arrives at apogee a prescribed distance from the target. This distance is based on the estimated minimum safe displacement between the manned vehicle and an assumed offensive target satellite, and the maximum range capability of a practical rendezvous radar design. The currently prescribed value is 50 miles. At apogee the manned vehicle injects into the target's orbit (in general this requires a planar transfer) and its displacement from the target is maintained at the prescribed value.

The manned vehicle carries a number of devices whose dual mission is to perform remote, close-in inspection of and, if necessary, to negate the target. If the target exhibits any sign of hostility then the inspection mission is immediately by-passed or interrupted in favor of the negation mission. A hostile sign might be any of the following: (a) destruction or attempted destruction of the manned vehicle, (b) jamming of the communication and radar links, and (c) an evasive maneuver.

After successfully engaging the primary target the manned vehicle will remain in orbit to perform similar missions as the opportunity arises. A three day life support is considered; however, the duration of the mission might be shortened due to consumption of maneuver fuel, use of all inspector/killer mechanisms carried, or occurrence of most opportune or practical time for reaching desired landing site on earth.



One possible system concept for performing this mission is illustrated in Fig. 1. The Titan III boost vehicle is employed to place the manned vehicle and mission module in earth orbit.

The three man command module is lenticular in shape and is the only portion of the system which re-enters the atmosphere. The reasons for selecting this particular configuration will be dealt with in the latter portions of this paper.

The mission module consists of four satellite inspector/killer mechanisms, the fire control radar, and the propulsion system for orbital maneuvers.

Exploded views illustrating the system components are given in Figs. 2 and 3. As can be seen, the cockpit can be separated from the command module for mission abort while on the launch pad or during the initial phases of ascent. For abort after attaining supersonic velocity, the complete command module would be separated from the booster by the maneuver propulsion system. The command module could glide to an emergency landing site and land in the normal manner or the cockpit could be ejected and landed by parachute.

A weight breakdown of the proposed system is given in Table 1.

Table 1. System Weight

Command Module	8,500 lb
Mission Module	20,500 lb
Four Inspector/Killer Devices	1,680
Engine	3,600
Propellant	14,300
Control, Radar, Misc.	920
Total	29,000 lb

#### Energy Management

For apparent reasons the propulsion requirements of both the inspector/killer device and the manned vehicle should be minimized. Furthermore, as much of the inspector/killer fuel as possible should be reserved for the possible negation mission against evasive targets. Accordingly, in the absence of a hostile sign, there is no justifiable reason for imposing a small upper limit on the time required for completion of the inspection mode. In the absence of a time constraint the inspector/killer can utilize the relative closing velocity which exists prior to orbital injection of the mother ship ahead of the target, for attaining inspection range.

Since plane transfer and orbital injection can be accomplished most economically as a combined operation requiring a single velocity impulse, the inspector should be released from the manned vehicle prior to this combined maneuver.



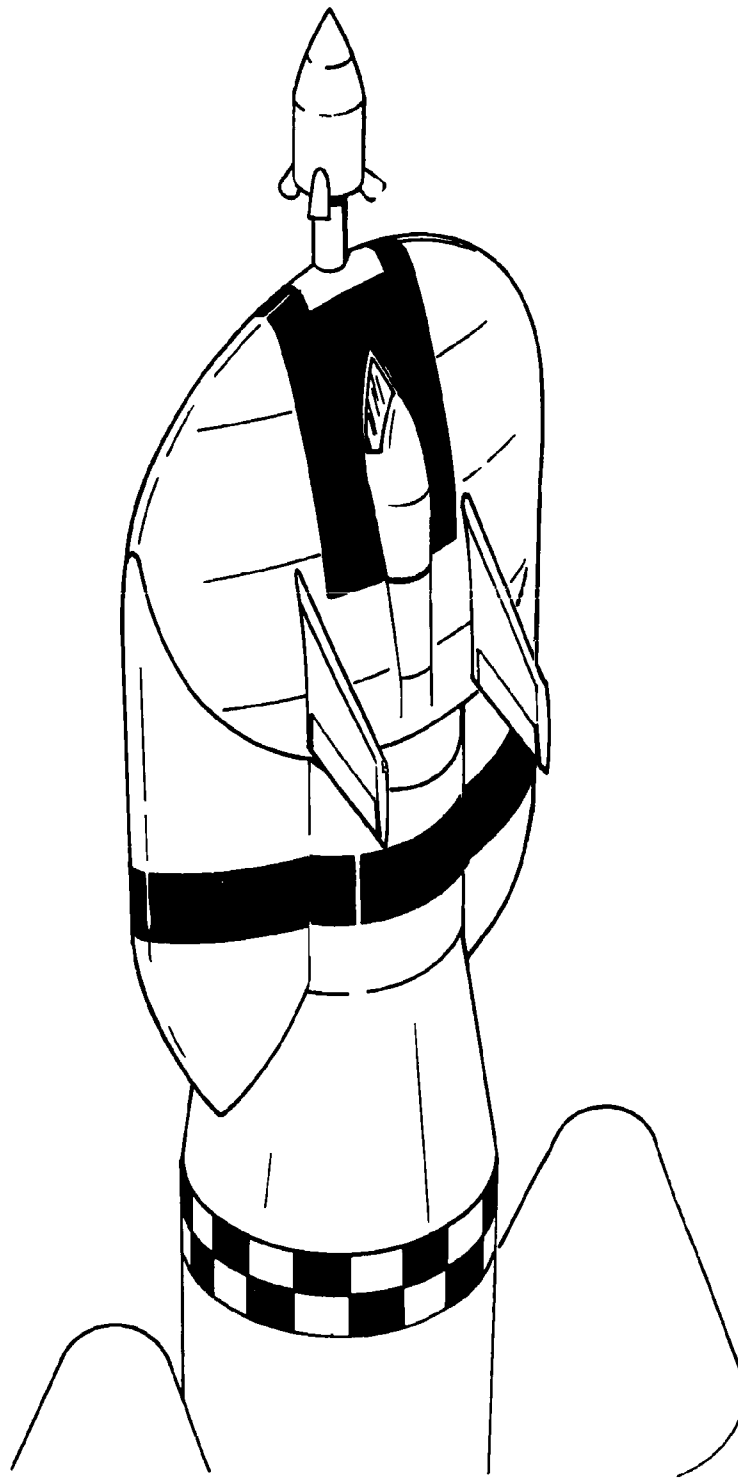


Fig. 1. Launch Configuration



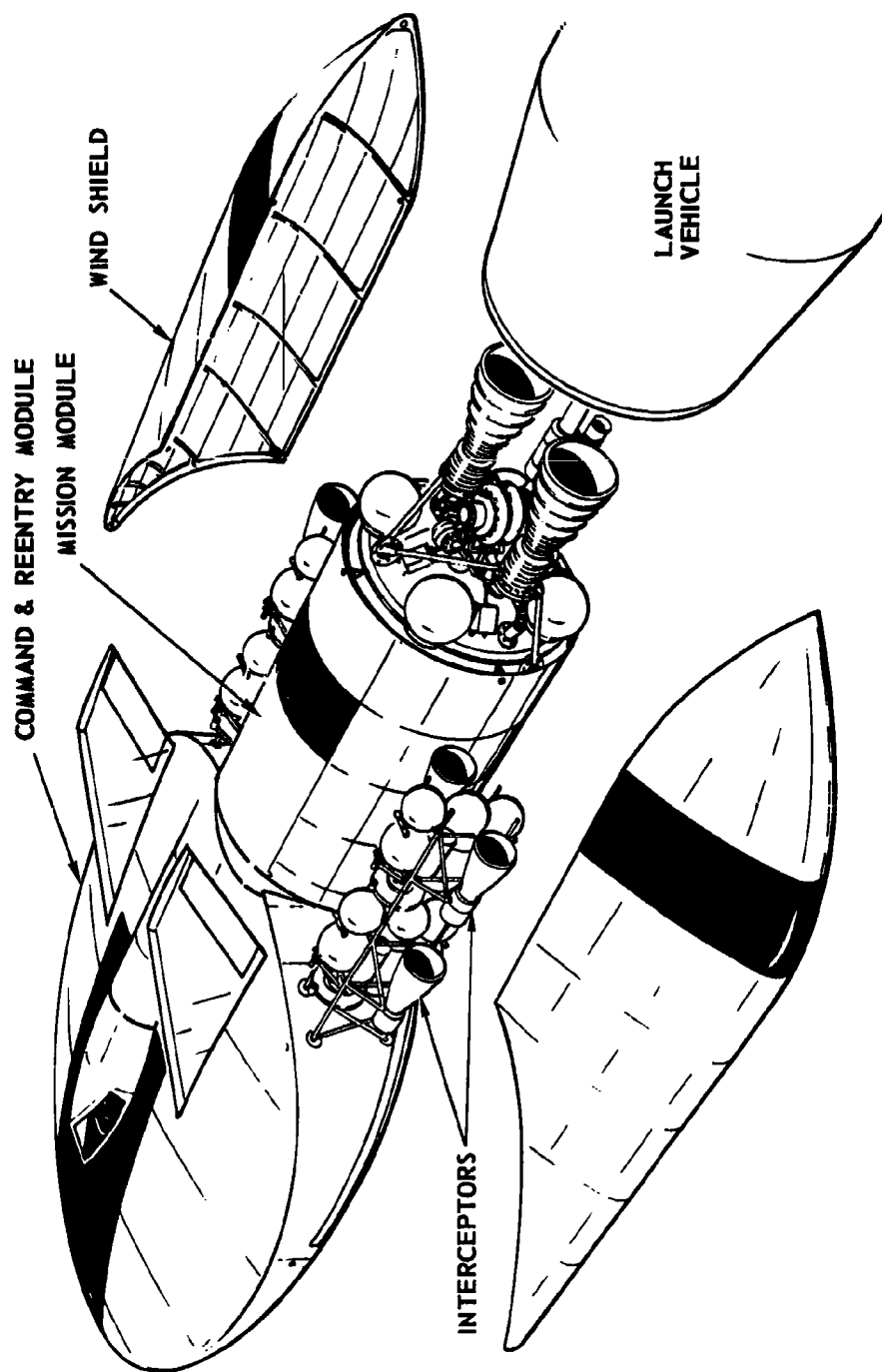


Fig. 2. System Configuration



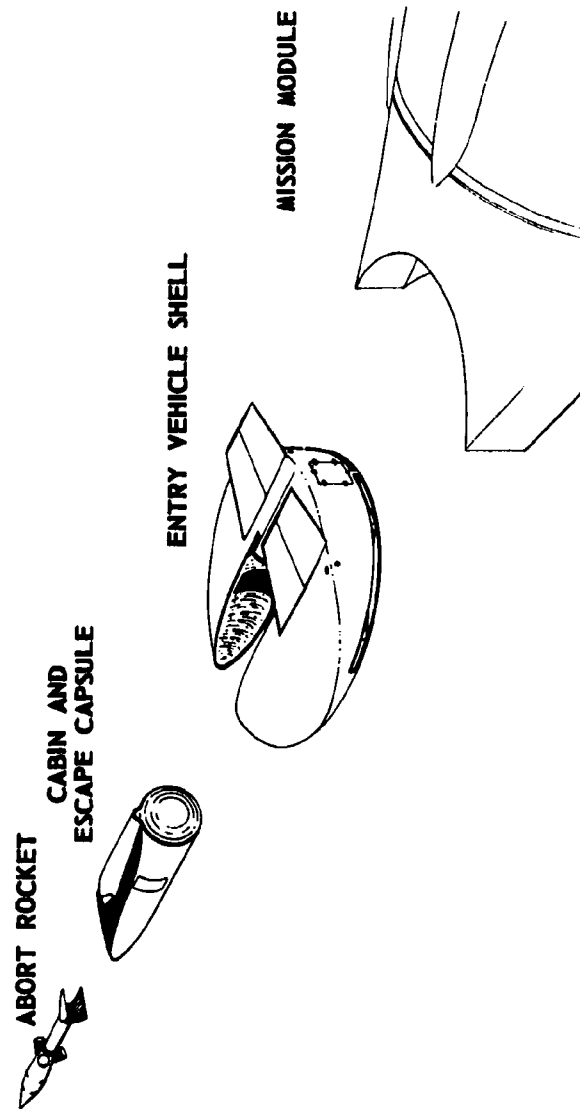


Fig. 3. Three-Man Space System; Exploded View



The minimum energy operation is illustrated in Fig. 4. During Phase 1 the manned vehicle is ascending to target satellite orbit and the radar is in a search mode. The manned vehicle radar has acquired the target in Phase 2 and is approaching ascent trajectory apogee (tangent to target orbit) approximately 50 miles ahead of the target. At this time the inspector is released and allowed to coast freely along the ascent trajectory. The manned vehicle reaches apogee in Phase 3 and is injected into the target orbit leading the target by approximately 50 miles. Target has not given any sign of hostility so the inspector remains on the slower transfer trajectory allowing target to catch up. Inspection is initiated when the target comes within range and the inspector makes orbit plane correction if required. During Phase 4 the target catches up with the inspector which then injects into target orbit. The inspector maneuvers around target to perform close inspection during Phase 5. During Phase 6 the target is determined to be hostile and the negation task is performed. This could have occurred at any time after the inspector/killer was released from the manned vehicle.

To illustrate the economy of the above procedure, the following points are made: (a) the fuel required for injecting the manned vehicle without the inspector/killer device on board was less than if it had been on board, (b) by allowing the inspector to coast on the ascent trajectory while the target catches up instead of orbit injection aboard the manned vehicle, the inspector does not have to decelerate from orbital velocity to match position with the target and then accelerate again to maintain station. For practical inspection times this would amount to considerable  $\Delta V$  (i.e., weight of propellants).

With this procedure, the inspector needs propulsion for only one orbit injection and/or intercept maneuver as well as a small amount for attitude control.

The required average relative velocity as a function of time to intercept is given in Fig. 5. As can be seen, for initial relative displacements typical of that desired for manned vehicles, quite high velocities are required for closure times of one to two minutes. If the closure maneuver can take as long as four minutes, for example, a velocity of only 1300 ft/sec is required for an initial separation of 50 miles. If the intercept transfer trajectory is made with a transition angle of 80 degrees such that apogee is in front of the target satellite, the closing velocity between the inspector and target is approximately 1300 ft/sec (see Fig. 6), the value required in the above example (this assumes the inspector was released from the manned vehicle which was injected into orbit ahead of the target).

It is interesting to note in Fig. 7 that the total  $\Delta V$  requirements for obtaining orbital velocity with a transition angle of  $80^\circ$  are very close to those for the optimum case of  $180^\circ$  transfer (Hohmann).

There are essentially an infinite number of examples to illustrate how the available maneuver propellant could be utilized to engage other targets after completion of the primary mission. This is due to the many parameters involved such as target orbit altitude, inclination and eccentricity relative to the interceptor, allowable intercept time, and propellant characteristics,



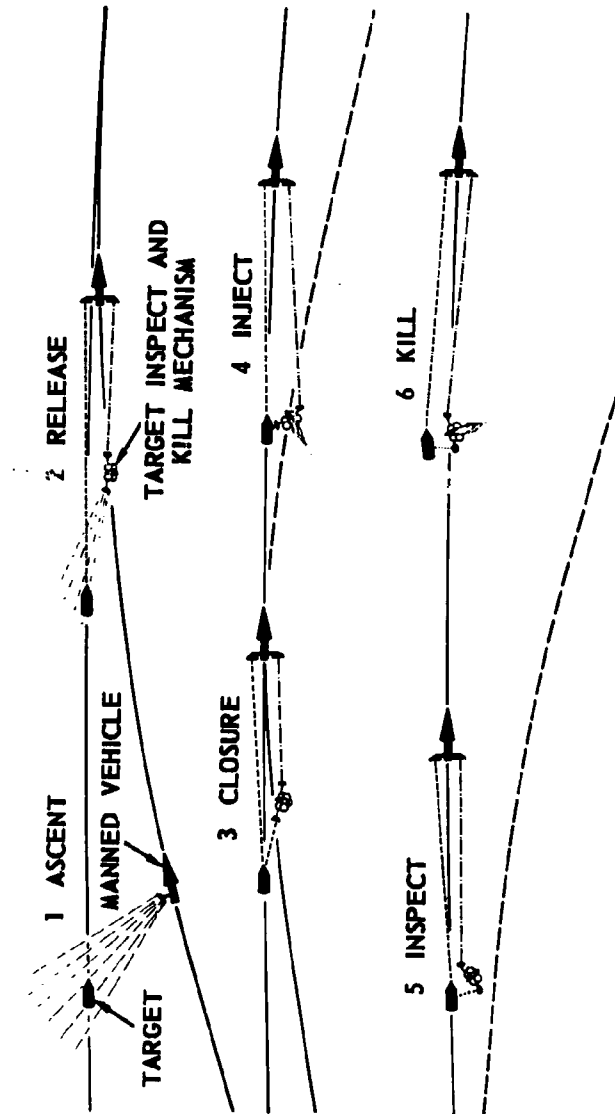


Fig. 4. Mission Sequence of Events



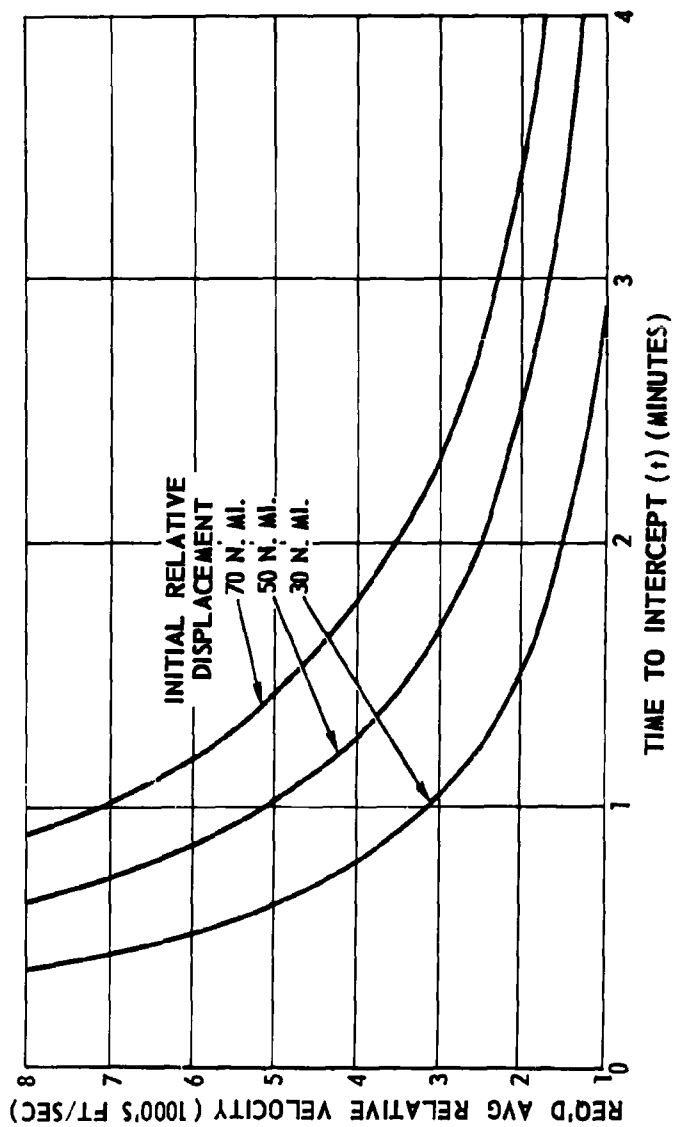


Fig. 5. Required Average Relative Velocity vs Intercept Time



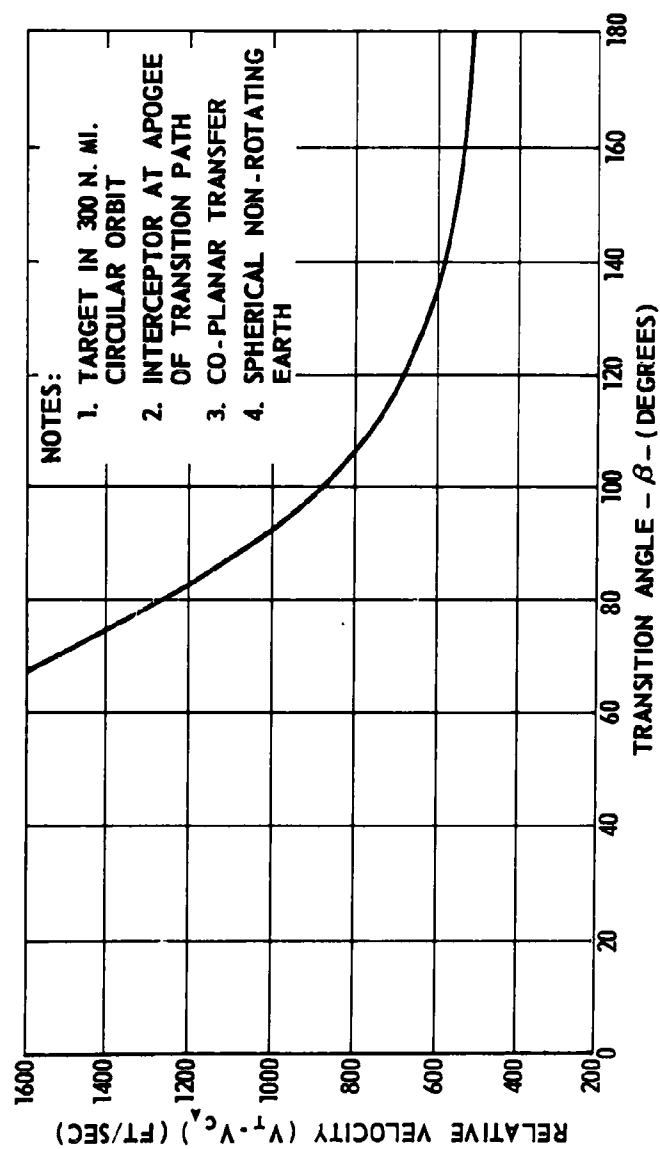


Fig. 6. Relative Velocity vs Transition Angle



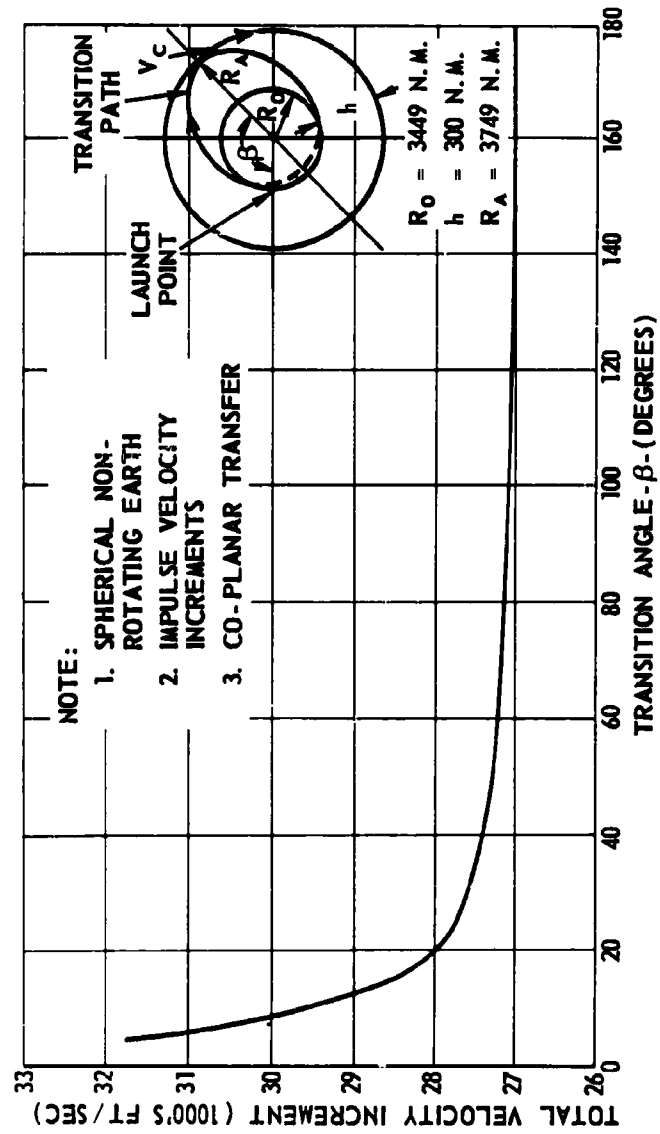


Fig. 7. Orbital Velocity Requirements vs Transition Angle



as well as others. For an example, we will restrict the orbits of the target and manned interceptor to the coplanar case. The geometry involved is illustrated in Fig. 8. Assuming a target orbit altitude ( $h_t$ ), envelopes of rendezvous capability can be determined as a function of the initial altitude of the interceptor ( $h_i$ ) and the central angle (i.e., the angle between the radius vector to the target and the interceptor,  $\theta$ ) for various values of available propellant weight-to-total weight. The resulting regions of rendezvous capability against a target in a 300 mile circular orbit are shown in Fig. 9 for an assumed maximum intercept time of 6000 sec and a propellant specific impulse of 300 sec. (1)

The decision to engage a particular target at a particular time must also consider the propellant requirement for orbit ejection to effect re-entry.

#### INSPECTOR/KILLER CONFIGURATION

The inspector/killer configuration (see Fig. 10) consists of two main thrust chambers and six separate attitude control motors with the required propellant and pressurization tanks, data link antenna, target tracking radar antenna, TV camera, IR sensor and warhead. A flood lamp is provided for inspection while the target is in the earth's shadow. As shown in Fig. 10, the radar and data link antenna are folded for minimum storage volume in the mission module; they are extended upon release. An arbitrary design requirement was that the inspector/killer fit in a volume of 47 in. by 38 in. by 38 in. when packaged in the launch configuration.

#### Guidance and Control

In order to orient the thrust axes properly it is necessary for the manned vehicle to know the orientation of this device with respect to the manned vehicle frame of reference. The inspector/killer mechanism has two tracking antennas which are both gyroscopically stabilized; one tracks the target and the other tracks the manned vehicle. If the antenna axes are not parallel it is possible to determine the inspector's orientation through knowledge of the outer and inner gimbal angles of these two antennas. However, when the axes are parallel additional information is needed to provide a measure of roll orientation.

Since the line of sight from the inspector to the manned vehicle remains essentially horizontal throughout the mission it can act as a good spin axis for an horizon detector. Since an antenna is directed along this line it is a simple matter to fix the detector on this antenna.

If the antenna is free to rotate about its pointing axis it is possible to position a reference line (the axis of symmetry of the detector which is normal to the spin axis) in the vertical plane by rotating the antenna until the detector output is nulled. This provides a roll reference known to the manned vehicle. The gimbal angles associated with this antenna completely define the inspector's orientation in the manned vehicle reference system.



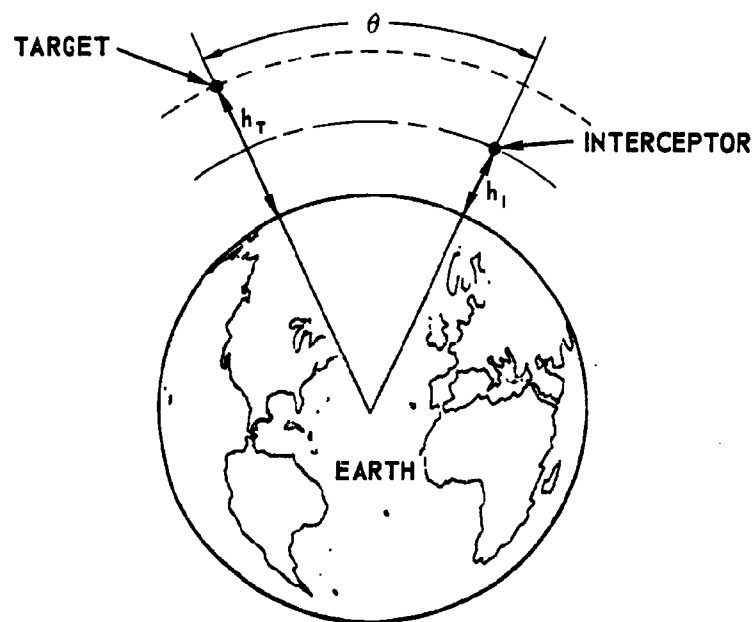


Fig. 8. Coplanar Coordinate System



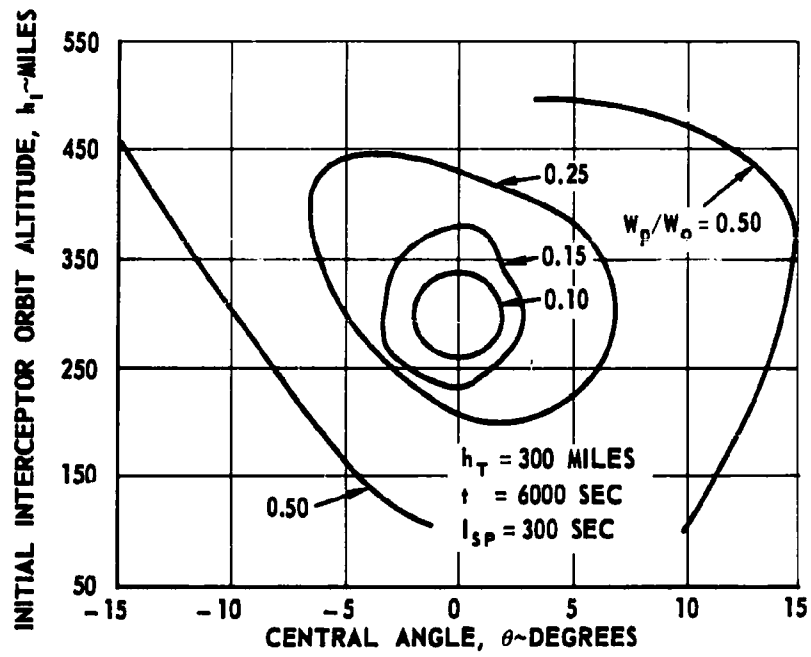


Fig. 9. Coplanar Rendezvous Capability



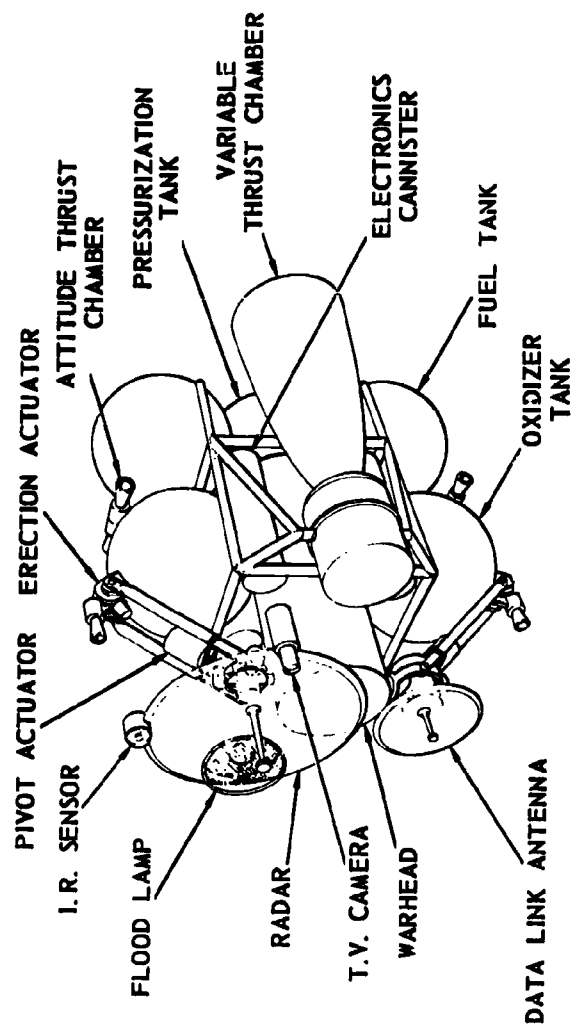


Fig. 10. Inspector/Killer Configuration



The inspector has eight reaction motors including the main rockets for controlling attitude; these were illustrated earlier. In addition, the primary rocket engines can also deliver a low level thrust (by incorporating a second set of control valves) which can be controlled independently of the main thrust. This in effect, provides ten attitude control motors which can be used to rotate the body about three axes. Translational capability is provided along two axes.

All motors except the two primary thrust chambers are low thrust devices. Each has a dual role in that each can be used to induce translation or rotation. It follows that each motor is shared by two control loops.

The simplest mode of operation for a reaction motor is the bistable mode since full-on and full-off commands are easily implemented. Control of thrust level is a more difficult and costly process. Bistable control can optimize the large error corrective capability of the attitude controller, but, it also introduces a small error chatter mode. The problems incurred by the chatter mode can be overcome or minimized by employing suitable filtering techniques.

#### Inspection Equipment

The basic function of the device just described is to provide the manned interceptor with a means of remotely inspecting and killing an enemy satellite. The main purpose of the inspection mode is to determine if the satellite is a threat to the interceptor or to national security. Fig. 11 illustrates the orientation of the vehicle during inspection.

Optical inspection is one of the most useful of inspection methods. Optical inspection by the crew can be performed from long range by the use of telescopes when the satellite is in the sunlight. However, when the inspection has to be done in the earth's shadow, illumination of the satellite is very difficult at a range of 50 miles. The inspector/killer device can provide this illumination since it can approach the target to a very close range.

Another prime advantage of inspecting with such a device is that it can maneuver around the target to view it from all aspects at a much lower fuel requirement than could the larger mother ship. IR scanning will also be more effective at close range.

It is proposed that the inspection equipment consist of a TV camera with optical illumination and an IR scanner. Characteristics of these components are listed in Table 2.

#### Data Link and Radar

The data link performs three primary functions: (a) transmit commands to the inspector/killer device, (b) provide range response and (c) transmit inspection data to the manned vehicle.



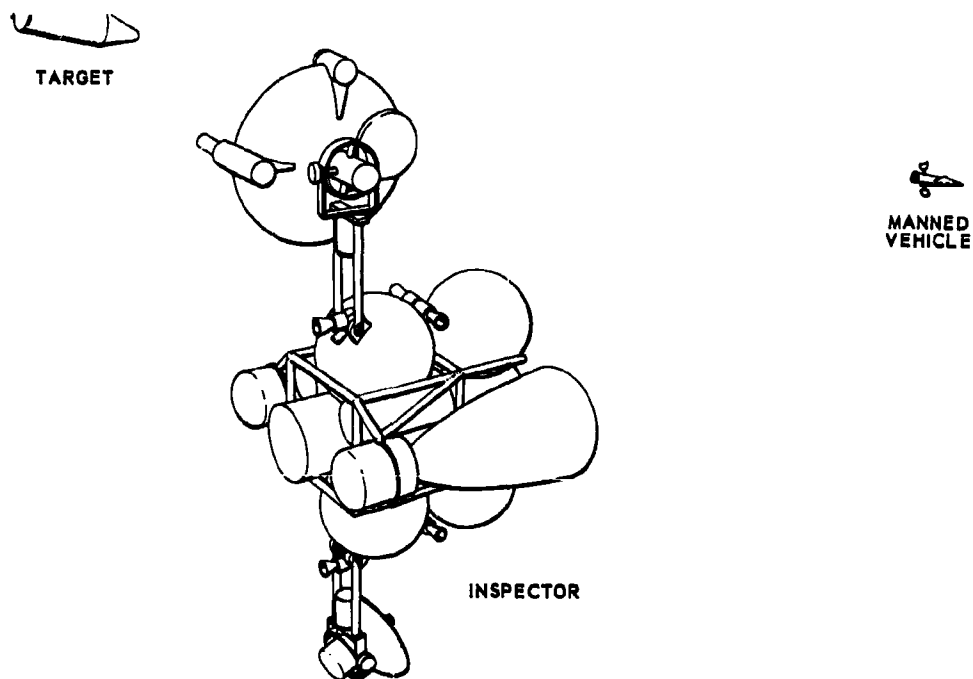


Fig. 11. Inspection Mode

Table 2. Inspection Components

TELEVISION

VIDICON TYPE

REAL TIME DATA IN DAYLIGHT

DATA RATE OF 0.5 SEC WITH FLOODLIGHT ILLUMINATION

PROVIDES CLOSE-IN ANGLE TRACKING

INFRARED

INDIUM ANTIMONIDE CELL

COOLED TO  $-20^{\circ}\text{C}$

SPECTRAL RESPONSE: 7 TO 10 MICRONS



The manned vehicle transmits commands by the use of pulse code modulation and the I/K device transmits FM inspection data and range indication. The parameters are given in Table 3 and block diagrams are shown in Figs. 12 and 13. The transmitters and receivers operate on different frequencies in the same band (about 16,000 mc) so they will not interfere with each other.

Table 3. Data Link Parameters

Frequency	16,000 mc
Antenna Size	1 ft diameter
Modulation	
Commands	Pulse code
Inspection Data	fm
Power	1 watt
Range	50 n.m.

Both of the antennas used in the data link system track the incoming signals. Conical scan tracking should provide sufficient accuracy and, when tracking, the scanning modulation should not interfere with the data. The 4° beam of the antenna should ease the acquisition problem so that extensive search patterns will not be necessary.

The parameters for the radar on board the manned vehicle are shown in Table 4. These values were used in determining the requirements of the I/K seeker.

Table 4. Assumed Fire Control Radar Parameters

Peak Power	150 kw
Frequency	16,000 mc
Antenna Diameter	5 ft
PRF	800
Pulse Width	0.25 sec
Dwell Time During Search	1/40 sec
Beam Width	0.8°
Detection Range at $P_o = 90\%$	50 n.m.

The I/K semi-active seeker is a pulse receiver to be compatible with the fire control radar on the manned vehicle. The R.F. section is a tunnel diode amplifier and mixer for low noise figure and simplicity. A separate local oscillator is not required.



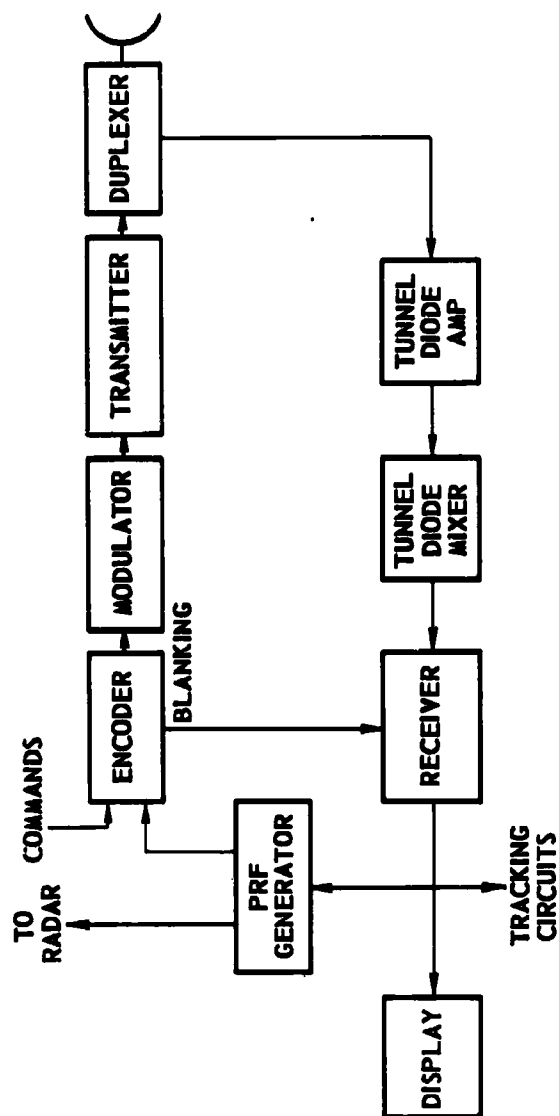


Fig. 12. Manned Vehicle Data Link



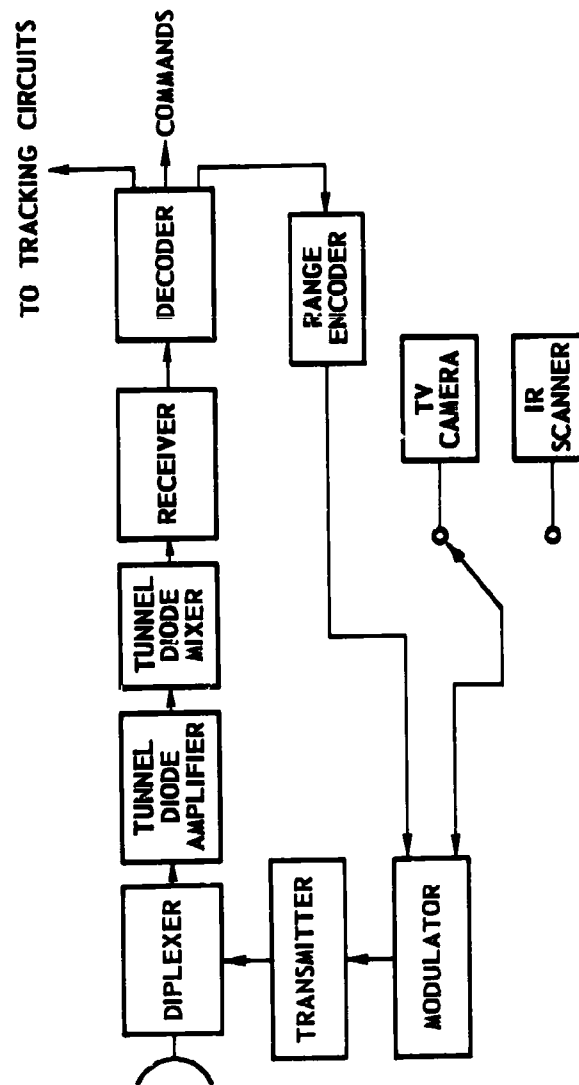


Fig. 13. Inspector/Killer Data Link



A range gate must be provided to gate out noise and unwanted pulses from the command system. Several range gates will be generated to aid acquisition. The timing of the range gate is controlled by signals received by the decoder via the data link. The manned vehicle knows the position of the I/K and the target and can then compute and command the proper range gate positions; conventional conical scan tracking circuits are provided. A home-on-jam mode can also be provided through proper circuit design.

The inspector/killer seeker parameters are given in Table 5 and a block diagram of the seeker is shown in Fig. 14.

Table 5. Inspector/Killer Seeker Parameters

Antenna Diameter	2 ft
Lock on Range Product	1700 (n.m) <sup>2</sup>
Noise Figure	4.5 db
Minimum Range Track	130 ft

#### Warhead

When it has been determined that the target should be destroyed the main thrust chambers will be aligned toward the target as shown in Fig. 15. If the target executes an evasive maneuver prior to warhead fuzing, the I/K will fly a modified proportional navigation course to intercept. The intercept capability against maneuvering targets will be presented later.

For the concept presented, sufficient kill probability can be provided with a non-nuclear device such as a shaped charge warhead. The fragmenting warhead concept shown in Fig. 16 has a theoretical kill probability of 95.3% for a target having a vulnerable area of 2 ft<sup>2</sup> and with an aiming error of 10 ft for example. The single shot kill probability of this warhead for various aiming errors is shown in Fig. 17 as a function of vulnerable area.

#### Inspector/Killer Propulsion System and Weight Summary

The propulsion design problem is basically to design a minimum weight, minimum volume system which will deliver the required performance. In general, the minimum weight and space requirements are not compatible and compromises must be made.

To yield some indication of the required system weight, parametric analyses, such as illustrated in Fig. 18 were utilized. The plot shows  $\Delta V$  capability as a function of propellant weight for several total I/K vehicle and payload weights. The chart is based on typical values of propulsion system mass fraction and  $I_{sp}$ ; 0.85 and 315 second, respectively. From this chart one can see that for an initial estimate of payload weight equal to 125 lb, for example, and if total weight is restricted to 450 lb, then the weight of propellant would be approximately 275 and the total  $\Delta V$  capability resulting would be about 9600 ft/sec. This  $\Delta V$  is more than sufficient to intercept most threats, as will be pointed out later; however, the payload



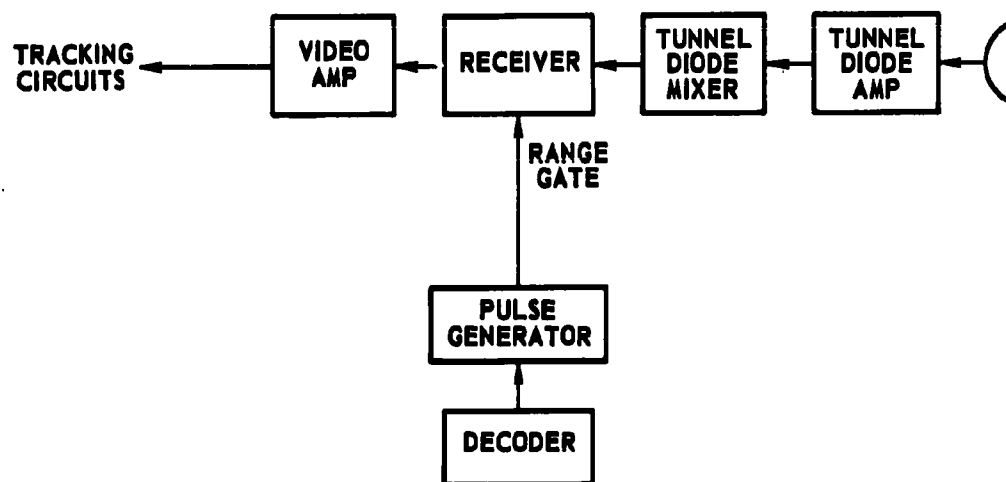


Fig. 14. Inspector/Killer Seeker



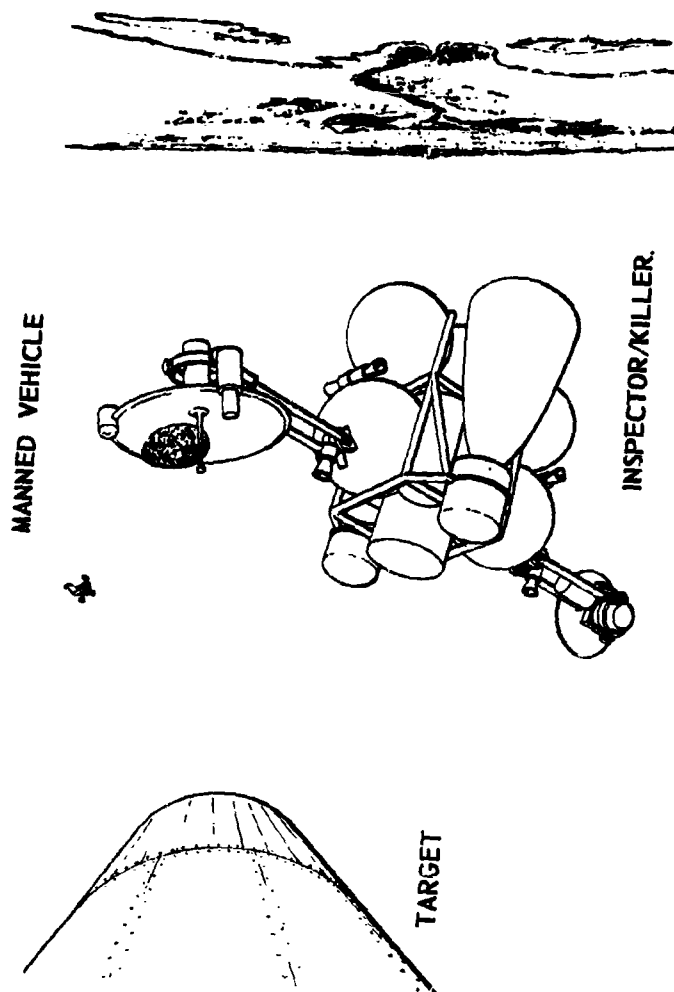


Fig. 15. Kill Mode



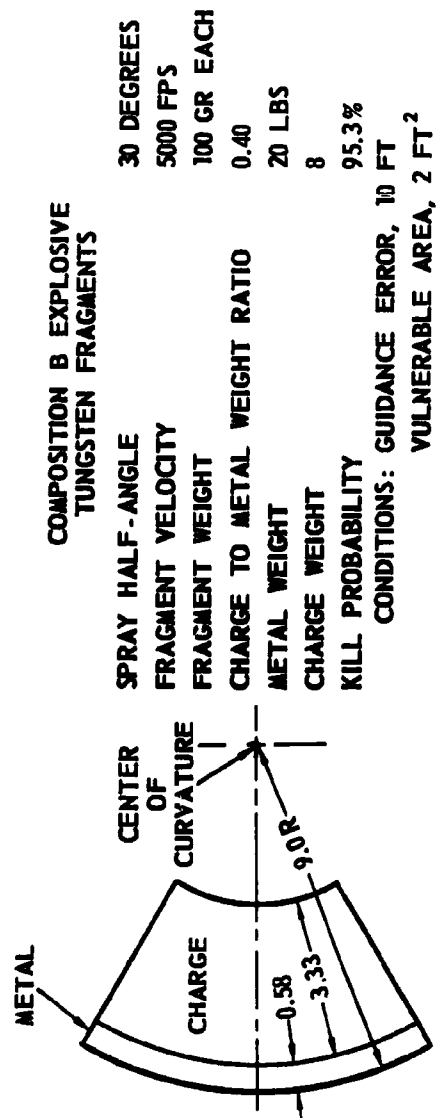


Fig. 16. Conical Charge Warhead



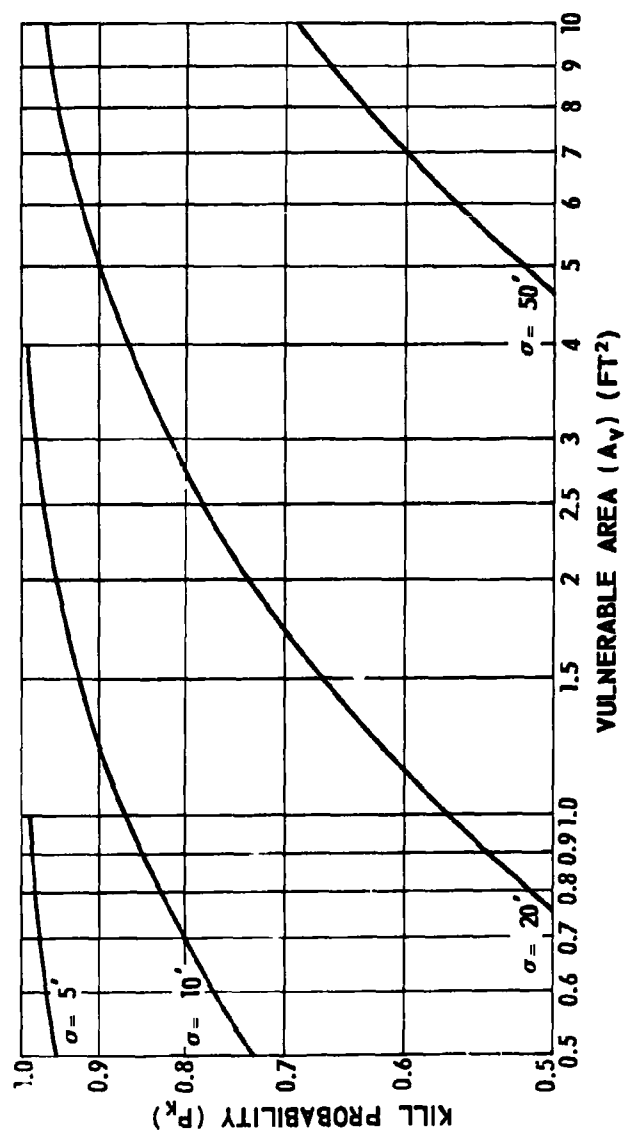


Fig. 17. Single Shot Kill Probability



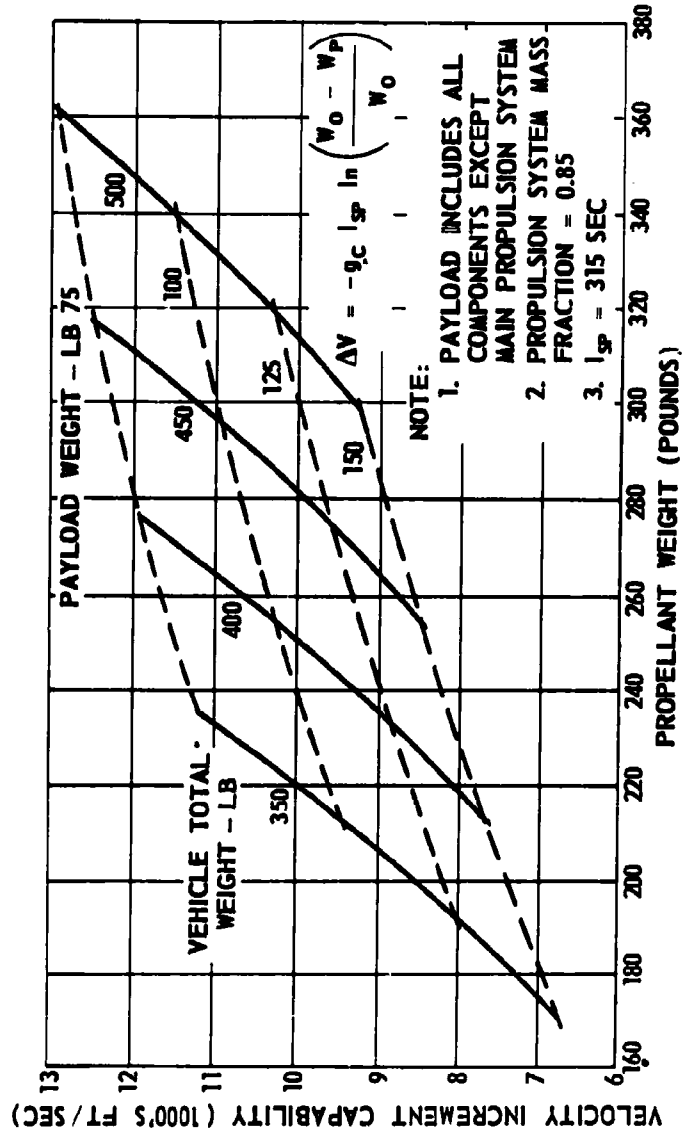


Fig. 18. Performance Chart



weight for the configuration shown earlier also is heavier than the above example weight.

In selecting the I/K propulsion system, solid propellants and hybrids were not given serious consideration because of the restart capability requirement and the logistic advantages of storable liquids. Also, if the storable liquid propellant is hypergolic, the same propellant can be used for attitude control, markedly reducing the number of vehicle components.

The following parameters were considered in selecting a propellant: specific impulse, density impulse, toxicity problems and storability. The propellant selected was nitrogen tetroxide for the oxidizer and 50% hydrazine - 50% unsymmetrical dimethyl hydrazine ( $N_2O_4/N_2H_4$  - UDMH) for the fuel.

To be as effective against the postulated threat as possible, analyses showed that an average acceleration of approximately 12 g's was desirable; therefore, a thrust level of 3200 lb was selected.

Due to arbitrarily selected space limitations (i.e. 38 in. x 38 in. x 47 in.) a single thrust chamber could not be configured which would deliver the required thrust in an economical manner; therefore, in a step towards optimizing the thrust chamber, two chambers which would fit in the envelope were selected. The resulting propulsion system characteristics are given in Table 6.

Table 6. Inspector/Killer Propulsion System

Oxidizer - Nitrogen Tetroxide ( $N_2O_4$ )  
 Fuel - 50% Hydrazine ( $N_2H_4$ ) and 50% UDMH  
 Oxidizer to Fuel Ratio - 2:1

Main Thrust Chambers

Nozzle Area Ratio	30:1
Chamber Pressure	300 psi
Length	25.1 in
Thrust (each)	1600 lb
Δ Thrust (each)	40 lb

Control Motors

Thrust (each)	5 lb
---------------	------

The dimension restriction also made it necessary to package the fuel and oxidizer in two tanks each, which is not optimum from a weight standpoint. A nitrogen pressurization system was selected. Propulsion system weights are given in Table 7.



Table 7. Propulsion System Weights

Main Thrust Chamber Assemblies	25.3 lb
Control Thrust Chamber Assemblies	10.0 lb
Fuel & Oxidizer Tanks	16.1 lb
Pressurization System	45.0 lb
Fuel & Oxidizer	<u>290.0 lb</u>
Total	386.4 lb

The weight estimates of the major systems and components of the I/K device are shown in Table 8. As can be seen, the total weight of the I/K is 472.5 lb.

Table 8. Weight Summary

Propulsion & Control System	386.4 lb
Warhead	38.0 lb
Structures	8.0 lb
Inspection System	8.0 lb
Communication Link	8.6 lb
Electronics	<u>23.5 lb</u>
Total Weight	472.5
Empty Weight	182.5

### Targets

The primary characteristics of the postulated threat which were considered in the design studies are given in Table 9. The Inspector/Killer concept presented has a  $\Delta V$  capability of around 9000 ft/sec. In comparing this with the postulated target  $\Delta V$ 's it is seen that the I/K can eventually overtake all of the example cases except the interceptor (priority #4). However, if the I/K is within 20 miles of the interceptor when it begins its evasive maneuver, the negation mission can be accomplished due to the I/K having a higher level of acceleration capability. The 20 miles is based on the target maneuvering straight along the initial line-of-sight between target and the I/K. If the target has an evasive velocity component normal to the line-of-sight, the maximum initial separation, for which the I/K can execute a kill, is increased. For this target, which is postulated to have a two man crew, the best evasive maneuver is essentially normal to the orbital plane (i.e., normal to initial line-of-sight) because, if the  $\Delta V$  is added to its orbital velocity, it is possible that the vehicle will attain earth escape velocity which is probably not desirable for several reasons. Even if escape velocity is not attained, its new orbit will be in the Van Allen radiation belts; also undesirable. If the  $\Delta V$  is subtracted from its orbital velocity the target will re-enter the earth's atmosphere and its primary mission will



Table 9. Target Characteristics

PRIORITY	MISSION	CREW	MANEUVERABILITY		COUNTERMEASURES
			g's	$\Delta V$ , fps	
1	BOMBARDMENT	0	1	2,000	BOOBY TRAP
2	RECONNAISSANCE	2	4	5,000	RADAR RANGE JAM
3	SURVEILLANCE	0	0	0	NONE
4	INTERCEPTOR	2	4	10,000	RADAR RANGE JAM
5	COMMUNICATION	0	0	0	NONE
6	LOGISTICS	3	1	2,000	NONE



probably have been negated.

#### COMMAND AND RE-ENTRY MODULE

##### Configuration Selection

The primary requirements for manned vehicles which must return to the Earth's surface after a space mission are to be capable of dissipating the enormous amount of kinetic energy without overheating or subjecting the passengers to intolerable decelerations. In addition to these primary requirements, the aspects of manned space missions are considerably improved if the atmospheric entry vehicle is capable of reaching and landing at a pre-selected or preferred site. This is also desirable from an economic point of view since this would enhance the feasibility of re-using the vehicle.

The results of extensive studies, which have been made at General Dynamics/Pomona since 1959 ((2) and (3)) show the lenticular configuration (Fig. 19) to be an excellent candidate for the optimum vehicle in terms of meeting the above requirements. The advantages offered by the lenticular configuration over other configurations are described in the following paragraphs.

During the initial phase of atmosphere entry the vehicle would be at a high angle of attack (60 to 75°) presenting a blunt surface which is near optimum from a total heat input standpoint for the velocities of interest. This blunt surface is also very desirable for the relatively high drag produced, even at the fringe of the atmosphere.

The configuration lends itself to a very attractive method of trajectory control, namely, rolling and directing the lift vector in the desired direction for control while still maintaining the high angle of attack. This is desirable since (a) extensive heat protection need be placed on the windward side only, (b) the astronaut does not experience oscillatory decelerations and (c) the vehicle continues to decelerate prior to reaching the very dense atmosphere. In essence, all these things widen the entry corridor.

After the critical heating and deceleration phase of entry, the vehicle can glide at an angle of attack which results in very favorable lift-to-drag ratios desired for long glide ranges and landing capability. Lift-to-drag ratios as good or better than other candidate entry configurations are attainable with the lenticular vehicle.

The lenticular configuration is superior to most other configurations in terms of weight. As pointed out above, the weight of the heat shield would be less than for most other vehicles; in addition, the configuration allows a highly efficient structural design since the cabin and wing are essentially an integral unit and no large bending moments are incurred. All surfaces of the body enclose volume which can be used for packaging subsystems, life support items, etc.





Fig. 19. Lenticular Entry Body



Analytical and experimental studies have been conducted to determine the best lenticular configuration. Wind tunnel tests were performed to determine the aerodynamic characteristics of the body shapes shown in Fig. 20. Model III was found to have superior lift, lower drag and better stability than the other configurations, as was predicted by theory. The lift-to-drag ratios which can be obtained with lenticular bodies are dependent upon the thickness-to-chord ratio. The significance of lift-to-drag ratio is illustrated in Fig. 21. As can be seen, for example, a glide range of 2,400 nautical miles is realizable for a vehicle with an L/D of 2 if an equilibrium glide is initiated at a velocity of 18,500 ft/sec.

The internal arrangement of the three man command module is illustrated in Fig. 22. As indicated by the sketch, adequate room is provided for the astronaut to move about or perform monitoring and maintenance tasks while the vehicle is in orbit.

The diameter of the configuration is 16 feet and the weight of the vehicle, crew and subsystem is approximately 8500 pounds. (2)

During transonic and subsonic flight, horizontal stabilizers are extended, as shown in Fig. 23. The stabilizers are required for subsonic stability; also, the stabilizers add a considerable amount of lift which is very desirable for the landing phase of the mission.

#### Re-Entry Performance

Studies (2)(3) have shown that the most desirable entry trajectory is one for which the deceleration throughout the initial entry phase approaches the maximum tolerable. This will prevent skipping, minimize range dispersion and minimize the duration of the heat flux. Fig. 24 presents the deceleration history for entry at several different initial angles from a 200 mile orbital altitude. These data illustrate the control logic employed which was to fly in such a manner that a deceleration of approximately 5 g's was realized until the vehicle velocity had dropped to some prescribed value, at which time the vehicle would be placed on an equilibrium glide trajectory.

The ability of a simple guidance system coupled with the configuration's aerodynamic characteristics, to compensate for errors in atmosphere injection is illustrated in Fig. 25. As can be seen, trajectories which are initially considerably different than the nominal can be corrected so that the desired landing site is reached.

#### Vehicle Structure and Heat Shield

The proposed design utilizes the double-wall structural concept (Fig. 26). The vehicle inner body wall is the load-bearing structure and the outer wall is of segmented panel construction and is attached to the primary structure by means of thermally insulated clips. Thus, thermal expansion is absorbed through over-lapping joints and flexibility in the attachment clips.



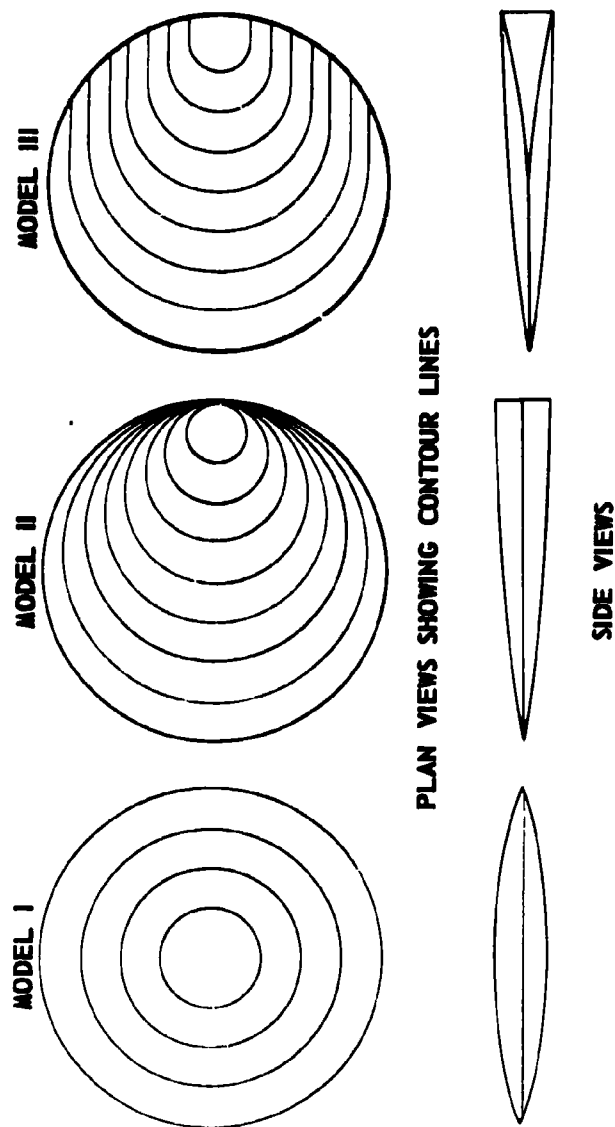


Fig. 20. Lenticular Configuration Cross Section Evaluation



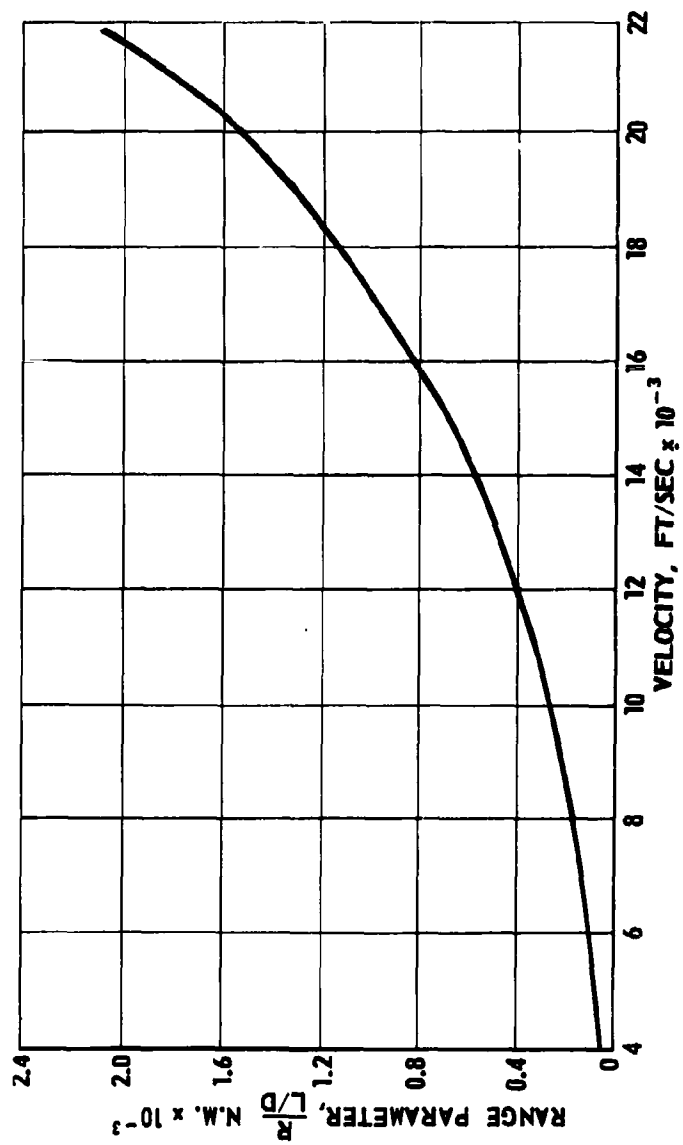


Fig. 21. Glide Range Parameter



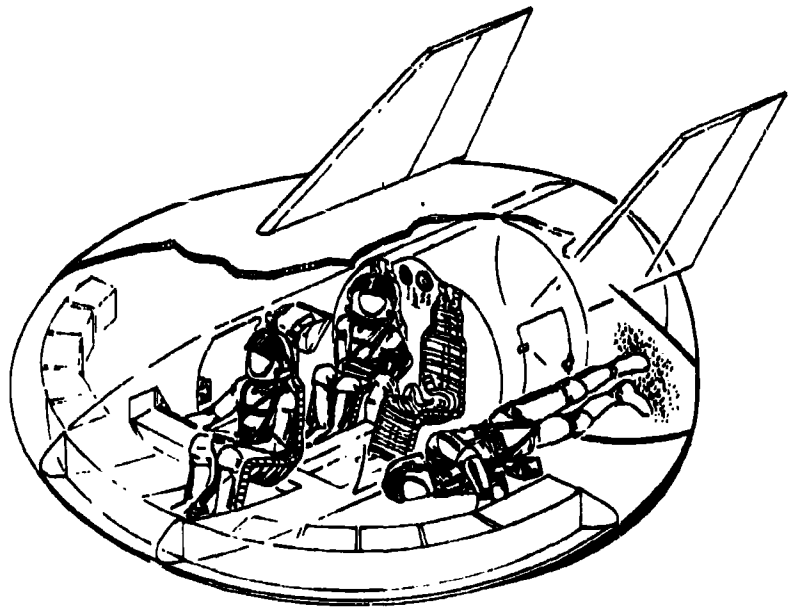


Fig. 22. Three-Man Entry Vehicle; Space Flight





**Fig. 23. Three-Man Entry Vehicle; Glide Phase**



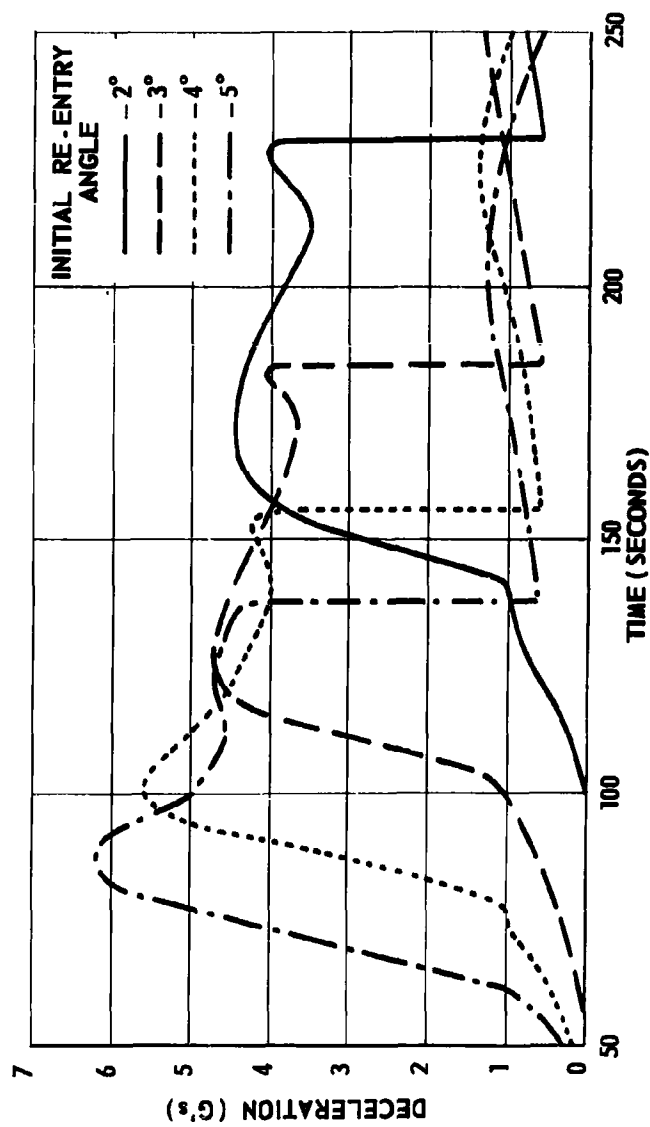


Fig. 24. Deceleration History



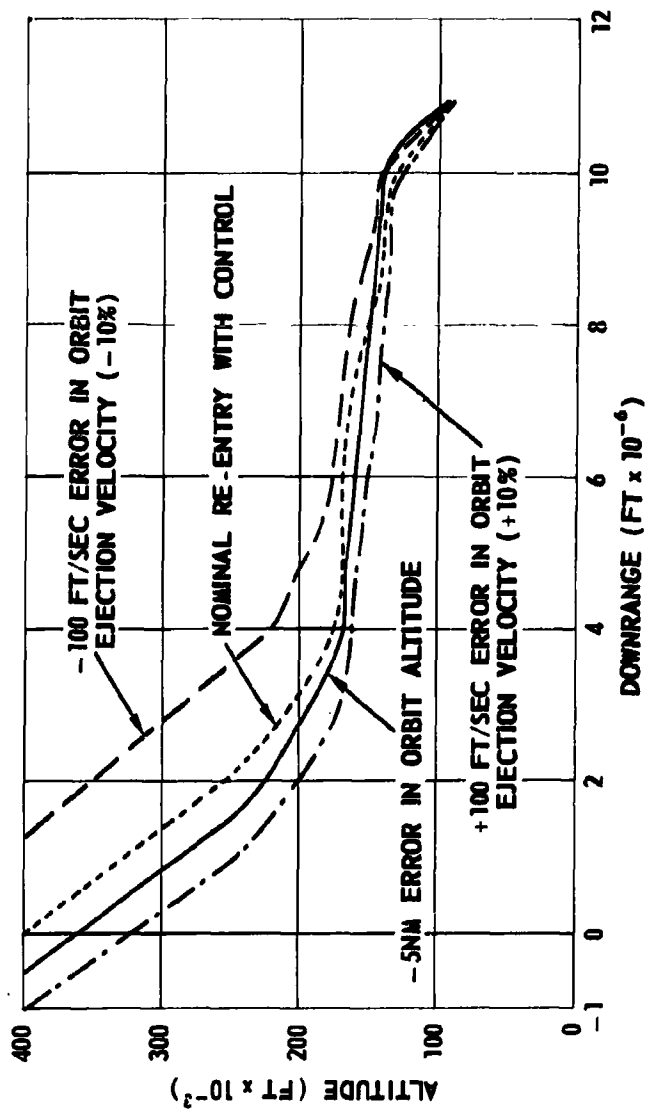


Fig. 25. Re-entry Trajectories



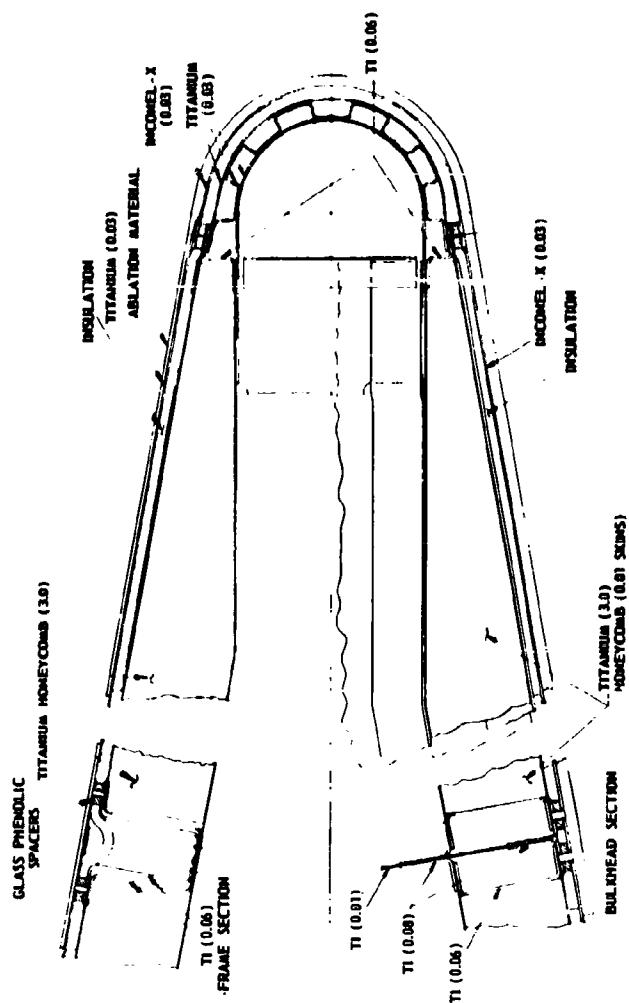


Fig. 26. Leading Edge Section



The primary structure, which is critical for the internal pressure loads, consists of deep-cored honeycomb sandwich panels. The fundamental design problem was to maintain stability of relatively flat upper and lower surfaces when subjected to the internal pressure loads. The upper and lower surfaces are internally braced by two inner and two outer fore and aft spars.

The perimeter of the vehicle is essentially an end closure fabricated of corrugated sheet. The transition from honeycomb to corrugation is made by extending the honeycomb skin facings and adding equally spaced tie-in ribs. This construction eliminates large moments in the end closure due to the pressure loads transmitted from the upper and lower surfaces into the closure.

The heat shield consists of ablative material over radiative skin and insulation material. The ablative material will be consumed during the initial phase of re-entry when the heating rates are high.

#### CONCLUSIONS

The system concept presented is believed to possess advantages over other possible approaches to satellite defense such as: (a) inspection from ground and then launching ground based interceptors, (b) unmanned orbital inspector/killer systems, or (c) manned orbital systems which requires close inspection of the target by the crew. The primary advantage of the proposed system over the first two approaches is that it includes man in the inspection process at a range which is short enough to allow good optical resolution. The advantages of including the target inspection and killer device in a manned satellite interceptor system are summarized in Table 10. Probably the prime advantage is a combination of those listed; that is, when the target is in the Earth's shadow so that it is impractical to illuminate from a safe distance, the I/K can provide a very thorough close-in inspection and destroy the target if desirable without extreme exposure of the crew to possible danger.

Table 10. Advantages of Inspector/Killer Concept

- Safe Stand-off Distance
- Inspection of Target While in Earth's Shadow
- Economically Inspect Target from all Aspects
- Effective IR Sensing
- Ready Negation Mechanism

Other functions which may be incorporated into the inspector/killer device are given in Table 11.

A potentially dangerous target that will have a high priority for kill is the orbital bomber. Therefore, a means of detecting a nuclear weapon would be highly desirable. Methods of inspecting a satellite for a nuclear bomb have been studied by General Dynamics.



Table 11. Potential Functions

Nuclear Bomb Detection  
 Target Mass Determination  
 Electromagnetic Detection  
 Decoy Exterminator

Mass measurement would be a possible indication of the presence of a bomb because of the inherent high density of the bomb. Such methods of measuring mass as gravitational, orbital deviation (both natural and induced) and observation of the change of path of an external object, have been considered, but none of these appear suitable for an initial I/K concept, however, they should not be discounted from future considerations.

At the present, there is not an effective, practical method available for measuring directly the presence of a nuclear bomb by a device such as the I/K, however, new developments may enhance the feasibility.

Useful information concerning the signature of any enemy communication link may be obtained by including ferret equipment on the I/K. Target satellites having low frequency links (300 mc and below) have broad beam patterns so that the manned vehicle could easily intercept the transmission and do a better job than the I/K because of the greater space available. However, frequencies in the microwave region can use narrow beams so their signals might not be readily available at the manned vehicle at a range of 50 miles. Therefore, there is a possible requirement for the I/K to carry ferret equipment.

It is also possible that some clever device can be installed on the I/K which will reveal or destroy decoys without requiring the firing of the warhead. This idea will be pursued further.

#### REFERENCES

1. Honeywell, E. E., "Satellite Inspector/Killer Mechanism Study", General Dynamics/Pomona, TM-341-177, January 1963.
2. Honeywell, E. E., "Manned Re-entry Vehicle Preliminary Design Study", General Dynamics/Pomona, TM-341-147, March 1961.
3. Honeywell, E. E., "Preliminary Design of a Three Man Orbital and Re-entry Vehicle," General Dynamics/Pomona, ERR-PO-086, October 1962.



**ELECTROMAGNETIC RADIATION HAZARDS  
TO ELECTROEXPLOSIVE DEVICES**

**Lt. Col. Reuben B. Moody**

**Deputy The Inspector General, USAF  
Directorate of Aerospace Safety  
Norton AFB, California**

**ABSTRACT**

This paper makes an elementary evaluation of three general proposals recently made as means or techniques to diminish electromagnetic radiation hazards to electroexplosive devices. The evaluation is predicated on basic antenna theory and the improbability of accidental detonation of electroexplosive devices by radio-frequency radiation. The paper recommends the safety practices of safe-separation distances, hazard assessment through the use of inert devices, and electromagnetic shielding techniques.



## ELECTROMAGNETIC RADIATION HAZARDS TO ELECTROEXPLOSIVE DEVICES

Lt. Col. Reuben B. Moody  
Deputy The Inspector General, USAF  
Directorate of Aerospace Safety  
Norton AFB, California

### INTRODUCTION

Throughout Air Force missile activities there is much concern over electromagnetic radiation hazards to electroexplosive devices (EEDs). The concern arises from the fact that electrical leads to an EED can, under certain conditions, act as an antenna. There have been incidents, albeit very few, when leads have abstracted sufficient energy from an electromagnetic environment to cause inadvertent detonation (1).

In order to reduce the hazard and to allay concern, several specifications have been proposed and, to a certain extent, placed in effect.

a. Foremost among these is the specification that EEDs dissipate, without firing, one watt of DC power for five minutes of one ampere current flow. The specification also prohibits the use of external shunts. Unless some type of heat sink is used this requirement, of course, imposes an EED bridgewire resistance of one ohm. The virtue of this proposal is based on the supposition that the sensitivity and susceptibility of the EED to electromagnetic radiation is reduced by the one watt/one ampere parameter.

b. Another recommended specification is that EEDs be designed so that the integral unit will survive in an electromagnetic field intensity of 100 watts per square meter.

c. Still another proposal suggests the application of classical antenna theory to make a field evaluation and hazard assessment on a case-to-case basis. The assessment would be derived from measurements, the known characteristics of the EED and adjacent radiators, and when necessary, through the use of "worst case" assumptions.

All of these proposals have been prompted by the probability that an EED in a particular configuration may, when immersed in an electromagnetic field, react as a receiving antenna. In order to explore the validity of the proposals it is therefore necessary to present some basic antenna theory.



### ANTENNA THEORY CONSIDERATIONS

The equivalent circuit of a receiving antenna may be represented by Figure 1, (2) (3).

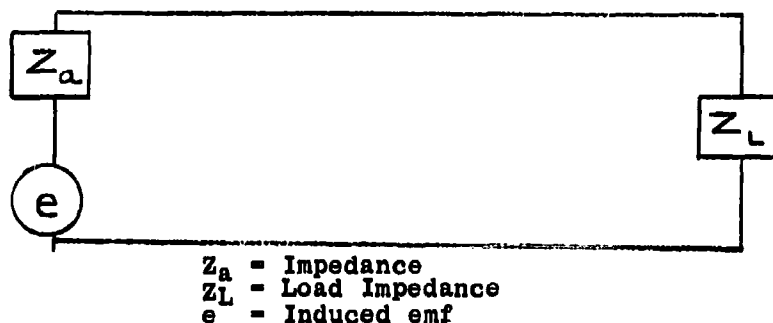


Figure 1 - Equivalent Circuit of a Receiving Antenna.

When an antenna length precisely accommodates a particular wave length it becomes a resonant circuit and its impedances become pure resistances. Therefore, the equivalent circuit for a resonant antenna reduces to that indicated by Figure 2.

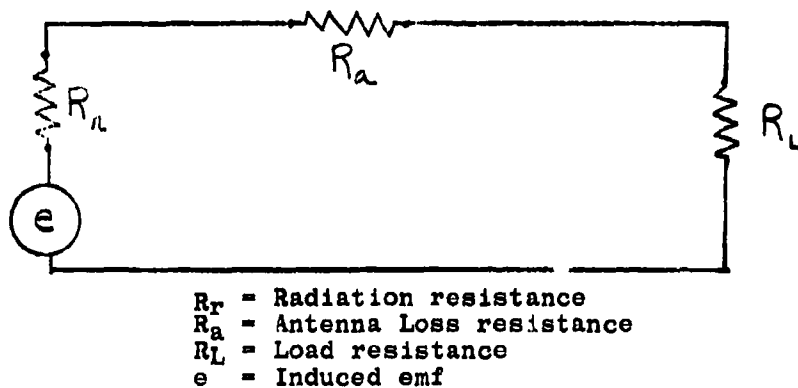


Figure 2 - Equivalent Circuit of a Resonant Receiving Antenna

The radiation resistance shown in Figure 2 is a fictitious quantity resistance which indicates the radiation properties of the antenna. It is defined as a resistance which, if inserted in the antenna circuit with current flowing, would dissipate the same energy as is actually radiated by the antenna (2) (3).



The antenna loss resistance is a lumped quantity to account for losses which arise from the presence of earth, the RF ohmic resistance of the antenna wires, dielectrics in the neighborhood, etc., (3) (4).

The total power ( $P_T$ ) that a receiving antenna abstracts from an electromagnetic field can be determined by the equation:

$$P_T = \frac{(\epsilon h)^2}{R_L + R_a + R_r} \quad (1)$$

where  $\epsilon$  = field strength (rms value) in volts per meter;  $R_L$ ,  $R_r$  and  $R_a$  are defined by Figure 2; and  $h$  is the effective height of the antenna in meters.

The effective height of an antenna is defined by Terman (3) as the ratio of the induced voltage ( $e$ ) to the strength ( $\epsilon$ ) of the radio wave. The effective height of a transmitting vertical wire antenna is that height it "would be required to have to radiate the same field along the horizontal as is actually present if the wire carries a current that is constant along its entire length and of the same value as at the base of the antenna". By virtue of the reciprocity theorem this latter definition can be applied to a receiving antenna. It also permits the deduction that a measure of effective height is the area ( $A$ ) under the current curve divided by the value of the current at the base of the antenna ( $I_b$ ) or  $h = A/I_b$ .

Of the total power abstracted from the environment a fraction is re-radiated by the antenna. Another fraction is dissipated through the antenna loss resistance, and a third fraction is delivered to the load. This latter or third fraction is represented by the ratio  $R_L/(R_L + R_a + R_r)$ . The power delivered to the load ( $P_L$ ) can therefore be determined by multiplying equation (1) by this ratio.

$$P_L = \frac{(\epsilon h)^2 R_L}{(R_L + R_a + R_r)^2} \quad (2)$$

Antenna configurations likely to be assumed by an EED and its leads are a half-wave dipole, a quarter-wave grounded stub, or a short-stub antenna (e.g., where the antenna length is 1/20th the wave length). These possible configurations are shown in Figure 3.



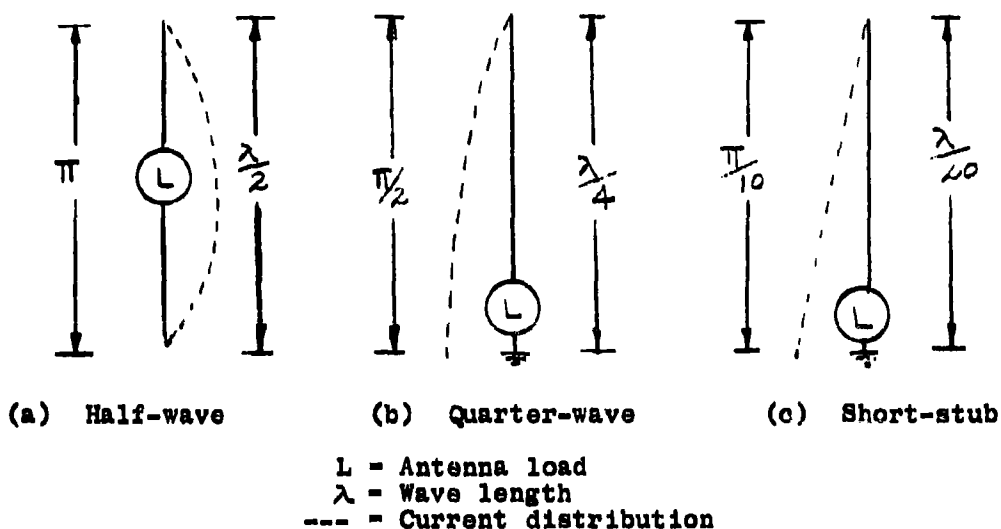


Figure 3 - Antenna Configurations

For a half-wave dipole or doublet antenna the radiation resistance ( $R_r$ ) is about 73 ohms and the effective height ( $h$ ) can be expressed as  $\lambda/\pi$  (2) (6). The volts per meter field strength can be expressed as a power density ( $P_D$  = watts per square meter) by the relationship  $e^2 = 120\pi P_D$  (7). Substituting these values in Equation (2) yields the power delivered to the load of a resonant dipole antenna.

$$P_L (\text{DIPOLE}) = \frac{120 P_D \lambda^2 R_L}{(R_L + R_a + R_r)^2 \cdot \pi} \quad (3)$$

The bridgewire resistance of an EED may be considered as the load resistance of an antenna when the leads are configured as a half-wave dipole as indicated in Figure 3(a). Ordinarily the bridgewire resistance is something less than one ohm and, consequently, is much less than the radiation resistance of 73 ohms. Also, the antenna loss resistance can be considered as negligible (4). Equation (2) can therefore be approximated by the simpler expression:

$$P_L (\text{dipole}) = (7.2 \times 10^{-8}) P_D \lambda^2 R_L \quad (4)$$

Also,  $P_L = I_L^2 R_L$ , so that

$$I_L (\text{dipole}) = \lambda \sqrt{(7.2 \times 10^{-8}) P_D} \quad (5)$$



Similarly, for a quarter-wave grounded antenna with the load located at the grounded end (Figure 3(b)), the radiation resistance is about 38 ohms and the effective height of the antenna is  $\lambda/2\pi$  (3). If, again, the antenna loss resistance is considered negligible and the bridgewire resistance is very much less than the load resistance, then equation (2) simplifies to:

$$P_L (\lambda/4) = (6.6 \times 10^{-3}) P_d \lambda^2 R_L \quad (6)$$

$$\text{and } I_L (\lambda/4) = \lambda \sqrt{(6.6 \times 10^{-3}) P_d} \quad (7)$$

Equations (4), (5), (6), and (7) are valid only when  $R_a$  is negligible and  $R_L$  is very much less than  $R_r$ . With these conditions in mind the equations permit the conclusions that (a) the power delivered to the load is directly proportional to the intensity of the electromagnetic field environment, the square of the wave length, and also to the ohmic value of the load resistance; and (b) the current through the load resistance is independent of the value of the load resistance.

For the short-stub grounded antenna (see Figure 3(c)), the load resistance can no longer be considered as very much less than the radiation resistance. In this case the radiation resistance is only one ohm and the effective height of the antenna is  $0.5\lambda/20$  (6). If the antenna loss resistance is negligible equation (2) becomes:

$$P_L (\lambda/20) = (0.24 P_d \lambda^2 R_L) / (R_L + 1.0)^2 \quad (8)$$

$$\text{and } I (\lambda/20) = \lambda \sqrt{0.24 P_d / (R_L + 1.0)} \quad (9)$$

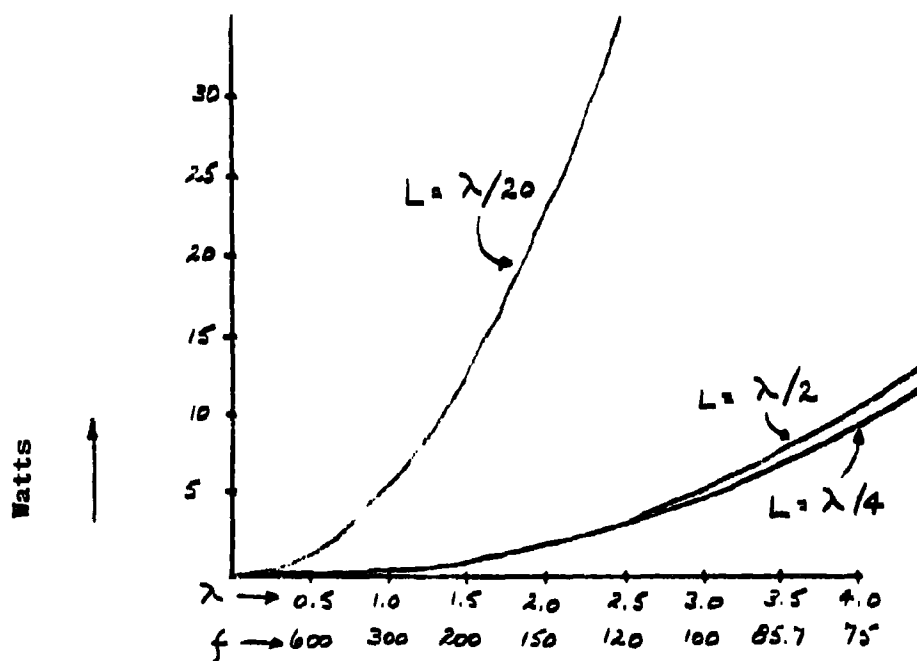
#### DISCUSSION

Equations (4), (6), and (8) are plotted in Figure 4 for the case where the bridgewire resistance is one ohm and the incident field strength is 100 watts per square meter. A surprising revelation is that under the given conditions, the power delivered to the one-ohm load of the short-stub antenna exceeds that of the quarter-wave and half-wave antennas by factors of 9.1 and 8.3, respectively. The plot and the analysis also indicates the one-watt/one-ampere criteria does not necessarily decrease the electromagnetic sensitivity of an EED. In fact, it definitely increases the hazard under certain conditions.

A power density of 100 watts per square meter was chosen for the foregoing illustration because it is that magnitude which has been recommended as an environmental criterion (10) (11). This particular value is arbitrary except for the fact that 100 watts per square meter is also that power density level which has been defined as a physiological hazard (8). The environmental criterion seems to have merit because, if for no other reason, of the formidable magnitude of the specified electromagnetic



Figure 4 - Power delivered by a resonant antenna to a one ohm load; when  $P_D = 100$  watts per square meter,  $L$  - antenna length,  $\lambda$  - wave length and  $f$  - megacycles.





field. Certainly an EED which can survive 100 watts per square meter over a broad frequency spectrum is relatively insensitive to RF radiation. Unfortunately, however, the proponents of the environmental criterion have not been precise or specific regarding the techniques, tests, and procedures whereby the survivability of an EED is to be proven. Moreover, the environmental proposal requires the evaluation of EEDs in all normal modes of storage, transportation, handling and installation. The impracticality of requisite tests, validations and costs is obvious in light of the infinite number of possible EED configurations. Also, the specification fails to consider or exploit the fact that power delivered to the EED bridgewire increases in direct proportion to the square of the wave length. For these reasons, the environmental criterion needs much more refinement and better definition.

The third proposal which has been mentioned is the theoretical hazard assessment on a case-to-case basis under actual field conditions (12). The merits of this recommendation are overshadowed by the following disadvantages:

- a. The procedures and techniques required are laborious and time consuming. They can only be applied by a trained team of knowledgeable technicians.
- b. Comprehensive coverage of a large inventory of missile sites and locations would require an extensive organization and effort. Personnel requirements and costs may well be prohibitive.
- c. The many "worst case" assumptions which are necessary and inherent in a theoretical hazard assessment may impose unnecessary operational penalties or restrictions on missile activities. They may also result in unnecessary and costly remedial measures.

To comply with any one of the three proposals just discussed would require considerable effort and retrofit of EED systems. For the most part these proposals have been made after the fact, and very few of existing EED configurations have been tested to meet the specified requirements. Why, then, is not accidental RF initiation of EEDs more prevalent?

The power levels indicated by Figure 4 are quite formidable. However, these power levels represent the worst possible case predicated on an ideal antenna and conditions. The validity of these values depend on a most improbable chain of circumstances.

- a. The EED must be immersed in a very strong electromagnetic field.
- b. The leads to the EED must be exposed and configured as an antenna.



- c. The EED itself must be configured as an antenna load.
- d. Leads must be of a precise length to provide a resonant circuit for the wave length of the electromagnetic field.
- e. Leads must be oriented in a three-dimensional space in order to accommodate the polarization and directivity of the electromagnetic field.

Deviation from any of the above conditions will diminish the magnitude of power transferred to the EED bridgewire. It is extremely improbable the several conditions can be accidentally met to the extent an inadvertent detonation occurs. An extensive research (1) has revealed only a handful of confirmed incidents wherein EEDs have been accidentally detonated by electromagnetic radiation. More to the point, in 1956 the Institute of Makers of Explosives published a pamphlet (5) which states, in part:

"From a practical viewpoint, the possibility of premature explosion due to RF energy is extremely remote. This has been demonstrated by numerous tests on representative transmitting equipment, and it is confirmed by many years of experience. The annual consumption of electric blasting caps is well over 100 million, and they are used in every section of the country. Yet there have been only two authenticated cases of a cap being accidentally fired by radio."

#### RECOMMENDATIONS

Notwithstanding the improbabilities, incidents have occurred and, because of the possibility of catastrophe, protective or safety measures should be taken.

- a. The power delivered to the bridgewire of an EED is directly proportional to the incident electromagnetic field. In turn, the power density of an electromagnetic field decreases as the square of the distance from the radiating source. Therefore, published distance tables (9) should be observed insofar as is operationally possible. This is particularly true for RF sources radiating long wave lengths or low frequencies.
- b. To facilitate hazard assessment of EED operational configurations under field conditions, manufacturers should supply "dummy", "dud", or inert EEDs having the same electrical characteristics and parameters as the real item. The use of inert EEDs would permit meaningful field evaluations by relatively unskilled, untrained personnel.
- c. The electromagnetic radiation hazard to ordnance depends on the probability of EED leads acting as an antenna. The hazard can therefore be reduced by any technique which destroys the EED antenna characteristics. The environmental criterion indirectly



imposes requirements for shielded components, twisted and shielded leads, RF attenuation devices, heat sinks, etc. Specifications and exhibits should therefore be written wherein effective, acceptable techniques are described and minimum shielding requirements are stipulated.

### BIBLIOGRAPHY

1. Investigation of Premature Explosions of Electroexplosive Devices and Systems by Electromagnetic Radiation Energy (U), Final Report - Volume I, April 1962, Midwest Research Institute; Ogden AMA, 2705th Munition Wing, Hill AFB, Utah. (Confidential)
2. H. P. Williams, Antenna Theory and Design, Volume Two (The Electrical Design of Antennae) Sir Issac Pitman and Sons, Ltd; London, 1952.
3. F. E. Terman, Radio Engineers Handbook, McGraw-Hill Book Co., Inc., N.Y., 1943.
4. The Radio Amateur's Handbook, American Radio Relay League, West Hartford, Conn., 29th Edition, 1952.
5. Radio Frequency Energy a Potential Hazard in the Use and Transportation of Electric Blasting Caps, Revised Edition, Pamphlet No. 20, Institute of Makers of Explosives, N.Y., 1956.
6. H. P. Williams, Antenna Theory and Design, Volume One (Foundations of Antenna Theory), Sir Issac Pitman and Sons, Lt; London, 1950.
7. Reference Data for Radio Engineers, 3rd Edition, Federal Telephone and Radio Corp., N.Y., 1949.
8. Radio Frequency Radiation Hazards, T.O. 31-1-80, USAF, 1958.
9. Explosives Safety Manual, AFM 32-6, USAF, 1961.
10. Interim Standards to Minimize the Hazards of Electromagnetic Radiation to Electroexplosive Devices, Hq AFSC, 1 Oct 1962.
11. Safety Design Criteria for the Development of Electroexplosive Ordnance System, Ballistic Systems Division, Hq AFSC, 20 Feb 1963.
12. RF Hazards to Electroexplosive Devices Measurement and Prediction, T.O. 31Z-10-7 (Proposed), Jan 1963.